The Eurasia Proceedings of Science, Technology, Engineering & Mathematics

EPSTEM

IConTES 2019 DECEMBER

Edited by: Mehmet Ozaslan
Articles: 1-51
Conference: IConTES 2019: International Conference on Technology, Engineering and Science
Dates: October 26 – 29
Location: Antalya, Turkey
Conference Chair(s): Prof.Dr. Mack Shelley, Iowa State University, USA & Prof.Dr. Mehmet Ozaslan, Gaziantep University, Turkey

CONTENTS

CFD Hydrodynamics Forces Determination for a Darrieus Turbine Rotating Blades Using K-ε Turbulence Model

Abdelouahab BENZERDJEB
Université des Sciences et de la Technologie "M. B." Oran

Bouabdellah ABED
Université des Sciences et de la Technologie "M. B." Oran

Habib ACHACHE
Université Mohamed Benahamed Oran 2

Abdeljellil BENMANSOUR
Université des Sciences et de la Technologie "M. B." Oran

Mohammed HAMEL
Université des Sciences et de la Technologie "M. B." Oran

Abderrahmane DEBZ
Université des Sciences et de la Technologie "M. B." Oran

Mohammed K. HAMIDOU
Université des Sciences et de la Technologie "M. B." Oran

Abstract: Determination of hydrodynamic forces acting on the blades of Darrieus turbine used to harness water energy from dams, rivers and ocean is very important to evaluate this turbine performance. Therefore, this paper presents the numerical results of CFD investigation using K-ε closure turbulence model. This simulation has been performed for a hydro Darrieus turbine that we have previously tested experimentally; this turbine has a diameter of 21.5 cm and it is composed of three NACA0020 blades, with a height of 23 cm and a cord of 7 cm, that are fixed with a separation angle of 120 °. The present simulation has been carried out for a water flow velocity of 0.67 m/s and the Darrieus turbine rotating velocity of 125 rpm. These values correspond to a specific velocity λ equal to 2, a flow Reynolds number Rev equal to 4.57 104, a rotational Reynolds number Reu equal to 1.97 105 and a relative Reynolds number Rew varying between 4.72 104 and 1.39 105. The graphical presentations of the simulation numerical results have shown practically identical curves, respectively for the hydrodynamic lift and drag forces variations versus the rotational angle (position angle of each blade) with a phase angle of 120° between the first blade and the second one and of 240° between the first blade and the third one. The hydrodynamic blade element lift force varies between 0.0454 and 0.641 N while the drag force varies between - 0.0968 and 0.342 N. The global turbine hydrodynamic lift and drag forces (for the three blades elements together) varies respectively between 0.5928 and 0.9251 N and between 0.0335 and 0.2497 N. The maximal values show that the lift is about twice the drag for each blade and about four times for this turbine. The turbine average lift and drag forces over three rotations are respectively 32.38 N and 6.61 N.

Keywords: Water energy, Darrieus turbine, Hydrodynamic forces, Simulation, Turbulence model

Introduction

Renewable energies, as an alternative to non-renewable fossil energies, are getting increasing attention, especially in remote areas. The main reasons are the continuous increase of global warming effects and fossil

energies decreasing availability. To harness water energy of hydraulic reservoirs with small head, rivers and sea currents the use of Darrieus turbine is getting growing interest and the prediction of the hydrodynamics forces acting on this turbine is becoming necessary and important.

Benzerdjeb, Abed, Hamidou, Bordjane and Gorlov (2017) conducted an experimental study for a vertical axis water Darrieus turbine. The experimental tests were carried out for a Darrieus turbine model with its three blades fixed with geometric angle of incidence equal to 0°. The experimental results have shown, for a relative increase of the water flow velocity of 100%, a 604% relative increase for the generated mechanical power by this turbine. Another experimental investigation on the effect a Darrieus turbine blades orientation angle, presented by Benzerdjeb, Abed, Achache, Hamidou and Gorlov (2018), have shown the optimal performance has been obtained when this angle is set to 1.75°.

To show the importance of water energy, Shahinur, Sabuj Shah, Nazmul and Ashraful (2013) presented an analysis of the possibility of using small-scale hydro power plant in Surma and Gumoti (Bangladesh) and deducted that these two rivers can produce respectively 14.804 MWhr and 18.834 MWhr per year. The experimental study presented by Rus T., Rus L.F., Abrudan, Domnita and Mare (2016) shows that, for the same velocity, vertical axis wind turbines rotate at lower RPM than water turbines. Maître, Amet and Peltone (2013) presented a wall grid analysis and comparison with experiments. Their study showed that a too coarse wall grid leads to early and overestimated stalls and have negligible contributions on the power. Ploesteanu, Tarziu and Maître (2003) conducted a study on the flow modeling for a Darrieus turbine at moderate Reynolds number and found that the determined effort coefficients results show significant deviations from the experimental ones.

The experimental study on a modified hydrokinetic four bladed Savonius turbine, conducted by Thyagaraj, Rahamathullah and Suresh Prabu (2016), has improved the power coefficient from 0.16 to 0.19. Sanusi, Soeparman, Wahyudi and Yuliati (2016) carried out and experimental study of a wind Savonius turbine with combined blades; their results show an increase of the maximum power coefficient by up to 11 % with respect to the conventional blades at the tip speed ratio (TSR) of 0.79. An experimental study, was carried out by Kaprawi, Santoso and Sipahutar (2015), for a combined Darrieus and Savonius water turbine placed in a river, during which, they found that the maximum power coefficient of 0.19 and torque coefficient of 0.107 were obtained when the attaching angle on the returning side of Savonius bucket β is set to 30°.

Work Objective

The objective of the present numerical work is to conduct a 2D CFD simulation to evaluate the hydrodynamic lift and drag forces acting on the three rotating NACA0020 blades elements of a water Darrieus turbine versus the rotational angle (position or azimuthal angle of each blade). The academic ANSYS CFX R18.1 and the K-ε closure turbulence model with sliding mesh technique are used. The simulation will be performed for a Darrieus turbine model that we have previously tested experimentally in water flowing at 0.67 m/s and for maximal mechanical power rotating velocity of 125 rpm (Benzerdjeb et al., 2017). The corresponding specific velocity λ is equal to 2, free flow Reynolds number Rev is equal to $4.57 \ 10^4$ and rotational Reynolds number Reu is equal to $1.97 \ 10^5$. This model has a diameter of 21.5 cm and a height of 23 cm and its blades cord is 7 cm.

(a)   **(b)**
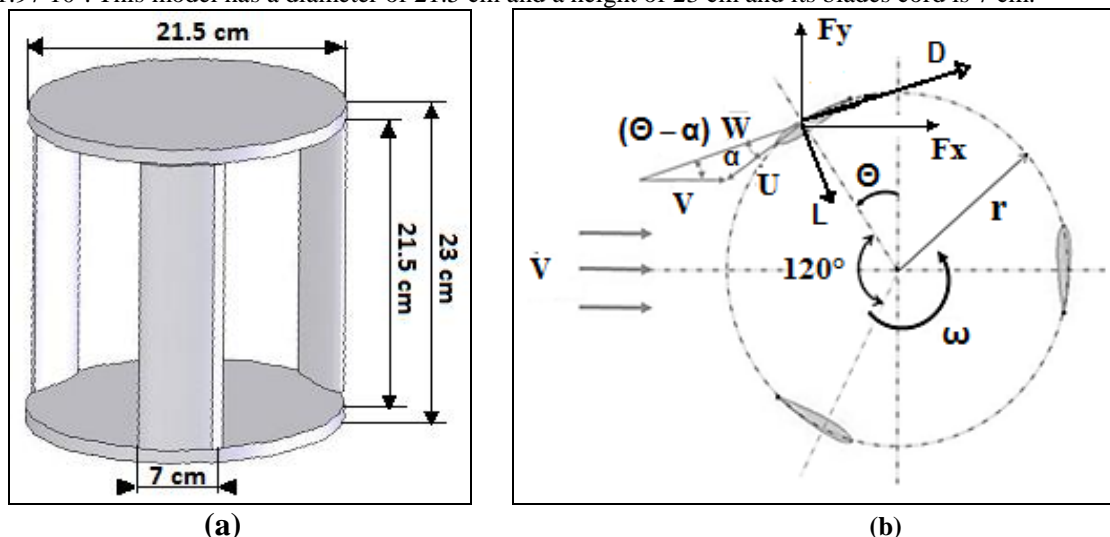
Figure 1. (a) Darrieus turbine model (b) section with velocities and forces

Numerical Presentation

The numerical simulation, of the water Darrieus turbine (figure 1), uses the academic ANSYS CFX R18.1, with a scheme of high resolution to estimate the convective terms of the transport equations. The numerical domain is divided into three part (figure 2): two fixed domains (D1 and D3) and a rotating one (D2) that models the turbine rotational zone. A hexahedral mesh is generated (Table 1) and the sliding mesh technique is used (ANSYS® Academic Research Mechanical, Release 18.1, 2017).
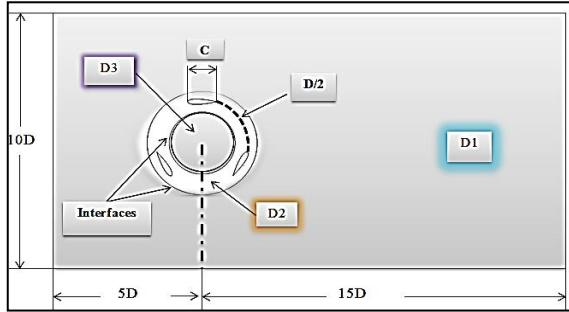
(a) Numerical domains and meshes
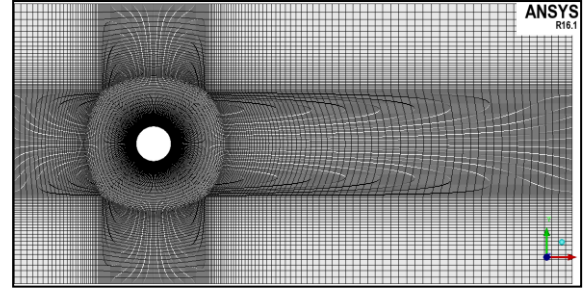
(b) Numerical meshes
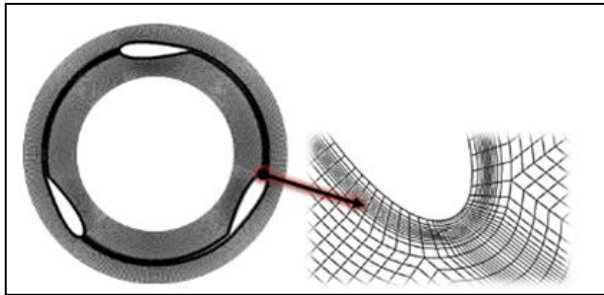
(c) Domain D2 mesh with zoom
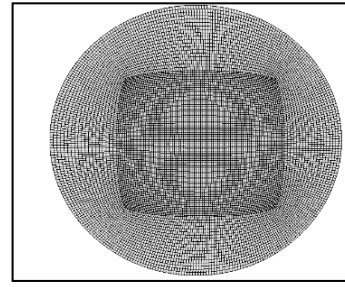
(d) Domain D3 mesh

Figure 2. Numerical domains and meshes

Table 1. Domains mesh nodes and elements

Domain	D3	D2	D3
Number of elements	31820	22321	13440
Number of nodes	64744	45770	27218

Formulation

Figure 1 (b) represents an axial section of the Darrieus turbine with the free flow velocity V, the rotational velocity U, the relative velocity W, the numerical forces Fx and Fy and the hydrodynamics lift and drag forces L and D acting on the turbine blades.

The relative velocity of the fluid W and the angle of attack α cannot be measured, therefore they will be expressed in terms of the known fluid velocity, Darrieus turbine rotational speed and the position angle of the blade θ which are shown in figure 1 (Arief., Musriyadi, & Aldara, 2018). From this figure, we can see that,

$$Usin\alpha = Vsin(\theta - \alpha) \qquad (1)$$

$$Ucos\alpha = W - Vcos(\theta - \alpha) \qquad (2)$$

After developing Sin (θ-α) and Cos (θ-α) equations 1 and 2 give,

$$\alpha = \tan^{-1}\left[\frac{V\sin\theta}{U+V\cos\theta}\right]$$

(3)

and

$$W = \sqrt{U^2 + V^2 + 2UV\cos\theta}$$

(4)

The free flow, the relative flow and the rotational Reynolds numbers, respectively Re_V, Re_W and Re_U, based on the blade chord C, are given (Maître et al., 2013) and (Paillard, Hauville and Astolfi, 2013) by,

$$Re_V = \frac{CV}{\nu}$$

(5)

$$Re_W = \frac{CW}{\nu}$$

(6)

$$Re_U = \frac{CU}{\nu}$$

(7)

where ν is the water kinematic viscosity.

The hydrodynamic lift and drag forces can be expressed in term of the simulation numerical forces as,

$$L = F_x\,\sin(\theta-\alpha) - F_y\cos(\theta-\alpha)$$

(8)

$$D = -F_x\,\cos(\theta-\alpha) - F_y\sin(\theta-\alpha)$$

(9)

Results and Discussion

As shown on figure 3, when the rotating turbine blade is in the first half of rotation (θ from 0° to 180°) the relative Reynolds number decreases from $1.39\ 10^5$ to $4.72\ 10^4$ then it increases again to $1.39\ 10^5$ when the blade is in the second half (θ from 180° to 360°). The free flow and rotational Reynolds numbers remain equal respectively to $4.57\ 10^4$ and $9.28\ 10^4$. We can see also, that the blade angle of attack increases from 0° to 29.5° when its position (azimuthal) angle changes from 0° to 120° then it deceases to 0° at θ =180°. In the second half of the rotation the angle of attack becomes negative with a minimum of -29.40° at θ =240°.
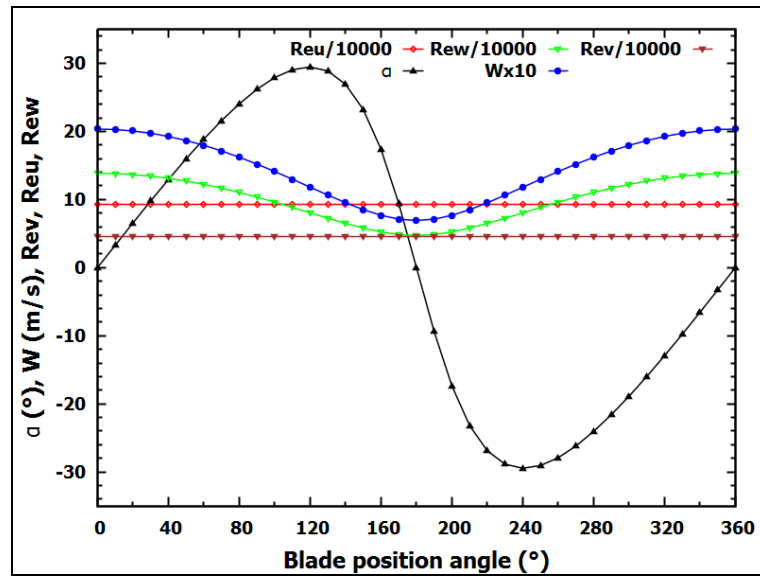
Figure 3. Attack angle, relative velocity and reynolds number

First, we should remind that the three blades are fixed apart with a phase angle of 120°. However, in figure 4 to 7 this phase angle is not considered mainly to get the right global force acting on the turbine, which is given by the summation of the forces acting on the three blades.

On figure 4, we can see that the curves of the numerical horizontal forces acting on the full blades are similar when considering the shift angle of 120° between the first and second blade and of 240° between the first and third blade. There is insignificant differences between these three forces for each blade position. .Indeed, the maximal values are 29.30 N, 29.37 N and 29.24 N respectively for blades 1, 2 and 3 (at $\theta \approx 80°$), while the corresponding minimal values are respectively -7.49 N, -7.53 N and -7.43 N. The total force varies between 3.89 and 23.07 N. The global turbine element horizontal forces (for the three blades elements together) are between 0.0904 and 0.5366 N (not presnetd on this figure). The average horizontal force for three revolutions is equal 13.7644 N.
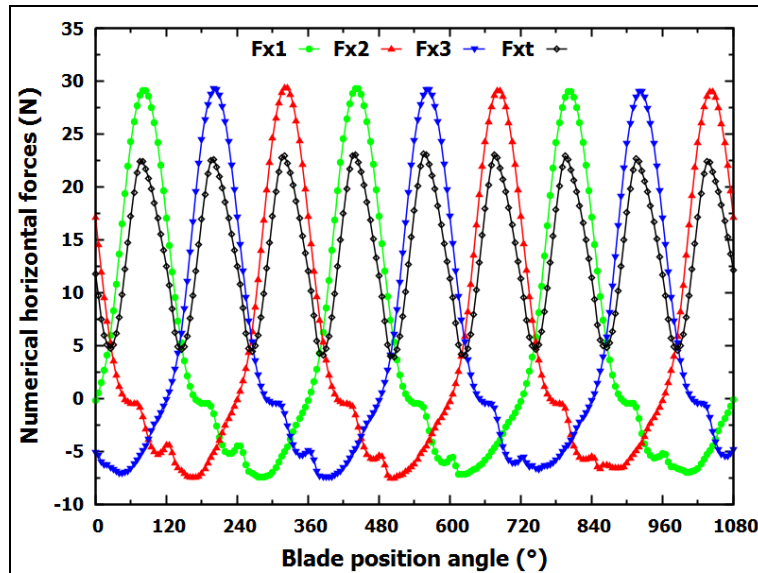
Figure 4. Horizontal forces for each blade and the turbine
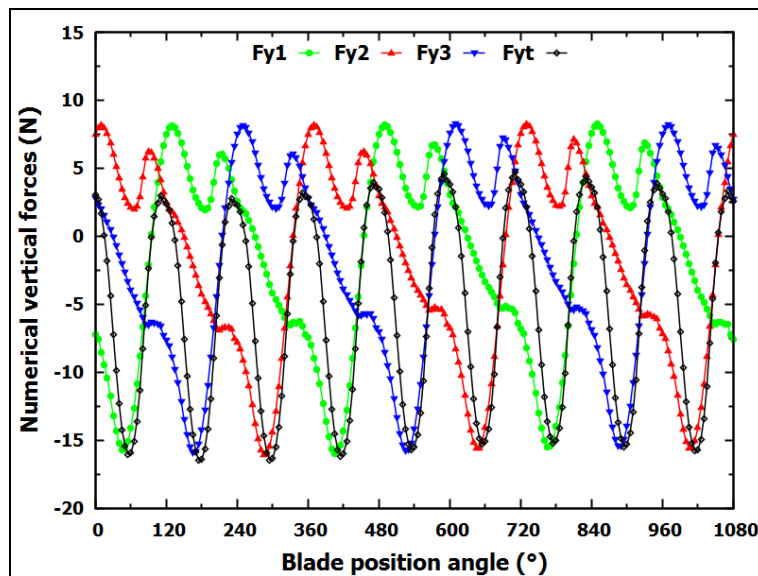
Figure 5. Vertical forces for each blade and the turbine

Figure 5 shows also similarity between the curves for the horizontal forces acting on the blades with a shift angle of 120° and 240°, respectively between the first and second blade and between the first and third blade. The maximal values are 8.22 N, 8.25 N and 8.27 N respectively for blades 1, 2 and 3 (at $\theta \approx 80°$), while the minimal values are respectively -16.00 N, -16.08 N and -15.91 N. The total force acting on the turbine is mostly negative and varies between 4.68 and -16.49 N. The global turbine element vertical forces (for the three blades elements together) are between -0.3836 and 0.1089 N (not presnetd). This maximal vertical force is 20% of the maximal

horizontal one. The average vertical force over three rotations is -5.3339 N, which is about 39% the horizontal average force.

As shown on figure 6, the curves of the hydrodynamic lift forces acting on the turbine blades have identical behavior and the differences are negligible. In fact, the lift force for the three blades L_1, L_2 and L_3 varies respectively between 27.64 and 2.01 N, 27.63 and 2.01 N and 27.5 and 2.04 N. Hence, the force acting on the turbine changes between 25.49 and 39.78 N. The global turbine element lift forces (for the three blades elements together) vary from 0.5978 to 0.9251 N (not presnetd). The turbine average lift force over three rotations is 32.38 N.
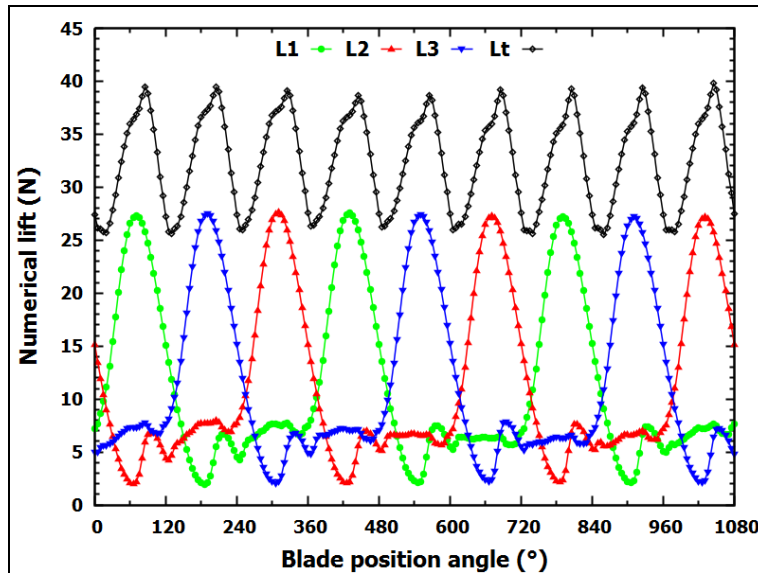
Figure 6. Lift forces for each blade and the turbine
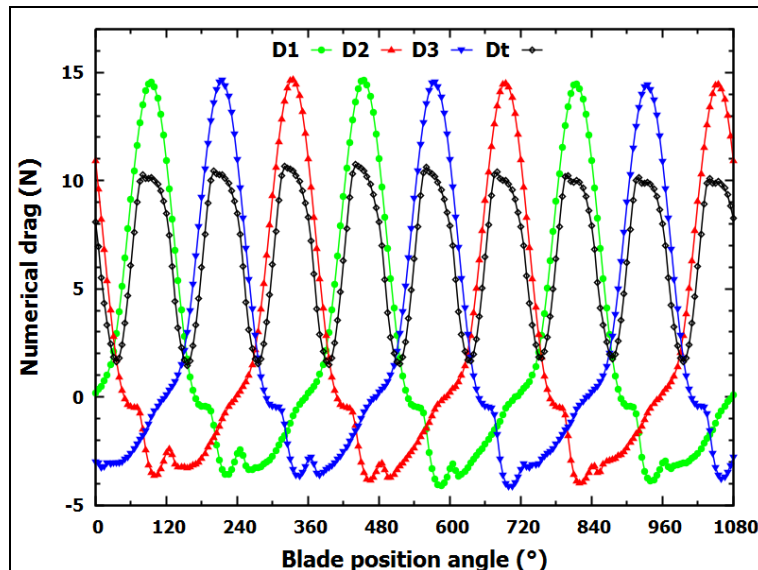
Figure 7. Drag forces for each blade and the turbine

We can see from figure 7 that the variations of the hydrodynamic drag forces acting on the turbine blades are the same with very small differences. The drag force for the three blades D_1, D_2 and D_3 changes respectively from -4.11 to 14.64 N, -3.98 to 14.69 N and -4.16 to 14.62 N. This gives a force acting on the turbine between 1.44 and 10.74 N.The corr'esponding global drag forces for the blades elements change between 0.0335 N and 0.2497 N (not presnetd on the figure). The average of the turbine drag force over three rotations is 6.61 N. This maximal drag force is equal to 20% of the maximal lift force.

6

Conclusion

To evaluate the hydrodynamic lift and drag forces acting on a water Darrieus turbine three rotating NACA0020 blades elements versus their azimuthal angle, a 2D CFD simulation, using the academic ANSYS CFX R18.1 and the K-ε closure turbulence model along with sliding mesh technique, has been conducted. This simulation has been performed for a 21.5 cm wide and 23 cm high turbine that we have experimentaly tested in a previous work in a 0.67 m/s water flow (free flow Reynolds number Rev equal to 4.57 10^4) and at rotational velocity of 125 rpm (rotational Reynolds number of 1.97 10^5).

The analysis of the simulation numerical results has given the following findings:

◆ there is a very close agreement between each type of forces acting on all three blades (horizontal, vertical, lift and drag forces);

◆ the global horizontal forces for the turbine three blades elements together vary from 0.0904 to 0.5366 N;

◆ the average for the global horizontal force for three revolutions is 13.7644 N;

◆ the global vertical forces for the turbine three blades elements are between -0.3836 and 0.1089 N;

◆ the maximal vertical force is 20% of the maximal horizontal one;

◆ the average vertical force over three rotations is -5.3339 N, which is about 39% the horizontal average force;

◆ the global turbine elements lift forces vary from 0.5978 to 0.9251 N;

◆ the turbine average lift force over three rotations is 32.38 N;

◆ the average of the turbine drag force over three rotations is 6.61 N;

◆ the maximal drag force is 20% of the maximal lift force.

Acknowledgements

References

ANSYS® Academic Research Mechanical, Release 18.1, *User's manual*, ANSYS, Inc., 2017.

Arief I.S., Musriyadi T.B., & Aldara D.R. (2018). Design and simulation of axial turbine for ocean thermal energy conversion (OTEC). *International Journal of Marine Engineering Innovation Research.* 3(1):8-17.

Benzerdjeb A., Abed B., Achache H.,Hamidou M. K., & Gorlov A. G., Achache, Hamidou and Gorlov (2019).

Proceedings from EPSTEM '18: *The International Conference on Technology, Engineering and Science* (IConTES2019). Antalya, Turkey.

Benzerdjeb A., Abed B., Hamidou M. K., Bordjane M. & Gorlov A. G. (2017) Experimental study on the effect of water velocity on the performance of a Darrieus turbine, *International Journal of Renewable Energy Research*, 7(4), 2011-2019.

Bertin J. & Smith M. L. (1998) *Aerodynamics for engineers*, Prentice-Hall International, Inc., Simon & Schusler / A Viacom Company, Upper Saddle River, New Jersey.

Cocina V., Leo P. D., Pastorelli M. & Spertino F. (2015, November 22-25) Choice of the most suitable wind turbine in the installation site: a case study, *4th International Conference on Renewable Energy Research and Applications*, (pp. 1631-1634), Palermo, Italy.

Faure T. D. (1984) Experimental results of a Darrieus type vertical axis rotor in a water current. -National Research Council of Canada, TR-NY-005.

Kaprawi S., Santoso D. & Sipahutar R. (2015) Performance of combined water turbine Darrieus-Savonius with two stage Savonius buckets and single deflector, *International Journal of Renewable Energy Research*, 5(1), 217-221.

Maître T., Amet E., C. Pellone, (2013). Modeling of the flow in a Darrieus water turbine: Wall grid refinement analysis and comparison with experiments, *Renewable Energy*, 51, 497-515.

Paillard B., Hauville F. & Astolfi J.A. (2013) Simulating variable pitch crossflow water turbines: a coupled unsteady ONERA-EDLIN model and stream tube model, *Renewable Energy*, 52, (pp. 209-217).

Ploesteanu C., Tarziu D. & Maitre T. (2003, Mars 10-12). Modélisation de l'écoulement dans une turbine Darrieus à nombre de Reynolds modéré, *9èmes Journées de l'Hydrodynamique*, Poitiers-Futuroscope, France.

Rus T., Rus L.F., Abrudan A., Domnita F. & Mare R. (2016) Experimental tests in equipping vertical axis Wind Turbine with electric generator, *International Journal of Renewable Energy Research*, 6(2), 465-471.

Sanusi A., Soeparman S., Wahyudi S. & Yuliati L. (2016) Experimental study of combined blade Savonius wind turbine, *International Journal of Renewable Energy Research,* 6(2), 614-619.

Shahinur Md. I., Sabuj D. G., Shah Md. M., Nazmul I. R. & Ashraful S. K. (2013) Potentiality of small-scale hydro power plant using the kinetic energy of flowing water of Gumoti & Surma river of Bangladesh: An energy odyssey, *International Journal of Renewable Energy Research*, 3(1), 172-179.

Thyagaraj J., Rahamathullah I. & Suresh Prabu P. (2016). Experimental investigations on the performance characteristics of a modified four bladed Savonius hydro-kinetic turbine, *International Journal of Renewable Energy Research,* 6(4), 1530-1536.

Vieira R. J. A. & Sanz-Bobi M. A. (2015, November 22-25) Power curve modeling of a wind turbine for monitoring its behavior, *4th International Conference on Renewable Energy Research and Applications*, (pp. 1052-1057), Palermo, Italy.

Author Information

Abdelouahab Benzerdjeb
University of Sciences and Technology M. B. Oran
Boite Postale 1505 El Menouar Oran, Algeria
Contact E-mail: *abdoubenzerdjeb@yahoo.com*

Habib Achache
University Mohamed Benahamed Oran 2
Boite Postale 1515 El Menouar Oran, Algeria

Mohammed Hamel
University of Sciences and Technology M. B. Oran
Boite Postale 1505 El Menouar Oran, Algeria

Abdeljellil Benmansour
University of Sciences and Technology M. B. Oran
Boite Postale 1505 El Menouar Oran, Algeria

Bouabdellah Abed
University of Sciences and Technology M. B. Oran
Boite Postale 1505 El Menouar Oran, Algeria

Abderrahmane Debz
University of Sciences and Technology M. B. Oran
Boite Postale 1505 El Menouar Oran, Algeria

Mohammed K. Hamidou
University of Sciences and Technology M. B. Oran
Boite Postale 1505 El Menouar Oran, Algeria

Acceleration Logger and Analyzer

Gizem KAYISOGLU
Istanbul Technical University

Seda CANPOLAT
Istanbul Technical University

Aysenur Dilara AYDIN
Istanbul Technical University

Nehir KUCUKTAS
Istanbul Technical University

Metin HUNER
Istanbul Technical University

Abstract: In the case of high acceleration values, it is important to obtain data on the vehicles used by third parties in order to prevent possible accidents. For this purpose, it is aimed to design an electronic system which will record the acceleration values of a vehicle during its journey and then to analyze it. Thanks to the accelerometer sensor placed in an experimental vehicle, the g force data that the vehicle was exposed to were obtained and analyzed by Arduino to determine which speeds the drivers were subjected to during the journey. The final product created in the study is an electronic device consisting of an Arduino, an accelerometer and an Arduino SD card reader module. After the physical connection between the elements were established, the Arduino interface was installed in the computer to obtain the instantaneous acceleration values in the direction of the acceleration of the accelerometer. After completing the physical installation of the circuit, different routes were determined within the scope of determined route in order to observe the acceleration values for different situations. The axes in each route obtained were analyzed separately by Matlab and the acceleration values were plotted. According to the results of the analysis, a maximum of +0.22 / -0.34 g at the x-axis and +0.26 / -0.25 g at the y-axis and +0.15 / -0.17 g at the z-axis were encountered during a normal driving. In contrast, in the case of unsafe use of the same vehicle, the values of +0.41 / -0.63 g on the highest x-axis, +0.33 / -0.36 g on the y-axis and +0.18 / -0.18 g on the z-axis were encountered. When the results obtained are shared with the sector and their view are received, the results of our study have been shown to be supportive of the data that the companies have already pursued, and have the characteristics that can meet the needs of the sector.

Keywords: Acceleration, Arduino, Matlab, Acceleration Logger, Sensor

Introduction

Although many positive developments have been achieved in the transportation sector today, the increase in traffic accidents raises the issue of taking some precautions. Traffic accidents, which causes both material and nonmaterial consequences for individuals and companies, have increased from 440,000 to 1,203,000 in a period of 15 years. Mortality rates in these accidents also doubled in the same period (TURKSTAT, 2018).

One of the prominent forces that act on the vehicle during accidents or their journeys is the gravitational force (G force). The force G is defined as the force exerted by gravity on a free falling object and is named after the word "gravitational". Acceleration values that can be measured with accelerometers are called g force. That is, the "weight" value that an object produces in any direction by accelerating and decelerating by a force applied

to it is called g-force (URL 1). A car is exposed to g-force in the direction of the component of the resistance forces exerted by the ground and air. This force can reach up to 2 g on high speed cars used in motor sports and up to 5.3 g during hard cornering (URL 2).

The human body has different tolerances to the g force. This tolerance depends on the duration, direction, intensity, body position and the center of the g force the person is exposed to (URL 1). For example, a violent slap can create momentary force up to hundreds of g, but the intensity is low. If the same event occurs a few minutes at 10-15 g, it can be fatal. In general, a normal human body is resistant to about 1 g of force. In the experiments performed, forces of 2 g or more are unusual forces and the tolerance limit of a human body can be referred to as being around 5 g (URL 1). For such reasons, it is important that data is obtained on how drivers drive during the day in company vehicles, especially in cargo companies, in order to warn drivers and prevent possible accidents when high acceleration values are recorded.

Alongside individual effects, financial losses caused by traffic accidents will also have a great impact on the logistics sector companies operating on the highway. Given the undeniable growth of the logistics sector, the identification of the factors causing traffic accidents and any positive development in any of these factors will undoubtedly have a reducing effect on these accident rates. The aim of this study was determined by considering these situations and the issue of damaged parcels which is common in customer returns for the cargo sector and has negative effects on customer satisfaction. In terms of safety of life and property, the acceleration values the vehicles have while traveling must not exceed certain limits. Otherwise, passengers and cargo will be subjected to great forces and the above-mentioned traffic accidents or customer satisfaction reducing events will occur. For the purpose of this study, we aim to obtain data on how the drivers' drive during the day and to determine what kind of dangerous situations may arise and to prevent the material and nonmaterial losses.

For this purpose, the aim is to design an electronic system to record the acceleration values of a land vehicle during its journey and then to analyze it. An accelerometer mounted on a vehicle is used in conjunction with an Arduino microprocessor, the g forces the vehicle is exposed to are obtained and later analyzed to determine the forces corresponding to different driving behaviors.

Literature Review

According to the information obtained from the literature, there are various forces acting on a vehicle. In this study, the effect of gravitational force on the vehicle and its contents is examined. During the literature review, various studies were found in this context.

In 2014, Mane and Rana demonstrated that the accelerometer can be used as a vehicle's impact or tipping detector during and after a collision, so that dangerous driving can be detected. They have used many modules such as AVR controller, accelerometer, GSM and GPS. In their architecture, when the system is found to be abnormal, it is confirmed that the accident occurred. The vehicle's vibration / acceleration is detected by the accelerometer to confirm the cause of the accident. The alarm turns on as soon as an accident is detected. In the event of a minor accident, the key remains open and messaging is terminated. In the event of a major accident, the key remains closed and a message is automatically sent to the rescue team after the location is detected by the GPS (Mane & Rana, 2014).

A similar study was conducted in 2017 by Mahamud et al. They have also developed an accident prevention system that reduces the likelihood of accidents that may occur on the roads every day, while simultaneously determining and transmitting the accident location automatically when an accident occurs. They developed an Arduino based system using Global Positioning System (GPS) and Global System for Mobile Communication (GSM). When the vehicle hits something, the speed of the vehicle and the amount of tilt are measured by an accelerometer. When the car's speed is greater than the maximum speed defined for the road, a warning is automatically issued. In addition, whenever an accident occurs, the GPS finds the geographic coordinates of that location and sends SMS using GSM (Mahamud, Monsur, & Zishan, 2017). Thus, it has been proven that a vehicle accident can be detected by an accelerometer and Arduino, which is an economical microcontroller platform.

Methodology

The method steps for the purpose of the study were completed as follows;
- circuit installation,
- writing the required codes,
- obtaining the data related to the targeted scenarios,
- displaying the written data,
- analyzing the obtained data and
- conducting the target group interviews

For these purposes, the materials used during the execution of the study are as follows;
- Arduino Uno R3
- ADXL345 3 Axis Accelerometer
- Micro SD Card Module
- Micro SD Card
- Cables
- Breadboard
- Resistance

After procuring the necessary parts, the originally planned module was started to put together. In this context, first, ADXL345 sensor connections were made with Arduino microcontroller as in Figure 1.
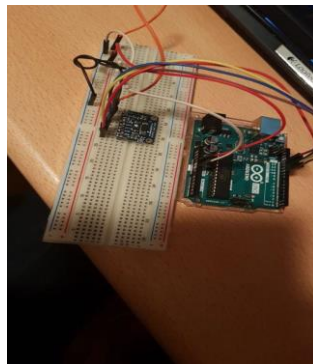
Figure 1. Connection of Arduino and ADXL 345 sensor

SPI (Serial Peripheral Interface) communication technique was used instead of I2C communication technique because of high data transfer requirements in this study. I2C is an example of synchronous communication from serial communication types. Due to the high number of transmission lines, it is not preferred for long distance communications. It is often used where short range and low data transfer rates are sufficient. SPI is one of the synchronous serial communication types that Arduino supports. In SPI protocol, unlike I2C, the data lines are unidirectional. In addition, the peripheral devices (slaves) do not need to have addresses. SPI communication technique has been chosen as the data transfer rate is suitable for this study (URL 3).

In the SPI protocol, there is one Master device just like I2C. This device controls peripheral devices connected to the transmission bus. There are three SPI lines, MISO (Master In Slave Out), MOSI (Master Out Slave In) and SCK (Serial Clock) connected to the master and peripheral devices (URL 3).
- MISO: The line where data sent from the peripheral devices (slave) is read by the master device.
- MOSI: The line where data sent from the master device is read by peripheral devices.
- SCK: This is the line where the clock signal that synchronizes the SPI communication is. The clock signal is generated by the master device.

Each peripheral device has a selection pin. This pin is called SS (Slave Select). The number of these lines is equal to the number of peripheral devices used. A separate SS line is output from the master device for each device. The peripheral device with the SS line at the LOW (0 volt) level starts to communicate with the master device. This is called "Active Low" (URL 3).

The connections between devices is made with the understanding gathered from the operating manuals of the Arduino and the accelerometer, the technical data sheets and the above information. Accordingly, the

connections with the structure as in Figure 2 are made between the two devices. In Figure 2, SDA and SDI pins are described as MOSI and SDO pin is described as MISO.

Arduino Pin	ADXL345 Pin
10	CS
11	SDA
12	SDO
13	SCL
3V3	VCC
Gnd	GND
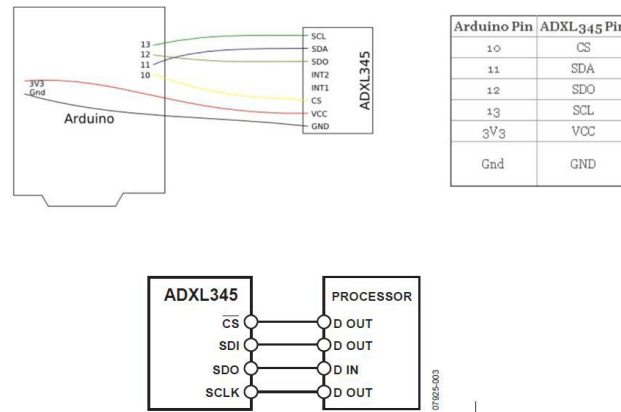
Figure 2. Arduino and ADXL345 accelerometer connection diagram

The SPI communication has either 3- or 4-wire configurations. A 4-wire configuration (CS, MOSI, MISO, SCLK) was used in this study. According to the ADXL345 accelerometer technical data sheet, it is necessary to reset bit D6 in the DATA_FORMAT register at address 0x31 to select the 4-wire SPI configuration. The maximum SPI clock speed is 5MHZ and the timing scheme follows clock polarity (CPOL) = 1 and clock phase (CPHA) = 1 (URL, 4).

The CS is the line for enabling serial communication and is controlled by the SPI master. As in Figure 3, when the data transfer starts, the CS is drawn to "low" and it becomes "high" at the end of the data transfer. SCLK is the clock of serial communication and is supplied by the SPI master. SCLK is "high" position, unless there is any data transfer. SDI and SDO are serial data input and serial data output respectively. Data is shifted on the falling edge of the SCLK and is sampled on the rising edge. To read or write multiple bytes in a single transport, the multi-byte bit must be set to "1" after the R / W bit in the first byte transfer (MB in Figure 3 and Figure 4). After the register at the address and the first data byte, each subsequent set of clock pulses (eight clock pulses) causes the ADXL345 to point to the next register for a read or write. This scroll continues until the clock pulses stop.
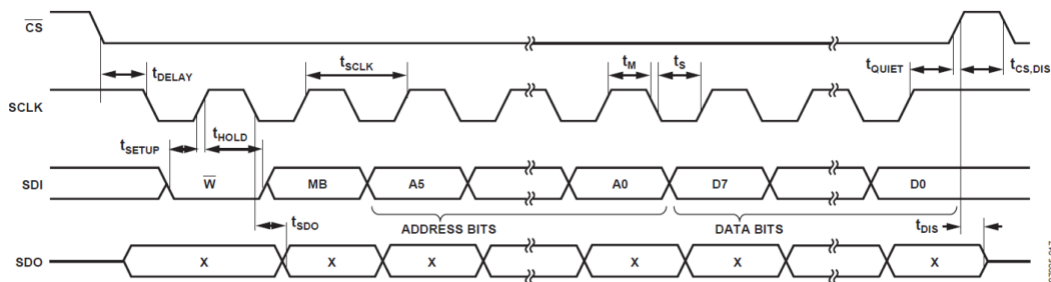
Figure 3. 4-Wire SPI writing
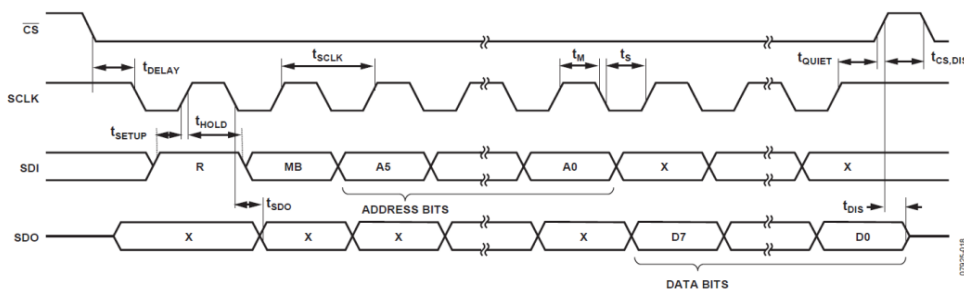
Figure 4. 4-Wire SPI reading

The use of 3200 Hz and 1600 Hz output data rates is recommended only at SPI communication speeds greater than or equal to 2 MHz. The 800 Hz output data rate is recommended only for communication rates equal to or greater than 400 kHz, and the remaining data rates are proportionally scaled. For example, for a 200 Hz output data rate, the recommended minimum communication speed is 100 kHz. Operating at an output data rate above

the maximum recommended value may cause unwanted effects on acceleration data, including missing samples or additional noise. In the study, the default SPI clock speed of Arduino of 4 MHz is used.

When the ADXL345 is used on an SPI bus with multiple devices, the CS pin is kept in the "high" position while the Arduino (host) communicates with other devices (SD card) (URL 4).

The circuit established after performing the steps according to the specified method is as shown in Figure 5.
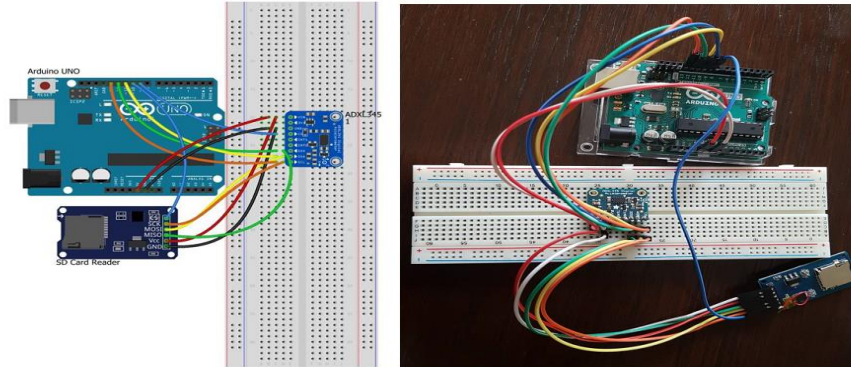
Figure 5. Completed circuit design

After the circuit was established, library codes in IDE language were added by using Arduino program and SPI communication was performed by receiving data from the sensor. In order to use SPI methods in Arduino, we had to add the library "SPI.h" to the study. The functions that initiate the SPI communication and take the SPI pins to their initial positions, set the time of the SPI communication, send or receive data to the SPI line became available when the library was added to study. First, the communication between the sensor and the Arduino with the written code was carried out with the help of the library of the ADXL345 sensor. The data was taken from the sensor and observed on the Arduino screen. In the last case, SPI communication with the sensor is provided by writing Arduino libraries and additional codes and the data is saved to SD card.

In brief, all codes are written in Arduino program in accordance with the technical information written in the user manual of the sensor and SD card and thus the data exchange of the installed circuit is ensured and the data obtained are recorded in the SD card (URL 5, 6).

Obtaining and Analyzing Data

In the process of obtaining the data, the circuit design was positioned in a vehicle and the routes determined before were followed. During this process, the computer screen for recording the path and data was recorded. After the data was written to SD card, necessary analysis process was completed via MATLAB.

Obtaining Data

In order to see changes in acceleration values, Istanbul Technical University Ayazaga Campus is chosen as the test location where many bumps, bends, slopes and distorted road characteristics are present. Before the discovery tour on the campus, the routes for the scenarios considered were determined. Afterwards, the necessary data were obtained by normal driving first and then unsafe driving based on the same starting and ending points on these routes. Unsafe driving is mainly intended to test situations that would adversely affect passenger comfort or endanger property. In addition, proceeding with two steps, namely normal and unsafe driving, makes it possible to observe the effects of changes on acceleration values according to driving style. In all figures given during routes, the first display represents normal and the second display represents unsafe driving.

Our first route is a route with certain small-scale bumps, normal bends and less inclined slopes. While there are no clear changes in the x and z coordinates while there is no skidding on a straight path along the route, the example of the magnitude of the value in y coordinate which shows an increase-decrease due to acceleration is as shown in Figure 6.

Figure 6. Route 1 speeding status

In addition, when constant speed and acceleration cases at the same locations during route 1 were examined, lower values in the y-axis was observed in the first case and greater values in the second case Figure 7.

Figure 7. Route 1 constant speed and accelerating comparison

Changes in the case of sudden braking at a constant speed or on a speeding road are as shown in Figure 8. In this scenario, positive values are read on y axis during acceleration and negative acceleration values are read on y axis when braking. The second display is for unsafe driving and it is clear that the values are more aggressive than normal driving.

Figure 8. Route 1 sudden braking attempt

As it is seen in Figure 9, while passing over a small-scale bump in our first route, the value 8 was observed in the first case and the value 13 in the second case in the z coordinates, meaning an acceleration value in the up-down direction.

Figure 9. Route 1 bump comparison

The first route involved some asphalt disturbances. It is also seen in Figure 10 that the vehicle undergoes significant acceleration value changes in all of the x, y and z coordinates while passing this point and these values reach much more prominent levels in unsafe driving.

Figure 10. Route 1 bad road comparison

The data during cornering on this route are shown in Figure 11. Visible changes in the x-coordinate of acceleration changes in the right-left direction and the magnitude of the affected acceleration values depending on the driver during normal or unsafe driving are clearly demonstrated.

Figure 11. Route 1 cornering comparison

The second route involved sharper corners than the first. In this way, we had the opportunity to compare the acceleration value changes to be observed during driving in a normal bend and a sharper bend. When we compare Figure 12 and Figure 13, we see that the values of the x coordinate have opposite signs because the bend direction is the opposite. In addition, the absolute differences in the values also reveal the differences of the sharpness of the bends.

Figure 12. Route 2 normal bend comparison

Figure 13. Route 2 sharp bend comparison

During unsafe driving, values while overtaking a vehicle at rest in Route 2 is seen in Figure 14. The x coordinate grows in negative values during the left turn and shows sharper increases in positive values during the right turn.

Figure 14. Route 2 crossover attempt

During unsafe driving of Route 2, the car is stopped with a sudden brake. At this stage, the sudden transition from -32 to 0 in y axis is shown in Figure 15.

Figure 15. Route 2 with sudden braking

In addition to route 1 and route 2, in order not to endanger the traffic and to see the changes more clearly, the parking lot on the campus was determined as route 3, where especially sudden changes in x and y coordinates were observed.

Analyzing Data

It is observed that the acceleration data from test drives have noise. Any noise should be eliminated in order to evaluate the data more accurately. MATLAB was used for the filtering of noise. As a way of filtering, Lowpass Chebyshev Type II filter was utilized. This filter was selected because it has no passband ripples and a sharper cutoff in the transition band. After implementing Fourier Transform to five different data sets acquired from 3 routes, it was realized that most of the valuable data were at 0.1 – 2 Hz. Therefore, cut-off frequency (fc) was determined as 2 Hz. Obtained data values were divided by 64 to turn them into g values, as per data sheet instructions. The noise was eliminated from the data at the time domain then all data set were represented as graphs.

As mentioned before, test drives cover 3 different routes and 2 different styles of driving for each route. The aim of choosing the first route was analyzing the effects of bumps, bad quality roads, and potholes on the acceleration values. Also, effects of bends, accelerating, and braking were also observed at this route.

During normal driving acceleration ranged from +0.22g to -0.31g on the x axis, +0.24g to -0.18g on the y axis, and +0.15g to -0.17g on the z axis.

During unsafe driving that was more careless and faster than the first one, acceleration ranged from +0.41g to -0.45g on the x axis, +0.33g to -0.36g on the y axis, and +0.18g to -0.18g on the z axis. Some of the consequences after these drives are as below.

The driver who was cornering very fast was exposed to an acceleration between +0.41g and -0.45g. The driver who was accelerating rapidly was exposed to about +0.33g. The driver who was braking suddenly was exposed to approximately -0.36g.

Contrary to expectations, the driver who passed a speedbump faster than normal was not subject to meaningfully larger amounts of g force. (+0.18g and -0.18g).
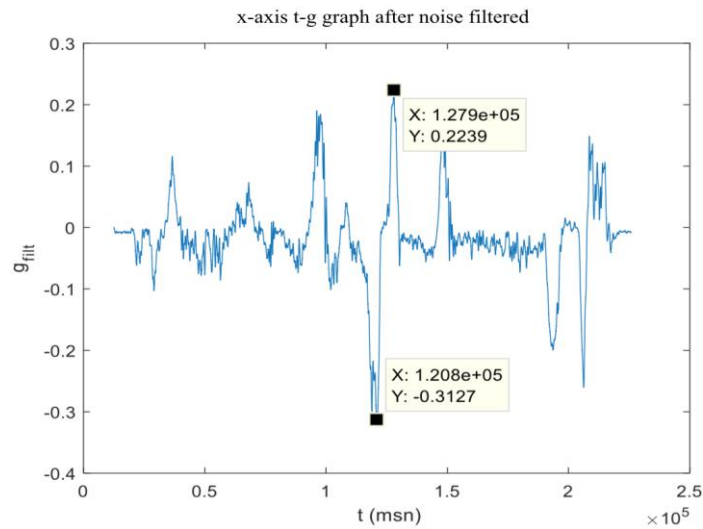
Figure 16. Route 1 x axis for normal driving
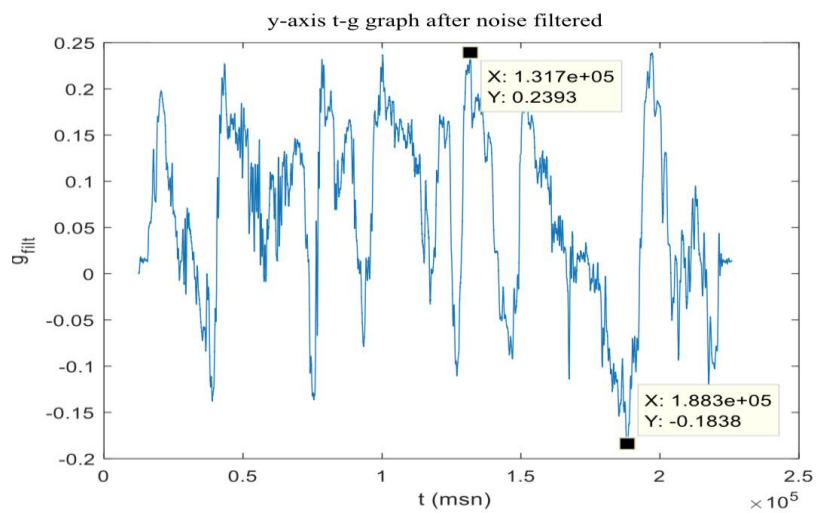
Figure 17. Route 1 y axis for normal driving
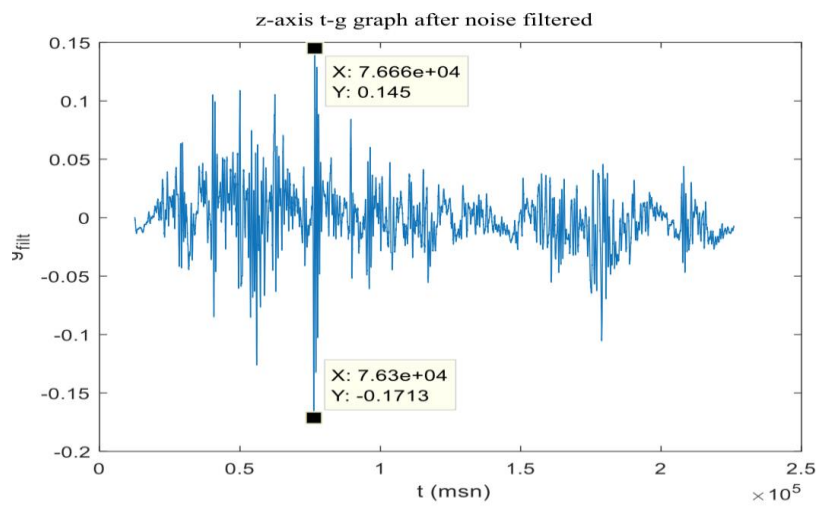
Figure 18. Route 1 z axis for normal driving

On the second route normal driving and unsafe driving were completed. In comparison with Route 1, there are sharper bends on Route 2.

During normal driving acceleration ranged from +0.34g to -0.18g on the x axis, +0.26g to -0.25g on the y axis, and +0.08g to -0.08g on the z axis. Maximum value of x axis on second route is smaller than on first route since we turned the sharper bend safer than the first route. Results for y axis is closer to first route and results for z axis are smaller because of having scarcely any bumps on second route.

During unsafe driving acceleration ranged from +0.51g to -0.39g on the x axis, +0.26g to -0.6g on the y axis, and +0.09g to -0.1g on the z axis. It is observed that these results obtained from unsafe driving are close to similar cases for Route 1.
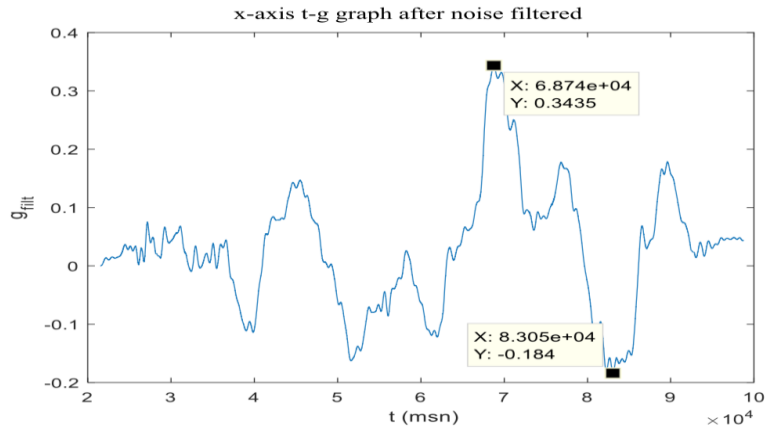
Figure 19. Route 2 x axis for normal driving
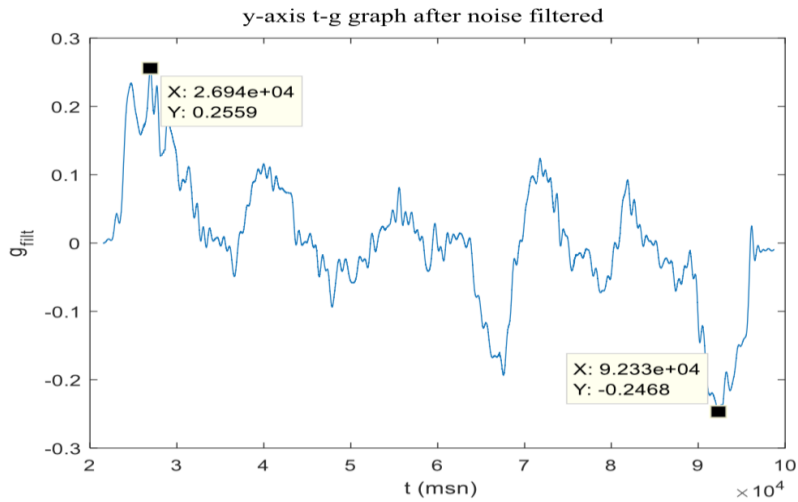
Figure 20. Route 2 y axis for normal driving
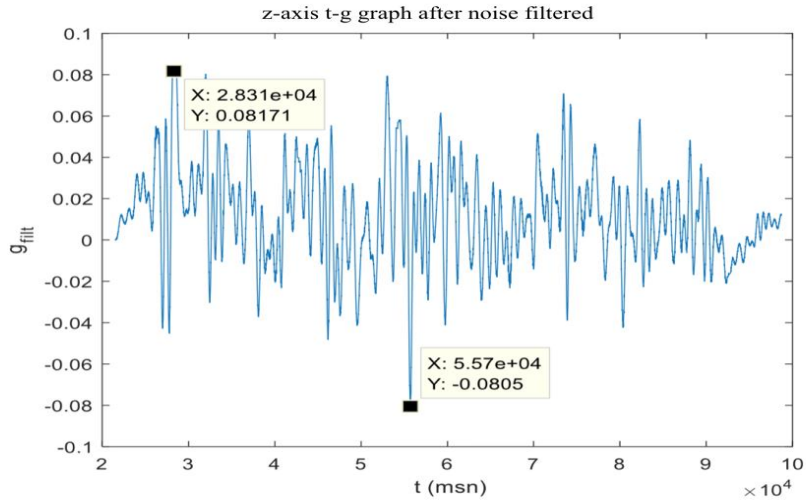
Figure 21. Route 2 z axis for normal driving
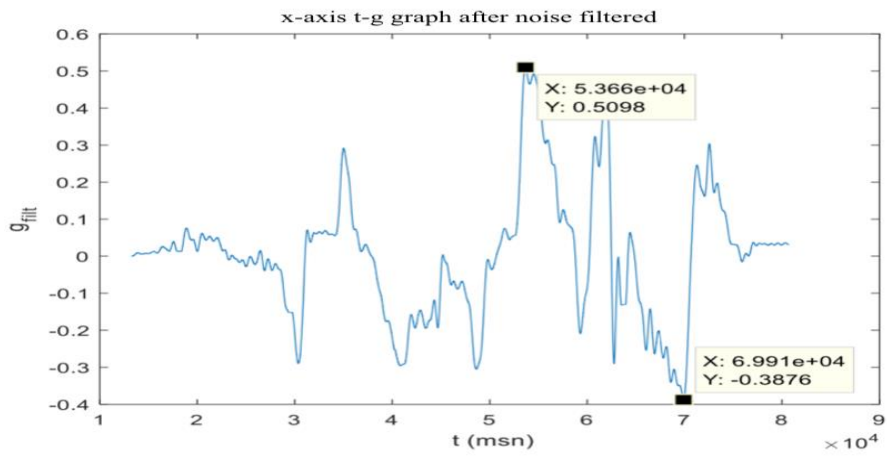
Figure 22. Route 2 x axis for unsafe driving
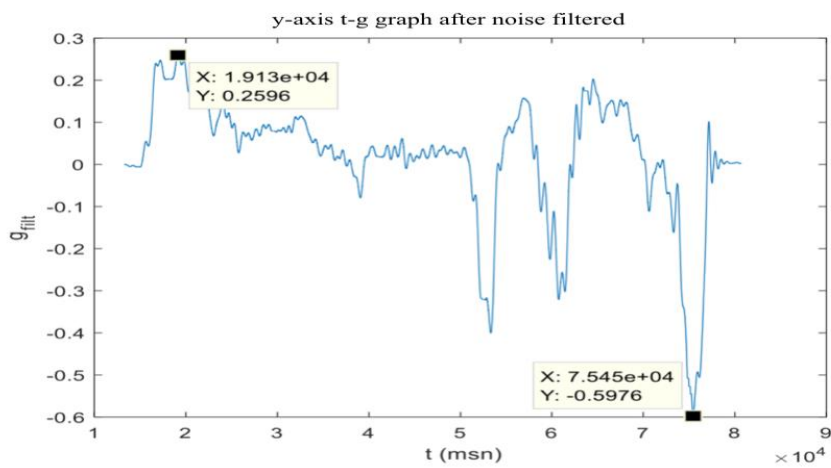
Figure 23. Route 2 y axis for unsafe driving
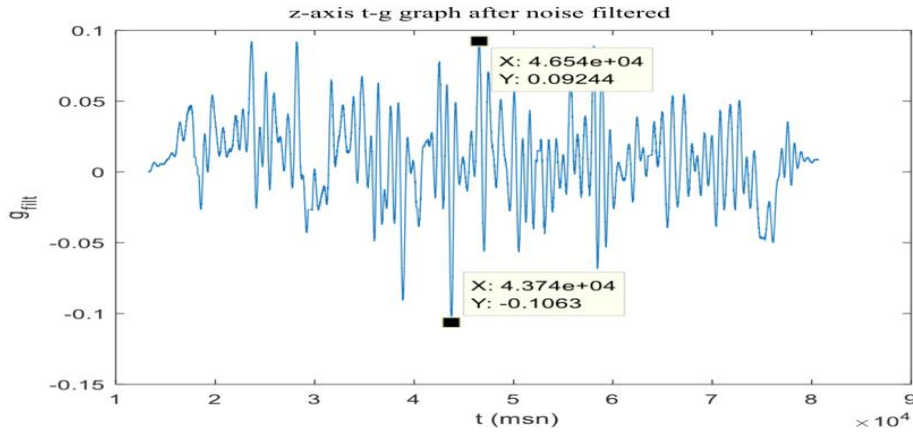
Figure 24. Route 2 z axis for unsafe driving

Route 3 is a straight road with no bumps and only one drive was completed. On this route, we turned the steering wheel hard right and left and acceleration values during speeding and braking were observed.

During driving acceleration ranged from +0.4g to -0.63g on the x axis, +0.17g to -0.35g on the y axis, and +0.04g to -0.08g on the z axis. According to results, acceleration values going up to +0.4g in the +x direction and -0.63g in the -x direction were observed because of sudden steering turns. Compared to Route 1, the values in the negative direction on the x axis were twice as much since we turned the steering wheel to the left to drive 2 or 3 rounds. Also, this driving pattern caused sudden skidding. Besides, it is observed that acceleration results obtained from sudden braking are similar between results from Route 1 and 3.
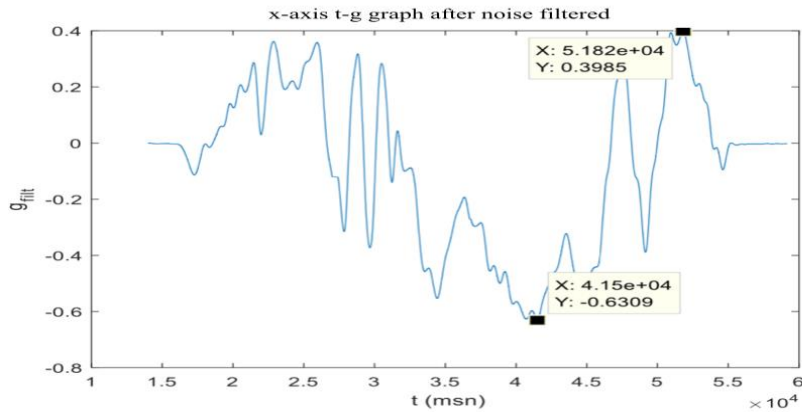
Figure 25. Route 3 x axis for normal driving
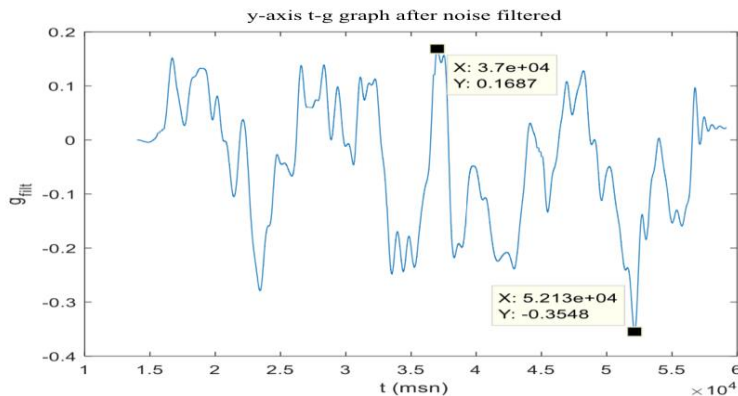
Figure 26. Route 3 y axis for normal driving
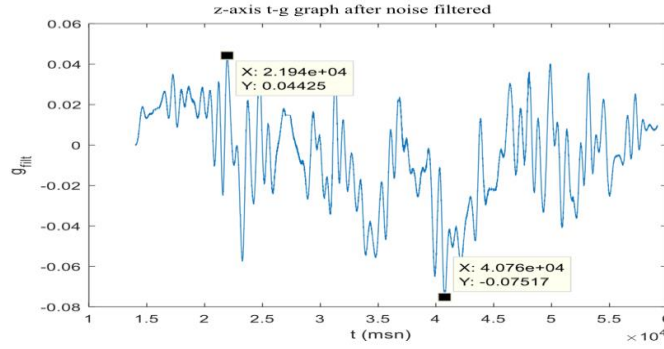
Figure 27. Route 3 z axis for normal driving

Results and Discussion

The data to be analyzed were obtained after performing normal driving and unsafe driving, which is more likely to cause damage to the vehicle, humans or transported cargo, on the specified routes and for the specified scenarios. According to the results obtained after the completion of the analysis process, the acceleration values encountered during normal driving and unsafe driving were as shown in the tables below.

When the tables are examined, we can conclude that we can see the changes to the z-axis more limited since the changes in the x and y axes are more dependent on the driving style, while the changes in the z-axis are more dependent on the road structure of the route. The absence of significant bumps in the routes we conducted our test drives also caused us to see relatively little changes in the values related to the z-axis.

Table 1. Acceleration values for normal and unsafe driving

	Acceleration values (g) (max)		
Axis	Normal driving	Unsafe driving	Difference
x	+0.34	+0.51	**+0.17**
	-0.31	-0.63	**-0.32**
y	+0.26	+0.33	**+0.07**
	-0.25	-0.60	**-0.35**
z	+0.15	+0.18	**+0.03**
	-0.17	-0.18	**-0.01**

Conclusion

In addition to the completion of the study process, one of the main objectives was for this study to address specific needs. We have achieved very positive results in our focus group discussions on the logistics sector, which was our target group. It is possible to say that the data obtained in this study could be very useful and is perceived as a security measure by big and small organizations in this sector, which are currently continuing to use information technologies and planning to do this in a wider way, after we have conducted interviews with them. In addition to this, we have achieved positive results in the questions that we aim to measure the usability for and in fact we have achieved the target of meeting the needs of and reaching the targeted audience.

References

Türkiye İstatistik Kurumu. (2018). *Ulaştırma istatistikleri*, Access adresi http://www.tuik.gov.tr/PreTablo.do?alt_id=1051

URL 1 < https://www.kozmikanafor.com/g-kuvveti-nedir/ >, access: 30.01.2019

URL 2 < https://www.telegraph.co.uk/motoring/motorsport/7681665/Formula-One-drivers-feel-the-G-force.html >, access: 30.01.2019.

Mane, A., & Rana, J. (2014). *Vehicle collision detection and remote alarm device using Arduino*. International Journal of Current Engineering and Technology, 4(3).

Mahamud, M. S., Monsur, M., & Zishan, M. S. R. (2017). *An arduino based accident prevention and identification system for vehicles*. Paper presented at the 2017 IEEE Region 10 Humanitarian Technology Conference (R10-HTC).

URL 3<https://gelecegiyazanlar.turkcell.com.tr/konu/arduino/egitim/arduino-401/spi-protokolu>, access: 03.02.2019

URL 4 < http://pdf1.alldatasheet.com/datasheetpdf/view/254714/AD/ADXL345.html >, access: 18.05.2019

URL 5 < https://www.vishnumaiea.in/projects/hardware/interfacing-catalex-micro-sd-card-module>, access 17.05.2019.

URL 6 < https://www.vishnumaiea.in/projects/hardware/interfacing-catalex-micro-sd-card-module >, access 15.05.2019

Author Information

Gizem Kayisoglu
Istanbul Technical University
Faculty of Electrical and Electronics
Engineering
Contact E-mail: *yukselg@itu.edu.tr*

Seda Canpolat
Istanbul Technical University
Faculty of Electrical and Electronics
Engineering

Ayşenur Dilara Aydin
Istanbul Technical University
Faculty of Electrical and Electronics
Engineering

Nehir Kucuktas
Istanbul Technical University
Faculty of Electrical and Electronics
Engineering

Metin Huner
Istanbul Technical University
Faculty of Electrical and Electronics
Engineering

Spectrophotometric Determination of Hydrazine Sulphate using Fe(II)-2,2'-Bipyridyl-Application to Various Water Samples

Sahba Y. MAJEED
Mosul University

Wadala A. BASHIR
Mosul University

Abstract: Hydrazine is an inorganic chemical compound with the chemical structure N_2H_4. Hydrazine a colorless flammable liquid compound. Hydrazine is very toxic and unstable compound, also hydrazine is a strong reducing agent. This compound easily ignites in the air, generating a large amount of heat and the composition of nitrogen gas and water. Symptoms of acute (short-term) exposure to high levels of hydrazine may include irritation of the eyes, nose, throat, dizziness, headache and nausea. Acute exposure can also damage the liver, kidneys and central nervous system. Cases of lungs, liver, spleen and thyroid infection in animals exposed to hydrazine have been reported by inhalation. Increased lung injury, nasal cavity, and liver tumors were observed in rodents exposed to hydrazine. This work involves the development of a fast and sensitive spectrophotometric method for the determination of trace of hydrazine, the method based on the reduction of ferric ions by hydrazing to ferrous ions, and finally the later reacts with the reagent (2,2'-bipyridyl) at 60°C to form a stable red-pink complex, this complex is soluble in water and gave absorption maxima at 523 nm. Beer's law was agreed with range (50-800) µg of hydrazine per 25 ml (i.e: 2-32 ppm), with a corresponding molar absorptivity of 5.6×10^3 $l.mol^{-1}.cm^{-1}$, Sandell's sensitivity index of 0.02 $µg.cm^{-2}$ limit of quantitation of 0.3 µg/ml, limit of defection 0.1 µg/ml , and finally average relative standard deviation of $\pm 1.25\%$, depend on the concentration level. This method had been applied successfully to determination of hydrazine amount in different samples water (tap water, river water and sea water).

Keywords: Hydrazine, Water samples, Molar absorptivity

Introduction

Hydrazine is an important inorganic chemical compound of formula N_2H_4, a base containing nitrogen, a colorless flammable liquid. Hydrazine is very toxic and unstable, and is a strong reducing agent. This compound easily ignites in the air, generating a large amount of heat and the composition of nitrogen gas and water [1-5].The name hydrazine was coined by Emile Fisher in 1875 and was attempting to produce organic compounds consisting of a single-substitution hydrazine. By 1887 [6], The odore Kirtius produced hydrazine sulfate by treating organic diazides with dilute sulfuric acid; however, he was unable to obtain pure hydrazine, despite the efforts mentioned [7]. Pure anhydrous hydrazine was first prepared by Dutch chemist Lopri de Bruyne in 1895[8]. The first use of hydrazine was during World War II as an element in rocket fuel mixtures[9,10]. Due to the many uses of hydrazine in the various fields mentioned above, a number of researchers have developed different methods for estimating hydrazine[11-15].

Various method were reported in the literatures for the estimation of hydrazine such as fluorescence determination of trace amount of Hydrazine[16,17] Chromatographic methods played an important role in the process of hydrazine estimation [18,19].

Spectrophotometric methods were also widely used for the determination of hydrazine after reacting with different ions [20-22], and corrective methods were used to estimate the said compound [23]. Potentiometric

methods are also approved and recommended in the determination of hydrazine by the use of selective electrodes for this purpose [24,25].

Practical Part

Devices used

Spectroscopic measurements were carried out by a double beam type spectrometer (JASCO 630 double beam UV-visible spectrophotometer) (Japan) Quartz cells with a light path of 1 cm were used. The pH readings were measured using (HANA Instruments pH 211 microprocesser pH meter) An ANDHR-200 type sensitive balance was used for weighing.

Reagents and chemicals used:

All chemicals and analytical reagents used were highly purified.

Solutions of Substances Used:

Standard hydrazine sulfate solution (1000 micrograms / ml):This solution was prepared by dissolving (0.1000 g) of hydrazine sulfate in 100 mL distilled water using a volumetric flask and was kept in a sealed dark bottle. - Working hydrazine solution (250μg / ml) This solution was prepared by diluting (25 mL) from the standard solution to (100 mL) with distilled water in a volumetric flask and was kept in a dark vial and remaining stable for 15 days.

Regulated solution (pH 2.9) *Prepare* this solution by dissolving (0.082 g) of sodium acetate at a concentration of (1×10^{-2} M) with distilled water and diluting the volume to (100 ml) in a volumetric flask.

Reagent solution 2 ', 2- dipyridyl (1×10^{-2} M): Prepare this solution (1×10^{-2} molar) by dissolving (0.156 g) of the reagent (supplied by ABCR GmbH & Co.KG) in 2 mL ethanol and then complete the volume to (100 mL) with distilled water in a volumetric flask. for a week.

iron ion solution(III) (1×10^{-1} M): *Prepare* this solution by dissolving (4.822 g) ammonium ferric sulfate $NH_4Fe (SO_4) 2.12H_2O$ from Dehaen AG-Riedel in distilled water containing 10 drops of concentrated sulphuric acid and diluting the volume to 100 mL in a volumetric bottle and preserving it. In an opaque bottle.

Interfering solutions (1000 μg / ml): These solutions were prepared by dissolving (0.1 g) of each substance in (100 ml) distilled water using a volumetric vial.

Results and Discussion

250 μ/ mL of hydrazine sulphate in final volume (25 mL) was used for subsequent experiments and the absorption of the solutions was measured against the solution.

Principle of method: The current developed spectral method involves two basic steps: The first step is based on the oxidation-reduction reaction between the hydrazine and the iron ion(III), which is reduced to the iron ion (II) by the hydrazine sulfate compound. The second step involves the interaction of the resulting iron-ion (II) with the ´2,2-dipyridyl reagent, which is a complex red-pink complex that gives the highest absorption at a wavelength of 523 nm.

Study of optimal reaction conditions: The effect of various conditions affecting the absorption of the complex formed by the reaction of the resulting iron ion with the reagent 2, 2-bypridyl in the aqueous solution was studied.

Effect of acid function

For the purpose of determining the optimal pH to obtain the reaction between Fe (II) ion and reagent 2 ', 2-bypyridyl and to form a stable and highly colored absorption complex, solutions were prepared with different pH by adding different volumes of HCl solution at 0.01 M. The sodium acetate solution (0.01 molar) to the reaction mixture and complete the volume to (25 mL) with distilled water. Absorption measurements were made for each solution versus the formal solution at a wavelength of 523 nm. The pH of each solution was measured as shown in Table 1. Previous same but using lotion Sodium acetate at a concentration of (0.01 molar) instead of hydrochloric acid and the results are recorded in Table 2.

Table1. Effect of acid addition on the absorption of the complex formed

ml of 0.01 M HCl solution	Absorbance		pH
	Sample vs. blank	Blank vs. water	
0	0.5560	0.1203	2.9
1	0.3371	0.1237	2.85
1.5	0.2590	0.1246	2.83
2	0.2541	0.1247	2.81
3	0.2465	0.1182	2.76
4	0.26866	0.1167	2.73
5	0.2414	0.1248	2.68

It is noted in Table 1 that the addition of acid led to a decrease in the absorption value of the complex formed and therefore was excluded in addition in subsequent experiments. The following table shows the effect of adding different amounts of sodium acetate to the reaction mixture.

Table 2. Effect of sodium acetate addition on complex absorption

ml of 0.01 M CH_3COONa solution	Absorbance		pH
	Sample vs. blank	Blank vs. water	
1	0.5943	0.0901	2.9
2	0.5745	0.0945	2.9
3	0.5598	0.0957	2.92
4	0.5560	0.0884	2.92
5	0.6113	0.1030	2.95
6	0.6438	0.1106	2.95
7	0.6764	0.1066	2.98

It is noted from Table 2 that the addition of sodium acetate gives a good absorption and better than hydrochloric acid and the same solution pH.

To control and preserve the pH at 2.9 for the reaction mixture solution, a number of different structured solutions with an pH of 2.9 were prepared and their effect on absorbance were studied: Glycine-HCl (B_2), KHphthalate-HC l(B_1),Citric acid-NaOH(B_3), Formic acid-NaOH(B_4).

Table 3. Effect of structured solutions on reaction mixture

ml of buffer solution	Absorbance /ml of buffer solution added			
	B_1	B_2	B_3	B_4
1	0.3327	0.3359	0.0864	0.3303
2	0.3076	0.3772	0.0587	0.2848
3	0.2803	0.3733	0.0031	0.2748
5	0.2319	0.3105	-0.1824	0.3305
7	0.2217	0.3309	-0.1050	0.3560
9	0.2213	0.3332	-0.1018	0.3453
Final pH	(3.0-2.8)	(3.0-2.8)	(3.04-2.89)	(3.0-2.8)

Effect of Sodium Acetate Addition Sequence

Table 4 shows the sequence of sodium acetate addition to the absorption.

Table 4. Effect of sodium acetate addition sequence

	Order	Abs. sample vs. blank	Abs. sample vs. blank
I	HS+SA+Fe+R+DW	0.5532	0.0806
II	HS+Fe+SA+R+DW	0.5316	0.1553
III	HS+Fe+R+SA+DW	0.5461	0.0853

HS= Hydrazin sulphate, SA= Sodium acetate, R= Reagent, Fe= Iron III Solution

Effect of Oxidizing Agent (Triple Iron Ion)

Different volumes (1-10) ml of oxidizing agent were studied. Iron ion(III) concentration of 1×10^{-1} M on the absorption of solutions containing different amounts of hydrazine sulfate and the results are shown in table 5.

Table 5. Effect of oxidizing agent quantity on absorption

ml of oxidant (1×10^{-1}M) solution	Absorbance /µg of HS in 25 ml						
	50	**100**	**250**	**500**	**1000**	**Blank**	**R^2**
1	0.1815	0.2458	0.5378	0.9435	1.7588	0.1911	0.9994
3	0.1317	0.2383	0.4721	0.6393	1.0321	0.0901	0.971
5	0.1159	0.2166	0.4382	0.6502	1.0294	0.0791	0.9753
7	0.0289	0.1162	0.1994	0.3217	0.6494	0.1010	0.9909
10	0.0499	0.0877	0.1498	0.2326	0.3426	0.0816	0.9701

Effect of the amount of reagent

The effect of different volumes (1-10) ml of the reagent at (1×10^{-2} M) concentration on the absorption of solutions containing different volumes of hydrazine sulfate (250µg / ml) was studied and the results are shown in Table 6.

Table 6.Effect of detector quantity

ml of reagent ($1*10^{-2}$M) solution	Absorbance /µg of HS						
	50	**100**	**250**	**500**	**100**	**Blank**	**R^2**
1	0.0099	0.0184	0.0404	0.0604	0.0956	0.0738	0.9734
3	0.0921	0.1963	0.3006	0.5008	0.8726	0.0923	0.9932
5	0.1841	0.2118	0.4009	0.6888	1.1858	0.1477	0.9988
7	0.2568	0.3562	0.6259	1.0089	1.6871	0.1556	0.9962
10	0.3216	0.4648	0.8991	1.5002	2.7654	0.2593	0.9932

Effect of iron (III) reduction time on the absorption of the product:
The effect of the time required to complete the oxidation process was studied as the solutions were left after the addition of sodium acetate solution and oxidizing agent solution to hydrazine sulfate solution for different time periods.

Table 7. Effect of tertiary iron reduction time on absorption

Time /min	Absorbance
Immediately	0.5563
5	0.5502
10	0.5560
20	0.5574
30	0.5572

It is noted from the results shown in the table above that the differences between the absorption of the solution at different times were few so the direct addition was adopted with little time in subsequent experiments. The effect of time was also studied after the addition of the reagent solution to the hydrazine sulfate solution and the oxidizing agent solution. The results are shown in Table 8.

Table 8. Effect of reagent addition time on absorption

Time /min	Absorbance
Immediately	0.5563
5	0.5539
10	0.5534
20	0.5625
30	0.5641

Effect of temperature and reaction time

The effect of different temperatures and time required to complete the reduction of Fe^{+3} to Fe^{+2} and give the highest absorption of the complex formed by using a water bath at different temperatures and for different periods of time, then the solutions were left at room temperature for 10 minutes to cool after That. The solutions were diluted with distilled water and the absorption measured for each solution versus the formal solution as shown in Table 9.

Table 9. Effect of temperature and reaction time

Temperature °C	Absorbance / Standing time (min)					
	10	20	30	40	50	60
R.T	0.0026	0.0045	0.0081	0.0101	0.0102	0.0134
30	0.0506	0.0616	0.0699	0.1568	0.1610	0.2368
40	0.1312	0.1779	0.2099	0.3119	0.3186	0.3841
50	0.2690	0.3157	0.3398	0.4125	0.4312	0.5324
60	0.3256	0.4814	0.5563	0.5591	0.5642	0.5690
70	0.4027	0.4931	0.5065	0.5241	0.5631	0.5661

Effect of superficially active substances

The effect of superficially active substances was studied by adding (3 mL) of different types of superficially active substances (positive, negative and neutral) to the reaction solution in different sequences (Table 10).

Table 10. Effect of surface active substances

Surfactant Solution 3 ml	Absorbance / order of addition (I-V)				
	I	II	III	IV	V
Triton X-100,1%	0.5568	0.5317	0.5349	0.5423	0.5673
C TAB,1×10^{-3}	0.5542	0.5262	0.5192	0.5235	0.5312
SDS, 1×10^{-3}	0.5549	0.5632	0.5561	0.5500	0.5553

I=HS+SA+O+R+DW,II=HS+S+SA+O+R+DW,III=HS+SA+S+O+R+DW,   IV=HS+SA+O+S+R+DW,
V=HS+SA+O+R+S+DW

HS=Hydrazine sulphate ,SA=Sodium acetate, O=Oxidant ,S=Surfactant ,R=Reagent

Complex Stabilization Time

For the purpose of determining the stability of the complex consisting of the reaction of iron and binary reagent ′2,2-dipride, three different amounts of hydrazine sulphate (125, 250 and 500 غرام g in a final volume of 25 mL) were used. 60 ° C and left for 10 minutes at room temperature to cool and then diluted to the mark with distilled water and measured its absorption against its formal solutions at fixed intervals of 5 minutes and the results are shown in Table 11.

Table 11. Effect of time on reaction output

Time (min)	Absorbance/µg of HS in 25ml		
	125	250	500
0	0.3559	0.5544	0.9145
5	0.3660	0.5650	0.9312
10	0.3725	0.5881	0.9437
15	0.3848	0.6010	0.9665
20	0.3930	0.6140	0.9980
25	0.4038	0.6349	1.0135
30	0.4141	0.6486	1.0313
35	0.4177	0.6527	1.0503
40	0.4264	0.6577	1.0599
45	0.4334	0.6679	1.0706
50	0.4385	0.6735	1.0825
55	0.4463	0.6805	1.0902
60	0.4472	0.6908	1.1018

From the results shown in the table above it is noted that the product is completed after 25 minutes and remains almost stable for more than 30 minutes and this time is enough to make several measurements at the same time.

For the purpose of improving stability, a masking agents (NaF, EDTA (sodium salt)) was added at a concentration of 0.01 molar each with a volume of 3 mL and the absorbance of the model was measured according to table 12.

Table 12. Adding masking agents

Time /min	Absorbance with EDTA 0.01M	Absorbance with NaF 0.01M
0	0.3848	0.3133
5	0.4570	0.3753
10	0.5220	0.4201
15	0.5725	0.4542
20	0.6149	0.4796
25	0.6544	0.5063
30	0.6881	0.5325
35	0.7156	0.5560
40	0.7483	0.5796
45	0.7746	0.5992
50	0.7997	0.6181
60	0.8105	0.6375

Final absorption spectrum

Under the optimal conditions previously established. The final spectrum of the colored product is plotted, and Figure 1 shows the final absorption spectrum of the colored product formed versus the formal solution, the absorption spectrum of the colored product formed against the distilled water and the spectrum of the solution of the formal solution versus the distilled water.
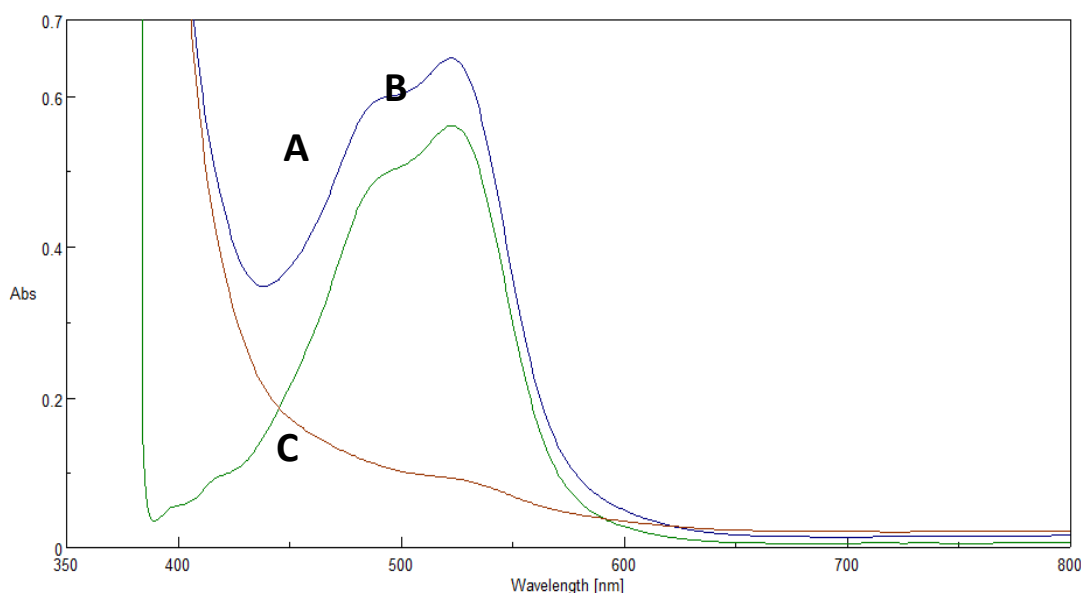
Figure 1. Absorption spectrum of 250μg /25 mL, Hydrazine sulfate is treated according to the method and measured by: (A) versus monomer, (B) versus distilled water, (C) monomer versus distilled water.

Standard working method and standard curve

The standard curve was obtained by adding increasing volumes (0.2-3.2) mL of 250μg /mL hydrazine sulphate solution to a group of 25 mL volumetric bottles and then adding 4 mL of 0.01 mL sodium acetate solution and 5 mL of oxidizing agent 1×10^{-1}M (Fe(NH$_4$) (SO4)$_2$.12H$_2$O) and 3 mL of the reagent solution ´2,2-bipyridyl at a concentration of 1×10^{-2}M and the solutions were placed in a water bath at 60 °C for half an hour, then Leave the bottles for 10 minutes at room temperature to cool and complete the volume with distilled water up to the mark and then measure the absorption of the complex formed at wavelength 523nm versus reagent blank as shown in Figure 2.
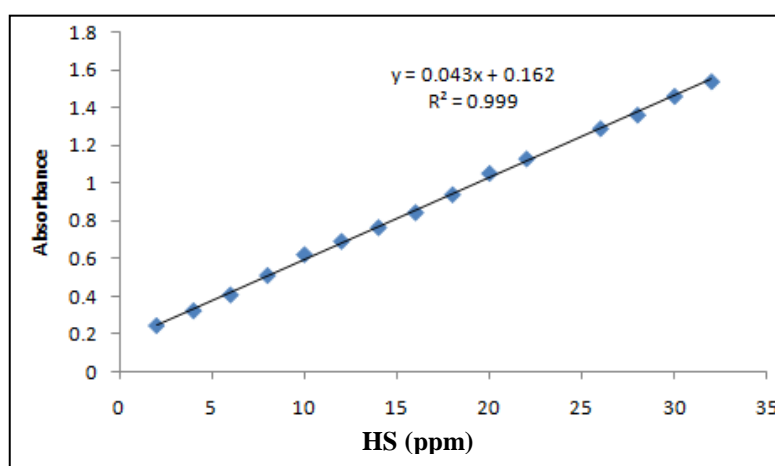
Figure 2. Standard curve for determination of hydrazine sulphate

Nature of the product formed

The Continuous variations method (Job's method) was used to find the ratio of reaction between hydrazine and ternary iron. The oxidizing agent at 1.925×10^{-3} M concentrations each was then added the optimum volumes of electrolyte solution and reagent and the solutions were placed in the water bath for half an hour at 60 °C. then, measure the absorption for each sample, the results are shown in Figure3.
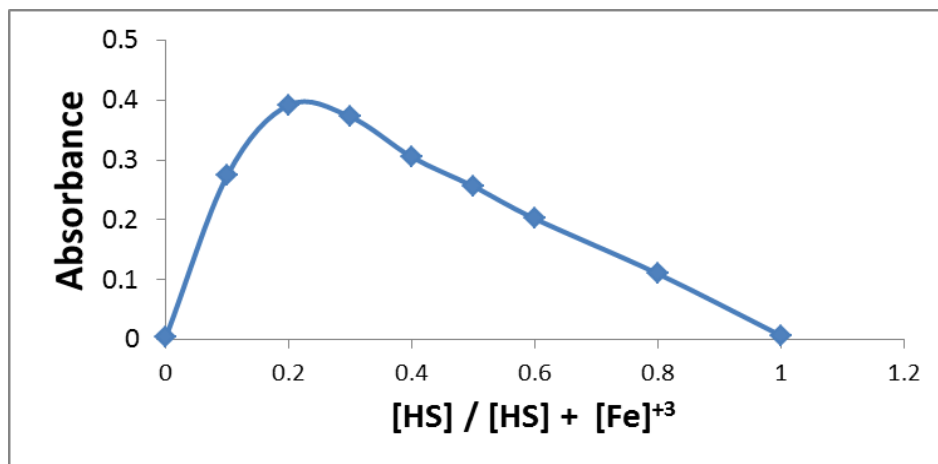
Figure **3**. Nature of the product

From Fig. 3, the molar ratio of the reaction Fe^{+3}: HS was 4: 1 and therefore the proposed reaction is consistent with the following equation

$$NH_2\text{-}NH_2 + 4Fe^{+3} \longrightarrow N_2 + 4Fe^{+2} + 4H^+$$
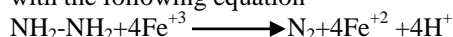
The molar ratio of the complex (Fe^{+2}-reagent) is constant and was 3: 1 and the proposed formula for the resulting complex: $[Fe(bipy)_3]^{+2}$
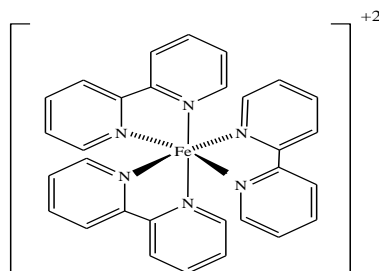
Effect of overlaps

In order to determine the method selectivity, the effect of the interference of a number of compounds was studied. These results are compared with a standard solution that does not contain any amount of interference and the results are shown in Table 13.

Table 13.Effect of interference

Foreign compound P	Recovery % of 250 µg HS /µg foreign compound present			
	25 µg	50 µg	100 µg	500 µg
Phenylhydrazine	123.34	139.73	153.00	275
Hydroxylamine- hydrochloride	140.2	187.8	235.12	408.89
Boric acid	99.7	102.8	105.2	107.2
Sucrose	106.9	100.5	99.9	102.2
Glucose	113.4	113.9	114.1	122.3
Urea	81.1	119.7	110.1	84.4
Thiourea	109.5	115.2	167.57	381.9
Borax	116.9	122.4	113.6	125.6
Sodium sulphate	109.4	116.7	116.3	Turbid
Sodium phosphate	133	107.5	109.9	Turbid
Sodiun persulphate	105.1	102.2	95	3.4
Glycerol	123.8	122.8	121	112.6
Sodium nitrite	16.7	40.8	36.4	106.6
Sodium nitrate	122.4	90.8	115.4	108.9
Sodium chloride	84.5	93.8	83	87.1
Potassium perchlorate	108.3	92.4	101.8	95.2
Ammonium chloride	113	103	102.3	110.9

Application Method

The proposed method for estimating hydrazine was applied in different water models such as tap water, river water (Tigris River, Rashidiya area) and sea water (Mediterranean). The results are shown in the table below:

Table 14. Results of application of method on water types

Sample	ml of sample	Recovery , (%)
Tap water	1	98.5
	3	95.35
	5	95.8
	10	96.88
River water	1	97.5
	3	96.8
	5	95.1
	10	95.3
Sea water	1	97.5
	3	90.5
	5	91.6
	10	91.7

Comparison of the two methods used to estimate hydrazine

A comparison has been made between the present methods with the literature[12] used to estimate hydrazine. From the table below, the present method have a good analytical properties and can be applied successfully in aqueous models.

Table 15. Comparison of the method

Analytical parameter	Present method	literature method[26]
pH	4.29	2.9
Temperature ,C°	R.T	60 C°
λ_{max} nm	730	523
Reagents used	3 reagents	3 reagents
Principle reagent	Potassium ferricyanide	2,2'-bipyridyl
Time of analysis , min	30 min	30 min
Determination range	1-22 ppm	2-32 ppm
Molar absorptivity	1.95×103	5.6×10^3
Redox stoichiomstry	1:4	1:4
Color	Prussian blue	Red-pink
Recovery%	100.1	100.8
RDS%	± 0.2	± 1.25
Determination coefficient (R^2)	0.990	0.999
Application	Could not be applied determination of hydrazine in waters	Has been applied successfully for determination of hydrazine in sea, river and tap water

Conclusions

A rapid and sensitive spectroscopic method for estimating hydrazine was developed. The method is based on the reduction of hydrazine triple iron ion to the binary iron ion which in turn reacts with 2,2-di-pyridil reagent to produce a complex (red-pink) color that is soluble and stable for a period of 60 minutes. At least it has a maximum absorption at a wavelength of 523 nm. The standard straight curve shows the PIR law following limits of concentrations (50-800) μg / 25 mL (2-32) ppm, and the standard relative deviation values (RSD) were Depending on the concentration level, the molar absorption coefficient was 103×5.6 liters.

References

https://ar.wikipedia.org/wiki/Hydrazine.

E.Fischer,"On aromatic Hydrazine compounds",Berichteder Deutschenchemischen Gesellschaft Zu Berlin,(1875),8,589-594.

T.Curtius,"On diamide(Hydrazine)",Berichte der Deutschen Chemischen Gesellschaftzu Berlin,(1887),20,1632-1634.

C.A.Lobryde Bruyn,"On the hydrate of Hydrazine",Recueil des Travaux Chimiques des Pays-Bas,(1895),13(8),85-88.

D.John Clark,"An informal history of liquid rocket propellants", New Jersey:Rutgers University Press,(1972),p.13.

J.P.Schirmann,P.Bourdauducy,"Hydrazine in Ullmann's Encycl -opedia of Industrial Chemistry",Wiley-VCH, Weinheim, (2002), 177.

R.Adams,B.K.Brown,"Hydrazine sulfate",Org.Synth. Coll., (1941), 1,307.

"Hydrazine:Chemical product info",Chem.industry, (2007),01-08.

"Chemistry of petrochemical processes",2nd edition ,Gulf Publishing Company, 2000,p.148.

Riegel,Emil Raymond,"Riegel's Handbook of Industrial Chemistry",(1992),p.192.

A.F.Holleman, E.Wiberg, "Inorganic Chemistry",Academic press, San Diego,(2001).

https://.Chemical Hazard Properties Tableat NOAAgov.

Stankovich,"Synthesis of graphene-based nanosheets via chemical reduction of exfoliated graphite oxide", Carbon.(2007), 45,1558-1565.

http://"HYDRAZINE SULFATE".Wikipedia and references in it.

"Criteria for a recommended standard: occupation Exposure to Trichloroethylene(73-11025)".CDC-NIOSH Publications and Products,(2016).

X.Chen , Y.Xiang , Z.Li , A.Tong , "Sensitive and selective fluorescence determination of trace Hydrazine in aqueous solution utilizing 5-chlorosalicylaldehyde", Anal .Chem. Acta, (2008), 625,41-42.

W.Chen, W.Liu, X.J.Liu, Y.Q.Kuang, R.Q.Yu and J.H.Jiang, "A novel fluorescent probe for sensitive detection and imaging of Hydrazine in living cells" Talanta,(2017),162,225-231.

H.L.Seifart, W.L.Gent, D.P.Parkin, P.P.Van Jaarsveld and P.R. Donald, "High-performance liquid chromatographic determination of isoniazid, acetylisoniazid and Hydrazine in biological fluids", J.Chro.Bio.Sci.,Appl., (1995),674,269-275.

G.Elias,W.F.Bauer,"Hydrazine determination in sludge samples by high-performance liquid chromatography", J.Sep.Sci., (2006), 29(3),460-4.

A.Safyavi and A.A.Ensafi,"Kinetic spectrophotometric determination of Hydrazine", Anal.Chim.Acta, (1995),300, 307-311.

S.Amlathe, V.K.Gupta," Spectrophotometric determination of Hydrazine in polluted water", Analyst,(1988),113,1481-1483.

M.George, K.S.Nagaraja and N.Blalasubramanian," Spectrophotometric determination of Hydrazine", Talanta, (2008) ,75, 27-31.

S.Lkeda and H.Satake,"Rapid method for the micro- determination of Hydrazine by amperometric titration with potassium iodate", Anal.Lett.,(1987),11,403-413.

P.Sahoo,N.Malathi,R.Ananthanarayanon,K.Praveen and N. Murali, "A novel approach for high precision rapid potentime- tric titration :application to Hydrazine assay", Rev.Sci,Inst,(2011) , 82(11),p.102-114.

S.Ganesh,F.Khan,MK. Ahmed and SK.Pandey," Potentiometric determination of free acidity in presence of hydrolysable ions and a sequential determination of Hydrazine",Talanta ,(2011), 85(2), 58-63.

S. Y. Majeedand W.A. Bashir "Spectrophotometric Determination of Hydrazine Sulphate using Fe(II)-2,2'-Bipyridyl-Application to various water samples

Author Information

Sahba Y. Majeed
University of Mosul
Mosul,Iraq
Contact E-mail:sahbayounis@gmail.com

Wadala A. Bashir
University of Mosul
Mosul,Iraq

IConTES 2019: International Conference on Technology, Engineering and Science

Design and Production of a Help Tool for Quick, Easy and Innovative Prototyping

Ghezail ABDI
University Oran 2

Habib ACHACHE
University Oran 2

Abstract: This paper describes a new tool developed in the IPSI laboratory (ENP of Oran) named (3 In 1). The latter was adopted as a powerful, easy and innovative tool and made available to the designer more features. Our rapid prototyping tool, which from a Computer-Aided Design file, corresponding to an object, allows you to quickly and easily visualize and generate a physical part on one of the lab printers. The validation was successfully completed .what makes (3 In 1) the first universal tool used ,aims to improve the field of prototyping in Algeria based on 3D printers available in the lab and trying to pass creative ideas, imaginary to the real realization. In the context of the globalization of increasingly competitive markets and increasing reactivity on the part of companies, a company wishing to maintain and / or acquire new market shares must ; control costs ; improve product and study quality ; reduce development time (design and delivery) .To meet these critical success criteria, companies need to adapt their design process and al so take into account the emergence of new technologies. In this way, it becomes crucial for companies to have the tools to quickly materialize the products under development, in order to facilitate the design and realization of all the different technical solutions chosen. This is the area of rapid prototyping research at the IPSI Laboratory.

Keywords: CAD, Prototyping, Technology, Rapid prototyping

Introduction and the Origin of Rapid Prototyping

Rapid prototyping is a technique for making solid objects from a digital model. The first CNC (Computer Numerical Control) machines were built in the 1950s. These were mainly towers and milling machines, but they were intended for production, not for prototyping. As this type of machine evolved, the G-Code was invented in the 1960s: a standardized language for operating digital machines. This language will later be used with RepRaps (Rapid Prototyper Replication or Rapid Replication Designer). It is a team made up of Alain Le Méhauté (Alcatel), Olivier de Witte (Cilas) and Jean-Claude André CNRS (National Centre for Scientific Research) who patented the first 3D printing process in 1984 : stereolithography. Little convinced of the value of this technique Alcatel and Cilas will quickly abandon these patents. In the second half of the eighties appeared the first commercial stereo Lithography machine, the process was patented by Chuck Hull and disseminated by his company 3D Systems. It is a system of photo-polymerization of a resin using lasers. Unlike traditional machine tools, this type of machine constructs objects by adding matter and not by shrinkage (it is additive manufacturing).You can therefore make an object directly from a 3D model, without any concern for the path of the tool, without mold, and thus create (relatively) quickly complex shapes that are impossible to make otherwise.

The STL (Stereo Lithography) format is created for this purpose. It is a 3D file format that describes the surface of an object, and is currently the standard used in 3D printing.

At the same time, Stratasys filed a patent on the FDM (Fused Deposition Modeling) process, which consists of building an object from molten plastic and extruded in successive layers.

This process is used by a Rep Rap under the name of (FFF : Fuse Filament Fabrication). Since then, various other processes have emerged, such as SLS (Selective Laser Sintering), which consists of polymerizing a powder in successive layers with a laser, or SLA (Stereolithography Apparatus) using photo-polymerizing resin sensitive to ultrasound. All these systems used by companies remain rather expensive (in machines, as in consumables), and have therefore remained inaccessible to the general public. It was not until 2005 and the RepRap project hat this technology was widely disseminated

Definition of Rapid Prototyping

Rapid manufacturing, or rapid prototyping, is a combination of processes and technologies for manufacturing parts by removing or adding layer-by-layer material. However, there are several methods of rapid prototyping. From a computer-aided design (CAD) model, it is possible to realize all types of parts, especially those with complex architectures.

The work piece is produced by machining, depositing, polymerizing or melting successive layers of organic, mineral or metallic raw material. It is thus possible to produce parts in routine materials such as plastic, ceramic or metal.

Rapid prototyping incorporates three key concepts: time, cost and form complexity.
- **Time:** the objective of rapid prototyping is to quickly realize the models, in order to reduce the time of product development.
- **Cost:** rapid prototyping allows prototypes to be made without the need for expensive tools, while guaranteeing the performance of the final product. It is therefore possible to explore the different variants of the product underdevelopment in order to select the most appropriate solution.
- **Complexity of forms:** machines operating by adding matter are capable of making extremely complex forms (inclusion, cavity, torsion, etc.).., unachievable by processes such as machining for example.

3D printing

3D printing is an additive production technique developed for rapid prototyping. Its goal is to quickly and easily generate a physical part. Different materials can be used, more generally ABS plastic, PLA plastic, and metal, but also wax, or even plaster.

The applications of 3D printing are varied, but in all cases aim at the concrete visualization of projects, or checking of ergonomics of parts.

The general principle is quite similar to that of a conventional 2D printer, that is, from a model created on a computer and giving a physical, concrete representation of it. From a CAD file, 3D printing allows the user to produce a part (through a software that cuts it into slices) by depositing or solidifying the material layer by layer, which makes it possible to obtain a physical part in 3D. The printing time, which varies depending on the volume of the work piece and the printing speeds, is a few hours.

The operation of the 3D printer

From the beginning, 3D printing can seem very complicated. But when you're experienced enough, it's all the easier to assemble parts mechanically. First of all, it is necessary to understand the principle of identical operation for any type of printer. This principle consists in creating, step by step, an object as if one were building a building with several floors. This principle is more commonly known as " layer by layer ".3 D printing consists of the deposition of molten material, selective laser filtering which will allow the object to be assembled and finally the solidification of the material thanks to UV lights.

To achieve this objective, the first step is to model the object to be realized on a CAD tool. This CAD tool is a software program that will make it possible to materialize the object in a printable format. A final step will be to transfer the file to the printer and promote its materialization. File transfer can be done in several ways: Wi-Fi, Bluetooth, or USB if necessary. Once the transfer is complete, the creation process can be initiated.

The press suite is taken care of by the machine itself. It is responsible for super imposing several layers of the material used until the desired result is achieved.

Les outils utilisés : (Logiciel CAD-Slic3r-G. code-Arduino)

Our 3D printer will be driven by several free software programs, capable of printing parts based on PLA and ABS wire coils. In what follows, We will present the various tools that we needed to use and their functionalities from the creation to the actual impression of apiece.
For this, we will use the following tools:

CAD software

A 3D CAD software, which will allow us to make the desired part in 3D and then save it in STL format for use afterwards.

STL

Short for Stereolythography, a 3D file format used for printing and working with most 3D modeling or printing software.

Slic3r

This software allows to convert SLT file to G-code. The G-code is a text-based language that is generated on the basis of a 3D model. These instructions are sent to our printer who will interpret these lines and execute them. The G-code instructions program by the coordinates X, Y and Z. These are points in the 3D space that the print head will move with some advance that will be adjustable.

Slic3r al so cuts the model into horizontal slices to calculate the amount of material to be extruded.

G-Code

Code used by most digital machines that gives the instructions they need to use (coordinates, travel speeds, tool parameters,..).

Operation of the application (3 In 1)

The use of the software (3 In 1) is to view the parts, generate the Rolling G-code and print with the 3D machine. It is a simple and efficient interface which facilitates USB connection to the 3D printer. This part is devoted to the design and realization of our work, thatis, the implementation of a rapid product development process. To do this, we will introduce and make available to the IPSI   (ENPO) (a 3in1 software) of rapid prototyping.

Rapid prototyping techniques, which rapidly lead to design validation models, make a major contribution to mechanical production. Because of this, our goal is to improve these techniques by developing an application that will allow many users to view and print files from 3D modeling.
We will start with the presentation of the *functioning of the application*
Figure 1 represents the main interface of our application , it contains design tools, prototyping, help and a work history.
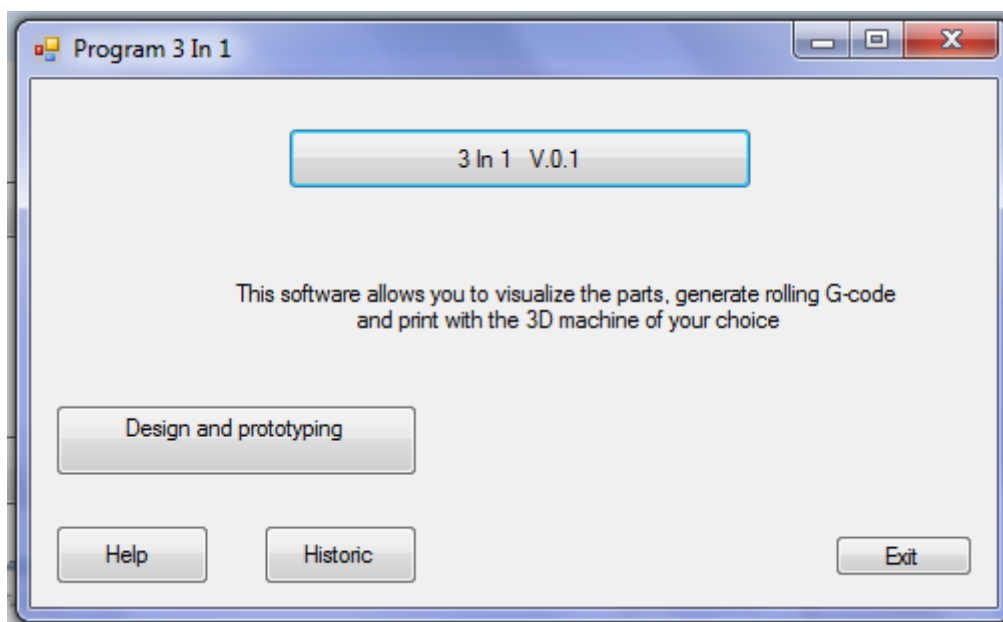
Figure 1. The main interface of the project 3 In 1

We can use our Software (3 In 1) to print our models and we will see that it is graphically more user friendly and offers more control options with visualization of formats STL and G-code.

- Open the file first .STL on the main software interface (3 In 1) by clicking on the ***design and prototyping*** button in Figure 1, we obtain the ***interface 2*** (See Figure 2).
- For this ***interface 2*** (figure2), it was preferred to set up a single window, making it easier for the user to follow the Three steps recommended for carrying out his work.
- The first step, we will see that we can select the settings and saved profiles that we would like for printing by clicking on the button ***open the DAO file***
- The second step, choosing the printer by clicking on the ***Choose 3D printer button***.
- The third step after selecting the STL file and selecting the printer, by clicking on the button ***g-code*** which will automatically generate the file g-code.
- Once we have a generated g-code format, we can print the piece we want by clicking on the ***print button***, this is the fourth step and the printer starts to print our work.
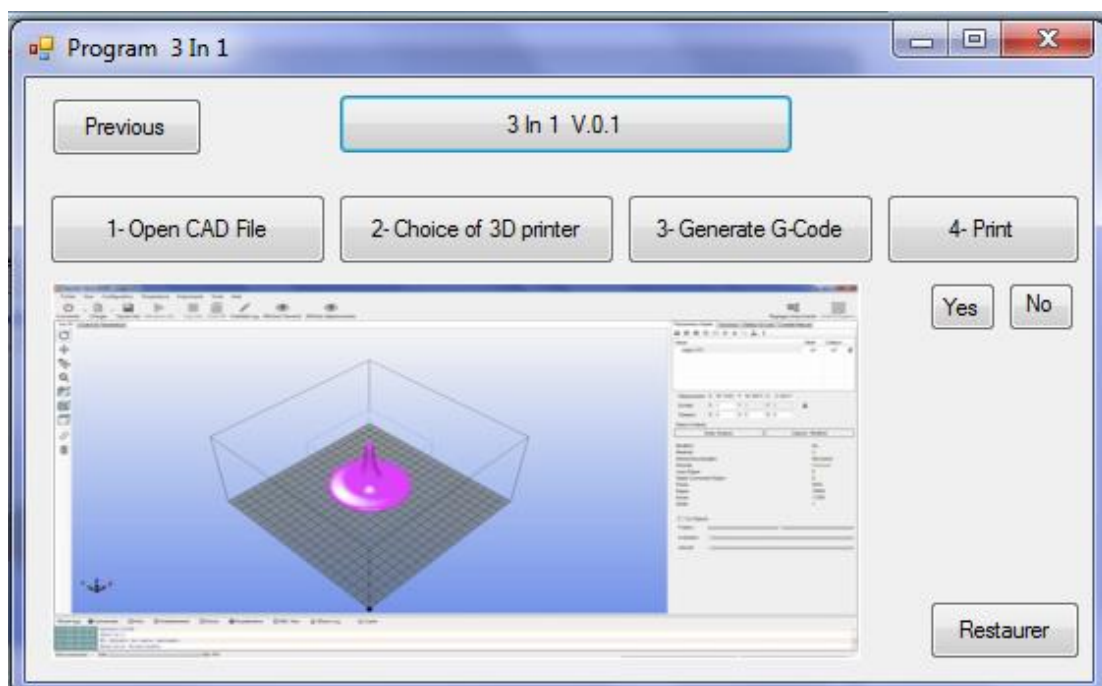
Figure 2. Design and prototyping Interface in step 3

The IPSI laboratory has solved one of the major problems for users, namely the import of files .STL, G-Code generation and direct printing of the part after choosing the 3D printer on the same software 3 In 1.

Conclusion and Outlook

Despite these seemingly temporary limitations, research is making great strides in the area of additive manufacturing, new materials, new models, new uses and new software ...etc. eachmonthbringsexcitingadvancesthatreallysuggestthatthistechnology (3D printing) can soon be used on a large scale.

Whether you are a designer or SME manager, a passionate amateur or an expert in CAD, 3D printing is a technique that is becoming impossible to do without.

A new generation of manufactured objects, designed by professional designers and made possible by end-user data, can be created: e-objects .These new digital objects, manufactured on demand with 3D printing technology, adapt to the needs of the end user and announce this wonderful world to suit every man, where mass production is giving way to mass customization.

Through this research work, we had the chance to discover this wonderful world of rapid prototyping and to make our contribution by developing and producing a tool (3in1) for end users, namely the researchers of the IPSI laboratory (ENP of Oran). An easy, simple and innovative tool, you just need to install the application (3en1) for more features, so this will give us the right to create, as we have the chance to challenge the prices of other parts that we will be able to buy from the Algerian market and reprint them using the imported printer, in order to reduce its price to 40% and to have an Algerian product that would give every Algerian customer the opportunity to benefit from the product exhibited and to increase the number of purchases, hence the interest to manufacture this type of machinery locally. Finally, as a major perspective for our work, we cite the realization of other Algerian products.

References

Nicholas A. Meisel, Christopher B. Williams, (2015) .Design and assessment of a 3D printing vending machine, *Rapid Prototyping Journal*, Vol. 21 Issue: 5/471-481,

Benjamin Weiss, Duane W. Storti, Mark A. Ganter, (2015) .Low-cost closed-loop control of a 3D printer gantry, *Rapid Prototyping Journal*, Vol. 21 Issue: 5/ 482-490,

Francesca Ostuzzi, Valentina Rognoli, Jelle Saldien, Marinella Levi, (2015) .+TUO project: low cost 3D printers as helpful tool for small communities with rheumatic diseases, *Rapid Prototyping Journal*, Vol. 21 Issue: 5/491-505,

Preston G. Smith, (1999) .The business of rapid prototyping. *Rapid Prototyping Journal*, Vol. 5 Issue: 4/ 179-186,

Munish Chhabra, Rupinder Singh, (2011) .Rapid casting solutions: a review. *Rapid Prototyping Journal*, Vol. 17 Issue: 5/328-350,

Sunil Kumar Tiwari, Sarang Pande, Sanat Agrawal, Santosh M. Bobade, (2015) .Selection of selective laser sintering materials for different applications. *Rapid Prototyping Journal*, Vol. 21 Issue: 6/ 630-648.

Syed H. Masood, (1996) "Intelligent rapid prototyping with fused deposition modeling. *Rapid Prototyping Journal*. Vol. 2 Issue: 1/ 24-33.

Neil Hopkinson, Phill Dickens, (2001) .Rapid prototyping for direct manufacture. *Rapid Prototyping Journal*. Vol. 7 Issue: 4/ 197-202

Belarbi Boumediene, Benabdallah Tawfik, Abdi Ghezail, (2016) .Implementation of a New Dimensional Qualification (DQ) Method for an Open Access Fused Deposition Modeling 3D Printer. *International Review of Mechanical (I.RE.M.E.)*. Vol 10/ N.2.

Rosario, J.M., Kubiak, D., De Oliveira, E., de Silveira, A.F., de Melo, L.F., (2015). Supervision and control architecture for CNC machine tool using rapid prototyping. *International Review of Mechanical Engineering (IREME)*, 9 (3)/ 212-222.

Castañeda, A., Ospina, N., Hurtado, D., (2015) . Position Control of a Vehicle Seat Using Rapid Prototyping and CAN Protocol. *International Review on Modeling and Simulations (IREMOS)*. 8 (5)/576-582.

Ajaamoum, M., Kourchi, M., Bouachrine, B., Ihlal, A., Bouhouch, L., (2014) .Photovoltaic Panel Emulators, Design and Implementation Using Rapid Prototyping Technique. *International Review of Electrical Engineering (IREE)*. 9 (5)/ 1012-1020.

Cheah, C., Chua, C., Lee, C. et al. (2005) . Rapid prototyping and tooling techniques: a review of applications for rapid investment casting. *The International Journal of Advanced Manufacturing Technology* ,Volume 25, Issue 3–4/ 308–320

G. Delaleux, (2013) .Putting 3D Printing into the Value Stream.

D. Scaravetti et al, (2001).Qualification Procedure Design of Rapid Prototyping Means

Jacobs PF (1996) Stereolithography and other RP&M technologies: from rapid prototyping to rapid tooling. ASME Press, NYGoogle Scholar

Radstok E (1999) Rapid tooling. Rapid Prototyping J 5:164–169CrossRefGoogle Scholar

Author Information

Ghezail Abdi	**Habib Achache**
Industrial Maintenance and Safety Institute , University Oran 2	Industrial Maintenance and Safety Institute , University Oran 2
Name of Institution or University	170 bp EL Mnawer, Oran, Algéria
170 bp 170 EL Mnawer, Oran, Algéria	
Contact E-mail: ghezailabdi@yahoo.fr	

IConTES 2019: International Conference on Technology, Engineering and Science

The Role of Cloud Computing in Smart Cities

Murat DENER
Gazi University

Abstract: With smart cities, people's living areas become better and their living standards rise. People can easily access the information they want and plan accordingly. In this way, they live a better quality and productive world. They can also remotely control and direct any smart system at home, in his car or in his office, regardless of time and location. In addition, thanks to intelligent systems, government agencies can control different parts of the city as well as foresee and take precautionary damages. Health, military, industrial, environmental, agricultural, logistics, transportation systems are realized with economic and social gains. All these smart systems require infrastructure. There are many technical and financial needs such as the servers that the devices that make up the systems can send the data, the servers where these data will be stored, the maintenance and security of these servers. At this point, Cloud Computing emerges. Cloud computing, a new generation of topics, is the general name of Internet-based IT services that can be used by computers and other devices at any time and provides shared resources among users. With Cloud Computing, users can access the system from anywhere on the internet. Cloud Computing is becoming a part of technologies in smart cities with its success in cost, global scale, speed, performance, efficiency, security and reliability. With cloud computing, servers, storage areas, databases and numerous application services are easily accessible over the internet, making integration of the systems in smart cities and the exchange of information between them more constructive. In this study, the role of Cloud Computing in smart cities will be explained. The current literature review will reveal the latest trends in these two areas. The study is considered to be beneficial for smart cities technology developers.

Keywords: Smart city, Cloud computing, Infrastructure, Living, Technology

Introduction

With the development of cloud computing and the rise of smart cities, smart city cloud service platforms are increasingly recognized by businesses and individuals. The data detected by thousands of smart devices that make up smart cities and provide data exchange can be stored in cloud systems. This makes it easier to exchange the data needed for different systems.

However, since all data collected are on the same platform, all processes related to this system need to be analyzed very well. While an efficient cloud system will make everything more accessible, in an inefficient cloud system all data can become more complex.

In this study, the current studies on cloud computing in smart cities are shared with the elements of smart city.

Smart City

According to the European Commission, a smart city is a place where traditional networks and services, city dwellers and business is made more efficient by the use of digital and information communication technologies. Some of the systems found in smart cities, as shown in Figure 1, are as follows.

Smart Industry, Smart Security, Smart Energy, Smart People, Smart Health, Smart Home, Smart Mobility, Smart Governance, Smart Retail.
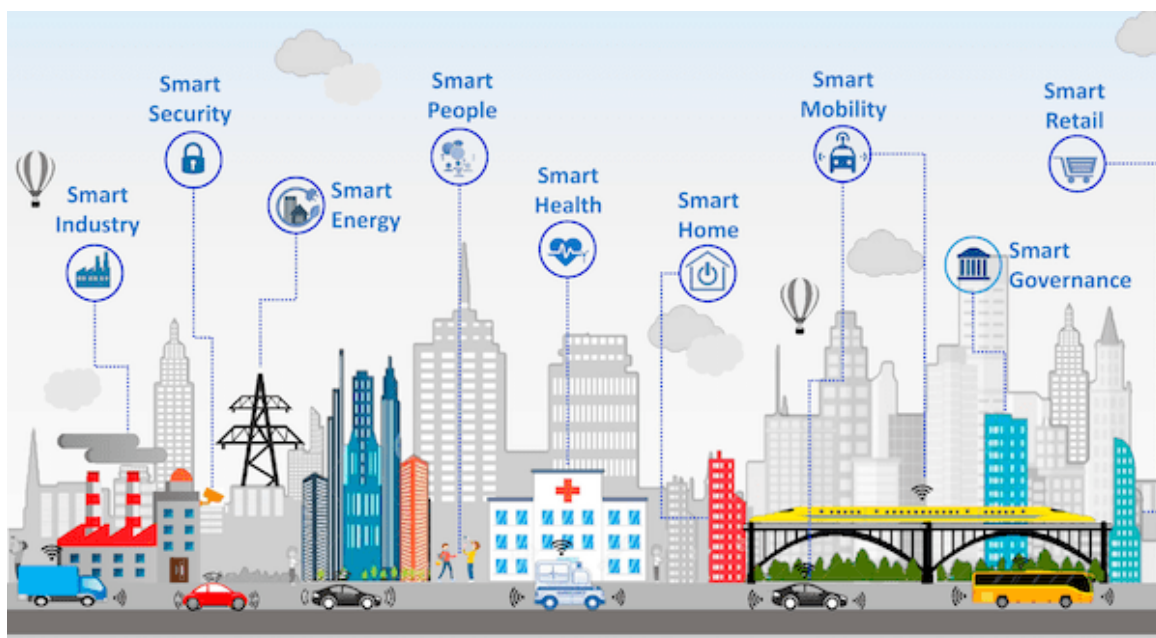
Figure 1. Smart City [Silva et al., 2018]

Smart city aims to improve the quality of life of citizens by creating sustainable mechanisms. In this respect, the issue of smart city should be considered as a concept that includes different economic, humanitarian or legal elements instead of being seen only as a technological issue. The main objective of the smart city initiative is to ensure the sustainability of cities, to increase the social activities and to facilitate the living conditions.

Cloud Computing

Cloud Computing, a new generation of topics, is the general name of Internet-based IT services that can be used by computers and other devices at any time and provides shared resources among users. With Cloud Computing, users can access the system from anywhere on the internet.

Cloud Computing is becoming a part of technologies in smart cities with its success in cost, global scale, speed, performance, efficiency, security and reliability. With cloud computing, servers, storage areas, databases and numerous application services are easily accessible over the internet, making integration of the systems in smart cities and the exchange of information between them more constructive.

Studies on Cloud Computing in Smart Cities

When the literature is examined, it is seen that there are many studies on cloud computing in smart cities. The most recent of these studies are described below.

The study [Araujo et al., 2019] presents a comprehensive performance assessment of FIWARE, a cloud-based IoT platform developed by the European Commission.

In the study [Jegadeesan et al., 2019], it has been stated that the number of mobile users has increased considerably recently. While users are using mobile applications, they can also exchange data from various cloud services. The study proposes a new authentication technique in order to ensure security between the end user and the service provider.

In the study [Huang et al., 2019], it is stated that it is very difficult to efficiently query the data pool in smart city cloud systems. Accordingly, a new technique is proposed for interrogation.

It is stated that [Esposito et al., 2019] although cloud computing is a very useful technology, it has security and privacy concerns. For this purpose, data access restriction technique has been developed when access to the same cloud from different sites.

In the study [Sinky et al., 2019], the caching and placement approach for circulating data within the network is suggested in order to be more positive in terms of data acquisition speed, network traffic congestion, memory usage efficiency for cloud computing to be more effective.

In the study [Sun et al., 2019], a new queue model is proposed to evaluate the demands coming to the cloud, to reduce delays and to respond to normal requests faster.

In the study [Alabdulatif et al., 2019], a cloud-based model for anomaly detection is presented to obtain accurate information from the data collected in smart cities and to operate a good decision-making mechanism.

The study [Khattak et al., 2019] proposes a new framework that integrates vehicle clouds and IoT.

In the study [Han et al., 2018], it is stated that data produced in smart cities are stored on cloud servers and privacy and integrity of stored data should be ensured. Therefore, a new cloud audit program has been proposed.

The study [Al Ridhawi et al., 2018] proposes a new technology to increase the performance and diversity of existing vehicle cloud services in smart cities.

In the study [Bangui et al., 2018], it is stated that cloud computing techniques are used to reduce costs, manage resource consumption, increase performance and connect IoT devices more effectively. Accordingly, a new intermediate layer is proposed by using fuzzy similarity and TOPSIS methods which cloud computing techniques should be used.

In the study [Liu and Lian, 2018], the minimum number of copy approaches for data security is proposed. For this purpose, a new replication strategy based on access pattern mining is proposed.

The study [Wang et al., 2018] proposes a new cloud-supported, lower latency, real-time framework for smart cities.

In the study [Barra et al., 2018], cloud based biometry services for smart cities are investigated.

The study [Eirinaki et al., 2018] proposes a new cloud-based framework to assist citizens and city authorities in the construction permit process.

The study [Hossain et al., 2018] proposes a new cloud-supported framework for secure video transmission and sharing.

In the study [Mazza et al., 2018], there are many smart mobile devices in smart cities and a new method has been developed with randomized algorithms in order to ensure fair allocation of resources to these devices.

In the study [Massobrio et al., 2018], big data analysis is performed using cloud computing infrastructures. Two case studies were analyzed using the historical bus location data, the service quality assessment of the public transport system, and the estimation of passenger mobility using ticket sales data from smart cards.

In the study [Yang et al., 2018], a decentralized image acquisition method is proposed for cloud computing based multi camera system for smart cities. The combination of cloud storage technology, data encryption and data retrieval technology enables efficient integration and management of multiple camera resources.

The study [Cheng et al., 2018] proposes a standard-based approach to design and implement FogFlow, a new sis-based framework for IoT smart city platforms.

In the study [Chen and Tsai, 2018], a new mobility management is presented using the follow-me cloud-cloudlet (FMCL) approach proposed in fog computing based radio access networks for smart cities.

The study [Enayet et al., 2018] proposes an optimal mobility-sensitive resource allocation architecture for remote big data task execution, providing greater efficiency in time and reliability in mobile cloud computing.

In the study [Simon and Mester, 2018], cloud based IoT platforms for smart cities are analyzed.

In the study [Miao et al., 2018], a new keyword search scheme based on verifiable attribute is proposed. In this way, it allows users to check and obtain the accuracy of the search results.

In the study [Kurdi et al., 2018], a trust management system is needed to help reliable peers when looking for reliable communication partners and a new trust management system is proposed.

The study [Muhammed et al., 2018] proposes a new cloud-based network health system for smart cities.

Conclusion

The work done with cloud computing in smart cities is increasing day by day. Studies are focused on using the cloud more effectively and safer. Many services in the smart city make it easier to access city services by expanding them with cloud systems. Cloud computing systems integrate data from many different sources over the network.

Cloud computing systems enables infrastructure, software and platforms to be used with common service logic. It offers both large enterprises and small entrepreneurs the opportunity to store large data, instantly access and operate without hardware, and share with third parties.

References

Al Ridhawi, I., Aloqaily, M., Kantarci, B., Jararweh, Y., Mouftah, H.T. (2018). A continuous diversified vehicular cloud service availability framework for smart cities, *Computer Networks*, 145, 207-218.

Alabdulatif, A., Khalil, I., Kumarage, H., Zomaya, A.Y., Yi, X. (2019). Privacy-preserving anomaly detection in the cloud for quality assured decision-making in smart cities, *Journal of Parallel and Distributed Computing*, 127, 209-223.

Araujo, V., Mitra, K., Saguna, S., Ahlund, C. (2019). Performance evaluation of FIWARE: A cloud-based IoT platform for smart cities, *Journal of Parallel and Distributed Computing*, 132, 250-261.

Bangui, H., Rakrak, S., Raghay, S., Buhnova, B. (2018). Moving towards Smart Cities: A Selection of Middleware for Fog-to-Cloud Services, *Applied Sciences-Basel*, 8, 1-20.

Barra, S., Castiglione, A., De Marsico, M., Nappi, M., Choo, K.K.R. (2018). Cloud-Based Biometrics (Biometrics as a Service) for Smart Cities, Nations, and Beyond, *IEEE Cloud Computing*, 5, 92-100.

Chen, Y.S., Tsai, Y.T. (2018). A Mobility Management Using Follow-Me Cloud-Cloudlet in Fog-Computing-Based RANs for Smart Cities, *Sensors*, 18, 1-26.

Cheng, B., Solmaz, G., Cirillo, F., Kovacs, E., Terasawa, K., Kitazawa, A. (2018). FogFlow: Easy Programming of IoT Services Over Cloud and Edges for Smart Cities, *IEEE Internet of Things Journal*, 5, 696-707.

Eirinaki, M., Dhar, S., Mathur, S., Kaley, A., Patel, A., Joshi, A., Shah, D. (2018). A building permit system for smart cities: A cloud-based framework, *Computers Environment and Urban Systems*, 70, 175-188.

Enayet, A., Razzaque, M.A., Hassan, M.M., Alamri, A., Fortino, G. (2018). A Mobility-Aware Optimal Resource Allocation Architecture for Big Data Task Execution on Mobile Cloud in Smart Cities, *IEEE Communications Magazine*, 56, 110-117.

Esposito, C., Castiglione, A., Frattini, F., Cinque, M., Yang, Y.J., Choo, K.K.R. (2019). On Data Sovereignty in Cloud-Based Computation Offloading for Smart Cities Applications, *IEEE Internet of Things Journal*, 6, 4521-4535.

Han, J., Li, Y.P., Chen, W.F. (2018). A Lightweight And privacy-preserving public cloud auditing scheme without bilinear pairings in smart cities, *Computer Standards & Interfaces*, 62, 84-97.

Hossain, M.S., Muhammad, G., Abdul, W., Song, B., Gupta, B.B. (2018). Cloud-assisted secure video transmission and sharing framework for smart cities, *Future Generation Computer Systems-The International Journal of Escience*, 83, 596-606.

Huang, H., Lu, Z.H., Peng, R., Feng, Z.W., Xuan, X.H., Hung, P.C.K., Huang, S.C. (2019). Efficiently querying large process model repositories in smart city cloud workflow systems based on quantitative ordering relations, *Information Sciences*, 495, 100-115.

Jegadeesan, S., Azees, M., Kumar, P.M., Manogaran, G., Chilamkurti, N., Varatharajan, R., Hsu, C.H. (2019). An efficient anonymous mutual authentication technique for providing secure communication in mobile cloud computing for smart city applications, *Sustainable Cities and Society*, 49, 1-7.

Khattak, H.A., Farman, H., Jan, B., Din, I.U. (2019). Toward Integrating Vehicular Clouds with IoT for Smart City Services, *IEEE Network*, 33, 65-71.

Kurdi, H., Alshayban, B., Altoaimy, L., Alsalamah, S. (2018). TrustyFeer: A Subjective Logic Trust Model for Smart City Peer-to-Peer Federated Clouds, *Wireless Communications & Mobile Computing*, 2018, 1-13.

Liu, X.J., Lian, X. (2018). Study on Replica Strategy Based on Access Pattern Mining in Smart City Cloud Storage System, *Wireless Personal Communications*, 103, 519-534.

Massobrio, R., Nesmachnow, S., Tchernykh, A., Avetisyan, A., Radchenko, G. (2018). Towards a Cloud Computing Paradigm for Big Data Analysis in Smart Cities, *Programming and Computer Software*, 44, 181-189.

Mazza, D., Pages-Bernaus, A., Tarchi, D., Juan, A.A., Corazza, G.E. (2018). Supporting Mobile Cloud Computing in Smart Cities via Randomized Algorithms, *IEEE Systems Journal*, 12, 1598-1609.

Miao, Y.B., Ma, J.F., Jiang, Q., Li, X., Sangaian, A.K. (2018). Verifiable keyword search over encrypted cloud data in smart city, *Computers & Electrical Engineering*, 65, 90-101.

Muhammed, T., Mehmood, R., Albeshri, A., Katib, I. (2018). UbeHealth: A Personalized Ubiquitous Cloud and Edge-Enabled Networked Healthcare System for Smart Cities, *IEEE Access*, 6, 32258-32285.

Silva, B.N., Khan, M., Jung, C., Seo, J., Muhammad, D., Han, J., Yoon, Y., Han, K. (2018). Urban Planning and Smart City Decision Management Empowered by Real-Time Data Processing Using Big Data Analytics, *Sensors*, 18, 1-19.

Simon, J., Mester, G. (2018). Critical Overview of the Cloud-Based Internet of Things Pilot Platforms for Smart Cities, *Interdisciplinary Description of Complex Systems*, 16, 397-407.

Sinky, H., Khalfi, B., Hamdaoui, B., Rayes, A. (2019). Adaptive Edge-Centric Cloud Content Placement for Responsive Smart Cities, *IEEE Network*, 33, 177-183.

Sun, D., Li, G.Q., Zhang, Y.Y., Zhu, L.M., Gaire, R. (2019). Statistically managing cloud operations for latency-tail-tolerance in IoT-enabled smart cities, *Journal of Parallel and Distributed Computing*, 127, 184-195.

Wang, P.M., Yang, L.T., Li, J.T. (2018). An Edge Cloud-Assisted CPSS Framework for Smart Cities, *IEEE Cloud Computing*, 5, 37-46.

Yang, J.C., Jiang, B., Song, H.B. (2018). A distributed image-retrieval method in multi-camera system of smart city based on cloud computing, *Future Generation Computer Systems-The International Journal of Escience*, 81, 244-251.

Author Information

Murat Dener
Gazi University
Emniyet Mahallesi Abant-1 Caddesi No:10/2E Kat:8
06500 Yenimahalle, Ankara/Turkey
Contact E-mail: *muratdener@gazi.edu.tr*

Recycling of Brick Waste for Geopolymer Mortar Using Full Factorial Design Approach

Nadia TEBBAL
M'sila University

Zine El Abidine RAHMOUNI
M'sila University

Abstract: Recently a full factorial design is an experiment allows the investigator to study the effect of each factor on the response variable, as well as the effects of interactions between factors on the response variable. The objective of this study is to identify the significant factors and interactions involved in maximizing compressive strength of geopolymer mortar when brick waste activated is used as cement. In this respect, experimental factors at two levels, which are alkaline activator type (Na_2SiO_3+ NaOH), curing temperature (40°C - 60°C) and cure duration (7-28 days), are selected as possible applicants affecting the compressive strength. According to the full factorial analysis, at the 60 °C curing temperature level when brick waste activated is added to mortar, the compressive strength will be good enough after 28 days. The physic - mechanical analysis shows an excellent agreement between the measured and the estimated values for both the compressive strength and only slight deviations were noticed for high curing temperature. The use of appropriate values of matrix strength and consideration of the improvement in mechanical behavior allow a good agreement between the experimental values and the estimated values .The results demonstrate that brick waste after activation can be used in construction industry.

Keywords: Brick waste, Experimental design, Geopolymer mortar, Curing temperature

Introduction

Globalization and the constant development of countries require the application of new and improved infrastructure to meet the needs and requirements, but without commit the resources of future generations [Kossi Ayenagbo et al , 2012]. Alkaline activation of aluminosilicate materials is known from the thirties of the last century. Alkali-activated materials (geopolymers) are good alternative to Portland and blended cements [Pavel Rovnanik et al , 2016].

Waste brick (WB) powder is a material with pozzolanic properties. Pozzolanicity is dependent on several characteristics, of which the main ones are the amount of amorphous phase, particle size distribution, and specific surface area [Pavel Rovnaník et al , 2018]. WB powder can be successfully used as a precursor in alkali activated materials or geopolymers [Jan Fořt et al , 2018]. These are generally composed of aluminosilicates with specific properties and an alkaline solution as an activator. Waste-based materials and by-products used in building industry are considered to be environmentally friendly, hence common aluminosilicate precursors are fly ashes from power plants, palm oil fuel ash, ash from biomass, slag, waste brick powder, waste glass, stone dust, incineration products of sludges, and similar materials containing amorphous silica and/or aluminosilicates [L.J. Provis et al , 2015].

Rakhimova and Rakhimov used blended binder prepared from granulated blast furnace slag (GBFS) and brick waste powder (BP) at different ratio by alkali-activation using mixed solution of sodium silicate, sodium hydroxide and sodium carbonate. The compressive strength of mixture with GBFS/BP ratio 60/40 was higher than for one component binders. The compressive strength reached 120 MPa when GBFS and BP were milled together [N.R. Rakhimova et al ,2015]. Mortars prepared using alkali-activated brick powder as binder and

siliceous sand as aggregate, cured at 65 °C for 7 days, exhibited 30-50 MPa compressive strength, 12-20% open porosity (decreasing with increasing sodium silicate used for activation) and pore size increasing for increasing sodium silicate [Enrico Sassoni et al , 2016]. Bilim et al .(2018) reported that curing conditions had a significant effect on the mechanical behavior of the hardened state of alkali-activated slag paste. This paper investigates the effect of curing conditions on compressive strength of geopolymer mortar when brick waste activated and used as cement. In this respect, experimental factors at two levels, which are alkaline activator type (Na_2SiO_3+ NaOH), curing temperature (40 °C – 60 °C) and cure duration (7-28 days), are selected as possible applicants affecting the compressive strength.

Experımental Investıgatıon

Method

Materials

Brick Waste (BW): The waste brick used was from a local manufacturing unit which was crushed in a laboratory mill. The waste brick powder has a density of 2.55 and a Blaine fineness of 3036 cm^2/g comparable to that of cement.

Sand: The sand used for making mortars is standardized sand, conforming to the requirements of EN 196-1.

The alkaline activator solution. The alkaline activator used in this study was a combination of sodium silicate (Na_2SiO_3) and NaOH. The NaOH was in pellet form with 100.5% purity and 10M solution was fixed . NaOH solution was prepared by dissolving the pellets in one liter of distilled water in a volumetric flask and stirred it. The Na_2SiO_3 consisted of 10.6% Na_2O, 26.5% SiO_2, and 62.9% H_2O (with a SiO_2/Na_2O weight ratio of 3 and a specific gravity of 1.39 at 20 °C. The properties of the materials used are shown in Table 1.

Table 1.Chemical composition of Brick Waste

Compositions (%)	SiO_2	CaO	Al_2O_3	Fe_2O_3	MgO	SO_3	Na_2O	K_2O	Cl^-	PAF
Brick Waste (%)	62.54	8.78	14.31	5.98	2.62	0.46	0.77	2.01	0.026	2.5

Preparation of Mortar Samples

To develop the alkali-activated brick waste materials were mixed with an alkaline solution. The activating solution was prepared by dissolving sodium hydroxide pellets with water and a sodium silicate solution. Brick waste was used at proportions of 100 % by weight. Therefore, these mortars were designed as MWB.

Geopolymer mortar mixes were prepared after replacing cement totally by the same amount of BW activating it by alkaline solutions of sodium hydroxide and sodium silicate. Geopolymer mortars were prepared using 1: 3 proportions of BW and standard sand. For the mixing procedure, NaOH solution, base water and binder of filler were first mixed for 5min in a pan mixer. Sand was then added and mixed for 5min.Finally, soduim silicate solution were included and were mixed for another 5min.This mixing procedure was test and found to produce high strength geopolymer. Subsequent to mixing, were molded in 2.5 cmx 2.5cmx 10cm prismatic , which were to a precured treatment that consisted of subjecting them to a relative humidity of 100% , with a temperature of 40°C and 60 °C for a period of 24 hours, in order to accelerate the activation process of mortar. After curing then subjected at an elevated temperature, the mortars were put in laboratory to cool down and demoulded the next day and kept in 25 °C room until testing age. The specimens were tested at the age of 7days and 28days. The reported results were the average of three samples.

Compresive strength: The mortar compressive strengths test were determined using prismatic specimens of square section 2.5 cm × 2.5 cm and length 10 cm in accordance with EN 196-1.

Results and Discussion

Modeling the compressive strength

When plotting the observed values of the quadratic model as a function of the predicted values (that is, the relationship between the predicted area and the actual area measured, it is found that the points are placed above the first arithmetic that is desirable.
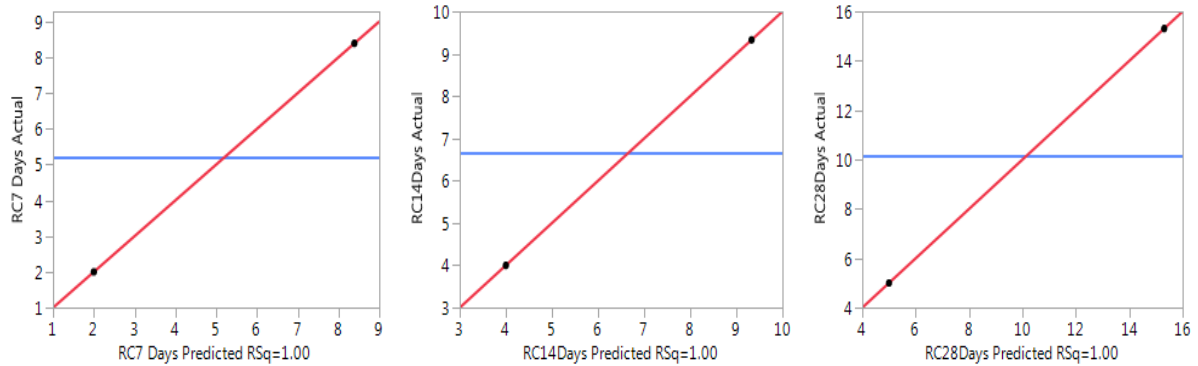
Figure 1. Graph of the values observed according to the expected values
(Compressive strength at 7days, 14 days and 28 days)
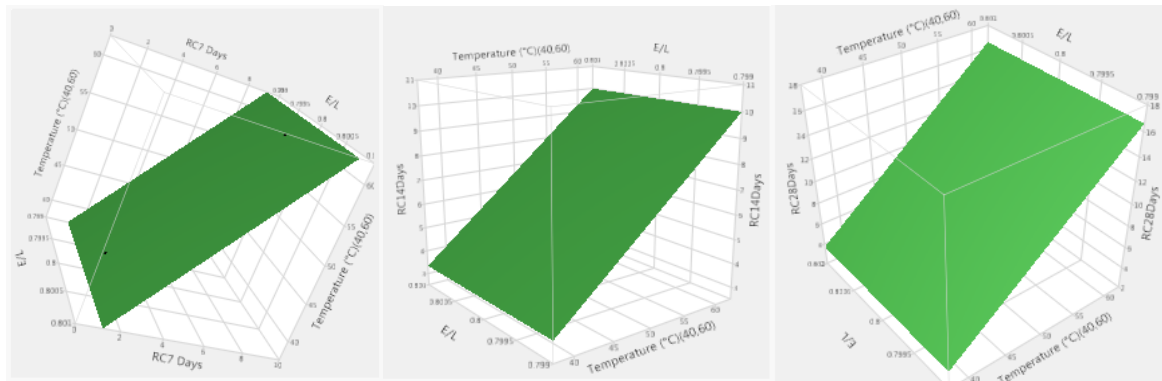
Figure 2. Evolution of compression strength as a function of curing temperature
(Compressive strength at 7days, 14 days and 28 days)

Fig. 2 shows the evolution of the compressive strengths as a function of the couring temperature. It can be clearly stated that the storage temperature strongly influences the compressive strength. An increase in the compressive strength was observed with the increase of the cooking temperature.

According to the results of estimate of coefficients drawn: the temperature effect is larger than the effect of the percentage interaction of brick waste. To simplify the model, we will eliminate this term from the equation. therefore the compressive strength response can be summarized in the following empirical model:

- Compressive strength at 7 days = $5.195 + 3.195[T \, (°C) - 50]/10$
- Compressive strength at 14 days = $6.665 + 2.665[T \, (°C) - 50]/10$
- Compressive strength at 28 days = $10.155 + 5.155[T \, (°C) - 50]/10$

Conclusion

By designing three geopolymer concrete mixtures, this paper studied the effect of curing temperature in the alkali-activated brick waste and glass powder mortar and their influence of mechanical resistances .The following conclusions are drawn:
1. For the polymerization the heat is required to the geopolymer mortar;
2. The mechanical strength increases with the incorporation of brick powder at early age;

3. At 60 °C, such strengths are improved, especially for the mix with 100% brick fines;
4. The interaction between the percentage of brick waste and the dosage of activans and the influence of these last two combined with the cooking temperature are more consistent with the mechanical response and development of mortar strength.

References

Kimatu, J. N., Wenjing, W., Rongcheng, W., Ayenagbo, K., Nguhi, S., & Makse, J. P. (2012). The impact of globalization on African countries economic development.

Rovnaník, P., Řezník, B., & Rovnaníková, P. (2016). Blended alkali-activated fly ash/brick powder materials. Procedia Engineering, 151, 108-113.

Pavel Rovnaník, PavlaRovnaníková, MartinVyšvařil, StefaniaGrzeszczyk, ElżbietaJanowska-Renkas .(10 November 2018). Rheological properties and microstructure of binary waste red brick powder/metakaolin geopolymer, Construction and Building Materials, Volume 188, Pages 924-933

Fořt, J., Vejmelková, E., Koňáková, D., Alblová, N., Čáchová, M., Keppert, M., ... & Černý, R. (2018). Application of waste brick powder in alkali activated aluminosilicates: Functional and environmental aspects. Journal of cleaner production, 194, 714-725.

Provis, J. L., Palomo, A., & Shi, C. (2015). Advances in understanding alkali-activated materials. Cement and Concrete Research, 78, 110-125.

Rakhimova, N. R., & Rakhimov, R. Z. (2015). Alkali-activated cements and mortars based on blast furnace slag and red clay brick waste. Materials & Design, 85, 324-331.

Sassoni, E., Pahlavan, P., Franzoni, E., & Bignozzi, M. C. (2016). Valorization of brick waste by alkali-activation: A study on the possible use for masonry repointing. Ceramics International, 42(13), 14685-14694.

Bilim, C., Karahan, O., Atiş, C. D., & Ilkentapar, S. (2013). Influence of admixtures on the properties of alkali-activated slag mortars subjected to different curing conditions. Materials & Design, 44, 540-547.

NF EN 196-1 Méthodes d'essais des ciments - Partie 1 : détermination des résistances mécaniques.

Author Information

Nadia Tebbal
Institute of Technical Urban Management
M'sila University, M'sila (28000), Algeria.
Contact E-mail: nadia.tebbal@univ-msila.dz

Zine El Abidine Rahmouni
Geomaterials Development Laboratory, M'sila University, M'sila, (28000), Algeria.

Electrochemical and Thermodinamic Study of Tyrosine and its Complexes in Aqueous solution by conductivity measurement

Fanar M. AL-HEALY
Mosul University

Yasir O. HAMEED
Mosul University

Abstract: The electrical conductivities of aqueous solutions of tyrosine was measured , in the beginning Kohlrausch equations was used to discover types of electrolyte through plot the relation between equivalent conductivity against the square root of molar concentration for tyrosine at 310.16K. The plot indicate that amino acid was weakly associated in water the molar conductivity of tyrosine measured by processing the obtained data using the conductivity equation of lee-Wheaton to calculation of the ionic molar conductivity (Λ)(64.9), the association constant (KA)(218610), distance parameter (R)(1.00E-06),stander and deviation ($\sigma\Lambda$)(0.91) the analysis shows that cation is association with anion to form contact ion –pair (CIP) . The prepared complexes of tyrosine with Co(II) , Mn(II) , Ni(II) , Fe(II) , to form [Ni(tyr)3]Cl2, [Co(tyr)3]Cl2, [Fe(tyr)3]Cl2, [Mn(tyr)3]Cl2 complexes are measured using in the temperature range from (288.16–313.16K) in steps of 5 K. To give information about ionic molar conductivity(Λ), the association constant (KA), distance parameter (R), and standard deviation ($\sigma\Lambda$). Standard thermodynamic information from association and examining the nature of the interaction was obtained and calculation of the thermodynamic quantities ($\Delta H°$, $\Delta G°$, $\Delta S°$) have been done. A multi parameter curve fitting procedure is used to give the lowest value of curve fitting parameter, $\sigma(\Lambda)$, between the experimental and calculated values The values differ from one complex in to another depending on the interactions in solution. the values of stander deviation proved that lee-wheaton equation suitable for this study.

Keywords: Tyrosine, Tyrosine complexes, Electrical conductivities, Lee-Wheaton equation, Thermodynamic parameter

Introduction

Amino acids are very important for human body for their regular biological activities. Amino acids are the building blocks of the body. Besides building cells and repairing tissue, they forms antibody to combat bacteria and virus; they are part of enzyme and hormonal system. Amino acids are very important for building nucleoproteins (RNA & DNA) (Hames *et al*., 2005)[1] .Eight amino acids areregards essential for human body: phenylalanine, valine, Threonine, Tryptophan, Isoleucine,Methionine , Lucien, and lysine (Ferrmand *et al*., 2001) [2] Additionally, Histidine and Arginine are required by infants and growing children (Adugana *et al*., 2004)[3] .Tyrosine intake in their food because the person living with Phenylketonuria PKU can't convert the Phenylalanine into Tyrosine .Many amino acids and their derived complexes were prepared and identified by using different methods (ex: spectral (U.V,IR), magnetic susptibility, elemental analysis and X-ray diffraction], since amino acids as ligands contain two donor atoms (N and O), therefore the complexes of amino acids with metals are interesting to study.here are some applications in this area The complexes of Ca(II),Ni(II) ,Fe(II)with mixed ligands of amino acids (Glycine, Histidine, Cysteine and Arginine) were prepared and identified by elemental analysis, electrochemical conductivity measurements at different temperatures at PH=7,the thermodynamic data were calculated then the conductivity data were compared with other electrical method(Abdel –Rahman, *et al*., 2007) [4] .Molar conductivities of dilute solutions for the complexes: Co(II)(alanine + valine),Ni(II)(valine + serine), Ca(II)(alanine + serine), Mg(II)(valine + serine) in water were measured in the temperature range from (293.16–313.16K) The ionic molar conductivity(Λ), the association

constant (KA), distance parameter (R), were determined by treating experimental data with Lee-Wheaton conductivity equation.Thermodynamic quantities for the ion association reaction were derived from the Temperature(Al-Allaf, *et al.*, 2013) [5]. Using the expanded Lee-Wheaton equation of electric conductivity, constants of ionic association are defined. It is determined that LiClO4 in propylene carbonate is a non-associated electrolyte. In order to account on the dynamics of ionic solvation, separation into ionic components is made, Results of conductometric investigations of solutions of several 1-1 electrolytes in propylene carbonate in the range of temperatures from 298 to 398 K are presented(Chernozhuk, *et al.*, 2016) [6].The electrical conductivities of aqueous solutions of quinic acid and its sodium salt were measured from 293.15 to 328.15 K in steps of 5 K. The molar conductivities of the sodium salt were treated by the Lee–Wheaton equation in the form of Pethybridge and Taba, and the Kohlrausch equations. The limiting molar conductivities of the quinate anion were estimated, as well as the corresponding ionic association constants and standard thermodynamic functions of the ionic association reaction. The hydrodynamic radius of the quinate anion was calculated from the Walden rule and compared with the van der Waals radius(Kloutar, *et al.*, 2007) [7]. The molar conductivities of dilute solutions of potassium chloride in binary mixtures of ethanol and water were measured in the temperature range from 288.15 to 308.15 K at 5 K intervals. The experimental data were treated by the Lee-Wheaton conductivity equation and parameters Λ_o and K_A derived. The ionic limiting molar conductivities (λ_o) were obtained using the literature values of the cation limiting transference number $to(K^+)$ from the same temperature range. The ionic Walden product ($\lambda_o\eta$), thermodynamic quantities for the ion-association reaction (ΔG^o, ΔH^o and ΔS^o) and the activation enthalpy of the ionic movement were calculated and discussed in terms of the ionic size, as well as solvent viscosity, permittivity, structure and basicity (Boskovic, *et al.*,2013) [8].

Experimental

Conductivity water was prepared by redistilling water three times with the addition of little amount of potassium permanganate and a small pellets of (KOH) (Palmer,1954)[9]. The complexes of Fe(II),Co(II), Mn(II) and Ni(II) with tyrosine was prepared by mixing (0.001mole,0.1988g) of ($FeCl_2.4H_2O$) , (0.001mole,0.2378g) from ($CoCl_2.4H_2O$), (0.001mole,0.238g) from ($NiCl_2.4H_2O$) and (0.001mole,0.197g) from ($MnCl_2.4H_2O$) in 25 ml of conductivity water with (0.003 mole,0.5435g) of the amino acid Tyrosine in 25 ml of conductivity water and refluxed for about two hours on cooling, each complex was precipitated. Magnetic electronic spectra, IR measurement was used to make sure of the resulting complexes . A general method has been used for measuring the conductance of the electrolytes, the conductivity cell was washed , dried and then weighed empty and kept at a constant temperature ($\pm 0.1^oC$) using a water circulating ultra thermostat . A certain amount of solution was injected into the conductivity cell and the conductivity of solution was measured by WTW Inolab 740 computerized conductivity meter. Another known amount of solution was injected by a syringe of 1ml and the measurement was repeated. Generally about (15) addition have been made by weighing the amount for each one.

Results and Discussion

It was found that Lee-Wheaton equation is applicable to the interpretation of conductance data for simple (2:1 + 1:1) in water at 298.16K [9]. This equation is used for complete analysis of mixed symmetrical and asymmetrical electrolyte at different temperatures. The electrical conductivity of the amino acid solution of tyrosine was studied in conductivity water, which was subtracted from acid continuation values , at 310.16 K .the tyrosine solution promised symmetrical electrolytes of type (1:1) if the positive ion is denoted by(M^+) and negative ion (X^-)when using the equation for these solution can be explain as follows.

$$M^+_{aq.} + X^-_{aq.} \xleftrightarrow{\quad Ka \quad} (M_{.aq}^{+n} X)$$

Ka: association constant
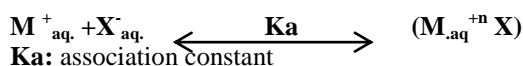
Kohlrausch has established the stability that the solution are weak electrolytes after electrical conductivity was measured at the above –mentioned temperature of the mother acid solution .the intent used is then to calculated the equivalent concentration for tyrosine solution using a special calculation program to extract the equivalent continuity after entering the conductivity information, physical parameter, temperature and weights of the additives, as it was shown that amino acid under study the behavior of the weak electrolytes was demonstrated by the relationship between the square root of the different concentration of the tyrosine solution versus the equivalent continuation calculated through the calculation program. Values indicating that solution behave like weak electrolytes(Dabbagh and Akrawi, 1992)[10], figure (1) demonstrates this behavior . The lee-Wheaton equation was applied to the amino acid solution described above , where the equivalent conductivity was

calculation program after it announced the electrical conductivity of all studied fixed cell concentration (0.5cm) ,density (0.99707gm/cm3) , the data including concentration and equivalent conductivity values,were analyzed using aspecial analysis software after giving information on both absolute temperature(T),viscosity of solution (0.0089pois) and dielectric constant (78.3D). after completing the analysis of the data it was confirmed that these solution were weak electrolytes .as aresult of the the analysis The ionic molar conductivity (Λ)(64.9), the association constant (Ka)(218610), distance parameter (R)(1.00E-06) and stander deviation (σΛ)(0.091). The analysis shows that cation is associated with anion to form contact ion –pair (CIP) ((Lee and Wheaton 1978))[11]. The values of stander deviation proved that lee-wheaton equation suitable for this study.

Table 1. Molar concentration (M) and Equivalent conductance of Tyrosine in water at 310.16K

Conc. Mole/L$*10^7$	√Conc. Mole/L$*10^3$	Λ (Ohm^{-1}. equive^{-1}.cm^2)
5.076851	0.712520245	98.48611
10.22603	1.01123835	78.89477
14.80581	1.216791272	60.65571
19.71295	1.404028134	52.046
24.55657	1.567053605	45.72224
29.27562	1.711011981	40.39238
33.99138	1.843675134	39.15806
38.60946	1.964929006	37.41918
43.29933	2.080849106	37.7599
47.86036	2.187701076	36.37544
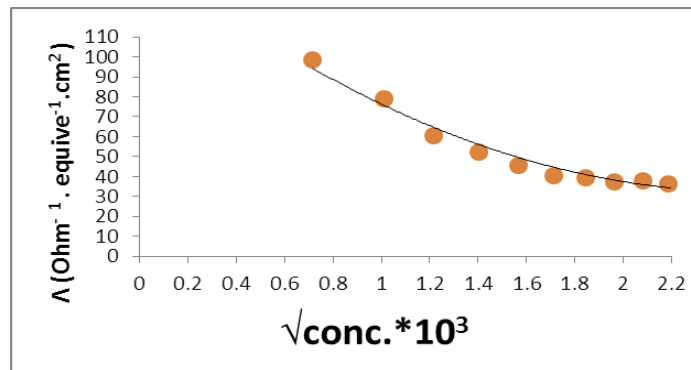
Figure 1. Molar concentration (M) and Equivalent conductance of Tyrosine in water at 310.16K

The following mixtures are chosen for this study. The equivalent conductivity ($\Lambda_{equiv.}$) at each concentration of each electrolyte solution was calculated by the following equation:

$(\Lambda_{equiv.}) = 1000\sigma / C_1C_2$ ………(1)

Where σ is the specific conductance obtained experimentally, C_1 and C_2 are the equivalent concentration of 2:1 and 1:1 electrolytes used respectively.The values of the equivalent conductivity and concentrations of the two electrolytes salts (2:1 and 1:1) determined experimentally.

$$M^{2+} + X^- \underset{KA2}{\overset{KA1}{\longleftarrow}} MX^+$$
$$MX^+ + X^- \longleftarrow MX_2$$
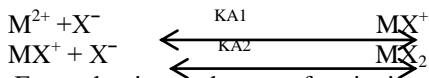
For each mixture there are four ionic species (M^{+2}, X^{-1}, MX^+ and MX_2) ions. The theoretical equivalent conductance is given by the following equation.

$\Lambda_{equiv.} = \Sigma | Z_i | m_i \lambda_i / \Sigma C_n$ …………(2)

Where Z_i is the charge, mi molar concentration, λ_i equivalent conductivity for each ionic species present in the solution and C_n is the stoichiometric equivalent concentration of electrolyte species n. It was found earlier that Ka and Λ value for single ion and for ion - pair are constant from one system to another for symmetrical, asymmetrical and mixed electrolytes by using lee-Wheaton equation (Lee and Wheaton (1978)[12] . Therefor the values of concentration and(Λ) in Tables and figures (2) (a-d) .The input data of computer program are solvent parameters (T, D, η), charges Zi and limiting conductivities λ°i for each ionic species.

Table 2a. Molar concentration (M) and Equivalent conductance of $[Co(C_9H_{11}NO_3)_3]Cl_2$ in water at different temperatures

Conc. Mole/L*10^7	Λ (Ohm^{-1}. equive^{-1}.cm^2) 288.16 °K	Λ (Ohm^{-1}. equive^{-1}.cm^2) 293.16 °K	Λ (Ohm^{-1}. equive^{-1}.cm^2) 298.16 °K	Λ (Ohm^{-1}. equive^{-1}.cm^2) 303.16 °K	Λ (Ohm^{-1}. equive^{-1}.cm^2) 308.16 °K	Λ (Ohm^{-1}. equive^{-1}.cm^2) 313.16 °K
2.383897	209.740	136.878	208.055	199.19	191.741	221.59
5.007807	133.125	99.0153	133.776	135.87	132.808	134.626
7.418538	112.331	90.2398	114.315	99.921	99.3843	102.543
9.521729	105.022	85.0816	114.454	84.774	85.4115	87.4339
11.88098	98.1961	80.4602	110.892	70.063	69.2089	84.0921
14.21494	93.7980	77.7961	108.193	58.007	67.8131	70.7315
16.45612	91.1515	75.6954	108.938	49.586	60.0880	70.8832
18.75926	88.8450	73.3356	107.429	44.019	58.7973	67.2633
20.90903	87.6814	73.6221	103.099	45.014	54.7795	66.7278
23.19345	86.2312	72.675	99.2228	42.747	49.6143	66.2269
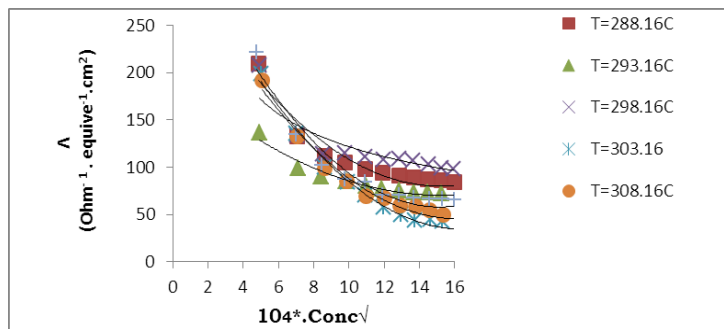
Figure 2a. The relation between the square root of concentration and the equivalent conductance of $[Co (C_9H_{11}NO_3)_3]Cl_2$ at different temperatures

Table 2b. Molar concentration (M) and Equivalent conductance of $[Fe(C_9H_{11}NO_3)_3]Cl_2$ in water at different temperatures

Conc. Mole/L*10^7	Λ (Ohm^{-1}. equive^{-1}.cm^2) 288.16 °K	Λ (Ohm^{-1}. equive^{-1}.cm^2) 293.16 °K	Λ (Ohm^{-1}. equive^{-1}.cm^2) 298.16 °K	Λ (Ohm^{-1}. equive^{-1}.cm^2) 303.16 °K	Λ (Ohm^{-1}. equive^{-1}.cm^2) 308.16 °K	Λ (Ohm^{-1}. equive^{-1}.cm^2) 313.16 °K
2.760822	181.1058	202.7705	185.529	238.5023	129.3583	133.6344
5.345241	144.7216	128.8271	127.284	159.0835	114.7457	99.238
7.828444	126.4495	108.4458	106.9917	129.653	86.67001	88.69511
10.22255	114.1267	99.24797	99.3177	99.54557	76.7261	80.94354
12.40562	107.4781	94.9043	92.5799	93.2404	66.28027	75.5241
14.95515	100.2999	90.84052	88.34605	89.97767	60.57096	70.57441
17.39708	101.3817	87.1188	86.21001	88.00488	58.50777	70.23684
19.52292	102.9806	85.79326	84.29774	85.76924	57.16596	65.07155
21.87674	101.2766	85.52024	85.75169	85.75169	56.12665	64.30665
24.15812	102.3839	86.74034	85.94481	76.55907	56.72736	64.81703
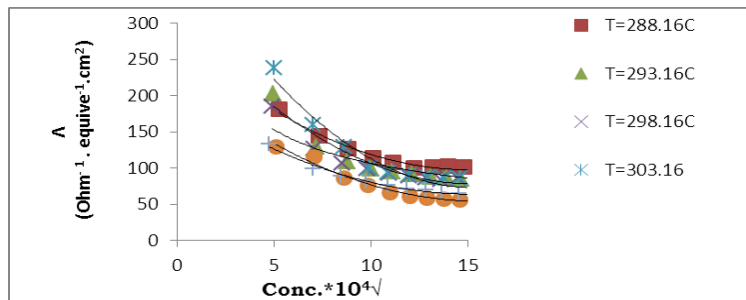
Figure 2b. The relation between the square root of concentration and the equivalent conductance of $[Fe (C_9H_{11}NO_3)_3]Cl_2$ at different temperatures

Table 2c. Molar concentration (M) and Equivalent conductance of $[Mn(C_9H_{11}NO_3)_3]Cl_2$ in water at different temperatures

Conc. Mole/L*10^7	Λ (Ohm^{-1}.equive^{-1}.cm^2) 288.16 °K	Λ (Ohm^{-1}.equive^{-1}.cm^2) 293.16 °K	Λ (Ohm^{-1}.equive^{-1}.cm^2) 298.16 °K	Λ (Ohm^{-1}.equive^{-1}.cm^2) 303.16 °K	Λ (Ohm^{-1}.equive^{-1}.cm^2) 308.16 °K	Λ (Ohm^{-1}.equive^{-1}.cm^2) 313.16 °K
2.511813	129.0591	136.2342	130.475	127.288	134.4554	125.075
4.914812	120.6442	126.8353	120.872	114.005	124.9509	95.4786
7.384514	112.8486	116.3184	111.441	107.831	109.3058	89.1087
9.615788	103.9956	106.1697	102.569	100.205	100.9905	84.8022
12.01134	97.13045	100.0837	96.6024	99.459	94.97099	81.5334
14.39375	92.63277	95.80995	92.0740	98.4071	89.70667	75.3756
16.53605	90.71085	92.44804	90.3886	97.0306	88.50784	71.2534
18.78537	88.72146	89.94707	89.2522	96.4747	86.47475	69.2593
21.03257	87.16635	89.4364	87.0967	95.7865	85.18074	67.9267
23.18772	86.25257	88.00122	86.1609	95.0657	83.99399	66.1585
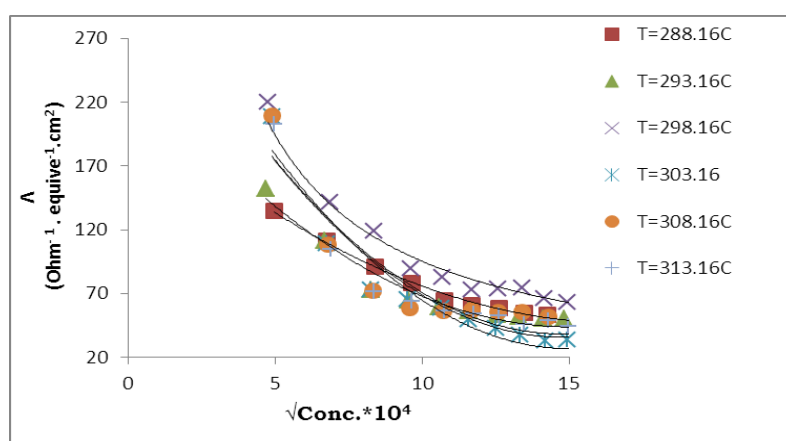
Figure 2c. The relation between the square root of concentration and the equivalent conductance of $[Mn (C_9H_{11}NO_3)_3]Cl_2$ at different temperatures

Table 2d. Molar concentration (M) and Equivalent conductance of $[Ni(C_9H_{11}NO_3)_3]Cl_2$ in water at different temperatures

Conc. Mole/L*10^7	Λ (Ohm^{-1}.equive^{-1}.cm^2) 288.16 °K	Λ (Ohm^{-1}.equive^{-1}.cm^2) 293.16 °K	Λ (Ohm^{-1}.equive^{-1}.cm^2) 298.16 °K	Λ (Ohm^{-1}.equive^{-1}.cm^2) 303.16 °K	Λ (Ohm^{-1}.equive^{-1}.cm^2) 308.16 °K	Λ (Ohm^{-1}.equive^{-1}.cm^2) 313.16 °K
2.472517	134.815	152.337	219.969	208.65	209.369	202.769
4.565327	111.262	111.262	141.322	109.20	108.038	104.586
7.05793	90.8423	72.9625	119.120	73.190	71.8239	71.2649
9.301885	77.9064	64.9064	89.7624	65.354	58.2693	63.6543
11.58103	64.5653	59.3859	82.4796	58.616	56.0497	56.0497
13.71313	60.7689	56.6456	73.0953	49.620	56.7080	54.0393
15.94772	58.7048	52.9220	73.6707	42.517	55.462	52.1944
18.21375	54.9035	51.5446	74.1549	37.465	55.6294	45.9321
20.38609	53.0530	50.1801	66.4267	33.077	51.9870	48.7971
22.63517	51.5422	50.0065	63.0171	33.349	51.8041	44.4636
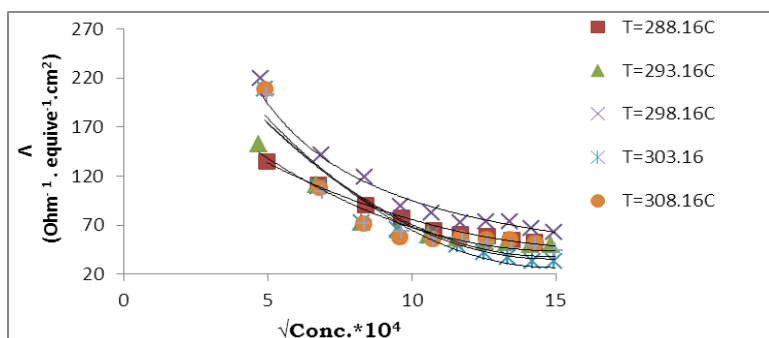
Figure 2d. The relation between the square root of concentration and the equivalent conductance of [Ni $(C_9H_{11}NO_3)_3$]Cl_2 at different temperatures

In Generally it can be observed the equivalent conductance (Λ) of Fe>Co>Ni>Mn compelexes gave higher value in the rang of temperatures between (293.16-303.16).   Probably because of the effect of the temperature on the properties of solution and with increase the degree of temperature decrease the density and the viscosity and may be increase association and decrease equivalent conductance (Λ) because effect of the asymmetric effect(or relaxation effect (Dabbagh and Akrawi, 1992)[10].

Tables 3(a-d) show the results of the analysis compelexes at different temperatures. where each table show the association constant (KA) and the equivalent conductance (Λ), the(R) values (distance parameter) and the best fit data standard deviation σs(Λ).

Table 3a. the values at constant Ka, Λ,the distance between R(A°) and $\sigma\Lambda$ of the[Co($C_9H_{11}NO_3$)$_3$]Cl_2 at different temperatures in water solvent

T(K)	Ka	Λ (Ohm^{-1}. equive^{-1}.cm^2)	R(A°)	$\sigma\Lambda$
288.16	1781	42	4	0.032
293.16	3201	45	8	0.015
298.16	9602	52	5	0.046
303.16	10440	35	4	0.112
308.16	11380	26	4	0.068
313.16	12001	18	8	0.063

Table 3b. the values at constant Ka, Λ,the distance between R(A°) and $\sigma\Lambda$ of the[Fe($C_9H_{11}NO_3$)$_3$]Cl_2 at different temperatures in water solvent

T(K)	Ka	Λ (Ohm^{-1}. equive^{-1}.cm^2)	R(A°)	$\sigma\Lambda$
288.16	5610	52	8	0.059
293.16	11010	36	7.9	0.063
298.16	14110	36	4	0.053
303.16	14502	34	4	0.116
308.16	15802	39	4	0.074
313.16	17702	18	8	0.047

Table 3c. the values at constant Ka, Λ,the distance between R(A°) and $\sigma\Lambda$ of the[Mn($C_9H_{11}NO_3$)$_3$]Cl_2 at different temperatures in water solvent

T(K)	Ka	Λ (Ohm^{-1}. equive^{-1}.cm^2)	R(A°)	$\sigma\Lambda$
288.16	16601	42	5	0.114
293.16	9810	46	8	0.073
298.16	8410	38	8	0.064
303.16	6610	42	8	0.026
308.16	6300	36	8	0.057
313.16	5910	20	4	0.069

Table 3d. the values at constant Ka, Λ,the distance between R(A°) and σΛ of the$[Ni(C_9H_{11}NO_3)_3]Cl_2$ at different temperatures in water solvent

T(K)	Ka	Λ (Ohm^{-1}.equive^{-1}.cm^2)	R(A°)	σΛ
288.16				
	42100	10	4	0.063
293.16				
	43701	5	8	0.138
298.16				
	45100	6	5	0.143
303.16				
	50100	3	8	0.069
308.16				
	58001	5	4	0.046
313.16				
	64810	3	4	0.045

In tables 3(a-d) the values of λM^{2+} deferent rom complex to another depend on the values of equivalent conductance (Λ) and Ka value of Ni>Mn>Co>Fe complexes because the electronic density of the element increase associations with decrease the radii of metal this mean that the solvent molecules will be attracted and thus ion association increase , The results of distance parameter R show that complexes electrolytes form solvent separated ion pairs (R is between4-8) these high values of R indicated that cations and anions are separated by many solvent molecules since the association was high with increase temperatures(Hemes ,P.J., 1974)[12]. The values of σΛ give an indication of good best-fit values (Akrawi,B.A. ,*et al*, 2008)[13].

Calculation of the thermodynamic parameters (ΔH, ΔG, ΔS)

The relation of lnKA against 1/T was shown in figure 3 (a-d) and the relation between them was illustrated by Vant-Hoff equation(Eggers *et al*., 1964)[14] .

$$lnKa = -\frac{\Delta H}{RT} + C$$

The relation gives a straight line for complex solutions, This behavior will be illustrated by the fact that the results of association depends on two opposite effects. The first one was the formation of ion pairs separated by solvent molecules (SSIP) and the other was the formation of contact ion pairs (CIP) (Dawod, 1995)[15]. The values of ΔH were calculated from Vant –Hoff equation and ΔG from the equation :

$\Delta G = - R T lnKA$
While ΔS values were calculated from the equation :
$\Delta G = \Delta H - T \Delta S$
From the tables below, the values of ΔH (enthalpy of association) were negative which show that the operation was hydration ,while ΔG (Gibbs free energy) has a negative values which depends upon the kind of ions and in agreement with the relation
$\Delta G = - RTLnKA$
which means that the reaction was spontaneous towards association , and the values of ΔS were also negative due to the negative values of ΔH which leads to the ordering of the system as a result of association under the influence of solvation and columbic effect in spontaneous continuum media (Nancollas, 1960)[16].

Table 4a. Thermodynamic parameters of $[Co(C_9H_{11}NO_3)_3]Cl_2$

T (K)	-ΔS (J.mol^{-1}.K^{-1})	-ΔG (KJ.mol^{-1})	-ΔH (KJ.mol^{-1})	Ln ka
288.16	140	17.92	58.13	7.485
293.16	131	19.66		8.071
298.16	119	22.72		9.17
303.16	115	23.31		9.253
308.16	111	23.92		9.34
313.16	108	24.44		9.393
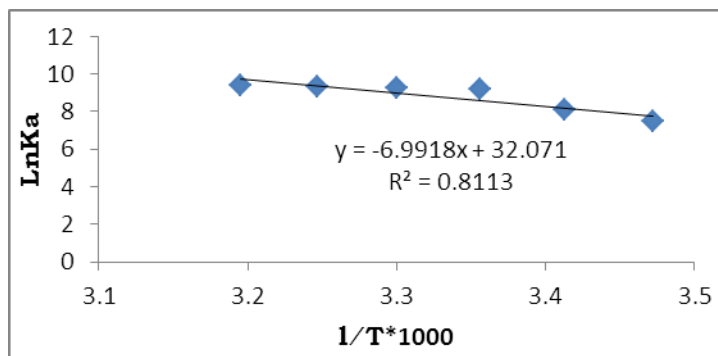
Figure 3a. The relation between the Ln ka &1/T of $[Co(C_9H_{11}NO_3)_3]Cl_2$

Table 4b. Thermodynamic parameters of $[Fe(C_9H_{11}NO_3)_3]Cl_2$

T (K)	$-\Delta S$ (J.mol^{-1}.K^{-1})	$-\Delta G$ (KJ.mol^{-1})	$-\Delta H$ (KJ.mol^{-1})	Ln ka
288.16			29.69	
	20.67	20.67		8.632
293.16				
	22.67	22.67		9.307
298.16				
	23.67	23.67		9.555
303.16				
	24.14	24.14		9.582
308.16				
	24.76	24.76		9.668
313.16				
	25.46	25.46		9.781
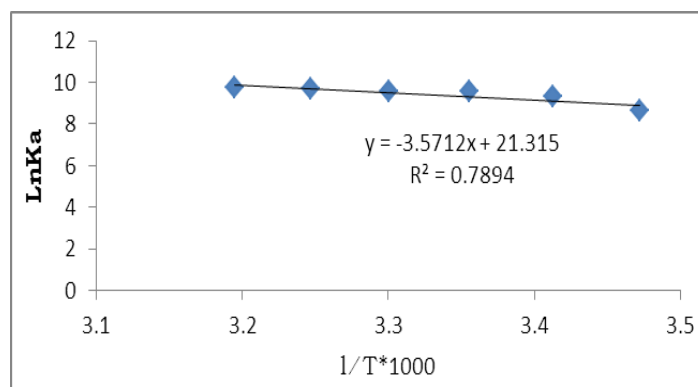
Figure 3b. The relation between the Ln ka &1/T of $[Fe(C_9H_{11}NO_3)_3]Cl_2$

Table 4c. Thermodynamic parameters of $[Mn(C_9H_{11}NO_3)_3]Cl_2$

T (K)	$-\Delta S$ (J.mol^{-1}.K^{-1})	$-\Delta G$ (KJ.mol^{-1})	ΔH (KJ.mol^{-1})	Ln ka
288.16			29.09	
	-20.2	23.27		9.717
293.16				
	-22.9	22.39		9.191
298.16				
	-22.5	22.39		9.037
303.16				
	-22.9	22.16		8.796
308.16				
	-21.7	22.4		8.748
313.16				
	-20.7	22.6		8.684
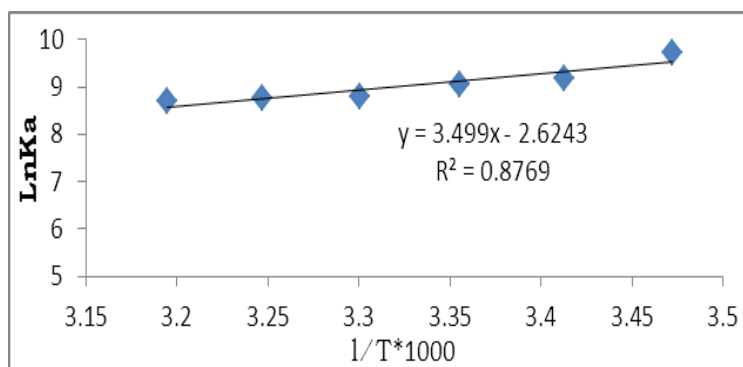
Figure 3c. The relation between the Ln ka &1/T of $[Mn(C_9H_{11}NO_3)_3]Cl_2$

Table 4d. Thermodynamic parameters of $[Ni(C_9H_{11}NO_3)_3]Cl_2$

T (K)	$-\Delta S$ $(J.mol^{-1}.K^{-1})$	$-\Delta G$ $(KJ.mol^{-1})$	$-\Delta H$ $(KJ.mol^{-1})$	Ln ka
288.16			13.24	
	42.55	25.5		10.65
293.16				
	43.64	26.03		10.69
298.16				
	44.66	26.55		10.72
303.16				
	46.27	27.26		10.82
308.16				
	48.2	28.09		10.97
313.16				
	49.81	28.83		11.08

Figure 3c. The relation between the Ln ka &1/T of $[Ni(C_9H_{11}NO_3)_3]Cl_2$

Conclusion

The present work reports conductivity data for the low concentration tyrosine solutions in water at 310.16 K. The electrical conductivities of Co , Fe , Mn , Ni complex with tyrosine in water at different temperatures were measured by using of lee-Wheaton equation at the best fit values of standard deviled (□□□□□for analyzing the data of unsymmetrical electrolytes including: The equivalent conductivity Λ , the association constant KA and the distance parameter R . The values differ from one complex to another depending on the interactions in solution and effect the electrophoretic , asymmetric effect and the type of metal.

Recommendations

The lee-wheaton equation is very important, it be used to determination of any ionic compound at very low concentration, with any solvent at different temperatures and give information about association constant

KA,equivalent conductivity at infinity dillution $\Lambda_\circ$ and the distance parameter R,Which is very important constant in Thermodynamic.Thermodynamic parameters can be calculated by using Vant-Hoff equation from association constant.

References

Hames,D. Hopper,N.(2005)" Biochemistry".Third edition.

Freemand,W.H. CO,N.(2001)"Exploring Chemical Analysis".

Adugna,S.Mekannen,L.A.(2004)"Medical Biochemistry".

Abdel –Rahman, H.A.(2007);M.Sc.Thesis, An Electrical Conductometric Study of Some Amino Acids and Their Complexes with Some Metals in Aqueous Medium at Different   Temperatures . Mosul University

Al-Allaf, Y.O.; Al-Tamer, M.Y. ; Abdulfattah, M.N.(2013). Conductometric Studies for Association Reaction of some Amino Acid complexes in Water.,*Raf.J.Sci*., 24, (6),(pp. 45-60).

Chernozhak,T. Kalugin,O. Conductivity and Interparticle Interactions in The Solutions of 1-1 Electrolytes in Propylene Carbonat in The wide range   of Temperatures , *Chemistry & Chemical Technologe* ,*10*,2016 Kolfutar,C. Segatin,N. (2007).Electrical Conductivity Studies of Quinic Acid and its Sodium Salt in Aqueous Solutions.J.Solution Chem,36,879-889.

Boškovi,p. Sokol,v. Tomaš,R.Prkic,A.(2013). Conductometric Study of Potassium Chloride in Ethanol -Water Mixtures . *Int. J. Electrochem. Sci., 8* **,** (pp**.**10961 – 10975)

Palmer, W.G. (1954). "Experimental Physical Chemistry". Cambridge at the University Press, London, 186 p.

Akrawi,B.A.,Hameed, Y.O.(2008),J.National.Chemistry,31,(pp.447-454).

Eggers, D.F.; Gregory, N.W.; Halsey, G.D.; Rabinovitch, B.S. (1964). "Physical Chemistry". John Wiley and Sons, Inc. New York, 198 p.

Eggers, D.F.; Gregory, N.W.; Halsey, G.D.; Rabinovitch, B.S. (1964). "Physical Chemistry". John Wiley and Sons, Inc. New York, 198 p.

Lee, W.H.; Wheaton, R.J.(1978) .Conductance of symmetrical, unsymmetrical and mixed electrolytes .J.C.S.Farady II,74,(pp.743-766).

Dabbagh, A.M.; Akrawi, B.A. (1992). "Kinetics and Electrochemistry".Dar Alkutub for printing and publishing, Mosul,(pp. 323-405).

Dawod, A.M. (1995). An application of the Lee_Wheaton Conductance Aquation To Single and Mixed (Symmetrical and Assymmetrical) Electrolytes in Different Media. Ph.D. Thesis, Mosul University, Iraq, 10 p.

Nancollas, G.H. (1966). "Interactions in Elctrolyte Solutions". Elsevier, Amsterdam, Tables A-1 and A-5.

Author Information

Fanar Al-healy	**Yasir Hameed**
Department of Chemistry	Department of Chemistry
College of Science,Mosul University	College of Science,Mosul University
Mosul/Iraq	Mosul/Iraq
Contact E-mail:Fm.alhealy@*gmail.com*	

IConTES 2019: International Conference on Technology, Engineering and Science

Synthesis of Triazole-Coupled Quinoline-Based Fluorescent Sensor

Aysegul GUMUS
Van Yuzuncu Yil University

Selcuk GUMUS
Van Yuzuncu Yil University

Abstract: Fluorescent sensor is one of the most important chemical sensors and is a powerful tool for imaging target molecules and ions in the living organism. Because it has high sensitivity and simultaneous imaging. In this work, fluorescence chemosensor was designed based on ionophore-bridge-fluorophore approach. In the structure of the designed chemosensor, anthracene unit was used as fluorophore. The receptoric hydroxy quinoline group to interact with the metal ion were incorporated into the structure by the triazole bridge which has high coordination properties. Detection of a specific type of a metal is very important in terms of biouse of the related compound. In addition to the synthetic approach, the metal coordination propertiess of the novel chemosensors will be investigated theoretically at the level of Density Functional theory with the application of B3LYP/6-31++G(d,p), which is a combination of hibrit exchange function and basis set.

Keywords: Fluorescent Sensor, Anthracene, Triazole

Introduction

In recent years, more and more attentions have been drawn to devise ingenious fluorescent sensors capable of selective recognition and effectively detecting the presence of alkali, alkaline earth and transition metal ions because of their importance in biological systems as well as to environmental concerned [1,2]. However, among different chemosensors, fluorescence-based ones present many advantages as fluorescence measurements are usually very sensitive, low cost, easily performed and versatile, offering subnanometer spatial resolution with submicron visualization and submillisecond temporal resolution [3,4].

8-Hydroxyquinoline is one of the widely used chelating moieties for metal ion coordination, and quite a number of chemically modified 8-hydroxyquinoline derivatives have been used as metal binding probes [5-9]. 8-HQ was introduced into fluorescent probes acting as a metal ion chelating agent for metal ions detection. Triazole substituted 8-HQ could furnish an extra binding site, and might inhibit the possible excited-state intramolecular proton transfer (ESIPT) event.

The chemistry of 1,2,3-triazole derivatives has gained interest over the past few years due to their wide range of applications in chemical, biological, medicinal, and materials science. The Huisgen 1,3-dipolar cycloaddition of azides and alkynes is the most efficient pathway for the synthesis of substituted 1,2,3-triazoles as chemotherapeutic agents [10-11], synthetic intermediates for bioactive compounds, agrochemicals, optical brighteners, photostabilizers, anticorrosive agents, and metal chelators [12-14]. The extraordinary stability toward metabolic transformations and aromatic nature of the triazole ring along with its high dipole moment and H-bonding capability, makes it an important functionality as a connecting group [15-18].

In the present study, the synthetic typical motif consist of a core fluorescent signaling unit of anthracene, which is well connected with oxyquinoline through triazole bridge, to generate a suitable ionophore site that has great affinity to coordinate with a metal ion.

Method

General

All the chemicals used in the biologic assay studies were purchased from Sigma (Sigma-Aldrich GmbH, Sternheim, Germany). ^{1}H NMR and ^{13}C NMR spectra were recorded in CDCl$_3$ on a Agilent NMR spectrometer (400 MHz). ^{1}H (400 MHz) and ^{13}C NMR (100 MHz) were recorded in CDCl$_3$ and the chemical shifts are expressed in ppm relative to CDCl$_3$ (δ 7.26 and 77.0 for ^{1}H and ^{13}C NMR, respectively) as the internal standard.

Flash column chromatography was performed by using thick-walled glass columns and silica gel (60-mesh; Merck). The reactions were monitored by thin-layer chromatography (TLC) using Merck 0.2-mm silica gel 60 F254 analytical aluminium plates, visualized by UV light.

Synthesis of Fluorescent Sensor

8-(prop-2-ynyloxy)quinoline-2-carbaldehyde, **2.**

8-hydroxyquinoline-2-carbaldehyde (1.0 g, 5.7 mmol) was dissolved in 30 mL THF. K$_2$CO$_3$ (2.0 g, 15 mmol) was added and the mixture was refluxed for 30 min. Then, propargyl bromide (1 mL, 6.8 mmol) was added slowly. Reaction mixture was refluxed overnight. After TLC control, reaction mixture was cooled and filtered. Solvent was evaporated under vacuum and crude product was purified by flash column chromatography (EtOAc: Hexane 1:4).

White solid. (1.03 g, 86% yield); ^{1}H NMR (CDCl$_3$, 400 MHz): δ 10.28 (s, 1H), 8.27 (dd, *J*=0.7 and 8.5 Hz, 1H), 8.04 (d, *J*=8.5 Hz, 1H), 7.63-7.59 (m, 1H), 7.50 (dd, *J*=1.2 and 8.3 Hz, 1H), 7.34 (dd, *J*=1.2 and 7.8 Hz, 1H), 5.08 (d, *J*=2.4 Hz, 2H), 2.57 (t, *J*=2.4 Hz, 1H); ^{13}C NMR (CDCl$_3$, 100 MHz): δ 193.6, 153.7, 151.6, 140.0, 137.3, 131.4, 129.4, 120.6, 117.9, 111.0, 77.8, 76.6, 56.9.

9-(azidomethyl)anthracene, **4.**

9-(Chloromethyl)anthracene (227 mg, 1 mmol) ve NaN$_3$ (130 mg, 2 mmol) were dissolved in 20 mL CH$_3$CN and refluxed overnight at 85 °C. After all starting compounds were consumed, reaction mixture was filtered and solvent was evaporated under vacuum. Crude product was purified by flash column chromatography by EtOAc:Hexane mixture (1:15).

Yellow solid. (228 mg, 98% yield); ^{1}H NMR (CDCl$_3$, 400 MHz): δ 8.51 (s, 1H), 8.32-8.28 (m, 2H), 8.07-8.06 (m, 1H), 8.05-8.04 (m, 1H), 7.62-7.58 (m, 2H), 7.54-7.50 (m, 2H), 5.33 (s, 2H); ^{13}C NMR (CDCl$_3$, 100 MHz): δ 131.4, 130.7, 129.3, 129.0, 126.8, 125.8, 125.2, 123.5, 46.3.

8-((1-(anthracen-9-ylmethyl)-1H-1,2,3-triazol-4-yl)methoxy)quinoline-2carbaldehyde, **5.**

8-(prop-2-ynyloxy)quinoline-2-carbaldehyde, **2** (211 mg, 1 mmol) and 9-(azidomethyl)anthracene, **4** (233 mg, 1 mmol) were dissolved in 5 mL THF:H$_2$O (4:1). CuSO$_4$.5H$_2$O (25 mg, 0.1 mmol) and sodium ascorbate (40 mg, 0.2 mmol) were added and reaction mixture was mixed overnight at room temperature. After the reaction was complete, water was added and extracted with EtOAc. Product was purified by flash column chromatography by EtOAc:Hexane (1:1) .

Yellow solid. (360 mg, 81% yield); ^{1}H NMR (CDCl$_3$, 400 MHz): δ 9.98 (s, 1H), 8.57 (s, 1H), 8.30-8.28 (m, 2H), 8.21-8.19 (m, 1H), 8.08-8.06 (m, 2H), 7.96 (d, *J*=8.5 Hz, 1H), 7.60-7.50 (m, 5H), 7.43-7.40 (m, 2H), 7.36-7.34 (m, 1H), 6.55 (s, 2H), 5.41 (s, 2H); ^{13}C NMR (CDCl$_3$, 100 MHz): δ 193.6, 154.6, 151.3, 143.7, 140.0, 137.2, 131.4, 131.2, 130.7, 130.0, 129.7, 129.5, 127.7, 125.4, 123.5, 123.0, 122.9, 120.2, 117.7, 111.3, 63.5, 46.5.

Computational Method

The three-dimensional ground state (S_0) geometry of the compound was geometry optimized using Density Functional Theory (DFT) by using the Gaussian 09W package program and the hybrid functional B3LYP. The B3LYP is composed of Becke's three parameter exchange functional (B3) and the nonlocal correlation functional by Lee, Yang, and Parr (LYP). The basis set used for all atoms was 6-31++G(d,p) in both DFT and time-dependent density functional theory (TD-DFT) method. We have applied default G09 grid for computations.

For the nonel compound, vibrational analyses were carried out using the same basis set employed in the corresponding geometry optimizations. The frequency analysis of none of the compounds yielded any imaginary frequencies, indicating that the structure of each molecule corresponds to at least a local minimum on the potential energy surface. The normal mode analysis was performed for 3N-6 vibrational degrees of freedom, N being the number of atoms in the molecule.

The low-lying triplet (T) and singlet excited states (S) of the compounds were relaxed to obtain their minimum energy geometries using the TD-DFT as implemented in G09 package program. The vertical excitation energies and oscillator strengths were obtained for the lowest triplet and singlet transitions at the optimized ground state equilibrium geometries by using TD-DFT at the same hybrid functional and basis set [22]. Optimized ground state structures were utilized to obtain the electronic absorption spectra, including maximum absorption wavelengths, oscillator strengths, and main configuration assignment by using TD-DFT.

Results and Discussion

The present molecular probe containing quinoline and anthracene fluorophores has been synthesized. The synthetic route adopted for preparation of **5** is shown in Scheme 1. Click chemistry, serving as a linking strategy for the 1, 3 dipolar cycloaddition of alkynes and azide by generating 1, 2, 3-triazoles, has been exploited in the wide variety of areas including bio conjugation, drug design and material chemistry. Meanwhile, the 1,2,3-triazole linker could be exploited for the binding of cations which might be useful in the recognition of metal ions. Based on this statement, the probe **5** was designed (Scheme 1). This could be easily synthesized using the anthracene azide **4** and alkyne of 8-oxyquinoline, **2** in the presence of $CuSO_4$ as a catalyst.
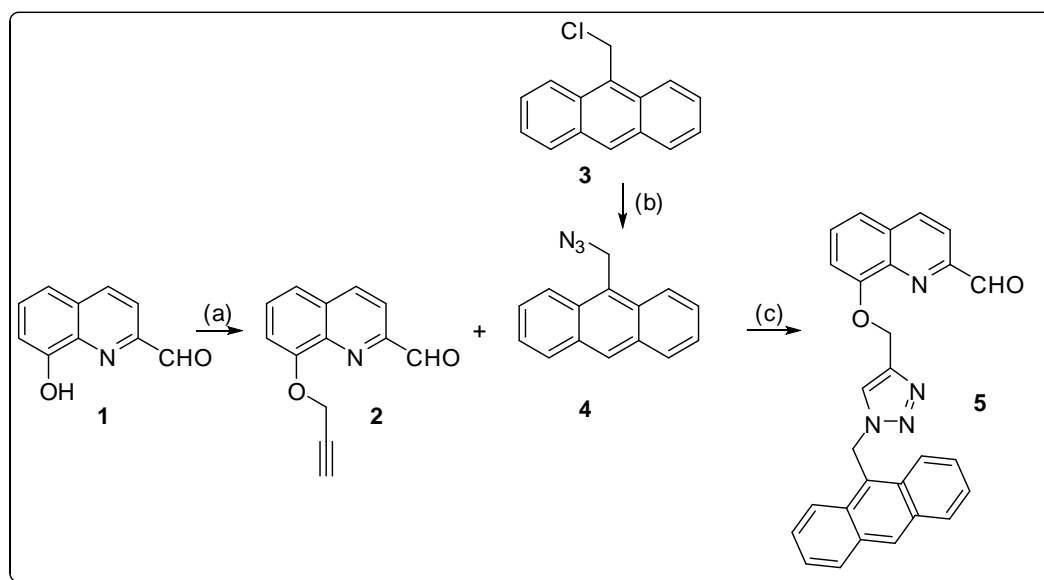
Scheme 1. (a) Propargyl bromide, K_2CO_3, THF; (b) NaN_3, THF; (c) $CuSO_4$, sodium ascorbate
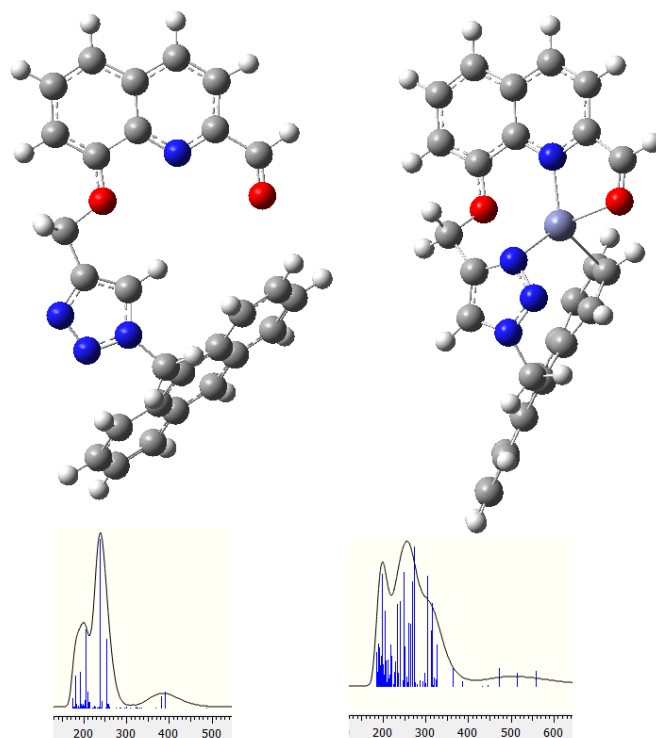
Figure 1. Geometry optimized structures and corresponding UV-VIS spectra of the compounds

Geometry optimizations of the compounds have been performed by the aforementioned method and corresponding UV-VIS spectra have been obtained by the application of TDDFT calculations. Metal coordination has been proven by the change in the UV-VIS spectra since some of the bands faced a red-shift. Upon coordination with the metal (Zn^{2+}) the triazole moiety moved toward the metal to make the coordination stronger.
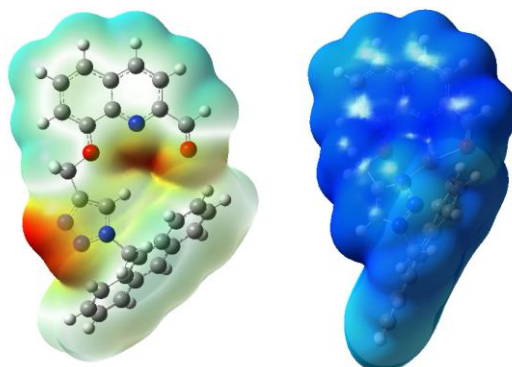
Figure 2. 3D electrostatic potential map for the present compounds.

3D electrostatic potential maps for the compounds indicate that upon coordination of the +2 charged metal cation the charge distribution in the compound changed completely a more uniform charge distribution has been obtained.

Conclusion

In conclusion, propargyl unit was attached to 8-OH of quinoline by O-propargylation and alkyne derivative was obtained. Then, anthracene azide was coupled with this quinoline-alkyne derivative in the presence of Cu(I) catalyst by forming triazole bridge and a novel fluorescent sensor was isolated in good yield. Computational calculations proved the coordination of the metal cation through changes in the electronic spectra and charge distribution in the system.

Acknowledgements

References

Krämer, R. (1998). Fluorescent Chemosensors for Cu^{2+} Ions: Fast, Selective, and Highly Sensitive. *Angew. Chem. Int. Ed*. 37, 772–773.

Uauy, R., Olivares, M., Gonzalez, M. (1998). Essentiality of copper in humans. *Am. J. Clin. Nutr.* 67, 952–959.

de Silva, A. P., Gunaratne, H. Q. N., Gunnlaugsson, T., Huxley, A. J. M., McCoy, C. P., Rademacher, J. T., Rice, T. E.(1997). Signaling Recognition Events with Fluorescent Sensors and Switches. *Chem. Rev*. 97, 1515–1566.

Czarnik, A.W. (1992). *Fluorescent Chemosensors for Ion and Molecule Recognition*, first ed., A.C.S, Washington.

Chen, Y., Wan, L., Yu, X., Li, W., Bian, Y. and Jiang, J. (2011). Rational Design and Synthesis for Versatile FRET Ratiometric Sensor for Hg^{2+} and Fe^{2+}: A Flexible 8-hydroxyquinoline Benzoate Linked Bodipy-Porphyrin Dyad. *Org. Lett.*, 13, 5774-5777.

Jotterand, N., Pearce, D. A. and Imperiali, B. (2001). Asymmetric Synthesis of a New 8-Hydroxyquinoline-Derived α-Amino Acid and Its Incorporation in a Peptidylsensor for Divalent Zinc. *J. Org. Chem.*, 66, 3224-3228.

Zhao, Y., Lin, Z., Liao, H., Duan, C. and Meng, Q. (2006). A highly selective fluorescent chemosensor for Al3+ derivated from 8-hydroxyquinoline. *Inorg. Chem. Commun.,* 9, 966-968.

Li, Z., Xi, P., Huang, L., Xie, G., Shi, Y., Liu, H., Xu, M., Chen, F. and Zeng, Z. (2011). A highly selective fluorescent chemosensor for Cd(II) based on 8-hydroxyquinoline platform. *Inorg. Chem. Commun.,* 2011, 14, 1241-1244.

Tian, H., Li, B., Wang, H., Li, Y., Wang, J., Zhao, S., Zhu, J., Wang, Q., Liu, W., Yaoa, X. and Tang, Y. (2011). A nanocontainer that releases a fluorescence sensor for cadmium ions in water and its biological applications. *J. Mater. Chem.*, 21, 10298-10304.

Huisgen, R. (1984). 1,3-Dipolar Cycloaddition–Introduction, Survey, Mechanism. In *1,3-Dipolar Cycloaddition Chemistry*. Padwa, A., Ed. Wiley: New York.

Agalave, S. G., Maujan, S. R., Pore, V. S. (2011). Click chemistry: 1,2,3-triazoles as pharmacophores. *Chem. Asian J.*, 6, 2696–2718.

Krivopalov, V. P., Shkurko, O. P. (2005), 1,2,3-Triazole and its derivatives. Development of methods for the formation of the triazole ring. *Russian Chem. Rev.*, 74, 339–379.

Yet, L. (2004). Progress in Heterocyclic Chemistry; Elsevier, Oxford, UK.

Katritzky, A. R., Zhang, Y., Singh, S. K. (2003). 1,2,3-Triazole formation under mild conditions via 1,3-dipolar cycloaddition of acetylenes with azides. *Heterocycles*, 60, 1225–1239.

Seo, T. S., Li, Z., Ruparel, H., Lu, J. (2003). Click chemistry to construct fluorescent oligonucleotides for DNA sequencing. *J. Org. Chem.*, 68, 609–612.

Sivakumar, K., Xie, F., Cash, B. M., Long, S., Barnhill, H. N. (2004). A fluorogenic 1,3-dipolar cycloaddition reaction of 3-azidocoumarins and acetylenes. *Org. Lett.* 6, 4603–4606.

Dondoni, A., Marra, A. (2006). *C*-Glycoside clustering on calix[4]arene, adamantane, and benzene scaffolds through 1,2,3-triazole linkers. *J. Org. Chem.*, 71, 7546–7557.

Hota, S., Kashyap, S. (2006). "Click chemistry" inspired synthesis of *pseudo*-oligosaccharides and amino acid glycoconjugates. *J. Org. Chem.* 71, 364–367.

Author Information

Aysegul Gumus	**Selcuk Gumus**
Van Yuzuncu Yil University	Van Yuzuncu Yil University
Department of Chemistry, Van 65080, Turkey	Department of Chemistry, Van 65080, Turkey
Contact E-mail: *gumusa@gmail.com*	

Methyl α-[(4-oxoquinazolin-2-yl)thio]acetate as Precursor to New Heterocyclic Compounds

Hiba Amin AL-ALAAF
University of Mosul

Mohammed Ahmed AL-IRAQI
University of Mosul

Abstract: Methyl α-[(4-oxoquinazolin-2-yl)thio]acetate (3) is one of the important heterocyclic compounds. It is used as a precursor to synthesize new derivatives of quinazolin-4-one moiety. The compound (4) was synthesized *via* a series of steps from anthranilic acid. Firstly, the anthranilic acid was converted to its methyl ester (1) by esterification with methanol under acidic condition. The ester (1) was reacted with chloroacetyl chloride to produce methyl α-chloroacetamido benzoate (2). The chloro compound (2) was converted to the to the target precursor (3) by boiling of the chloro compound (2) with ammonium thiocyanate for 12 h. The compound (3) was used as synthon to synthesize new series of five membered ring heterocyclic derivatives, *via* its conversion to the corresponding acid hydrazide (4). The acid hydrazide (4) was reacted with carbon disulfide under boiling condition to produce 1,3,4-oxadiazole-5-thione derivative (5). The oxadiazole compound (5) was reacted with alkyl halides to afforded the corresponding alkylthio compounds (6-11), and with aromatic aldehydes to afforded the carbinol derivatives (12-18). The synthesized compounds were identified *via* the physical and spectral data.

Keyword: 2-Mercaptoquinazolin-4-one, Methyl 2-chloroacetaminobenzoate, Methyl anthranilate, 1,3,4 Oxadiazol, Alkylthio derivatives, Acetohydrazide compounds

Introduction

Quinazolin-4(3)-one is one of most important nucleus in heterocyclic chemistry owing to its participation in building block enormous number of biologically active compounds, by incorporation of the quinazolin-4(3)-one nucleus with deffirent heterocyclic moieties, such as triazole, thiadiazole and oxadiazole moieties. These compounds have been entice the medicinal chemists to find and design novel structures having pharmacological activity (Vijai Anand etal., 2009)[1]. Quinazolin-4(3H)-one derivatives showed diversity of biological activity such as analgesic, anti-inflammatory (Bhalla et al ;1993),[2] anti-hypertensive (Kotto et al; 1985),[3] anti-histaminic, anti-cancer (Brana et al; 1994),[4] (Boyle et al; 1993),[5] (Parasharya and Parkh, 1994),[6] anti-tumor (Al-Omary et al; 2012),[7] sedative, hypnotic and anti-microbial activity (Khalil; 1989)[8] (Vogel's; 1994),[9] anti-leishmanial activity (Agarwal et al; 2009)[10] and as anti-oxidant (Decker; 2008).[11] So, the previous views encouraged us to synthesize novel compounds containing quinazolin-4(3H)-one nucleus incorporated with oxadiazole moiety starting from methyl α-[(4-oxoquinazolin-2-yl)thio]acetate.

Experimental

Melting points were recorded on a Stuart melting point SMP30 apparatus and were uncorrected. IR spectra were recorded as neat using Bruker system 2000 FT.IR spectrophotometer. 1H NMR spectra were measured on a Bruker DPX(400) super conducting NMR Spectrometer (400 MHz) using DMSO-d6 as a solvent and TMS as an internal standard.

Synthesis of methyl anthranilate (1) (Bhasker et al.1996)[12]

A solution of anthranilic acid (0.1mol, 14.7 g) in absolute methanol (250 ml) was cooled to 0-5 ^{o}C, then a concentrated sulfuric acid (20 ml) was added dropwise with stirring. After the addition was completed, the mixture was refluxed for 72 h. The volatile components were evaporated under reduced pressure. A cold water (100 ml) was added to the residue. The mixture was basified by dropwise addition of (5 %) sodium bicarbonate solution, then the resulted mixture extracted with (20 * 30 ml) dichloromethane. The organic layers were collected, dried over magnesium sulfate, then evaporated. The crude product was recrystallized from methanol to give red crystals in 85% yield: melting point 22-23 ^{o}C. IR spectrum (neat, ν Cm^{-1}): 3369 (N-H), 1704 (C=O), 1604 (C=C), 1442 (CH3), 1245 (C-O). 1H NMR (DMSO-d6) (δ, ppm): 3.39 (s, 3H, CH3), 6.66 (s, 2H, NH2), 6.53 (t, 1H, H5), 6.79 (d, 1H, H3), 7.25 (t, 1H, H4), 7.71 (d, 1H, H6).

Methyl N-(α-chloroacetyl)anthranilate (2) (Behbehani and Ibrahim, 2013)[13]

To a solution of methyl anthranilate (0.01mol, 1.52 g) in chloroform (50 ml), chloroacetyl chloride (0.012 mol, 1.36 g) and potassium carbonate (0.015 mol, 2.1 g) were added. The reaction mixture was refluxed for 12 h. the volatile material was evaporated under reduced pressure. The residue was washed thoroughly with water then with 5% sodium bicarbonate solution and finally with water. The resulted product was dried then recrystallized from ethanol to give white crystals, in 98% yield, m.p. 90-91 oC, IR (neat, ν, cm -1): 3194 (N-H), 1682, 1676 (2C=O), 1441 (CH3),1226 (C-O). 1H NMR (DMSO-d6): δ, ppm: 3.89 (s, 3H, CH$_3$), 4.45 (s, 2H, CH$_2$), 7.27 (t, 1H, H5) , 7.66 (t, 1H, H4), 7.99 (d, 1H, H3), 8.40 (d, 1H, H6), 11.33 (s,1H, NH).

Synthesis of methyl α-[(4'-oxoquinazolin-2'-yl)thio]acetate (3):

To a solution of methyl 2-(α-chloroacetamino)benzoate (2) (0.01 mol, 2.27 g) in methanol (30 ml), ammonium thiocyanate (0.015 mol, 1.15 g) was added with stirring. The mixture was refluxed for 12h then cooled to room temperature. The resulted precipitate was filtered off, washed with water, dried then recrystallized from methanol to give pale yellow crystals in 98 % yield, m.p. 191-192 ^{o}C. IR (neat, ν,cm $^{-1}$): 3170 (N-H), 1734, 1682 (2C=O), 1375 (CH$_3$), 681 (C-S). 1H NMR (DMSO-d6): δ, ppm: 3.69 (s, 3H, CH$_3$), 4.11 (s, 2H, CH$_2$), 7.4 (t, 1H, H6) , 7.75 (t, 1H, H7), 7.98 (d, 1H, H5), 8.23 (d, 1H, H8), 11.14 (s,1H, NH).

Synthesis of α-[4'-oxoquinazolin-2'-yl)thio]acetohydrazide (4):

A solution of methyl α-(4'-oxoquinazolin-2'-yl)thio]acetate (3) (0.01 mol, 2.64 g), hydrazine hydrate (99.5 %) (0.015 mol, 0.75 g) in absolute ethanol (30 ml) was refluxed with stirring for 12 h. The solid product was separated by filtration, washed with cold water, dried, then recrystallized from ethanol to give green crystals in 90 % yield, m.p. 248 ^{o}C. IR (neat, ν, cm-1): 3289, 3128 (NH$_2$, N-H), 1662 (2 C=O), 682 (C-S). ^{1}H NMR (DMSO-d6): δ, ppm: 4.41 (s, 2H, CH$_2$), 5.43 (s, 2H, NH$_2$) (D$_2$O exchangeable), 5.88 (s, 1H, NNH), 7.14 (t, 1H, H6), 7.31 (d,1H, H5), 7.70 (d, 1H, H8), 7.48 (t, 1H, H7), 8.23 (s, 1H, H3).

Synthesis of 5-[(4'-oxoquinazolin-2'-yl)thiomethyl]-1,3,4-oxadiazol-2-thiole (5) (Behbehani and Ibrahim, 2013)[13]

To a solution of potassium hydroxide (0.01 mol, 0.65 g) in absolute ethanol (100 ml), the acetohydrazide (4) (0.005, 1.25 g) was added with stirring, followed by carbon disulfide (0.02 mol, 1.52 g). The mixture was refluxed for about 24h or until the release of H$_2$S was ceased (using lead acetate paper). The volatile materials were evaporated and the residue was added to a crushed ice. The mixture was acidified with diluted hydrochloric acid and the precipitate was filtered off, washed thoroughly with water, dried and recrystallized from ethanol to give yellow crystals in 85 % yield, m.p. 213-215 ^{o}C. IR (neat, ν, cm^{-1}): 3148, 3183 (N-H),1685(C=O); 1234 (C=S). ^{1}H NMR (DMSO-6d): δ, ppm: 4.56 (s, 1H, CH$_2$), 7.34 (t, 1H, H6), 7.38 (d,1H, H5), 7.79 (t, 1H, H7), 8.45 (d, 1H, H8), 10.2 (d, 1H, SH).

Synthesis of of 5-[(4'-oxoquinazolin-2'-yl)thiomethyl]-1,3,4-oxadiazol-2-alkylthiole (6-11)

A solution of 5-[(4'-oxoquinazolin-2'-yl)thiomethyl]-1,3,4-oxadiazol-2-thiole (5) (0.01mol, 0.3 g) and (0.01 mol) of alkyl halide (methyl iodide or other alkyl bromide) in (25 ml) methanol was refluxed for 10 h, then cooled and poured on ice water (50 ml). The precipitate was filtered off, washed with water, dried then recrystallized from ethanol . The physical and the IR spectral data of compounds (6-11) were listed in Table 1.
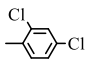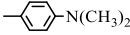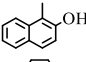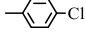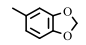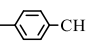
Table 1. The physical and IR spectral data of compounds (6-11)

Compd. No.	R	Yield %	m.p. °C	color	IR (neat, v, Cm^{-1})		
					C=O	C=N	N-H
6	CH_3-	98	235-237	green	1689	1632	3080
7	$CH_3CH_2CH_2CH_2$-	85	179-180	White	1680	1639	3090
8	CH_2=CH-CH_2-	98	195-197	Green	1685	1636	3108
9	ph-$COCH_2$-	98	167-169	Orange	1683	1635	3082
10	phCH_2-	98	269-270	White	1688	1635	3107
11	2-Br-phCH_2-	95	230-231	Yellow	1681	1633	3108

Synthesis of 5-[(4'-oxoquinazolin-2'-yl)thiomethyl]-2-(subistituted carbinol)-1,3,4-oxadiazol-2-thione (12-18):[12]

To an ice cooled solution of 5-[(4'-oxoquinazolin-2'-yl)thiomethyl]-1,3,4-oxadiazol-2-thiole (5) (0.02 mol, 0.3 g) in (50 ml) of ethanol, an aldehyde (0.02 mol) was added with stirring. The stirring was continued for further 10 h. The resulted precipitate was filtered off, washed with cold ethanol then recrystallized from ethanol. The physical and the IR spectral data of compounds (12-18) were listed in Table 2.

Table 2. The physical and chemical properties of compounds (12-18).

Compd. No.	R'-	Yield %	m.p. °C	color	IR (neat) , v (Cm^{-1})			
					C=N	C=O	C=S	O-H
12	H-	90	345-346	light yellow	1604	1672	1205	3393
13	Cl / -Cl (dichlorophenyl)	90	296-297	white	1606	1674	1207	3389
14	-N(CH_3)$_2$ (phenyl)	90	268-269	brown	1602	1668	1210	3399
15	-OH (naphthyl)	90	235-237	yellow	1611	1675	1212	3390
16	-Cl (phenyl)	90	256-257	brown	1610	1670	1202	3377
17	dioxole (phenyl)	90	295-296	white	1608	1678	1208	3392
18	-CH_3 (phenyl)	90	287-288	white	1606	1665	1209	3378

Result and Discussion

The synthetic route of the quinazolin-4(3H)-one derivatives (3-18) was illustrated in Scheme 1. The primal precursor for these heterocyclic compounds is α-[(4'-oxoquinazolin-2-yl)thio]acetohydrazide (4). This compound was synthesized from anthranilic acid via four steps. The anthranilic acid was converted to its methyl ester through
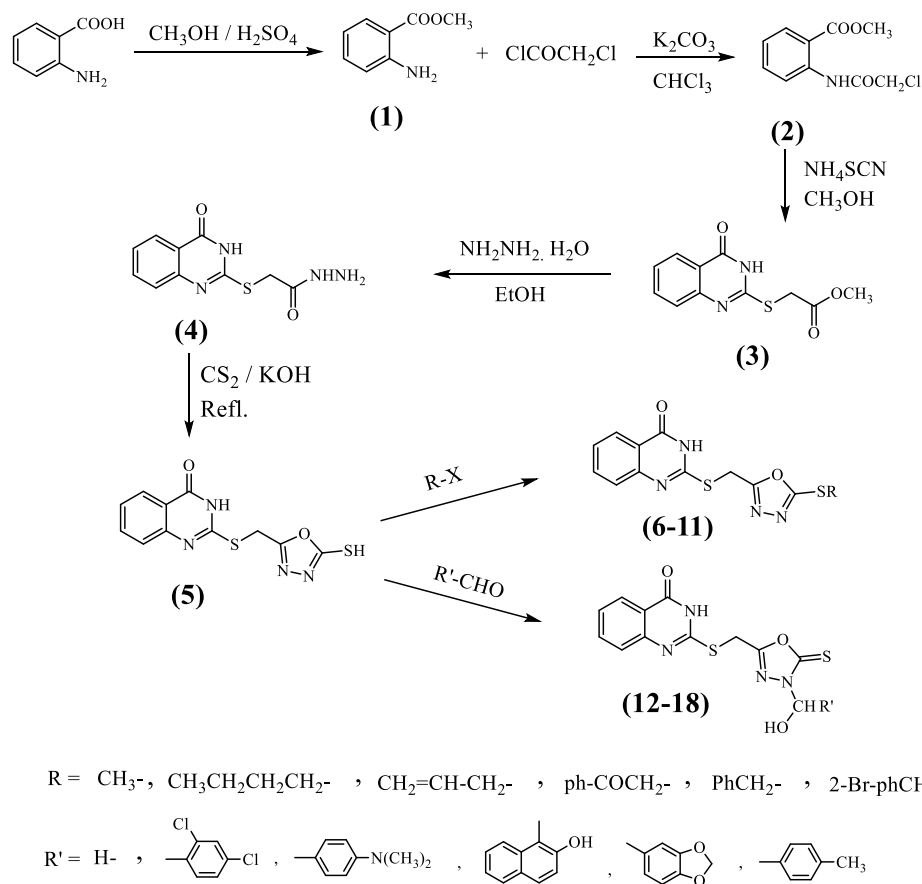
Scheme 1

the conventional acid catalyzed esterification method. The ester (1) was reacted with chloroacetyl chloride in the presence of potassium carbonate as a base to afford methyl 2-(α-chloroacetamino)benzoate (2). The ^{1}H NMR spectrum of compound (2) showed the following chemical shifts (δ, ppm): 3.89 (s, 3H, CH_3), 4.45 (s, 2H, CH_2), 7.27 (t, 1H, H5) , 7.66 (t, 1H, H4), 7.99 (d, 1H, H3), 8.40 (d, 1H, H6), 11.33 (s,1H, NH) [Crews et al, 1998].[14] The reaction of compound (2) with ammonium thiocyanate in absolute ethanol under reflux for 12 h afforded methyl α-[(4-oxoquinazolin-2-yl)thio]acetate (3) via the formation and cyclization of un-isolated methyl 2-(α-thiocyanato acetamino)benzoate (I) as an intermediate compound.
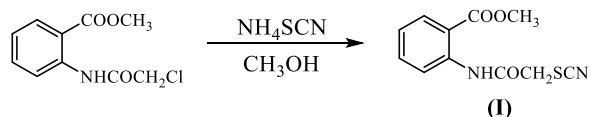
The IR spectrum of the quinazolinone compound (3) showed IR absorption bands at 3170 Cm^{-1} for the N-H bond stretching of the quinazolinone nucleus, and two absorption bands at 1734, 1682 Cm^{-1} for the C=O bond stretching of the ester and the amide respectively. The proton NMR spectrum of compound (3) showed the following chemical shifts (δ, ppm): 3.69 (s, 3H, CH_3), 4.11 (s, 2H, CH_2), 7.4 (t,1H, H6), 7.75 (t, 1H, H7), 7.98 (d, 1H, H5), 8.23 (d, 1H, H8), 11.14 (s, 1H, NH). The ester (3) was converted to the corresponding hydrazide compound (4) by its refluxing with hydrazine hydrate in absolute ethanol. The absence of the C=O bond stretching of the ester at 1704 Cm^{-1} indicates the full conversion of the ester (3) to the hydrazide (4). The ^{1}H NMR spectrum of the hydrazide (4) (DMSO-d6) showed the following chemical shifts: δ, ppm: 4.41 (s, 2H, CH_2), 5.43 (s, 2H, NH_2), 5.88 (s, 1H, NNH), 7.14 (t, 1H, H6), 7.31 (d,1H, H5), 7.70 (d, 1H, H8), 7.48 (t, 1H, H7), 8.23 (s, 1H, H3). The hydrazide (4) was used as precursor to synthesize the posterior heterocyclic compounds (5-18). Firstly, the hydrazide (4) was reacted with carbon disulfide in presence of ethanolic potassium hydroxide solution to give 5-[(4'-oxoquinazolin-2'-yl)thiomethyl]-1,3,4-oxadiazol-2-thiole (5). This compound was present in a tautomeric thiol-thione equilibrium as indicated from the IR and ^{1}H NMR spectra. It present as thione in the solid state, while present as thiol in the solution. The IR spectrum of the oxadiazole compound (5) showed absorption bands at 3148, 3183 Cm^{-1} for the (N-H) bond stretching of quinazolinone and

oxadiazole moieties respectively, at 1685 for the (C=O) bond stretching and at 1234 for the (C=S) bond stretching. The ^{1}H NMR (DMSO-6d) spectrum of compound (5) showed the following chemical shifts: δ, ppm: 4.56 (s, 1H, CH$_2$), 7.34 (t, 1H, H6), 7.38 (d, 1H, H5), 7.48 (t, 1H, H7), 7.82 (d, 1H, H8), 8.21 (s, 1H, H3), 10.2 (d, 1H, SH). Furthermore, two series of derivatives were prepared from the 1,3,4-oxadiazol-5-thiole compound (5). The first one involves the reaction of compound (5) with different alkyl halides to synthesize the alkyl thio derivatives (6-11). This reaction takes place *via* S$_N$2 mechanism. These compounds showed an absorption bands in the IR spectra at 1680-1689 Cm^{-1} for C=O bond stretching, in addition to absorption band at 1704 Cm^{-1} for the ketonic C=O bond stretching related to compound (9), and at 1632-1639 Cm^{-1} for C=N bond stretching. The [1]H NMR (DMSO-6d) spectrum of compound (6) showed the following chemical shifts: δ, ppm: 2.63 (s, 3H, CH$_3$), 3.90 (s, 2H, CH$_2$), 7.47 (d, 1H, H5), 7.73 (t, 1H, H6), 7.85 (t, 1H, H7), 7.93 (d, 1H, H8), 8.29 (s, 1H, H3). The [1]H NMR (DMSO-6d) spectrum of compound (8) showed the following chemical shifts: δ, ppm: 1.24 (d, 2H, allylic CH$_2$), 3.90 (s, 2H, CH$_2$), 4.09 (d, 1H, =CH), 6.1 (d, 2H, =CH$_2$), 7.37 (t, 1H, H6), 7.48 (t, 1H, H7), 7.47 (d, 1H, H5), 7.83 (d, 1H, H8), 8.19 (s, 1H, H3). The [1]H NMR (DMSO-6d) spectrum of compound (10) showed the following chemical shifts: δ, ppm: 3.18 (s, 2H, benzylic CH$_2$), 3.86 (s, 2H, CH$_2$), 7.39 (t, 1H, H6), 7.46 (t, 1H, H7), 7.48 (d, 1H, H5), 7.71(d, 1H, H8), 7.81-8.21 (m, 5H, ph-H), 8.26 (d, 1H, H3). The second series involves the reaction of compound (5) with different aldehydes to synthesize the carbinol derivatives (12-18). These compounds showed an absorption bands in their IR spectra at 1665-1678 Cm^{-1} for C=O bond stretching, at 1602-1611 Cm^{-1} for C=N bond stretching, at 1202-1212 Cm^{-1} related to C=S bond stretching and at 3377-3399 Cm^{-1} for the O-H bond stretching. The [1]H NMR (DMSO-6d) spectrum of compound (12) showed the following chemical shifts: δ, ppm: 2.09 (s, 2H, SCH$_2$), 3.18 (s, 2H, NCH$_2$), 7.39 (t, 1H, H6), 7. 62 (t, 1H, H5), 7.85(t, 1H, H7), 8.00 (s, 1H, H3), 8.21 (d, 1H, H8), 13.48 (s, 1H, OH). The [1]H NMR (DMSO-6d) spectrum of compound (13) showed the following chemical shifts: δ, ppm: 2.09 (s, 2H, SCH$_2$), 3.17 (s, 1H, NCH), 7.24-7.35 (m, 3H, Ar-H), 7. 78 (t, 1H, H6), 7.97 (t, 1H, H7), 8.20 (d, 1H, H5), 8.50 (d, 1H, H8), 9.60 (s, 1H, H3), 13.48 (s, 1H, OH). The [1]H NMR (DMSO-6d) spectrum of compound (17) showed the following chemical shifts: δ, ppm: 2.09 (s, 2H, SCH$_2$), 3.18 (s, 1H, NCH), 6.17 (s, 2H, OCH$_2$O), 7.20-7.41 (m, 3H, Ar-H), 7. 76 (t, 1H, H6), 7.84 (t, 1H, H7), 7.96 (d, 1H, H5), 8.82 (d, 1H, H8), 9.81 (s, 1H, H3), 13.83 (s, 1H, OH).

References

Vijai Anand P.R., Kumar K.S., Kumar, Siva Kumar R., Sam Solomon V.D.; Jayaveera K.N., (2009), Asian Journal of Chemistry, 21, 9, 6656-6660.

Bhalla M., Srivastava V.K., Bhalla T.N., Shanker K., (1993), Arzeneimettelfoschug, 43, 595.

Kotto K. ,Koeshmstedt H. ,Konke D. ,Wahlam H., Heder G.; (1985), Patent, 31, 225.

Brana M.R., Castellano.J.M. , Keihauer G., Martin Y., Redondo C.; (1994), Anticancer drugs, 9 ,527.

Boyle F.T., Matusiuk Z.S., Hughes L.R., Slater A.M., Smith M.N., Stephens T.C.; Kimbell R., Jackman A.L., (1993), Adv. Exp. Med. Boil, 338, 585.

Parasharya P.M., Parkh A.R.; (1994), Chem. Abstr., 121, 108675.

Al-Omary F., Hassan G.S., El-Messery S.M., El-Subbage; (2012), Eur. J. Med. Chem., 47, 65-72.

Khalil M.A.; (1989), Alexandria J. Pharm. Sci., 3, 221.

Vogel's A.I.; (1994), Text book of practical organic chemistry, Ed. 5, 964-965.

Agarwal K.C.,Sharma V. Shakya N.; (2009) ,Gupta S. Bioorg. Med. Chem. Lett. ,19 ,5474-5477.

Decker M., Kraus B.;(2008), Biorg. Med. Chem., 16 ,4252-4261.

Bhasker D., Hosangadi, Rajesh H. Dave; (1996) Tetrahedron Letters ,37(35), 6375-6378.

Behbehani H. and Ibrahim M.H; (2013), Chemistry Central Journal , 7, 82.

Crews Ph; Rodriguez J; Jaspars M, "Organic Structure Analysis" ,Oxford University press, (1998).

Author Information

Hiba A. Ibraheem AL-Alaaf	**Mohammed A. Al-Iraqi**
Department of Chemistry,	Department of Chemistry,
College of Science,	College of Science,
University of Mosul, Iraq	University of Mosul, Iraq
Contact E-mail: *hibaalaf80@gmail.com*	

Mechanical Behavior of Mode I Delamination of a Laminated Composite Material

Habib ACHACHE
IMSI University of Mohamed Ben Ahmed Oran2

Abdi GHEZAIL
Université Mohamed Benahamed Oran 2

Bouabdellah ABED
Université des Sciences et de la Technologie

Abdelouahab BENZERDJEB
Université des Sciences et de la Technologie

Abstract: The objective of our work is to analyze numerically in three dimensions by the finite element method of the effect of a mechanical load on the delamination of unidirectional and multidirectional stratified composites in order to determine the energy release rate G in Mode I and the Von Mises equivalent stress distribution along the damaged area under the influence of several parameters such as applied load and delamination size. The results obtained in this study show that unidirectional composite laminates have better mechanical strength on the loading line than multi-directional composite laminates.

Keywords: Delamination, Release energy rate, Stratified composite, Finite element method and ply

Introduction

Composite laminates are used in different sectors such as transportation (including aerospace and automotive). They are widely used in applications where weight reduction is essential. In addition, the use of a material is enlarged, the more the probability of a possible failure is increased. The ability to characterize failures, for example by identifying failure modes, characteristic parameters or critical failure values, is essential to ensure the integrity of parts and services when designing future products. The main aspect of this failure is the crack, which provides the location and progression of the fracture. The study of an existing crack and its stability is of great importance. In fact, the propagation of a crack can lead to the breakage of a component that can lead to the complete collapse of the structure. The fracture mechanics is the ideal tool to analyze this situation according to the breaking characteristics of the material, namely the critical stress intensity factor (Kc) and the critical energy release rate (Gc), also called tenacity. This composite degradation has been studied by several authors.

According to Bai, T and Pollard, D.D, Cracking, delamination crack tip and longitudinal or interlaminar cracking describe the different mechanisms of damage in transverse transversal laminates. The result of the spread and accumulation of these three types of damage causes the final collapse of the composite. The order and sequence of occurrence of such damage depends mainly on the following parameters: nature of the constituents of the fiber / matrix architecture of the laminated plate, fabrication process of the shaping and different types of charges.

In the literature, these damages have generally been studied separately: the studies concern either the propagation of cracks by an analytical or numerical method (Berthelot, J.-M. and Le Corre, J.-F), or on an analytical model delamination (Rebière, J.-L et al.). Haneef, M et al. performed a finite element analysis to analyze the delamination effect on composite structures with two models. Smith B. W determined the angle of

propagation of the crack; . A survey was again conducted by Todo, M., and Jar, PYB Using the Model and ENF (End Notched Flexure) Mode II (Todo, M., and Jar, Composite Fiberglass / Ester Composite) SEM). It was concluded that in mode II crack growth is a function of the properties of the fiber / matrix interface.

However, some authors have studied the role of transverse cracks in the initiation of inter-layer delamination as a function of properties. For example, Wang, J. and Karihaloo, B. L study the best stack (0 °, 45 °, 90 °) to reduce the stress concentration at the bottom of the crack and the shear stress at the interface in mode II . Dasa, Subhankar et al. have studied the effect of overlap and winding on the reduction of the stress concentration at crack, which leads to suggest the propagation of cracks. He presented a finite element study of the micro-macro-mechanical growth of DCB fiberglass / interlaminar epoxy crack network samples for Mode I (Todo, M., and Jar, P. Y. B.). Because of the heterogeneity of the composite material, probabilistic studies have also been conducted according to two approaches: some Manders, P.W. et al. use a probabilistic criterion for the distribution of critical stress, while Katerelos, D.T.G et al. use a criterion of the random critical energy release rate. Szekrényes, András showed that shear stress at the interface contributes significantly only to the rate of energy release in mode II. Qing n, G.H et al. have located a semi-analytical model of energy release rate for delamination analysis of composites. Yao, Liaojun et al. used the energy deformation reimbursement rate for the characterization of fatigue delamination.

Our study is about the determination of the release energy rate G in mode I and the distribution of Von Mises equivalent stress along the damaged area. Different parameters were considered: - Effect of the applied loading. - Effect of the delamination size. The results show clearly better mechanical resistance on the loading line fort the unidirectional stratified composites than for the multidirectional stratified composites.

Geometric Model

The composite laminate studied is a carbon/epoxy, it is composed of 20 plies, each with a thickness of 0.13 mm, with a symmetrical fiber; the first 8 plies are oriented at 0° and the other adjacent plies at 90°. Our analysis goal is to show the effect of several parameters such as the applied load and the delamination length on mode opening (model) for a test composite material with a length of 150 mm, width of 20 mm and a thickness of 2.6 mm.

The unsticking of layers was observed for a constant static load from 10 N to 60 N applied to the half-width of the specimen. For a distance of 5 mm, of his free end. The delamination is created according to the width of the composite material, and is located between the ten and the eleven layer of the stratified. The composite material is manufactured such as the initial length of the delamination area is 35 mm. The stratified composite material uses in this study is a carbon\epoxy, its mechanical characteristic are presented in table 1:
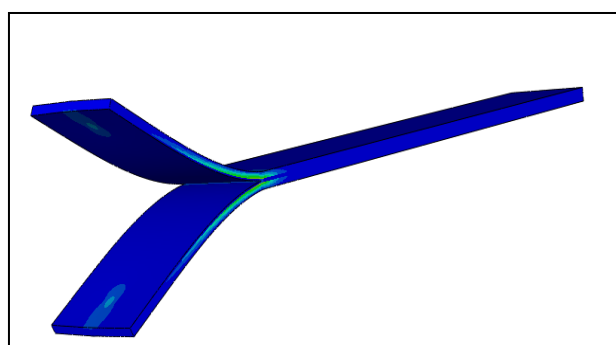
Fig. 1. Schematic representation of the geometrical model

Modeling

The adopted approach in this analysis is to use a reasonable modeling with a good refinement of the critical area [6]. In this digital analysis by the finite elements method, the specimen is modeled by quadrilaterals mesh elements of eight nodes, isoparametric type.
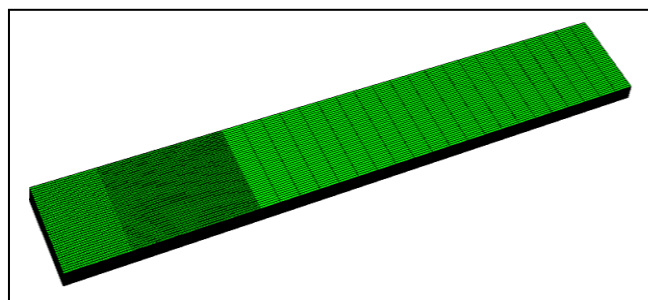
Fig. 2. Schematic representation of the geometrical model with modeling

Table 1. 0rthotropic proprieties of unidirectional carbon/epoxy layer

Designation	Young's modulus E_{12}, MPa	Young's modulus E_{23}, MPa	Young's modulus E_{13}, MPa	Shear's modulus G_{12}, MPa	Shear's modulus G_{23}, MPa	Shear's modulus G_{13}, MPa	Poisson's ratio v_{12}	Poisson's Ratio v_{23}	Poisson's ratio v_{31}
Carbon/epoxy	140000	10000	10000	5000	3850	5000	0.3	0.3	0.0214

Results

Effect of Applied Load

Case 1: Delamination Length of 35 mm

We represent, in Fig. 3, the variation of the equivalent release energy rate G in function off the length of delamination line (width of the specimen), for different load, we remark the increasing of G parameter with accretion of load. The minimal values of G parameter where observed in the free edge of the specimen, and begin to increase until a maximal value in the middle of his width. The style of the curve is almost a parabolic curve. For the low loads the release energy rate G is almost constant along the width of the specimen. The increasing rate of the failure parameter G is accented when in accordance with the applied load accretion
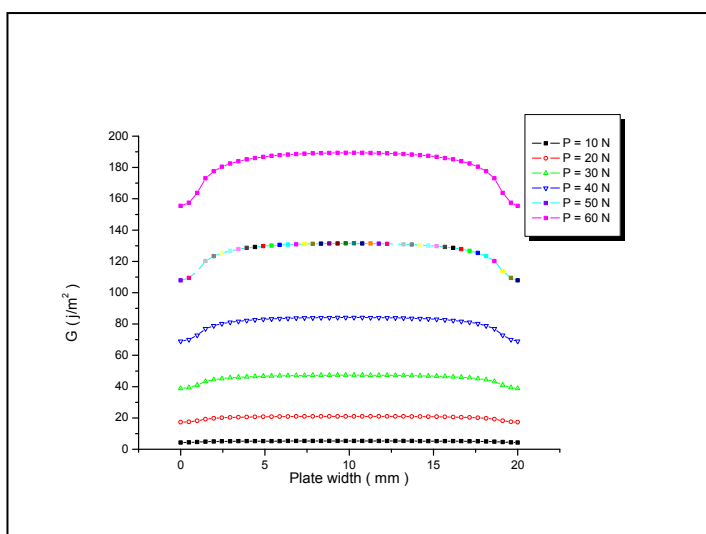
Fig.3. Energy release rate distribution versus plate width for delamination length of 35 mm

Case 2: Delamination Length of 45 mm

We observe the same behavior like the precedent figure, but in this time we remark that an increasing rate of G parameter most marked is as the one of the precedent case.

With the same load of 40 N; we remark that the maximum value of G parameter gives a rise of 77% as the precedent case.
- 20 N increasing of 70%
- 30 N increasing of 75%

The release energy rate G reached his critical value for applied loads breaking the 40 N barriers.

Case 3: Delamination Length of 55 mm

We registered an important increasing of the release energy rate G in relation to the precedent case, defined by s:
- 20 N increasing of 50%
- 30 N increasing of 53%
- 40 N increasing of 55%

The increasing rate of G parameter is more intense. Fig. 5 shows that for loads inferior of 40 N, there is no damage for the composite material.
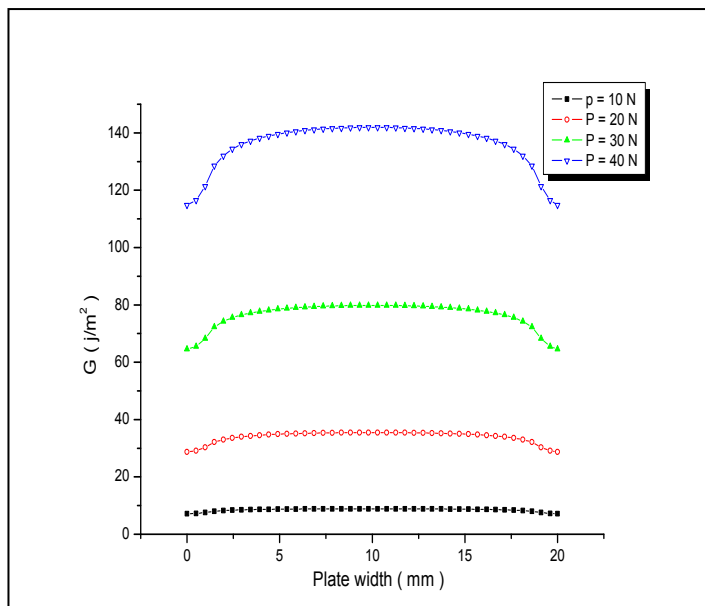
Fig.4. Energy release rate distribution versus plate width for delamination length of 45 mm
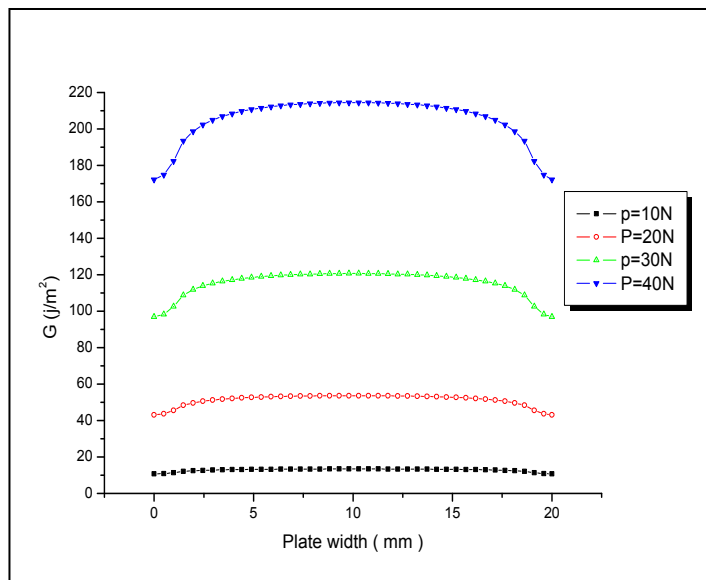
Fig.5. Energy release rate distribution versus plate width for delamination length of 55 mm

Case 4: Delamination Length of 65 mm

Fig. 6 shows that the length of delamination has a big influent on the G parameter. However, relatively to the length delamination of Fig. 5, this one present a significant values of G parameter with those percentages:

- 20 N increasing of 35%
- 30 N increasing of 39%

Fig. 7 shows the variation of G equivalent for the two positions P_1 and P_2. The difference between the two values of G parameter are due principally to the increasing of applied load, and reach his maximal value for a delamination length of 65 mm.

Comparatively to Fig.3, we mark an important difference of G equivalent for the two positions P_1 and P_2 for a load near of an average equal to 20 N. this difference increase with the accretion of load, and it reach the 16% for a load of 30 N, for wish the G parameter approach the critical value in the position P_2.
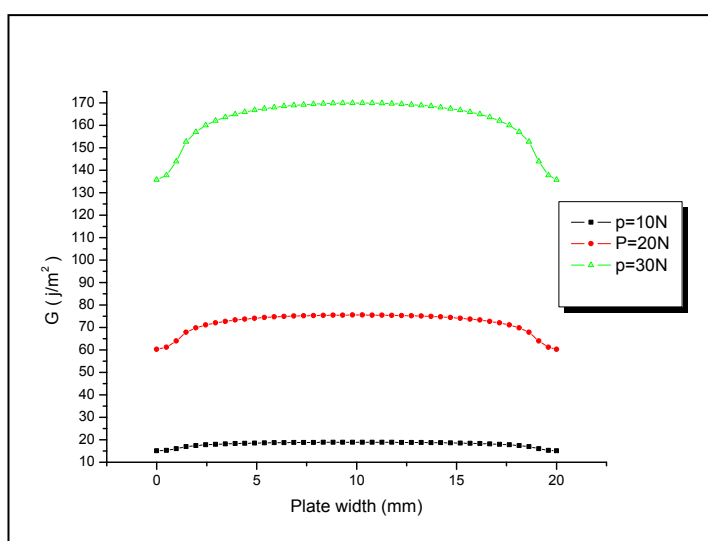
Fig.6. Energy release rate distribution versus plate width for delamination length of 65 mm
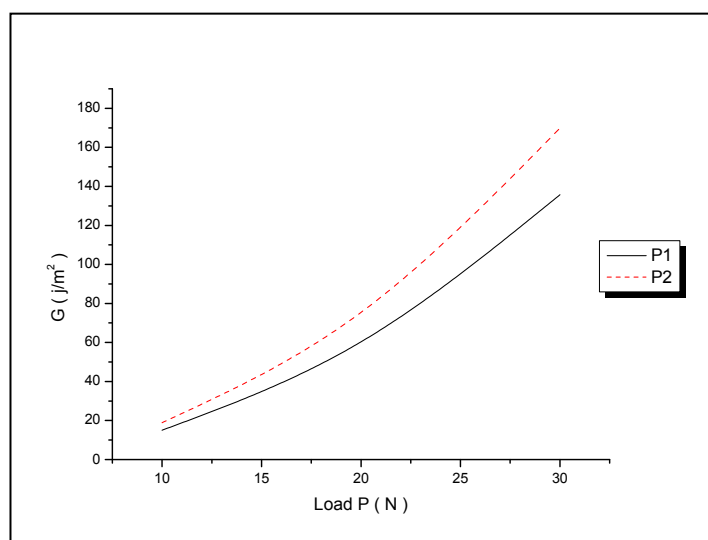
Fig.7. Evolution of G parameter with applied loads for the two positions P_1 and P_2

Comparison between the Unidirectional and Multidirectional Stratified

Fig. 8 represents the distribution of release energy rate G in function with the applied loads for a unidirectional stratified composite with a delamination length of 35 mm. We remark from a part, that whatever the stratified composite material, the release energy rate G proportionally varied with the applied load, other part, from the digital results obtained, we observe that the multidirectional stratified composite (Fig. 3), present a most marked

level of release energy rate G equivalent as the unidirectional stratified composite. This attenuation of G parameter is due principally to the mechanical resistance of unidirectional fibers on opened mode in the delamination area.
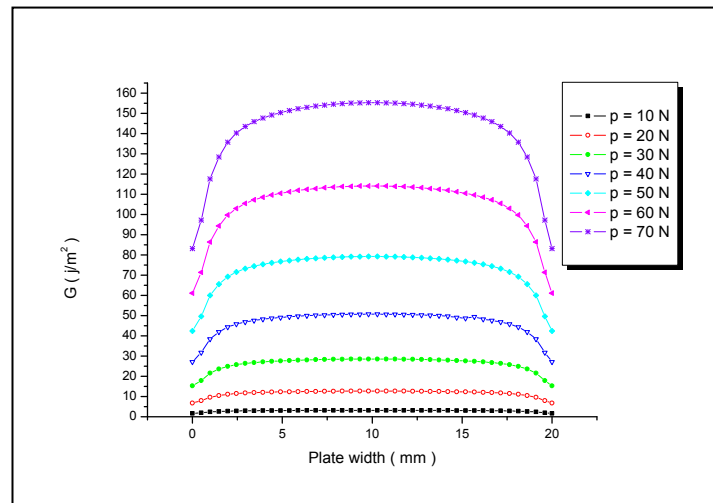
Fig. 8. Energy release rate distribution versus plate width for delamination length of 35 mm

Stress Distribution

We represent the variation of Von Mises stress equivalent intensity and distribution on the requested zone defined by the both position P1 and P2. We recall that the mesh was refined at the level of this zone to obtain accurate results. The stresses are determined in the various layers of the laminated composite according to the inter distance going from the undamaged zone to the one where the load is applied.

Through the line of delamination, whatever the two positions P1 and P2, the stresses growing in from the undamaged area, reaching a maximum value at the delaminated line and decrease proportionally away from the latter, towards the point of load application.
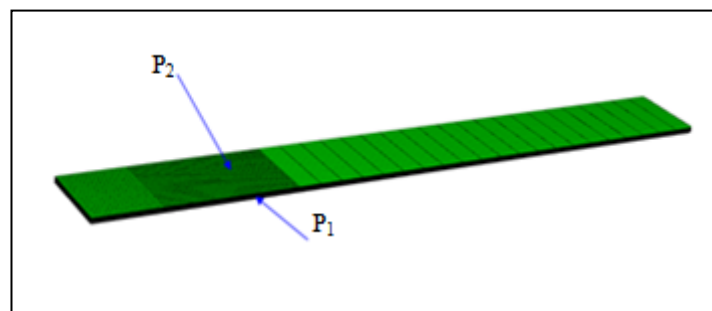
Fig. 9. Mesh model and representation of the positions P_1 and P_2

Position P_1

Laminated Unidirectional

We observe that the stress field is localized at the level of the line gouged (between ply 10 and its symmetrical, ply 11) for the composite unidirectional. The stresses decrease as we go further from the defect where the stresses are concentrated.
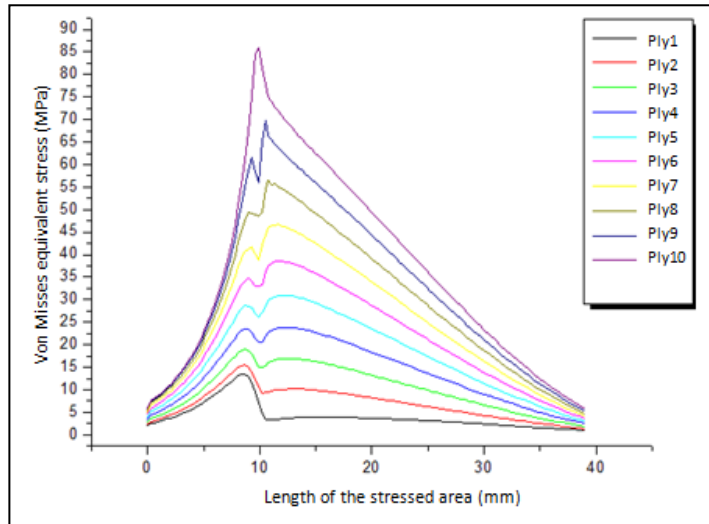
Fig. 10. Distribution of G versus platewidth for P_1 position (UL)

Cross Laminated

There is a considerable fall of the stress field at the level of ply 9 and 10 oriented to 90° and constraints in the other folds are more intense than those of the composite laminate one-way. The plies9 and 10 oriented 90° have a low resistance to the opening of the composite and therefore constraints are transferred to the other folds facing 0°.
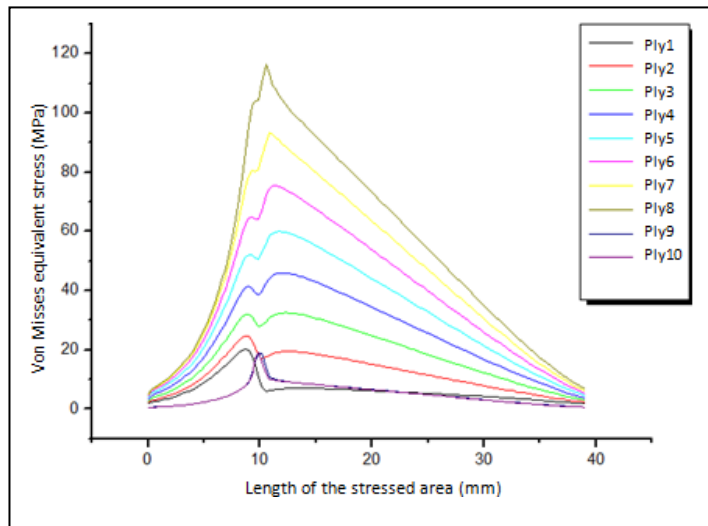
Fig. 11.Distribution of G versus plate width for the P_1 position(CL)

Conclusions

This numerical study, can draw the following conclusions:
- The delamination of composite laminate in mode I depends on the intensity of the applied load and the surface of the damaged area.
- The rate of refund of energy values are maximum in the middle of the width of the plate composite laminate and they are minimum two free ends of the laminated composite material, specifically at the level of the line of delamination.
- Compared to the cross laminatecomposite, composite unidirectional presents a good mechanical strength, because oriented at 0° ply better resist the imposed load those oriented at 90°.
- Under the effect of the same loading type and the presence of an identical defect, it is noted that the high level of the equivalent von Mises stress of the cross laminate composite in the ply close to the defect is due to the transfers of constraints following the non-solicitation of adjacent fibers that are oriented at 90 ° and

that have a low von Mises equivalent stress; but that of the unidirectional composite increases gradually from the first ply to the one that is at the closest vicinity of the delamination line.

References

Bai, T. and Pollard, D.D. 1999, "Spacing of fractures in a multilayerat fracture saturation",*International Journal of Fracture*, 100(4),pp. 23–24.

Berthelot, J.-M. and Le Corre, J.-F. 2000, "Statistical analysis of the progression of transverse cracking and delamination in cross-ply laminates", *Composites Science and Technology,* 60(3), pp. 2659–2669.

Haneef, M., R M S. A. & Ali, M. M. 2011, "Studies on Delaminating Effects on Stress Development in Composite Structures", *Proceedings of the World Congress on Engineering* Vol. III WCE, July 6 - 8, London, U.K..

Katerelos, D.T.G., Kashtalyan, M., Soutis, C. and Galiotis, C. 2008, "Matrix cracking in polymeric composites laminates Modeling and experiments",*Composites Science and Technology*, pp. 2310-2317.

Manders, P.W., CHOU, T.-W., Jones, F. R. and Rock, J. W. 1983" Statistic al analysis of multiple fracture in 0/90/0 glass fiber/epoxy laminates".*J Mater Sci*18, pp. 2876-2889.

Product DassaultSystèmesSimuliaCorp2010, ABAQUS Standard Version 6.10, Providence, RI, USA..

Qing n, G.H., Liu,Y.H. and Li, D.H. 2011, "A semi-analytical model for the energy release rate analyses of composite laminates with a delamination". *Finite Elements in Analysis and Design,* 47, pp. 1017–1024.

Rebière, J.-L, Maâtallah, M.-N and Gamby, D. 2002, "Analysis of damage mode transition in a cross-ply laminate under uniaxial loading", *Composites structures,* 55,pp. 115-126.

Smith B. W. 1993, "Fractography for continuous fiber composites", in "Engineered materials handbook", volume 1: composite, Ohio, USA, ASM International, pp: 786-793, ISBN 0871702797 (v.1).

Dasa, Subhankar, Choudhurya, Pannalal, Haldera, Sudipta and Sriramb, P. 2013 "Stress and free edge delamination analyses of delaminated composite structure using ANSYS", *Procedia Engineering*, , 64 1364 – 1373

Szekrényes, András, 2012 "Interlaminar stresses and energy release rates in delaminated orthotropic composite plates. *International Journal of Solids and Structures*, 49 2460–2470.

Todo, M., JAR, P. Y. B. and Takahashi, K. 2000, "Initiation of a Mode-II Interlaminar Crack from an Insert Film in End-Notched Flexure Composite Specimen", *Composites Science and Technology*, 60, pp. 263–272.

Todo, M.,Jar, P. Y. B. 1998, "Study of Mode-I Interlaminar Crack Growth in DCB Specimens ofFibre-Reinforced Composites", *Composites Science and Technology*, 58, pp. 105–118.

Wang, J. and Karihaloo, B. L. 1997, "Matrix crack-induced delamination in composite laminates under transverse loading", *Composites structures,* 38, 661-666.

Yao, Liaojun, Alderliesten, R.C., Zhao, Meiying and Benedictus, R. 2014, "Discussion on the use of the strain energy release rate for fatigue delamination characterization".*Composites: Part A,* 66 65–72.

Author Information

Habib Achache
University of Sciences and Technology M. B. Oran
Boite Postale 1505 El Menouar Oran, Algeria
Contact E-mail: *abdoubenzerdjeb@yahoo.com*

Abdi Ghezail
Industrial Maintenance and Safety Institute , University
Oran 2 Name of Institution or University 170 bp 170 EL
Mnawer, Oran, Algéria

Bouabdellah Abed
University of Sciences and Technology M. B. Oran
Boite Postale 1505 El Menouar Oran, Algeria

Abdelouahab Benzerdjeb
University of Sciences and Technology M. B. Oran
Boite Postale 1505 El Menouar Oran, Algeria

Evaluation of Rans Turbulence Models for Turbulent Flow over Nrel S809 Airfoil

Bouabdellah ABED
Université des Sciences et de la Technologie

Abdelouahab BENZERDJEB
Université des Sciences et de la Technologie

Habib ACHACHE
Université Mohamed Benahamed Oran 2

Abiddine DEBAB
Université des Sciences et de la Technologie

Mohamed-Kamel HAMIDOU
Université des Sciences et de la Technologie

Abstract: In this presented work, a numerical investigation was conducted to evaluate the performance of RANS turbulence models implemented in ANSYS CFX to predict flow field and aerodynamic characteristics of the NREL S809 Airfoil. The simulations were carried out with ANSYS CFX R18.2 (academic version). The blade geometry was simplified into a 2D airfoil and the flow analysis around the profile was conducted at various angles of attack equal to 0°, 5.13°, 9.22°, 11.24° and 20.15°, at a constant and same Reynolds number equal to 2×10^6. In this paper, the turbulence flow patterns and separation around the profile were represented using the most turbulence models used in CFD codes, the standard k-ε and its modifications RNG k-ε. The moment coefficient (C_m), the lift coefficient (C_l) and the drag coefficient (C_d) were determined and plotted as a function of the angle of attack. The pressure distributions around this profile, for each angle of attack, were also presented. The results and the plots obtained have shown good agreements with published experimental results. From the simulations, the two turbulence models provided near prediction to the experimental values at low angle of attacks, but over predict the Cd values. Calculations have also shown that the standard k-ε model and RNG k-ε model produced similarly results but with partly differences in pressure magnitude.

Keywords: NREL S809 Airfoil, CFD simulations, RANS turbulence models, Aerodynamic characteristics

Introduction

For the last three decades, fluid dynamics (CFD) approach has been the most appropriate method used almost exclusively by researchers to evaluate the hydrodynamic properties of the flow field over wind. This method provides a detailed description of a phenomenon and consequently gives a good description of flow fields around wind turbine blades. With the recent advances in computing power, together with advanced solvers that enable to give robust solutions of the flow field in a reasonable time, CFD approach provides a practical tool to model and simulate the aerodynamic performances of wind turbine airfoils.

Some of the interesting work concerning CFD analyses of the flow field around S809 airfoil are presented below:
- Wolfe and Ochs (1997) studied the aerodynamic characteristics of S809 and compared the numerical results with experimental data. They used the standard k-ε turbulence model, a fully turbulent and a mixed

laminar/turbulent flow. Their calculated results agree well with the experimental data for smaller angles but failed for 14.24° and 20.15°;

- Guerri et al. (2006) employed a 2D Navier–Stokes simulation of steady and unsteady flow for the S809 airfoil. They studied different turbulence models, SST k-ω and the RNG k-ε model. They establish that k-ω model is better to simulate flow instability region than the k-ε model;

- David Hartwanger et al. (2008) conducted a CFD analysis for NREL S809 airfoil using the various codes, 2D panel code, X-Foil ANSYS CFX 2D code. They concluded that using a high-resolution mesh with advanced turbulence models provide an excellent match with experimental;

- Haipeng et al. (2017) investigated by the fluid dynamic method the aerodynamic performance of the airfoil S809 without and with the use of vortex generators. They discussed the effects of vortex generators on the airfoil S809 boundary layer and analyzed quantitatively the lift coefficient, drag coefficient, x-velocity gradient vorticity.

The main objective of this work is to evaluate the performance of different RANS turbulence models implemented in ANSYS CFX solver code. There are several RANS models available in ANSYS CFX and each model has been developed with different objectives, strategies, and measures in mind. In this work, two Linear Eddy Viscosity models have been tested, the standard k-ε model (Launder and Spalding, 1974) and it variants, RNG k-ε model (Yakhot wet al. 1992). The objective is to evaluate the ability of these two models to determine the hydrodynamics coefficients, pressure coefficient (C_p), moment coefficient (C_m), lift coefficient (C_l), and drag coefficient (C_d), of NREL S809 airfoil at fixed Reynolds number of $2.0 \times 10^{+06}$. The simulated results will be compared to wind tunnel test results of the wind turbine dedicated airfoils made by Delft University of Technology (DUT) (Somers, 1997).

We will not try to explain in depth why models fails or succeed in approximating these quantities, it will simply state that a model gives good results or failed results.

For the evaluation, the software ANSYS CFX R18.2 version academic (ANSYS, Inc, 2018) is used for calculation of the flow field over the NREL S809 airfoil.

Method

Turbulent flow calculations have been performed in two-dimensional steady state flow over a S809 NREL airfoil at different angles of attack. In a steady flow, hydrodynamics coofficients and mean velocity field of the airfoil have been calculated by two turbulence models, k-ε model and RNG k-ε model.

Turbulence Modelling

The governing equations used in the simulations are the RANS equations. The RANS Eddy Viscosity Models are commonly used in the engineering applications for their robustness, low computation costs and providing good results. In order to model and simulate the turbulent flow in the present study we have selected both k-ε turbulence and RNG k−epsilon models. The simulations were done for a Reynolds number of $2.0 \times 10^{+06}$ with three different grids.
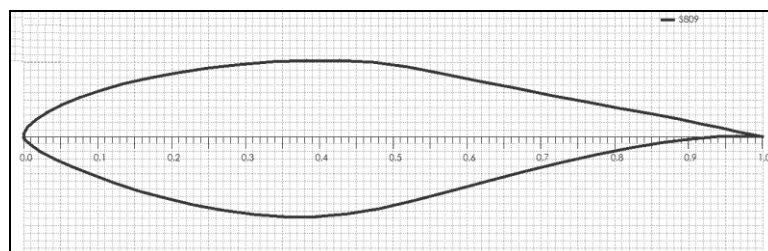
Figure 1 . Schematic of the NREL S809 airfoil

The NREL S809 airfoil is a laminar flow aerodynamic profile 21% thick (Figure 1), specifically designed for horizontal axis wind turbine (HAWT) applications (Somers, 1997). This profile is justified by the existence of a very large number of studies carried out in the field of wind turbines, which makes it easier to obtain

experimental data (Butterfield et al., 1992) and (Somers, 1997) and numerical results from other CFD software. This will allow more comparisons and gives a better evaluation of the models proposed by CFX solver.

Computational Mesh

The computational domain is defined as 2-D; extend to a distance of 5C (C = airfoil cord) long in all directions from the airfoil aerodynamic center and 20C long at the wake. The two-dimensional C-H structured mesh around the S809 airfoil shape is generated using ICEM CFD code. The numerical domain is divided into 22 blocks with 4 blocks lying very close to the airfoil, which have very refined mesh size when compared with the remaining blocks far from the airfoil (Figures 2-a and 2-b).

Three mesh sizes are done, namely coarse, medium and fine mesh, as shown in the Table 1. A boundary layer mesh is used at the wall of the airfoil, with the first near-wall node placed at $Y_{Plus} \approx 60$. Figures 3-a and 3-b show, respectively, the whole mesh of the domain and the refinements near the airfoil with a coarse mesh (Figure 3-b).
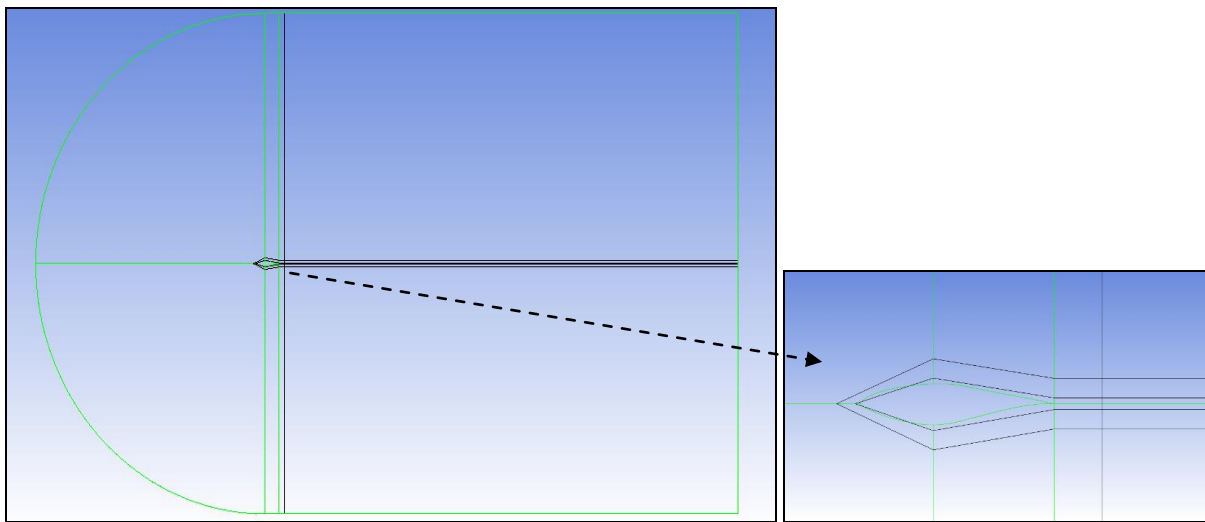
Figure 2. C-H grid topology around the NERL s809 airfoil

| (a) | (b) |
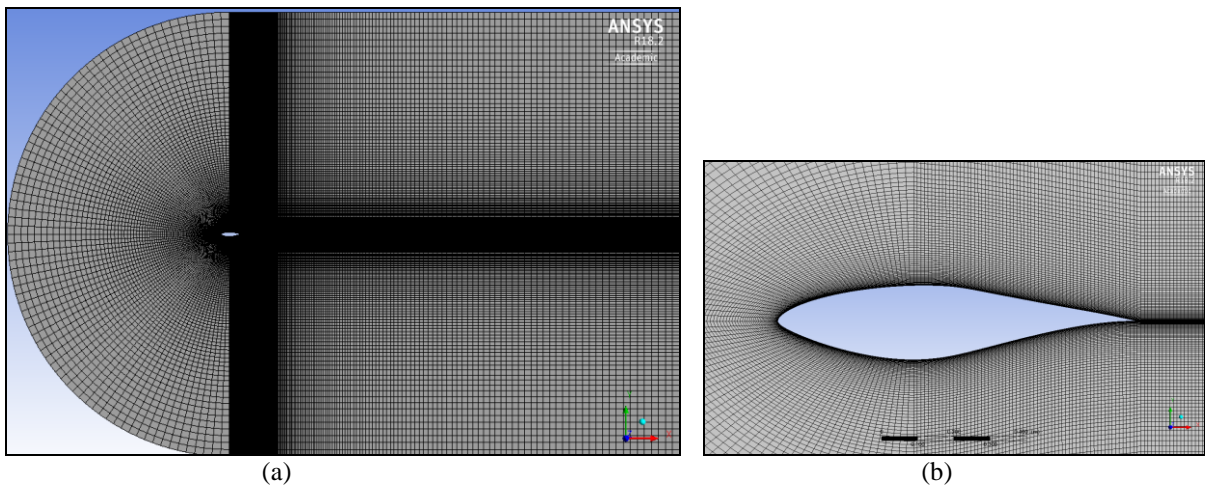
Figure 3. Numerical Domain and Mesh
(a) Domain with Coarse Mesh ; (b) Mesh detail around S809 airfoil shape

Table 1. Mesh Information

Mesh	Local Mesh Size on Airfoil shape	Number of Hexahedra Elements
Coarse	0.010 C	71 484
medium	0.005 C	41 514
Fine	0.001 C	302 697

Boundary Conditions and solver setting

Velocity components are specified at the inflow boundary of the computational domain as follow: $U_x = U_\infty \cos(AOA)$ and $U_y = U_\infty \sin(AOA)$, where (AOA) is the angle of attack. The free stream velocity is $U_\infty = 1 \ [m/s]$ and the dynamic viscosity μ is calculated based on the fixed Reynolds number, $\mathrm{Re} = 2.0 \times 10^{+06}$ chord length, $C = 1[m]$, and the Density $\rho = 1[kg/m^3]$.

The reference pressure is set to 1 atmosphere and the relative pressure is zero at the outflow boundary placed at the right side of the numerical domain. Along the airfoil surface, no-slip boundary conditions are imposed, while the top and the bottom of the numerical domain are considered as inflow boundary conditions. Considering the RANS, simulations are carried out on two-dimensional meshes, the two sides of the domain in the *z*-direction are set to symmetry boundary condition. Finally, the value of turbulence intensity at the inflow boundary is set to 5% .

The analysis is performed using steady state RANS models. ANSYS CFX use pseudo-transient solution approach for steady-state computations. Here the timescale is specified to local timescale with factor 5. The high-resolution scheme is used to evaluate advection terms that are second-order accurate and bounded. The solver stops iterating when RMS residual error values are below to 10^{-06} for all variables or when achieving a maximum number of 10.000 iterations. Initial conditions for simulations are set to the free stream velocity $U_\infty = 1. \ [m/s]$ and turbulence values to 5% .

Results and Discussion

Post processing has been performed for different parameters such as velocity and aerodynamics coeficients for both turbulence models and also for different meshes.

The lift, drag and pitch moment coefficients are dimensionless numbers used to measure the aerodynamic characteristics of the airfoil. These coefficients are expressed as follows:

Lift coefficient :
$$C_L = \frac{L}{\frac{1}{2}\rho U_\infty^2 A} \tag{1}$$

Drag coefficient :
$$C_D = \frac{D}{\frac{1}{2}\rho U_\infty^2 A} \tag{2}$$

Pitch moment coefficient (calculed about 0.25 chord) :
$$C_m = \frac{M}{\frac{1}{2}\rho U_\infty^2 C A} \tag{3}$$

Where: U_∞ is the freestream velocity, A is a reference area and C is a reference length, D is the drag force, L is the drag force, M is the pitching moment and ρ is the mass density of the fluid.

Grid resolution analysis

The graphs below (Figure 4, 5 and 6) show the lift, drag and moment coefficients as a function of the angle of attack, obtained by k-ε and RNG k-ε models.

The values of the coefficients are almost identical for angles of attack less than or equal to 9.22 degrees. Indeed, we observe the same shape and almost the same values obtained by three different meshes. There is little effect of the mesh density on the values of the lift, drag and moment coefficients calculated by the two turbulence models for the small angles of attack.

For the values of the lift at the angle of attack equal to 14.24°, the numerical results obtained by both turbulence models are larger than the experimental results except for the case of the k-ε model for the coarse mesh. Same results are observed for 20.15°, except for this case the k-ε model underestimates the lift for the average mesh.

For the numerical results of the drag coefficient, the curves look the same except for the results obtained for the coarse mesh. The drag values are underestimated for the fine mesh at angles of attack greater than 9.22 degrees, and are closer to the experimental values for the values calculated for the mean mesh.

For the moment coefficient, the curves obtained by the simulations and the experimental curves have the same shape. A slight difference is observed at the 20.15° angle for the results obtained for the three different meshes.
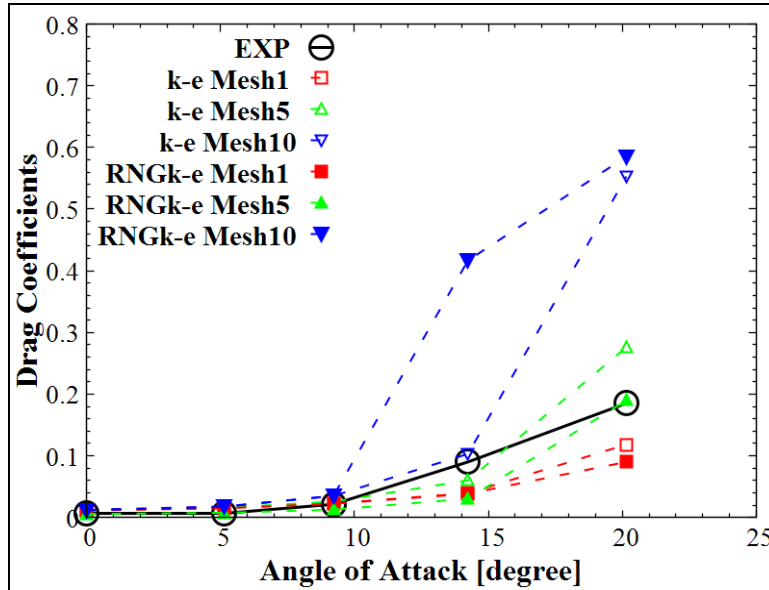
Figure 4. Predicted drag coefficient
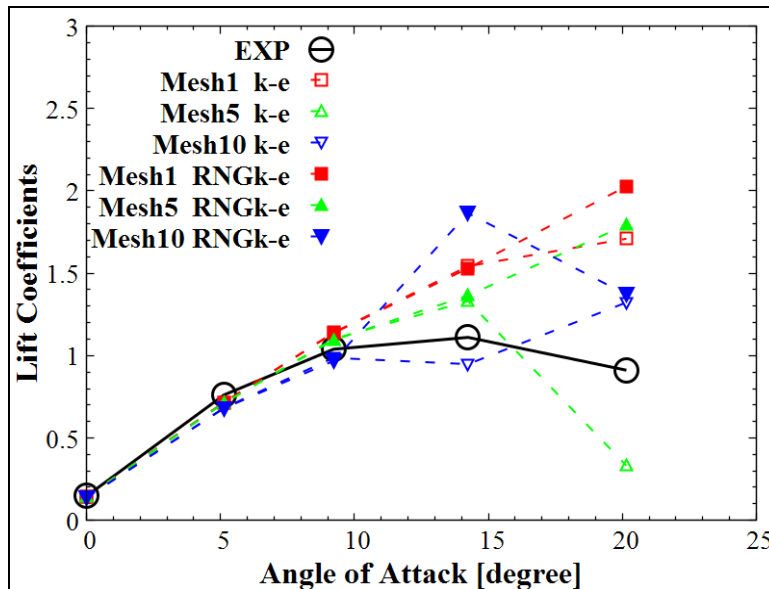
Figure 5. Predicted lift coefficient
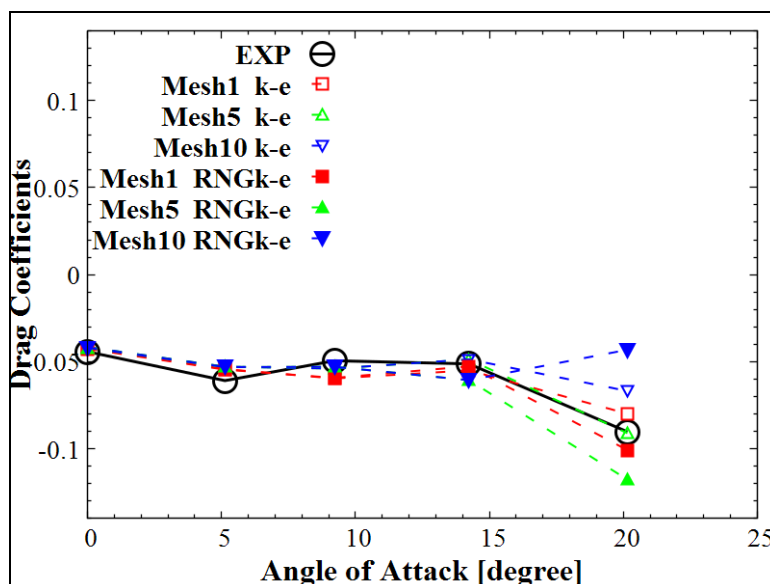
Figure 6. Predicted moment coefficient

3.1 Pressure Coefficient

Figure 7 shows comparisons between numerical and experimental distribution of pressure coefficient of the NREL S809 airfoil at various angles of attack for fine mesh.

We can notice that both turbulence models predict similar results. The graphs show that the pressure coefficient at the upper surface of the airfoil is negative and positive at the bottom surface. They indicate more clearly that the pressure coefficient varies depending on the angle of attack and show a significant difference in pressure coefficient between the leading edge and the trailing edge of the airfoil. We can also see that at 5.13°, the profile indicates a large difference in pressure coefficient between the lower and upper surfaces compared to the other angles of attack.

At angles of attack equal to 14.14° and 20.15°, the two turbulence models k-ε and RNG k-ε failed to predict the pressure coefficient except over the lower surface of the airfoil.

Aerodynamic coefficients

Figures 8, 9 and 10, respectively, show calculated values of drag (C_D), lift (C_L) and moment coefficients (C_m) for fine mesh compared with experimental data. Generally, all the coefficients predicted by the two turbulence models show reasonably good agreement with the experimental results. It seems that the predicted drag and lift coefficients are in quite good agreement with experimental data for the linear part of the curves.

However, for the lift coefficients both models fail to predict stall location. The calculated results compare quite well with experimental data for the angle of attack only up to 9.22 degrees. Figure 8 clearly shows that both turbulence models give the same magnitude of C_L for an angle of attack of up to 14.24°, and shows a separation in the results for AOA > 9.22°, which is found in the calculations obtained by both turbulence models. While for both turbulence models, k-ε and RNG k-ε, smaller values of the C_D are predicted for AOA ≥ 10° (Figure 9), and the divergences with experimental data are more important for AOA greater than this value.

Figure 10 shows the moment coefficient versus angle of attack. The predicted moment coefficient is calculated by assuming that the aerodynamic center is about 25% of chord. The calculated results of the moment coefficient for both k-ε model and RNG k-ε model are in good agreement with experiment data. Again, the comparison looks similar for both turbulence models.
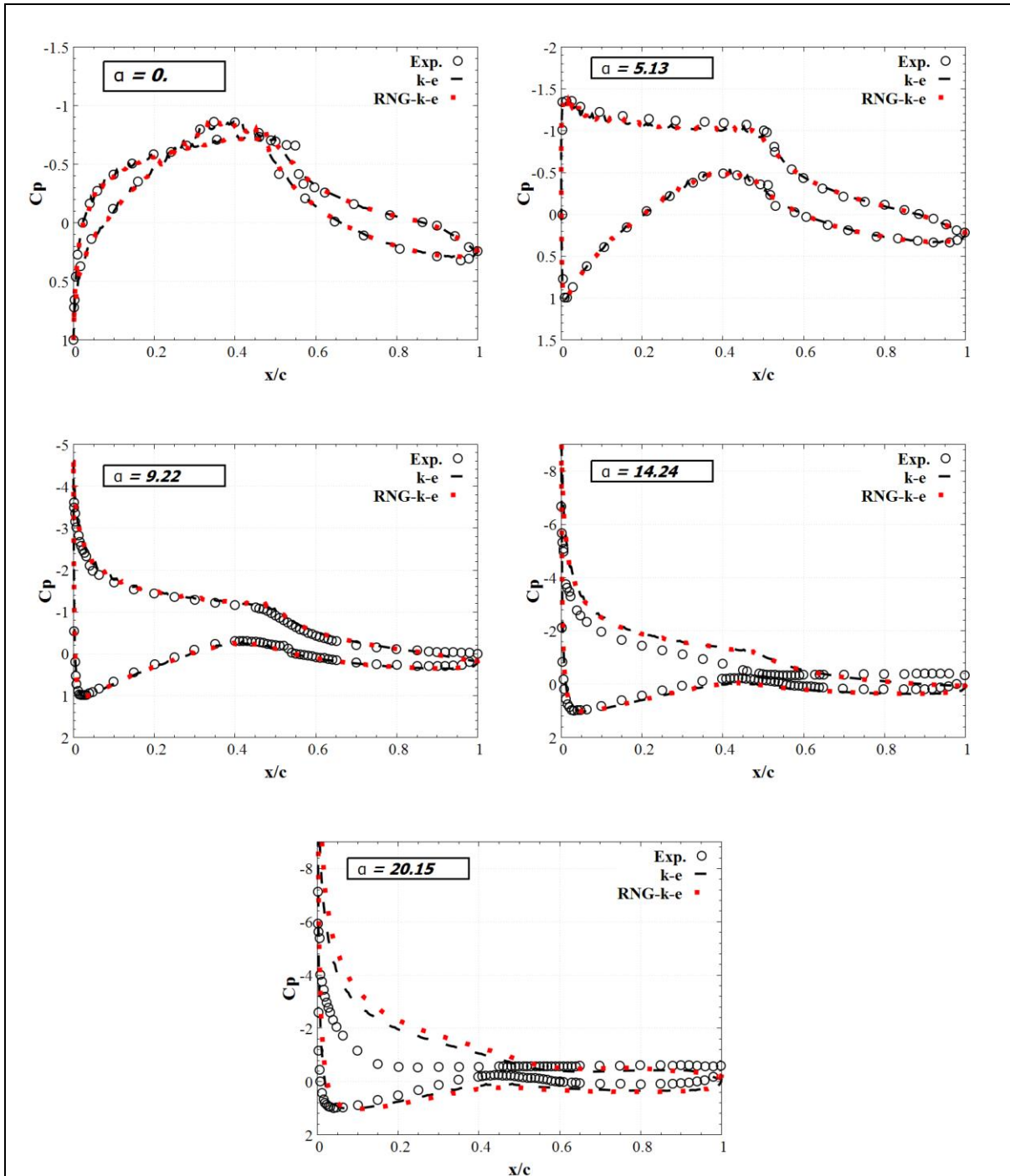
Figure 7. Pressure coefficient at various angles of attack for fine mesh
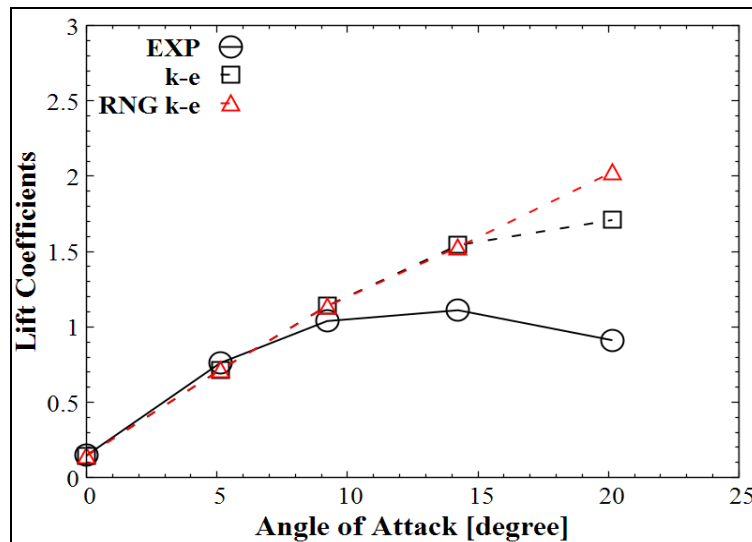
Figure 8. S809 Lift coefficients for fine mesh
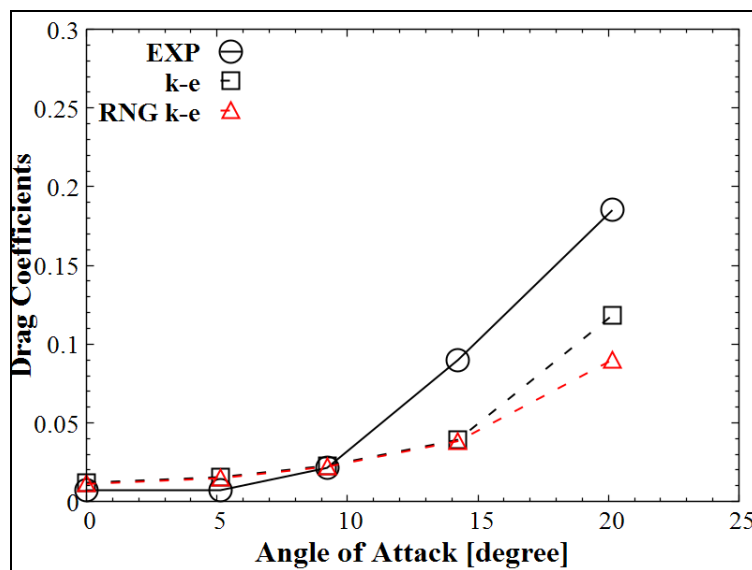
Figure 9. S809 Drag coefficients for fine mesh
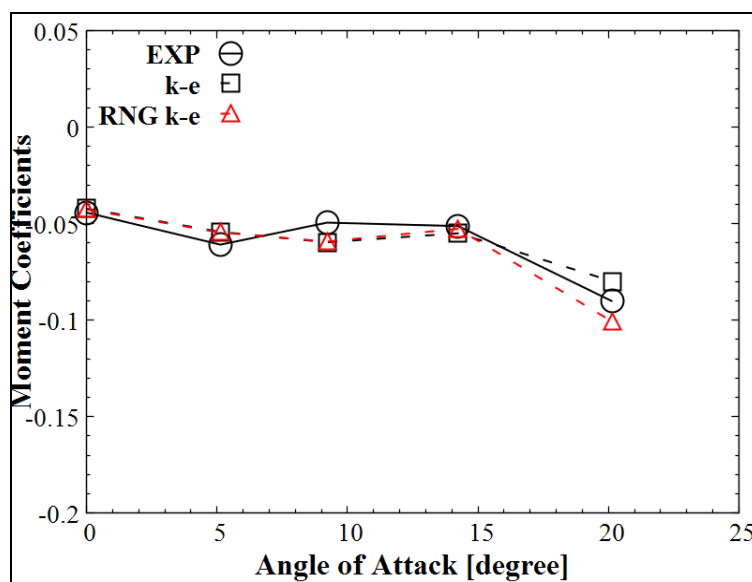
Figure 10. S809 Moment coefficients about 25% chord for fine mesh

Figures 11-12 and 13 show the velocity fields predicted by both turbulence models at 0.0°, 9.22° and 20.15° angle of attack. It should be noted that the k-ε and RNG k-ε models present almost identical velocity contours. Except for AOA = 20.15°, the shape of the wake region formed behind the airfoil present a slight difference. With both models, the turbulent flow remains attached to airfoil surface for AOA = 0° and 9.22°, and is fully separated on the upper surface; separation is predicted at distance superior to 50% from the leading edge. Note that the wake region with zero velocity is important for AOA = 20.15° than AOA = 9.22°, and it is almost nulle for AOA = 0°. In addition, a higher-velocity zone is formed on the extrados close to the leading edge of the airfoil. This zone of increase of speed is more or less important according to angle of attack. The maximum velocity calculated for angle of attack 20.15° is about three times larger than for AOA =0° , and it is about twice times larger than for AOA =9.22°.

k-ε   RNG k-ε
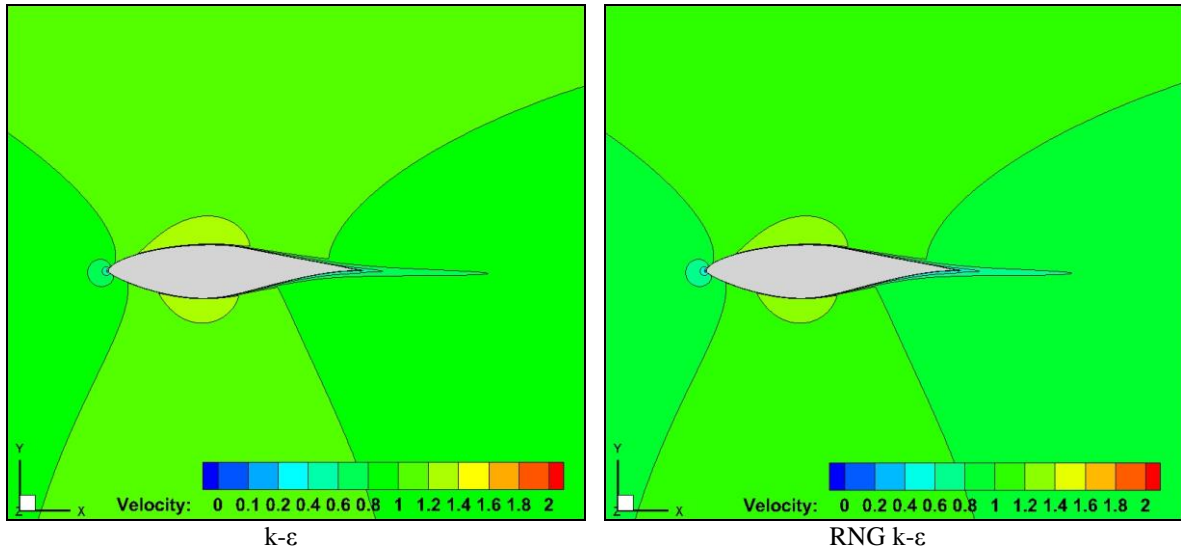
Figure 11. Calculations velocity contours for the angle of attack α = 0°
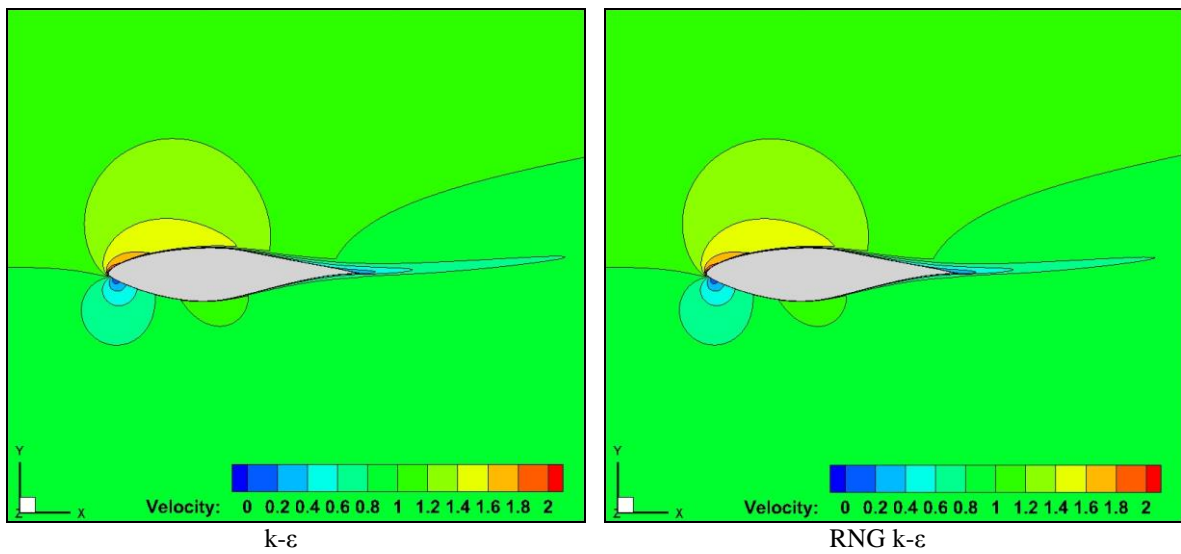
k-ε   RNG k-ε

Figure 5: Calculations velocity contours for the angle of attack α = 9.22°.

| k-ε | RNG k-ε |
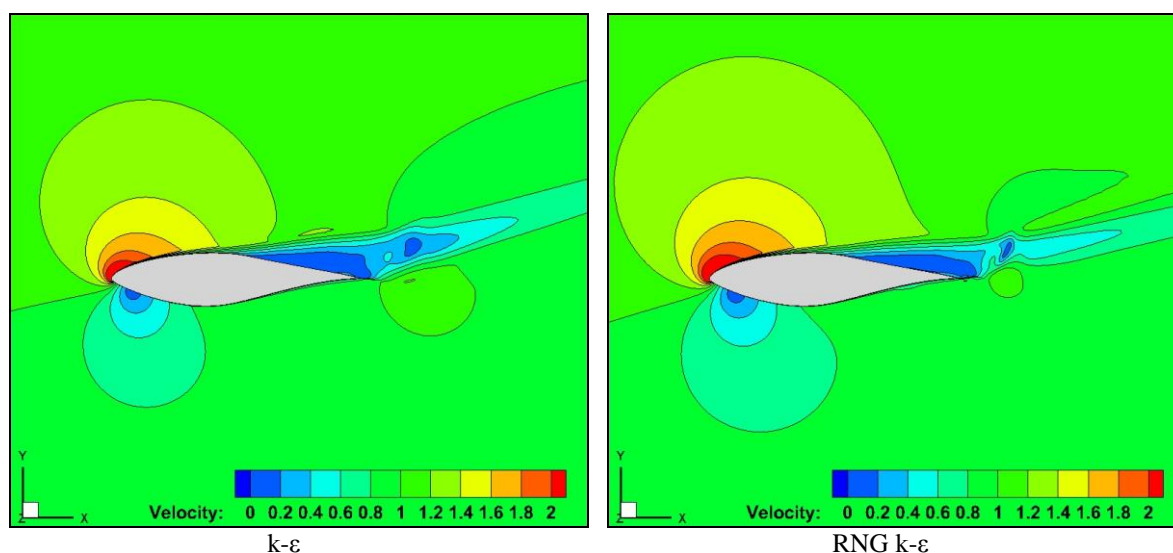
Figure 5. Calculations velocity contours for the angle of attack α = 20.15°.

Conclusion

An analysis of two-dimensional incompressible turbulent flow around NREL S809 airfoil was performed using ANSYS CFX CFD code. The analysis was carried out using two turbulence models, k-ε and RNG k-ε, for fixed Reynolds number of 2.0×10^6. From the calculations, both k-ε and RNG k-ε models gave near prediction to the experimental values at low angle of attacks, whereas they failed to give good prediction in both pre-stall and post-stall regions. Both models used in this analysis gave more satisfactory predictions of the hydrodynamics characteristics for this airfoil. However, while taking drags and lifts into account, these two models under predict the C_d values and over predict the C_l at higher angles of attack (AOA >= 9.22°), whereas C_d and C_l values of both models lies close to the experimental values at smaller angles of attack (AOA <= 9.22°). The obtained results of k-ε and RNG k-ε models can be improved by increasing the mesh density in the direction of the flow.

Acknowledgements

References

ANSYS, Inc. (2017). *ANSYS CFX Reference Guide*. Release 18.2 academic version.

Butterfield, C. P., Scott, G., & Musial, W. (1992). Comparison of wind tunnel airfoil performance data with wind turbine blade data. *Journal of solar energy engineering*, *114*(2), 119-124.

Chang, Y. L., Yang, S. L., & Arici, O. (1996). *Flow field computation of the NREL S809 airfoil using various turbulence models* (No. CONF-960154-). American Society of Mechanical Engineers, New York, NY (United States).

Guerri, O., Bouhadef, K., & Harhad, A. (2006). Turbulent flow simulation of the NREL S809 airfoil. *Wind Engineering*, *30*(4), 287-301.

Hartwanger, D., & Horvat, A. (2008, June). 3D modelling of a wind turbine using CFD. In NAFEMS Conference, United Kingdom.

Launder, B. E. & Spalding, D. B. (1974). The numerical computation of turbulent flows. Computer methods in applied mechanics and engineering, 3(2),269–289.

Wang, H., Zhang, B., Qiu, Q., & Xu, X. (2017). Flow control on the NREL S809 wind turbine airfoil using vortex generators. Energy, 118, 1210-1221.

Wolfe, W. P. and Ochs, S. S., *CFD calculations of S809 aerodynamic characteristics*, AIAA-97-09

Yakhot, V. S. A. S. T. B. C. G., Orszag, S. A., Thangam, S., Gatski, T. B., & Speziale, C. G. (1992). Development of turbulence models for shear flows by a double expansion technique. Physics of Fluids A: Fluid Dynamics, 4(7), 1510-1520.

Author Information

Bouabdellah Abed
Laboratoire de Mécanique Appliquée,
Université des Sciences et de la Technologie-Mohamed
Boudiaf- Oran, Algérie.
El Mnaouar, BP 1505, Bir El Djir 31000, Oran - Algérie.
Contact E-mail: bouabdellah.abed@univ-usto.dz

Habib Achache
University Mohamed Benahamed Oran 2
Boite Postale 1515 El Menouar Oran, Algeria

Mohamed-Kamel Hamıdou
Laboratoire de Mécanique Appliquée,
Université des Sciences et de la Technologie-Mohamed
Boudiaf- Oran, Algérie.
El Mnaouar, BP 1505, Bir El Djir 31000, Oran - Algérie

Abdelouahab Benzerdjeb
Laboratoire de Mécanique Appliquée,
Université des Sciences et de la Technologie-Mohamed
Boudiaf- Oran, Algérie.
El Mnaouar, BP 1505, Bir El Djir 31000, Oran - Algérie

Abiddine Debab
Departement de Génie Maritime,
Université des Sciences et de la Technologie d'Oran,
Algérie.
El Mnaouar, BP 1505, Bir El Djir 31000, Oran - Algérie

IConTES 2019: International Conference on Technology, Engineering and Science

Synthesis of Novel Triazole-Linked Schiff Base Derivative

Aysegul GUMUS
Van Yuzuncu Yil University

Selcuk GUMUS
Van Yuzuncu Yil University

Abstract: The nitrogen atom of azomethine C=N double bond in Schiff base exhibits a strong affinity for transition metal ions. Schiff base derivatives incorporating a fluorescent moiety are appealing tools for optical sensing of metal ions. In this work, fluorescent Schiff base derivatives were synthesized by reacting triazole-linked salicylaldehyde derivative with aminopyrene and aminoanthracene, which are very good fluorophores. These compounds have high potential to be used as metal chemosensors. Detection of a specific type of a metal is very important in terms of biouse of the related compound. In order to determine the sensitivity of the novel compounds, a series of spectroscopic measurements were caried out upon synthesis. Moreover, the metal coordination characteristics of the new compounds were also be investigated theoretically at the level of Density Functional theory with the application of B3LYP/6-31++G(d,p), which is a combination of hybrid exchange function and basis set.

Keywords: Schiff base, Anthracene, Pyrene, Triazole

Introduction

The evolution of fluorescence sensing has been known as an essential and fascinating research field of analytical chemistry at present, due to its simplicity in measurements, low detection limit, low cost, real-time analysis and quantified applications in the environment, biological systems and molecular catalysis[1-6].

Molecular probes containing pyrene or anthracene framework were well suited for the development of chemosensors due to their extended π-conjugation property, chemical stability, high quantum yield and effective photoluminescence features [7-10].

Schiff bases are known to be good ligand for metal ions [11] and used to develop chemosensors since the nitrogen atom of azomethine C=N double bond in Schiff base exhibits a strong affinity for transition metal ions. Schiff base metal complexes have numerous applications like antitumor properties [12], antioxidative activities [13], and attractive electronic and photophysical properties [14]. In addition, Schiff base derivatives incorporating a fluorescent moiety are appealing tools for optical sensing of metal ions. Tetradentate ligands such as salen- or pyridine-type symmetrical Schiff bases are capable of forming complexes with certain metal ions which can exhibit unusual coordination, high thermodynamic stability, good fluorescent properties and biological activities [15].

Triazole-containing compounds show various biological activities including antimicrobial [16], anti-inflammatory [17], antidepressant [18], anticonvulsant [19], antifungal [20], enzyme inhibition [21] activities. 1,2,3-Triazoles have also a wide range applications in industry as anticorrosive agents, dyes, photostabilizers, photographic materials, and agrochemicals [22–24]. Remarkable stability toward metabolic transformations, H-bonding capability, and high dipole moment make triazoles attractive building components [25–27].

Motivated by these studies, Schiff base structure was built between benzyl substituted salicylaldehyde and amino anthracene. Trizole bridge connecting benzyl and salicylaldehyde could furnish an extra binding site.

Salicylaldehyde was connected with anthracene by C=N structure. Anthracene and pyrene were employed as fluorophore due to their outstanding photophysical properties and easy modification [28]. The C=N structure might provide another binding state, which could improve the selectivity.

Experimental

General

All experiments were carried out in pre-dried glassware an inert atmosphere of argon. All the chemicals used in the biologic assay studies were purchased from Sigma (Sigma-Aldrich GmbH, Sternheim, Germany). ^{1}H NMR and ^{13}C NMR spectra were recorded in CDCl$_3$ on a Agilent NMR spectrometer (400 MHz). ^{1}H (400 MHz) and ^{13}C NMR (100 MHz) were recorded in CDCl$_3$ and the chemical shifts are expressed in ppm relative to CDCl$_3$ (δ 7.26 and 77.0 for ^{1}H and ^{13}C NMR, respectively) as the internal standard.

Flash column chromatography was performed by using thick-walled glass columns and silica gel (60-mesh; Merck). The reactions were monitored by thin-layer chromatography (TLC) using Merck 0.2-mm silica gel 60 F254 analytical aluminium plates, visualized by UV light.

Synthesis of 2-(prop-2-ynyloxy)benzaldehyde, 1.

Salicylaldehyde (1.2 g, 10 mmol) was dissolved in 30 mL THF. K$_2$CO$_3$ (4.14 g, 30 mmol) was added and the mixture was refluxed for 30 min. Then propargyl bromide (1.7 mL, 12 mmol) was added slowly. The mixture was refluxed overnight and cooled. After filtration solvent was evaporated. Crude product was purified by column chromatography (EtOAc: Hexane 1:5).

White solid. (1.52 g, 95% yield); ^{1}H NMR (CDCl$_3$, 400 MHz): δ 10.49 (s, 1H), 7.86 (dd, J=1.8 and 7.7 Hz, 1H), 7.59-7.55 (m, 1H), 7.13-7.07 (m, 2H), 4.83 (d, J=2.4 Hz, 2H), 2.57 (t, J=2.4 Hz, 1H); ^{13}C NMR (CDCl$_3$, 100 MHz): δ 189.5, 159.7, 135.7, 128.6, 125.5, 121.7, 113.2, 56.4.

Synthesis of 2-((1-benzyl-1H-1,2,3-triazol-4-yl)methoxy)benzaldehyde, 2.

A mixture of benzyl bromide (1 mmol), 2-(prop-2-ynyloxy), salicylaldehyde (1 mmol), L-proline (24 mg, 0.2 mmol), Na$_2$CO$_3$ (24 mg, 0.2 mmol), NaN$_3$ (65 mg, 1 mmol), sodium ascorbate (20 mg, 0.1 mmol), DMSO/H$_2$O (18:2, 2.0 mL), and CuSO$_4$·5H$_2$O solution (1 M, 0.05 mL) in a 20 mL scintillation vial was stirred overnight at 65°C. The crude mixture was poured into cold dilute NH$_4$OH solution (30 mL) and extracted with ethyl acetate (3×20 mL). The collected organic layer was washed with brine, dried over MgSO$_4$, and concentrated in *vacuo*. The crude product was purified by flash column chromatography.

White solid. (264 mg, 90% yield); ^{1}H NMR (CDCl$_3$, 400 MHz): δ 10.40 (s, 1H), 7.80 (dd, J=1.8 and 7.7 Hz, 1H), 7.58 (s, 1H), 7.56-7.51 (m, 1H), 7.40-7.35 (m, 3H), 7.28-7.26 (m, 2H), 7.14 (d, J=8.4 Hz, 1H), 7.04 (t, J=7.7 Hz, 1H), 5.54 (s, 3H), 5.30 (s, 3H); ^{13}C NMR (CDCl$_3$, 100 MHz): δ 189.5, 160.4, 143.7, 136.0, 134.3, 129.2, 128.9, 128.6, 128.1, 122.8, 121.3, 113.0, 62.6, 54.3.

General procedure for the synthesis of Schiff Bases, SB-1 and SB-2.

2-((1-benzyl-1H-1,2,3-triazol-4-yl)methoxy)benzaldehyde **2** (147 mg, 0.5 mmol) and aryl amine (0.5 mmol) were dissolved in 5 mL ethanol. Reaction mixture was mixed at room temperature overnight. Solid was filtered and dried.

(E)-N-(2-((1-benzyl-1H-1,2,3-triazol-4-yl)methoxy)benzylidene)anthracen-1-amine, SB-1.

Yellow solid. (190 mg, 81% yield); ^{1}H NMR (CDCl$_3$, 400 MHz): δ 8.99 (s, 1H), 8.86 (s, 1H), 8.42 (s, 2H), 8.00 (s, 2H), 7.87-7.82 (m, 1H), 7.48-7.40 (m, 5H), 7.28 (s, 3H), 7.16 (s, 4H), 6.93 (s, 1H), 5.43 (s, 2H), 5.28 (s, 2H); ^{13}C NMR (CDCl$_3$, 100 MHz): δ 158.2, 156.1, 150.3, 143.9, 136.0, 132.9, 132.1, 131.9, 131.5, 129.2, 129.1,

128.7, 128.3, 128.1, 128.0, 127.9, 127.8, 125.9, 125.8, 125.6, 125.5, 125.3, 122.9, 122.8, 121.6, 112.8, 111.4, 62.6, 54.2.

(E)-N-(2-((1-benzyl-1H-1,2,3-triazol-4-yl)methoxy)benzylidene)pyren-1-amine, SB-2.

Yellow solid. (214 mg, 87% yield); ^{1}H NMR (CDCl$_3$, 400 MHz): δ 9.08 (s, 1H), 8.63 (d, *J*=9.1 Hz, 1H), 8.44 (dd, *J*=1.8 and 7.7 Hz, 1H), 8.17-8.13 (m, 3H), 8.08-7.98 (m, 4H), 7.65 (d, *J*=8.1 Hz, 1H), 7.50-7.47 (m, 2H), 7.28-7.25 (m, 3H), 7.19-7.15 (m, 4H), 5.47 (s, 2H), 5.32 (s, 2H); ^{13}C NMR (CDCl$_3$, 100 MHz): δ 158.3, 156.7, 146.5, 144.1, 134.3, 132.8, 131.5, 129.4, 129.1, 128.8, 128.1, 128.0, 127.3, 126.9, 126.5, 126.0, 125.5, 125.2, 124.9, 124.8, 123.4, 122.7, 121.6, 115.7, 112.9, 62.7, 54.2.

Computational Method

The three-dimensional ground state (S$_0$) geometry of the compound was geometry optimized using Density Functional Theory (DFT) by using the Gaussian 09W package program and the hybrid functional B3LYP. The B3LYP is composed of Becke's three parameter exchange functional (B3) and the nonlocal correlation functional by Lee, Yang, and Parr (LYP). The basis set used for all atoms was 6-31++G(d,p) in both DFT and time-dependent density functional theory (TD-DFT) method. We have applied default G09 grid for computations.

For the nonel compound, vibrational analyses were carried out using the same basis set employed in the corresponding geometry optimizations. The frequency analysis of none of the compounds yielded any imaginary frequencies, indicating that the structure of each molecule corresponds to at least a local minimum on the potential energy surface. The normal mode analysis was performed for 3N-6 vibrational degrees of freedom, N being the number of atoms in the molecule.

The low-lying triplet (T) and singlet excited states (S) of the compounds were relaxed to obtain their minimum energy geometries using the TD-DFT as implemented in G09 package program. The vertical excitation energies and oscillator strengths were obtained for the lowest triplet and singlet transitions at the optimized ground state equilibrium geometries by using TD-DFT at the same hybrid functional and basis set [22]. Optimized ground state structures were utilized to obtain the electronic absorption spectra, including maximum absorption wavelengths, oscillator strengths, and main configuration assignment by using TD-DFT.

Results and Discussion

The key substrate 2-(prop-2-ynyloxy)benzaldehyde was synthesized by the addition of propargyl bromide to commercially available salicylaldehyde by O-propargylation method (Scheme 1). Terminal acetylene unit on 2-(prop-2-ynyloxy)benzaldehyde **1** make it a valuable candidate for one-pot synthesis of the target triazole structure **2**. Aliphatic and aromatic azides from corresponding halides can easily be generated as intermediates in one-pot synthesis method and converted to desired triazole derivatives without isolation. The operational simplicity of this method makes it attractive for wide variety of applications. Initially, 2-(prop-2-ynyloxy)benzaldehyde was employed in one-pot, two-step procedure by reacting with sodium azide and benzyl bromide (Scheme 1).

(a) Propargyl bromide, K$_2$CO$_3$, THF; (b) benzyl bromide, NaN$_3$, one-pot click reaction; (c) aryl amine, EtOH.
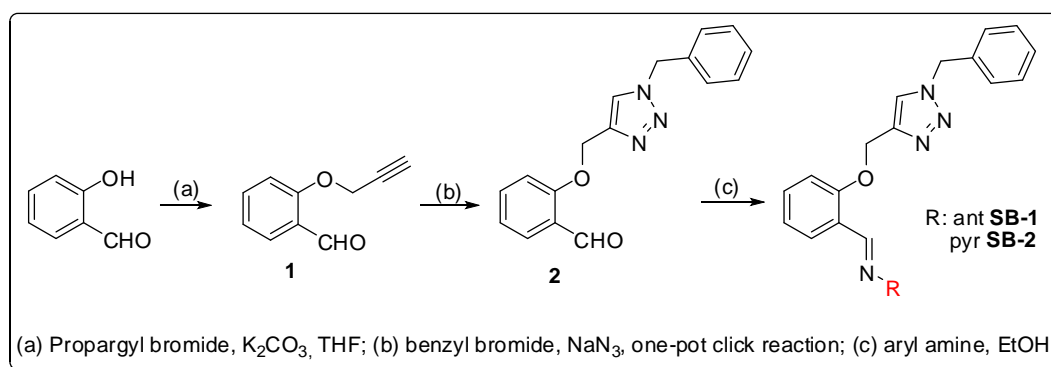
Scheme 1. Synthesis of Schiff-base derivatives

The Schiff bases **SB-1** and **SB-2** were prepared by the condensation reaction of triazole-substituted salicyaldehyde with the corresponding amino anthracene and amino pyrene as illustrated in Figure 1 below.
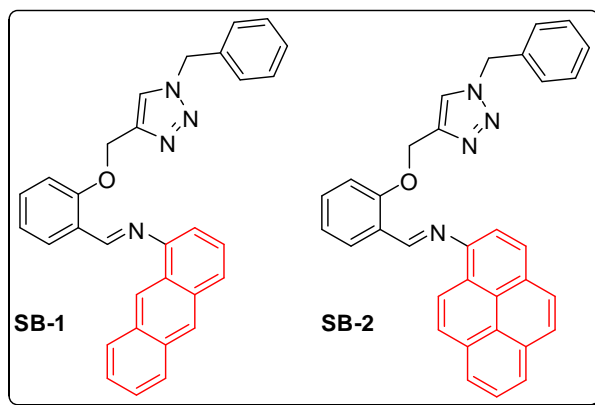
Figure 1. Synthesized Schiff bases
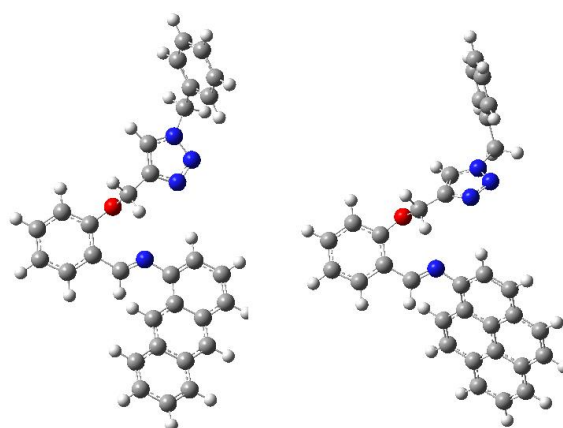
Figure 2. Geometry optimized structures of Schiff bases

The geometry optimizations of the compounds have been performed at B3LYP/6-31++G(d,p) level of theory. After obtaining the ground state geometries of the Schiff bases we have went through the metal coordiation process with Zn^{2+} ion. The metal coordination is proven upon TDDFT investigation of the UV-Vis spectra of the compounds. In Figure 3, the structures of the compounds and correcponding spectra are given. As can be observed there exist a visible band at aroun 420 nm on both structure without metals. We observe a red-shift at these band upon metal addition to the system, which proves the metal coordination at triazole and imine nitrogens.
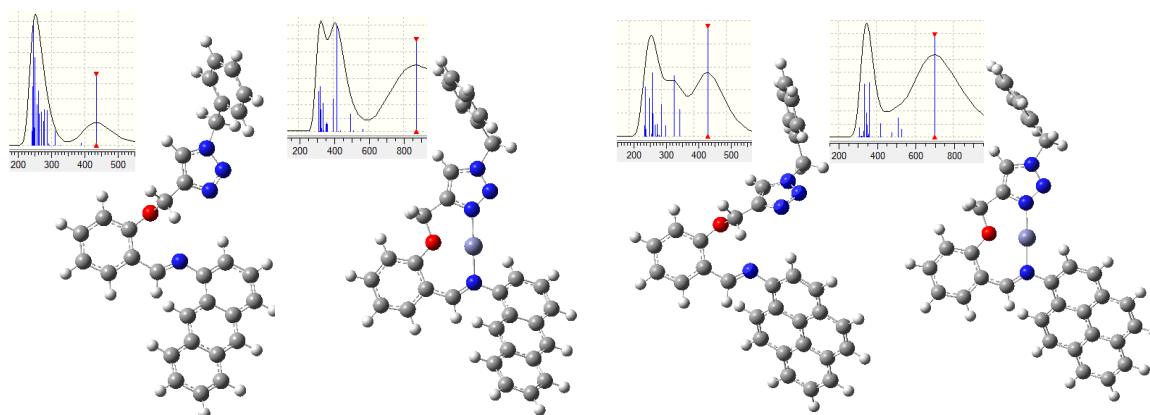
Figure 3. Geometry optimized structures and corresponding UV-Vis spectra of the Schiff bases.

Conclusion

In conclusion, propargyl unit was attached to salicylaldehyde by O-propargylation and alkyne derivative was obtained. Then, triazole-substituted salicylaldehyde **2** was synthesized with high yield by one-pot method.

Target fluorescent Schiff-bases were isolated from the reaction of aldehyde group on salicylaldehyde ring with amino anthracene and amino pyrene successfully.

Theoretical calculation on the coordination ability of the compounds showed that the UV-Vis spectra of the compounds are highly sensitive to metal coordination. TDDFT computations of the metal coordinated Schiff bases yielded red-shifted bands.

Acknowledgements or Notes

References

A.P. de Silva, H.Q. Gunaratne, T. Gunnlaugsson, A.J.M. Huxley, C.P. McCoy, J.T. Rademacher, T.E. Rice, Signaling Recognition Events with Fluorescent Sensors and Switches, *Chem. Rev*. 97 (1997) 1515-1566.

R. Hu, J. Feng, D.H. Hu, S.Q. Wang, S. Li, Y. Li, G.Q. Yang, A Rapid Aqueous Fluoride Ion Sensor with Dual Output Modes, *Angrew. Chem., Int. Ed.* 49 (2010) 4915-4918.

J. Fan, M. Hu, P. Zhan, X. Peng, Energy transfer cassettes based on organic fluorophores: construction and applications in ratiometric sensing, *Chem. Soc. Rev*. 42 (2013) 29-43.

Y. Yang, Q. Zhao, W. Feng, F. Li, Luminescent Chemodosimeters for Bioimaging, *Chem. Rev.* 113 (2013) 192-270.

X. Lim, The Nanoscale Rainbow, *Nature*. 531 (2016) 26.

M. Gao, B.Z. Tang, Fluorescent Sensors Based on Aggregetion-Induced Emission: Recent advances and perspectives, *ACS Sens.* 2 (2017) 1382-1399.

G.B. Demirel, B. Daglar, M. Bayindir, Extremely fast and highly selective detection of nitroaromatic explosive vapours using fluorescent polymer thin films, *Chem Commun.* 55 (2013) 6140-6142.

(a) L. Ding, Y. Fang, Chemically assembled monolayers of fluorophores as chemical sensing materials, *Chem Soc Rev*. 11 (2010) 4258-4273. (b) G. Sivaraman, A.Gulyani, Chemically diverse small molecule fluorescent chemosensors for copper ion. *Coord. Chem rev.*, 357 (2018) 50-104

S. Shanmugaraju, H. Jadhav, R. Karthik, P. S. Mukherjee, Electron rich supramolecular polymers as fluorescent sensors for nitroaromatics, *RSC Adv.* 15 (2013) 4940-4950.

R. Pandey, L. Reddy, S. Ishihara, A. Dhir, V. Krishnan, Conformation induced discrimination between picric acid and nitro derivatives/anions with a Cu-pyrene array: the first decision making photonic device , *RSC Adv*. 3 (2013) 21365-21368.

D.M. Epstein, S. Choudhary, M.R. Churchill, K.M. Keil, A.V. Eliseev, J.R. Morrow, Chloroform-Soluble Schiff-Base Zn(II) or Cd(II) Complexes from a Dynamic Combinatorial Library, *Inorg. Chem*. 40 (2001) 1591–1596.

V.C. Da Silveira, J.S. Luz, C.C. Oliveira, I. Graziani, M.R. Ciriolo, A.M. Ferreira, Double-strand DNA cleavage induced by oxindole-Schiff base copper(II) complexes with potential antitumor activity, *J. Inorg. Biochem*. 102 (2008) 1090–1103.

Y. Li, Z.Y. Yang, DNA binding affinity and antioxidative activity of copper(II) and zinc(II) complexes with a novel hesperetin Schiff base ligand, *Inorg. Chim. Acta* 362 (2009) 4823–4831.

S. Kasselouri, A. Garoufis, A. Katehanakis, G. Kalkanis, S.P. Perlepes, N. Hadjiliadis, 1:1 Metal complexes of 2-(2′-pyridyl)quinoxaline, a ligand unexpectedly formed by the reaction between 2-acetylpyridine and 1,2-phenylenediamine, *Inorg. Chim. Acta* 207 (1993) 255–258.

G. A. Morris, H. Zhou, C.L. Stern, S.T. Nguyen, A General High-Yield Route to Bis(salicylaldimine) Zinc(II) Complexes: Application to the Synthesis of Pyridine-Modified Salen-Type Zinc(II) Complexes, *Inorg. Chem.* 40 (2001) 3222–3227.

S. Esvaran, A. V.,Adhikari, N. S. Shetty, Synthesis and antimicrobial activities of novel quinoline derivatives carrying 1,2,4-triazole moiety, *Eur. J. Med. Chem. 44* (2009) 4637–4647.

S. S. Kumar, H. P. Kavitha, Synthesis and biological applications of triazole derivatives, *Mini-Rev. Org. Chem*. 10 (2013) 40–65.

C. Radhika, A. Venkatesham, M. Sarangapani, Synthesis and antidepressant activity of disubstituted-5-aryl-1,2,4-triazoles, *Med. Chem. Res*. 31 (2012) 3509–3513.

T. Plech, J. J. Luszczki, M. Wujec, J. Flieger, M. Pizon, Synthesis, characterization and preliminary anticonvulsant evaluation of some 4-alkyl-1,2,4-triazoles, *Eur. J. Med. Chem*. 60 (2013) 208–215.

P. M. Chaudhary, S. R. Chavan, F. Shirazi, M. Razdan, P. Nimkar, S. P. Maybhate, A. P. Likhite, R. Gonnade, B. G. Hazara, S. R. Deshpande, Exploration of click reaction for the synthesis of modified nucleosides as chitin synthase inhibitors, *Bioorg. Med. Chem. Lett*. 17 (2009) 2433–2440.

J. P. Zhou, H. B. Zhang, H. Qian, L. Lin, W. L. Huang, S. J. Ni, Synthesis and biological evaluation of aromatase inhibitors, *Lett. Drug Design Discov*. 6 (2009) 181–185.

B. S. Holla, N. S. Mahhalinga, Synthesis, characterization and antimicrobial activity of some substituted 1,2,3-triazoles, *Eur. J. Med. Chem*. 40 (2005) 1173–1178.

M. A. Elmorsi, A. M. Hassanein, Corrosion inhibition of copper by heterocyclic compounds, *Corros. Sci*. 41 (1999) 2337-2352.

D. K. Kim, J. Kim, H. J. Park, Synthesis and biological evaluation of novel 2-pyridinyl-[1,2,3]triazoles as inhibitors of transforming growth factor beta 1 type 1 receptor, *J. Bioorg. Med. Chem. Lett.* 14 *(*2004) 2401–2405.

T. S. Seo, Z. Li, H. Ruparel, J. Lu, Click chemistry to construct fluorescent oligonucleotides for DNA sequencing, *J. Org. Chem*. 68 (2003) 609–612.

K. Sivakumar, F. Xie, B. M. Cash, S. Long, H. N. Barnhill, A Fluorogenic 1,3-dipolar cycloaddition reaction of 3-azidocoumarins and acetylenes, *Org. Lett*. 6 (2004) 4603–4606.

A. Dondoni, A. Marra, "Click chemistry" inspired synthesis of *pseudo*-oligosaccharides and amino acid glycoconjugates, *J. Org. Chem*. 71 (2006) 364–367.

J. Chan, S. C. Dodani and C. J. Chang, Reaction-based small-molecule fluorescent probes for chemoselective bioimaging, *Nature Chemistry* 4 (2012) 973-984.

Author Information

Aysegul Gumus
Van Yuzuncu Yil University
Department of Chemistry
Contact E-mail: *gumusa@gmail.com*

Selcuk Gumus
Van Yuzuncu Yil University
Department of Chemistry

Synthesis of New 3-Substiuted Quinazolin-4(3H)-one Compounds

Rand Arshad SAAD-ALDEEN
University of Mosul

Mohammed Ahmed AL-IRAQI
University of Mosul

Abstract: Quinazolin-4(3H)-one is a well-known heterocyclic compound with a unique place in medicinal chemistry, and it has drawn much attention due to its diversified biological activity. In this research we report the synthesis of some quinazolin-4-one derivatives containing acetylenic moiety. The quinazolin-4(3H)-one (1) was synthesized from the reaction of anthranilic acid with formamide under the conventional or microwave irradiation conditions. The quinazolin-4(3H)-one was converted to the corresponding 3-propargyl derivative (2) by its reaction with propargyl bromide in presence of potassium carbonate as a base and acetone as a solvent. The 3-propargyl quinazolin-4(3H)-one (2) was used as a precursor to synthesize new three series of heterocyclic compounds containing quinazolin-4(3H)-one moiety. Compound (2) was treated with ethyl magnesium bromide, then the resulted solution treated immediately with carbon disulfide and sublimed sulfur to synthesize 1,2-dithiol-3-thione compound (3). The 1,2,3-triazole compounds (5a-d) were synthesized by the reaction of compound (2) with alkyl azides (4a-d) according to Click reaction. The Mannich bases (6a-i) were synthesized *via* Mannich reaction by reaction of the acetylenic compound (2) with secondary amines in presence of paraformaldehyde in1,4-dioxane as a solvent. All the synthesized compounds were characterized by physical and spectral measurements.

Keywords: Quinazolin-4-one, 1,2-dithiol-3-thione, 1,2,3-triazole, Click reaction, Mannich reaction

Introduction

Quinazolin-4(3H)-one and its derivatives occupy a distinct position among the heterocyclic compounds and they considered as a building block for a huge number of synthetic and natural products such as alkaloids, agrochemicals, drugs, antibiotic and antimicrobial agents. These compounds have gained great attention owing to their wide and distinct biological and therapeutic activity. Many therapeutic activities were determined for the quinazolin-4(3H)-one derivatives, including anti-bacterial [Hess et al., 1968],[1] antifungal [Ghorab 2000; Bartroli et al., 1998] [2,3] anticancer [Dohle et al., 2018; Abdel-Hamid, 1997; EI-Brollosy et al., 2003; Shab et al., 1995] ,[4-7] anti-HIV [Khili et al, 1994],[8] anti-inflammatory [Shivaram et al, 1998],[9] anticonvulsant [Noureldin et al, 2017],[10] anti-oxidant [Saravanan et al, 2010],[11] anti-obesity [Sasmal et al, 2012].[12] The above facts encouraged us to synthesize several newer quinazolin-4(3H)-one derivatives by incorporating a set of biologically active moieties, such as acetylenic (oxotremorine analog), [Sjoqvist and Gilette, 1965; Leslie and Maxwell, 1904; Tang et al, 1993; Disingrini et al, 2006; Dallanoce et al, 1999],[13-17] 1,2,3-trizole [Xu et al, 2014; Saqlain et al, 2014],[18,19] and 1,2-dithiol-3-thione [Lee et al, 1986; Kensler et al, 1987][20,21] moieties at position-3 of quinazolinone nucleus, in order to improve the efficacy and biological activity of quinazolin-4(3H)-one.

Experimental

Melting points were determined with an open capillary tube by Stuard-SMP30 melting point apparatus, and were uncorrected. Microwave irradiation was performed by microwave oven with power output 900 W. Infrared spectra were recorded as neat on Alfa Bruker ATR- FT.IR Co. Germany, 2003, College of Pharmacy.

^{1}HNMR and ^{13}CNMR spectra were recorded on Bruker Bio Spin 400 MHz spectrometer, Turkey , using TMS as internal standard and (DMSO-d6) as a solvent.

Synthesis of Quinazolin-4(3H)-one (1):

This compound was synthesized *via* two synthetic methods, the conventional method and the green method *via* the free solvent, microwave irradiation.

The Conventional Method:

A mixture of anthranilic acid (0.1 mol, 13.7 g) and formamide (0.5 mol, 22.5 g) was heated on a sand bath at 150-160 ^{o}C for 8h, then left to cool. The resulted precipitate was filtered off, washed thoroughly with water, dried then recrystallized from methanol to afford shiny white powder in 61% yield, m.p. 214-216 ^{o}C.

The Green Method:

In a Pyrex beaker, anthranilic acid (0.1 mol, 13.7 g) and formamide (0.5 mol, 22.5 g) were mixed well. The beaker was covered with a turned over funnel, then placed in the microwave oven and irradiated at two stages: in the first stage the content of the beaker was irradiated with a power of 30% (270 W) for 5 min. then left for 15 min. In the second stage the beaker was subjected to microwave for further 5 min. at a power at a level 50% (450 W), then left to cool to room temperature. The resulted residue was washed thoroughly with water, dried then recrystallize from methanol to give shiny honey crystal in 86.4% yield, m.p. 216-2017 ^{o}C.

Synthesis of 3-Propargylquinazolin-4(3H)-one (2):

A mixture of quinazolin-4(3H)-one (1) (0.005 mol, 0.73 g), propargyl bromide (0.005 mol, 0.59 g) and potassium carbonate (1 g) in dry acetone (15 ml) was refluxed with stirring for 6h, then cooled and poured on 25 ml of an ice-water. The resulted precipitate was filtered off, washed thoroughly with water, dried and recrystallized from ethanol : water (90%) to give hazel shiny needle crystals in 76% yield, mp. 115-117 ^{o}C.

Synthesis of 4-Mercapto-5-[(4'-oxoquinazolin-3'-yl)methyl]-1,2-dithiol-3-thione (3):

Synthesis of Ethyl Magnesium bromide:

To dry magnesium turning (0.008 mol, 0.87 g) in dry diethyl ether (25 ml), a solution of ethyl bromide (0.008 mol, 0.87 g) in 10 ml of dry diethyl ether was dropwise added. The reaction was worked up according to the conventional method for preparation of Grignard reagent [Furniss et al, 1989].[22] After consuming of all magnesium, the mixture was cooled, and a solution of the acetylenic compound (2) (0.008 mol, 1.47 g) in 15 ml of dry diethyl ether was dropwise added with stirring. The stirring was continued for further 0.5h at room temperature to form the solution of magnesium acetylide, which is used immediately to synthesize 4-mercapto-5-[(4'-oxoquinazolin-3'-yl)methyl]-1,2-dithiol-3-thione (3).

Synthesize 4-Mercapto-5-[(4'-oxoquinazolin-3'-yl)methyl]-1,2-dithiol-3-thione (3):

The resulted solution from the previous step was cooled to (0-5 ^{o}C) in an ice-bath, then carbon disulfide (0.008 mol, 0.5 ml) and excess of sulfur (0.026 mol, 0.86 g) were added with stirring. The stirring was continued for further 1h in an ice-bath, and 6h at room temperature. The reaction mixture was filtered and the filtrate acidified with 10% hydrochloric acid. The ether layer was separated and the aqueous layer extracted with (2 * 20 ml) diethyl ether. The ether fractions were collected, dried with magnesium sulfate, filtered and the ether was evaporated to afford the crude 1,2-dithiol-3-thione compound (3) which recrystallized from ethanol to give faint yellow crystals in 65% yield, m.p. 199-200 ^{o}C.

Synthesis of 1-Alkyl-4-[(4'-quinazilin-3-yl)methyl]-1,2,3-triazoles (5a-d):

Synthesis of Alkyl azides (4a-d):

An alkyl halide (0.01mol) was added with stirring to a mixture of sodium azide (0.01 mol, 0.71 g) in (22 ml) of dimethyl sulfoxide (DMSO). The stirring was continued overnight at room temperature. The resulted reaction mixture was added to an ice-water (50 ml), then extracted with (2 *30 ml) diethyl ether. The collected ether fractions were washed with water, then with brine, dried with magnesium sulfated, then evaporated under reduced pressure at room temperature to give an oily product in ~ 90% yield. Their meting points are not measured because the azides classified as explosive materials. The IR spectral data of compounds (4a-d) were shown in Table 1.

Synthesis of 1,2,3-Triazole Derivatives (5a-d) (Click Reaction).

A mixture of acetylenic compound (2) (0.005 mol, 0.92 g), one of alkyl azides (4a-d) and catalytic amount (10 mg) of cuprous chloride in 15 ml of dry toluene was refluxed for 10h. The reaction mixture was filtered then the solvent evaporated and the residue was recrystallized from methanol to give 1,2,3-triazole derivatives (5a-d). The physical and IR spectral data are listed in table 2.

Synthesis of 1-(4'-Oxoquinazolin-3'-yl)-4-disubstituted amino-2-butyne (6a-i): General Procedure:

A mixture of the acetylenic compound (2) (0.03 mole, 0.69 g) and secondary amine (0.036 mole) was cooled to (0 °C). A solution of paraformaldehyde (0.036 mole, 0.13 g) in dry dioxane free peroxide (16 ml) was added dropwise slowly with stirring and finally catalytic amount of cuprous chloride (0.06 g) was added. After the completion of addition at (0 °C), 4.5 ml of glacial acetic acid was added in 5min period. The mixture was heated to 90 °C for 1.5h, then cooled and a cold water (100 ml) was added to the reaction mixture. The mixture was acidified with diluted hydrochloric acid (1:1) to pH=1 with continuous stirring. The mixture was extracted with (2*20 ml) diethyl ether, and the ether fractions were neglected and the aqueous layer was basified with sodium carbonate to pH=9 then extracted with five (20 ml) portion of chloroform. The collected chloroform was dried over magnesium sulfate, filtered and evaporated under reduced pressure to provide the acetylenic Mannich bases (6a-i). The physical and the spectral data were listed in Table 3.

Result and Discussion

The synthetic strategy for this research to obtain the targeted compounds (1-6) is depicted in Scheme 1.

Scheme 1

The first route of this strategy involves the synthesis of the starting material, quinazolin-4(3H)-one (1), which was synthesized from the reaction of one equivalent of anthranilic acid and five equivalents of formamide, either by the conventional method or by the green method *via* the irradiation with microwave radiation. The second method is more favorable than first method because the green method performed in few minutes with high yield (87%), while the conventional method required at least 6h heating at 150-160 ^{o}C with a lower yield (61%). The IR spectrum of compound (1) showed a characteristic absorption bands at 1696 and 1604 Cm^{-1} for C=O bond stretching and C=N bond stretching respectively. The ^{1}HNMR spectrum [Crews et al, 1998][23] of compound (1) showed the following chemical shifts δ (ppm) at: 7.5 (t, 1H, H6) 7.65 (d, 1H, H5), 7.81(t, 1H, H7), 8.11(d, 1H, H8), 8.14 (s, 1H, H2), 12.26 (s, 1H, OH). The spectral data indicate that the compound present as quinazolin-4(3H)-one in the solution and as 4-hydroxyquinazoline in a solid state.

1
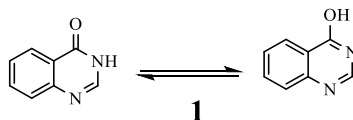
Quinazolin-4(3H)-one (1) was converted to its acetylenic derivative (2) *via* alkylation process with propargyl bromide in dry acetone in presence of potassium carbonate. Quinazolin-4(3H)-one (1) is known to be alkylated at either N-3 or oxygen depending on the reaction conditions. In this study, the alkylation of quinazolin-4(3H)-one (1) was occurred at the nitrogen in the 3-position to produce 3-propargyl quinazolin-4(3H)-one (2), on the dependence on the spectral data. The appearance of a characteristic absorption bands at 1657 Cm^{-1} in the IR spectrum for C=O bond stretching supported the alkylation at N-3 position. Moreover, the IR spectrum of compound (2) showed a characteristic absorption bands for the acetylenic moiety at 3214 and 2120 Cm^{-1} for the acetylenic ≡C-H and C≡C bond stretching respectively. The ^{1}HNMR spectrum of compound (2) showed the following chemical shifts, δ (ppm) at: 3.34 (s, 1H, ≡C-H), 4.84 (s, 2H, CH$_2$), 7.57 (t, 1H, H6), 7.7 (d, 1H, H5), 7.85 (t, 1H, H7), 8.17 (d, 1H, H8), 8.47 (s, 1H, H2). The ^{13}C NMR spectrum shows the following chemical shifts, δ (ppm) at: 35.59 (<u>C</u>H$_2$), 76.1(≡<u>C</u>-H), 78.99 (<u>C</u>≡C-H), 121.9 (C8), 126.56 (C6), 127.8 (C5), 127.88 (C10), 135.11 (C7), 147.5 (C2), 148.24 (C9), 159.96 (C5). The chemical shift of the C-13 of <u>C</u>H$_2$ gives a further support for the alkylation at the nitrogen-3. If the alkylation occurred at the oxygen, the spectrum must give a chemical shift at more than 50 ppm.

The acetylenic compound (2) was used as a precursor to synthesize new heterocyclic derivatives of quinazolin-4(3H)-one through three routes. The first route involves the synthesis of 4-mercapto-5-[(4-oxoquinazolin-3-yl)methyl]-1,2-dithiol-3-thione (3), which synthesized by conversion of the acetylenic compound (2) to the corresponding Grignard reagent (acetylide intermediate) by its reaction with ethyl magnesium bromide, then the resulted acetylide intermediate reacted with carbon disulfide in presence of elemental sulfur. The IR spectrum of compound (3) showed an absorption bands at 2447,1153 and 491Cm^{-1} for S-H, C=S and S-S bond stretching respectively, in addition to absorption band at 1645 Cm^{-1} for the C=O bond stretching of the quinazolinone moiety. Moreover, the absorption bands of ≡C-H and C≡C bonds stretching at 3214 and 2120 Cm^{-1} are disappeared from the spectrum, which indicates the acetylenic moiety was converted to the 1,2-dithiol-3-thione moiety. The ^{1}HNMR of compound (3) showed the following chemical shifts δ (ppm) at: 3.46 (s, 1H, SH), 4.85 (s, 2H, CH$_2$),), 7.63 (t, 1H, H6), 7.74 (d, 1H, H5), 7.89 (t, 1H, H7), 8.19 (d, 1H, H8), 8.7 (s, 1H, H2).
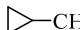
The second route involves the synthesis of 1-alkyl-4-[(4'-oxoquinazolin- 3'-yl)methyl]-1,2,3-triazole derivatives (5a-d) *via* the reaction of the acetylenic compound (2) with alkyl azides (4a-d). The azides (4a-d) were synthesized, as oily products, by the reaction of alkyl halide with sodium azide in DMSO as a solvent at room temperature. Their melting points are not measured owing to the azides are explosive materials. The characteristic absorption band for azide compounds is the bond stretching band of the N=N=N bonds which appeared at 2093-2099 Cm^{-1}.

Table 1. The physical and IR spectral data of the azides (4a-d)

Compd. No.	R	Yield %	IR (neat) ν (Cm^{-1}) N=N=N str.
4a	CH$_3$-	82	2093
4b	C$_2$H$_5$-	90	2095
4c	PhCH$_2$-	91	2094
4d	▷—CH$_2$-	92	2099
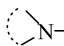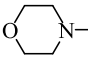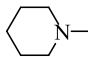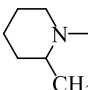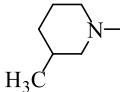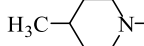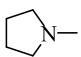
The synthesized alkyl azides (4a-d) were used to synthesize the 1-alkyl-4-[(4'-oxoquinazolin-3'-yl)methyl]-1,2,3-triazole derivatives (5a-d) *via* Click reaction by its reaction with the acetylenic compound (2) in presence of catalytic amount of cuprous chloride in dry toluene. The IR spectra of compounds (5a-d) showed a characteristic absorption bands at 1467-1468 cm^{-1}for N=N bonds stretching, and absorption bands at 1661-1672 Cm^{-1} for the C=O bond stretching for quinazolinone moiety. The absence of the absorption bands at 3214 and 2120 Cm^{-1} for ≡C-H and C≡C bonds stretching supported the conversion of the acetylenic moiety to the triazole moiety.
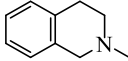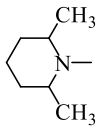
Table 2. The physical and IR spectral data of 1,2,3-triazoles (5a-d)

Compd. No.	R	Yield %	m.p. ^{o}C	Color	IR (neat) ν (Cm^{-1})		
					C=O	N=N	=C-H
5a	CH$_3$-	70	203-204	Light green	1672	1467	3055
5b	C$_2$H$_5$-	71	165-167	Brown	1668	1468	3055
5c	PhCH$_2$-	77	134-135	Brown	1661	1467	3058
5d	▷—CH$_2$-	75	86-88	Light brown	1672	1467	3048

The third route in this research is the synthesis of acetylenic Mannich bases [1-(4'-oxoquinazolin-3'-yl)-4-disubstituted amino-4-butyne] (6a-i). The synthesis of the Mannich bases performed by reaction of the acetylenic compound (2) with secondary amines in presence of paraformaldehyde and catalytic amount of cuprous chloride in dioxane free peroxide. The IR spectra of the Mannich bases (6a-i) showed a characteristic absorption bands at 2124-2220 cm^{-1}for the C≡C bonds stretching, and absorption bands at 1660-1679 cm^{-1} for the C=O bond stretching of quinazolinone moiety. It is notice that the absorption bands of the ≡C-H bond stretching is absent, which indicates the formation of the titled Mannich bases. The ^{1}HNMR spectrum of compound (5d) showed the following chemical shifts (δ, ppm): 0.8 (d, 3H, CH$_3$), 1.69-2.83(m, 9H, piperidine-H), 3.49 (s, 2H, piperidine-CH$_2$-C≡), 4.9 (s, 2H, quin-CH$_2$-C≡), 7.53 (t, 1H, H6), 7.59 (d, 1H, H5), 7.85 (t, 1H, H7), 7.17 (d, 1H, H8), 8.5 (s, 1H, H2). Moreover, the ^{1}HNMR spectrum of compound (5f) showed the following chemical shifts (δ, ppm): 1.48-1.94 (m, 8H, pyrrolidine-H), 2.49 (s, 2H, pyrrolidine -CH$_2$-C≡), 4.87 (s, 2H, quin-CH$_2$-C≡), 7.57 (t, 1H, H6), 7.69 (d, 1H, H5), 7.84 (t, 1H, H7), 8.17 (d, 1H, H8), 8.48 (s, 1H, H2).

Table 3: The physical and IR spectral data of the acetylenic Mannich bases (6a-i):

Compd. No.	◌N—	Yield %	m.p. ^{o}C	color	IR (neat) ν (Cm^{-1})		
					C=C	C≡ C	C=O
6a	O⬡N—	50	51-53	Orang	1606	2203	1679
6b	⬡N—	64	60-62	Faint green	1606	2154	1673
6c	⬡N—(CH$_3$)	62	148-150	Faint brown	1606	2184	1670
6d	H$_3$C-⬡N—	65	68-70	brown	1606	2175	1669
6e	H$_3$C-⬡N—	69	88-89	brown	1606	2214	1669
6f	⬠N—	70	66-68	yellow	1602	2135	1666

6g		61	72-74	brown	1597	2168	1664
6h		52	73-75	brown	1636	2148	1660
6i	PhCH$_2$NCH$_3$	62	79-80	Faint brown	1603	2215	1667

References

Hess, H. J.; Cronin, T. H.; Scriabine, A., (1968), *J. Med. Chem. 11*, 140.

Ghorab, M. M. (2000), *Farmco. 55*, 249.

Bartroli, J.; Turmo, E.; Alguero, M.; Boncompte, E.; Vericant, M. L.; Conte Ramis, J.; Merlos, M.; Gracia-Rafanell, J. F., (1998), *J .Med .Chem. 48*, 1869.

Dohle, W.; Jourdan, F.L.; Menchon, G.; Prota, A.E.; Foster, P.A.; Mannion, P.; Hamel, E.; Thomas, M.P.; Kasprzyk, P.G.; Ferrandis, E.; (2018), J. Med. Chem. 61, 1031–1044.

Abdel-Hamid, S. G. (1997), *J. Indian Chem. Soc. 74*, 613.

El-Brollosy, N. R.; Abdel-Megeed, M. F.; Genady, A. R. (2003), *Alexandria J. Pharm. Sci. 17(1)*, 17.

Shab, B. R.; Bhatt, J. J.; Patel, H. H.; Undavia, N. K.; Trivedi, P. B.; Desai, N. C. (1995), *Indian. J.Chem. 34B*, 201.

Khili, M. A.; Soliman, R.; Furghuli, A. M.; Bekhit, A. A. (1994), *Arch. Pharm. 327*, 27.

Shivaram, H. B.; Padmaja, M. T.; Shivnanda, M. K.; Akbarali, P. M. (1998), *Indian. J. Chem. 37B*, 715.

Noureldin, N.A.; Kothayer, H.; Lashine, E.-S.M.; Baraka, M.M.; El-Eraky, W.; El Awdan, S.A. (2017), Arch. Pharm. Chem. Life Sci. 350, e1600332.

Saravanan G., Alagarsamy V., Prakash CR; (2010), Int. J. Pharm. Pharm. Sci., 2010, 2:83–86.

Sasmal S, Balaji G, Kanna R. HR, Balasubrahmanyam D, Srinivas G, Kyasa S, Sasmal PK, Khanna I, Talwar R, Suresh J, Jadhav VP, Muzeeb S, Shashikumar D, Harinder Reddy K, Sebastian VJ, Frimurer TM, Rist Ø, Elster L, Högberg T; (2012), Bioorg. Med. Chem. Lett. 22:3157–3162.

Sjoqvist F and Gilette J, (1965) *Life Sci.* 4, 1031.

Leslie G.B. and MaxwellD. R. (1904), *Nature, 202,* 97.

Tang C, Castoldi AF, Costa LG, (1993) *Biochem. Mol. Biol. Int*. **29** (6): 1047–54.

Disingrini T, Muth M, Dallanoce C, Barocelli E, Bertoni S, Kellershohn K, Mohr K, De Amici M, Holzgrabe U; (2006), *J. Med. Chem.* 491, 366-372 .

Dallanoce, C.; Conti, P.; De Amici, M.; De Micheli, C.; Barocelli, E.; Chiavarini, M.; Ballabeni, V.; Bertoni, S.; Impicciatore, M., (1999), *Bioorg. Med. Chem. 7*, 1539-1547.

Xu J M, Zhang E, Shi X J, Wang Y C, Yu B, Jiao W W, Guo Y Z, Liu H M, (2014), *Eur.J. Med. Chem.* **80,** 593.

Saqlain H, A. Sarwar A M, Hinna H, Syed S, Abhijeet D, Firasat H, Perwez A, Sadiq U, Pasha M A Q, Sameena B, Syed N, Yakub A, Chetna K, (2014), *Eur. J. Med. Chem.* **81**, 204.

Lee W. W, Bueding E, (1986), Carcinogenesis, 7(8), 1379–1381.

Kensler T W, Egner P A, Dolan P M, Groopman J D, B. D. Roebuck B D, (1987), Cancer Research, 47, 4271-4277.

Furniss B S; Hannaford A J; Smith P W; Tatchell A R; (1989) "Vogel's Textbook of Practical Organic Chemistry", John Wiley & Sons. Inc. New York, pp.534.

Crews Ph; Rodriguez J; Jaspars M, "Organic Structure Analysis" ,Oxford University press, (1998).

Author Information

Rand A. Saad-Aldeen
Department of Chemistry,
College of education of girl,
University of Mosul, Iraq

Mohammed A. Al-Iraqi
Department of Chemistry,
College of Science,
University of Mosul, Iraq
Contact E-mail: *mohammedaliraqi@uomosul.edu.iq*

Production, Analysis, and Evaluation of Biodiesel from mixed Castor SEED oil, Bitter Almond oil, and Waste Fish Oil

Saba H. SEDEEQ
Mosul University

Neam M.T. AL-LAYLA
Mosul University

Abdelrahman B. FADHİL
Mosul University

Abstract: Utilization of priceless raw materials for biodiesel (BD) production is an essential target to reduce its production cost. Therefore, this work inspects the exploitation of a non-conventional feedstock, namely a mixture of non-edible oils (40% castor bean oil+ 30% bitter almond oil, and 30% waste fish oil w/w) in the production of ethylic biodiesel (EBD) and methylic/ethylic biodiesel (MEBD) through KOH-catalyzed transesterification reaction with ethanol and mixed methanol/ethanol, respectively. Effect of alcoholysis variables, such as alcohol/oil molar ratio, reaction period, reaction temperature and KOH amount, were examined. The alcoholysis outcomes revealed that the kind of implemented alcohol affected the optimum conversion of the oils mixture to BD. The maximum yield of FAMEE (96.33± 1.0 %) was attained at 0.75 wt.% KOH,6/1 alcohol/oils blend molar ratio, 45 minutes, and 55ºC reaction temperature, while the best FAEE yield (95.11 % ± 2.50%) was obtained at 1.0 %wt.KOH,7/1 ethanol/oils blend molar ratio, 65ºC, and a reaction time of 60 minutes. The fuel properties of the prepared fuels were assessed and discussed following ASTM D 6751 specifications. The results also exhibited that properties of FAMEE and FAEE were much better than those of BD from castor bean oil, suggesting their suitability as realistic alternative fuels to diesel fuel. ^{1}H NMR and FTIR techniques affirmed the transformation of the oils blend to BD. Pseudo-first-order kinetics was obeyed on the alcoholysis of the said mixed oils.

Keywords: Mixed non-eatable oils, Biodiesel, Fuel properties assessment, Identification of biodiesels, Kinetics

Introduction

The liquid biofuel that is obtained by the chemical processes of different vegetable oils or animal fats with alcohol is named biodiesel (BD). It is utilized separately or as a blend with petrodiesel (PD) in diesel engines. The most common method employed for BD synthesis is the TE reaction. It involves the reaction of triglycerides with an alcohol in the existence of a base catalyst (KOH or NaOH), an acid catalyst (H_2SO_4 or HCl or) or an enzyme catalyst (lipase) (Verma et al.,2016; Kudre et al.,2017). First-generation biodiesels (BDs) have generated from edible oils, which their utilization in BD synthesis was associated with many drawbacks, including energy versus food dispute. Besides, it was reported that about 80% of the final price of BD production relates to the production cost of the parent oil employed in its preparation. Additionally, utilization of food crops for energy production might also increase acreage, which in turn causes deforestation. As such, production of the second-generation BDs has been accomplished relying on the exploitation of non-edible oils (NEO) to avoid issues generated during exploiting eatable oils for BD production (Ong et al.,2019).

Many NEO, such as *Hevea brasiliensis*(Karnjanakom et al.,2016), *Ceiba Pentandra* (Silitonga et al.,2014), *Cerbera manghas*, *Calophyllum inophyllum* (Silitonga et al.,2014), *Jatropha curcas* (Silitonga et al.,2014), *Madhuca indica* (Lamba et al.,2019),*Sterculia foetida* (Silitonga et al.,2013) *Silybum marianum* L.(Fadhil et al.,2016), Wild (*Brassica juncea* L.)(Aldobouni et al., 2016), Bitter almond (*Prunus dulcis* var. amara) (Al-

Tikrity et al.,2107), waste fish oils (Fadhil et al.,2015; Al-Tikrity et al.,2016), and waste cooking oils (Vanessa et al.,2015) were explored as feedstocks for producing different BDs.

The castor (Ricinus communis L.) which is a non-eatable plant has a high commercial value besides its industrial applications as an outcome of its oil which could be employed in the synthesis of various products, like high profitable value polymers, pharmaceuticals and BD fuel. The high oil level of castor beans which ranges between 40-55% makes it a valuable raw oil for BD synthesis. However, the density, polarity and viscosity of castor bean oil (CBO) are higher than other oils, as a consequence of its chemical composition which is mainly composed of ricinoleic acid (R-12-hydroxy-9-cis-octadecenoic acid) as a superlative fatty acid (±89%). Hence, BD form CBO possesses high density and viscosity as well. Accordingly, BD from CBO is blended with PD or other low density and viscosity BDs to become a useful fuel for diesel engines (Barbosa et al.,2010; Saez-Bastante et al.,2015; Keera et al.,2018).

Almonds (*Prunus amygdalus*) is one of the Rosacea's family. Based on its taste, two kinds of almonds were distinguished: sweet almond and bitter almond. Sweet almond is widely utilized as the main component in the manufacture of food products, while bitter almond supplies the main source of bitter almond oil (BAO) which acts as an ingredient in cosmetics. The presence of cyanogenic glucosides, like amygdalin and prunasin added the bitter flavor in bitter almonds (Borras et al.,2014;Cortes et al.,2018). The BAO has considered as a non-eatable oil as a consequence of its content of Hydrocyanide, Benzaldehyde, and glycoside amygdaline. The occurrence of Hydrocyanide made the crude bitter almond oil (BAO) poisonous so that a dosage of 7.7 mL may cause death. As such, it was exploited as a useful precursor for BD creation (Fadhil and Mohammed,2018).

The occurrence of different water sources, like Tigris, Euphrates Rivers and Marshes made Iraq a fish producing country. Besides, certain species of fish were bred in ponds to meet the increasing need for white meats due to their health and nutritional importance. Production of fish leaves behind various solid waste, such as viscera, frame, head and skin scales(Fu et al.,2017). These parts are rich with fat and could be a significant threat to the environment. As an actual solution to eliminate the accumulation of such fatty wastes is the reclamation of oil from those wastes to be utilized for producing BD fuel(Fadhil et al.,2015; Al-Tikrity et al.,2016). The transesterification (TE) of mixed NEO with methanol to produce BD with favorable physical and chemical properties was established in the literature. The synthesis of BD from mixed Jatropha curcas and Ceiba pentandra oils has resulted in the production of BD with higher oxidation stability than that produced from Ceiba pentandra oil separately (Damanik et al.,2017). The TE of mixed CBO and WCO with methanol improved the Cetane number to 100 (Hadiyanto et al.,2018). Methanolysis of a mixture of CBO and waste fish oil (WFO) (50:50 w/w)(Fadhil et al.,2017) and mixed CBO and waste chicken oil (50:50 w/w)(Fadhil and Ahmed, 2016) produced BDs with kinematic viscosities much lower than that produced from CBO individually, and also within the safe limits prescribed by ASTM standard. The preparation of BD from CBO mixed with NEO or edible oils has also reported in the literature (Barbosa et al.,2010). Nonetheless, TE reaction of a mixture of NEO, namely CBO, BAO and WFO with ethanol and mixed methanol/ethanol, to yield ethylic biodiesel (EBD) and mixed methylic/ethylic biodiesel (MEBD) has not been yet declared in the literature to the best of our knowledge.

The present context reports the synthesis of EBD and MEBD from a blend of NEO viz. CBO, BAO and WFO via alcoholysis reaction. The oils blend has assessed for its chemical and physical features, and then transesterified with various alcohols to yield varied alkyl esters via the optimized procedure was inspected. The resulting BDs were identified by ^{1}H NMR and FTIR spectroscopy in addition to the assessment of their fuel properties.

Methods

Materials and chemicals

The castor beans and bitter almond kernels were collected from trees planted in Mosul and Dohuk cities, respectively in July 2018, while the fish wastes have obtained from the fish Slaughterhouse in the city of Mosul. Analytical grade solvents and chemicals implemented were purchased from different origins (Merck, Germany and Scharlau, Spain) and utilized without any pre-treatment.

Extraction and analysis of oils

The extraction of oils from castor and bitter almond kernels was accomplished in a Soxhlet extractor with hexane as a solvent. After stripping the solvent form the oils via vacuum distillation by the aid of a rotary

evaporator, the yields of the got oils were calculated on a weight basis. Extraction of WFO from the fish waste was carried out following the procedure presented in our previous work (Fadhil and Ahmed,2018). The oils were well-mixed at the following ratios: 40% CBO, 30% BAO and 30% WFO w/w. Properties of the oils and their blend including the density at 15.6ºC, kinematic viscosity at 40ºC, flash point, acid value, refractive index, pour point and the saponification number have specified as per the ASTM standard methods.

Biodiesel production and analysis

The oils blend was fed to a 500 mL round-bottomed flask joined with a mechanical stirrer, condenser and thermostat to prepare MBD and MEBD. KOH was completely dissolved in alcohol under stirring. The alcoholic solution of KOH was added to the oil. The mixture was refluxed with stirring at 600 rpm using a magnetic stirrer for given reaction time. At the end of the operation, the attained mixture was transferred to a separator to yield two layers, while the alkyl ester layer was washed with distilled water to remove water-soluble impurities, such as soaps and alcohol. Lastly, it was dried over Na2SO4. The following formula was applied in the calculation of BD yield(Fadhil and Ahmed,2018):

$$\text{BD yield (\%)} = \frac{\text{Weight of the purified alkyl ester (g)}}{\text{Weight of oils blend used (g)}} \times 100$$

Adsorption chromatography method was applied to specify the purity of the as-produced fuels (Bindhu et al.,2012). Proton nuclear magnetic resonance (^{1}H NMR) was also employed to affirm the conversion of the oils blend to its alkyl esters on 1H NMR spectrophotometer, GmbH 400.22 Mhz. The MEBD was identified using Fourier transform infrared (FTIR) spectrometer (Model: A Bruker EQUINOX 55, USA) equipped with a detector having a spectral range 4,000-400 cm-1. Assessment of the properties of the obtained fuels achieved as per ASTM standard test methods. Content of soaps in the biodiesels was specified based on AOCS Cc 17-95, while the total glycerin content was determined as suggested by Pisarello et al.(2010). Various blends of BD and PD have prepared and then evaluated for their properties following the ASTM standard test methods.

Results and Discussion

Oils yield and properties

The content of oils in the castor beans, bitter almond kernels and fish waste, were 51.55, 42.0 and 76.0 % w/w, respectively. The oils contents in these precursors are higher than those published for *Sterculia striata* seed (40.0% %)(Ong et al.,2013) and pork waste (Dias et al.,2009). As a result, BD synthesis from such NEO or their blends is reliable. It is obvious from Table 1 which displays physicochemical properties of the CBO, BAO, WFO and their blend that the density, kinematic viscosity and refractive index of the CBO, have been markedly reduced as a consequence of blending with the other NEO. This result attributes to the lower density, kinematic viscosity and refractive index values of the other NEO compared to CBO. As fixed in **Table 1**, the properties of the oils blend were comparable to those of conventional NEO utilized for the synthesis of BD in literature (Reshad et al.,2015; Ong et al.,2019).

Table 1. Properties of the oils and their blend compared to other non-edible oils

Property	CBO	BAO	WFO	Oils blend	CCIO [a]	CI60CP40 [b]	Rubber seed oil [c]
Density @ 15.6 g/mL	0.9730	0.9200	0.9188	0.9376	0.9640	906.2	0.9100
Kinematic Viscosity@ 40°Cmm²/s	261.33	41.39	35.99	57.47	56.74	29.57	30.0
Flash Point °C	185	200	272	193	-	-	-
Acid Value mg KOH / g oil	0.10	1.11	1.31	1.15	36.26	15.82	24
Refractive index@20°C	1.4780	1.4682	1.4680	1.4674	-	-	1.4700
Pour Point °C	-<15	-7	0.0	-10	-	-	3.0
Saponification Value mg KOH / g oil	188.47	216.12	211.60	196.70	-	-	235.28

[a] Crude *Calophyllum inophyllum* oil from Ong et al.,2019；[b] *Calophyllum inophyllum-Ceiba pentandra* oil mixture (60:40 wt%) from Ong et al.,2019;[c] from Ong et al.,2019

Alcoholysis reaction of the oils blend

The main characteristic that influences the conversion of oil to its alkyl esters, as well as the selection of the optimum base catalyst for the alcoholysis process, is free fatty acid (FFA) content of it (Armendáriz et al.,2015). The oils blend used for BD synthesis in this work has an FFA content of 0.575%, which is much below that announced for other NEO, like Nigella *sativa* (15.17 %)[33] and *Ceiba pentandra* (10.11%) (Khan et al.,2015). Thus, BD production from the said oils blend is reasonable. Moreover, utilization of low FFA content oils for the synthesis of BD reduces its production cost comparing to those with high FFA contents, which their conversion to BD required a dual-step process, namely acid-base TE process, leading to a higher cost of production.

Different amounts of KOH ranged from 0.25-1.50 wt.% were tried on the alcoholysis reaction of mixed NEO to MBD and MEBD. The experiments were performed using 6/1 alcohol/ NEO molar ratio, 60 ºC, 600 rpm rate of stirring, and 60 minutes reaction time as fixed in **Fig.1a**. With increasing KOH amount from 0.25 wt.% to 1.50 wt.%, growth in the BD yield was noticed. This outcome suggested that increasing the KOH amount will provide more active sites for the reaction, leading to a better conversion of the oil to BD (Syazwani et al.,2107). Nonetheless, ethanolysis of NEO mixture required a higher amount of KOH (1.0 wt.%) to reach the highest conversion than that required to get the maximum yield of MEBD (0.75 wt.%). When the KOH % exceeded the optimal amount, the BD yield declined as a result of the reaction of more triglycerides with KOH, leading to a more formation of soaps. So, the BD yield diminished (Syazwani et al.,2107).
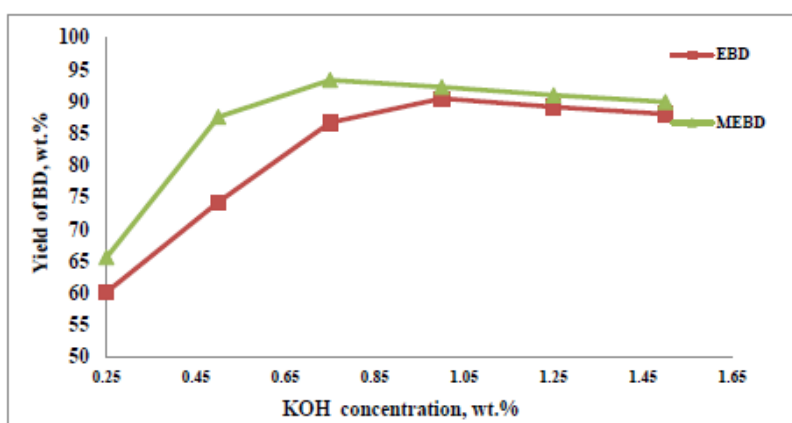
Figure 1.Effect of KOH concentration on FAEE and FAMEE yield

As alcoholysis reaction is greatly affected by varying alcohol/oil molar ratio, transesterification of the NEO mixture with the said alcohols was accomplished using different molar ratios of alcohol/NEO as given in **Fig.1b**. The experiments were accomplished at 65ºC using the optimal amounts of KOH obtained earlier for 60 minutes with a stirring speed of 600 rpm. It is evident from **Fig.1b** that the conversion of NEO mixture to EBD and MEBD raised as the molar ratio of alcohol/NEO increased. The TE with mixed alcohols gave the highest yield of MEBD at a molar ratio of 6:1, while a molar ratio of 7:1 ethanol/NEO blend has given the best conversion. Nonetheless, the molar ratio of alcohol/NEO might increase the polarity of the reaction mixture, giving rise to a higher solubility of glycerin in the ester phase. As a result, it drives the equilibrium back to the reactants side. Hence, the BD yield declined (Gaurav et al.,2014).
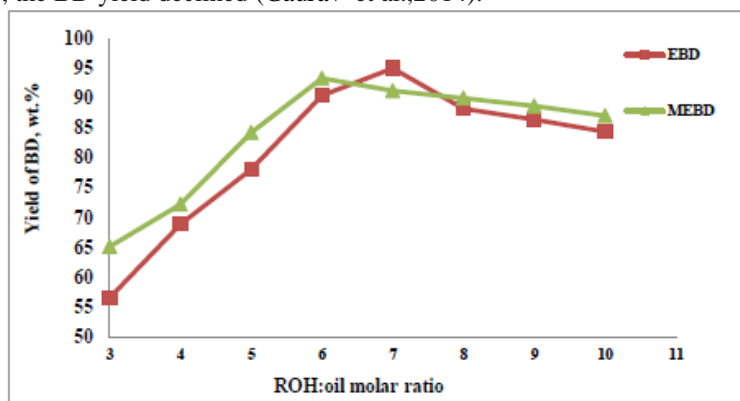
Figure 2.Effect of alcohol/NEO molar ratio on FAEE and FAMEE yield

The BD yield and alcoholysis reaction rate are greatly influenced by altering the reaction temperature. Raising the reaction temperature decreases the oil viscosity, and also lessens the reaction time. So, the impact of the reaction temperature on the EBD and MEBD yields has studied through conducting the alcoholysis reaction at different temperatures, namely 30 ℃,40 ℃,50,55℃ ℃,60 ℃,65 ℃ and 70℃. The experiments were carried out by employing the optimal amounts of KOH and the optimal alcohol/NEO molar ratios obtained previously for 60 minutes at 600 rpm rate of stirring. **Fig.1c** showed that the BD yield raised with the rise of the reaction temperature.
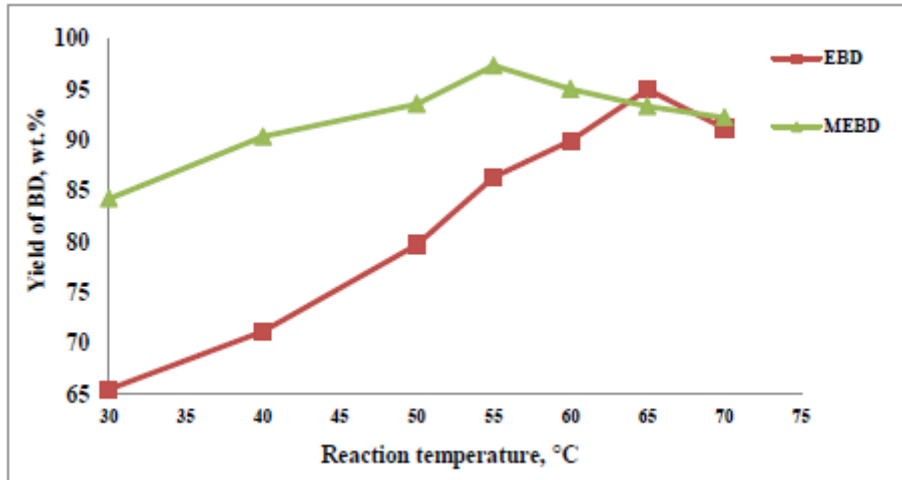
Figure 3.Effect of reaction temperature on FAEE and FAMEE yield.

The optimal temperature for alcoholysis of NEO with mixed alcohols was 55°C. On the other hand, ethanolysis of NEO blend produced the maximum EBD yield at 65°C. Both temperatures are below the boiling points of the utilized alcohols. Thus, such an outcome may lessen the cost of BD production. Soap formation was noticed when the reaction temperatures exceeded the optimal temperature (Hassen et al.,2014).

The influence of the reaction time on the yield of alcoholysis products was studied through changing the time from 15 to 90 minutes with 15 minutes increments. All experiments were done by fixing KOH, alcohol: NEO and the reaction temperatures at their optimal values obtained earlier, while a stirring rate of 600 rpm was employed. It can be seen from **Fig.1d** that increasing the reaction period improved the BD yield. A reaction time of 45 minutes was the optimal period, as it yielded the highest conversion of the mixed NEO to MEB, while 60 minutes were enough to give the highest yield of the EBD. The loss of BD in the form of soaps as a consequence of the hydrolysis of the formed alkyl esters has noticed as the reaction periods exceeded the optimal values (Silitonga et al.,2015).
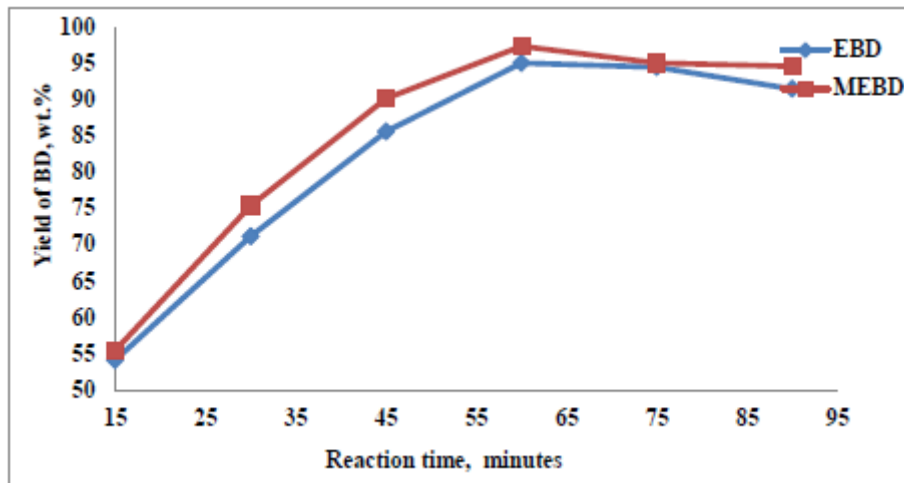
Figure 4.Effect of reaction time on FAEE and FAMEE yield

Above results disclosed that the transesterification reaction of NEO blend with ethanol and mixed alcohols produced the highest yield of MEBD at conditions lower than those required for the ethanolysis reaction. These outcomes might ascribe to the solubility of the oil in the implemented alcohol, which expected to be better in mixed methanol/ethanol than ethanol, resulting in a better mass transition between the oil and alcohol phases.

Analysis of BDs from NEO mixture

The EBD and MEBD prepared from mixed CBO, BAO and WFO have analyzed by 1H NMR spectroscopy. The conversion of oil mixture to its EBD was confirmed through the appearance of a quartet peak at 4.09-4.14 ppm, which attributes to the methylenic protons (-OCH2-) of the ester group as depicted in **Fig.5**. Conversion of the mixed oils to EBD was quantified making use of the equation suggested by Hincapié et al.(2011).

$$CEE\ (\%) = 100 \ X \ [I_{TGA+EE} - I_{TGA}] \ /[I_{\alpha CH2}]$$

where ITGA+EE represents the integration of peak assigned to the glyceryl methylenic and (-OCH2-) of the ethoxy protons appeared at 4.07-4.14 ppm, IαCH2 is the integration of peak corresponding to the a-methylene protons (2.3 ppm), and ITAG is the integration of peak corresponding to the glyceryl methylenic protons (4.27-4.33 ppm) in the 1H NMR spectra of EBD.
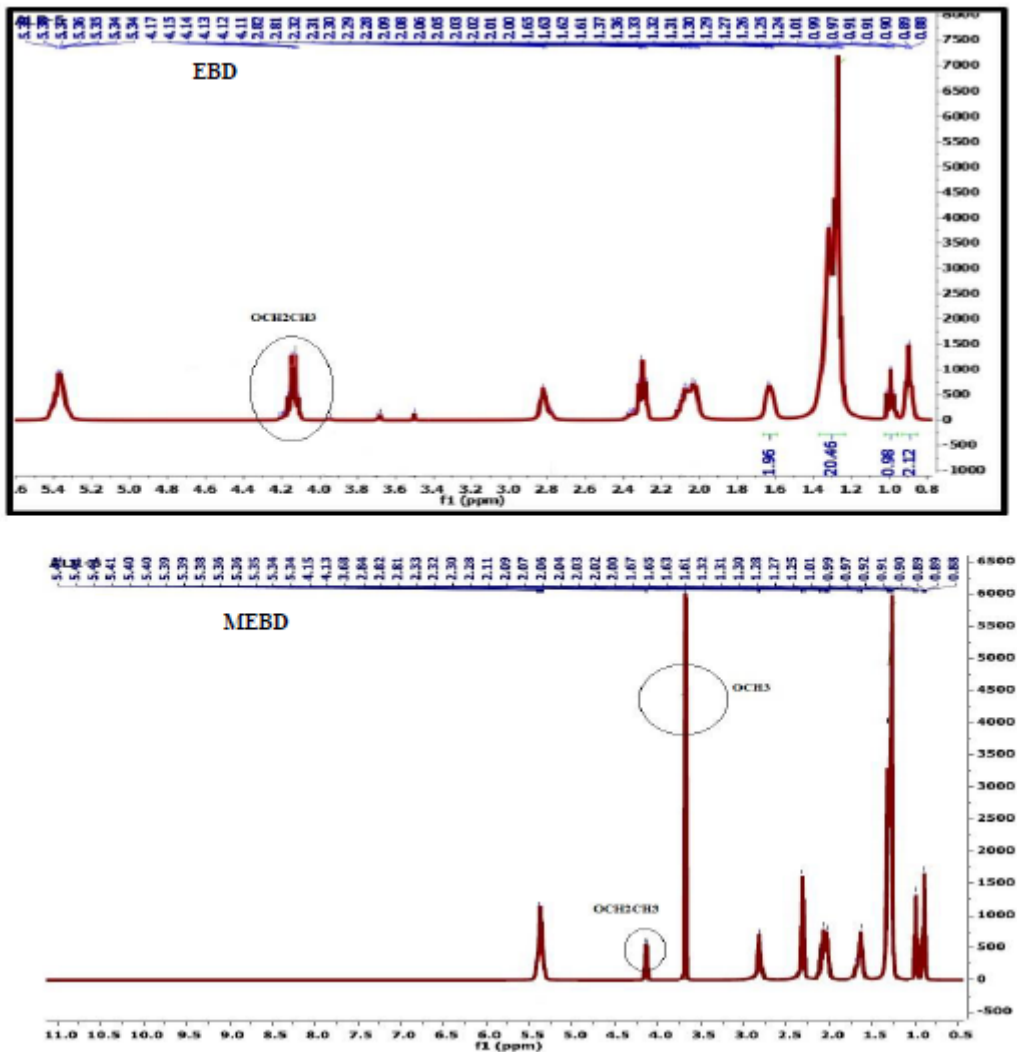
Fig.5. ^{1}HNMR spectra of EBD and MEBD.

Following the above equation, conversion of the NEO blend to EBD was 92.64 %, which is close to that obtained practically (95.11 % ± 2.50). The presence of both methylic and ethylic esters in the MEBD was affirmed through the appearance of a strong singlet at 3.7 ppm which relates to the methoxy ester protons (-O-CH$_3$), a triplet of α-methylene protons (α-CH$_2$) at 2.01–2.75 ppm, and a quartet at 4.07– 4.14 ppm, which attributes to the methylenic protons from the ethoxylated group (-O-CH$_2$-CH$_3$) as depicted in **Fig.5**.

The NEO mixture and its MEBD have also characterized by the FTIR technique, and the spectrums are presented in **Fig.6**.
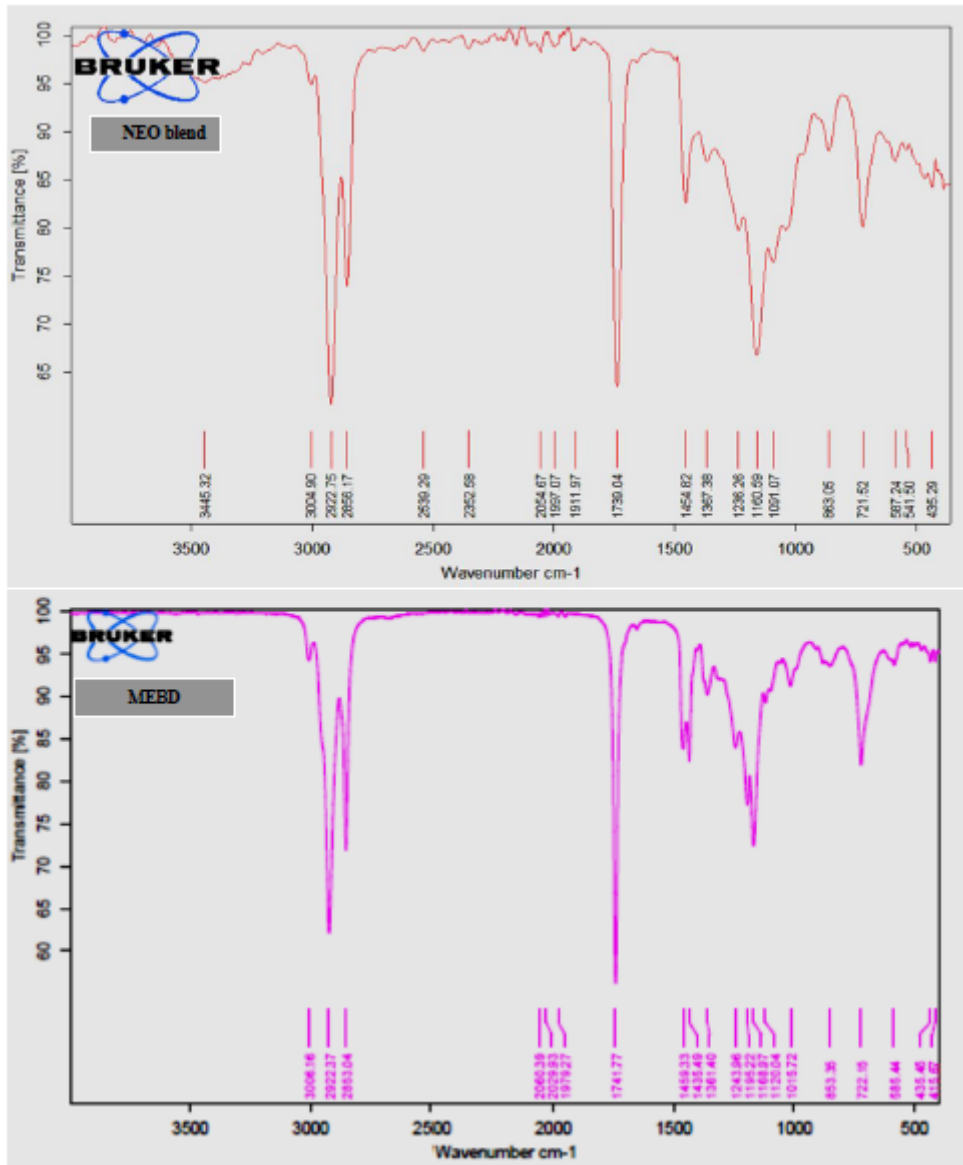
Fig. 6. The FTIR spectra of the NEO mixture and its MEBD

The symmetric and asymmetric stretching vibrations of the methyl group (□ CH3), which appeared between 3006-2853 cm-1 are characteristic bands of the alkyl esters. The absorption bands in the region of 1741-1737 cm-1, may be assigned to the stretching vibration of the carbonyl group (□ C=O), while that belongs to the symmetric stretching vibration of (C□ O□ C) was noticed at 1246-1170 cm-1. The absorption peak observed in the region of 912-723 cm-1 may ascribe to the hydrocarbon chain rocking vibration (Ali and Fadhil,2013; Gupta et al.,2106). **Fig.6** also disclosed that the spectrums of the authentic NEO blend and its MEBD are nearly the same with a bit differences in the frequencies of the absorption peaks. Besides, the bands, which appeared at 3445,2539,2352,20154,1997 and 1911 cm-1 were present in the oils blend but absent in the obtained MEBD. Moreover, new absorption peaks, such as those noticed at 1435,1193 and 1119 cm-1 were found in the BD and absent in the oils blend. These findings affirmed the conversion of fatty acid to fatty acid alkyl esters. The area below the absorption peaks of stretching vibration of the (□ C□ H) band, bending band of (□ C□ H), and stretching vibration of (□ C=O) were lower than those observed in the authentic oils blend. These observations might also affirm the conversion of the oils blend to its alkyl ester (Fadhil et al.,2019).

Kinetics study

Kinetics of the alcoholysis reaction of NEO mixture with the said alcohols at different temperatures is demonstrated in **Fig.7** and **Fig.8.** The pseudo-first-order kinetic model was followed to investigate the kinetics of the alcoholysis process.

$$- ln (1- X) = - k.t.$$
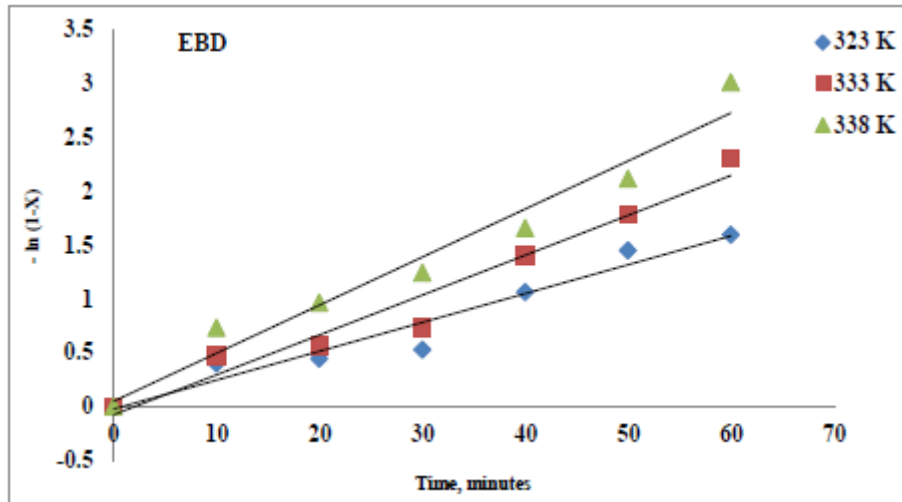
Figure 7. Plotting of - ln (1- X) versus time for ethanolysis of NEO mixture.
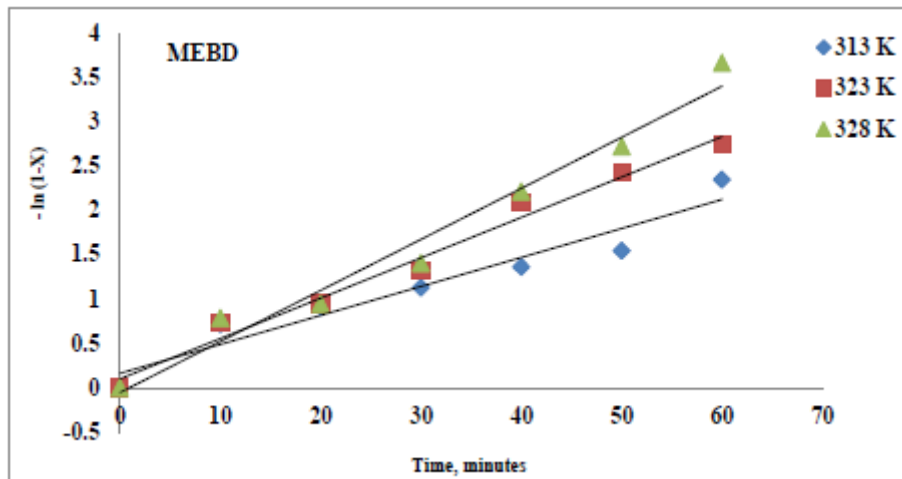
Figure 8. Plotting of - ln (1- X) versus time for transesterifcation of NEO mixture with mixed alcohols

where, X is the conversion of triglyceride (TG) at any given time t, and k is the rate constant. As seen from **Fig.6** and **Fig.7**, plotting $-ln(1 - X)$ versus time will give k which could be obtained from the slope of the curve. The obtained outcomes have revealed that increasing the reaction temperature improved the rate constant for the forward reaction. The high value of R^2 coefficient assures that the reaction followed a pseudo-first-order kinetic model. The obtained consequences were in line with results performed by other authors(Birla et al.,2012; Berchmans et al.,2013).The relationship among the reaction rate constant, temperature and activation energy can be given by the Arrhenius equation:

$$k = A e^{-Ea/RT} \quad ……………………………….(4)$$

where A is the frequency factor, E_a is the activation energy, R is the universal molar gas constant, and T is the temperature (°K). As the activation energy is temperature dependent; the rate constant at any temperature can be expressed using the following Eq. :

$$ln\ k = ln\ A – Ea\ /RT…………………..\quad (5)$$

The linear plot of ln k versus $1/T$ has given the activation energy as depicted in **Fig.8 and Fig.9**.The activation energy values for the transesterifcation of the oils blend with ethanol and mixed methanol/ethanol were 30.57 KJ mol^{-1}and 32.65 KJ mol[-1,] respectively. These values were relatively small, which reveals the great catalytic

activity of basic catalyst (KOH) and also support that reaction is chemically controlled and not by diffusion or mass transfer limitations (Fadhil et al.,2015).
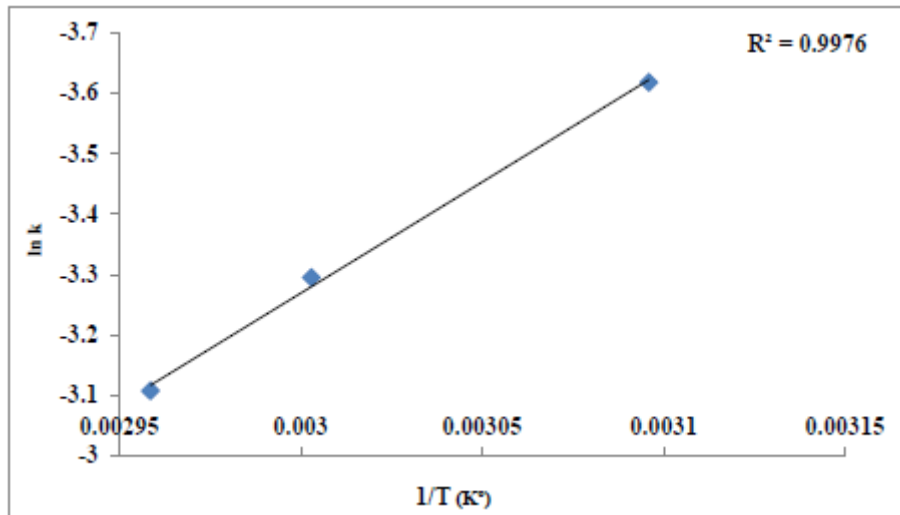
Figure 8. Arrhenius plot, *lnk* versus *1/T* for ethanolysis of NEO mixture
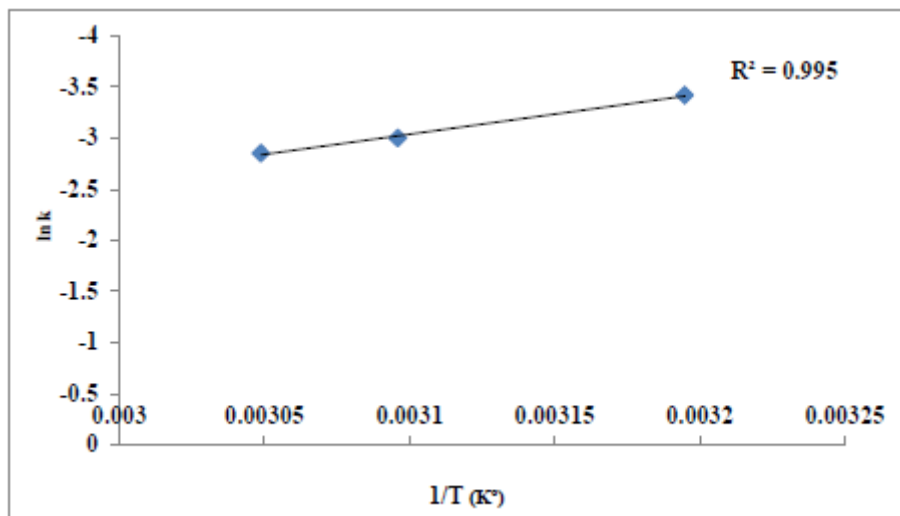
Figure 9. Arrhenius plot, *lnk* versus *1/T* for transesterifcation of NEO mixture with mixed alcohols

Properties assessment of biodiesels

Basic physicochemical features of both EBD and MEBD produced from mixed non-edible oils were assessed according to ASTM standards, and compared with those of BD from CBO as established in **Table 2**. The results in **Table 2** exhibited that properties of the prepared fuels, were lower than those of the parent oils mixture, suggesting that alcoholysis reaction has positively changed features of the feedstock to more useful fuels. Moreover, properties fulfilled the limits given by ASTM D 6751 except the density and kinematic viscosity of the EBD. Besides, the density and kinematic viscosity of the produced fuels were superior to those of BD derived from CBO. This outcome is due to the presence of BAO and WFO, which possess much lower density and kinematic viscosity than the CBO.

Table 2. Physicochemical properties of biodiesels produced from mixed NEO

Property	BD from CSO	EBD	MEBD	ASTM D6751
Yield (wt.%)	94.55	95.11±1.0	96.33±1.0	-
Ester content (w/w %)	94.01	96.64±1.0	96.89±1.0	96.50
Density @15.6 °C g/mL	0.9202	0.9121± 0.0011	0.8940± 0.0011	0.9000
Kinematic viscosity @ 40 °C mm^2/s	9.22	8.89± 0.25	4.33±0.11	3.0 – 6.0
Flash point °C	145	±1.0160	120±1.0	130.0
Acid value mg KOH/g	0.08	0.38± 0.01	0.39± 0.01	0.50
Refractive index @ 20°C	1.4611	1.4509± 0.0010	1.4505± 0.0010	-
Pour point °C	<-15	-8	-7.0	-
Total glycerin content (wt.%)	0.08	0.14± 0.10	0.12± 0.01	0.24
Soaps (ppm)	0.62	0.98± 0.11	0.85± 0.01	5.0
Water content (%)	< 0.01	< 0.01	< 0.01	

Table 2 also shows that the properties of MEBD were superior to those of EBD. This achievement could be accredited to the ester level of each BD and the kind of alcohol used in the synthesis of BD. Blending results of MEBD with PD at various percentages are listed in **Fig.10**. The BD and PD can be blended at any percentages causing an improvement in their properties. Fig.10 shows that the density, kinematic viscosity, flash point and pour point of PD have been increased with the increment of BD content in the prepared blends, while the acid number decreased. These consequences could have belonged to the molecular mass of BD, which is higher than that of PD (Fadhil et al.,2019). Based on the above results, EBD and MEBD produced from the suggested oils mixture are suitable fuels for diesel engines or/and they can be successfully mixed with PD.
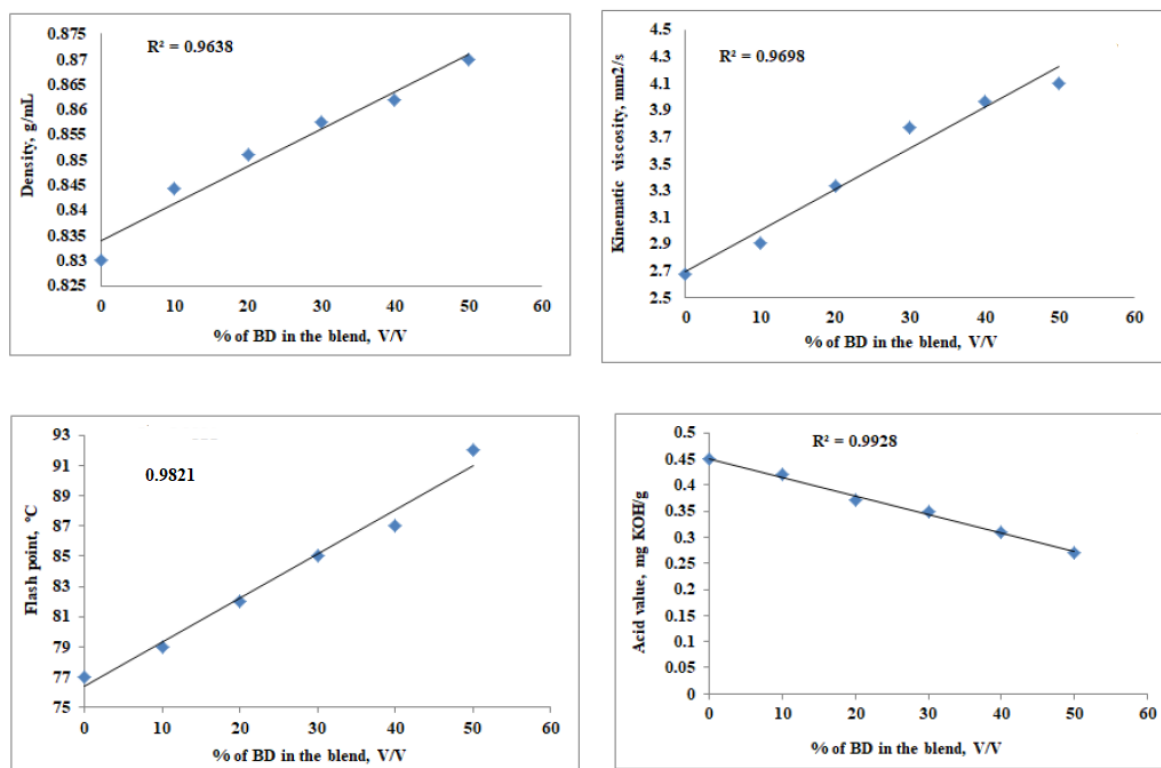
Figure 10. Effect of BD blending with petro diesel on properties of the latter

Conclusion

This paper introduces a new non-edible feedstock, namely a mixture of CBO, BAO and WFO for the synthesis of BD. This oils mixture was utilized for the production of EBD and MEBD by direct KOH-catalyzed TE process as a consequence of its low acid number. Additionally, the fuel properties of the obtained fuels lied within the limits specified by ASTM D 6751 except the density and kinematic viscosity of the EBD. The BD and conventional diesel fuel blends met the specifications fixed by ASTM D7467-17 standard. Both the [1]H

NMR and FTIR spectroscopy affirmed the conversion of non-edible oils mixture to more valuable products. Finally, transesterification of the oils blend with ethanol and mixed alcohols followed the pseudo-first-order-kinetics.

Acknowledgements

References

Al-dobouni, I. A., Fadhil, A. B., and Saeed, I. K. (2016). Optimized alkali-catalyzed transesterifcation of wild mustard(*Brassica juncea* L.) seed oil. Energy Sources, Part A. 38:2319–2325.

Al-Tikrity,E.T.B.,Fadhil, A.B., Ibraheem, K.K.(2017). Biodiesel production from bitter almond oil as new Feedstock. Energy Sources part a;39:649-656. non-edible oil.

Al-Tikrity, E.T.B., Fadhil, A.B., Albadree, M.A.(2016). Cyprinus carpio fish oil: A novel feedstock for biodiesel production. Energy Sources, Part A 38 (22),3367-3374.

Armendáriz,J., Lapuerta, M., Zavala, F., García-Zambrano, E., Ojed, M.C. (2015). Evaluation of eleven genotypes of castor oil plant (*Ricinus communis* L.) for the production of biodiesel. Industrial Crops and Products 77, 484–490 .

Bindhu, C.H., Reddy, J.R.C., Rao, B.V.S.K., Ravinder, T., Chakrabarti, P.P., Karuna, M.S.I., et al. (2012).Properties and evaluation of biodiesel from Sterculia foetida seed oil. J Am Oil Chem Soc. 89,891–6.

Birla,A., Singh,B., Upadhyay, S. N., Sharma, Y.C. (2012) . Kinetics studies of synthesis of biodiesel from waste frying oil using a heterogeneous catalyst derived from snail shell. Bioresource Technology 106 : 95–100.

Berchmans,HJ., Morishita, K.;Takarada,T. (2013) . Kinetic study of hydroxide-catalyzed methanolysis of Jatropha curcas–waste food oil mixture for biodiesel production. Fuel ,104 : 46–52.

Barbosa, D. da-Costa, T. Serra, S.M.P. Meneghetti, M.R. Meneghetti,(2010). Biodiesel production by ethanolysis of mixed castor oil and soybean oil. Development of biodiesel from castor oil, Fuel 89 : 3791–3794.

Borras, E., Amigo, J.M., Van den Berg, F., Boque, R., Busto, O. (2014). Fast and robust discrimination of almonds (*Prunus amygdalus*) with respect to their bitterness by using near infrared and partial least squares-discriminant analysis. Food Chemistry 153 : 15–19.

Barbosa, D.C., Serra, T.M., Plentz Meneghetti, S.M., Meneghetti, M.,R. (2010). Biodiesel production by ethanolysis of mixed castor and soybean oils. Fuel 89,3791–4 .

Cortes, V., Talens, P., Barat, J. M., Lerma-García, M.J. (2018). Potential of NIR spectroscopy to predict amygdalin content established by HPLC in intact almonds and classification based on almond bitterness . Food Control 91 : 68-75.

Damanik, N., Ong, H.C., Chong, W., Silitonga, A.,(2017). Biodiesel production from *Calophyllum inophyllum*-palm mixed oil. Energy Sources, Part A. 39,1283-1289.

Dias, J.M., Maria, C.M., Alvim-Ferraz,Almeida, M.,F. (2009).Production of biodiesel from acid waste lard. Bioresour Technol.100,6355–61.

Fadhil, A. B., Aziz, A. M., and Altamer, M. H.(2016). Biodiesel production from Silybum marianum L. seed oil with high FFA content using sulfonated carbon catalyst for esterification and base catalyst for transesterification. Energy Convers. Manage. 108:255–265.

Fadhil, A.B., Al-Tikrity, E.T., Albadree, M.A.(2017). Biodiesel production from mixed non-edible oils, castor seed oil and waste fish oil. Fuel 210, 721-728.

Fadhil, A. B., and Ahmed, A. I. (2016). Production and evaluation of biodiesel from mixed castor oil and waste chicken oil, Energy Sour., 38(Part A), 2140–2147.

Fadhil, A. B., and Ahmed, A., I. (2018). Production of mixed methyl/ethyl esters from waste fish oil through TE with mixed methanol/ethanol system. Chemical Engineering Communications 205 (9):1157–66.

Fadhil, A. B., Saleh, L. A. Altamer, D. H. (2019). Biodiesel production from spent fish frying oil via alkali-catalyzed transesterification. Energy Sources, Part A: Recovery, Utilization, and Environmental Effects. https://doi.org/10.1080/15567036.2019.1604893.

Fadhil,A.B., Mohammed, H.M. (2018). Co-solvent transesterifcartion of bitter almond oil into biodiesel: Optimization of variables and characterization of biodiesel. TRANSPORT 33(3) 686–698.

Fu, J., Hue. B.T.B., Turn, S.Q. (2017) Oxidation stability of biodiesel derived from waste catfish oil. Fuel 202 - 455–463.

Gaurav, D., and Sharma, M. P..(2014). Prospects of biodiesel from pongamia in India. Renewable Sustainable Energy Rev. 32,114–122.

Gupta, Jharna, Agarwal, M., Dalai A.K. (2016). Optimization of biodiesel production from mixture of edible and non-edible vegetable oils . Biocatalysis and Agricultural Biotechnology8:112–120.

Hadiyanto, H., Yuliandaru, I., Hapsari, R.(2018). Production of biodiesel from mixed waste cooking and Castor oil. In: MATEC Web of Conferences. EDP Sciences.

Hassen, M. S., Imededdine, A. N., Chin, P. T., and Saud, I. A.(2014). Production and characterization of biodiesel from Camelus dromedaries (Hachi) fat. Energy Convers. Manage. 78,50–57.

Hincapié, G., Mondragon, Fanor, Lopez, D. (2011). Conventional and in situ TEof castor seed oil for biodiesel production Fuel 90 ,1618–1623 .

Karnjanakom, S., Kongparakul, S., Chaiya, ., Reubroycharoen, P., Guan, G., Samart, C . (2016) . Biodiesel production from Hevea brasiliensis oil using SO3H-MCM-41 catalyst. Journal of Environmental Chemical Engineering 4 47–55.

Keera, S.T., El Sabagh, S.M., Taman, A.R.(2018). Castor oil biodiesel production and optimization. Egyptian Journal of Petroleum 27 : 979–984.

Khan, T.M.Y., Atabani, A.E., Badruddin, I.A., Ankalgi R.F., Khan, T.K. M., Badarudin, A .(2015). *Ceiba pentandra*, *Nigella sativa and* their blend as prospective feedstocks for biodiesel. Industrial Crops and Products

65 :367–373.

Kudre, T.G., Bhaskar, N., Sakhare, P.Z. (2017) . Optimization and characterization of biodiesel production from rohu (Labeo rohita) processing waste. Renewable Energy 1131408-1418.

Lamba, N., Gupta, R., Modak, J.M., Madras, G. (2014) . ZnO catalyzed TEof Madhuca indica oil inupercritical methanol . Fuel 242 (2019) 323–333.

Liu, J., Cui, Q., Kang, Y., Meng, Y., Gao, M., Efferth, T., Fu, Y. Euonymus maackii Rupr. (2019).Seed oil as a new potential non-edible feedstock for biodiesel. Renewable Energy 133: 261-267.

Ong, H. C., Silitonga, A. S., Masjuki, H. H., Mahlia, T. M. I., Chong, W. T., and Boosroh, M. H.. (2013).Production and comparative fuel properties of biodiesel from non-edible oils: Jatropha curcas, Sterculia foetida and Ceiba pentandra . Energy Convers. Manage. 73,245–255.

Ong,,H.C., Milano, J., Silitonga, A.S., Hassan, M. H.i, Shamsuddin,A., Wang, C., Mahlia,T.M.I., Siswantoro, J., (2019). Biodiesel production from Calophyllum inophyllum- Ceiba pentandra Kusumo, F., Sutrisno, J. oil mixture: Optimization and characterization. Journal of Cleaner Production 219: 183-198.

Pisarello, M.L., Dall-Csta ,B.O, Veizaaga, N.S., Querini, C.,A.. (2010).Volumetric method for free and total glycerin determination in biodiesel. Ind Eng Chem Res;49, 8935–41.

Reshad,A.S., Tiwari, P., Goud, V.V. (2015). Extraction of oil from rubber seeds for biodiesel application: Optimization of parameters Fuel 150, 636–644.

Silitonga, A.S., Ong, H.C., Mahlia, T.M.I., Masjuki, H.H., Chong, W.T.(2014). Biodiesel conversion from high FFA crude jatropha curcas, calophyllum inophyllum and ceiba pentandra oil. Energy Procedia 61 480 – 483.

Silitonga, A.S., Ong, H.C., Masjuki,H.H., Mahlia, T.M.I. , Chong, W.T., Yusaf, T.F.(2013). Production of biodiesel from Sterculia foetida and its process optimization. Fuel 111 478–484.

Silitonga, A.S., Masjuki, H.H., Mahlia, T.M.I., Ong, H.C., Kusumo, F., Aditiya, H.B., Ghazali, N.N.N.. Schleichera oleosa, L .(2015).oil as feedstock for biodiesel production Fuel 156 ,63–70.

Saez-Bastante, J., Pinzi, S., Jiménez-Romero, F.J., M.D. de Castro, L.F. Priego-Capote, Dorado, M.P.(2015). Synthesis of biodiesel from castor oil: Silent versus sonicated methylation and energy studies, Energy Convers. Manage. 96 : 561–567.

Syazwani, O.N. , Teo, S.H. , Islam, A. , Taufig-Yap ,Y.H. .(2017). TEactivity and characterization of natural CaO derived from waste venus clam (Tapes belcheri S.) material for enhancement of biodiesel production, Process Saf. Environ. Protect. 105: 303-315.

Ullah, Z, Bustam, M.A., Man, Z., A., Khan, S., Muhammad, N. Sarwono, A. (2017). Preparation and kinetics study of biodiesel production from waste cooking oil using new functionalized ionic liquids as catalysts, Renew. Energy 114 :755-765.

Verma, D., Raj, J., Pal, A., Jain, M. (2016) . A critical review on production of biodiesel from various feedstocks, J. Sci. Innov. Res. 5 (2) 51-58.

Vanessa, F. de Almeida,A. Pedro J. García-Moreno Antonio Guadix, B., Emilia M. Guadix.(2015) .Biodiesel production from mixtures of waste fish oil, palm oil and waste frying oil: Optimization of fuel properties. Fuel Processing Technology 133 152–160.

Author Information

Saba H. Sedeeq
University of Mosul/College of Science
Department of Chemistry, Mosul/Iraq

Neam M.T. Al-Layla
University of Mosul/College of Science
Department of Chemistry, Mosul/Iraq

Abdelrahman B. Fadhil
University of Mosul/College of Science
Department of Chemistry, Mosul/Iraq
Contact E-mail: *abdelrahmanbasil@yahoo.com*

IConTES 2019: International Conference on Technology, Engineering and Science

Potential TADF Structures with Benzophenone Moieties

Selcuk GUMUS
Van Yuzuncu Yil University

Aysegul GUMUS
Van Yuzuncu Yil University

Abstract: The architectures of organic solar cells are based on two kinds of materials: electron donors (D) and electron acceptors (A), respectively. Organic compounds which possess donor-acceptor units exhibit important optical and photophysical characteristics. Donor-acceptor compounds are widely used in molecular electronics applications, and it is of interest to investigate how their properties can be manipulated and probed. The πelectronic characteristics of molecular donor (D) – acceptor (A) compounds have been attracting attention in solid state science as well as for their potential technological development in organic electronics. The DA solar cells apply the photoinduced electron transfer to separate the electron from the hole. The photo-induced electron transfer takes place from the excited state of the donor to the LUMO of the acceptor. One of the most important design considerations of TADF molecules is obtaining a small energy gap between the S1 and T1 states ($\Delta \varepsilon_{ST}$). A molecule meets this requirement only when its lowest-energy transition has low singlet–triplet exchange energy. Current trends in the research into novel TADF emitters are mainly focused on intramolecular donoracceptor (D-A)-type molecules, as in the present case In this work, we have constructed benzophenone based butterfly compounds and investigated the structural and electronic properties theoretically at the level of Density Functional Theory (DFT). These D-π-A type compounds may be potential candidates for organic solar cell applications, organic lightemitting diodes or fluorescent organic materials.

Keywords: TADF, Solar cells, OLED, DFT

Introduction

The amount of energy that the sun produces is enormous such that Earth receives enough energy to fulfill the yearly world demand of it in less than an hour although not all of that energy reaches the Earth's surface due to absorption and scattering [1]. The continous supply of energy from sun introduces the photovoltaic conversion of solar energy as an important challenge. Solar cells of inorganic materials have a record energy conversion efficiency of around 39%, [2] whereas commercially available solar panel systems, have a significantly lower efficiency range between 15 and 20%.

Solar energy industry is seeking for both high power conversion efficiency and low cost materials. Yet, the prices of silicon based solar cell power plants or solar energy panels are still not competitive with other traditional combustion rivals. Use organic materials can serve an alternative approach for lowering the manufacturing costs of solar cells which can be processed under less demanding conditions. The research for novel organic photovoltaic's has been continued for more than 30 years, however, within the last decade the developments in the field gained considerable momentum [3,4]. Organic solar cells bring the advantages of mechanical flexibility, ease of processing, and low cost of production. Moreover, chemical modification is easy for customization of desired properties. However, the energy conversion efficiency for these organics still needs to be improved, since a maximum efficiency of 4-5% could have only been reached, up to date [5].

The architectures of organic solar cells are based on two kinds of materials: electron donors (D) and electron acceptors (A), respectively. Organic compounds which possess donor-acceptor units exhibit important optical and photophysical characteristics [6]. Donor-acceptor compounds are widely used in molecular electronics

applications, and it is of interest to investigate how their properties can be manipulated and probed. The π-electronic characteristics of molecular donor (D)–acceptor (A) compounds have been attracting subjects for the solid state science as well as for the potential technological development in organic electronics. The DA solar cells apply the photo induced electron transfer [7] to separate the electron from the hole. The photo induced electron transfer takes place from the excited state of the donor to the LUMO of the acceptor.

In order to gain higher efficiencies for organic solar cells, the primary strategy can be adjusting the highest occupied molecular orbital (HOMO) and the lowest unoccupied molecular orbital (LUMO) energy levels by chemical tailoring. This strategy is rather usefull since the difference between HOMO and LUMO determines the light absorption regions [8], the open-circuit voltage (V_{oc}) heavily depends on the gap of $LUMO_{acceptor}$-$HOMO_{donor}$ [9] and sufficient $\Delta\varepsilon$ (the difference between HOMOs or LUMOs of donor and acceptor), which usually needs to be at least 0.3 eV, is necessary for excitons dissociation at the interface of donor and acceptor [10]. Recently, two main methods have been used to modify the energy levels of potential molecules: (1) to establish a donor-acceptor (D-A) conjugated backbone by choosing appropriate donors and acceptors [11,12], (2) to introduce electron-donating or electron-withdrawing atoms and groups, such as F-atom, alcoxyl, cyano, rhodanine, etc. [13–17].

In this work, we have constructed a triazophenone centred butterfly compound and investigated the structural and electronic properties theoretically at the level of Density Functional Theory. These D-π-A type compounds may be potential candidates for organic solar cell applications or organic light emitting diodes or fluorescent organic materials.

Method

The three-dimensional ground state (S_0) geometry of the compound was geometry optimized using Density Functional Theory (DFT) [18] by using the Gaussian 09W [19] package program and the hybrid functional B3LYP. The B3LYP is composed of Becke's three parameter exchange functional (B3) [20] and the nonlocal correlation functional by Lee, Yang, and Parr (LYP) [21]. The basis set used for all atoms was 6-31++G(d,p) in both DFT and time-dependent density functional theory (TD-DFT) method. We have applied default G09 grid for computations.

For the nonel compound, vibrational analyses were carried out using the same basis set employed in the corresponding geometry optimizations. The frequency analysis of none of the compounds yielded any imaginary frequencies, indicating that the structure of each molecule corresponds to at least a local minimum on the potential energy surface. The normal mode analysis was performed for 3N-6 vibrational degrees of freedom, N being the number of atoms in the molecule.

The low-lying triplet (T) and singlet excited states (S) of the compounds were relaxed to obtain their minimum energy geometries using the TD-DFT as implemented in G09 package program [22]. The vertical excitation energies and oscillator strengths were obtained for the lowest triplet and singlet transitions at the optimized ground state equilibrium geometries by using TD-DFT at the same hybrid functional and basis set [22]. Optimized ground state structures were utilized to obtain the electronic absorption spectra, including maximum absorption wavelengths, oscillator strengths, and main configuration assignment by using TD-DFT.

Results and Discussion

The demand for economically viable for large-scale power generation based on environmentally green materials with limitless availability and variaty force people to search for novel ideas and applications. Organic semiconductor materials are a cheaper alternative to inorganic counterparts like Si. Organic photovoltaics can have extremely high optical absorption coefficients which provide the potential for the production of very thin solar cells, therefore, they can be fabricated as thin flexible devices.

Semiconductor Properties

The electronic structure of all organic semiconductors is based on conjugation of π-electrons. A conjugated organic system consists of an alternation between single and double carbon-carbon bonds. Single bonds are named as σ-bonds and are associated with localized electrons, and double bonds are composed of a σ-bond and

a π-bond. The π-electrons are mobile and can jump between carbon atoms due to the mutual overlap of pi orbitals along the conjugation path, which causes the wave functions to delocalize over the conjugated skeleton. The empty π-bands are called the Lowest Unoccupied Molecular Orbital (LUMO) and π-bands filled with electrons are called the Highest Occupied Molecular Orbital (HOMO). The band gap (Δε) of semiconductor materials ranges from 1 to 4 eV.

Rigid polyaromatic planar carbon or heterocyclic compounds with donor-π-acceptor architecture have attracted much attention in recent years due to their special electro-optical properties originating from their low band gap [23,24]. Benzophenone was used in literature a building block for butterfly compounds. It has strong ability as an acceptor. Triazophenone, a derivative of benzophenone electronically, is a thought to be a very well acceptor unit to be used in organic photovoltaics which can connect either side with donors to provide semiconductor system (Figure 1).
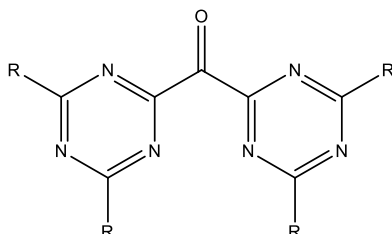
Figure 1. Chemical structure of triazophenone

Pyrene is a polycyclic aromatic hydrocarbon consisting of four fused benzene rings, resulting in a flat aromatic system. This yellow solid is the smallest peri-fused polycyclic aromatic hydrocarbon (one where the rings are fused through more than one face). Pyrene forms during incomplete combustion of organic compounds. Pyrene and its derivatives are used commercially to make dyes and dye precursors, for example pyranine and naphthalene-1,4,5,8-tetracarboxylic acid. It has strong absorbance in UV-Vis in three sharp bands at 330 nm in DCM. The emission is close to the absorption, but moving at 375 nm. The morphology of the signals change with the solvent. Its derivatives are also valuable molecular probes via fluorescence spectroscopy, having a high quantum yield and lifetime (0.65 and 410 nanoseconds, respectively, in ethanol at 293 K). Pyrene was the first molecule for which excimer behavior was discovered.

In the present research, a triazophenone based structure has been studied computationally at B3LYP/6-31++G(d,p) level of theory. These highly conjugated systems are important in terms of their structural and electronic properties. They may be strong candidates for organic semiconductors and their potential applications as organic solar cells. The structures are designed in the form of D-π-A type organic systems. The geometry optimized ground state structure of the pyrene triazophenone structure is shown in Figure 2.
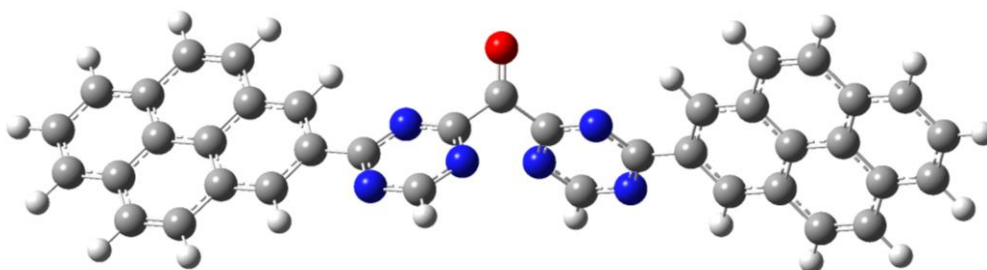
Figure 2. Geometry optimized structure of pyrene triazophenone

The interfrontier molecular orbital energy gap (Δε) provides information about the conductivity of the system. According to the literature data, $\Delta\varepsilon \leq 0.1$ eV conductors, $\Delta\varepsilon = 0.5$-3.5 eV semiconductors and $\Delta\varepsilon \geq 4.0$ eV insulator. The interfrontier molecular orbital energy gap (Δε) for the present structure is 3.22 eV. Therefore, the novel compound is a potential semicoductor for OLED.

TADF Properties

One of the most important design consideration of TADF molecules is to obtain a small energy gap between the S_1 and T_1 states ($\Delta\varepsilon_{ST}$). A molecule meets this requirement only when its lowest-energy transition has a small

singlet–triplet exchange energy. Current trends in research of novel TADF emitters are mainly focusing on intramolecular donor-acceptor (D-A)-type molecules as in the present case. Therefore, appropriate donor-acceptor units have to be selected carefully to obtain full-color TADF molecules, with their HOMO and LUMO being localized on different constituents. To obtain details about the geometric and electronic structures of the present compound time-dependent density functional theory (TD-DFT) calculations were performed at the B3LYP/6-31++G(d,p) level.

The clear separation of the frontier molecular orbitals results in narrower $\Delta\varepsilon_{ST}$ values. $\Delta\varepsilon_{ST}$ data for the pyrene triazophenone unit is coputed top be 0.42 eV. Thus, ΔE_{ST} predicted by the TD-DFT calculation is small enough for thermal repopulation of the S_1 state via $T_1 \rightarrow S_1$ reverse intersystem crossing (RISC) for all the compound. It might suggest a very high potential as TADF emitters by possessing the narrow S_1-T_1 energy difference and well separated HOMO and LUMO schemes. All computed lowest-energy excited states may be described by the HOMO-LUMO transition corresponds to an intramolecular charge transfer (ICT) with small exchange energy (Figure 3).
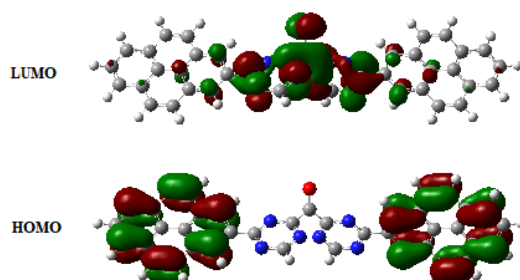
Figure 3. 3D frontier molecular orbital schemes of the present compound

Conclusion

In the present study, we performed a computational study by the application of Density Functional Theory at B3LYP/6-31++G(d,p) level on a triazophenone derivative.

The structure was constructed as D-A motif in order to increase the ability to achieve intramolecular charge transfer so that it may act as potential solar cell organic semiconductor. The interfrontier energy gap of the compound was obtained from DFT calculations and found to be 2.52 eV. Thermally activated delayed fluorescence (TADF) properties of the compound were discussed upon the results obtained by TDDFT calculations. Two critical points for potential TADF structures are; (i) separate distribution HOMO and LUMO orbitals throughout the molecule for small exchannge energy and (ii) nanrow energy gap between the S_1 and T_1 states ($\Delta\varepsilon_{ST}$). The $\Delta\varepsilon_{ST}$ data was computed to be 0.42 eV. Thus, it may be considered for future TADF applications.

Acknowledgements or Notes

References

A.S. Bagher, Introduction to Organic Solar Cells, *Sustainable Energy* **2**, 85-90 (2014).

H. Spanggaard, F.C. Krebs, A brief history of the development of organic and polymeric photovoltaic's, *Sol. Energy Mater. Sol. Cells* **83**, 125-146 (2004).

C. Brabec, V. Dyakanov, J. Parisi, N.S Sariciftci, *Organic photovoltaics: Concepts and Realization*, Springer, New York, 2003.

H. Hoppe, N.S. Sariciftci, Organic solar cells: an overview, *J. Mater. Res.* **19**, 1924-1945 (2004).

G. Li, V. Shrotriya, J. Huang, Y. Yao, T. Moriarty, K. Emery, Y. Yang, *Nature Mater.* **4**, 864-868 (2005).

H.N. Kim, Z.Q. Guo, W.H. Zhu, J.Y. Yoon, H. Tian, Recent progress on polymer-based fluorescent and colorimetric chemosensors, *Chem. Soc. Rev.* **40**, 79-93 (2011).

N.S. Sariciftci, L. Smilowitz, A.J. Heeger, F. Wudl, Photo induced electron transfer from a conducting polymer to buckminsterfullerene, *Science* **258**, 1474-1476 (1992).

Y. Lin, Q. He, F. Zhao, L. Huo, J. Mai, X. Lu, C.J. Su, T. Li, J. Wang, J. Zhu, Y. Sun, C. Wang, X. Zhan, A facile planar fused-ring electron acceptor for as-cast polymer solar cells with 8.71% efficiency, *J. Am. Chem. Soc.* **138**, 2973–2976 (2016).

S.H. Liao, H.J. Jhuo, Y.S. Cheng, S.A. Chen, Fullerene derivative-doped zinc oxide nanofilm as the cathode of inverted polymer solar cells with low-bandgap polymer (PTB7-Th) for high performance, *Adv. Mater.* **25**, 4766–4771 (2013).

M.C. Scharber, D. Mühlbacher, M. Koppe, P. Denk, C. Waldauf, A.J. Heeger, C.J. Brabec, Design rules for donors in bulk-heterojunction solar cells-towards 10% energy-conversion efficiency, *Adv. Mater.* **18**, 789–794 (2006).

J.A. Love, C.M. Proctor, J. Liu, C.J. Takacs, A. Sharenko, T.S. van der Poll, A.J. Heeger, G.C. Bazan, T.-Q. Nguyen, Film morphology of high efficiency solution-processed small-molecule solar cells, *Adv. Funct. Mater.* **23**, 5019–5026 (2013).

L. Liang, J.-T. Wang, X. Xiang, J. Ling, F.-G. Zhao, W.-S. Li, Influence of moiety sequence on the performance of small molecular photovoltaic materials, *J. Mater. Chem.* A **2**, 15396-15405 (2014).

B. Kan, Q. Zhang, M. Li, X. Wan, W. Ni, G. Long, Y. Wang, X. Yang, H. Feng, Y. Chen, Solution-processed organic solar cells based on dialkylthiol-substituted benzodithiophene unit with efficiency near 10%, *J. Am. Chem. Soc.* **136**, 15529-15532 (2014).

B. Kan, M. Li, Q. Zhang, F. Liu, X. Wan, Y. Wang, W. Ni, G. Long, X. Yang, H. Feng, Y. Zuo, M. Zhang, F. Huang, Y. Cao, T.P. Russell, Y. Chen, A series of simple oligomer-like small molecules based on oligothiophenes for solution-processed solar cells with high efficiency, *J. Am. Chem. Soc.* **137**, 3886-3893 (2015).

T.L. Nguyen, H. Choi, S.J. Ko, M.A. Uddin, B. Walker, S. Yum, J.E. Jeong, M.H. Yun, T.J. Shin, S. Hwang, J.Y. Kim, H.Y. Woo, Semi-crystalline photovoltaic polymers with efficiency exceeding 9% in a 300 nm thick conventional single-cell device, *Energy Environ. Sci.* **7**, 3040-3051 (2014).

J. Lu, J. Peng, Y. Wang, J. Yuan, C. Sheng, H.-Q. Wang, W. Ma, Benzo[1,2-b:4, 5-b0] dithiophene-fumaronitrile-based D-A type copolymers with different p-bridges: synthesis, characterization and photovoltaic properties, *Synth. Met.* **188**, 57-65 (2014).

Z. Du, W. Chen, M. Qiu, Y. Chen, N. Wang, T. Wang, M. Sun, D. Yu, R. Yang, Utilizing alkoxyphenyl substituents for side-chain engineering of efficient benzo[1,2-b:4,5-b']dithiophene-based small molecule organic solar cells, *Phys. Chem. Chem. Phys.* **17**, 17391-17398 (2015).

W. Kohn, L.J. Sham, Self-consistent equations including exchange and correlation effects. *Phys. Rev.* **140**, 1133-1138 (1965).

M. J. Frisch, G. W. Trucks, H. B. Schlegel, G. E. Scuseria, M. A. Robb, J. R. Cheeseman, G. Scalmani, V. Barone, B. Mennucci, G. A. Petersson, H. Nakatsuji, M. Caricato, X. Li, H. P. Hratchian, A. F. Izmaylov, J. Bloino, G. Zheng, J. L. Sonnenberg, M. Hada, M. Ehara, K. Toyota, R. Fukuda, J. Hasegawa, M. Ishida, T. Nakajima, Y. Honda, O. Kitao, H. Nakai, T. Vreven, J. A. Montgomery, Jr., J. E. Peralta, F. Ogliaro, M. Bearpark, J. J. Heyd, E. Brothers, K. N. Kudin, V. N. Staroverov, T. Keith, R. Kobayashi, J. Normand, K. Raghavachari, A. Rendell, J. C. Burant, S. S. Iyengar, J. Tomasi, M. Cossi, N. Rega, J. M. Millam, M. Klene, J. E. Knox, J. B. Cross, V. Bakken, C. Adamo, J. Jaramillo, R. Gomperts, R. E. Stratmann, O. Yazyev, A. J. Austin, R. Cammi, C. Pomelli, J. W. Ochterski, R. L. Martin, K. Morokuma, V. G. Zakrzewski, G. A. Voth, P. Salvador, J. J. Dannenberg, S. Dapprich, A. D. Daniels, O. Farkas, J. B. Foresman, J. V. Ortiz, J. Cioslowski, and D. J. Fox, *Gaussian 09, Revision D.01*, Gaussian, Inc., Wallingford CT, 2013.

A.D. Becke, Density-functional exchange-energy approximationwith correct asymptotic behavior. *Phys. Rev. A* **38**, 3098–3100 (1988).

C. Lee, W. Yang, R.G. Parr, Development of the Colle–Salvetti correlation energy formula into a functional of the electron density. *Phys. Rev. B* **37**, 785–789 (1988).

M.E. Casida, C. Jamorski, K.C. Casida, D.R. Salahub, Molecular excitation energies to high-lying bound states from timedependent density-functional response theory: characterization and correction of the time-dependent local density approximation ionization threshold. *J. Chem. Phys.* **108**, 4439–4449 (1998).

Author Information

Selcuk Gumus
Van Yuzuncu Yil University
Department of Chemistry, Van/Turkey
Contact E-mail: *gumuss@gmail.com*

Aysegul Gumus
Van Yuzuncu Yil University
Department of Chemistry, Van/Turkey

Analysis the Strength Reduction Factor in the Shear Strength of Geopolymer Concrete Beams

Sema ALACALI
Yıldız Technical University

Mehdi OZTURK
Yıldız Technical University

Guray ARSLAN
Yıldız Technical University

Abstract: In recent years, the rapidly developing and growing construction sector has brought about an increase in environmental concerns. Therefore, within the framework of sustainable development, researchers intensify their work on the reuse of environmentally friendly materials called geopolymer concrete. As a result of the studies of many researchers, geopolymer concrete which composed of sustainable materials has been proposed instead of traditional concrete. While a substantial amount of researches has focused on the flexural behavior of geopolymer concrete beams, there exists a relatively limited amount of studies concerning the shear behavior of geopolymer concrete beams with stirrup. Design codes use a strength reduction factor that reflects the degree of uncertainty associated with the probability of the design equations. In this study, the strength reduction factor in predicting the shear strength of geopolymer concrete beams with stirrups according to ACI318 was investigated for different coefficients of variation of concrete compressive strength by using the first-order second moment approach.

Keywords: Geopolymer concrete, Beam, Shear strength, Reduction factor

Introduction

In recent years, natural resources are consumed in an unplanned and wrong way, nature and environment is rapidly destroyed as the increasing population of the world urbanization and industry have developed. In order to prevent this negative situation, many institutions and organizations carry out various campaigns to raise awareness. One of them is the concept of sustainability that suggests the reuse of waste materials in the industry. The usability of various environmentally friendly materials is being investigated in the construction sector. One of these research topics is the use of more economical and sustainable materials instead of portland cement, which is known for its harm to nature during production. Scientists conducting many experimental and analytical studies on this subject have found geopolymer concrete formed by activating pozzolan substances with various alkalis. Portland cement consumes very high energy and produces carbon dioxide (CO_2). As a result of this production, 1 ton of CO_2 is released to nature for 1 ton of cement production. Approximately 7% of the world's CO_2 emissions are generated by the Portland cement production process (Roy, 1999). It is recommended to use many pozzolanic wastes instead of this substance which has a serious impact on global climate change. Thus, this serious harm to nature will be eliminated.

Nowadays , the most commonly used pozzolans for geopolymer concrete production are accepted as kaolin clay, metakaolin, fly ashes, blast furnace slag, red sludge, silica fume and zeolite. However, sodium hydroxide, sodium carbonate, sodium sulfate and sodium silicate are the best alkalis to activate these pozzolanic substances. The materials produced by changing the chemical composition and crystal structure of natural minerals by various methods are called "geopolymers".

Technological developments and recent studies have given cause for using new materials instead of traditional construction materials. Various researchers have studied on the shear and flexural strength prediction and safety factor of traditional construction materials. But, it has not been observed on the literature related to the safety factor of geopolymer concrete materials. Safety factor provisions utilize load and strength reduction factors. These factors for elements made of traditional concrete materials have been evaluated in many studies (Arslan et al. 2015, Alacalı and Arslan 2018). However, in the literature, there is no study on the reduction factor of shear strength for geopolymer concrete elements. In this study, when the shear strength relation given for traditional concrete according to ACI318 is used for geopolymer concrete, it has been investigated which value the safety factor corresponds.

The strength reduction factor ϕ considered in design of structural components to insure performance correspond to specified reliability index β. The main concept in most reliability-based design codes is to determine the target reliability index β. The scope of current codes for building design is to maintance the reliability index as close to the target index as possible. For this purpose, the 1995 edition of ACI 318 ''Building code requirements for reinforced concrete'' suggests a ϕ of 0.85 for shear design of the reinforced buildings. However, in ACI 318 (2002, 2011), the ϕ for shear design is decreased to 0.75.

This study assesses the change of the ϕ in predicting the contribution of geopolymer concrete to shear strength by using second-moment approach according to ACI318. The change in the ϕ against the coefficient of variation of geopolymer concrete compressive strength (V_{f_c}) and the failure probability (p_F) were examined through the database of 9 shear test results obtained from literature (Chang, 2009).

Design recommendations for RC Beams

According to ACI318, the nominal shear strength (v_n) is comprised two components: concrete and stirrups. This relationship is given as follows;

$$v_n = v_c + v_s \tag{1}$$

in which v_s is the shear strength of stirrup based on yield and v_c is the shear strength of concrete, respectively. ASCE-ACI426 (1973) reported that the shear strength of RC beams is given as follows;

$$v_n = \frac{1}{6}\sqrt{f_c} + \rho_w f_{yw} \tag{2}$$

in which ρ_w is the ratio of stirrups, f_c and f_{yw} are the compressive strength of concrete and yield strength of stirrup in MPa, respectively.

In the codes (ACI318, TS500), the basic requirement for strength design may be explained that the design shear capacity of a member must exceed the shear demand as shown in Eq. (3).

$$\phi v_n \geq v_u \tag{3}$$

In which ϕ is the shear strength reduction factor and given as 0.75 in ACI318 (2002, 2011) and 0.85 in ACI318 (1995), v_u is the ultimate shear strength. In this study, the change in the strength reduction factor considered in predicting the shear strength according to ACI318 (1995) was investigated and compared for different failure probabilities and coefficients of variation of geopolymer concrete compressive strength.

The Reliability Problem

In probability theory, the capacity R and the load S involve different basic variables. Hence the performance function, $Z = R - S = g(X_1, X_2.......X_n)$, contains uncertainties in the all design variables. When the performance function equals to zero, $Z = 0$, it is called a failure surface. The safety or reliability is defined by

the condition $Z > 0$ and therefore, failure by $Z < 0$. The probability of safety or reliability is $p_S = \Phi(\beta)$, and the probability of failure is $p_F = 1 - \Phi(\beta)$. In the case of with normal distribution of R and S, the failure probabilities p_F corresponding to different reliability indexes β (5.2, 4.75, 4.27, 3.72, 3.09, 2.33) are 10^{-7}, 10^{-6}, 10^{-5}, 10^{-4}, 10^{-3} and 10^{-2}, respectively.

In the reliability based design, the problem is to determine the partial safety factors of the variables according to target reliability index β. In this study, the first-order second moment approach (FOSM) was used and the design points $(\gamma_i . m_{X_i})$ corresponding to the target reliability index β were obtained. This method is generally used by committees in calibrating codes for the evaluation of partial safety factors (Ang and Tang, 1984, Ranganathan, 1990).

The performance function g(**X**) for the shear failure mode is expressed as

$$g(\mathrm{X}) = \gamma_i . v_n - \gamma_j . v_{u,\exp.} \tag{4}$$

in which v_n is the nominal shear strength, $v_{u,\exp}$ is the experimental shear strength, γ_i and γ_j are the safety factors corresponding to the related variables. By calculating weighted averages of these factors (γ_i), the strength reduction factor ϕ, defined in Eq.(3) is determined. The change in the ϕ considered in predicting the shear strength according to ACI318 against the different V_{f_c} (0.10, 0.12, 0.15, 0.18, 0,20) and p_F (10^{-7}, 10^{-6}, 10^{-5}, 10^{-4}, 10^{-3}, 10^{-2}) was investigated by using experimental studies available in the literature (Chang, 2009).

Uncertainties of random variables

The uncertainties included in the prediction of shear strength were modelled as random variables. Since there is no information about the measurement sensivity in the experiments, the values of the coefficient of variation taken into account in the calculations were determined by considering the previous statistical studies.

The coefficient of variation of concrete compressive strength (V_{f_c}) under average construction quality control usually depends on the concrete strength and varies in between 0.10 and 0.21 through the literature (Arslan et. al 2015). The standard deviation for geopolymer concrete was measured in between 5.0% and 7.8% of concrete compressive strength (Pan et al. 2010). This value corresponds to a coefficient of variation of 0.08 for the geopolymer concrete samples examined this literature. In this study, the coefficient of variation of geopolymer concrete compressive strength (V_{f_c}) ranges from 0.10 to 0.20.

Although the stirrup ratios depend on the structural dimensions, they are assumed to be statistically independent from each other and from the other random structural parameters. In the study of Hao et al. (2010), it is assumed that the coefficient of variation of stirrup ratio (V_{ρ_w}) is 0.15, which is the value used in this study. The coefficient of variation of reinforcement strength ($V_{f_{yw}}$) were also reported by many researchers. Slightly different values were given by different researchers, where the $V_{f_{yw}}$ ranges from 0.05 to 0.15 (Arslan et al. 2015). It is taken as 0.10 in the present study to model variations of $V_{f_{yw}}$. In the studies of Hognestad (1951) and Mirza (1996), it is assumed that the coefficient of variation of strength due to test procedure is 0.04, which is the value used in this study.

Analysis of the strength reduction factor in predicting the shear strength

The properties of the beams in the database of 9 shear test results are shown in Table 1 (Chang, 2009). As seen in Table1, f_c varies from 44 MPa to 56 MPa. In this study, normal strength geopolymer concrete (NSGC) is defined as concrete having compressive strength less than 50 MPa, and high strength geopolymer concrete (HSGC) having compressive strength equal to or more than 50 MPa. The shear span-to-depth ratio (a/d) and

stirrup yielding strength (f_{yw}) equal to 2.5 and 597 MPa, respectively, for all beams. The stirrup percentage (ρ_w) ranges from 0.1 to 0.168.

Table 1. The properties of the beams (Chang, 2009)

Name of beams	a/d	f_c (MPa)	ρ_w%	f_{yw} (MPa)	v_u (MPa)
S1-1	2.5	45	0.100	597	4.06
S1-2	2.5	45	0.126	597	3.95
S1-3	2.5	44	0.168	597	3.63
S2-1	2.5	56	0.100	597	5.03
S2-2	2.5	50	0.126	597	5.10
S2-3	2.5	50	0.168	597	5.07
S3-1	2.5	49	0.100	597	5.13
S3-2	2.5	49	0.126	597	5.42
S3-3	2.5	56	0.168	597	6.54

The change in the strength reduction factor ϕ for the shear design of geopolymer concrete beams obtained from the analysis is compared for different values of V_{f_c} and p_F in Table 2. As shown in Table 2, ϕ decreases as β increases and the reduction in the ϕ increases with V_{f_c}. For given V_{f_c} and p_F, the ϕ for HSGC beams were found to be greater than the one for NSGC beams, so it can be inferred that the ϕ for HSGC beams is more safe than the one for NSGC beams. In ACI318 (1995), the ϕ considered in predicting the shear strength equals to 0.85. It is indicated that this value corresponds to the target values of $p_F = 10^{-4}$ ($\beta = 3.72$) and $V_{f_c} = 0.10$, for NSGC and HSGC beams (Figure 1). It is observed that this value is conservative for $p_F > 10^{-4}$ and a variation coefficient of 0.10. In ACI318 (2002) and ACI318 (2011), the factor of 0.85 was replaced by a factor of 0.75, which corresponds to the target values of $p_F = 10^{-7}$ ($\beta = 5.2$) and $V_{f_c} = 0.20$ for all beams. According to the study published by Arslan et al. (2015) for traditional concrete, the ϕ of 0.85 corresponds to the target values of $p_F = 10^{-2}$ ($\beta = 2.33$) and $V_{fc} = 0.10$, and the ϕ of 0.75 corresponds to the target values $p_F = 10^{-5}$ ($\beta = 4.27$) and $V_{fc} = 0.10$ for all beams.

Table 2. Changing the average values of ϕ

V_{f_c}	p_F (β)						Beams
	10^{-7} (5.2)	10^{-6} (4.75)	10^{-5} (4.27)	10^{-4} (3.72)	10^{-3} (3.09)	10^{-2} (2.33)	
0.10	0.811	0.823	0.836	0.853	0.873	0.899	NSGC (5 beams)
0.12	0.798	0.811	0.826	0.843	0.865	0.892	
0.15	0.778	0.792	0.808	0.827	0.851	0.882	
0.18	0.757	0.780	0.789	0.811	0.836	0.869	
0.20	0.742	0.758	0.776	0.798	0.825	0.861	
0.10	0.820	0.831	0.844	0.859	0.878	0.903	HSGC (4 beams)
0.12	0.808	0.820	0.834	0.850	0.870	0.897	
0.15	0.790	0.803	0.818	0.836	0.858	0.887	
0.18	0.770	0.784	0.800	0.820	0.844	0.875	
0.20	0.756	0.771	0.788	0.808	0.834	0.867	
0.10	0.815	0.826	0.839	0.856	0.875	0.901	NSGC & HSGC (9 beams)
0.12	0.803	0.815	0.830	0.846	0.867	0.894	
0.15	0.783	0.797	0.812	0.831	0.854	0.884	
0.18	0.762	0.782	0.794	0.815	0.839	0.872	
0.20	0.748	0.764	0.781	0.803	0.829	0.864	
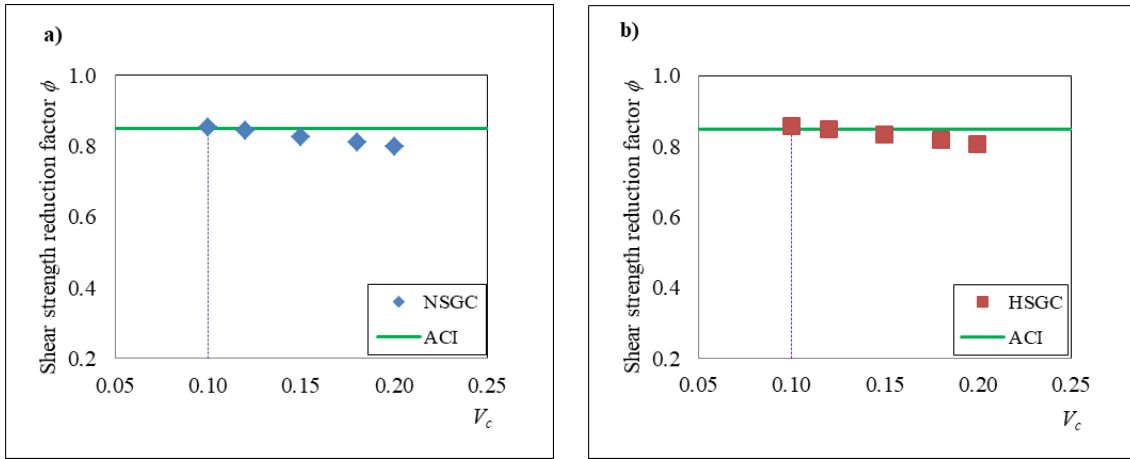
Figure 1. ϕ values for $\beta = 3.72$ ($p_F = 10^{-4}$) and V_{f_c}

In this study, the effects of f_c, a/d, ρ_w and f_{yw} on the ϕ are discussed below.

Figure 2a shows the variation of ϕ with f_c for $\beta = 3.72$ ($p_F = 10^{-4}$) and $V_{f_c} = 0.10$ for all (NSGC & HSGC) beams. It is observed that the ϕ increases with increasing f_c for all beams. This result means that the shear reliability of the beam increases as the strength of the geopolymer concrete increases. Figure 2b shows the variation of ϕ with ρ_w for $\beta = 3.72$ ($p_F = 10^{-4}$) and $V_{f_c} = 0.10$ for all (NSGC & HSGC) beams. It is observed that the ϕ decreases with increasing ρ_w for all beams.
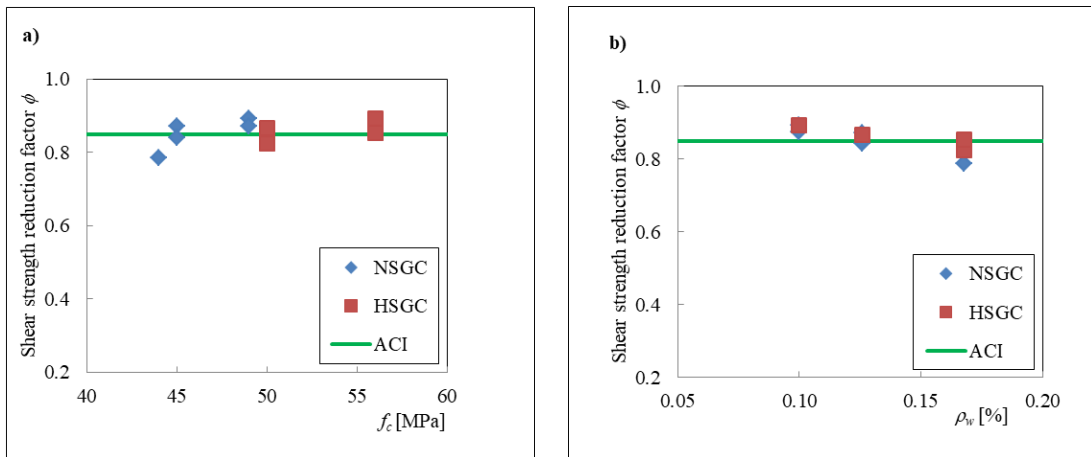
Figure 2. Range of ϕ values determined using evaluation database for $\beta = 3.72$ ($p_F = 10^{-4}$) and $V_{f_c} = 0.10$

It can be stated that the ϕ values are not equally distributed with respect to f_c, a/d and f_{yw}. The beams with a/d higher than 2.5 ($a/d = 2.5$) are limited for all (NSGC & HSGC) beams; further research is therefore required to verify the founded p_F.

Conclusions

The change in the shear strength of geopolymer concrete beams with stirrups according to ACI318 is investigated for different coefficients of variation and failure probabilities. On the basis of results obtained in this study, the following conclusions are drawn:

- It is found that a ϕ of 0.85, which is a value recommended by ACI318 (1995), corresponds to the target values of $p_F = 10^{-4}$ ($\beta = 3.72$).

- It is shown that the ϕ increases with increasing f_c for all beams. So, this result means that the shear reliability of the beam increases as the strength of the geopolymer concrete increases.
- It is observed that the ϕ decreases with increasing ρ_w for all beams.
- For given V_{f_c} and p_F, the ϕ for HSGC beams was found to be greater than the one for NSGC beams, so it can be inferred that the ϕ for HSGC beams is more safe than the one for NSGC beams.

References

American Concrete Institute Committee 318 (ACI 318). (1995). *Building Code Requirements for Structural Concrete (ACI 318M-95) and Commentary.* Farmington Hills, MI.

ACI (American Concrete Institute). (2002). ACI 318: Building Code Requirements for Structural Concrete (ACI 318M-02) and Commentary. Farmington Hills, MI.

Alacalı, S., & Arslan, G. (2018). Assessment of the strength reduction factor in predicting the flexural strength, *Journal of Theoretical and Applied Mechanics*, 56, 4, pp. 1043-1053.

American Concrete Institute Committee 318 (ACI 318). (2011). *Building Code Requirements for Structural Concrete (ACI 318M-11) and Commentary.* Farmington Hills, MI.

Ang, A.H.S., & Tang, W.H. (1984). *Probability concepts in engineering planning and design. V.II, Decision, risk, and reliability*, Wiley, New York.

Arslan, G., Alacalı, S.N., & Sagiroglu, A. (2015). The investigation of the strength reduction factor in predicting the shear strength. *Journal of Theoretical and Applied Mechanics* 53, 2, pp.371-381, Warsaw

ASCE-ACI 426. (1973). The shear strength of reinforced concrete members. *Proc Am Soc Civil Eng*, 99; ST6, 1091–1187.

Chang, E.H. (2009). Shear and Bond Behaviour of Reinforced Fly Ash-Based Geopolymer Concrete Beams. *Doctoral Thesis*, Curtin University of Technology.

Hao, H., Stewart, M.G., Li, Z.-X., & Shi, Y. (2010). RC Column Failure Probabilities to Blast Loads. *International Journal of Protective Structures* -Volume 1, Number 4.

Hognestad., E. (1951). A study of combined bending and axial load in reinforced concrete members. *Engineering Experiment Station Bulletin*, No. 399, University of Illinois, Urbana.

Mirza, S.A. (1996). Reliability-based Design of Reinforced Concrete Columns. *Structural Safety* Vol. 18, No. 2/3, pp. 179-194.

Pan, Z., Sanjayan, J.G., & Rangan, B.V. (2010). Fracture properties of geopolymer paste and concrete. *Magazine of Concrete Research*, Volume 63, Issue 10.

Ranganathan R. (1990). Reliability analysis and design of structures. *tata McGraw-Hill offices*. New Delhi.

Roy, D. (1999). Sulfoaluminate-Belite Cement From Low-Calcium Fly Ash and Sulfur-Rich and Other Industrial by-Products", *Cement and Concrete Research*, 29(8):1305-1311.

TS500 (2000). Requirements for design and construction of reinforced concrete structures, Ankara, *Turkish Standards Institute* (in Turkish).

Author Information

Sema Alacali
Yıldız Technical University
Faculty of Civil Engineering, Civil Engineering Department,
Structural Engineering Division, 34210
Esenler-Istanbul- Turkey

Mehdi Ozturk
Yıldız Technical University
Natural and Applied Sciences
Esenler-Istanbul- Turkey

Guray Arslan
Yıldız Technical University
Faculty of Civil Engineering, Civil Engineering Department,
Structural Engineering Division, 34210
Esenler-Istanbul- Turkey

Design and Implementation of an Experimental Setup for Automated Photothermal Spectroscopy

Mustapha DJABAR
Université Ferhat ABBAS Sétif 1

Ameur ZEGADI
Université Ferhat ABBAS Sétif 1

Abstract: Recent developments in solar energy research have led to new technologies in solar cells. Materials based on chalcopyrite ternary semiconductors have gained great interest because of their excellent optical properties. It has been shown that the compound's defect structure affects strongly the optoelectronic properties of these alloys. In order to obtain more efficient devices these defects need to be detected and identified. The best way to characterize those novel materials is to use new techniques based on the exploitation of the photothermal effect. The main objective of this work is to study and implement an automated photothermal spectrometer. The first measurement technique that can be done with this apparatus is the photoacoustic spectroscopy. Wavelength scanning and data acquisition and logging are done automatically by a program written in LabVIEW. The second measurement technique is a transition from the former one. It is done by modifying only a few devices. Thus, one can make the photothermal beam deflection spectroscopy simply by adding a laser source and the position sensor detector that goes with it. The last measurement technique that can be done with the implemented setup is photothermal imaging analysis. We just add a motorized X-Y stage and a suitable focusing optics. The assembled apparatus conceived in this work constitutes an essential tool for analyzing and characterizing ternary and quaternary absorbing materials for photovoltaic and microelectronic applications. This setup can also be used by a large number of scientists in various disciplines such as biology, medicine, physics and optics, since the analysis is nondestructive and without contact. It provides researchers with information on non-radiative de-excitation processes regardless of the form of the samples (solid, liquid, gel or gas). Finally, the test and calibration procedures necessary to have a functional and accurate system are reviewed.

Keywords: Photothermal, Spectroscopy, Photoacoustic, Chalcopyrite, Characterization

Introduction

Recent developments in solar energy research have led to new technologies in solar cells. The developments based on ternary semiconductors have aroused great interest because of their excellent optical properties. The use of solar cells heterostructures obtained by deposition of thin layers by low cost process is considered as a priority research track to optimize the cost of manufacture / yield. In addition, it has been shown that the properties of the different layers and the different interfaces are mainly responsible for limiting the photovoltaic conversion. Several phenomena remain unexplained, in particular the phenomena of recombination in such structures. The best way to characterize them is to use a new technique based on the exploitation of the absorption spectrum obtained by photoacoustic spectroscopy (PAS). [Rosencwaig]

The technique of photoacoustic spectroscopy (PAS) has shown a very important development in several directions in recent years. It is used by a large number of scientists in various disciplines such as biology, medicine, physics, electronics and optics [Sell]. PAS is unique in that it provides researchers with information on non-radiative de-excitation processes with the potential to give deep profiles of samples regardless of their form (solid, liquid, gel and gas) [Zegadi1]. The analysis is nondestructive and without contacts. The spectrum

obtained is based on the heating of the material considered as the origin of the greatest loss in the conversion process, therefore, it will analyze the channel responsible for these losses.

In this work we will go through the steps of the development of the photothermal spectrometer intended for material characterization especially for photovoltaic and microelectronic applications. The different variants of this system will also be exposed. Finally, the test and calibration procedures necessary to have a functional and accurate system are reviewed.

We want to mount a spectrometer that allows us to do the three spectroscopic techniques related to the photothermal effect which are: photoacoustic spectroscopy, photodeflection spectroscopy and photothermal imaging.

Photoacoustic Spectrometer

The photoacoustic spectrometer is based on the irradiation of a sample with a modulated monochromatic light source (Figure 1). A lens transforms the divergent beam of the lamp into a beam of small diameter. The latter is modulated by a mechanical optical chopper. The monochromator is used to disperse this luminous radiation, thus allowing to select the excitation wavelength. After passing through a filter (elimination of unwanted wavelengths), an elliptical mirror focuses the light beam thus obtained on the sample to be studied which is placed in the photoacoustic cell.
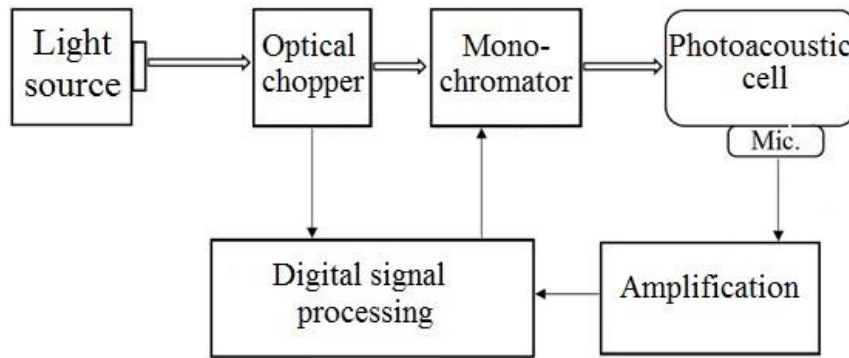
Figure 1. Synoptic diagram of the system [Zegadi2]

As a consequence of the absorption, the interaction of the surface layer of the sample is manifested by a thermal release which produces pressure fluctuations, which would result in a photoacoustic signal. The latter can be detected either by an acoustic or piezoelectric sensor. This low-amplitude signal is then amplified using a high-sensitivity AC amplifier and then extracted from noise by a lock-in amplifier and analyzed by a computer using the various signal processing methods.

Each instrument or element of the assembly must be appropriately chosen according to its possibilities and characteristics so as to construct a homogeneous assembly which fulfills the function for which it is designed and thus to obtain reliable and reproducible data. In the following, we detail the choice and the usefulness of each instrument of the assembly.

Excitation source

The sources of electromagnetic radiation that can be used are of two types: sources with a wide spectral range and narrow band ones (laser sources). For an analysis that requires wavelength variation, it is preferred to use the first type of source. For other analysis one opts for a laser source (continuous or pulsed).

In our assembly we use a radiation source with a wide spectral range: a short arc Xenon halogen lamp with a power of 300 W. A lens transforms the divergent beam of the lamp into a spot that fits between the slots of the chopper wheel.

Modulator (Optical Chopper)

The light beam is modulated ON-OFF using a variable frequency mechanical optical chopper. The model used is a MC2000 from Thorlabs (Figure 2). The wheel that comes with the chopper allows frequencies ranging from 20Hz to 1000Hz. The reference output signal is set to the actual frequency of the modulation wheel. This signal is injected into the lock-in amplifier to facilitate the extraction of the useful signal embedded in noise.

Figure 2. Head and wheel of the mechanical optical chopper

Monochromator

To select the excitation wavelength, the input light beam is dispersed using a high precision monochromator. The chosen model is the TRIAX 180 from HORIBA Scientific. The latter has an aperture of f/3.9 with a focal length of 19 cm and a spectral dispersion of 3.53 nm/mm. The monochromator has motorized adjustable slots located at the input and output ports (0-7 mm in 6.25 μm increments). It also has a triple turret dispersion network. The network of 1200gr/mm allows a spectral range of 0-1400nm.

Filter and focalization

The modulated monochromatic beam is then filtered using a filter that only passes light of wavelengths close to the region of interest. The beam is then directed using an elliptical mirror f/0.7. This serves to focus the light beam so that the incident ray only illuminates the desired part of the sample.

Photoacoustic cell

The photoacoustic cell is the chamber containing the sample to be studied as well as the microphone or transducer. It represents the heart of the spectrometer and directly influences the measurements made on different types of samples. All theoretical studies predict that the amplitude of the PA signal reaching the microphone depends on the size of the cell. In general, the amplitude of the PA signal increases when the dimensions of the cell are reduced. Different forms of PA cells have been reported in the literature [Zegadi2]. These cells can be classified according to the sample to be studied: cells designed for gaseous samples and others for solid samples. For the first case, the most used detector is the microphone. Regarding the second case one can use either a microphone or a piezoelectric sensor or both simultaneously.

The method of indirect detection is based on the thermal coupling from the sample to the gas column, the detector used is a microphone. This method was chosen for our assembly. The direct detection method uses a piezoelectric transducer as a sensor. The latter offers a greater range of modulation frequencies. Figure 3 shows a diagram of a photoacoustic cell. The window material is usually transparent to the studied wavelengths.
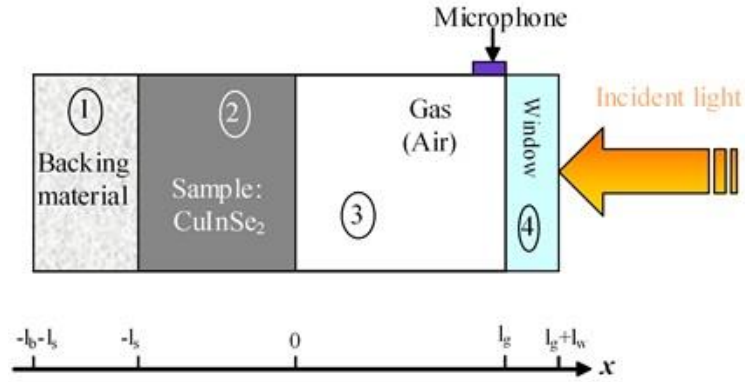
Figure 3. PA cell diagram

The study and design of photoacoustic cells is necessary for a good measurement of the photoacoustic signal. The cells may be parallelepipedal or cylindrical. The cell material may be stainless steel or plexiglass. Two examples of PA cells are shown in figure 4.
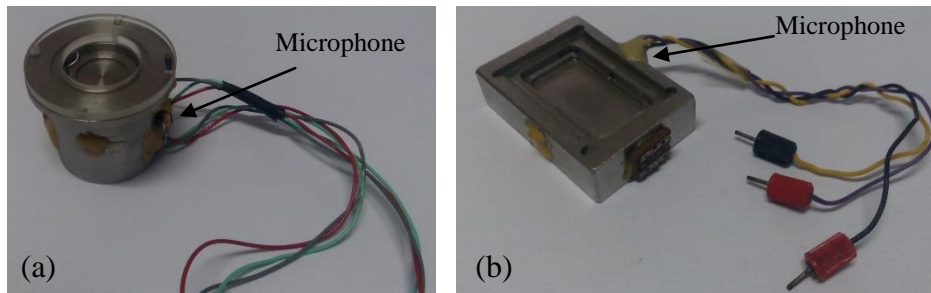
Figure 4. Photoacoustic cell a) cylindrical b) parallelepipedic

We chose a high sensitivity microphone to detect the generated PA signal. It is model BT1753, manufactured by Knowles Electronics. It is attached to the outside of the cell using a resin to prevent any kind of gas leakage or gas exchange between the inner part of the cell and the outside. It is connected through a channel leading to the sample compartment, to avoid any contact with light that might affect the signal.

Preamplifier and Lock-in

The output signal from the microphone (PA signal) is of very low amplitude. A high sensitivity AC amplifier amplifies this signal. The SR560 model from Stanford Research Systems was chosen.

The preamplified photoacoustic signal can be embedded in noise. A synchronous detection amplifier (lock-in) is used to separate the wanted signal from the noise. It is the model LI5640 from NF-corporation that was chosen. It is a digital multifunction lock-in amplifier in which high stability is achieved by a DSP processor. The instrument has a base capacity for frequencies ranging from 1mHz to 100KHz and a voltage sensitivity ranging from 2nV to 1V at full scale.

Signal processing

A microcomputer (PC) is used for storage and processing of the measured data. The same PC Controls the entire measurement system (optical chopper, monochromator, lock-in). Data acquisition is done through the IEEE 488 interface (GPIB). The exploitation of the photoacoustic signal, i.e analysis of the in-phase and in-quadrature signals as a function of the wavelength at a fixed modulation frequency, makes it possible to deduce certain optical properties from the sample under test. Figure 5 shows the mounted photoacoustic spectrometer. The optical chopper is connected to the PC through USB interface. The monochromator uses IEEE 488 interface.
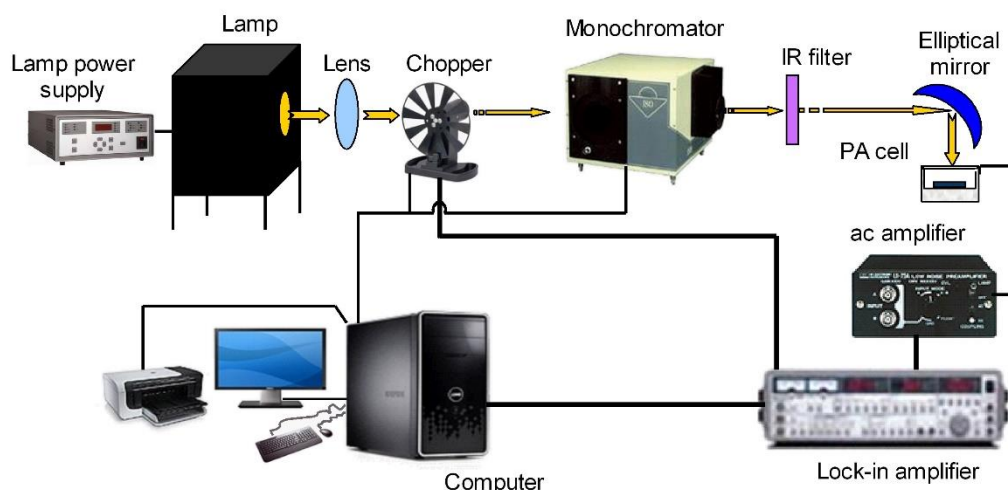
Figure 5. The photoacoustic spectrometer

Control software

The various instruments shown in Figure 5 are controlled by the famous LabVIEW language from National Instruments. LabVIEW is typically used for data acquisition, instrument control, and industrial automation. It can support interfaces such as RS232, GPIB, USB, etc. A control program has been written using version 17 of LabVIEW. Figure 6 gives an overview of the front face of our spectrometer while figure 7 gives the block diagram which is the graphical code itself.
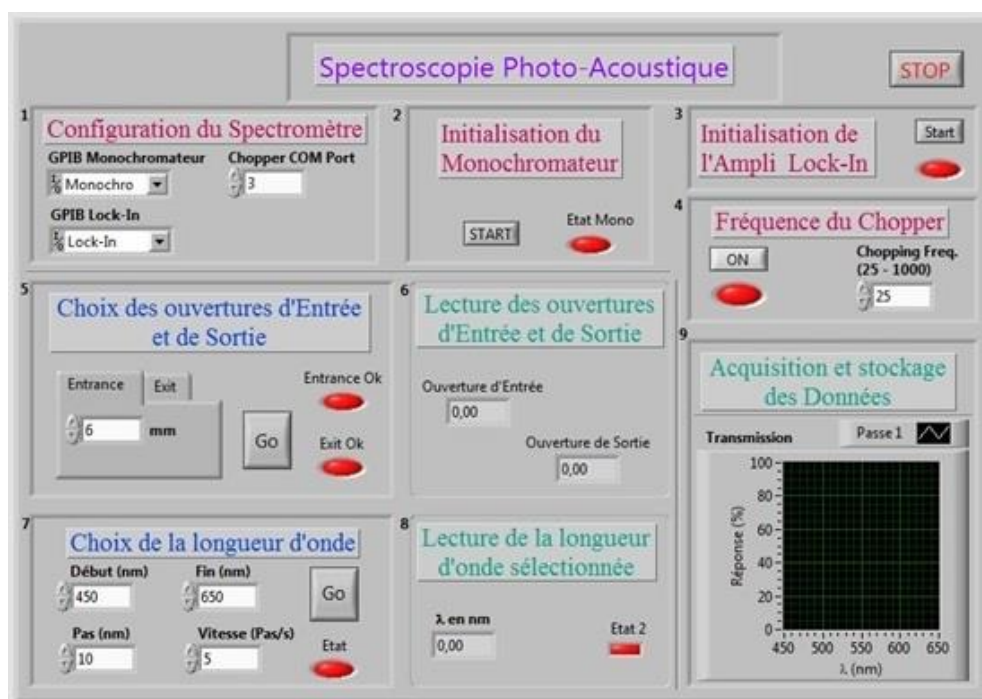
Figure 6. Front panel of the Virtual Instrument Spectrometer PAS
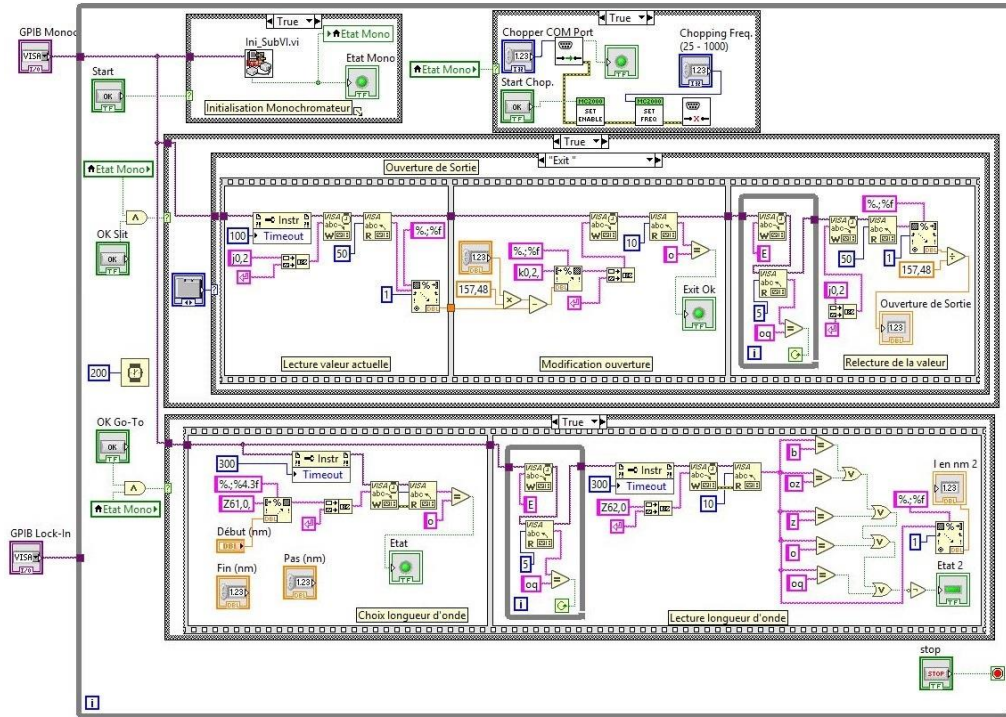
Figure 7. LabVIEW block diagram (graphical program) of the PA Spectrometer

Photodeflection Spectrometer

The principle of photodeflection spectroscopy (PDS) is as follows: a sample is irradiated by a modulated (periodic or pulsed) monochromatic light beam. The energy released as a result of the absorption of light causes a variation of certain physical parameters of the sample itself or the surrounding environment. A probe beam traversing this medium will be deflected and the amplitude of the deviation and its phase are a function of the thermal and optical properties of the sample under test. Figure 8 shows a block diagram of a photodeflection spectrometer using the principle just mentioned.
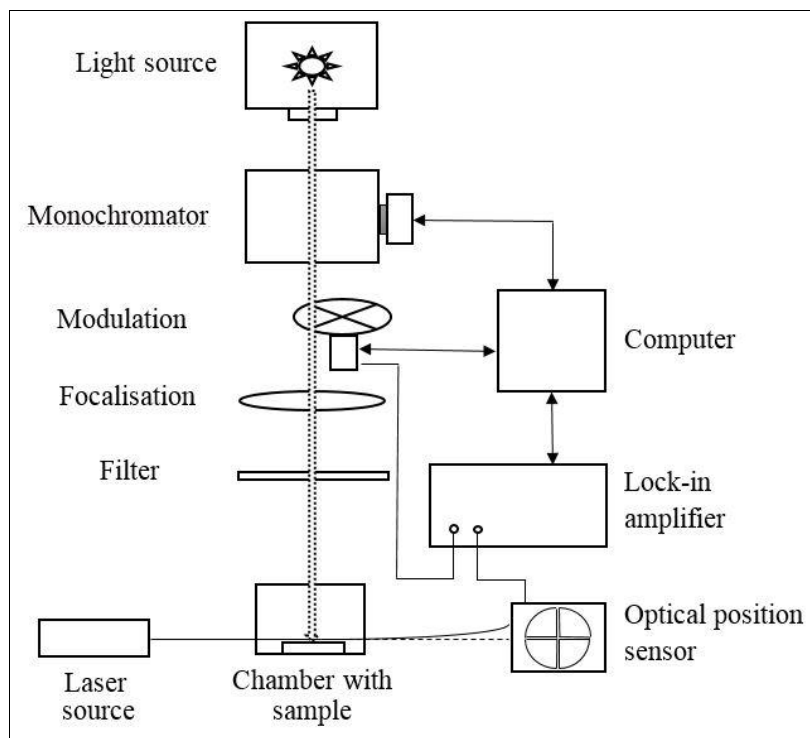
Figure 8. Block diagram of a PDS system " mirage " [Bocara]

Figure 9 illustrates a diagram of the cell containing the test sample and the surrounding fluid.
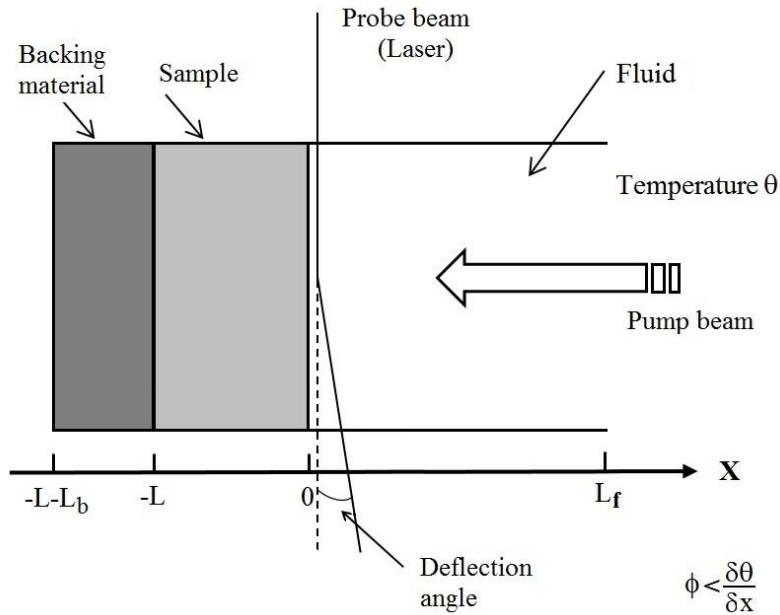
Figure 9. The geometry of a one-dimensional cell

The same setup used in photoacoustic spectroscopy can be used here with some small modifications. The excitation source can remain the same as it can be replaced by a laser source (continuous or pulsed). The sample cell must be transparent to let the laser probe beam passes through. The microphone is replaced by a position sensitive device which is often a 4-segment photodiode detector. Figure 10 depicts the assembled photodeflection spectrometer.
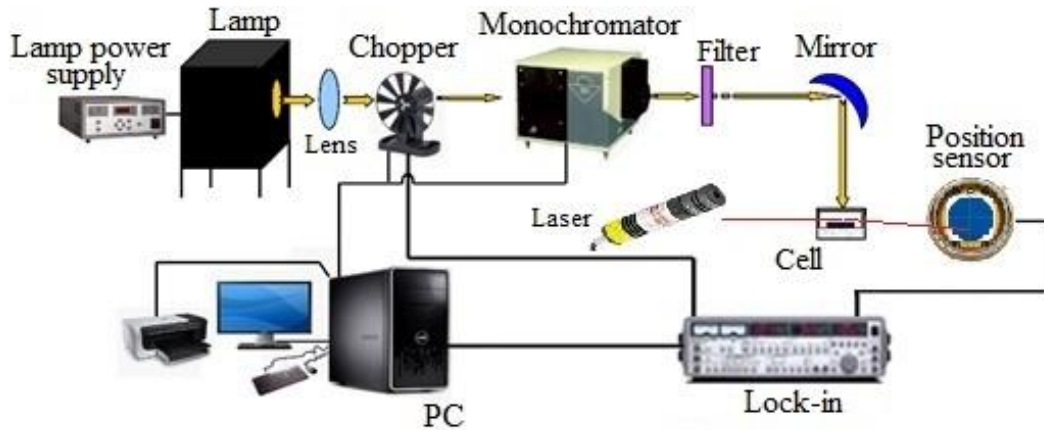
Figure 10. Photodeflection spectrometer

Photothermal imaging

The light source and the monochromator have been replaced by a laser source. The photoacoustic cell now rests on a XY positioning stage controlled by the PC. The scan step is very fine (5μm). Focusing optics replace now the elliptical mirror. It must provide a sharp focus to have a good resolution image. The motorized XY stage provides up to 13mm travel on both axes. Figure 11 depicts the photothermal imaging setup.
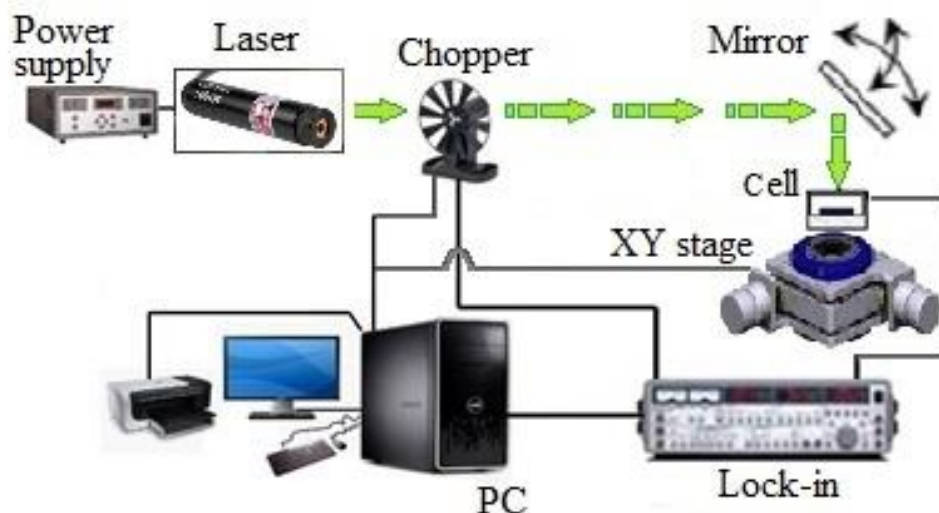
Figure 11. The photothermal imaging setup

Conclusion

To facilitate the characterization of new materials developed (in the field of photovoltaics and microelectronics) we have made available to researchers some powerful tools with very high sensitivity. The instrumentation of the three spectroscopy techniques is now assembled, it lacks only a few small accessories to make these techniques completely functional (focusing optics and mirrors). Once all the material is present one has to calibrate all three setups using reference or known samples.

References

Rosencwaig, A. (1980). *Photoacoustics and Photoacoustic spectroscopy*, New York, Wiley.

Sell, J.A. (1989). *Photothermal Investigations of Solids and Fluids*, Academic Press.

Zegadi, A. (1994). *Photoacoustic Study of CuInSe2 Single Crystals*, PhD thesis, University of Salford, UK.

Zegadi, A. Slifkin, M.A. Tomlinson, R.D. (1994). *Review of Scientific Instruments*, 65, 2238-2243.

Boccara, A.C. Fournier, A.D. Badoz, J. (1980). *Applied Physics Letters*, 36, 130-131.

Author Information

Mustapha Djabar	**Ameur Zegadi**
Université Ferhat ABBAS Sétif 1	Université Ferhat ABBAS Sétif 1
Campus Maabouda, Sétif 19000 Algérie.	Campus Maabouda, Sétif 19000 Algérie.
Contact E-mail: m_djabar@*yahoo.fr*	

IConTES 2019: International Conference on Technology, Engineering and Science

Evaluation of Shear Strength Approaches of SFRC Deep Beams without Stirrups

Mustafa Irfan BIRINCIOGLU
Yıldız Technical University

Guray ARSLAN
Yıldız Technical University

Abstract: The addition of steel fibres can be developed the mechanical properties and the crack control characteristics of concrete. In the last four decades, a lot of methods have been developed to estimate the shear strength of steel fiber reinforced concrete (SFRC) deep beams. In this study, seven different researchers' predictions are compared with the test beams without stirrups. Although calculating of the shear strength of steel fiber reinforced concrete deep beams is a complex phenomenon, these researchers proposed different reasonable equations. Twenty nine beams has been obtained from existing sources of RC deep beam shear test results covering a wide range of beam properties and test methods. All the equations compared with their mean values, standard deviations and coefficient of variation. It is found that the equation proposed by Ashour et al. (1992) shows good agreement with regard to existing test results, giving the less coefficient of variation value than the other equations.

Keywords: Reinforced concrete, Deep beam, Shear strength, Steel fiber

Introduction

Concrete is a brittle structural material that easily fails under the shear force due to the behavior of its low tensile strength. Thus, shear reinforcement should be included in the concrete by using stirrups or different types of fibers. Calculation method of the shear strength of a beam changes clearly depending on the shear span to effective depth ratio (α/d). When α/d is lower than 2.5, it can be called as a deep beam and all evaluations should be made according to this phenomenon. Nowadays, there are many theoretical and experimental studies in prediction of steel fiber reinforced concrete (SFRC) deep beams. Especially, predicting of the shear strength of deep beams is an important issue for researchers because the behavior of beams is complex to propose a simple empirical equation.

In order to predict the shear strength of deep beams more accurately, many researchers developed different acceptable equations. Researchers usually suggest shear equations to calculate the shear strength, and compare the equations' results with experimental ones. High-strength SFRC beams that subjected to combined flexure and shear were examined to figure out the impact of fibers on beam behavior (Ashour et al. 1992). Ashour et al. (1992) predicted an equation for the shear strength of SFRC beams and the equation showed good correlation with the experimental results. The main parameters of the equation were the steel fiber factor (F), the longitudinal steel reinforcement ratio (ρ) and α/d. Similarly, in the study of Imam et al. (1994), some high strength SFRC beams that subjected to bending moment and shear force were tested to suggest more accurate shear strength prediction. Khuntai et al. (1999) studied in shear behavior for not only normal and high strength SFRC beams but also the other factors such as F, α/d, ρ and size effect. Based on this factors, an equation was presented to estimate the ultimate shear strength.

In the study of Narayanan and Darwish (1987), to determine shear behavior of SFRC beams, simply supported rectangular beams were tested under concentrated loads. An empirical equation was suggested to calculate shear strength of SFRC deep and slender beams, comparing computed and experimental values. Similar to this

research, Kwak et al. (2002) proposed shear strength equation for deep beams considering some effective parameters. Li et al. (1992) tested SFRC beams under three point bending test to examine the shear strength equation considering the flexural and splitting tensile strength and size effect. The research concluded with the fact that the fiber reinforcements turned the tensile properties improvements into shear improvements.

The aim of this research is to determine the most reasonable estimation, comparing the shear strength equations which proposed by seven researchers that exist in the literature. Therefore, this study includes 29 SFRC deep beams obtained from earlier approaches (Ashour et al. 1992; Imam et al. 1995; Kwak et al. 2002; Li et al. 1992; Lim et al. 1987; Mansur et al. 1986; Narayanan and Darwish 1987). The changing parameters that are examined with respect to various proposed empirical equations, can be summarized as follows; the volume fraction of steel fiber (V_f), compressive strength of concrete (f_c) and F, ρ and α/d.

Shear Strength of Deep Beams with Steel Fiber

Existing Shear Strength Predictions

Seven investigators (Ashour et al. 1992; Imam et al. 1994; Khuntai et al. 1999; Kwak et al. 2002; Li et al. 1992; Narayanan and Darwish 1987; Sharma 1986) predicted the shear strength of SFRC deep beams without stirrups via empirical equations. These seven various equations for evaluation of the ultimate shear strength are provided in Table 1.

Table 1. Shear Strength Equations

Researchers	Equations
Ashour et al. (1992)	$v_u = \left(0,7 * \sqrt{f_c} + 7F\right) * \dfrac{d}{a} + 17,2\rho * \dfrac{d}{a}$
Imam et al. (1994)	$v_u = 0,7\left(\dfrac{1}{\sqrt{1 + \dfrac{d}{25d_a}}}\right) * \sqrt[3]{\rho} * \left(f_c^{0,44}(1 + F^{0,33}) + 870 * \sqrt{\dfrac{\rho}{\left(\dfrac{a}{d}\right)^5}}\right)$
Khuntai et al. (1999)	$v_u = \left(0,167\left(2,5\dfrac{d}{a}\right) + 0,25F\right)\sqrt{f_c}$
Kwak et al. (2002)	$v_u = 3,7\left(3,4\left(\dfrac{d}{a}\right)\left(\dfrac{f_c}{20 - \sqrt{F}} + 0,7 + \sqrt{F}\right)^{2/3}\left(\rho\dfrac{d}{a}\right)^{1/3}\right) + 0,8(0,41\tau F)$
Li et al. (1992)	$v_u = 9,16\left((f_t)^{2/3}(\rho)^{1/3}\left(\dfrac{d}{a}\right)\right)$
Narayanan and Darwish (1987)	$v_u = \left(2,8\dfrac{d}{a}\right)\left(0,24\left(\dfrac{f_c}{20 - \sqrt{F}} + 0,7 + \sqrt{F}\right) + 80.\rho\dfrac{d}{a}\right) + 0,41\tau F$
Sharma (1986)	$v_u = \dfrac{2}{3}f_t\left(\dfrac{d}{a}\right)^{0,25} \qquad f_t = 0.79\sqrt{f_c}$

The equation of Sharma (1986) includes tensile strength of concrete (f_t) that depends on f_c and α/d. Narayanan and Darwish (1987) and Kwak et al. (2002) introduced the ultimate bond stress (τ) that equals to 4.15MPa in their equations. In the predictions, F depending on length of fiber (L_f) diameter of fiber (D_f), volume fraction of fiber (V_f) and a constant value which called bond factor (d_f) were assigned a relative value of 0.75 for crimped fibers and 1.0 for indented fibers. These factors were involved into the fiber factor formula given by F=(L_f/D_f)*V_f*d_f and α/d as in Sharma's equation. Li et al. (1992) proposed an equation as a modified form of Sharma's equation through introducing ρ. The expression of Ashour et al. (1992) incorporates the same factors that were included in the equation of Narayanan and Darwish (1987) except τ. Kwak et al. (2002) proposed a shear strength equation which has the same parameters of Narayanan and Darwish's equation, involving different constants. Similar to the expression of Ashour et al. (1992), Khuntai et al. (1999) proposed their prediction which does not include ρ. The maximum aggregate size (d_a) is considered in the prediction of Imam et al. (1994) which differs from Ashour et al.'s equation.

Experimental Shear Strength Beams

The test beams obtained from the literature divided into two different groups according to their f_c values. Some of the SFRC deep beams' f_c values less than 50 MPa so they have been called as normal strength concrete (NSC) deep beams, similarly the others have been called high strength concrete (HSC) deep beams that have f_c values which are greater than 50 MPa.

Narayanan and Darwish's (1987) beams have crimped fibers whereas the others have hooked end fibers. The beams also have different values of α/d to determine size effect and these values range from 1.0 to 2.0. In addition to α/d, V_f values range from 0.25% to 2%. The shear strength equations that obtained in the literature incorporate the length of steel fiber to diameter of steel fiber ratios (L_f/D_f) ranging from 60 to 133 and ρ values ranging from 0.011 to 0.057.

Evaluation of Shear Strength Predictions

The ultimate shear strength values of SFRC deep beams have been predicted by calculating with the seven equations and compared with the experimental data. For this comparison among the equations, the mean values (MV), standard deviations (SD) and coefficient of variation (COV) values are given in Table 2.

Table 2. Statistics of the ratios of experimental values to predictions

Researchers	MV	SD	COV
Ashour et al. (1992)	0.958	0.184	0.192
Imam et al. (1994)	0.775	0.250	0.323
Khuntai et al. (1999)	1.832	0.367	0.200
Kwak et al. (2002)	0.907	0.187	0.206
Li et al. (1992)	0.813	0.240	0.295
Narayanan and Darwish (1987)	1.119	0.245	0.219
Sharma (1986)	1.571	0.463	0.295

The proposed equations by Khuntai et al. (1999) and Sharma (1986) overestimate the ultimate shear strength of the SFRC deep beams included in this research, predicting the shear strength values approximately 83% and 57% higher than the test data respectively, whereas the equations proposed by Imam et al. (1994) and Li et al. (1992) underestimate the experimental shear strength, giving approximately 22% and 19% less values than the test results respectively. It is clearly observed that the equation proposed by Ashour et al. (1992) provides the most accurate estimation for the beams. The estimations of the equations by Kwak et al. (2002) and Narayanan and Darwish (1987) also give good agreements with regard to existing test results. When the statistics of the Table 2 were considered, it can be observed that MV corresponding to the equation by Ashour et al. (1992) is the closest value to 1, equals to 0.958 with the least COV value that equals to 0.192.

The equation of Ashour et al. (1992) should be examined in terms of α/d, V_f, f_c and ρ since the best estimation was provided by this equation according to Table 2. The expression has been examined through the following Figure 1 to figure out how it shows agreement with the phenomena for both NSC and HSC.
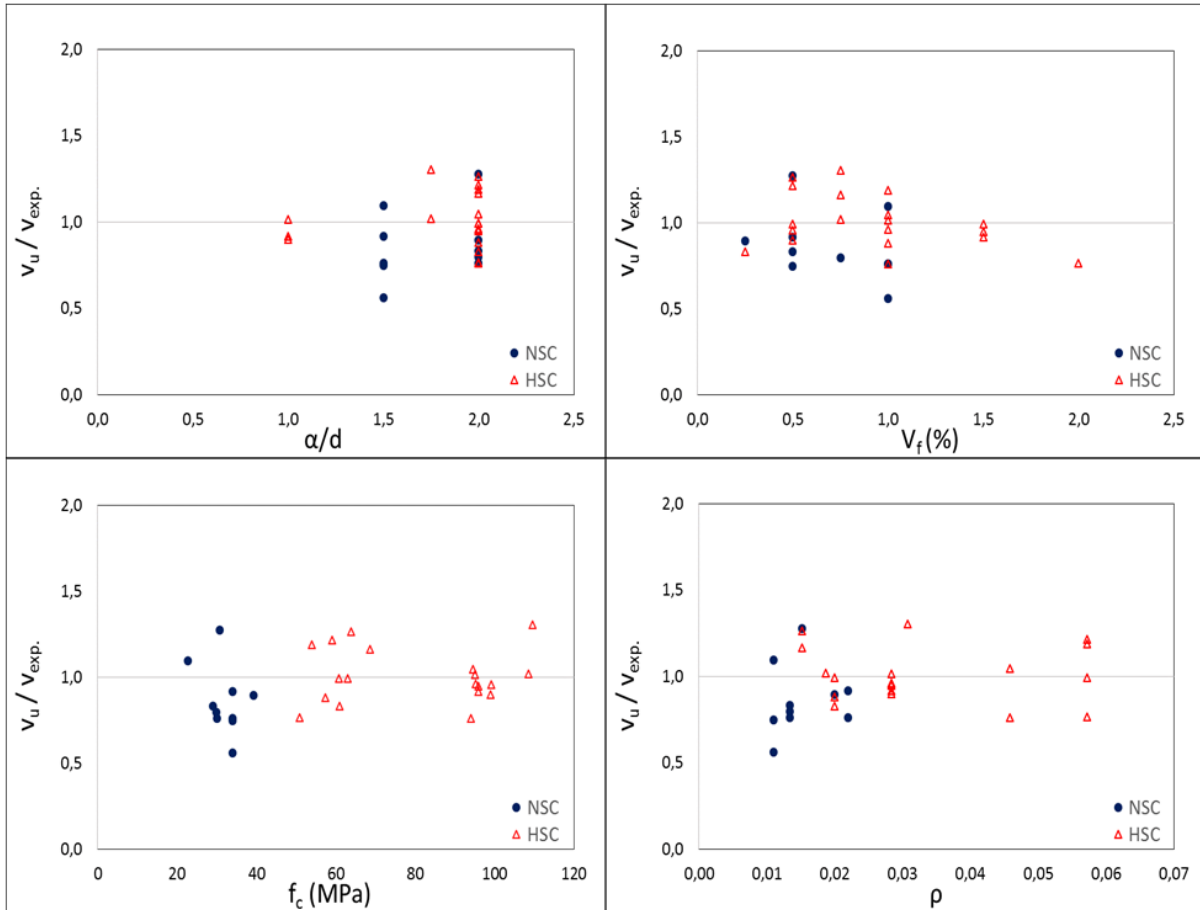
Figure 1. Comparison of test results with Ashour et al.'s prediction

The experimental data of this research were limited for NSC and HSC deep beams to determine how the equation predicts the shear strength whereas α/d, V_f, f_c and ρ change respectively. As shown in Figure 1, the calculated values by the equation to experimental one of the ultimate shear strength ratio $v_u/v_{exp.}$ yields large scatter in the results for both NSC and HSC deep beams when the α/d is higher than 1. However, $v_u/v_{exp.}$ Values range from 0.902 to 1.014 when α/d is 1, hence it can be said that the equation shows good agreements with regard to existing test results if α/d equals to 1 with a success ratio which is approximately 96%. Even if ρ shows changing values from 1.1% to 5.7% or V_f shows changing values from 0.25% to 2%, $v_u/v_{exp.}$ also provides a large scatter in the results. If f_c is higher than 50 MPa, the predictions are more reasonable though the equation gives the results that are a little far from the experimental shear strength values through decreasing f_c. It can be concluded that, α/d and f_c are more critical than V_f and ρ for the ultimate shear strength predictions that obtained from the equation.

Conclusion

When the ultimate shear strength predictions of SFRC deep beams by seven researchers' equations obtained in the literature, the consequences were determined as follows:

Sharma (1986) and Khuntai et al. (1999) overestimate the ultimate shear strength of the SFRC deep beams, on the other hand Imam et al. (1994) and Li et al. (1992) predict the ultimate shear strength, giving lower values than the test results.

The predictions of Kwak et al. (2002) and Narayanan and Darwish (1987) are more reasonable with a realistic approach of the ultimate shear strength. The best prediction of the ultimate shear strength of SFRC deep beams was provided by Ashour et al. (1992), yielding predictions near to experimental data and the lowest COV value.

Changing of V_f and ρ have no significant impacts on the ultimate shear strength prediction of the equation by Ashour et al. (1992) for NSC and HSC deep beams. When α/d equals to 1 or f_c is high, Ashour et al. (1992) equation has the most accurate estimations.

References

Ashour, S. R., Hasanain, G. S. & Wafa, F. F. (1992). Shear Behaviour of High-Strength Fiber-Reinforced Concrete Beams. *ACI Structural Journal, 89(2)*, 176-184.

Imam, M., Vandewalle, L. & Mortelmans F. (1994). Shear Capacity of Steel Fiber High-Strength Concrete Beams. *High Perform Concrete, SP 149, American Concrete Institute*, 227-241.

Imam, M., Vandewalle, L., & Mortelmans, F. (1995). Shear–moment analysis of reinforced high strength concrete beams containing steel fibres. *Canadian Journal of Civil Engineering*, *22(3)*, 462-470.

Khuntai, M., Stojadinovic, B. & Goel, S. (1999). Shear Strength of Normal and High-Strength Fiber-reinforced Concrete Beams without Stirrups. *ACI Structural Journal, 96(2)*, 282-290.

Kwak, Y., Eberhard, M. O., Kim, W. & Kim, J. (2002). Shear Strength of Steel Fiber-reinforced Concrete Beams without Stirrups. *ACI Structural Journal, 99(4)*, 530-538.

Li, V. C., Ward, R. & Hamza A. M. (1992). Steel and Synthetic Fibers as Shear Reinforcement. *ACI Materials Journal, 89(5)*, 499-508.

Lim T. Y., Paramasivam, P. & Lee, S. L. (1987). Shear and moment capacity of reinforced steel-fiber-concrete beams. *Magazine of Concrete Research, 39(140),* 148-160.

Mansur, M. A., Ong, K. C. G. & Paramasivam, P. (1986). Shear Strength of Fibrous Concrete Beams without Stirrups. *J. Struct. Eng., 112(9)*, 2066-2079.

Narayanan, R., & Darwish, I. Y. S. (1987). Use of Steel Fibers as Shear Reinforcement. *ACI Structural Journal, 84(3)*, 216-227.

Sharma, A. K. (1986). Shear Strength of Steel Fiber Reinforced Concrete Beams. *ACI Structural Journal, 83(4),* 624-628.

Author Information

Mustafa Irfan Birincioglu	**Guray Arslan**
Yıldız Technical University	Yıldız Technical University
Davutpaşa Street 34220 Esenler İstanbul/Turkey	Davutpaşa Street 34220 Esenler İstanbul/Turkey
Contact E-mail: *mibirincioglu@gmail.com*	

Effect of Stirring on the Microstructure and Mechanical Properties of ZAMAK-12 Alloy

Ibrahim CELIKYUREK
Osmangazi University

Osman TORUN
Kocatepe University

Abstract: Zinc alloy ZAMAK-12 was melted in an induction melting process. The melted alloy was stirred mechanically at 400 ± 10 ^{o}C for 5 minutes using a cast iron mixer. The speed of stirring was 1500 rpm. After stirring the melt was casted in a mold made from graphite immediately and quenched with water. The microstructures of unstirred and stirred samples were investigated with optical microscopy. The hardness' of samples were measured with Vickers indenter. The strengths of samples were determined by compression testing. The microstructural investigations showed that both stirred and unstirred ZAMAK-12 alloys have a dendritic microstructure. But, the grain size of Al-rich dendrites was finer and longer into the stirred samples. The hardness of stirred ZAMAK-12 was slightly higher than unstirred alloy. The compression yield strength and Elastic Modules of the stirred sample was lower than unstirred alloy, whereas the compression yield strain of the stirred alloy was higher.

Keywords: Zinc based alloys, Microstructure, Strength, Hardness

Introduction

Zinc based alloys are very attractive engineering materials due to their low density, very good cast ability, low energy consumption for shaping, low cost and intermediate strength and hardness etc. (Prasad et al. 1996, Pürçek et al. 2002). The commercial zinc based alloys called as ZAMAK, ALZEN and ZA are binary Zn-Al alloys and include small amounts of Cu. These alloys are based on Zn-Al eutectic, eutectoid or monotectoid composition. (Savaşkan et al. 2004).

Although their poor strength and hardness the Zn-Al alloys have been used widely in a variety of industry due to their excellent fluidity. With these alloys very thin walled and complex shaped parts can be casted using gravity or pressure die casting with/without heating the mold (Hanna et al. 1997). In recent years some works have been made intend to improve the strength and hardness of Zn-Al alloys. In these studies, some authors suggested the alloying of Zn based alloys (Prasad et al. 1996, Savaşkan et al. 2004, Pürçek et al. 2002, Hanna et al. 1997, Şevik 2014), whereas some of them suggested to reinforce the alloy with particulates or fibres (Pola et al. 2016, Li et al. 2001, Tao et al. 1995, Xu et al. 2014, Alaneme et al. 2017, Madronero et al. 1997,Almomani et al. 2016,Liu et al. 2009).

In addition to low strength and hardness low using temperature compared to other metallic materials limits the use of Zinc based alloys. Beside these properties, the Zn based alloys have been found to be an alternative material to bronzes which are used in tribological applications. It is reported that, Zn based bearings have good wear and seizure resistance, and lower coefficient of friction than bronzes under heavy load and slow to medium friction speed conditions. (Prasad et al. 1996).

Further studies have been focused on the increasing the hardness, strength and wear resistance of zinc based alloys. Abou El-Khair et al. (2004) investigated the effects of Al content on the properties of the Zn-Al binary alloys. They reported that hardness, strength, and wear resistance of alloy is increased with increasing Al

content, however ductility was degreased. Furthermore, the strength is degreased and ductility is increased with increasing temperature for Zn-Al binary alloys. Higher strength at elevated temperature was also observed with increasing Al content.

Türk et al. (2007) modified the ZA8 commercial alloy with Pb, Sn, and Cd. The samples were subjected to the wear tests and the results were compared with commercial SAE 660 bearing bronze. They found that ZA8 and modified ZA8 alloys have higher wear resistance, but also higher coefficient of friction than bearing bronze.

On the other hand, Savaşkan et al. (2014) investigated the effects of Cu and Si on the Zn-Al alloys. They increased the Si and Cu content systemically while the Al content was 15%. They found that the hardness, tensile, and compressive strength are increased whereas the elongation and impact energy were decreased with increasing Copper content for Zn-Al-Cu ternary alloys. For Zn-Al-Cu-Si quaternary alloys, the hardness and compressive strength were increased while the tensile strength, elongation, and impact energy were decreased with increasing Si content.

In this study, zinc alloy ZA12 was stirred mechanically at a temperature which was between liquidus and solidus, and subsequently quenched using water. The effect of stirring on the microstructure and mechanical properties of alloy was investigated.

Method

Zinc alloy ZAMAK-12 was produced by an induction melting furnace at the nominal composition of 88%Zn, 11.0%Al and 1.0%Cu (wt%). Firstly, Zn was melted, then Al was added, finally Cu was dissolved in the melt. The melted liquid was stirred slowly using a steel rod. After obtain a homogenous mixture the alloy was gravity casted into a graphite mold and quenched under running water. Then, the pre-casted ZAMAK-12 alloy was remelted by induction melting again and stirred mechanically at 400±10 °C for 5 minutes using a cast iron mixer. The speed of stirring was 1500 rpm. After stirring was completed the melt was casted into a graphite mold and quenched immediately using running water. The alloy has liquid and solid phases at the stirring temperature (Figure 1). The stirring was carried out to break up the primer □□solids and the quenching was applied to prevent grain coarsening. The casted samples were in the rod form with diameter of 8mm.
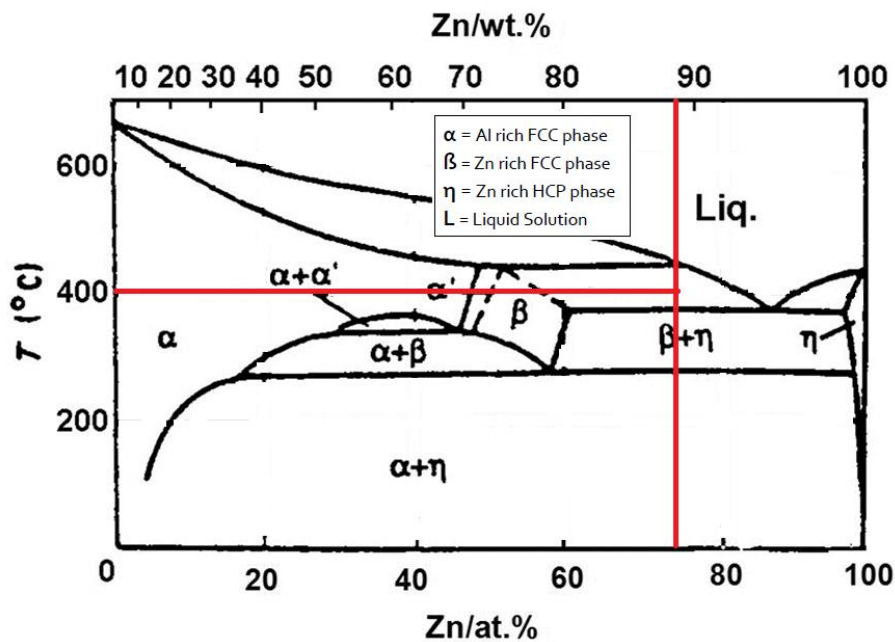
Figure 1. Al-Zn phase diagram

The alloys that are stirred and un-stirred were characterized in terms of the microstructural and mechanical properties. The microstructures of alloys were examined using optical light microscopy and the mechanical properties were determined by compression test and the hardness measurements. The compression tests were carried out at ambient temperature with crosshead rate of 10 mmmin^{-1}. Three test were done for each alloy. The

hardness of the samples was measured using Vickers indenter under 300gf load at 15s duration. The hardness values were determined from mean of 5 measurements for each alloy.

Results and Discussion

The light optical micrographs of the as-cast and stirred alloys in different magnifications were given in Figure 2. From the micrographs, it is seen that both as-cast and stirred alloy have a dendritic microstructure. However, when compared with the as-cast structure the dendrites in the stirred alloy are longer and thinner. The primer Zn rich FCC □ □solid phase was broken when stirring at 400 ^oC, and as a result, since □ transforms to Al rich FCC □ phase with cooling, the final grain size of □ was finer. On the other hand, while as-cast alloy has a smooth microstructure without pore, in the stirred alloy some pores were observed. These pores are result of stirring.
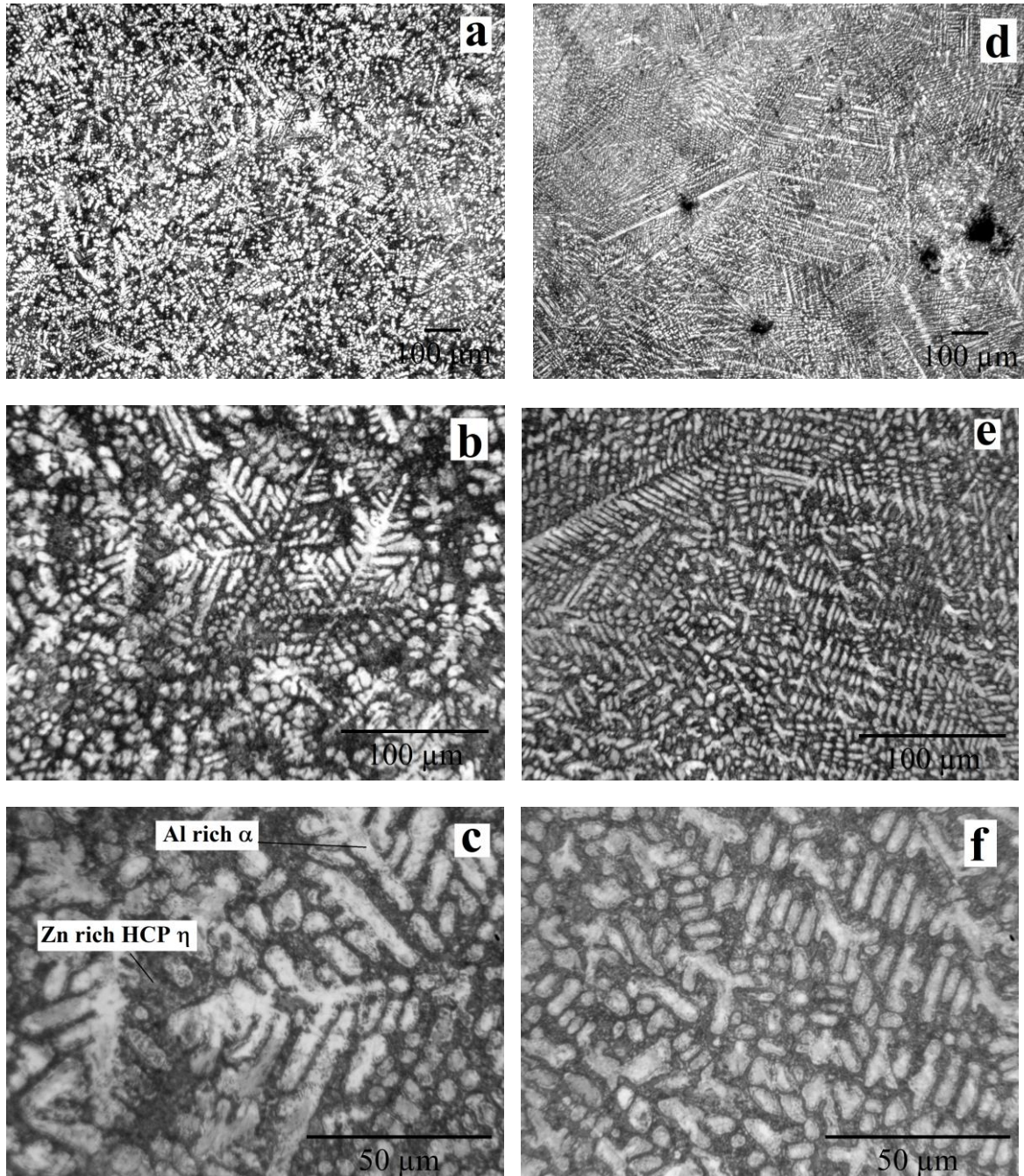
Figure 2. Light optical micrographs of the as-cast (a, b, and c) and stirred (d, e, and f) alloys at different magnifications

The mechanical properties of as-cast and stirred alloys are summarized in table 1, and figure 3 shows the compression test diagram. The hardness of stirred ZAMAK-12 was slightly higher than unstirred alloy. The compression yield strength and Modulus of Elasticity of the stirred sample are lower than unstirred alloy, whereas the compression yield strain of the stirred alloy was higher. Generally, hardness and strength are increase with reduction in grain size for metallic materials. The pores formed in the stirred alloy might be responsible for reduction in strength.

Table 1. Mechanical properties of the as-cast and stirred alloys

ZAMAK-12	Hardness (HV)	Compression Yield Strength, (MPa)	Compression Yield Strain, (%)	Elastic Modulus, (GPa)
As-cast	81	374	0,51	73
Stirred	86	332	0,56	59
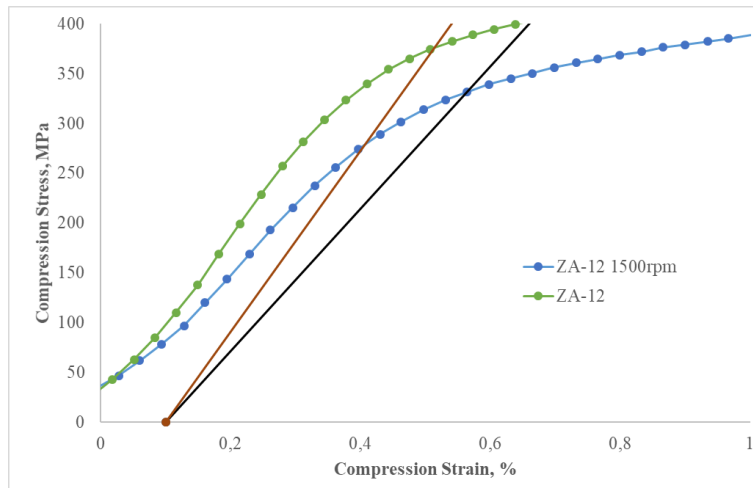
Figure 3. Compression tests of the alloys

Conclusion

The microstructure of ZAMAK-12 alloy is affected by stirring. When the alloy is stirred between solidus and liquidus temperature, the primary □ solid phase is broken and final grain size of □ dendrites is finer. The microstructural evaluation effects the mechanical properties. The finer grain size increases the hardness and yield strain, whereas it decreases the yield strength and Modulus of Elasticity.

Recommendations

The effect of the stirring on the sliding friction and wear behavior of ZAMAK-12 ally should be investigated. Because, the microstructural evolution and different mechanical properties may affect the friction and wear behavior.

References

Abou El-Khair M.T., Daoud A., Ismail A. (2004). Effect of different Al contents on the microstructure, tensile and wear properties of Zn-based alloy. Materials Letters, 58, 1754-1760.

Alaneme K.K., Ajayi O.J. (2017). Microstructure and mechanical behavior of stir-cast Zn-27Al based composites reinforced with rice husk ash, silicon carbide, and graphite. Journal of King Saud University-Engineering Sciences, 29, 172-177.

Almomani M., Hayajneh M.T., Draidi M. (2016). Tribological investigation of Zamak alloys reinforced with alumina (Al2O3) and fly ash. Particulate Science and Technology, 34, 317-323.

Hanna M.D., Carter J.T., Rashid M.S. (1997). Sliding wear and friction characteristics of six Zn-based die-casting alloys. Wear, 203-204, 11-21.

Li Z.Q., Zhang S.Y., Wu B.Y. (2001). Solidification and microstructure of ZA27/SiCp composite fabricated by mechanical – electromagnetic combination stirring process. Materials Science and technology, 17, 465-472.

Liu J., Yu S., Zhu X, Wei M., Luo Y., Liu Y. (2009). Correlation between ceramic additions and compressive properties of Zn-22Al matrix composite foams. Journal of Alloys and Compounds, 476, 220-225.

Madronero A., Cruz J., Foruria C., Coleto J. (1997). Rheocasting a Zn-Al Composite reinforced with Coke dust. Journal of Minerals, Metals and Materials Society, 49, 46-49.

Narimannezhad A., Aashuri H., Kokabi A.H., Khosravani A. (2009). Microstructural evolution and mechanical properties of semisolid stir welded zinc AG40A die cast alloy. Journal of Materials Processing Technology, 209, 4112-4121.

Pola A., Montesano L., Gelfi M., La Vecchia G.M. (2016). Comparison of the sliding wear of a novel Zn alloy with that of two commercial Zn alloys against bearing steel and leaded brass. Wear, 368-369, 445-452.

Prasad B.K., Patwardhan A.K., Yegneswaran A.H. (1996). Dry sliding wear characteristic of some zinc-aluminium alloys: a comparative study with a conventional bearing bronze at a low speed. *Wear*, 199, 142-151.

Pürçek G., Savaşkan T., Küçükömeroğlu T., Murphy S. (2002). Dry sliding friction and wear properties of zinc-based alloys. Wear, 252, 894-901.

Savaşkan T, Hekimoğlu A.P., Pürçek G. (2004). Effect of copper content on the mechanical and sliding wear properties of monotectoid-based zinc-aluminium-copper alloys. *Tribology International*, 37, 45-50.

Savaşkan T., Hekimoğlu A.P. (2014). Microstructure and mechanical properties of Zn-15Al-based ternary and quaternary alloys. Materials Science and Engineering A, 603, 52-57.

Şevik H. (2014). The effect of silver on wear behavior of zinc-aluminium-based ZA-12 alloy produced by gravity casting. *Materials Characterization*, 89, 81-87.

Tao L., Dellis M.A., Boland F., Delannay F. (1995). Comparison of fibres for creep strengthening of zinc-aluminium foundry alloys. *Composites*, 26, 611-617.

Türk A., Kurnaz C., Çevik H. (2007). Comparison of the wear properties of modified ZA-8 alloys and conventional bearing bronze. Materials and design, 28, 1889-1897.

Xu Z., Ma L., Yan J, Chen W., Yang S. (2014). Solidification microstructure of SiC particulate reinforced Zn-Al composites under ultrasonic exposure. *Materials Chemistry and Physics*, 148, 824-832.

Author Information

Ibrahim Celikyurek	**Osman Torun**
Eskişehir Osmangazi University	Afyonkocatepe University
Büyükdere Mah. 26040 Odunpazarı, Eskişehir, Turkey	Ahmet Necdet Sezer Kampüsü, Gazlıgöl Yolu, 03200,
Contact E-mail: cibrahim@*ogu.edu.tr*	Afyonkarahisar, Turkey

Synthesis a Series of 2-Pyrazolideno-1,3,4-Thiadiazoline Compounds Derived from Thiocarbohydrazide

Shaymaa K.Y. Al-AZZAWI
University of Mosul

Aemn Y.S. Al-ZEBARI
University of Mosul

Abstract: A series of some 2-pyrazolideno-1,3,4-Thiadiazoline Compounds [10-15] was prepared under conventional and thermal conditions using an active starting material thiocarbohydrazide [1] as a good precursor. Thiocarbohydrazide [1] was firstly prepared through direct addition reaction between (80%) hydrazine hydrate and carbon disulfide in aqueous media and reflux conditions, then it will be converted to it's hydrazone derivative via condensation reaction with benzophenone in acidic media at room temperature to afford compounds 1-(diphenyl methylene) thiocarbohydrazone [2], and the later one was underwent catalytic intracyclization reaction to give 2-hydrazinyl-5,5-diphenyl-2,5-dihydro-1,3,4-thiadiazoline compound [3] in presence of ferric chloride as a selective catalyst . Finally compound [3] reacted with freshly prepared chalcones (using diffrent substituted benzaldehyde and two types of ketones represented by acetophenone and m-methoxy acetophenono) [4-9] via traditional method to yield the titled compound represented by 1-(5,5-diphenyl-2,5-dihydro-1,3,4-thiadiazol-2yl)-3,5-diaryl-4,5-dihydro pyrazolidine compounds [10-15]. All prepared compounds were illustrated by the available physical and spectral data represented by U.V, FT-IR, H^1-NMR & C^{13}-NMR.

Keywords: Thiocarbohydrazide, Pyrazolidines, 1,3,4-thiadiazolines, Hydrazones

Introduction

Since many decades, active heterocyclic compounds are one of the main topic of interest for the medical chemists as it displays a number of pharmacological activities [1]. The most important types are nitrogen and sulfur containing five membered ring which occupied enormous significance in the medical chemistry field. First of all, 1,3,4-thiadiazoles are heterocyclic compounds which perform an important role as anticancer[2], while in agricultural field they play an important role as pesticide against rot, mice, and anti insects[3]. Additional, these compounds used as anti corrosion of metals in industrial field[4].The second important type are pyrazoles a five membered ring with two nitrogen atoms which accepted a great deals of attention especially in medical field[5] as anti breast cancer and anti liver cancer[6]. wherease in pharmaceutical field they show a wonderful activity as anti inflammatory and anti microbial[7,8]. To synthesis these active types of heterocyclic compounds , it must be starting from active materials with wide biological applications, here in this presentation the active starting material is thiocarbohydrazide [1] which have supreme role in heterocyclic synthesis [9], so it used to prepared the titled compounds [10-15] through traditional thermal methods.

Method

Melting points (M.P.) were measured on Stuart SMP10.MeltingPoint apparatus and are uncorrected. Proton-Nuclear Magnetic Resonance (^{13}C & ^{1}H-NMR) spectra were recorded using, Bruker DMX-500 NMR Spectrophotometer (300MHz); with TMS as internal standard, and DMSO-d_6 as solvents; Jorden, University of Al-Bayt. [(s) singlet; (d) doublet; (m) multiplet]. Infrared (FT-IR) spectra were recorded as (KBr) disc using a

Thermo Mattson300 Infrared Spectrophotometer. Ultraviolet (UV) spectra were performed on ShimadzuUV-160Ultraviolet–Vissible Spectrophotometer using methanol as a solvent.

Synthesis of Thiocarbohydrazide [1] [10]:

(0.22 mole,13 ml) of carbon disulphide was added drop wise to vigorously stirred solution (0.44 mole, 24 ml) of hydrazine hydrate (85%) in (15 ml) dis. water during (30 minutes). Then the temperature of the reaction was raised to (100-110°C) and the reaction mixture was refluxed for (2 hrs.), then cooled in ice bath to (0° C). The precipitated thiocarbohydrazide was filtered off, washed with ethanol followed by diethyl ether and then air dried. the product thus obtained was recrystallized from minimum amount of hot water. Yield (76%), M.p.(169-170°C). ^{1}H NMR (CDCl$_3$,δ ppm):(s, 3.34, 2H ,1H, NH$_2$ & NH); FT- IR(cm^{-1}): NH$_2$ (3306), NH (3274,3203), N-N (1489), C-N (1384) and C=S (1282); U.V DMSO λ $_{max (nm)}$ (355,272).

Synthesis of thiocarbohydrazone [2] [11]:

In round bottomed flask (100ml), benzophenone (0.02 mole,2.4 gm)was dissolved in abs. ethanol (100ml) and a solution of thiocarbohydrazide (0.02mole, 2.21 gm) in HCl (1N, 20ml) was adding drop wise with stirring at room temp. until the appearance of yallow precipitant which filtrate off , washed and recrystallized with abs. ethanol then dried to afford the yellowish hudrazone [2]. M.P. (199-200 $^°$C) ; yield 94% ; ^{1}H NMR (CDCl$_3$,δ ppm):(s, 3.35, 1H,2H, NH-NH$_2$), (s, 8.5, 1H, =N-NH) and (m, 7.2-7.7, 10H, aromatic); FT- IR(cm^{-1}):3328, 3247, 3269, 1342, 1484 and 1231; U.V DMSO λ $_{max (nm)}$ (308 &313).

Synthesis of 2,2-diphenyl-5-hydrazino-1,3,4-thiadiazole [3] [12]:

The hydrazone[2] (0.0017, 4.59gm) and FeCl$_3$ (0.0005 mole, 0.134 gm) were desolved in abs. ethanol (25 ml), then the reaction mixture refluxed for (1.5 hrs) in water bath then the reaction solvent was concentrated to the half volume and poured onto ice-water. The resulting product was filtered off and recrystallized from abs. ethanol to afford compound [3] with M.P.(120-121 °C); Yield 45%; ^{1}H NMR (CDCl$_3$,δ ppm): (s,3.5 , 1H,2H, NH-NH$_2$), (s, 7.01,1H,NH), (m, 7.1-7.5, 10H, aromatic); FT- IR(cm^{-1}): 3351, 3328,3261,1539,768; U.V DMSO λ $_{max (nm)}$ (318 &331).

Synthesis of chalcons [4-9] [13]:

All chalcons were prepared according to the literature method in reference (13) through Claisen-Schmidt condensation and the (Table 1) show all it's physical and spectral data.

Synthesis of 1-(5,5-diphenyl-2,5-dihydro-1,3,4-thiadiazol-2-yl)-3,5-diaryl-4,5-dihydro pyrazoline [10-15] [14]:

A mixture of freshly prepared chalcons (4-9) (0.005 mole) and compound (3) (0.005 mole, 1.34 gm) were refluxed for (9- 10 hrs.). After cooling, the reaction mixture poured into ice-water with stirring. The precipitated product was filtered off and washed with cold water then recrystallized from ethanol to affored compounds (10-15). All physical and spectral data were illustrated in Table (2).

Results and Discussion

Pyrimidines [10-15] has been achieved via traditional methods starting from an active material represented by thiocarbohydrazide [1]. The general synthetic pathway illustrated in (Scheme 1) below:
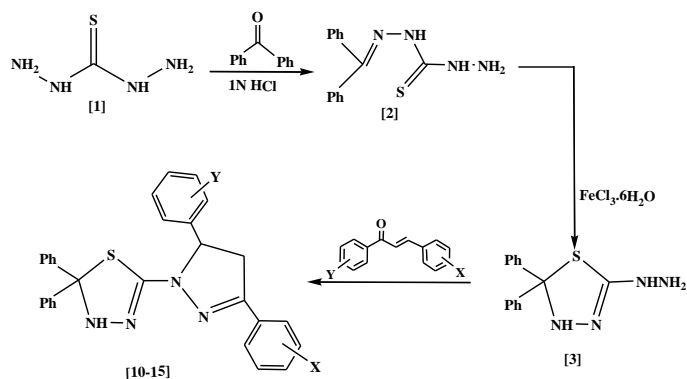
Scheme (1)
The synthetic pathway of pyrimidines [10-15]

Initially, Thiocarbohydrazide [1] was prepared in aqueous media through direct neucleophilic addition reaction with high percentage yield. Compound [1] characterized by spectral methods represented by ^{1}H-NMR, FT-IR and U.V., as shown in experimental section. this compound was used as a good and an active synthon to prepared the hydrazone compound [2] via condensation reaction with benzophenone. This reaction was activated by few drops of hydrochloric acid (1N) , (Scheme 2).
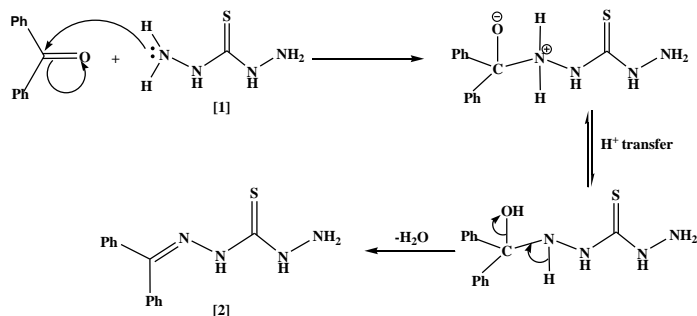
Scheme (2)

The formation of hydrazone [2] was proved by spectral methods, so, in ^{1}H-NMR spectra it shown shifting (δ, ppm) (s, 3.35, 1H,2H, NH-NH$_2$), (s, 8.5, 1H, =N-NH) and (m, 7.2-7.7, 10H, aromatic).

In FT-IR spectra it shown the following stretching absorption bands (cm^{-1}) (3328,3247,3169, 1484, 1342 and 1231) which refer to the functional groups (NH$_2$, NH, NH=NC, C=N, C=S, and N=N) respectively. While in U.V. spectra it gave two absorption bands at λ_{max} (308 &313 nm) due to the n→π* and π→π* and also due to the increasing of conjugation. The hydrazone [2] underwent intracyclization reaction in presence of catalytic amounts of ferric chloride (FeCl$_3$) to afford 2-hydrazino-1,3,4-thiadiazole [3]. The reaction proceeded easily under thermal conditions as shown in the following (Scheme 3) mechanism[15].
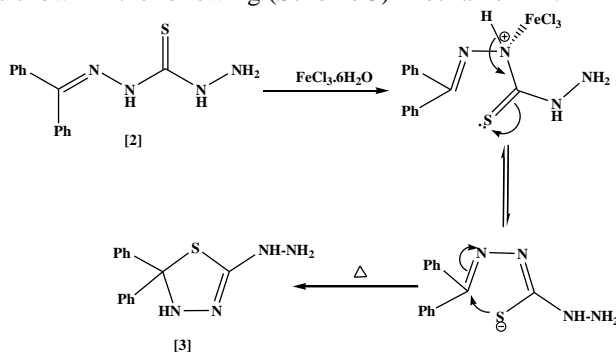
Scheme (3)

Compound [3] was characterized via ^{1}H-NMR spectra which shown shifting (δ, ppm) at (s, 3.35, 2H,1H,NH$_2$-NH), (s,7.01, 1H, cycl. NH) and (m, 7.1-7.5, 10H, aromatic). FT-IR spectra was used as further identification to proving the right structure, so, it shown the following absorption peaks (cm^{-1}) (3351, 3328, 3261,1531 and 768) refer to the following functional groups respectively (NH$_2$, cycl. NH, acycl. NH, cycl.C=N and C-S). whereas,

in U.V. spectra it gave absorption bands at λ_{max} (nm) (318 & 331) due to the n→π* and π→π* and also due to the cyclic system. Finally , compound [3] was reacted with different freshly prepared chalcons [4-9], (Table 1), to afford the substituted pyrimidines [10-15]. The mechanism reaction was illustrated below (Scheme 4).
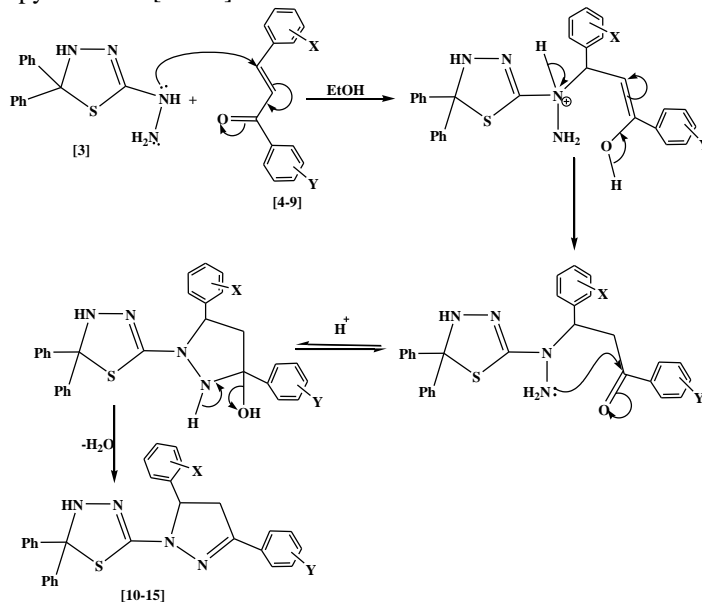
Scheme (4)

The structure of compounds [10-15] were also proved by using the spectral methods and the (Table 2) shown their physical and spectral data. The must important proof here is the absence of (NH$_2$) absorption band at (3351 cm^{-1}) and the appearance of stretching absorption bands at (1624-1659 cm^{-1}) due to the (C=N) functional group in formation pyrazole ring. Moreover, in U.V. spectra they show absorption bands at λ_{max} (nm) (323 - 386) & (307-375) due to the increasing the ring system additionally to the electronic transition represented by n→π* and π→π* respectively. Also, the ^{1}H-NMR spectrum for compound [10] revealed signals for substituted pyrazole at (δ, ppm): (d, 2.5,2H, CH$_2$) , (t,3.9, 1H, CH), (m, 7.85-7.98, 5H, phenyl) and (m, 8.0-8.2, 4H, p-bromo phenyl). While, the substituent 1,3,4-thiadiazole ring showed the absorption bands at (s, 7.0, 1H, NH) and (m,7.55-7.75, 10H, aromatic). Actually, ^{13}C-NMR was also used to prove the structure of compound [11], so, it gave signals at (δ, ppm): (128.1, phenyl), (123.8, p-bromo phenyl) and (129.3, m-methoxy phenyl) , so, this absorption values were supported the formed structure of compound [11].

Table 1. The physical and spectral data for chalcons [4-9]

Comp. No.	X	Y	M.p. ºC	Yield %	FT-IR (KBr) , v (cm^{-1})			U.V DMf $\lambda_{max(nm}$
					C=O	C=C	Others	
4	H	p-Br	118-119	92	1656	1607	C-Br 530	320
5	H	p-Cl	110-111	92	1656	1600	C-Cl 688	305
6	H	p-NO$_3$	163-164	49	1646	1602	NO$_2$ sym.1385 asym.1504	292
7	m-OMe	p-Br	155-156	96	1656	1593	C-Br 532 C-O-C sym. 1072 asym.1276	244
8	m-OMe	p-Cl	149-150	90	1655	1607	C-Cl 689 C-O-C sym. 1088 asym. 1277	259
9	m-OMe	p-NO$_3$	124-126	78	1684	1617	NO$_2$ sym. 1370 asym. 1575 C-O-C sym. 1073 asym.1279	332

Table 2. The physical and spectral data for compounds [10-15]

Comp. No.	X	Y	M.P.°C	Yield %	FT-IR (KBr) , v (cm^{-1})						U.V DMf $\lambda_{max(nm)}$
					N-H cycl.	C=N cycl.	C□C arom.	Others			
10	p-Br	H	114-115	66	3328	1658	1583	C-Br 532 C-S 736			319,323
11	p-Br	m-OMe	124-125	69	3328	1659	1583	C-Br 530 C-S 716 C-O-C sym. asym.	1033 1225		310,380
12	p-Cl	m-OMe	112-113	73	3282	1654	1587	C-Cl 668 C-S 703 C-O-C sym. asym.	1032 1225		322,386
13	p-Cl	H	215-216	89	3328	1658	1585	C-Cl 669 C-S 707			307,329
14	p-NO$_2$	H	100-101	80	3327	1624	1584	C-S 703 NO$_2$ sym. asym.	1345 1521		375,380
15	p-N(CH$_3$)$_2$	m-OMe	102-103	91	3209	1645	1576	C-N 1370 C-S 704 C-O-C sym. asym.	1035 1229		341,391

Conclusion

From the foregoing survey, it seems that thiocarbohydrazide provide a useful and convenient strategy for synthesis of numerous fused heterocyclic compounds containing 1,3,4-thidiazole , so, aseries of some 2-pyrazolideno-1,3,4-Thiadiazoline Compounds was prepared under conventional thermal conditions using thiocarbohydrazide. Thiocarbohydrazide converted to its hydrazonederivatives , and the later underwent catalytic intracyclization reaction to give 2-hydrazinyl-5,5-diphenyl-2,5-dihydro-1,3,4-thiadiazoline compound which reacted with different freshly prepared chalcones to yield the titled compound represented by1-(5,5-diphenyl-2,5-dihydro-1,3,4-thiadiazol-2yl)-3,5-diaryl-4,5-dihydro pyrazolidine compounds.

Recommendations

Thiocarbohydrazid is prepared so easily from hydrazine and carbon disulfide and it is very active in organic synthesis. In this presentation we prepare only one line from thiocarbohydrazide, but we believed that this active unite building will be used to prepare many different active heterocyclics which will show high activity in many different fields

Acknowledgements

References

Abdel Rahman.D E.,Mohamed.K O. (2014). Synthesis of novel 1,3,4-thiadiazole analogues with expected anticancer activity, *Der Pharma Chemica*, 6(1) ,P: 323- 335.

Ansari K F., Lal. C. (2009). Synthesis and biological activity of some heterocyclic compounds containing benzimidazole and beta-lactam moiety, *J. Chem. Sci.*, Vol. 121, No.6, 1017-1025.

Azarifar.D., Shaebanzadeh.M. (2002). Synthesis and characterization of new 3, 5-dinaphthyl substituted 2-pyrazolines and study of their antimicrobial activity, *Molecules*, 7, 885-895.

Bheru S.K., Man S. (2014). Synthesis, characterization, antibacterial, antioxidant, DNA binding and SAR study of a novel pyrazine moiety bearing 2-pyrazoline derivatives, *New J. Chem.*, 38, 4290-4299.

Fatondji.H.R.,Gbaguidi.F.,Kpoviessi.S.,Bero.J.,Hannaert.V.,QuetinLeclercq.J.,Poupaert.J.,Moudachirou.M.,Accrombessi.G.C. (2011). Synthesis, characterization and trypanocidal activity of some aromatic thiosemicarbazones and their 1,3,4-thiadiazolines derivatives, *African Journal of Pure and Applied Chemistry*, Vol. 5(1), p:59-64.

Francis A.G., Robert M.G. (2011). *Organic Chemistry*, 8th edition,MeGraw-Hill Comparies,Inc, pp:880.

Jumbad H. T., Mustafa S. K., Ammar H. A. (2014). Synthesis and characterization of novel Schiff bases containing pyrimidine unit, *Arabian Journal of chemistry*, 7, P:157-163.

Manjula.P.S., Sarojini.B.K., Darshan Raj.C.G. (2015). Antibacterial and in vitro antioxidant activities of some 4 4-amino-1,2,4-triazole-5(4h)-thione derivatives, *J Fundam appl Sci.*, 7(3), 394-407.

Nitulescu.G.M., Draghici.C.,Olaru.O.T. (2013). New Potential Antitumor Pyrazole Derivatives: Synthesis and Cytotoxic Evaluation ,*Int. J. Mol. Sci.* , 14, 21805-21818.

Noto R ., Buccheri F ., Cusmano G ., Gruttadauria M ., Werber G. (1991). Substituent effect on oxidative cyclization of aldehyde thiosemicarbazones with ferric chloride, *J. Heterocyclic Chemistry*, 28 , 1421.

Patil.C B., Mahajan.S.K., Katti.S.A. (2009). Chalcone: A Versatile Molecule*, J.Pharm.Sci*, 3,11- 22.

Rajin M., Devinder K.,Satbirm. (2014). Synthesis and Antimicrobial Activity of Some 1,3-Disubstituted Indeno[1,2-*c*]pyrazoles*, J.Heterocyclic Chem,* 51,203 .

Saha, G.C., Khayer, K., Islam.M.R. (1992). Syntheses of thiocarbohydrazide, some thiocarbohydrazones and their cyclized products as probes for pharmacological studies, *Indian J. Chem.*, 31, 547–551.

Shailesh H.S., Pankaj S.P., Mitesh P., Bharat V., Jayesh P. (2014). Synthesis, Characterization and Antimicrobial Activity of Azetidin-2-one based Phenyl Sulfonyl Pyrazoline Derivatives*, Global Journal of Science frontier Research*, (14):Issue 1.,Version 1, 33-38.

Shui-Lin Y., Ming-Yan Y., Zhao-Hui S., Li-Jing M., Cheng-Xia T., Jian-Quan W.,Hong-Ke W., Xing-Hai L. (2014). Synthesis and Antifungal Activity of 1,2,3-thiadiazole Derivatives Containing 1,3,4-thiadiazole Moiety *, Letters in Drug Design & Discovery,*11*,* 940-943.

Valentiny.M., Martvon.A. (1982). Synthesis of N-glucosyl derivatives of 5-amino-1, 2, 3- thiadiazole and 5-substituted 2-amino-1, 3, 4-thiadiazole*, Chem. Zvesti*, 36 (1), 111-116.

Xue-Ru. L., Hua W., Ze-Yu H., Zhi-Qing M., Jun-Tao F., Xing Z. (2014) . Design, Synthesis and Fungicidal Activities of Some Novel Pyrazole Derivatives , *Molecules*, 19 , 14036-14051.

Yousif.E A., Hameed.A S., Bakir.E T. (2007). Synthesis and photochemical study of of poly(vinyl chloride)-1,3,4-oxadiazole and 1,3,4-thiadiazole, *Journal of Al-Nahrain University*, Vol.10(1), pp:7-12.

Author Information

Shaymaa K.Y. Al-azzawi
University of Mosul, Iraq
College of Science
Chemistry Department
Contact E-mail: *khazaalyounis@yahoo.com*

Aemn Y.S. Al-zebari
University of Mosul, Iraq
College of Science
Chemistry Department

Effects of Superstrate Layer on the Resonant Characteristics of Annular-Ring printed Antenna

Fadila BENMEDDOUR
University of M'Sila

Christophe DUMOND
Université d'Orléans

Elhadi KENANE
University of M'Sila

Abstract: In practice, it was found that the choice of the substrate or superstrate material of printed antennas is of a great importance and plays a significant role in achieving the optimum resonant characteristics of the antenna; Uniaxial dielectrics have drawn more attention due to their availability in materials such as sapphire, boron nitride and Epsilam-10 ceramic-impregnated Tefon. Previous studies of anisotropic materials used in microwave devices indicate that the effects of anisotropy on the performance of such structures particularly in high frequencies cannot be ignored. Three very popular full wave methods that can be used to characterise microstrip patch antennas are: the finite element method, the finite difference time domain method, and the moment method. The last one also known as the full-wave method is arguably the most popular method for the analysis of microstrip antennas. In this work, resonant characteristics (the resonant frequency, the Half-power bandwidth) of an annular microstrip patch printed on uniaxially anisotropic substrate and covered with an anisotropic superstrate layer are studied using an electric field integral equation and the spectral domain Green's function. In order to validate the present method, we have confronted our results with theoretical and experimental data from the literature and very Good agreements were obtained between our computed data and measurements, and the convergence of the method is proven.

Keywords: Annular-ring patch, Anisotropic, Superstrate, Resonance frequency

Introduction

Because microstrip antennas are small, lightweight, and low-cost, they have found widespread applications in satellite and wireless mobile communication systems (Garg, Bhartia, Bahl, & Ittipiboon, 1995) (James, P. S. Hall, Hall, & Wood, 1981) (Sung & Kim, 2005) (Balanis, 1997).

In practice, it was found that the choice of the substrate or superstrate material is of a great importance and plays a significant role in achieving the optimum resonant characteristics of the antenna (Bhartia, Rao, & Tomar, 1991).

Uniaxial dielectrics have drawn more attention due to their availability in materials such as sapphire, boron nitride and Epsilam-10 ceramic-impregnated Teflon. Previous studies of anisotropic materials used in microwave devices indicate that the effects of anisotropy on the performance of such structures particularly in high frequencies cannot be ignored (Gurel & Yazgan, 2003).

Several methods exist for the analysis of annular microstrip antennas. These methods can be classified as the approximate and the full-wave methods. Some of the popular approximate models include: the transmission-line model, the cavity model and the segmentation model. These models usually consider the microstrip patch as a transmission line or as a cavity resonator (Lee, Luc, & Dahele, 1988) (Biswas & Guha, 2009).

Although the accuracy of these approximate models is limited, they are nevertheless useful in providing the preliminary design and predicting the trends of these characteristics with the variation of the design parameters. Three very popular full wave methods that can be used to characterise microstrip patch antennas are: the finite element method, the finite difference time domain method, and the moment method (Kumar & Ray, 2003). The last one also known as the full-wave method is arguably the most popular method for the analysis of microstrip antennas (Losada, Boix, & Horno, 1999) (Bouttout, Benabdelaziz, Benghalia, Khedrouche, & Fortaki, 1999) (BahI & Bbartia, 1980) and will be used in our work. For that, a rigorous full-wave analysis with basis modes involving is developed and applied.

Superstrate dielectric layer (or layers) or earlier known as cover layers, are often used to protect printed antennas (PA) from environmental hazards, or may be naturally formed for example: ice layers during flight or severe weather conditions (POZAR, 1983). Only after the year 1985, it was discovered that the superstrate layer many prove beneficial or detrimental to printed antenna radiation characteristics, depending on the thicknesses of the substrate and cover, as well as relative dielectric and permeability constants , it may affect adversely the antenna basic performance characteristics (POZAR, 1983) (Nicolaos, Alexopoulos, & Jackson, 1984).

For this reason, in this work the effects of superstrate Annular- Ring printed antennas using the moment method are considered in detail, so that the printed antenna performance may be understood better or a proper choice of cover parameters may be implemented to advantage in the enhancement of printed antennas.

Theory

The problem to be solved is illustrated in Figure 1. A annular-ring patch of thickness e is printed on a grounded dielectric slab of thickness h_1.
The annular ring patch dimensions are the inner radius a and the outer radius b. The substrate is characterized by the free-space permeability μ_0 and a permittivity $\varepsilon_0 \varepsilon_{r1}$.
Above the radiating patch is the superstrate layer of thickness h_2 with free-space permeability μ_0 and a permittivity $\varepsilon_0 \varepsilon_{r2}$.The permittivity tensor in this region is given by (Losada, Boix, & Horno, 1999) (Benmeddour, Dumond, Benabdelaziz, & Bouttout, 2011) :

$$\bar{\varepsilon} = \varepsilon_0 \begin{vmatrix} \varepsilon_x & 0 & 0 \\ 0 & \varepsilon_y & 0 \\ 0 & 0 & \varepsilon_z \end{vmatrix} \tag{1}$$

Where $\varepsilon_x = \varepsilon_y \neq \varepsilon_z$.
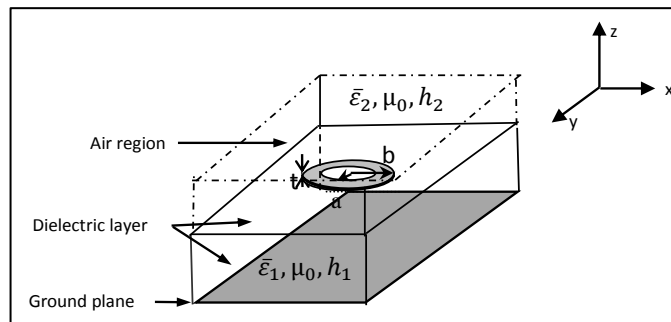
Figure 1. Geometrical structure of a superstrate loaded annular patch on a uniaxial substrate

The transverse fields components in the jth layer can be obtained using the vector Hankel transform formulation (Losada, Boix, & Horno, 1999) (Benmeddour, Benabdelaziz, Bouttout, & Aouabdia, 2004) (Benmeddour, Dumond, Benabdelaziz, & Bouttout, 2011).

$$E(\rho,\varphi,z) = \begin{bmatrix} E_\rho(\rho,\varphi,z) \\ E_\varphi(\rho,\varphi,z) \end{bmatrix} = \sum_{n=-\infty}^{\infty} e^{jn\varphi} \int_0^\infty dk_\rho \, k_\rho \bar{\mathbf{H}}_n(k_\rho\rho). \, e_n(k_\rho,z) \tag{2}$$

$$H(\rho,\varphi,z) = \begin{bmatrix} -H_\varphi(\rho,\varphi,z) \\ E_\rho(\rho,\varphi,z) \end{bmatrix} = \sum_{n=-\infty}^{\infty} e^{jn\varphi} \int_0^\infty dk_\rho \, k_\rho \bar{\mathbf{H}}_n(k_\rho\rho). \, \boldsymbol{h}_n(k_\rho,z) \tag{3}$$

$\overline{\mathbf{H}}_n(k_\rho\rho)$ is the kernel of the vector Hankel transform given by (Chew & Kong, 1980).

$$\overline{\mathbf{H}}_n(k_\rho\rho) = \begin{bmatrix} j_n(k_\rho\rho) & \dfrac{-in}{k_\rho\rho} J_n(k_\rho\rho) \\ \dfrac{in}{k_\rho\rho} J_n(k_\rho\rho) & j_n(k_\rho\rho) \end{bmatrix} \tag{4}$$

$\bar{A}$ and $\bar{B}$ are two unknown vectors and is determined by :

$$\begin{aligned} \overline{\mathbf{G}}(k_\rho) &= \mathrm{diag}\big[G^{TM}, G^{TE}\big] \\ &= -(\overline{\Gamma}_<)_{12} \cdot \big[\overline{\mathbf{g}}_0 \cdot (\overline{\Gamma}_>)_{12} - (\overline{\Gamma}_>)_{22}\big] \cdot \big[\overline{\mathbf{g}}_0 \cdot (\overline{\Gamma})_{12} - (\overline{\Gamma})_{22}\big]^{-1} \end{aligned} \tag{5}$$

Where

$$\overline{\Gamma}_< = \prod_{j=M}^{1} \overline{\mathbf{T}}_j, \ \overline{\Gamma}_> = \prod_{j=N}^{M+1} \overline{\mathbf{T}}_j, \text{ and } \overline{\Gamma} = \overline{\Gamma}_> \cdot \overline{\Gamma}_< \tag{6}$$

$\displaystyle\prod_{j=M}^{1}$, and $\displaystyle\prod_{j=N}^{M+1}$, means the product of matrices below and above the annular ring patch.

Here, the expression of the matrices $\overline{\mathbf{T}}_j$ for the anisotropy in the dielectrics is given by :

$$\overline{\mathbf{T}}_j = \begin{bmatrix} \cos\overline{\theta}_j & i\overline{\mathbf{g}}_j^{-1} \cdot \sin\overline{\theta}_j \\ -i\overline{\mathbf{g}}_j \cdot \sin\overline{\theta}_j & \cos\overline{\theta}_j \end{bmatrix} \tag{7}$$

Where
$$\overline{\theta}_j = \overline{\mathbf{k}}_{jz}\mathbf{d}_j \tag{8}$$

In which

$$\overline{\mathbf{k}}_{jz} = \begin{bmatrix} k_{jz}^e & 0 \\ 0 & k_{jz}^h \end{bmatrix} = \begin{bmatrix} \left(\varepsilon_{jx}k^2 - \dfrac{\varepsilon_{jx}}{\varepsilon_{jz}}k_\rho^2\right)^{\frac{1}{2}} & 0 \\ 0 & (\varepsilon_{jx}k^2 - k_\rho^2)^{\frac{1}{2}} \end{bmatrix} \tag{9}$$

$$\overline{\mathbf{g}}_j(k_\rho) = \begin{bmatrix} \widetilde{g}_j^e(k_\rho) & 0 \\ 0 & \widetilde{g}_j^h(k_\rho) \end{bmatrix} = \begin{bmatrix} \dfrac{\omega\varepsilon_{jx}\varepsilon}{k_{jz}^h} & 0 \\ 0 & \dfrac{k_{jz}^e}{\omega\mu} \end{bmatrix} \tag{10}$$

and

$k = \omega\sqrt{\mu_0\varepsilon_0}$: is the free space wavenumber.

$k = \omega\sqrt{\mu\varepsilon}$: Note that the presence of an arbitrarily number of layers above and / or below the annular patch is easily included in the matrix product $\overline{\Gamma}_<$ and/ or $\overline{\Gamma}_>$.

In applying Galerkin method to solve the vector dual integral equations express the unknown annular patch current in terms of appropriate expansion modes formed expansion basis functions (Sami, Chew, & Kong, 1982).

$$\kappa_n(\rho) = \begin{cases} \sum_{P=1}^{P} a_{np}l_{np}(\rho) + \sum_{q=1}^{Q} b_{nq}f_{nq}(\rho) & a < \rho < b \\ 0 & \rho > b, \rho < a \end{cases} \tag{11}$$

Here a_{np} and b_{nq} are unknown coefficients

Principal system

$$l_{nm}(\rho) = \begin{cases} \begin{bmatrix} \psi_n\left(\frac{\beta_{nm}\rho}{a}\right) \\ \frac{n}{\frac{\beta_{nm}\rho}{a}}\psi_n\left(\frac{\beta_{nm}\rho}{a}\right) \end{bmatrix} & a < \rho < b \\ 0 & \rho > b, \ \rho < a \end{cases} \tag{12}$$

The Hankel transform of l_{nm} is:

$$L_{nm}(k_\rho) = \begin{bmatrix} \frac{\beta_{nm}/a}{(\beta_{nm}/a)^2 - k_\rho^2}Y'_{nm}(k_\rho) \\ \frac{n}{(\beta_{nm}/a)k_\rho}Y_{nm}(k_\rho) \end{bmatrix} \tag{13}$$

Where
$$Y_{nm}(k_\rho) = \psi_n \tag{14}$$
$$Y_{nm}(k_\rho) = \psi_n(\beta_{nm}b/a)J_n(k_\rho b) - \psi_n(\beta_{nm})J_n(k_\rho a)$$

Orthogonal system

$$f_{np}(\rho) = \begin{cases} \begin{bmatrix} \frac{n}{\alpha_{np}\rho/a}\phi(\alpha_{np}\rho/a) \\ \dot{\phi}(\alpha_{np}\rho/a) \end{bmatrix} & a < \rho < b \\ 0 & \rho > b, \rho < a \end{cases} \tag{15}$$

The Hankel transform of f_{np} is:

$$F_{np}(k_\rho) = \begin{bmatrix} 0 \\ \frac{k_\rho a}{k_\rho^2 - (\alpha_{np}/a)^2}Z_{np}(k_\rho) \end{bmatrix} \tag{16}$$

Where
$$\phi_n(\alpha_{np}\rho/a) = J_n(\alpha_{np}\rho/a)Y_n(\alpha_{np}) - J_n(\alpha_{np})Y_n(\alpha_{np}\rho/a) \tag{17}$$
$$\phi_n(\alpha_{np}b/a) = \phi_n(\alpha_{np}) = 0 \tag{18}$$
$$Z_{np}(\rho) = \frac{b}{a}\phi_n(\alpha_{np}b/a)J_n(k_\rho b) - \phi_n(\alpha_{np})J_n(k_\rho a) \tag{19}$$

Vector Hankel transform of the current basis functions can be written as:

$$K_n(k\rho) = \sum_{m=1}^{M} a_{nm}L_{nm}(k\rho) + \sum_{q=1}^{Q} b_{nq}F_{nq}(k\rho) \tag{20}$$

The expression of the spectral dyadic Green function of the stratified medium, in which the patch is embedded, is shown to be given by : (Losada, Boix, & Horno, 1999) (Benmeddour, Benabdelaziz, Bouttout, & Aouabdia, 2004) (Benmeddour, Dumond, Benabdelaziz, & Bouttout, 2011).

$$E(k_\rho) = G(k_\rho) \times \kappa(k_\rho) \tag{21}$$

$$e_n(\rho) = \int_0^\infty dk_\rho k_\rho \bar{H}_n(k_\rho\rho).\left(\bar{G}(k_\rho) - \bar{Z}_s\right).K_n(k_\rho) = 0 \quad a < \rho < b \tag{22}$$

$$\kappa_\rho = \int_0^\infty dk_\rho k_\rho \bar{H}_n(k_\rho\rho).K_n(k_\rho) = 0 \qquad \rho > b, \ \rho < a \tag{23}$$

Where

The electric field integral equation which enforces the boundary condition must vanish on the patch surface, as discretized into a matrix form shown as:

$$\tag{24}$$

$$\begin{bmatrix} \left(\bar{Z}^{\psi\psi}\right)_{M\times M} & \left(\bar{Z}^{\psi\varphi}\right)_{M\times P} \\ \left(\bar{Z}^{\varphi\psi}\right)_{P\times M} & \left(\bar{Z}^{\varphi\varphi}\right)_{P\times P} \end{bmatrix} \cdot \begin{bmatrix} (A')_{M\times 1} \\ (B')_{P\times 1} \end{bmatrix} = 0$$

Each element of the submatrices $\bar{Z}_{ij}^{CD}$ is given by:

$$\bar{Z}'^{CD}_{ij} = \int_0^\infty dk_\rho k_\rho C^+_{ni}\left(k_\rho\right) \cdot G\left(k_\rho\right) \cdot D_{nj}\left(k_\rho\right) \tag{25}$$

Where
C and D represent either φ or ψ for every value of the integer n.

The system of linear equation has non-trivial solutions when the determinant of system equation (30) vanishes, that is:

$$\textbf{det} \left(\left[\bar{Z}'(f)\right]\right) = 0 \tag{26}$$

The equation (26) is the characteristic equation of the complex resonant frequencies of the microstrip antenna having stacked configuration as shown in figure 1.
The real parts of the complex resonant frequencies correspond to the resonant frequencies of the antenna, whereas, the imaginary parts are due to radiation loss of the antenna. Once the resonant frequencies are obtained, we can determinate the half power bandwidth.

$$BW = 2\,f_i\,/\,f_r \tag{27}$$

With f_i is the imaginary part of the resonant frequency, and is f_r the real part of the resonant frequency.

Numerical results and discussions

Validation of results

In order to confirm the computation accuracy of the approach described in the previous section, our numerical results are compared with those obtained from other works Table 1 shows the calculated resonant frequencies for the modes of Annular-ring Microstrip Single Layer Antenna (TM^{11}, TM^{21}, and TM^{31}). These results are compared with theoretical and experimental data, which have been suggested in (Richard, Bhasin, & Claspy, 1993) (Lee, Yho, & Dahel, 1984) (Lee & Dahele, The two-layered annular ring microstrip antenna, 1986).
The annular patch is printed on a substrate of thickness $h_1 = 1.59mm$, and $b = 2a$.
Note that the agreement between our computed results and experimental and the theoretical results is very good.

Table 1. Comparison of measured and theoretical resonant frequencies for different modes TM^{11}, TM^{21}, TM^{31}, $\varepsilon_{r1} = 2{,}32$, $b = 2a$, $h_1 = 1.59mm$ $h_2 = 0mm$

Modes	ε_{r1}	a [Cm]	Measured frequencies f_r[GHz] (Richard, Bhasin, & Claspy, 1993)	Calculated frequencies f_r[GHz]		
				(Lee, Yho, & Dahel, 1984)	(Lee & Dahele, The two-layered annular ring microstrip antenna, 1986)	This paper
TM^{11}	2.32	2.5	0.877	0.878	0.875	0.876
TM^{21}	2.32	2.5	1.722	1.723	1.732	1.732
TM^{31}	2.32	2.5	2.517	2.515	2.556	2.525
TM^{11}	2.32	3.5	0.626	0.623	0.621	0.622

Table 2. Comparison and calculated resonant wave number times the inner radius of the ring (k_r)

h_1/a	Mode TM^{11}					
	Results of (Gomez-Tagle & Christodoulou, 1997)			Our results		
	Re $(k_r a)$	Im $(k_r a)$	BP%	Re $(k_r a)$	Im $(k_r a)$	BP%
0.005	0.67	$1.6.10^{-4}$	0.048	0.676	$1.6.10^{-4}$	0.047
0.01	0.68	$1.7.10^{-4}$	0.05	0.682	$1.8.10^{-4}$	0.053
0.05	0.70	$5.4.10^{-4}$	0.15	0.695	$5.5.10^{-4}$	0.151
0.1	0.71	0.0012	0.34	0.705	0.0012	0.345

As a validation of the different results, in table 2, we have compared the results obtained with this theory and previously published data (Gomez-Tagle & Christodoulou, 1997). We have calculated the resonant wave number (k_r) times the inner radius a of the ring $k_r a$ ($(k_r a = 2\pi f_r \sqrt{\varepsilon_x \varepsilon_0 \mu_0})$), as functions of different sizes of the ratio of the substrate thickness h_1 normalized by the inner radius a (for the modes TM^{11}). The annular antenna printed on a substrate of permittivity $\varepsilon_{1x} = \varepsilon_{1z} = 2.65$, for the inner radius $a = 0.71cm$, thickness $h_2 = 0$ and the outer radius $b = 2a$ and, for various thickness h_1.

Again, the comparisons show a good agreement between our results and those of literature.

Effet of Isotripic Superstrate

In this sub section, a rigorous analysis of the annular-ring printed patch is obtained using the vector Henkek transform and Galerkin's method. Figure 3 depicts the variation of the resonant characteristics for annular-ring printed antenna as function of thicknesses h_2 and permittivity ε_{r2} of superstrate.
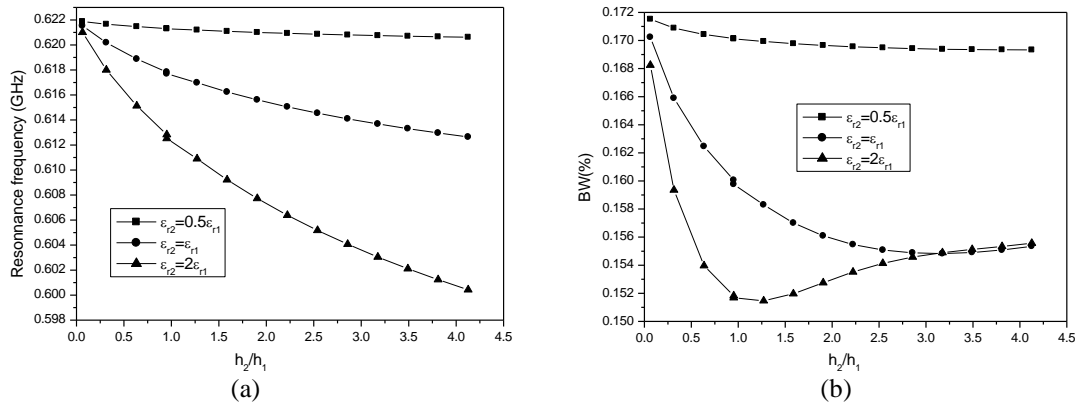
Figure. 2. Resonance frequency and half-power bandwidth of the annular-ring printed antenna with different thicknesses of superstrate layer against permittivity of superstrate layer;
(a) Resonance Frequency, (b) Half-power bandwidth

Results show that in addition to its protective action, the presence of a dielectric cover has two major interests in the field of antennas: (1) it decreases the resonant frequency which allows a reduction in the patch size for the same target frequency and (2) it increases the half-power bandwidth which improves the narrow-band characteristics of printed antenna. It can be observed both in Fig. 2a. and 2b that these effects are more pronounced for thicker superstrate and for increasing ratio of $\varepsilon_{r2}/\varepsilon_{r1}$. As it is well-known in printed antenna design, a low value of substrate permittivity ε_{r1} is generally preferred because it increases the fringing field at the patch periphery and then the radiated power. Thus the use of high permittivity superstrate ε_{r2} leading to high ratio $\varepsilon_{r2}/\varepsilon_{r1}$ is possible and could give significant improvements in condition of sufficient thickness. Indeed, from Fig. 2b, we can note that for ratios h_2/h_1 less than 3.1, the bandwidth is degraded and this especially as the permittivity ε_{r2} of the superstrate is high.

Conclusion

This work presents the resonant characteristics of superstrate loaded annular printed antenna. The analysis has been based on a full-wave model with London's equations and the Gorter-Casimir two-fluid model. It is shown that resonant frequency of the Annular-Ring printed Antenna is seriously affected from the anisotropy of superstrate layer. These results indicate that the effect of the superstrate layer on the resonant characteristics of

the Annular-Ring printed Antenna is stronger for higher superstrate thickness and permittivity. The accuracy of our results has been checked with different approaches and shows a very good agreement. The optimal operating frequency of the structure is shifted and wider bandwidth operation is achieved. These results must be taken into account in shielding applications in order to avoid unwanted characteristics and better protection of the structure.

References

Garg, R., Bhartia, P., Bahl, I., & Ittipiboon, A. (1995). *Microstrip Antenna Design Handbook.* Norwood: MA: Artech House.

BahI, I., & Bbartia, P. (1980). *Microstrip Antennas.* USA: Dedham, Mass. : Artech House.

Balanis, C. (1997). *Antenna Theory: Analysis & Design* (éd. 2). New York, USA: John Wiley & Sons, Inc.

Benmeddour, F., Benabdelaziz, F., Bouttout, F., & Aouabdia, N. (2004). Resonance characteristics of circular microstrip antennas using moment method and various current representations. *First International Symposium on Control, Communications and Signal Processing*, 339-342.

Benmeddour, F., Dumond, C., Benabdelaziz, F., & Bouttout, F. (2011). Improving the performances of a high Tc superconducting circular microstrip antenna with multilayered configuration and anisotropic dielectrics. *18*, pp. 169-183.

Bhartia, P., Rao, K., & Tomar, R. (1991). *Millimeter Wave Microstrip and Printed Circuit Antennas .* Boston, London: Artech House.

Biswas, M., & Guha, D. (2009). Input impedance and resonance characteristics of the superstrate –loaded triangular Microstrip patch. *IET Microw. Antennas propag, 3*, pp. 92- 98.

Bouttout, F., Benabdelaziz, F., Benghalia, A., Khedrouche, D., & Fortaki, T. (1999). Uniaxialy anisotropic substrate effects on resonance of rectangular microstrip patch antenna. *Electonics. Letters, 35*(4), pp. 255-256.

Chew, W., & Kong, J. (1980). Resonance of non-axial symme- tric modes in circular micro strip disk. *Mathematical. Physics, 21*(10), pp. 2590-2598.

Gomez-Tagle, J., & Christodoulou, C. (1997, November). Extended cavity model analysis of stacked microstrip ring antenna. *IEEE Trans. Antennas Propagat, 45*(11).

Gurel, C., & Yazgan, E. (2003). The effects of uniaxially anisotropic superstrate shielding on the resonant characteristics of circular microstrip patch. *IEEE International Symposium on Electromagnetic Compatibility, 2003. EMC '03.* Istanbul, Turkey.

James, P. S. Hall, J., Hall, P., & Wood, C. (1981). *Microstrip Antenna Theory and Design.* London, U.K: Peter Peregrinus.

Kumar, G., & Ray, K. (2003). *Broadband Microstrip Antennas, Artech House, Boston London ISBN 1- 58053- 244-6,.* Boston London: Artech House.

Lee, K., Luc, K., & Dahele, J. (1988, November). Characteristics of the equilateral triangular patch antenna. *IEEE Transactions on antennas and propagation, 36*(11), pp. 1510- 1518.

Lee, K., & Dahele, J. (1986). The two-layered annular ring microstrip antenna. *Int. J. Electronpp*, pp. 207-217.

Lee, K., Yho, K., & Dahel, J. (1984, August). Circular-disk microstrip antenna with an air gap. *Antennas and Propagation, IEEE Transactions, AP. 32*(8).

Losada, V., Boix, R., & Horno, M. (1999, April). Resonant Modes of Circular Microstrip Patches in Multilayered Substrates. *IEEE Transactions on Microwave Theory and Techniques, 47*(4), pp. 488–498.

Nicolaos, G., Alexopoulos, G., & Jackson, D. (1984). Fundamental Superstrate Effets on Printed circuit Antenna Efficiency. *IEEE MTT-S DIGEST*.

POZAR, D. (1983, September). Considerations for Millimeter Wave Printed Antennas. *IEEE TRANSACTIONS ON ANTENNAS AND PROPAGATION, 31*(5), pp. 740-747.

Richard, M., Bhasin, K., & Claspy, P. (1993, July). Superconducting microstrip antennas: an experimental comparison of two feeding methods. *Antennas and Propagation, IEEE Transactions, 41*, pp. 967 – 974.

Sami, M. A., Chew, W., & Kong, J. A. (1982, July). Vector Hankel transform analysis of annular ring microstrip antenna. *IEEE Transactions on Antennas and Propagation, AP-30*(4).

Sung, Y., & Kim, Y.-S. (2005, may). An Improved Design of Microstrip Patch Antennas Using Photonic Bandgap Structure. *IEEE transactions on antennas and propagation, 53*(5).

Author Information

Fadila Benmeddour
Electronics Department, University of M'Sila,
Laboratoire de Génie Electrique (LGE), M'sila, Algeria
benmeddourfadila@yahoo.fr
Contact E-mail: *fadila.benmeddour@univ-msila.dz*

Christophe Dumond
Institut Prisme, IUT de Chartres,
Université d'Orléans,
Chartres, France

Elhadi Kenane
Electronics Department, University of M'Sila,
Laboratoire de Génie Electrique (LGE), M'sila, Algeria

Synthesis, Characterization and Biological Activity of Binuclear Cu(II) Complexes with Unsymmetrical Brighted Tetradentate Schiff Bases

Moza M. AL-JIBOURY
Mosul University

Khansaa Sh. AL-NAMA
Mosul University

Abstract: Unsymmetrically brighted tetradentate Schiff bases   H2L1= [1-(E)-((3-((E)-2hydroxybenzlidene) amino) phenyl)imino) methyl), naphthalene-2-ol], H2l2= [2-((E)-1-((3(((E) 2hydroxybenzlidene) amino)phenyl) imino) phenyl) imino)ethyl)phenol], H2L3= [2-((E)-1-((3(((E) 2hydroxybenzlidene) amino)phenyl)methyl)-5methoxyphenol] Which derived from m-phenylenediamine with salicyaldehyde and 2-hydroxynaphthaldehyde or 2-hydroxyacetophenone or 2-hydroxy-4methoxybenzophenone and their complexes of the type [Cu2Ln2], where n=1,2,3 have been synthesized. Adduct complexes of the type [Cu2Ln2 (py)4] were also prepared in (1:4) (complex : py) molar ratio. The complexes and adducts were characterized by elemental analysis (C.H.N), metal content, (IR, UV-Vis, 1H-NMR) spectroscopy, conductivity and magnetic measurements. The resulted data suggested that the Schiff bases containing ONNO donor atoms acts as dibasic tetradendetate ligands through coordinated with Cu(II). Conductivity data in DMSO solution showed that all complexes are non-electrolyte. Magnetic moment and electronic spectra data indicat that the complexes have either tetrahedral or octahedral geometry. The ligands and their complexes were screened for antibacterial activity against Bacillus and Morganella Morgani. The ligands and their complexes showed some biological activities.

Keywords: Antibacterial activity, M-phenylenediamine, Schiff base, Unsymmetrical tetradentate

Introduction

Both symmetrical and unsymmetrical Schiff bases have been widely used as prepare metal complexes (Prakash et al., 2011). These complexes have played ligands to a major role in the advancement of coordination chemistry whose field of application varies from physicochemical studies (Luo et al., 2003), to biological aspects (El-Motalb et al., 2011). In biological systems, transition metal ions are as a heme ring or to donor atoms of peptide chains in distorted enviroment (Li et al., 2015), and this unsymmetrical coordination of ligands around central metal ions had lead to a growing interest in the design and synthesis of unsymmetrically substituted Aromatic diamines have the ability to coordinate to a metal directly on their relative ortho meta or para positions (Hernandez et al., 1997), m- phenyelenediamine derived Schiff bases can only coordinate one nitrogen atom to any metal ion. This is due to the big proximity range between the nitrogen atoms of 1998). Generally, m-phenylenediamine Schiff bases have the ability to acquire the formation of dimer complexes, where the Schiff bases act as bridges connecting the two metal cations (Clarke et al, 1998) thus producing dinuclear complexes. The uniqueness of such behaviour however has never been applied and studied in the biological field as bases derived from the other two aromatic diamines namely its ortho and para - analogues. Such complexes were suggested to have an even better presence of two metal ions compared to complexes with one metal ion. Therefore synthesis, characterization and the biological activity of two unsymmetrical tetradentate Schiff bases derived from m- described in this work usually bound to a macrocycle such transition metal complexes of Schiff base ligands as synthetic models (Hernandez et al., 2004) phenylenediamine and its rigid structure (Torayama et al, -u compared the Schiff biological activity due to the phenylenediamine and their Mn(II), Co(II), Ni(II) and Cu(II) complexes are described in this work.

Experimental

All reagents and solvents were of analytical grade used as BDH chemical companies, Infrared spectra were recorded on BRUKER mauf. U.K. (400-4000 cm-1) using KBr disc. Conductivity measurements were carried out on of the supplied from fluka or (10-3) M solution complexes in DMSO using Conductivity meter Model PCM3-JENWAY at ambient DMSO (10-3) M solution on temperature.The electronic spectra were recorded SPECTRO UV-VIS AUTO, 110 v 60 HZ using lcm quartz cell (200-1000)nm. Metal content was determined using instrument, AA-7000- UN. BG. IBN- H.C.S.L Atomic Absorption (Flamecont). Elemental analysis were performed on Euro EAE Elemental Analyzer Euro EA 3000 Italy H-NMR Spectra were recorded in DMSO-d6 using NMR edy 60 prrouser, Manual Version 1.0 (Nanalysis Crop, 2015). Melting point was recorded on Electro-thermal 9300 Engineering LT D. The magnetic measurements were carried out at 25 °C on the solid state by (Magnetic Susceptibility Balance Sherwood Scientific Cambridge/UK)

Method

Preparation of the ligands. H2L1, H2L2 , H2L3

Schiff base ligands were prepared according procedure (Pethe et al., 2017) by reacting equimolar amounts of m-phenylenediamine (0.01 mole, 1.08g) in methanol (15 ml) was added slowly to methanolic solution (15 ml) containing (0.01 mol, 1.22g) of salicyaldehyde and refluxed for 2h, then, fllowed by addition of 2-hydroxynaphthaldehyde (00.1 mole, 1.72g) or a 2-hydroxacetophenone (00.1 mole, 1.36g) or 2-hydroxy-4-methoxybeenzphenone (00.1 mole, 2.28g) each one dissolved in methanol (15 ml) the resulting cdoured mixture was refluxed with stirring for 3h and cooled, then the precipitate was filtered and washed with cold methanol and dried under vacuum, (schem-1-)
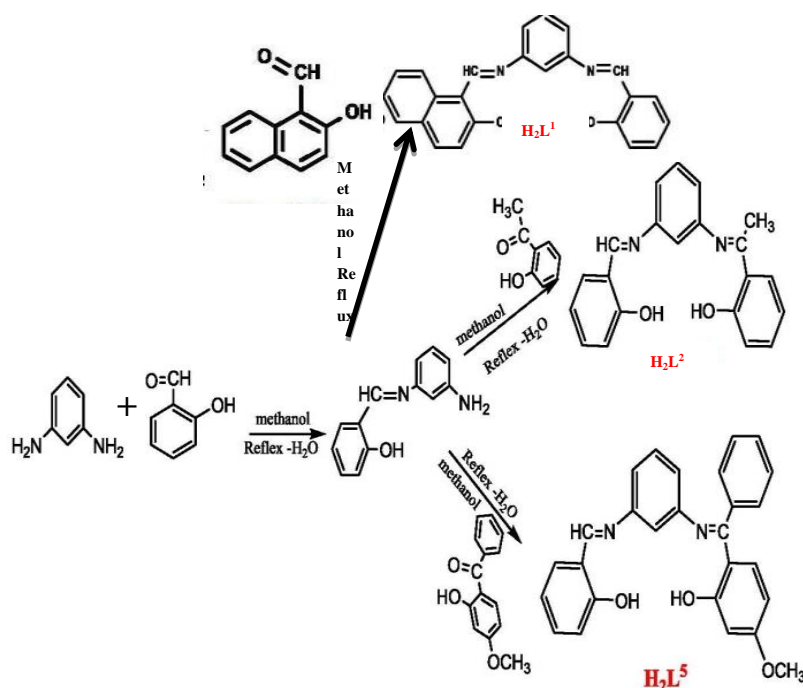
Scheme 1. Synthesis of Schiff bases ligands (H2L1, H2L2 and H2L3)

Preparation of the complexes. [Cu2Ln2]

The ligands H2L1 (00.1 mole, 3.66g) or H2L2 (001 mole, 3.30g) or H2L3 (00.1 mole, 4.22g), was dissolved in methanol (25 ml) in (50 ml) round bottom flask. Solution of Cu2L2. 2H2O (00.1 mole, 1.70 g) in methanol (15 ml) was added dropwise for 10-15 min. with continuos stirring at room temp. The mixture was refluxed for (3-4) h, after cooling the precipitate filtered off and washed with cold methanol then dried under vacuum.

Preparation of base adduct complexes. [Cu2Ln2 (py)2]

These complexes were prepared by the addition of pyridine (0.04 mole, 3.16g) to (0.01 mole) of the prepared complexes in methanol (50 ml) with continuous stirring until complete precipitation the precipitate was filtered off washed with cold methanol and dried under vacuum (Osowole 2008).

Antibacterial Activity

Antibacterial activity was evaluated using agar diffusion method (Kethcum, 1988), Gram - positive bacteria Bacillus and Gram - negative bacteria Morgaella Morgani were cultivated in nutrient agar on petri dishes. The test solution was prepared by dissolving (10 mg) of the tested substances in DMSO (1 mL). A6 mm diameter filter discs were socked in the tested solutions. After 24 h cultivation at 37 °C, diameter of zones of inhibition was determined. DMSO was inactive under applied conditions.

Results and Discussion

All the metal complexes are quite stable in dry air and insoluble in common organic solvents but soluble in DMF and DMSO. The elemental analysis shows (2:2) (Cu:L) molar ratio for [Cu2 Ln2] and (2:2:4) (Cu: Ln: py) molar ratio for [Cu2 Ln2 (py)4]. Some physical properties of ligands and their complexes are listed (Table 1.). The molar conductance in (10-3) M DMSO solution of complexes are in the range (16.0-20.4) ohm-1 cm2 mol-1, indicating a non electrolytic nature of the complexes (Gerry, 1971).

Infrared Spectra

The IR Spectrum of the free ligands was studied and assigned on the bases of careful comparison of the complex spectra with that of the free legends, (Table 2). The IR Spectrum of the ligand show characteristic band at (3465, 3416, and 3498) cm-1 attributed to the phenolic hydroxyl group in H2L1 H2L2 and H2L3 respectively (Alias et al., 2014). The absence of this band in the spectra of the complexes indicates the coordination of phenolic oxygen to the metal ion after deprotonation (Pethe et al., 2017). This is further supported by the shifting of ν (C-O) phenolic band to lowers frequency (1240-1260) cm-1 in the spectra of all complexes (Nagajothi et al., 2013). The IR spectrum of ligands show band at (1612, 1583 and 1582) cm-1 due to ν (C=N) stretch. On complexation this band shifted to higher frequency in all complexes by (10 - 34) cm-1 indicating participation of azomethine nitrogen in complexation (Ramesh et al., 1996). The stretching vibration of ν (C=N) bond of pyridine ring was observed at the region (1506-1515) cm-1 in complexes (2,4,6) which indicates the coordination of the nitrogen atom of pyridine ring with the metal ions (Ceraldo et al., 2011). Some new bands apper in the spectra of the complexes which include of the stretching vibrations of ν (M-N) and ν (M-O). These bands apper in the ranges (425-463) cm-1 and (491-429) cm-1 respectively (Pathan et al., 2012). The I.R Spectra of ligands H2L2, H2L3 and complexes (3, 5) had been shown Fig. 1 and 2.
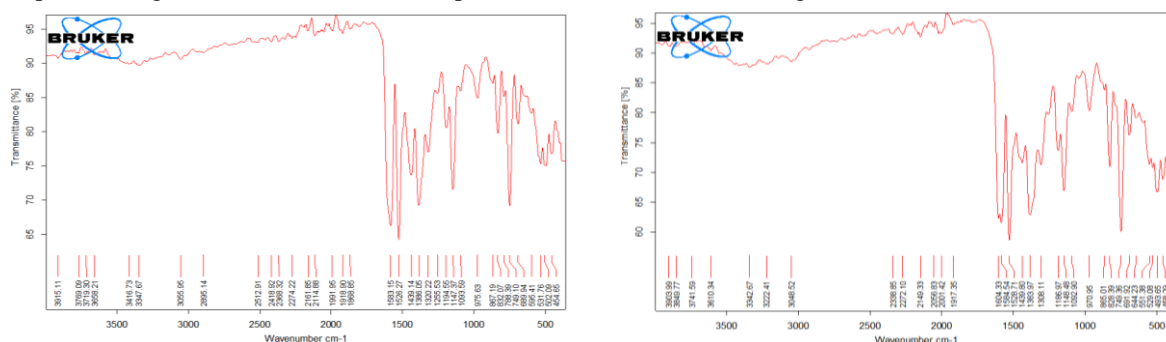
Fig (1) I.R spectra of (H_2L^2) and complex (3)
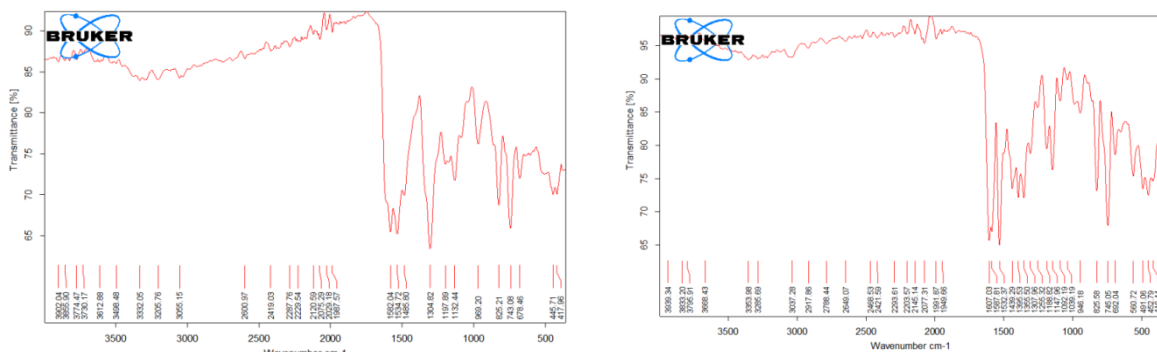
Fig (2) I.R spectra of (H_2L^3) and complex (5)

The magnetic moments and electronic spectra data at 25°C of the ligands and their complexes are listed (Table 3). The electronic spectra of the ligands H2L1, H2L2 and H2L3 in DMSO solution show intense bands at (37037–38167) cm-1 and (28985-31948) cm-1 attributed to benzene $\pi\rightarrow\pi^*$ and $n \rightarrow \pi^*$ transition of the non-bonding electrons present on the nitrogen of the acomethine group respectively, these transitions are also found in the spectra of the complexes but they are shifted to confirmed the coordination of the ligand to the metalion (Elmali et al 2005). New bands in spectra of all complexes at range (26221–38167) cm-1 may be associated with the charge transfer transition (Aranha et al 2016).

The obtained magnetic moment values of Cu (II) complexes (1-6) has been found in the range (1.83-2-11) B.M, which indicate the presence of one unpaired electron of for Cu (II). The electroic. spectra of Cu (II) complexes (1,3,5) showed a broad band at (10427-10686) cm-1 attributed to 2T2→ 2E transition which is comparable with complexes having a tetrahedral structure (Turan et al., 2009) while complexes (2, 4, 6) showed a broad absorption band at (14816 15157) cm-1arises due to d-d transition 2Eg →2T2g suggest that the Cu (II) ion exhibits an octahedral geometry (Jayaseelan et al., 2010).

^{1}H-NMR Spectra of H₂L[1] and H₂L[2] : The H-NMR spectra of free ligands to at room temperature in DMSO-d6 shows the following signals (Garces et al., 1988) For H2L1. δ = 12.95 ppm (s, 2H, phenolic) δ = (6.89 - 8.55) ppm (m, 14 H, Aromatic) δ =9.03 ppm (s, 2H, a zomethine). For H2L2 .   δ =9.71 (s, 2H, phendic), δ =(7.06-8.01) ppm (m, 17H, Aromatic), δ =8. 44ppm (s, 2H, azomethine), δ = 3.79 ppm (s, 3H, O-CH3).

(a)   **(b)**
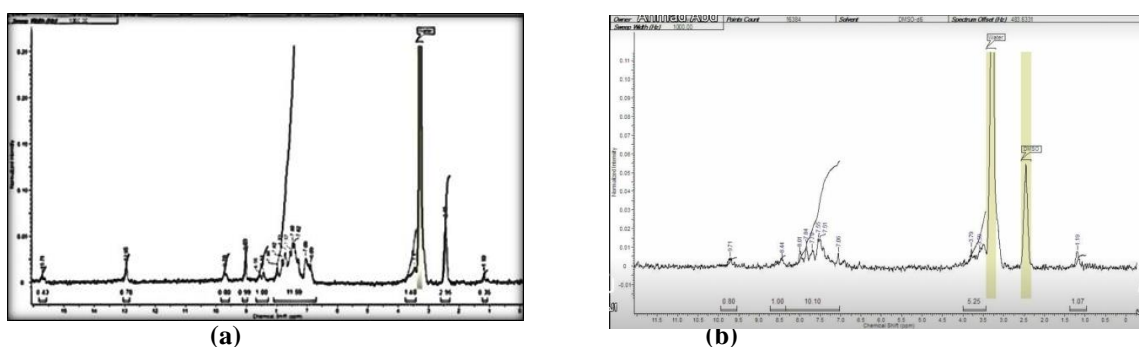
Fig. 3: ^{1}H-NMR Spectra of (a) H_2L^1; (b) H_2L^2

Antibacterial Activity

The tested compounds were screened in vitro of their antibacterial activity against Gram-negative and Gram-positive (Morganella Morgani, Bacillus) bacteria, the antibacterial rusults are given in (Table 4) compared with those of standard drug (Ciprofloxacin). The results evidently. show that all tested complexes were active against the Gram-positive and Gram-negative bacteria a generally the activity order against (Bacillus) of the synthesized compounds is as follows:

$[Cu_2L^3_2 > Cu_2L^2_2 (Py)_4] = [Cu_2L^2_2 (Py)_4] > [Cu_2L^1_2] > [Cu_2L^3_2] > [Cu_2L^3_2] > [Cu_2L^2_2 (Py)_4] > [Cu_2L^3_2] > [Cu_2L^2_2]$
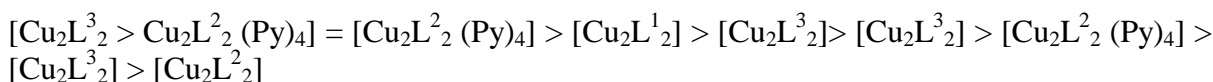
While the activity order against (Morganella *Morgani*) of the synthesized compounds is as follows:
$[Cu_2L^1_2] > [Cu_2L^1_2 (Py)_4] > [Cu_2L^2_2] = [Cu_2L^3_2 (Py)_4] > [Cu_2L^2_2(Py)_4] = [Cu_2L^3_2] > H_2L^3 > H_2L^1$
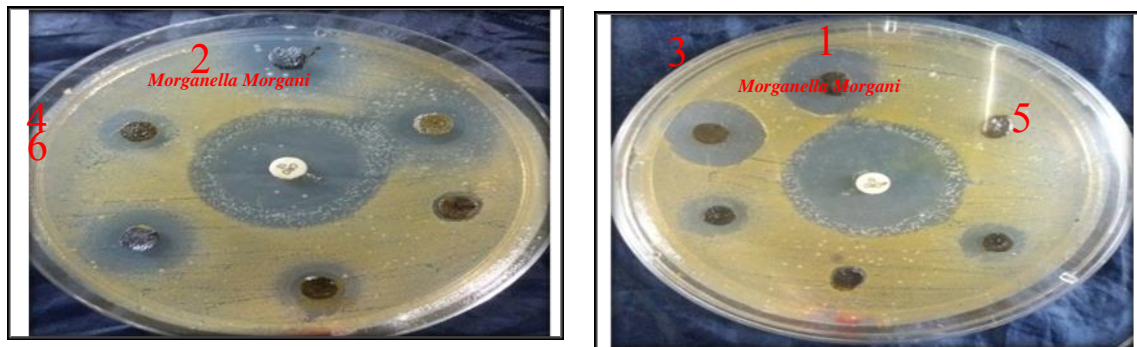
Fig.4 (a): Antibacterial activity of complexes agents gram negative bacteria *Morganella Morgani*
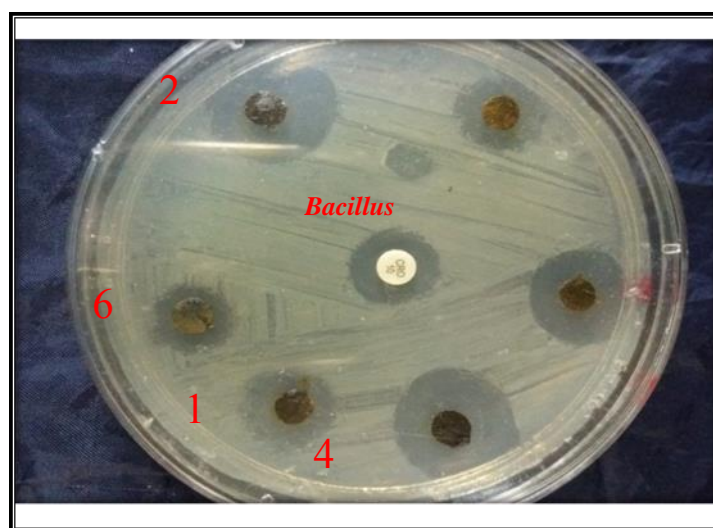
Fig.4 (b): Antibacterial activity of complexes agents gram positive bacteria *Bacillus*

Conclusion

New cu (II) complexes of unsymmetrical brighted tetra dentate Schiff bases ligands H2L1, H2L2 , H2L3 have been prepared and characterized by conventional measurements. The data revealed that all the complexes are dinuclear and have an either tetrahedral or octahedral geometry Fig (4). The ligands act as N2O2 tetra dentate dibasic chelating e ligands coordinated through phenolic oxygen and imine nitrogen atoms. The ligands and their complexes were tested against Gram positive and Gram-negative bacteria which indicate that all complexes are active against this bacteria as compared with standard drug (Ciprofloxaic).
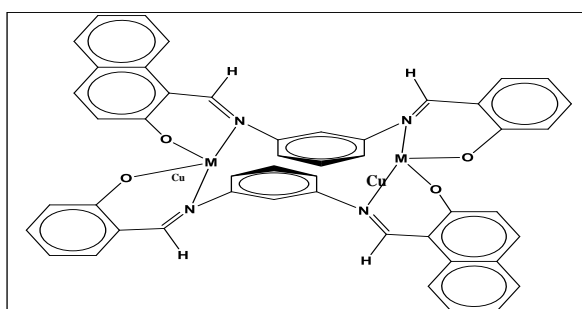
Complex (1)
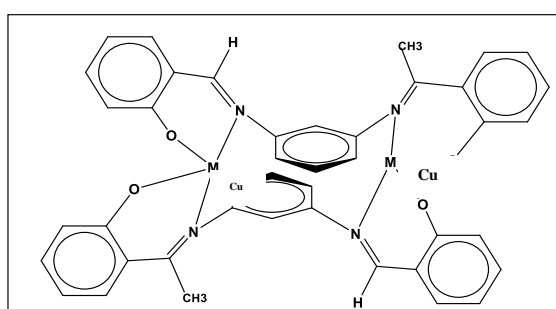
Complex (2)
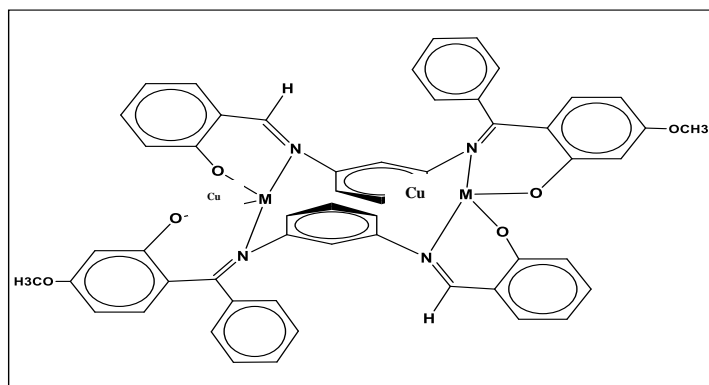
Complex (3)
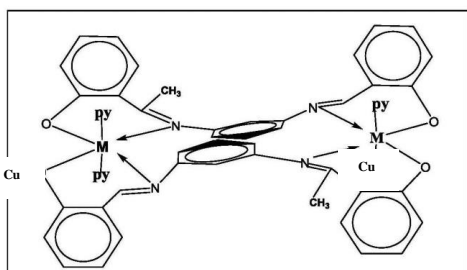
Complex (4)
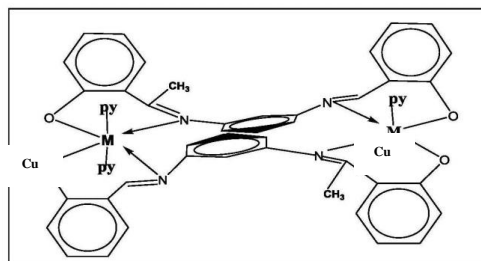
Complex (5)
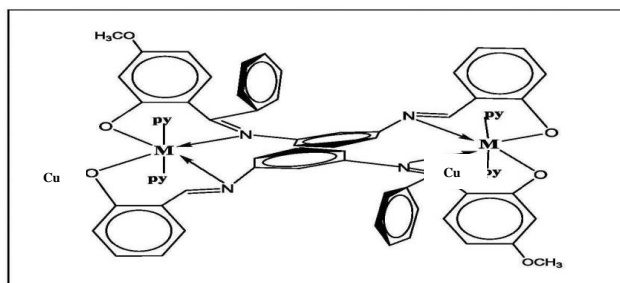
Complex (6)

Fig (5) Suggested Structure of complexes

Table 1.Tthe physical properties and analytical data of the ligands and their complexes

NO.	COMPOUND	COLOUR	m.p ($^{\circ}$C)	Am ohm^{-1} Cm^2 mol^{-1} DMSO	M% Calc (found)	Analysis calc (found) %		
						C%	H%	N%
H_2L^1	$C_{24}H_{18}N_2O_2$	Green Yellow	175	--------	--------	78.67 (77.73)	4.95 (4.78)	7.65 (8.18)
1	$Cu_2 L^1_2$	Brown	185	20.4	14.86 (15.22)	67.42 (68.11)	3.74 (4.12)	6.54 (7.21)
2	$[Cu_2L^1_2 (Py)_4]$	Green	195	19.8	--------	--------	-------	--------
H_2L^2	$C_{21}H_{18}N_2O_2$	Silver	180	-------	--------	76.38 (77.12)	5.45 (5.95)	8.74 (9.12)
3	$Cu_2 L^2_2$	Gray	220	17.0	11.50	67.68	4.77	10.19

						(10.05)	(66.81)	(4.55)	(9.87)
4	$[Cu_2L^2_2 (Py)_4]$	Green	195	17.3		--------	--------	-------	--------
H_2L^3	$C_{27}H_{22} N_2O_2$	Gray	195	--------	--------	76.73	5.21	6.63	
						(77.41)	(5.91)	(7.36)	
5	$Cu_2 L^3_2$	Pale green	290	16.0		13.18	67.30	4.15	5.81
						(14.00)	(68.21)	(4.91)	(6.21)
6	$[Cu_2L^3_2 (Py)_4]$	Brown Green	225	19.4		--------	--------	-------	--------

Table 2. Characteristic Infrared Spectral data (cm-1) of the ligands and their complexes

NO.	v (O-H) cm^{-1}	v (C-O) cm^{-1}	v (C=N) imine v (C=N) py-ring	v (M-O) cm^{-1}	v (M-O) cm^{-1}
H_2L^1	3465	1275	1612		
1		1270	1622	522	463
2		1260	1623 1506	523	458
H_2L^2	3416	1270	1583		
3		1240	1604	529	458
4		1251	1616 1515	496	425
H_2L^3	3498	1265	1582		
5		1255	1602	491	452
6		1245	1616 1506	420	465

Table 3. Magnetic moments and the electronic spectral data of theligands and Cu (II) complexes

No.	Meff (B.M)	Assignment	Band maxima λ (Cm^{-1})	structure
H_2L^1	…….	$n \rightarrow \pi^*,$ $\pi \rightarrow \pi^*$	31446 , 37037	……
1	2.11	$T_2^2 \rightarrow E^2, C.T$	10686 , 27954	Th
2	1.83	$E_g^2 \rightarrow E_{2g}^2, C.T$	15151, 27977	Oh
H_2L^2	……	………	31948, 38167	…….
3	2.09	$T_2^2 \rightarrow E^2, C.T$	10480, 29011	Th
4	1.99	$E_g^2 \rightarrow E_{2g}^2, C.T$	15157, 31152	Oh
H_2L^2	……..	……	28985, 37735	………
5	1.89	$T_2^2 \rightarrow E^2, C.T$	10427, 26221	Th
6	2.09	$E_g^2 \rightarrow E_{2g}^2, C.T$	14826, 26873	oh

Table 4. The antibacterial activity of ligand and their complexes

No.	Compound	Gram (+) bacteria Bacillus (mm)	Gram (-) bacteria Morga.
H_2L^1	$C_{24} H_{18} N_2O_5$	0	3
1	[cu$_2$ L_2^1]	14	22
2	[cu$_2$ L_2^1 (py)$_4$]	20	20
H_2L^2	$C_{21} H_{18} N_2O_5$	0	0
3	[cu$_2$ L_2^2]	7	18
4	[cu$_2$ L_2^2 (py)$_4$]	20	12
H_2L^3	$C_{27} H_{22} N_2O_3$	0	6
5	[cu$_2$ L_2^3]	10	12
6	[cu$_2$ L_2^3 (py)$_4$]	12	18

Inhibition zone diameter (mm) (% inhibition): 6-10 (27-45%); 10-14 (45- 64 %) ; 14-18 (64- 82 %) 18- 22 (82-100%)

References

Alias, M.; Kassum, H.; Shkir, C. (2014). Synthesis, physical characterization and biological evaluation of Schiff base M (II) complexes. J.AAUBAS, 15, 28-34.

Aranha, P.E.; Dosanto, M.P.; Romera, S.; Dockal, E.R. (2016). Polyhedron., Anovel Schiff base derived from the gabapentin drug and Cu(II) complex: synthesis, interaction with DNA/ protein and cytotoxic activity. J. Photo. V., 162, 34-44.

Ceraldo, M.; Menezes, D.C.; Cavalcanti, C.A.; Santos, J.F.; Ferreira, I.P.; Wadrall, M.S. (2011). Synthesis, characterization and biological aspects of Cu (II) dithiocarbamate complexes, [Cu{S2CNR(CH2CH2OH)}2]. J.Mol. Str. 988, 1-8.

Clarke, B.; Clarke, N.; Cunningham, D.; Higgins, T.; McArdle, P.; Cholchuin, M.N.; O'Gara, M. (1998). Transition metal Schiff base complexes as ligands in tin chemistry. Part 7. reaction of organotin (IV) Lewis acids with [ML] [M=Ni, Cu and Zn; H2L=N,N-bis(3-methoxysa licylidend) benzene-1,3-diamine and its-1,4-diamine analog). J. Org. Chem.,559, 55-64.

Elmali, C.T.; Elerman, A.; Svoboda, Y. (2005). Crystal structure and magnetic exchange inter action in a binuclear copper(II) Schiff base complex with a bridging m- phenylenedi amine ligand. Z. Naturforsch, 60b, 143-148.

El-Motaleb, A.; Ramadan, M.; Mohamed, M.; Shaban Y. (2011). Synthesis, Characterization, and tyrosinase biomimetic catalytic activity of Cu(II) complexes with Schiff base ligands derived from a- diketones with 2- methyl-3-amino-(3H)- quinazolin- 4-one. J. Mol. Struct., 1006, 348 -355.

Garces, f. O., King, K. A.; Watts, R.J. (1988). Synthesis, structure, electrochemistry, and photo physics of methyle-substituted phenylpyridine orth -metalated iridium(III) Complexes. J. Ino. Chem. 27(10), 3464 -3471.

Gerry, W.J. (1971). The use of conductivity measurements inorganic solvents for characterization of coordination compounds. J. Coord. Chem. Rev., 7, 8 - 122.

Hernandez -Molina, R.; Mederos, A.; McCleverty, J.A.; Meyer, T.J. (2004). (Eds.), "Compr ehensive Coordination Chemistry II". Elsevier Pergamon, Oxford, 1, 411p.

Hernandez-Molina, R.; Mederos, A.; Gili, P.; Dominguez, S.; Lioret, F.; Cano, J.; Julve, M.; Ruiz Perez, C.; Solans, X. (1997). Dimer species in dimethyl sulfoxide-water (80: 20 wlw) solution of N,N-

bis(salicylideneamine (H2sal-m-phen) and similar Schiff bases with CuII, NII, CoII and ZnII. Crystal structure of [Co2 (sal-m-phen)2]. CHC13. Dalton Transac tions, 1, 4327-4334.

Jayaseelan, P.; Prasad, S.; Vedanayaki, S.; Rajavel, R. (2010). Synthesis, spectral characterization, thermal and antimicrobial studies of new binuclear metal complexes containing tetra dentate Schiff base ligand. Inter. J. Chem. Env. Pharm. Res. 1, 80-88.

Kethcum, P.A. (1988). "Microbiology: Concept and Applications". John-Wiley and Sons. New York, 384 p.

Li, Y.G., Shi, D.H.; Zhu, H.L.; Yan, H.; Ng, S.W. (2015). Synthesis, structure, unease inhibitory, and cytotoxic activities of two complexes with protocatechuic acid derivative and phenanthroline. J. Coord. Chem. 68, 1571- 1582.

Luo, X.F.; Hu, X.; Zho, X.Y.; Goh, S.H.; Li, X.D. (2003). Miscibility and interactions in blends and complexes of poly (4-methyl-5-vinylthiazole) with proton -donating polymers. Polymer., 44(18), 5285-91.

Nagajothi, A.; Kiruthika, A.; Chitra, S.; Parameswari, K. (2013). Fe(III) Complexes with Schiff base ligands: synthesis, characterization, antimicrobial studies. India, Res. J. Chem., 3(2), 35-43.

Osowole, A.A. (2008). Synthesis and characterization of some tetra dentate schiff base complexes and their heteroleptic analogues. J. Chem., 5(1), 130-135.

Pathan, A.H.; Naik, G.N.; Bakale, R.P.; Machakanur, S.S.; Gudasi, K.B. (2012). Ligational behavior of new mononuclearting nooethyl pyruvate schiff base towards 3d metal(II)ions an emphasis on antiproliferative and photo cleavage property. Appl. Organoment. Chem., 26, 148-155.

Pethe, G.B.; Bansod, A.D., Devhade, J.B.; Maldhure, A.K.; Aswar, A.S. (2017). Synthesis, spectral, thermal and biological studies of some unsymmetrical Schiff base metal complexes. India, Res .J. Chem. Sci., 7(1), 8-12.

Prakash, A.; Gangwar, M.P.; Singh, K.K.(2011). Synthesis, spectroscopy and biological studies of Ni(II) complexes with tetradentate schiff base N2O2 donor group. Int. J. Chem. Tech. Res. 3(1), 222-229.

Torayama, H.; Nishide, T.; Asada, H.; Fujiwara, M.; Matsushita, T. (1998). Preparation and characterization of novel cyclic tetranuclear manganese (III) complexes: Mn 4(xsalmphen).(x-salmphen H2=N,N-disubstituted-salicylidene-1,3-diamin-Br)). Pol., 16(21), 3787-3794.

Turan, N.; Sekerci, M. (2009). Synthesis and characterization of Co(II), Ni(II), Cd(II) and Cu(II) complexes of bis- Schiff base obtained from 1,8-diaminonaphthalene. J. Chem. Soc., 31, 564 - 568.

Author Information

Moza M. Al-Jiboury
University of Mosul
Department of Chemistry, College of Science
Mosul/Iraq
Contact E-mail: Mmohammedsaleh9@gmail.com

Khansaa Sh. Al-Nama
University of Mosul
Department of Chemistry, College of Science
Mosul/Iraq

IConTES 2019: International Conference on Technology, Engineering and Science

Efficiency of Silver Nanoparticles against Bacterial Contaminants Isolated from Water in Basra

Hassanein HASSOON
University of Baghdad

Mais AHMED
University of Baghdad

Yasir QADDOORI
University of Baghdad

Abstract: The increased rates of morbidity and mortality due to contamination with pathological microorganisms that continuously develop antibiotic resistance has re-emphasized the need for alternative antimicrobial methodologies. Previous evidence showed such activity of *Punica* nanoparticles. The sources of microorganisms and plants are playing a major role in reduction of metallic nanoparticles such as silver, as it emerges as an eco-friendly and exciting approach in nanotechnology. The purpose of the present work is to investigate the potential antibacterial efficiency of silver nanoparticles obtained from pomegranate peel. Silver *Punica* nanoparticles with a size of 42 nm were prepared. The synthetized nanoparticles were analyzed by different techniques including UV-VisSpectrophotometer, atomic force microscopy and transmission electron Microscope. The potential of the silver *Punica* nanoparticles for water disinfection was examined on *Enterobacter* spp. isolated from Basra river. The results have shown that silver nanoparticles display a high antibacterial activity against bacterial contamination in the water samples of Basra river. In conclusion, nanotechnology provides an alternative solution to clean germs in water.

Keywords: Nanoparticles*, Punica grantum,* Antibacterial

Introduction

Waterborne diseases are major drive of mortality in the present world, especially in less developed communities. Data from international agencies indicates that a minimum of 15% of the world population do not have access to healthy water (Bohn et al., 2009). As a result, an annual mortality of approximately 760.000 deaths in children under the 5 years of age was recorded (Griffiths, 2016), which is an amelioration as compared to 2.2 million deaths majorly in children during 1998 due to diarrhea (Prüss-Üstün & Corvalän, 2007). Due to this un-negligible significance of water contamination, measures of microbial control were strengthened and permitted levels of drinking water contamination with coliforms/ *E. coli* should not exceed 0/100ml (Barrell, Hunter, & Nichols, 2000).

To avoid environmental contamination with wastewater, providing a suitable strategy to remove these contaminants could be of great importance in maintaining a healthy environment. For efficient removal of toxicants from water sources, different physiochemical mechanisms have been extensively used, including precipitation, adsorption, ion exchange, reverse osmosis, treatments, membrane filtration, flotation, oxidation and biosorption (Amin, Alazba, & Manzoor, 2014; Rasalingam, Peng, & Koodali, 2014).

The use of nanoparticles is among currently interesting applications for water-detoxification purposes, mainly due to their remarkably small size of 1 to 100nm, and hence their larger surface area per unit mass. Nanomaterials commonly exert remarkably improved physicochemical and biological characteristics in

comparison with macro-sized particles (Morose, 2010). Microorganisms are of major significance to environmental systems as they form the ground floor for the provision of various functions such as primary productivity, nutrient cycling and waste decomposition, therefore a comprehension of nanoparticles toxicity effects on microorganisms is a matter of concern, which requires an estimation of these particles influence on the environment (Klaine et al., 2008).

In order to get an environmentally friendly nanotechnology, delicate experimental design should be performed in order to provide best conditions that take into consideration nanoparticle physical and chemical features such as size, shape and stability. Such conditions involve dynamics of reaction between metal ions and the used reducing agents, as well as the adsorption reactions between the stabilizing agents and the nanoparticles(Guzmán, Taylor, & Banfield, 2006) .

Punica granatum is a fruit whose trees are extensively cultivated around the Mediterranean areas. Previous reports have indicated the presence of several active compounds species (e.g. flavonoids and anthocyanidins) isolated from this plant with powerful anti-oxidant activity (Abdelmonem & Amin, 2014).

Pomegranate peel, the most essential constituent of the plant, contains several phenolic compounds, gallic acid and other fatty acids, flavonols. flavones and flavanones. Recent research has focused on finding alternative environmentally-safe antimicrobial approaches, among which the employment of plant extracts in the biosynthesis of nanoparticles. Particles produced by plant extracts have been shown to ensure higher level of biocompatibility as compared to those chemically synthesized (GnanaJobitha, Shanmugam, Gurusamy, & Kannan, 2013).

Methods

Samples Collection

Three water samples were collected from river, tap water and RO (reverse osmosis installation) units. Water was sampled from different places within the same region of Basra city (Iraq) during the period from October to December 2019. For sampling, sterile bottles and caps were first rinsed three times with the source water and then filled to 1-2 inches below the top of the bottle aseptically in sterile 500 mL Duran Schott glass bottles from different sampling points by directly dipping the bottles into the surface of the water.

Cultivation of Bacteria

Samples were processed as previously described (Forbes, Sahm, Weissfeld, & Bailey, 2007). Briefly, 10ml of water sample was diluted in 90ml sterile enrichment peptone water and incubated at 37°C for 18- 24 hrs. Using a sterile standard loop (1ml), a loopful of the incubated culture was then successively cultured on mannitol salt agar and MacConkey agar plates to differentiate between Gve+ and Gve- bacteria. Following incubation at 37°C for 24 hours, the bacteria were identified by Gram's stain and standard biochemical tests.

Antibiotic Sensitivity Test

Antibiotics and antimicrobial susceptibility tests were performed by Bauer-Kirby method (Hoelzer et al., 2011) for Both Gve+ and Gve- bacteria detected by antibiotic disk.

Molecular assay

DNA extraction

Genomic DNA was extracted from the detected bacterial isolates according to the protocol of Wizard Genomic DNA Purification Kit, Promega. Quantus Florometer was used to detect the concentration of extracted DNA.

Primers Selection

Sets of primers 27F (AGAGTTTGATCTTGGCTCAG) and 1492R (TACGGTTACCTTGTTACGACTT) were used for amplification of 16s rRNA and so identification of bacteria at gene level (Srinivasan et al., 2015).

Preparations of *Punica granatum* peel extract

Punica granatum obtained from local Baghdad markets was washed, the peel was scrapped and brought to room temperature (24℃) for two days. Thereafter, 40 grams of dried *Punica granatum* peel powder was soaked in 300 ml of deionized water. In this process, extraction was performed by incubating the mixture-containing flask on an orbital shaker (Genex. Cat.No. 60HZ, USA) at room temperature with agitating at 100 rpm for 48 hours. After the extraction process was accomplished, the aqueous solution was filtrated twice by using Whatman filter paper No.1 (Whatman. Cat.No. Q/FML61-2004, England) (Jurenka, 2008)(11).

Preparation of 1mM Silver Nitrate

Silver nitrate was purchased from Lobachemie and a weight of 0.0169gm was dissolved in 100mL of distilled water in an amber colored bottle.

Synthesis of Silver nanoparticles under Room temperature

9 ml of 2mM silver nitrate solution was prepared. 1 ml of freshly prepared pomegranate peel extract was added separately to the silver nitrate solution. The bio-reduction of AgNO3 ions occurred within 3hrs (figure1). Color of peel extract solution has slowly changed from gray to brown indicating the formation of silver nanoparticles (figure1) (G. Gnana Jobitha, S. Rajeshkumar, G. Annadurai, & C. Kannan, 2013).

Figure 1. Preparation of *Punica granatum* peel extract – nanosilver

Preparation of Silver Nitrate

Silver nitrate was brought from Lobachemie. Weigh 8.49 gm of silver nitrate and dissolve in 1L of distilled water to obtain   three concentration 50 mM and prepration another concentration (25, and 75) mM in amber coloured bottle.

Transmission Electron Microscope (TEM Analysis)

For transmission electron microscopy (TEM) imaging, the AgNP suspensions (approximately 7 µL for each sample) in the absence or in the presence of anesthetics were deposited on the specimen grids and adsorbed for 1 minute. The excess solution was removed with filter paper, and the samples were air-dried (Sadowski, 2010).

Optical, Size and Morphological Characterization of Silver nanoparticles

Surface plasmon resonance of the samples was studied with a UV-VisSpectrophotometer (Cary 300 Conc spectrophotometer) at wavelength range of 250-600 nm with a resolution of 1 nm (Abimbola, Kolawole, Ajanaku, & Adeyemi, 2019) .The size of nanoparticles was examined with Atomic Force Field Microscopy (AFM). Preparation of the sample was performed through mounting one drop of the colloidal solution of the nanometal on a carbon-coated copper grid, with complete dryness being achieved by using the vacuum desiccators. Images of atomic force microscopy (AFM) were taken on the nanostructured film of AgNPs obtained by vertical adsorption from the colloid solution on glass plates for 5 minutes and dried out in air (Mocanu et al., 2013).

Well Diffusion Method

Well diffusion method (WDA) then carried out to test the antimicrobial activity of the synthetized sliver nanoparticles (Balouiri, Sadiki, & Ibnsouda, 2016; Charannya et al., 2018).100μL of the suspension was spread on the test plate (Muller Hinton Agar). And put(10 μL) of the essential oils and placed on well in agar. Plates were incubated at 37° C for 24 hours and the zone of inhibition was measured. The experiment was performed in triplicate and the average diameter of inhibition was calculated.

Results and Discussion

Isolation and identification of Bacteria

Isolation and Identification of Gram positive: (Staphylococcus. epidermidis, Staphylococcus. aureus) and Enterobacter spp.

The microscopic examination of the cultured bacteria showed that gram positive cocci appear as single cells, pairs, tetrads and chains. The macroscopic examination of the isolates on Mannitol Salt Agar showed that they have the ability to ferment mannitol and turn the color of medium from red to yellow. The isolates were on MacConkey agar as a presumptive *S. aureus and S. epidermidis* isolates (Figure2) and Enterobacter spp as pale colonies.

The isolates on blood agar showed yellow-gray colonies which are 4-3mm in diameter on the zones of β-hemolysis (Figure3).The result showed (Figure4) *S. aureus* colony on milke agare yellow while *S. aureus* appeared white color this medium using differential between *staphylococcus* spp.
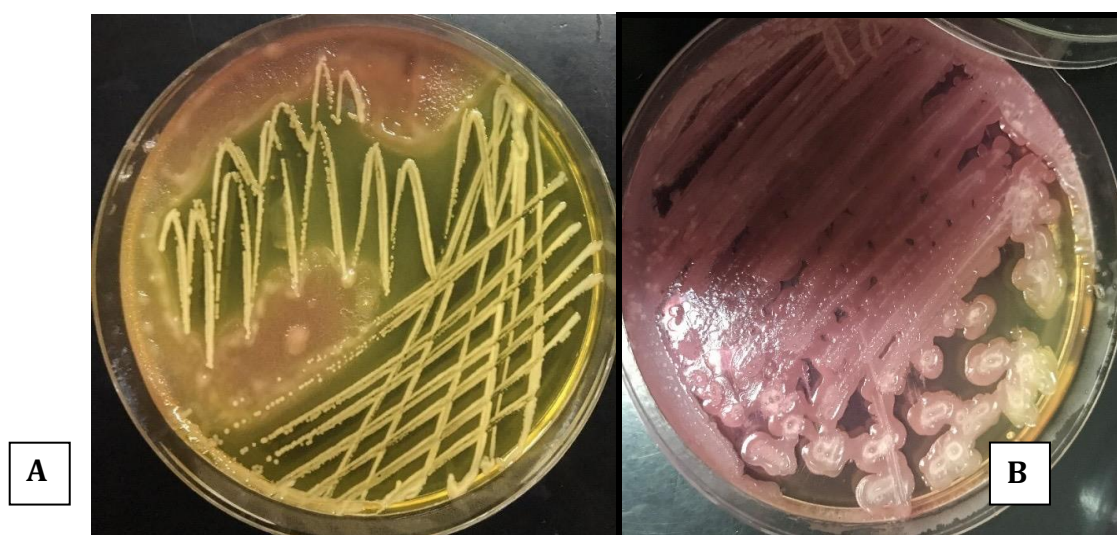
Figure 2. A presumptive of **A**: *S. aureus* **B:** *S. epidermidisS. epidermidis* on mannitol salt agar **C**:*Enterobacter* spp

Figure 3. A presumptive of *S. aureus* on blood Agar

Figure 4. A presumptiveof **A**: *S. aureus* **B**: *S. epidermidis* on Milk agar

Isolation and Identification of Gram Negative Bacteria

The macroscopic examination of presumptive (*E. coli,* and *Klebsiella* spp) isolates gave large flat colonies that produced zones of -haemolysis with odor on the blood agar and pale colonies on MacConkey agar (lactose fermenting and non fermenting).
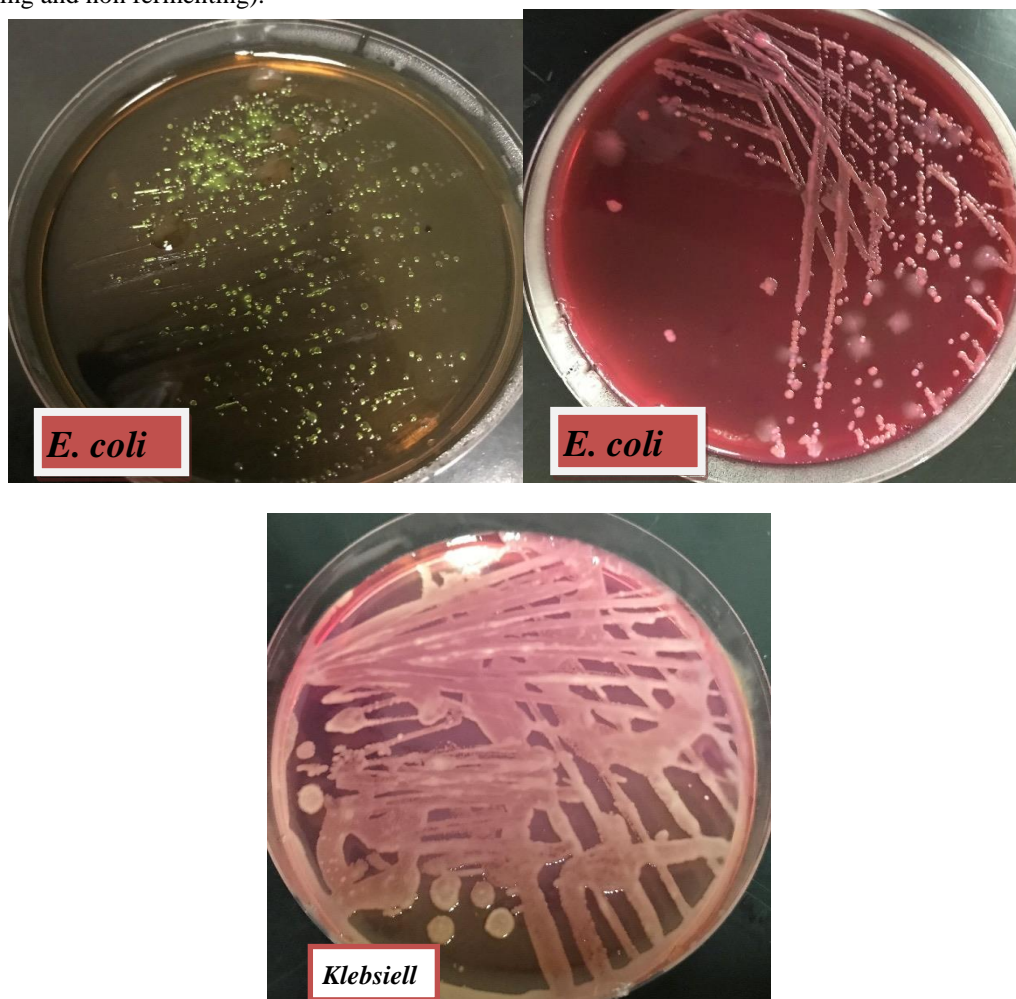
Figure 5. Bacterial isolation from Water sample *E. coli* on MacConkey and Eosin methicillin blue agar , while *Klebsiell* on MacConkey agar for 24hrs at 37°C.

Antibiotic susceptibility test (AST)

Resistance patterns for the isolated bacteria against different antibiotics demonstrated that the Gr-ve isolates had the highest resistance to Ampicillin, Amikacin and Ceftazidim, whereas for Gr+ve isolates they were Methicillin, and Gentamycin, with sensitivity was shown to Vancomycin (figure 6).
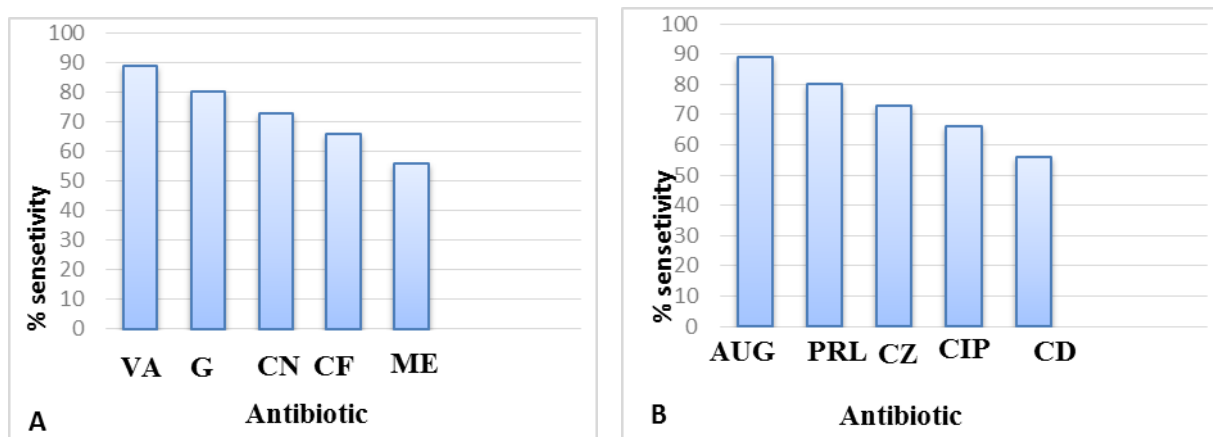
Figure 6. Antibiotic susceptibility test of **A**: Gram positive. **B**: Gram negative

Genomic DNA Extraction

In this study, the genomic DNA of bacterial isolate was successfully extracted of Gram positive and the extracted DNA had an appropriate quality to perform PCR (10 ng/µl). 16S rDNA was amplified by PCR using specific primers that gave a distinct amplicon pattern with a size of 1500 bp when analyzed by gel electrophoresis (Figure7).
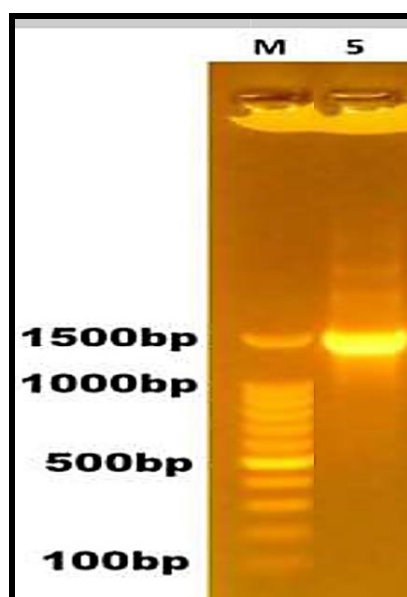
Figure 7. PCR product the band size 1500bp. The product was tested by electrophoresis on 2% agarose at 5 volt/cm^2. 1x TBE buffer for 1:30 hours. N: DNA ladder (100). *Enterobacter* spp

Study of Silver Nanoparticles compounds characterization

Spectral Properties of the Silver Nanoparticles

The strong interaction of the silver nanoparticles with light occurs because the conduction electrons on the metal surface undergo a collective oscillation when excited by light at specific wavelengths Surface .Plasmon resonance of the samples was studied with a UV-Vis Spectrophotometer (Figure 8).
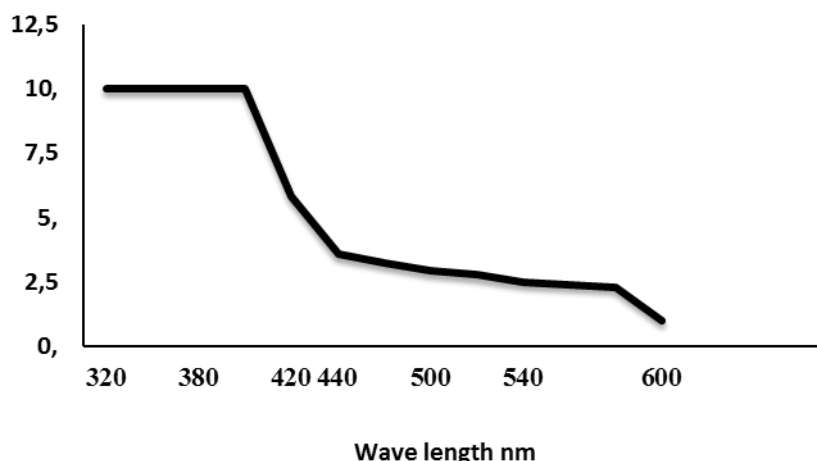
Figure 8. Absorption spectra of -silver nanoparticles

Atomic Force Electron Microscopy (AFM)

The AFM micrograph obtained for the silver nanoparticles (Figure 9) indicates the surface roughness changes as identified by the root mean square (Rp) values. For the sample, the roughness value was 56 nm and the section analysis of the sample's grain size resulted in a value of 42 nm.
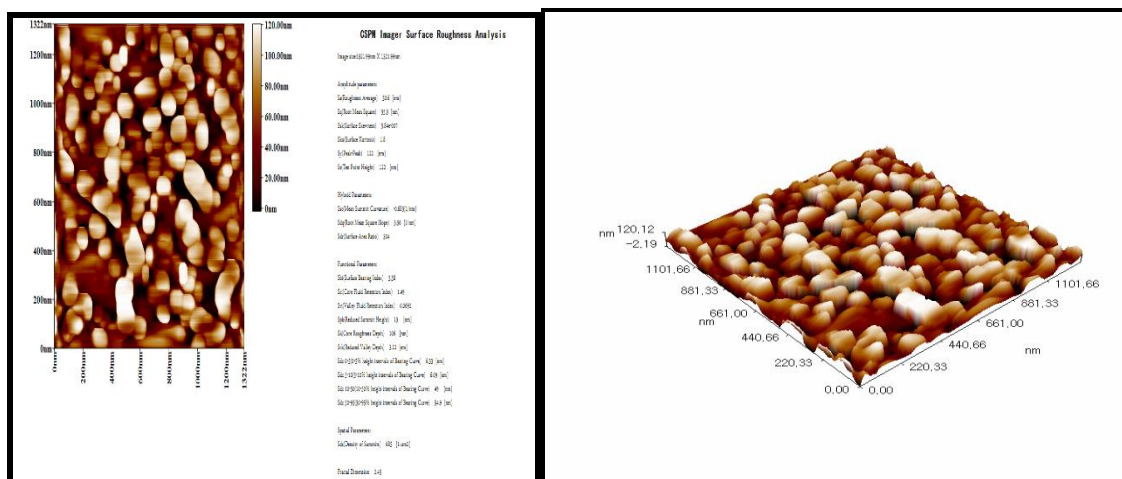
Figure 9. AFM for -silver nanoparticles

Transmission ElectronMicroscopy analysis (TEM)of silver nanoparticles:

TEM micrographs for Silver *Punica* nanoparticles was shown in Figure (10), the diameter of nanoparticles was measured to be 42 nm.show figure (10-A).

The figure showed *Enterobacter* spp before treatment appeared as cocci and had regular arrangement of cell wall figure (10-B), while after treatment with Silver *Punica* nanoparticles the bacteria swelled and had irregular cell wall Figure (10-C).
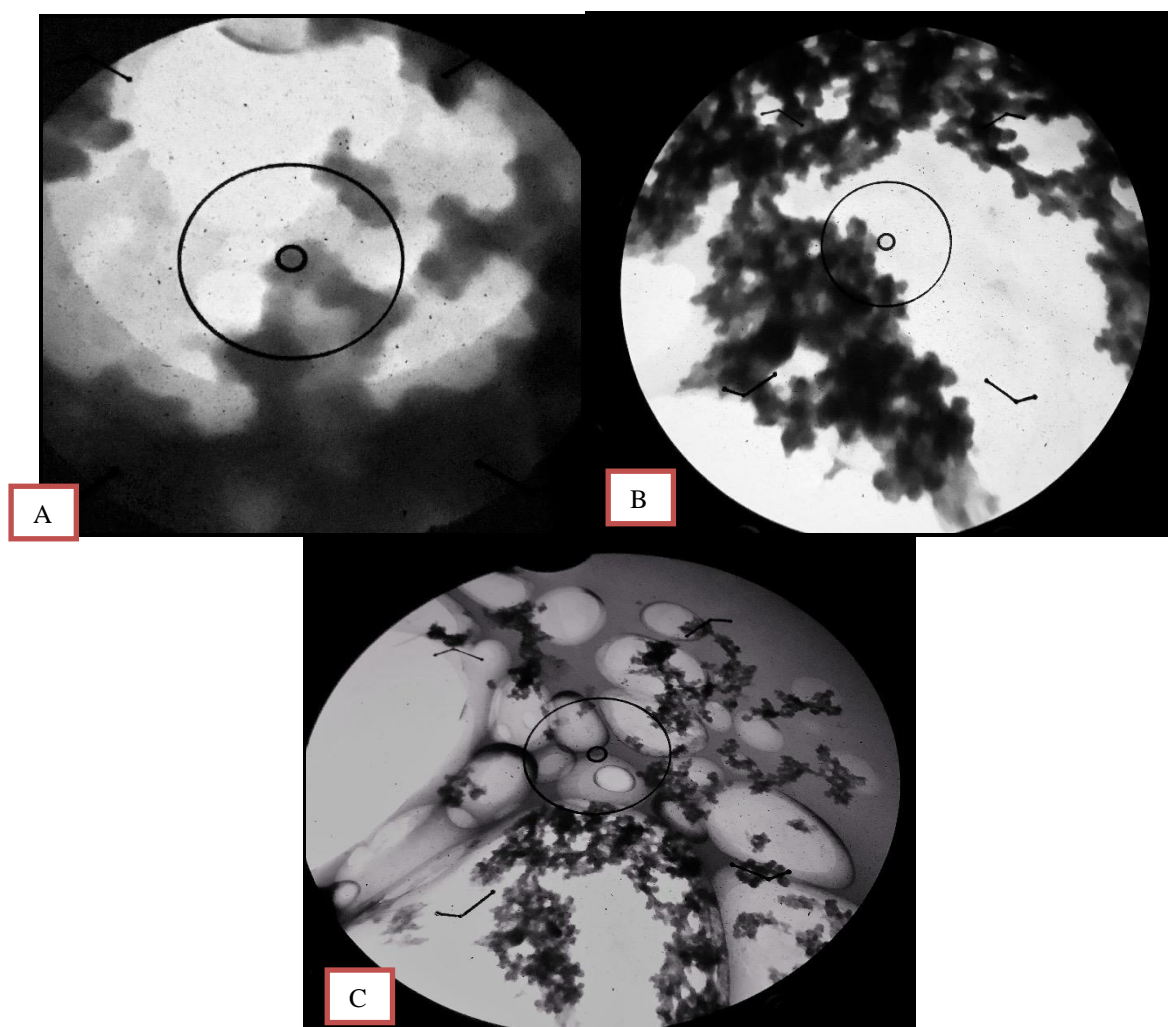
Figure 10. TEM of **A**: Sliver nanopartical **B**: *Enterobacter* spp before treatment -Silver Nanoparticles
C: *Enterobacter* spp after treatmentwith Nisin-Silver Nanoparticles

In the present study, we have successfully used the peel (exocarp and mesocarp) as well as the Peel pomegranates as a source to green-senthesize silver nanoparticles from silver nitrate.

We have also investigated the antimicrobial potential for these particles using various Gr-ve and Gr+ve bacteria as targets (Figure11). The results showed that **S.aureus** and *Enterobacter* spp were sensitive for the extractions of pomegranate as compared to the antibiotic zones nearer to standard antibiotic.

The present study concludes the obvious potential of nanoparticles synthesized using pomegranate to be invested as alternative antimicrobial agents against waterborne microorganisms.

Figure 11. Antibacterial activity of Sliver nanopa pomegranate nanoparticles against *Enterobacter* pp by WDA for 24-48 hrs at 37°C on Muller Hinton agar 1: Sliver nanoparticles 2: Sliver pomegranate nanoparticles

The present results shows the antimicrobial activities as compared with a previous study (Haniff Nisha, Tamileswari, & Jesurani, 2015), although with different microorganisms. In that study, antibiotic zones for peel demonstrated 16mm inhibition for Pseudomonas and resistance for Proteus. By using the seed extracts, they obtained the antibiotic zones against Pseudomonas and Proteus as 13 mm and resistant respectively, while using the leaf extracts (Haniff et al., 2015).

Conclusion

Introducing nanotechnology to various health fields has brought clear advantages that can be observed in the areas of nano-medicine and alternative medicine. In line with this, the present work could provide the evidence that pomegranate can be successfully used as a source of silver nanoparticles which in turn showed a remarkable antimicrobial potential against different bacteria. This work provides the basis for further investigations on the bio-medical activities of those pomegranate-synthesized silver nanoparticles.

References

Abdelmonem, A. M., & Amin, R. (2014). Rapid Green Synthesis of Metal Nanoparticles using Pomegranate Polyphenols. *International Journal of Sciences: Basic and Applied Research (IJSBAR)*.

Abimbola, A., Kolawole, A., Ajanaku, O., & Adeyemi, J. (2019). Combined green synthesis and theoretical study of Ag / Co nanoparticles from biomass materials. *Applied Physics A*, 1–7. https://doi.org/10.1007/s00339-019-2931-z

Amin, M. T., Alazba, A. A., & Manzoor, U. (2014). A review of removal of pollutants from water/wastewater using different types of nanomaterials. *Advances in Materials Science and Engineering*, *2014*. https://doi.org/10.1155/2014/825910

Balouiri, M., Sadiki, M., & Ibnsouda, S. K. (2016). Methods for in vitro evaluating antimicrobial activity: A review. *Journal of Pharmaceutical Analysis*, *6*(2), 71–79. https://doi.org/https://doi.org/10.1016/j.jpha.2015.11.005

Barrell, R. A., Hunter, P. R., & Nichols, G. (2000). Microbiological standards for water and their relationship to health risk. *Communicable Disease and Public Health / PHLS*.

Bohn, P. W., Elimelech, M., Georgiadis, J. G., Mariñas, B. J., Mayes, A. M., & Mayes, A. M. (2009). Science and technology for water purification in the coming decades. *Nanoscience and Technology: A Collection of Reviews from Nature Journals*, (March), 337–346. https://doi.org/10.1142/9789814287005_0035

Charannya, S., Duraivel, D., Padminee, K., Poorni, S., Nishanthine, C., & Srinivasan, M. R. (2018). Comparative Evaluation of Antimicrobial Efficacy of Silver Nanoparticles and 2% Chlorhexidine Gluconate When Used Alone and in Combination Assessed Using Agar Diffusion Method: An In vitro Study. *Contemporary Clinical Dentistry*, *9*(Suppl 2), S204–S209. https://doi.org/10.4103/ccd.ccd_869_17

Forbes, B. A., Sahm, D. F., Weissfeld, A. S., & Bailey, W. R. (2007). *Bailey & Scott's diagnostic microbiology*.

St. Louis, Mo.: Elsevier Mosby.

G. Gnana Jobitha, S. Rajeshkumar, G. Annadurai, & C. Kannan. (2013). Preparation and characterization of fruit-mediated silver nanoparticles using pomegranate extract and assessment of its antimicrobial activities. *Journal of Environmental Nanotechnology*, *3*, J.Environ. Nanotechnol., Volume 2, No. 1 (2013) pp. https://doi.org/10.13074/jent.2013.02.121023

GnanaJobitha, G., Shanmugam, R., Gurusamy, A., & Kannan, C. (2013). Preparation and Characterization of Fruit-Mediated Silver Nanoparticles using Pomegranate Extract and Assessment of its Antimicrobial Activities. *Journal of Environmental Nanotechnology*, *2*, 4–10.

Griffiths, J. K. (2016). Waterborne Diseases. In *International Encyclopedia of Public Health* (Second Edi, Vol. 7). https://doi.org/10.1016/B978-0-12-803678-5.00490-2

Guzmán, K. A. D., Taylor, M. R., & Banfield, J. F. (2006). Environmental risks of nanotechnology: National nanotechnology initiative funding, 2000-2004. *Environmental Science and Technology*, *40*(5), 1401–1407. https://doi.org/10.1021/es0515708

Haniff, M., Tamileswari, R., Jesurani, S., Samikannu, K., Hashim, M., Catherine, S., & Alexander, P. (2015). *GREEN SYNTHESIS OF SILVER NANOPARTICLES FROM POMEGRANATE (PUNICAGRANATUM) LEAVES AND ANALYSIS OF ANTI-BACTERIAL ACTIVITY.*

Haniff Nisha, M., Tamileswari, R., & Jesurani, S. (2015). Analysis of Anti-Bacterial Activity of Silver Nanoparticles from Pomegranate (Punicagranatum) Seed and Peel Extracts. *International Journal of Engineering Research And*, *V4*. https://doi.org/10.17577/IJERTV4IS041104

Hoelzer, K., Cummings, K. J., Warnick, L. D., Schukken, Y. H., Siler, J. D., Grohn, Y. T., … Wiedmann, M. (2011). Agar disk diffusion and automated microbroth dilution produce similar antimicrobial susceptibility testing results for Salmonella serotypes Newport, Typhimurium, and 4,5,12:i-, but differ in economic cost. *Foodborne Pathogens and Disease*, *8*(12), 1281–1288. https://doi.org/10.1089/fpd.2011.0933

Jurenka, J. S. (2008). Therapeutic applications of pomegranate (Punica granatum L.): a review. *Alternative Medicine Review : A Journal of Clinical Therapeutic*, *13*(2), 128–144.

Klaine, S. J., Alvarez, P. J. J., Batley, G. E., Fernandes, T. F., Handy, R. D., Lyon, D. Y., … Lead, J. R. (2008). Nanomaterials in the environment: Behavior, fate, bioavailability, and effects. *Environmental Toxicology and Chemistry*. https://doi.org/10.1897/08-090.1

Mocanu, A., Pasca, R. D., Tomoaia, G., Garbo, C., Frangopol, P. T., Horovitz, O., & Tomoaia-Cotisel, M. (2013). New procedure to synthesize silver nanoparticles and their interaction with local anesthetics. *International Journal of Nanomedicine*, *8*, 3867–3874. https://doi.org/10.2147/IJN.S51063

Morose, G. (2010). The 5 principles of "Design for Safer Nanotechnology." *Journal of Cleaner Production*, *18*(3), 285–289. https://doi.org/10.1016/j.jclepro.2009.10.001

Prüss-Üstün, A., & Corvalän, C. (2007). Preventing disease through healthy environments: Towards an estimate of the environmental burden of disease. *Engenharia Sanitaria e Ambiental*, *12*(2), 115–116.

Rasalingam, S., Peng, R., & Koodali, R. T. (2014). Removal of hazardous pollutants from wastewaters: Applications of TiO 2-SiO2 mixed oxide materials. *Journal of Nanomaterials*, *2014*. https://doi.org/10.1155/2014/617405

Sadowski, Z. (2010). Biosynthesis and Application of Silver and Gold Nanoparticles. In *Silver Nanoparticles* (pp. 257–277). https://doi.org/10.5772/8508

Srinivasan, R., Karaoz, U., Volegova, M., MacKichan, J., Kato-Maeda, M., Miller, S., … Lynch, S. V. (2015). Use of 16S rRNA gene for identification of a broad range of clinically relevant bacterial pathogens. *PloS One*, *10*(2), e0117617. https://doi.org/10.1371/journal.pone.0117617

Author Information

Hassanein Hassoon
Department of Biology, College of Science,
University of Baghdad, Baghdad 10071, Iraq
Contact E-mail:hassanainabbood@yahoo.com

Mais Ahmed
Department of Biology, College of Science,
University of Baghdad, Baghdad 10071, Iraq

Yasir Qaddoori
Department of Biology, College of Science,
University of Baghdad, Baghdad 10071, Iraq

Raghad Mohammed
Department of Biology, College of Science,
University of Baghdad, Baghdad 10071, Iraq

The Effect of the Friction Pressure on the Friction Welding of AZ91 and Fe₃Al Alloys

Osman TORUN
Kocatepe University

Ibrahim CELIKYUREK
Osmangazi University

Abstract: In this study, Fe₃Al and AZ91 magnesium alloys were welded by friction welding method. The samples were machined to a cylindrical form having a diameter of 8 mm and 40 mm in length. Friction welding processes were carried out for 20, 40 and 60 MPa friction pressures under a friction time 12 s, 100 MPa forging pressure, 10 s forging time and 1000 rmp rotational speed. A continuous drive friction welding was used for friction welding process. After welding, the microstructures of welding interfaces of the welded samples were examined with optical microscopy and scanning electron microscopy (SEM). The optical microscopy and SEM investigations were revealed that the welding interfaces of the friction welded of AZ91 magnesium and Fe₃Al alloys have a smooth morphology without any crack or pore. Diffusion zone was occurred in the interfaces of the welded samples. The mechanical properties of welding interfaces were determined using a specially designed shear test apparatus. The samples inserted in the apparatus were cut on the universal tension-compression testing machine. The hardness values were measured from the center of the welding interface to both sides. The micro hardness measurements of the welding interfaces showed that the hardness values differ slightly at welding interface.

Keywords: Friction welding, AZ91 Magnesium alloy, Fe₃Al, Hardness

Introduction

Magnesium alloys have attracted much interest in academic studies, space, automobile and electronics industries in recent years due to its low density, dimensional stability, good machinability and low casting cost. In order to expand the use of these alloys, welding with other materials is of great importance (Sun et al. 2004, Fernandus et al. 2011, Elthalabawy et al. 2011). Recently, many automobile and space components are manufactured using magnesium alloys Therefore, the joining of these alloys is critical in the manufacture of parts. The combination of magnesium alloys and other materials presents various problems by conventional melt welding methods due to the different physical and metallurgical properties (Campell, 2006). In the literature, there are many studies on the weldability of Mg alloys, especially AZ91 alloys. AZ91 alloys can be welded by conventional melt welding methods such as laser welding, MIG welding and TIG welding. In addition, these alloys can be welded by solid state welding methods such as diffusion welding, spot welding, friction stir welding (Çelikyürek and Önal, 2016). On the other hand, Mg alloys have some problems arise from the nature of magnesium during the melt welding. The most important problems are the affinity of magnesium alloys to oxygen and nitrogen. Most of these problems disappear because of the lack of melting in solid state welding techniques.

Fe₃Al based iron aluminides have recently received considerable attention in engineering area. The ordered structure is found to exhibit low diffusion and lower creep rate. The formation of Al₂O₃ scales causes excellent corrosion resistance at high temperatures in oxidizing and sulfidizing environments (David et al. 1996). The welding is an important fabrication technology for iron aluminides to be used widely in engineering applications. Investigations of welding of Fe₃Al alloys have mainly focused on fusion weldability using gas tungsten arc (GTA) and electron beam welding (EB) processes (Santella 1997, David et.al 1993 and David et. Al 1998). Friction welding is one of the applicable solid-state welding techniques and is widely used in metals

and alloys (Özdemir 2005, Lee et al. 2004, Sketchley et al. 2002). In this study, AZ91 magnesium alloy and Fe_3Al alloy were welded for different the friction pressures by friction welding.

Method

Fe_3Al alloy was produced with vacuum arc melting in argon atmosphere from iron and aluminum with 99,99 wt.% and 99.7 wt.% purity, respectively. The AZ91 alloy was proved a private firm. The Fe_3Al and AZ91 alloys were machined as cylindrical, 8 mm diameter and 40 mm length, at lathe machine for friction welding process. The friction welding experiments were performed out by a continuous-drive friction welding machine for under constant a friction time, forging pressure, forging time, rotational speed for different the friction pressure (Table 1).

Table 1. Parameters of the friction welding.

Rotational speed, rmp	Forging pressure (MPa)	Forging time (s)	Friction time (s)	Friction pressure (MPa)	Burn-Off (axial shortening) (mm)
1000	100	10	12	20	0,3
1000	100	10	12	40	1,8
1000	100	10	12	60	4,2

The friction welding principle is shown schematically in Figure 1. Four the welding process were performed for each a test condition. One of the welded samples was used for microstructure examinations. The shear tests were applied to the other welded samples to determine the shear strength of the joint and the results obtained were averaged. The shear strength tests were carried out at room temperature using a specially manufactured apparatus in a universal electromechanical tensile-compression device (Shimadzu AG-IS-250) (Figure 2).
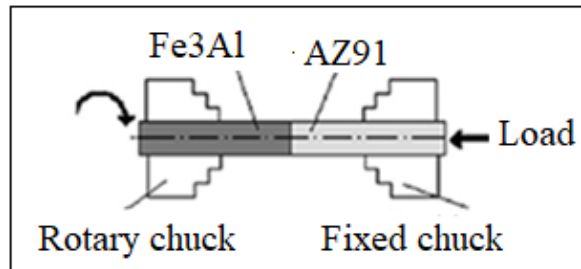
Fig. 1. Schematically illustration of the friction welding process.
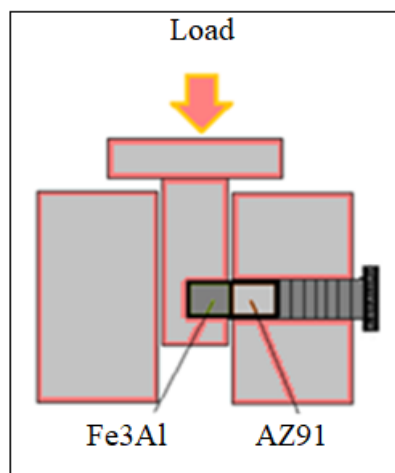
Fig 2. A specially designed specimen holder

The welded samples were cut perpendicular to the joint interface for microstructure investigations. The surfaces of the welded samples were ground with 600, 800 and 1200 mesh grinding paper and polished with a 3 μm diamond paste. Fe_3Al side of welded samples were etched with a mixture of H_2O (30 ml), HNO3 (30 ml), HCl (20 ml) and HF (20 ml). The AZ91 side was etched with 20 alcohol (20 ml), 2 H_2O and 1 gr $C_6H_3N_3O_7$. The

interfaces of the welded samples were examined were optical microscopy. After the shear test, the surfaces of the fracture samples were examined by SEM and EDS analyzes were taken from these surfaces.

Results and Discussion

Flash formation was observed in all welded samples because of plastic deformation during the welding process. The friction pressure plays an important role in the flash formation. More plastic deformation occurs because of higher the friction pressure, which produces higher heat in the weld interface. Hence, the burn-off (axial shortening) increases with the increase in plastic deformation. The different physical and mechanical properties of the materials exhibit different deformation rates during the friction welding. Fe_3Al alloy has greater strength at high temperatures compared with AZ91. Therefore, Fe_3Al alloy does not show deformation during friction welding. All mass is transferred to the flash from the AZ91 side. Optical micrographs of the samples welded for 40 and 60 MPa the friction pressure are presented in Fig. 3. As seen micrographs, all of the welded samples were of sound quality and, they did not exhibit any pores or crack formation along the weld interface.
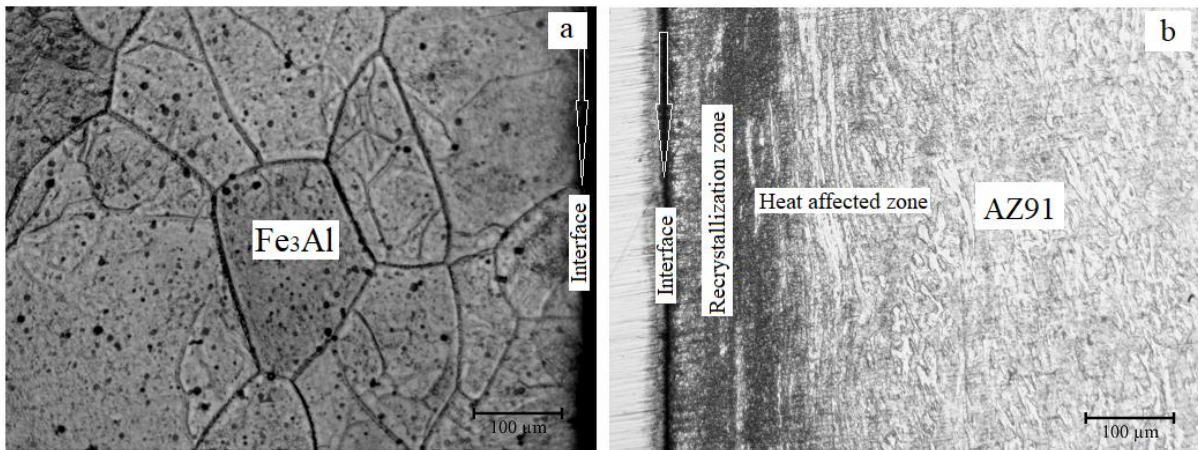
Fig. 3. Optical micrograph of the sample welded for 40 MPa friction pressure.

Two main regions are observable on the AZ91 side of the interface of all of the welded samples: a dynamically recrystallized zone with very fine grains and heat affected zone (Fig. 3b). The width of the dynamically recrystallized zone for all of the welded samples was approximately 190-200 μm. The micrographs demonstrated a slight variation in the width of dynamically recrystallized zone dependent on the friction pressure. There was not any change on the Fe_3Al alloy side (Fig. 3a).

The shear strengths of the welded samples and the base alloys are shown in Fig. 4. The results showed that the values of the shear strength of the welded samples increase with increase in the friction pressure. Under these experimental conditions, it can be said that the shear strength of the welded samples was depend on the friction pressure.
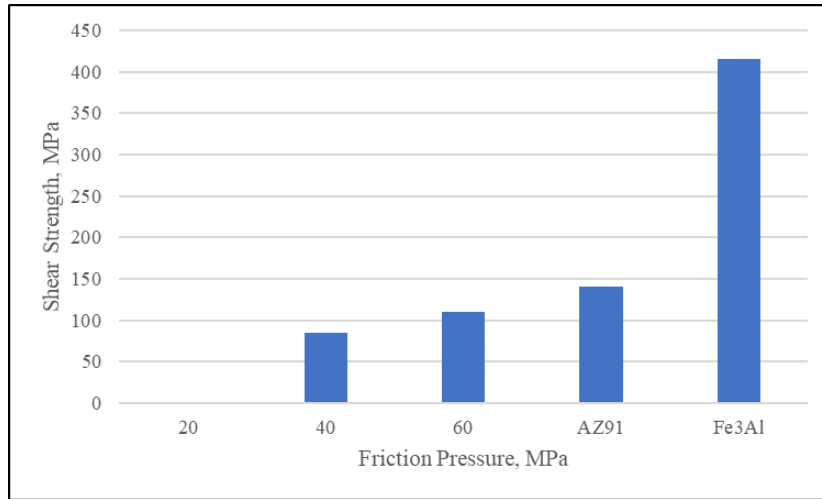
Fig. 4. The shear strengths of the welds and the base alloys

Microhardness values were measured in the direction from the center of the weld to both sides of the welded samples. The micro hardness profiles for all of the friction welding pressure were found to be similar. Fig. 5 shows the hardness values obtained from all the welded samples. The hardness of the dynamically recrystallized zone and heat affected zone is higher than that of the base alloy on the AZ91 side. The hardness of the dynamically recrystallized zone is higher the heat affected zone because of its fine-grained microstructure. There was not any changing on hardness of Fe_3Al alloy side.
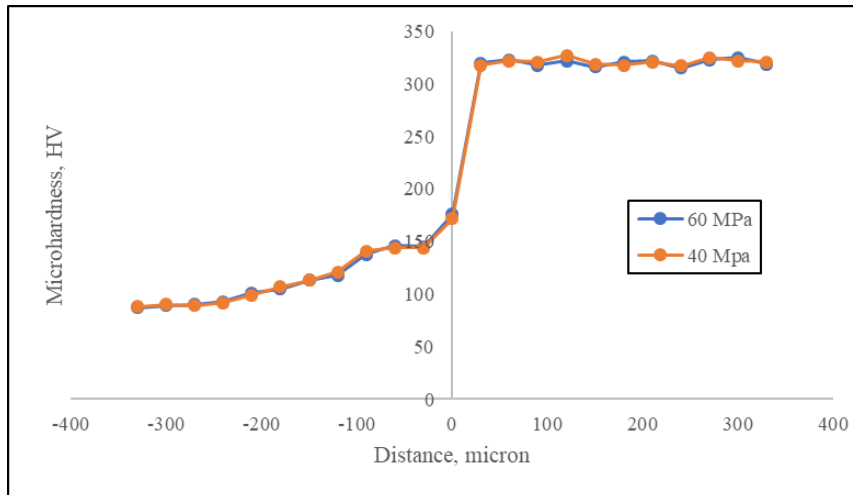
Fig. 5. The hardness values obtained from the welded samples for 40 and 60 MPa the friction pressure

Fig. 6 the SEM fractographs belonging to Fe_3Al side and AZ91 side of the welded sample that were treated for 60 MPa the friction pressure. The SEM and EDS analysis indicated that the failures took place in different zones, including interface of welded samples and the recrystallized zone of AZ91 side during the shear test. However, this situation was observed for all of the welded samples.
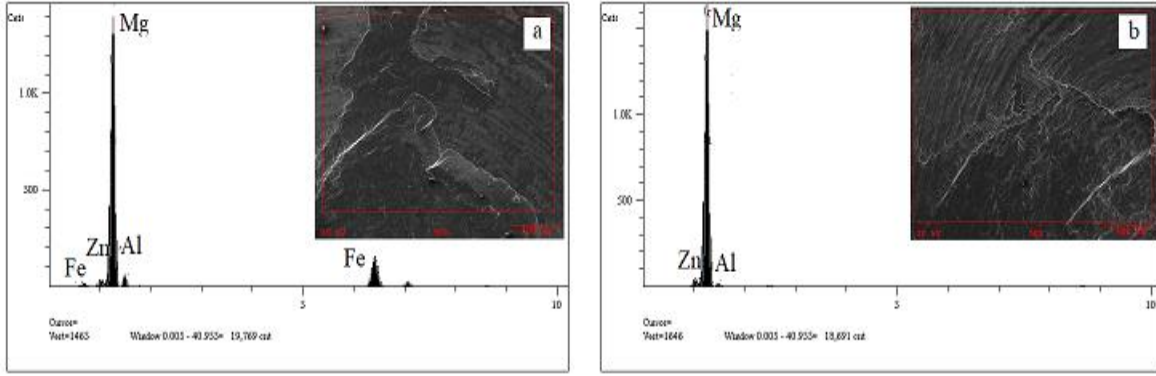
Fig. 6. SEM fractographs and EDS analysis of Fe$_3$Al side and AZ91 side

Conclusion

Fe$_3$Al and AZ91 alloys were welded by friction welding method. All of the welded samples were of sound quality, and they did not exhibit any pores or crack formation along the weld interface. The friction pressures play an important role in flash formation and welds shear strength. The welds shear strength and Burn-Off increase with increase in the friction pressure. After welding, while two different zone observed in the AZ91 side, there was not any difference on the Fe$_3$Al side. The hardness profiles for all friction pressure are similar. It was observed that AZ91 side has different hardness values. EDS analysis indicated that the failures took place in different zones during the shear test.

Acknowledgements or Notes

References

Baker H. (eds) (1997). ASM Handbook, Welding, Brazing, and Soldering, *ASM International*, A.B.D. 6

Barlas, Z. (2009). Sürtünme Karıştırma Kaynak Yöntemiyle Birleştirilen Cu ile CuZn37 Levhaların Mekanik ve Mikroyapı Özellikleri, Doktora Tezi, Sakarya Üniversitesi, Fen Bilimleri Enstitüsü,

Campell F.C. (2006). *Manufacturing Technology for Aerospace Structural Materials*, Elsevier Ltd., UK,

Çelikyurek İ., Torun O., Baksan B. (2011). Microstructure and strength of friction-welded Fe–28Al and 316 L stainless steel. *Materials Science and Engineering A 528 8530– 8536*

Çelikyürek İ., Önal E., (2016). Effect of the weldingöconditions on the microstructure and mechanical properties of friction welded AZ91 Mg alloy. *Anadolu Üniversitesi Bilim ve Teknoloji Dergisi A-Uygulamalı Bilimler ve Mühendislik, 17,3, 563-571.*

David SA, Zacharia T. (1993). Weldability of Fe3Al-type aluminide. *Weld J, 72(5), 201–227.*

David SA, Santella ML. 1996, In: Stoloff NS, Sikka VK, (eds). Physical metallurgy and processing of intermetallic compounds. Chapman & Hall; *655–75.*

David SA, Horton JA, McKamey CG, Zacharia T, Reed RW. (1989). Welding of iron aluminides. *Weld J, 68(9), 372–381.*

Elthalabawy W. and Khan T., J. (2011). Liquid Phase Bonding of 316L Stainless Steel to AZ31 Magnesium Alloy. *Materials Science Technology, 27,1, 22-28.*

Fernandus M., Senthilkumar T., Balasubramanian V., (2011). Developing Temperature –Time and Pressure–Time diagrams for diffusion bonding AZ80 magnesium and AA6061 aluminum alloys. *Materials and Design, 32, 1651–1656.*

Kurt B., J. (2007). The interface morphology of diffusion bonded dissimilar stainless steel and medium carbon steel couples. *Journal of Materials Processing Technology. 190, 38–143.*

Lee WB, Kim YJ, Jung SB., (2004). Effects of copper insert layer on the properties of friction welded joints between TiAl and AISI 4140 structural steel. *Intermetallics, 12, 671-678.*

Özdemir N., (2005). Investigation of the mechanical properties of friction-welded joints between AISI 304L and AISI 4340 steel as a function rotational speed. *Materials Letter, 59, 2504-2509.*

Ouyang, J., Yarrapareddy, E., Kovacevic, R., (2006). Microstructural Evolution in the Friction Stir Welded 6061 Aluminum Alloy (T6-Temper Condition) to Copper", *J Mater Process Tech*, *172, 1, 110-122*.

Öztemiz H. (2013). Bakır ve alaşımlarının sürtünme karıştırma kaynağı ile birleştirilmesi ve kaynak parametrelerinin mikroyapı ve mekanik özelliklere etkisinin araştırılması. Yüksek lisans tezi, Fen Bilimleri Enstitüsü, İnönü üniversitesi, Malatya.

Russell, A.M., Lee, K.L. (2005). Structure-Property Relations in Nonferrous Metals, *John Wiley & Sons*, Inc., Publication, A.B.D.

Santella ML. (1997). An overview of the welding of Ni3Al and Fe3Al alloys. In: Deeevi SC, Sikka VS, Maziasz PJ, Cahn RW, editors. Ni_3Al and Fe_3Al alloys, in: S.C. Deeevi, V.S. Sikka, P.J. Maziasz and R.W. Cahn(Eds.), Proceedings of Materials Week '96 on Nickel and Iron Aluminides: Processing, Properties, and Applications, Ohio, 7-9 October 1996. USA: ASM International*; 321–329.*

Satyanarayana V.V., Reedy G.M, Mohandas T., (2005). Dissimilar metal friction welding of austenitic–ferritic stainless steels. *Journal of Materials Processing Technology. 160, 128–137.*

Sketchley PD, Threadgill PL, Wright IG. (2002). Rotary friction welding of an Fe_3Al based ODS alloy. *Material Science Engineering*, *A329, 756- 762.*

Stephen D. Cramer and Bernard S. (1999). Properties, and Selection: Irons, Steels, and High-Performance Alloys. *ASM Handbook*, E-Publishing Inc. *1–2.*

Sun D.Q., Gu XY, Liu W.H., (2005). Transient liquid phase bonding of magnesium alloy (Mg–3Al–1Zn) using aluminum interlayer. *Materials Science and Engineering*, A 391, 29–33.

Vaidya, W.V., Horstmann, M., Ventzke, V., Petrovski, B., Kocak, M., Kocak, R., Tempus, G. (2009). Structure-Property Investigations on a Laser Beam Welded Dissimilar Joint of Aluminium AA6056 and Titanium Ti6Al4V for *Aeronautical Applications Part I*: Local Gradients in Microstructure, Hardness and Strength", Matwiss u Werkstofftech, *40, 8, 623-633.*

Author Information

Osman Torun
Afyon Kocatepe Üniversitesi, Teknoloji Fakültesi,
Mekatronik Mühendisliği Bölümü,
Afyonkarahisar/Türkiye
Contact E-mail:otorun@aku.edu.tr

Ibrahim Celikyurek
Eskişehir Osmangazi Üniversitesi, Müh. Mim. Fak.
Metalürji ve Mal. Müh. Bölümü, Eskişehir/Türkiye

Spectral Analysis of Experimental Ultrasonic NDT Signals

Samira DIB
University of Jijel

Toufik BOUDEN
University of Jijel

Messaoud BOUCHEFIRAT
University of Jijel

Fares DJERFI
University of Jijel

Abstract: Non Destructive Testing (NDT) plays an important role in different fields. It allows materials control or structures to check their condition, as well as detect defects without damaging inspected parts. The practical difficulty of extracting information to characterize materials led to use different methods of signal processing. Real ultrasonic signals considered in this paper are collected from Steel plate with defect and Aluminum cubic sample without defects prepared in LEND laboratory of Jijel University in Algeria. Two experiments are used: pulse-echo by contact and immersion techniques wherein ultrasonic energy is transmitted by piezoelectric transducer. The reflected signals are received by the same transducer where the energy is converted into an electrical signal. Signals are treated by three techniques adapted for nonstationary signals, and based on energy distribution in time-frequency plan; namely: Continuous Wavelet Transform (CWT), Wigner Ville (WVD) and Choi-Williams (CWD) distributions. This energy distribution allows an easy flight of time's measurement of different echoes, and thereafter velocity's calculation and defect's localization. Advantages and limits of each method are as follows: WVD achieves good resolution of interfaces; however, its capacity remains limited by the appearance of non-desirable terms which may limit results readings. CWD avoids interferences phenomenon. It allows exactly extraction and clearly representation of signal components in time/frequency. Application of CWT clearly shows that temporal resolution is improved by contrast frequency resolution is degraded for high frequency terms. Also the disadvantage of this method comes from the absence of criterion of mother wavelet choice. Comparative study shows that CWD makes it possible to have a velocity closer to that given in theory. While the CWT and WVD give more accurate results regarding the defect's position. This justifies the use of these efficient methods for non-destructive ultrasonic testing for defect localization and material characterization (Velocity and Young's modulus).

Keywords: Ultrasonic, NDT, Wigner-Ville, Choi-Williams, Wavelet

Introduction

Non-destructive testing (NDT) has become a field of continuous growth. It plays a very important role in various fields, particularly in the pipeline and storage industry, especially in the oil and gas, nuclear, automotive and aeronautics sectors. NDT groups together a set of methods whose general purpose is to control a material without modifying it, either during production or during maintenance. They can be classified according to the physical phenomena involved: acoustic, radiation, material flow or electromagnetic fields. The choice of a method depends on the structure to be examined, the conditions under which the control will be carried out, as well as the time and cost constraints.

In this work, we are interested in the ultrasound control method, in which ultrasound waves are emitted in the material to be examined. The waves propagate in the medium and retrieved by a receiver allowing in the possible, to identify the defects contained in the material and thus determine nature of material and/or sample size. The same method can be applied to characterize it, ie to estimate the physical parameters proper. Ultrasonic testing is frequently used because it has many advantages such as the ease of implementation, the ability to work on one side of the part to be controlled (no need for access to the second side), and the ability to cross large thicknesses of material depending on the working frequency. In addition, the existence of relationships between the ultrasonic propagation material and the characteristics of the material allows its characterization. Signal processing is the discipline that develops and studies signal analysis techniques (Malik & Saniie, 1996), (Dib, Djerfi, Merdjana, & Bouden, 2017). In this paper, we focus on the separation of near echoes and the localization of ultrasound echoes. This analysis will be done using some signal processing methods based on energy distribution in Time-Frequency plan, namely: WVD, CWD and CWT and test their feasibility on experimental ultrasonic signals.

The remainder of this paper is organized as follows: the selected time-frequency techniques which can be applied to ultrasonic NDT of materials are first presented. Then results and discussion are expressed. The paper is closed by conclusions highlighting the main advantages and disadvantages of each considered method.

Time-frequency methods

Wigner Ville Distribution (WVD)

The WVD is a method of describing the energy distribution of a signal in the time-frequency plan. It provides time-frequency decomposition without any restriction on temporal and frequency resolutions. It appears perfectly suited to the analysis of nonstationary signals. The DWV is defined as

$$WVD_{xx}(t,f) = \int_{-\infty}^{+\infty} x\left(t + \frac{t}{2}\right) x^*\left(t - \frac{t}{2}\right) e^{-j2\pi fx} dt \tag{1}$$

Unfortunately, the non-linearity of this transform has disastrous consequences manifested by the appearance of interference and negative energies in the time-frequency distribution of the signal energy. In practice, a smoothed version of the DVW is often preferred. It is named the Wigner-Ville Smoothed distribution and is defined by

$$WVD_x(t,f) = \int_{-\infty}^{+\infty} p(t) x\left(t + \frac{t}{2}\right) x^*\left(t - \frac{t}{2}\right) e^{-j2\pi fx} dt \tag{2}$$

where *p (t)* is the smoothing window that reduces the amplitude of the interference terms (Gaohui, Jun, Dezhi, Huasong, Wulan, & Yan, 2008).
In our work, one will seek the temporal positions of maxima of the WVD which indicate the positions of the echoes in order to characterize and/or locate the defect in specimens.

Choi-Williams Distribution (CWD)

The CWD was first proposed by H.I. Choi and J. Williams in 1989. It is a transformation that represents the spectral content of the nonstationary signal as a two-dimensional time-frequency map. It largely avoids one of the main problems of the WVD: the presence of interference limits in areas where one would expect values of zero power. CWD employs an exponential grain in the generalized class of time-frequency bilinear distributions to achieve a reduction in cross-boundary components of the distribution (Choi & Williams, 1989).
The mathematical representation of the CWD is given by the following equations

$$CWD_x(t,f) = \iint_{-\omega}^{\omega} A_x(\eta,\tau) \Phi(\eta,\tau) \exp\left(2j\pi(\eta.t - \tau.f)\right) d\eta d\tau \tag{3}$$

$$A_x(\eta,\tau) = \int_{-\omega}^{\omega} z(t + \tau).z^*t - \tau) \exp(-2j\pi t\eta) dt \tag{4}$$

$$\Phi(\eta,\tau) = exp[-\alpha(\eta\tau)^2] \tag{5}$$

$\Phi_x(\eta,\tau)$ is the kernel function which is usually a low-pass function. Choi and Williams have shown that there is a trade-off between the auto term resolution and the cross-term suppression.

The main objective to minimize the interferences terms results in choosing a kernel function which depends with the type of analyzed signal to make it smooth. Smoothing time-frequency will have to include very few samples on the frequency axis and many on the temporal axis in order to estimate the reasons for signal as well as possible. Indeed, in the case of real signals, the reasons time frequency are often varied and it is difficult, to find optimal characteristics of the core which allowing to insulate, at the same time of the pure frequencies and the impulses (Djerfi, 2017).

Continuous Wavelet Transform (CWT)

General expression of the CWT is given by

$$T_x(a, b) = \frac{1}{\sqrt{a}} \int_R x(t) \Psi^* \left(\frac{t-b}{a}\right) dt \tag{6}$$

$|T_x(a, b)|^2$ represents the scalogram of $x(t)$ (Ding, 2007).

The CWT is a multi-resolution representation of a signal. It has become a very powerful tool for filtering the signal, and also, it allows to locate and detect the main components of the signal (locate defect and characterize material in our case).

The CWT is a plot on which the abscissa axis represents the temporal variations and the ordinate axis those of the scale (inversely proportional to the frequency). The pronounced color at each point (x,y) represents the importance of the amplitude of the coefficients. Thus, we obtain the coefficients produced at different scales for different sections of the analyzed signal. The contours provide a very clear frequency-temporal representation. We apply the CWT on measured ultrasonic signals, with a choice of an analysis wavelet and an adapted scaling factor. This adaptation is done by calculating the most powerful coefficients, ie classification of the local maxima .

$$Echo_i = Max(C_i) \tag{7}$$

Once we find the high coefficients, we can deduce the temporal positions corresponding to each echo which composes the ultrasonic wave. This knowledge facilitates the characterization, detection and/or localization of defects by calculating the time of flight (Djerfi, 2017).

Results and Discussion

Experimental signals analyzed in this paper are collected from samples of Steel with a defect (*signal 01*) and Alluminum without defects (*signal 02*) prepared in the NDT laboratory of Jijel University in Algeria. The main objective is to detect reflected echoes from different interfaces (E1: face-echo, E2: defect-echo and E3: Depth-echo) and improve their visibility. Thus, we have to calculate the velocity of propagation in the Alluminum (the thickness of the piece is $e_p = 6\ cm$) and detect the defect in the Steel ($v_2 = 6082\ m/s$)). The equation used to calculate the propagation velocity and the defect thickness is based on the knowledge of time of flight: $T_v = 2. e_p / v$.

Experiment 1

This experiment is based on pulse-echo contact technique. The transducer is placed directly on the part to be controlled and the acoustic connection is ensured by a special gel. The piece under test is a steel plate of dimension (1x5) cm with a defect inserted at the depth of 0.5 cm. The defect is an empty crack or internal porosity. This experiment requires only one transducer to emit the ultrasonic signal and receive the echoes of the interfaces.

The measurement system consists essentially of a contact transducer of 2.25 MHz placed directly on the part to be controlled; it represents the generating source of the ultrasonic wave beam. It allows the transmission and reception of pulses. The pulses emitted (received) by the transducer are generated by an ultrasonic transmitter / receiver (Panametrics 5077PR, 606V) connected with a digital oscilloscope (Tektronics TDS 1002) to visualize echoes (ultrasound waves) emitted and reflected which is connected to a computer with data acquisition software (WaveStar) in turn, Figure 1(a). Notice that velocity in steel is equal to 5950 m/s.

Experiment 2

The experiment is based on the pulse echo by immersion technique. It consists essentially of a vessel comprising the sample holder. It includes the same devices as illustrated in Figure 1(b). The transducer works at 1MHz. We use a sample of Aluminum (2017A) realized as a cube of (6x6) cm placed at 4 cm from the transducer. Notice that velocity in alluminum is 6700 m/s and in water is 1480 m/s.

During the two experiments, the ultrasonic waves undergo a normal incidence. Indeed, they fall vertically on the face of the sample so that the echoes received are longitudinal waves. (Bouden, Nibouche, Djerfi , & Dib, 2012) (Dib, Djerfi, Merdjana, & Bouden, 2017).

Figure 2 shows the two received signals. In the Signal 01 providing from the steel plate, the first peak represents the first face of the sample (E1); the following echoes are peaks that represent the interior of the material : the defect echo (Ed) and the bottom echo (E2). In Signal 02, provided from the alluminum sample, the first peak represents the emitted signal; appeared echoes are consecutively face-echo (Face.E) and depth-echo (Depth. E). It's possible to determine the propagation velocity in the material if it is unknown. It has checked on this case and found the propagation velocity in water, aluminium and steel.

(a)   (b)
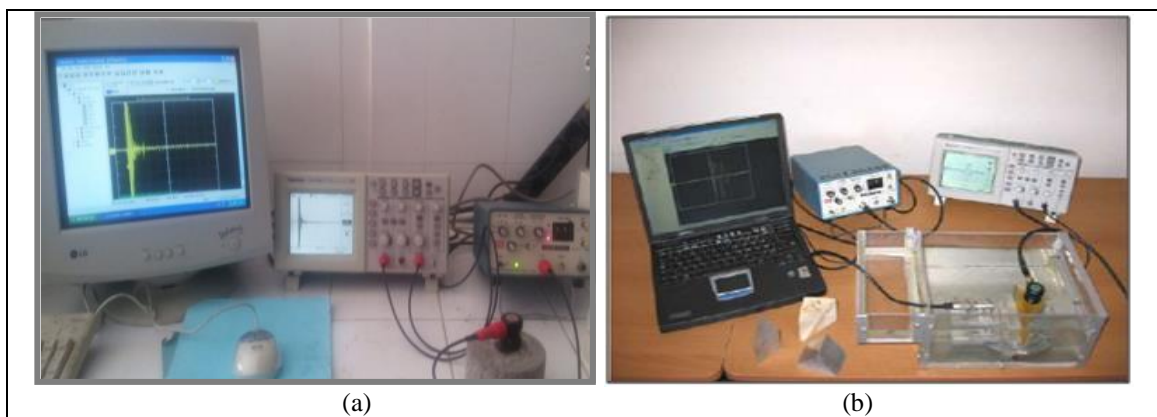
Figure 1. General view of measurement systems: (a) Experiment 1 and (b) Experiment 2
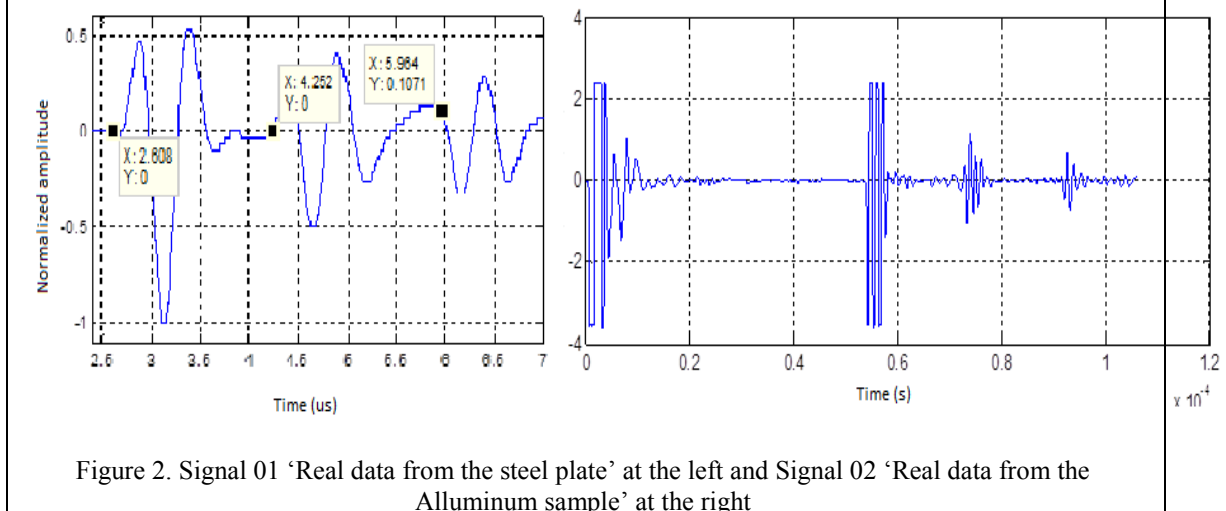
Figure 2. Signal 01 'Real data from the steel plate' at the left and Signal 02 'Real data from the Alluminum sample' at the right

Results are illustrated by Figures 3 to 9. The objective is to compare the performances of the considered techniques applied on the two samples of materials.Figures 3 and 7 show that WVD has a good joint resolution and thus enable to locate the time-frequency positions of each echo. Unfortunately, one notices clearly the appearance of interferences which can harm the legibility of the time-frequency representation.

The results obtained when applying Choi-Williams distribution are presented on Figures 4 and 8. We notice that the echoes of the external and internal faces appear clearly. We show by this the effectiveness of this method for ultrasonic signals, and give an advantage of eliminating all additional echoes. Therefore, one can say that it brings a solution to the problem of defects localization.

Figures 5, 6 and 9 illustrate the good performances of CWT. In fact, we apply the wavelets with a judicious choice of the mother wavelet and the scale coefficient. The results obtained proved that the wavelet coefficients calculated by the wavelet family 'db4', 'Haar' and 'Meyer' are better than the other families for analyzing Signal 01. However, 'Morlet' and 'Meyer' give good results for analyzing Signal 01.

The scalogram allows us to detect the temporal and frequency positions of the echoes in each signal. So CWT has demonstrated its ability to locate defects, since it acts as a "microscope" with which we can observe different parts of the signal.
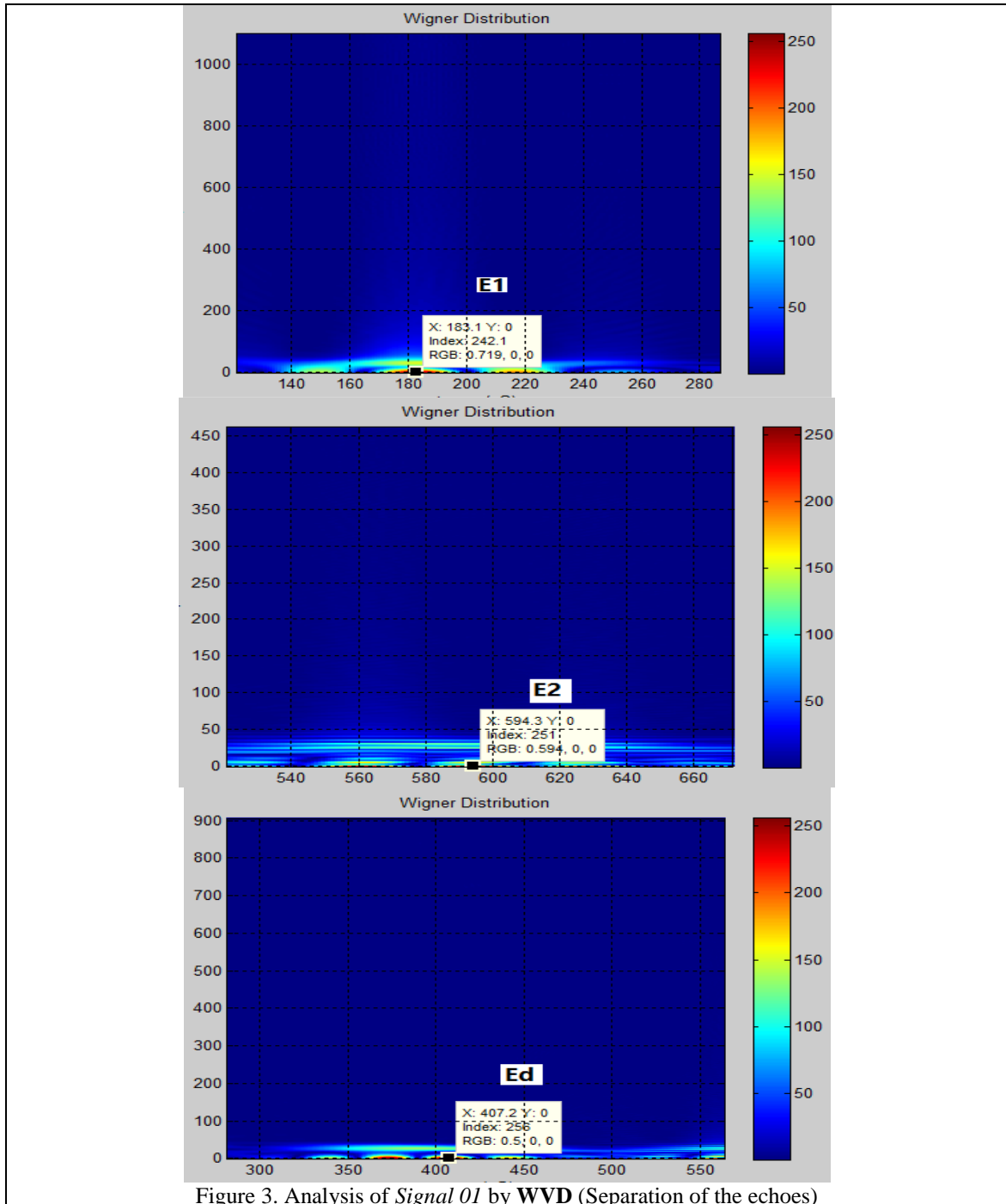
Figure 3. Analysis of *Signal 01* by **WVD** (Separation of the echoes)

(a)   (b)
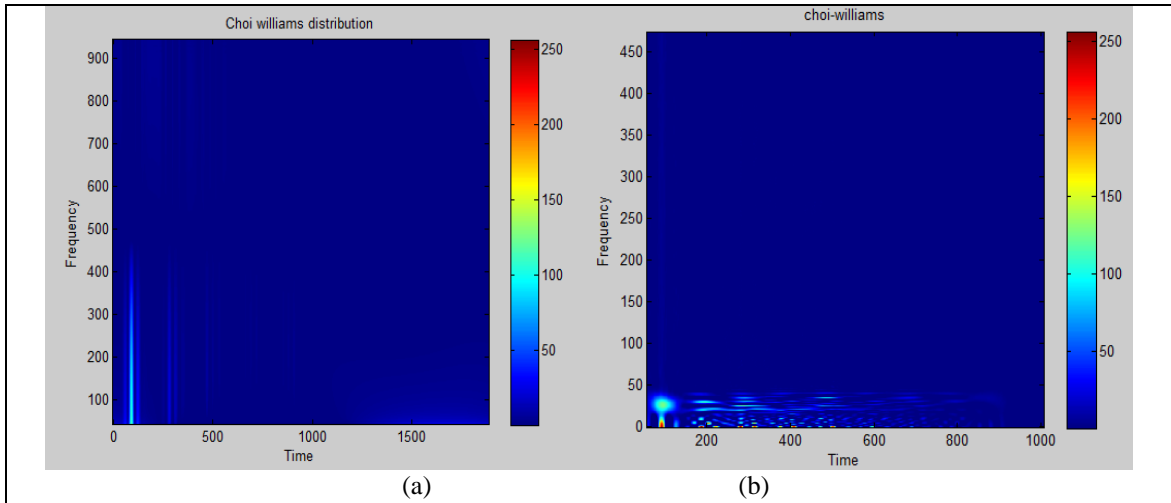
Figure 4. Analysis of *Signal 01* by **CWD**: (a) σ → 1 and (b) σ → ∞

(a)
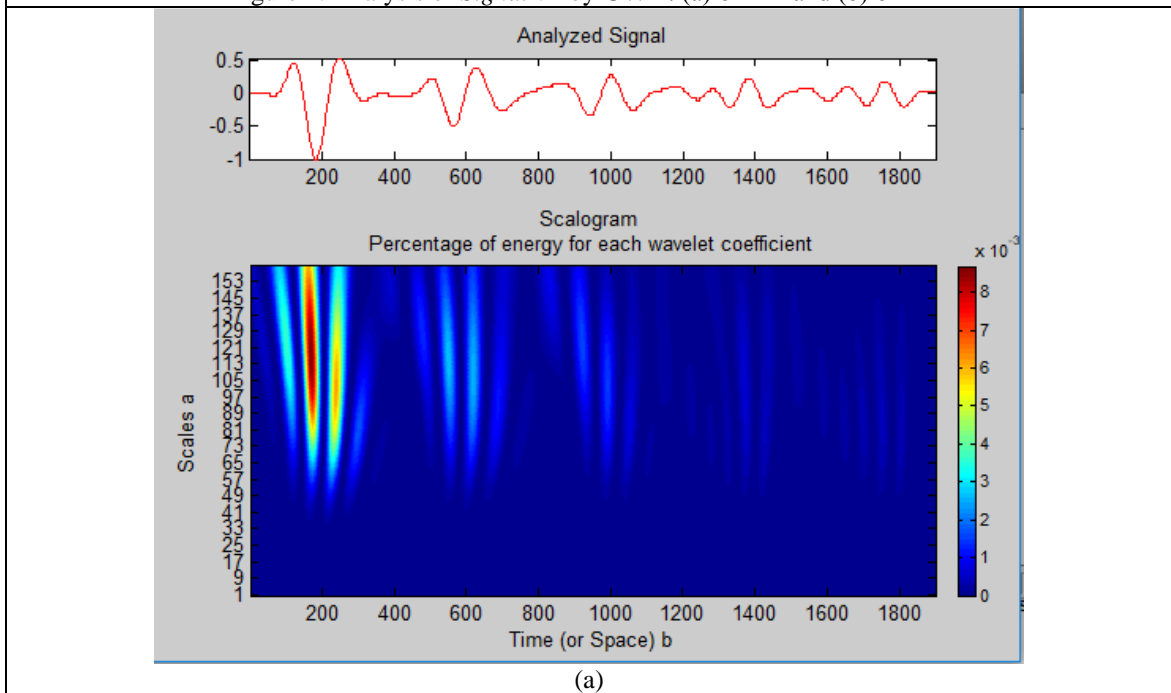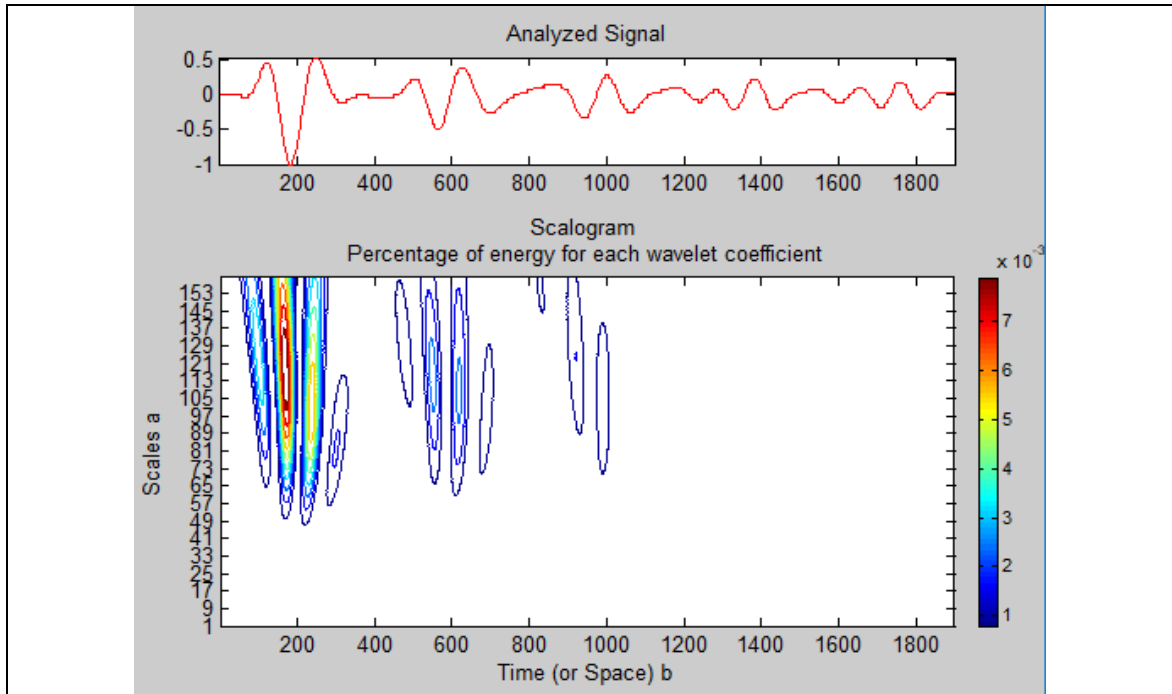
(b)

Figure 5. Analysis of *Signal 01* by **CWT**: (a) Scalogram of Signal 01 on scale at 160
(b) Contour time-scale

Figure 6. Analysis of *Signal 01* by **CWT**(separation of the echoes)

Figure 7. Analysis of *Signal 02* by **WVD**

Figure 8. Analysis of *Signal 02* by **CWD**

188
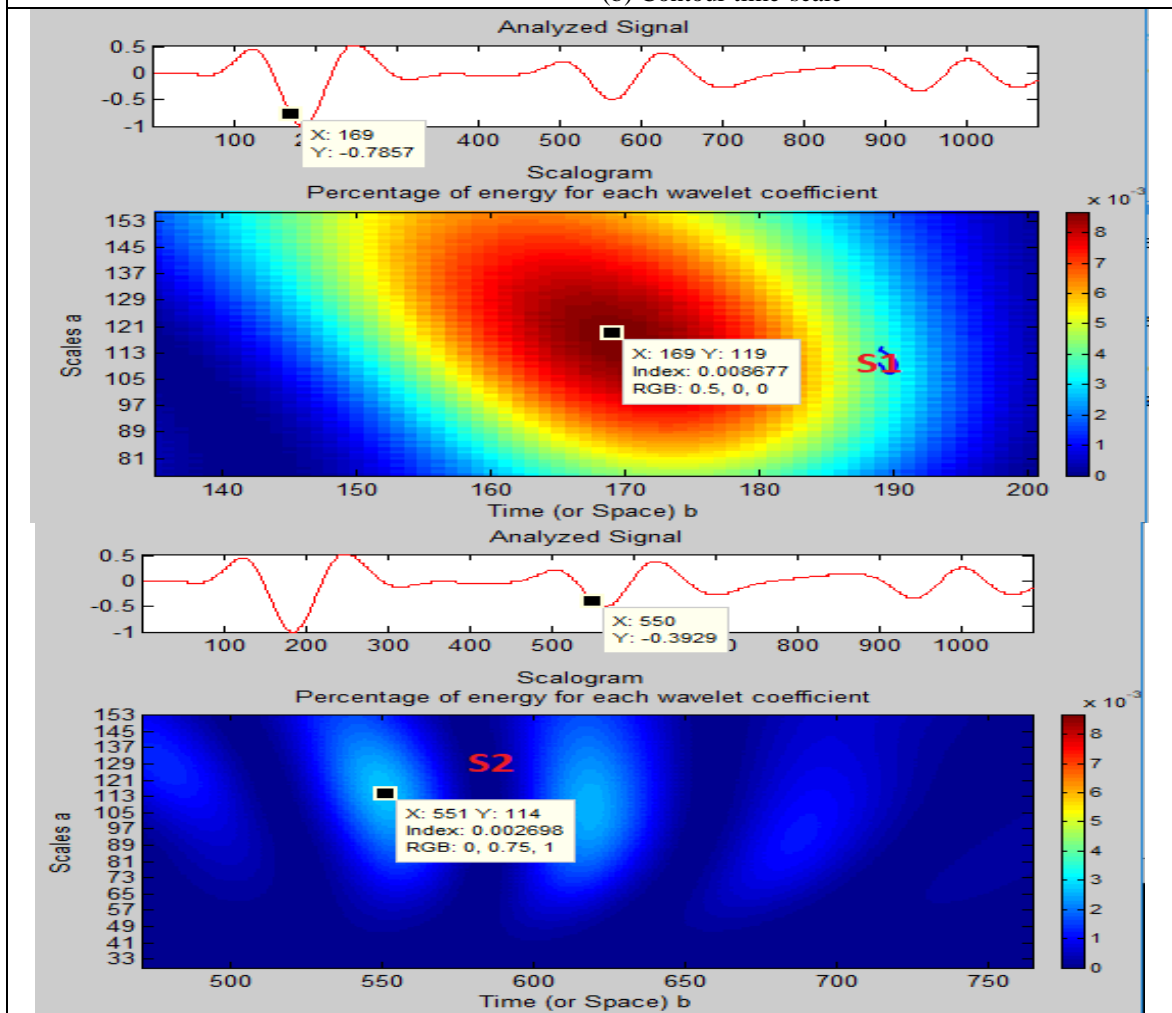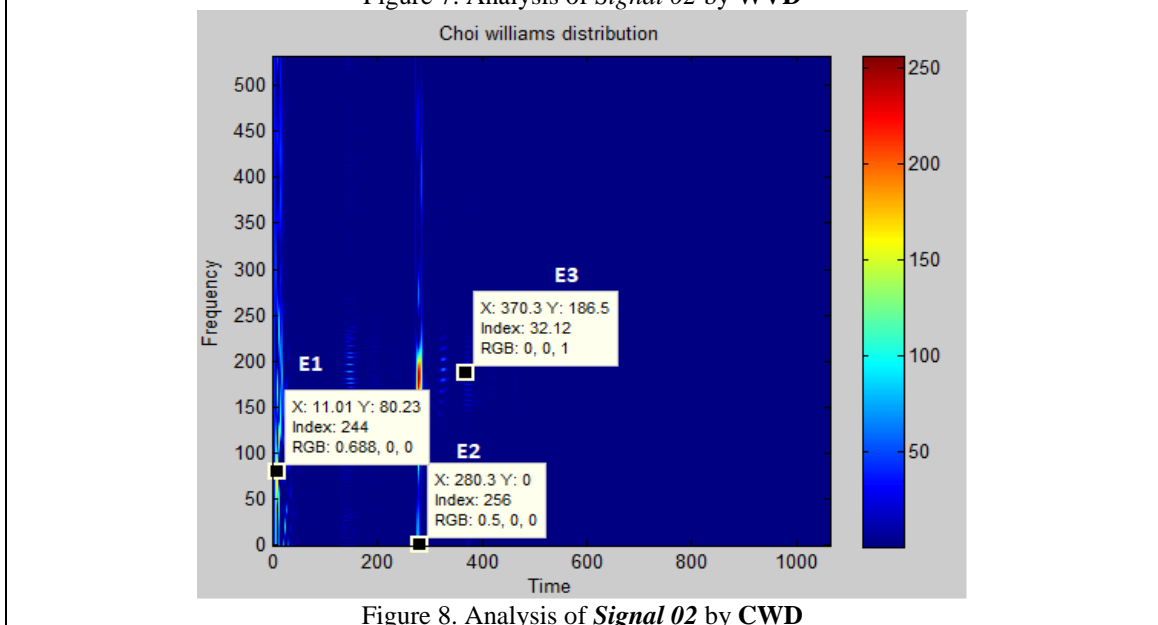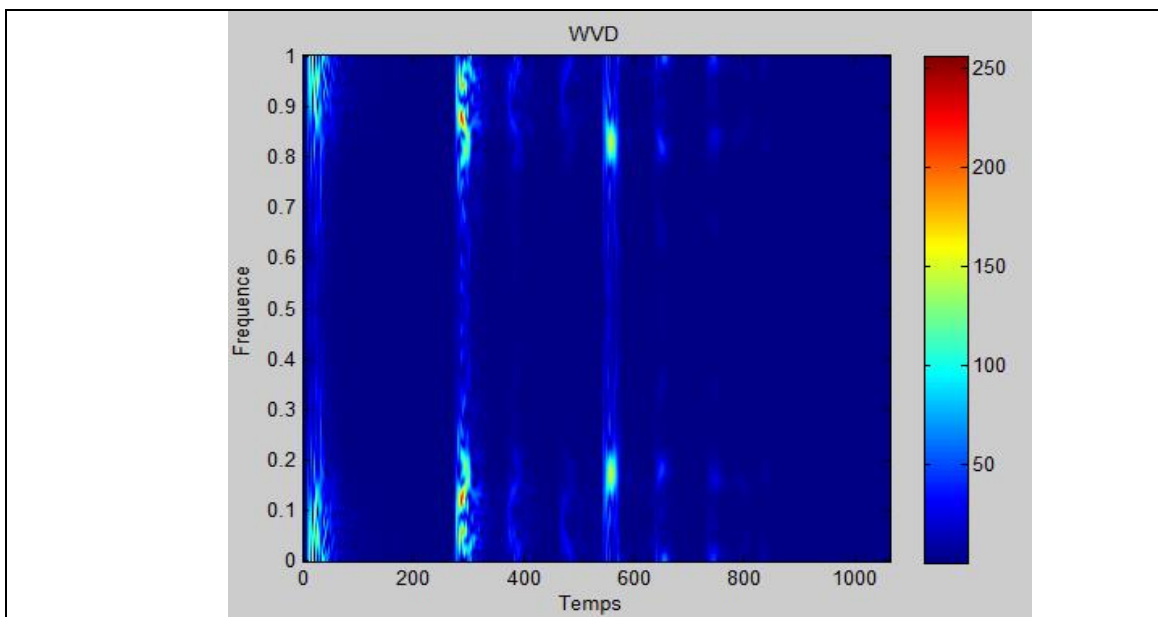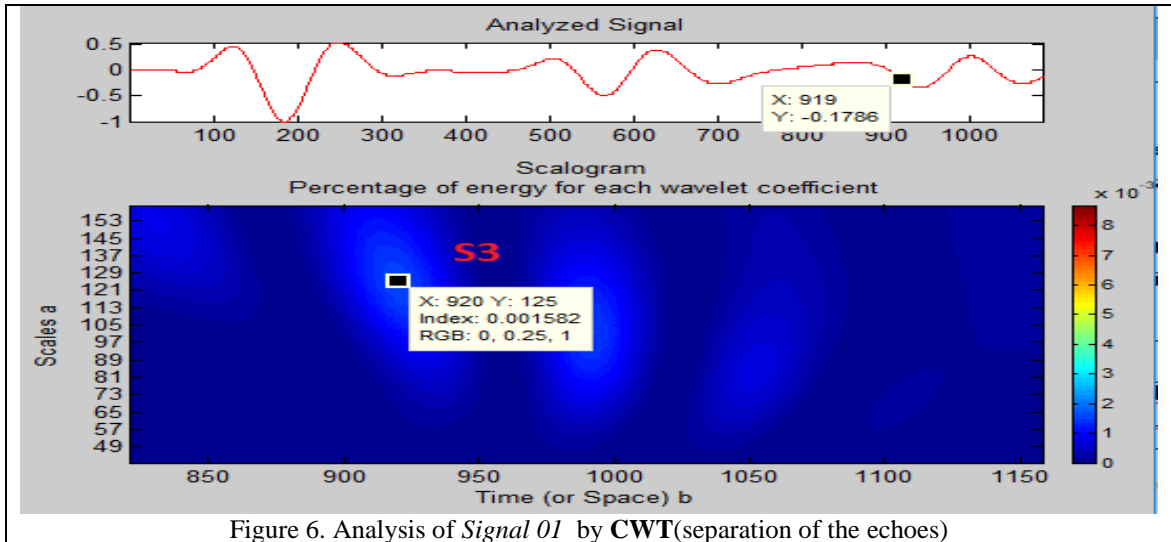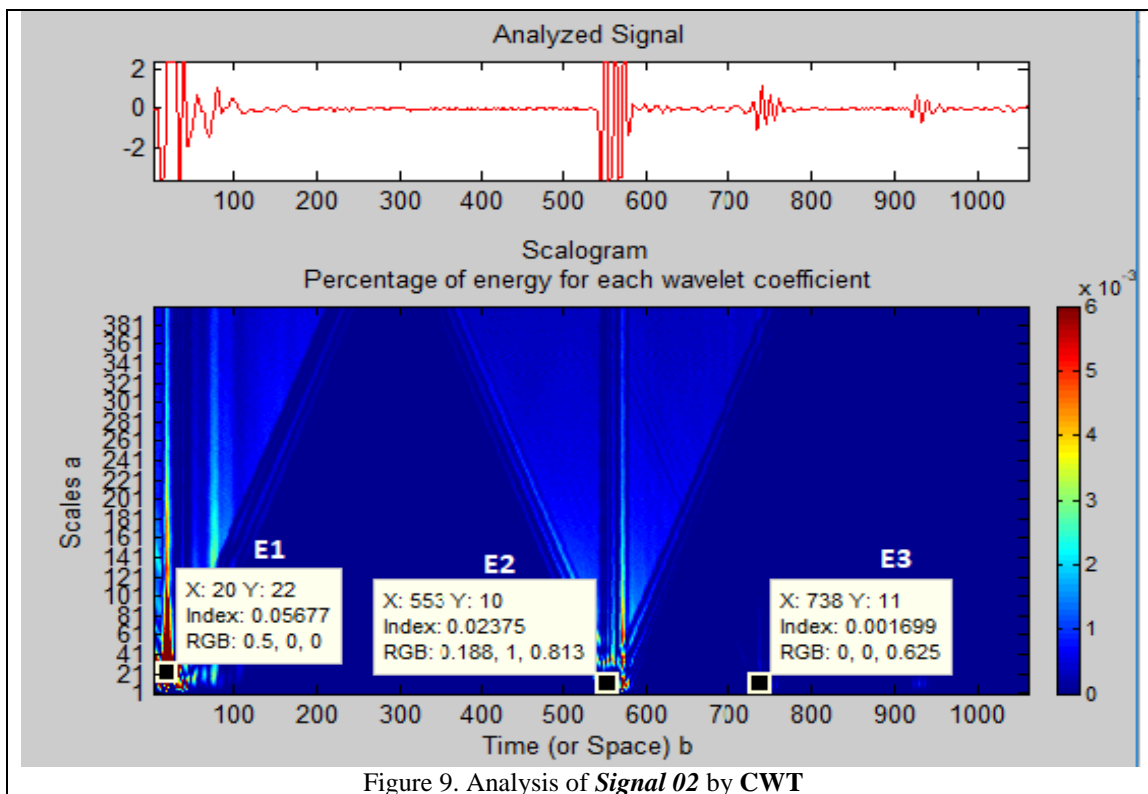
Figure 9. Analysis of *Signal 02* by **CWT**

When calculating the longitudinal velocities using the different methods, we note according to the Figures that each technique showed its capacity to locate the time-frequency positions of each interface. Numerical results are summarized in tables 1 and II. For the first experiment, CWT give relatively good measures for the characterization (velocity mesurement) and defect localization. For the second experiment, CWD is much better than WVD and CWT for the characterization (velocity mesurement).
This justifies the use of these efficient methods for non-destructive ultrasonic testing.

Table 1. Propagation velocity, sample thickness and defect position from *experiment 1*

	Experiment 1		
	Velocity	*Thikness*	*Defect position*
Theoritical	5950 m/s	1 cm	5 mm
WVD	5814 m/s	**0.99 cm**	**5.1 mm**
CWD	6622 m/s	0.97 cm	4.5 mm
CWT	**6025 m/s**	0.9 cm	**4.9 mm**

Table 2. Propagation velocity, sample thickness and transducer position from *experiment 2*

	Experiment 2		
	Velocity	*Thikness*	*Transducer position*
Theoritical	6700 m/s	6 cm	4 cm
WVD	6350 m/s	6.3 cm	4 cm
CWD	**6666 m/s**	**6 cm**	4 cm
CWT	6486 m/s	6.2 cm	4 cm

Young's modulus determination E

We know that: $V_l = \sqrt{E/\rho}$ and $E = V_l^2.\rho.$

Theoretically: ρ=7.85 g/cm³ for steel and ρ=2.79 g/cm³ for aluminum, we obtain results in Table 3.

Table 3.Young modulus determined by different methods

	Theoritical	*WVD*	*CWD*	*CWT*
Steel	278 GPa	**265 GPa**	344 GPa	**285 GPa**
Aluminum	121 GPa	109 GPa	**120 GPa**	113 GPa

Conclusion

In this paper, pulse-echo technique has been used to characterize materials. Two specimens were considered: a steel plate (with crack in the middle) and an aluminum cube (without defect). Longitudinal wave velocities were determined from flight time calculations in the specimens. A comparative study of different methods, used for material characterization and defects localization via ultrasonic NDT, was carried out inside the class of Cohen and wavelet. We used three tools of signal processing: Wigner Ville distribution, Choi-Williams distribution and Wavelet.

First, we applied these methods on two materials: Steel plate and Aluminum sample. The simulation results showed advantages and limits of each method. In fact, the implementation of the WVD is adequate to achieve good resolution of interfaces. However, its capacity remains limited by the appearance of interferences which can harm the legibility of the representation time- frequency. The CWD allowed the exactly extraction and clearly representation of the various components of the signal in time and frequency. Finally, compare to the Wigner Distribution Function, the Cohen's class distribution may avoid the cross term. The application of CWT performs the localization of the defect especially when making judicious choice of the analysis wavelet and the scale factor.

We can conclude that CWD and CWT are approved for their superiorities in the detection and localization of echoes and the exact calculation of propagation velocities.

References

Boashash, B. (2003). Time-Frequency Signal Analysis and Processing – A Comprehensive Reference. *Elsevier Science* .

Bouden, T., Nibouche, M., Djerfi , F., & Dib, S. (2012). Improving Wavelet Transform for the Impact-Echo Method of Non Destructive Testing. *Lecture Notes in Electrical Engineering, vol. 141. Springer-Verlag* , 241-217.

Chen, C. H. (2007). Ultrasonic and Advanced Methods for Non-destructive Testing and Material Characterization. *University of Massachusetts* , 3-33.

Choi, H., & Williams, W. J. (1989). Improved time-frequency representation of multicomponent signals using exponential kernels. *IEE transactions on Acoustics, Speech and Signal Processing, vol. 37, no. 6* , 862-871.

Dib, S., Djerfi, F., Merdjana, H., & Bouden, T. (2017). Time Frequency Techniques for Detection and Characterization of Experimental Ultrasonic Signals. *ICATS*. Annaba, Algeria.

Ding, J. (2007). *Time frequency analysis and wavelet transform class notes.* Taipei, Taiwan: National Taiwan University.

Djerfi, F. (2017). Techniques avancées de traitement du signal adaptées aux contrôle non destructifs par ultrasons. *PhD Thesis* . Jijel, Algeria.

Fuente J.V., V. L. (2002). Time-frequency analysis of ultrasonics backscattering noise for nondestructive characterisation on cement pastes. *8th ECNDT*. Barcelona.

Gaohui, W., Jun, S., Dezhi, Z., Huasong, G., Wulan, S., & Yan, L. (2008). Ultrasonic NDE of thin Composite plate Based on an enhanced Wigner-Ville distribution. *17th World Conference on Non destructive Testing*, (pp. 25-28). Shanghai, China.

Khan, N. A. (2010). Cross-term Suppression in Wigner Distribution. *PhD. Disertation* . Islamabad, Patistan.

Malik, M. A., & Saniie, J. (1996). Performance comparison of time-frequency distributions for ultrasonic non destructive testing. *IEEE Ultrason Symposium* , 701-704.

Qian, S., & Chen , D. (1996). Joint Time-Frequency Analysis: Methods and Applications. New York: Prentice Hall.

Zhao, Y., Atlas, L. E., & Marks, R. J. (1990). The use of cone-shape kernels for generalized time-frequency representations of non stationary signals. *IEEE Transactions on Acoustics, Speech and Signal Processing* , 1084-1091.

Author Information

Samira Dib
University of Jijel
BP Ouled Aissa, Jijel, Algeria
Contact E-mail: samiradib@yahoo.fr

Toufik Bouden
University of Jijel, Algeria

Messaoud Bouchefirat
University of Jijel, Algeria

Fares Djerfi
University of Jijel, Algeria

PbO₂ Synthesis by Complexation and Electrooxidation of Pb²⁺ in Poly[4-(pyrrol-1-yl methyl) benzoic acid] Film

Ahmed ZOUAOUI
Université Ferhat Abbas Sétif 1

Abstract: Actually, lead dioxide (PbO2) is used as electrodes (cathode) in electrochemical power generators in particular in car batteries. The synthesis of lead dioxide is essentially obtained by chemical or electrochemical oxidation of lead salts processes. A very ambitious objective of this study is based on preparing lead dioxide by a newly developed method carried out in our laboratory. This consists in a first step to deposit a conductive polymer film poly[4-(pyrrol-1-yl methyl) benzoïc acid] having complexing properties performed by electrochemical oxidation in acetonitrile medium of the monomer 4-(pyrrol-1-yl methyl) benzoïc acid on the surface of a substrate such as carbon felt having a very high specific surface. In a second step, we proceed to the incorporation of lead dioxide by complexing the metal cations of lead in the polymer film performed by immersion of the modified electrode in a solution of lead nitrate to complex the Pb2 + cation with the carboxylic group COOH present in the polymer structure followed by electrooxidation in a solution free of lead to precipitate lead dioxide into the polymer in the form of metal microparticles. This material is used as the cathode material in batteries.

Keywords: Conductive polymer, Modified electrodes, Lead dioxide, Batteries

Introduction

The structure of the electrode/electrolyte interface, where the electrochemical reaction takes place, is of great importance in the orientation of the reaction that occurs at the surface of the electrode. The work published in recent years on the modification of the surface of an electrode shows the interest granted by the researchers in the development of efficient electrode / electrolyte interface structures allowing a good orientation of the electrochemical reaction that occurs at the electrode and control techniques of physicochemical properties. Modification of the electrode surface with polymer films containing metal particles is an effective technique for developing modified electrodes having specific electrocatalytic, electronic and magnetic properties.

In this paper, we describe a novel method and easiest way to synthesis lead dioxide by complexation Pb²⁺ ions in a poly[4-(pyrrol-1-yl methyl) benzoïc acid] film and electrooxydation of the complex formed (polymer-lead) to the formation and precipitation of lead dioxide in the polymer film. We may expect from this procedure a better dispersion of the metal in the polymer film and the formation of particles of smaller sizes [1-8].

Experimental

After the deposition of poly[4-(pyrrol-1-yl methyl) benzoïc acid] on a platinum electrode obtained by controlled potential electrochemical oxidation of the monomer in acetonitrile solution 10^{-1} M $LiClO_4$ as electrolyte, the modified electrode is either oxidized in aqueous 10^{-1} M in $NaNO_3$ and containing 5×10^{-3} M in Pb $(NO_3)_2$, or it is immersed in an aqueous solution in a metal salt of Pb $(NO_3)_2$ 10^{-2} M for a few minutes to complex ions lead by the polymer film due to the protons of H^+ that are present in the carboxyl group of polypyrrole. The electrode is then washed with distilled water several times to remove excess metal cations associated with the non-polymer, and then immersed in aqueous solution of 10^{-1} M in $NaNO_3$ to oxidize the lead ions in complexed lead dioxide. This process can be repeated several times. Both deposition techniques of lead dioxide on the surface of the modified electrode are shown in Figure 1.

$$N-CH_2-\Phi-COOH$$

Oxydation sur électrode de
carbone vitreux dans une
solution organique $CH_3CN +$
$10^{-1}M$ en $LiClO_4$

Pt/polymer

direct electrochemical oxidation in $10^{-1}M$
of $NaNO_3$ and $5x10^{-3}M$ of $Pb(NO_3)_2$

soaking in an aqueous solution
in $10^{-1}M$ of $NaNO_3$ and $10^{-2}M$
of $Pb(NO_3)_2$

Pt/ polymer, PbO_2

Pt/poly, Pb^{+2}

n répétitions

electrochemical oxidation in
an aqueous solution $10^{-1}M$ of
$NaNO_3$

Pt/ polymer, PbO_2
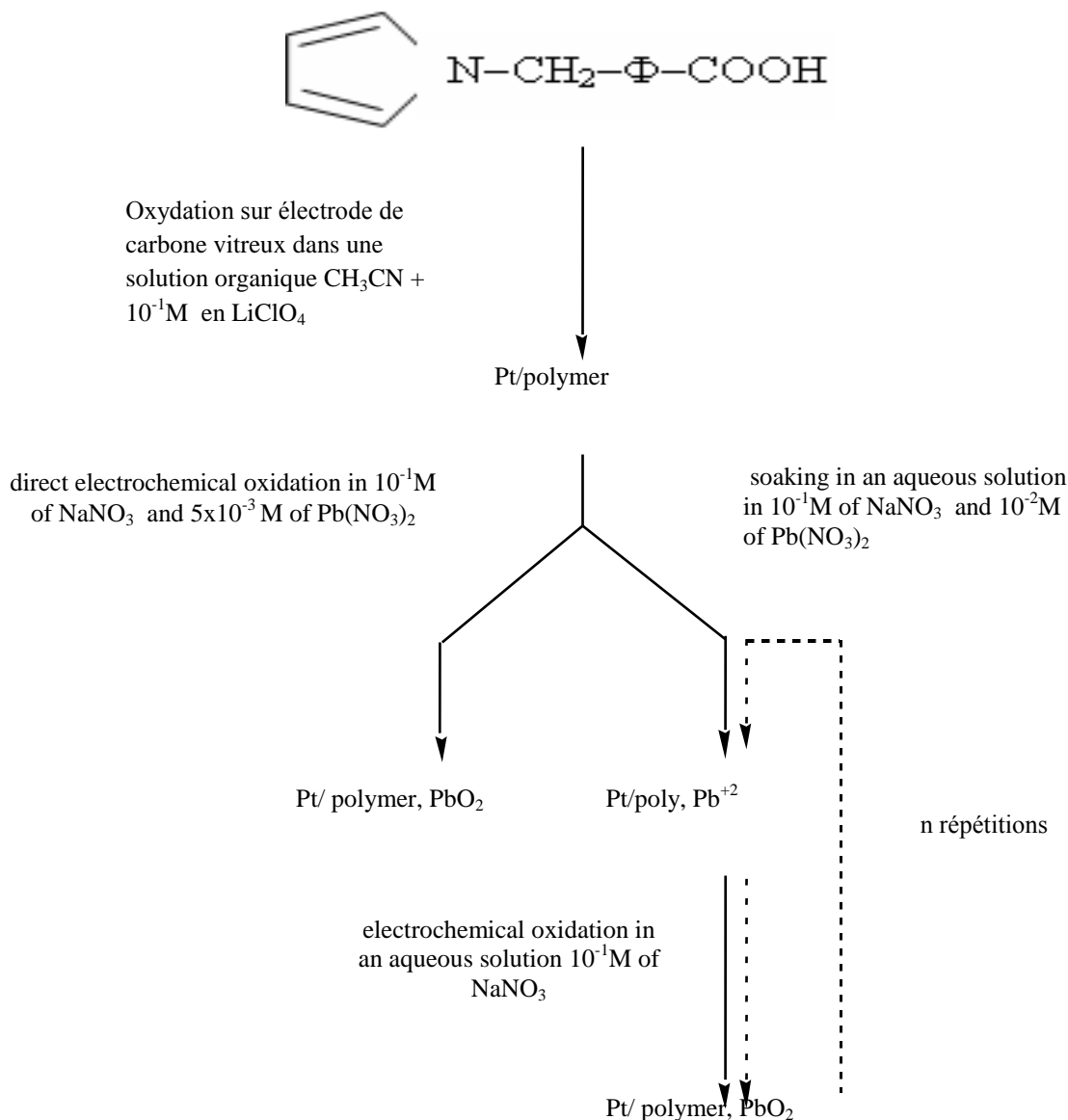
Figure 1. Techniques of preparing a platinum electrode modified with PbO_2 particles

Electropolymerization of 4-(pyrrol-1-yl methyl) benzoïc acid

The electrochemical behavior of the monomer was studied by cyclic voltammetry on platinum electrode ($\Phi = 3$ mm) in an acetonitrile medium (CH_3CN), 10^{-1} M of lithium perchlorate ($LiClO_4$) and $4x10^{-3}$ M of 4-(pyrrol-1-yl methyl) benzoïc acid. The presence of an irreversible oxidation peak around 1,2 V/ECS corresponding to the oxidation of monomer (polymerization) and consequently to the formation of poly [4-(pyrrol-1-yl methyl) benzoïc acid] deposited on the surface of the electrode (figure 2 a). The record shows a subsequent increase in current waves of oxidation and reduction peaks observed around 0,6-0,8 V, indicating that the polymer is starting to be deposited on the surface of the electrode. The current intensity of the peaks is seen to stabilize after several cycles (figure 2 b).
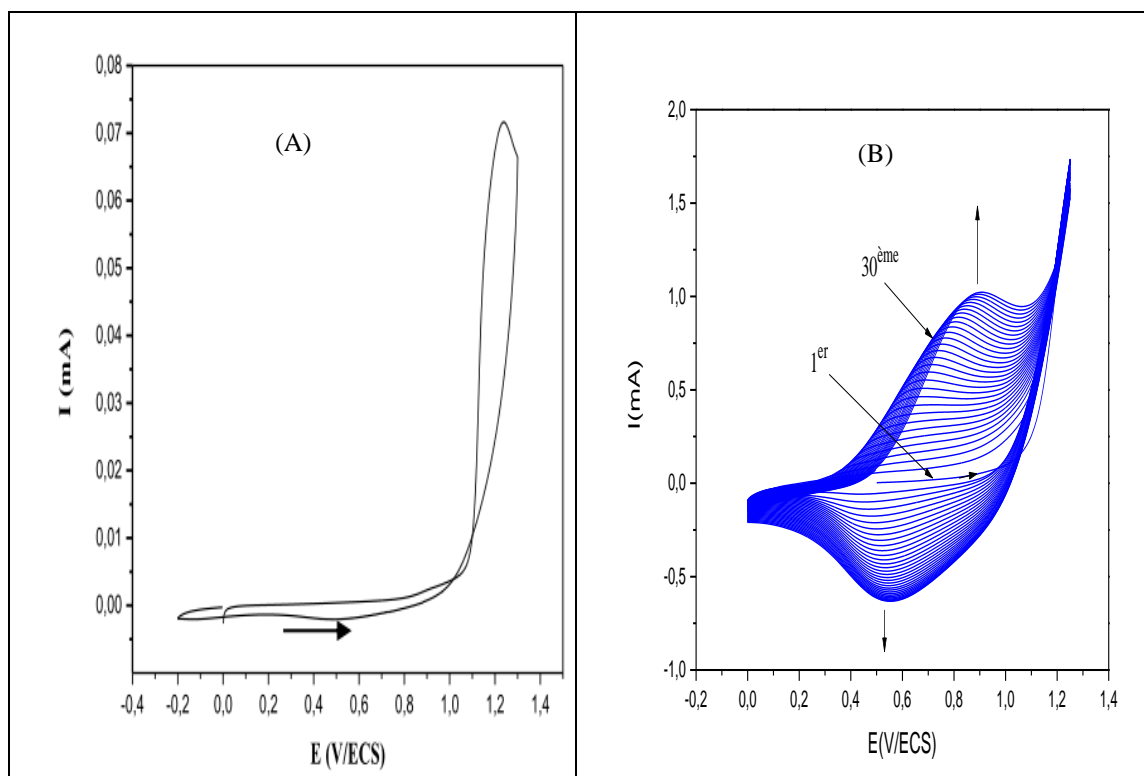
Figure 2: Electropolymerization of monomer on a platinum electrode in CH_3CN in 0.1 M $LiClO_4$ and 4×10^{-3} M of monomer at the speed of v = 100 mV/s.

Study of the electrochemical behavior of lead (II) on platinum electrode

The electrochemical behavior of lead (II) was studied on a platinum electrode of 0.07 cm^2 (ϕ = 3 mm) of area by digital cyclic voltammetry in an aqueous solution containing 10^{-2} M of $Pb(NO_3)$ and 10^{-1} M of $NaNO_3$ (figure 3) . The obtained curve is characterized by the presence of oxidation peak in the vicinity of 1,4 V/SCE corresponding, to the oxidation of lead II ions in lead IV. In the return sweep is also observed one peak in the vicinity of 0,9 V/SCE corresponding to the reduction of oxidized specie (figure 3 a).

Successive scans show an increase in the intensities of the reduction and oxidation peaks. The increase in peaks is due to the change in the state of surface of the electrode during sweeps (figure 3 b)

Effect of concentration

In order to see the influence of the concentration of the solution on the electrochemical behavior of lead, different concentrations were prepared and studied by cyclic voltammetry. The curves obtained (figure 4) show an increase in the intensity of the peak of oxidation and reduction with the increase of the concentrations. A slight displacement of the peak potential has been observed due to the surface of the electrode. These results confirm that the peaks obtained correspond well to those of lead reduction and oxidation.

.
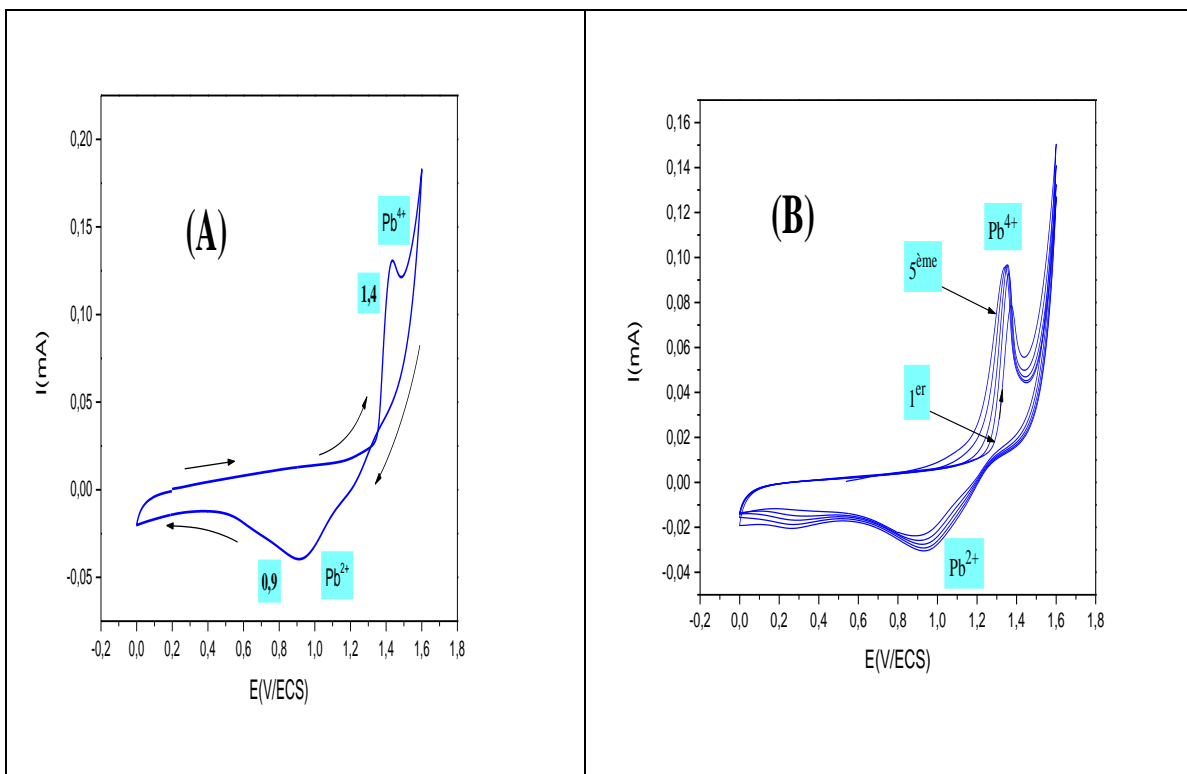
Figure 3: Cyclic voltammetry curve of Pb (II) in an aqueous solution 10^{-1} M NaNO$_3$ and 5x10^{-3} M Pb(NO$_3$)$_2$ at the scan speed of 100 mV/s, at pH =5.
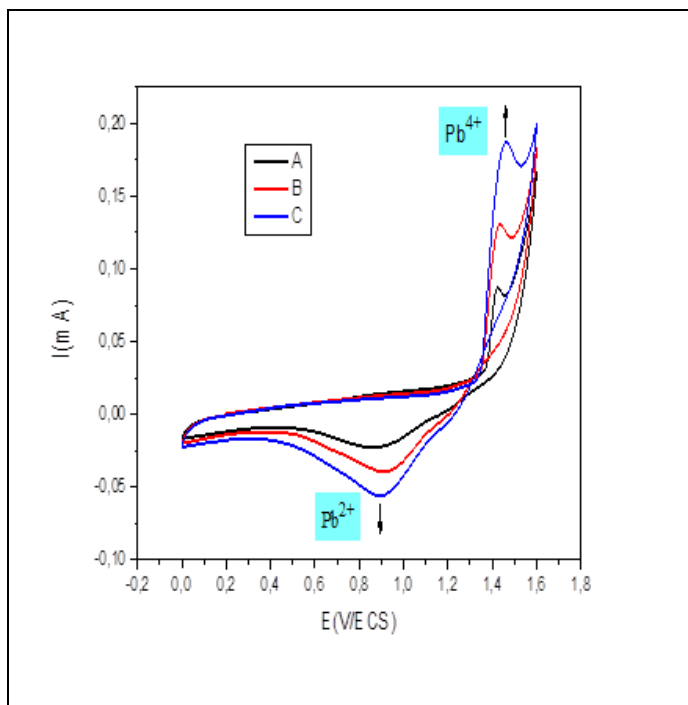
Figure 4 : Voltammograms of lead nitrate at different concentrations, plotted in aqueous solution 0,1 M of NaNO$_3$ at v =100 mV/s and PH=5 (A) 2. 10^{-3} M; (B) 5.10^{-3}M ; (C) 10^{-2}M

pH effect

In order to see the influence of the pH of the medium on the electrochemical behavior of lead, we have prepared three solutions, at pH = 2, pH = 5 and pH = 7 by adding a few drops of sodium hydroxide (NaOH) or 1M of nitric acid (HNO$_3$). Then studied by cyclic voltammetry. The curves obtained are grouped together in figure 5.

It can be seen from the curves obtained that the current density of the oxidation and reduction peaks at pH = 2 and 5 are the most intense. The latter decrease by increasing the pH of the medium and become insignificant from 5. In fact, the solution becomes cloudy indicating the beginning of the formation of a white precipitate of lead hydroxide observed especially at pH 7. According to results obtained it can be concluded that the best pH of the medium for lead is the strongly acidic medium. We also note from the curves obtained a displacement of the potential of the peak, which shows that the activated electro lead species are not the same.
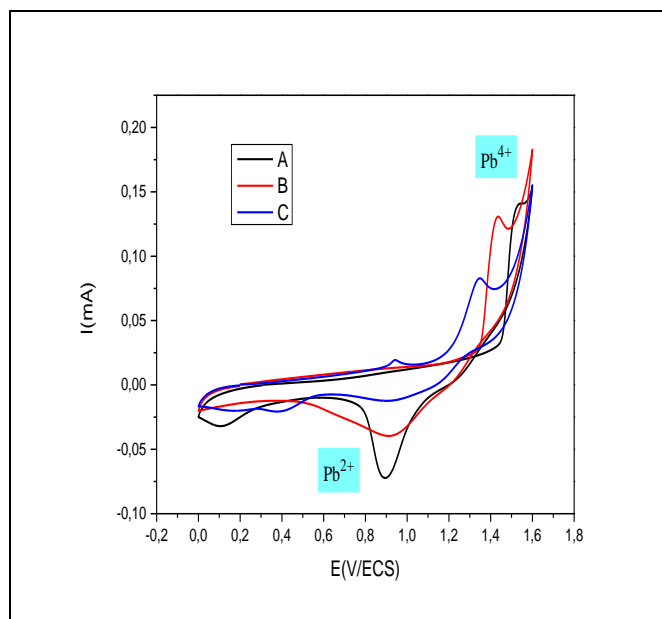
Figure 5 : Voltammograms of lead nitrate at differents pH, plotted in aqueous solution 0,1 M of $NaNO_3$ at v =100 mV/s *(A) : pH = 2, (B) : pH = 5, (C) =7.*

Insertion of lead dioxide in the polymer film

After depositing a benzoic pyrrole film on the platinum electrode, the latter was studied in a solution of 0.1M acetonitrile in $LiClO_4$, and after polymer overoxidation, we studied the electrochemical behavior. cations of lead by cyclic voltammetry in a 0,1 M aqueous solution in $NaNO_3$ after soaking for 30 minutes of the electrode modified by the polymer film in a solution of Pb $(NO_3)_2$. The curve obtained is shown in figure 6. It is characterized by the presence of an intense oxidation peak in the vicinity of 1,5V / ECS corresponding to the oxidation of Pb^{2+} to Pb^{4+}. In the return scan, a peak near 1,1 V / ECS is also observed, due to the reduction of Pb^{4+} to Pb^{2+} (figure 6 a).

Successive scans (figure 6 b) show that the Pb^{2+} cations remain in the polymer film after several cycles. A slight shift of the peak potential to the most positive values has been observed. This result clearly shows the insertion of the lead dioxide in the polymer film by complexation of the lead cations by the carboxylic group present in the polymer backbone followed by its electrooxidation to precipitate the lead dioxide in the form of microparticles.

Characterization of the composite material by impedance spectroscopy

In Figure 6 are shown the impedance diagrams of the different electrodes. The impedance diagrams are composed of an arc of circles at high frequencies corresponding to a charge transfer process and of a straight line at low frequencies corresponding to a diffusion regime (Figure 7 (A), curves b, c , d, e), except the case prior to deposition the electrode diagram presents a line all across the spectrum characteristic of a diffusion process (Figure 7 (A), diagram a). After an increase in the range of frequencies between 0 and 7 $k\Omega cm^2$, we observe that the platinum electrode has the best electrical properties, Figure 7 (B), diagram a). The impedance diagram of the electrode after deposition of lead oxide has an arc and then a very steep right slope corresponding to a blocking system. Although the electrical properties of the material decreases after deposition of the polymer film (Figure 7 (B), diagram c) and the complexation of lead (Figure 7 (B), diagram d), the latter becomes more important after oxidation of lead in the film polymer (Figure 7 (B), diagram e).
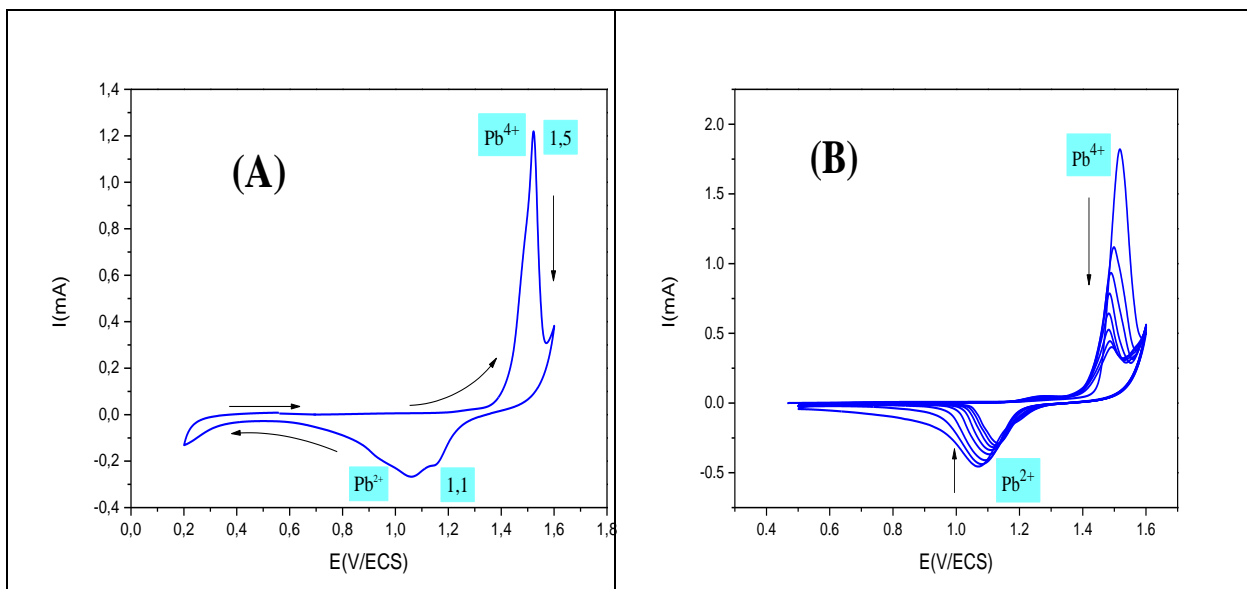
Figure 6 : Cyclic voltammetry of lead on a platinum electrode modified with a polymer film in a 0.1 M aqueous solution in NaNO₃ after dipping in Pb(NO₃)₂. at v =100 mV/s. (A) : first cycle, (B) : repetitive scanning
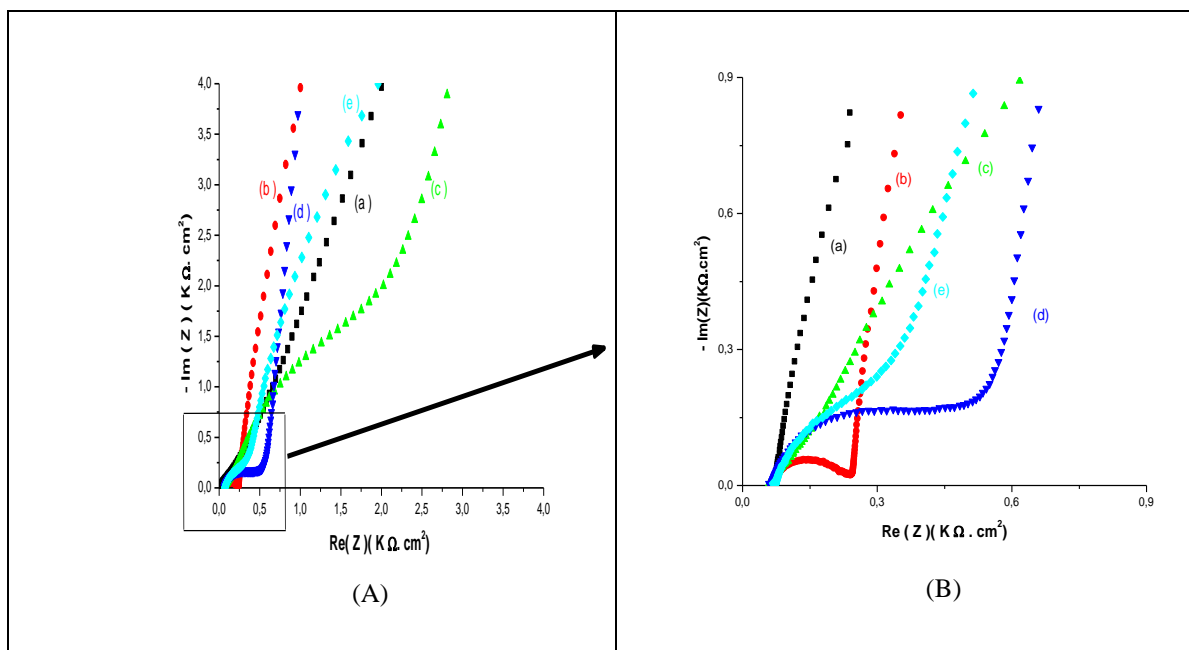
Figure 7: (A) - Impedance diagrams of an aqueous 0.1 M NaNO₃ in the frequency range between 100 kHz and 10 MHz on an electrode (a) platinum electrode, (b) electrode covered with a layer of lead in an applied potential to 1,5 V/SCE, (c) polymer film alone, (d) platinum electrode modified with a film of poly [4-(pyrrol-1-yl methyl) benzoïc acid] and then soaked in a solution of 10⁻² M of Pb(NO₃)₂ for 30 minutes, (e) platinum electrode modified with a polymer film and then dipped in a solution of 10⁻² M of Pb(NO₃)₂ for 30 minutes and oxidized at the potential of 1,5 V/SCE in the absence of Pb(NO₃)₂. **(B)** After expansion of the frequency domain.

Conclusion

I have presented a new method of preparing lead dioxide PbO₂ by complexation of lead ions in polymer films by the carboxylic group (COOH) of the polymer and thereafter by carrying an electrooxidation to precipitate the particles of PbO₂ into the polymer films. The electrochemical study showed the deposition of a polymer film on the surface of the platinum electrode and the insertion of lead dioxide particles.

The impedance diagram of the electrode after deposition of metallic lead has an arc and then a very steep right slope corresponding to a blocking system. The electrical properties of the material become more important after incorporation of lead dioxide in the film of polymer. We obtained a new material composite for applications in electrochemical generators as a cathode in batteries and in electrocatalysis.

References

Sih, B.C. and M.O. Wolf. (2005), Metal nanoparticle—conjugated polymer nanocomposites. *Chemical communications*, 27, 3375-3384.

Abrantes, L. and J. Correia, (1998), Poly (3-methylthiophene) incorporating electrolessly deposited Ni–P particles. *Surface and Coatings Technology*, 107, (2-3), 142-148.

Moutet, J.-C., (1992), Electrocatalytic hydrogenation on hydrogen-active electrodes. *A review. Organic preparations and procedures international*, 24 (3) 309-325.

Zouaoui, A., et al., (2005), *Electrodeposition of copper into functionalized polypyrrole films.* Journal of Electroanalytical Chemistry,. 474(2) 113-122.

Zouaoui, A., et al., (2000), Electrocatalytic hydrogenation of ketones and enones at nickel microparticles dispersed into poly (pyrrole-alkylammonium) films. *Electrochimica Acta*, 46 (1) 49-58.

Melki, T., et al., (2009), Electrosynthesis and catalytic activity of polymer-nickel particles composite electrode materials.*Journal of the Brazilian Chemical Society*, 20(8) 1523-1534.

Shiu, K.-K. and O.-Y. Chan, (2005), Electroanalysis of copper species at polypyrrole-modified electrodes bearing alizarin red S ligands. *Journal of Electroanalytical Chemistry*, 388(1-2) 45-51.

Hakimi N., Zouaoui A.,Satour F. Z., Sahari A., Zegadi A. (2005), Electrochemical Synthesis and Properties of the Composite MaterialITO/PolypyrroleBenzoic:Cobalt for Electronic Storage Applications, *Journal of Inorganic and Organometallic Polymers and Materials* 1-7.

Author Information

Ahmed Zouaoui
Laboratoire de Croissance et Caractérisation de Nouveaux
Semiconducteurs, Faculté de Technologie, Université Ferhat
Abbas Sétif 1, 19000 Sétif, Algérie
Contact E-mail: a_zouaoui_dz@yahoo.fr

A Drone IFF and Tracking Algorithm with the Relay Drone and the Beacon System

Yunseok CHANG
Daejin University

Abstract: A beacon system can easily be applied to recognize the registered drone information since the beacon can be worked as a sort of IoT device. But most of the beacon device can work in a short-range, the control center has lots of troubles to receive the beacon signal in it's out of range. In this study, we designed the drone IFF and tracking algorithm that can track the current position and the flight route of the target drone through the beacon information and the GPS positioning data from the approached relay drone in the beacon range of the target drone. The relay drone has the beacon receiver and GPS sensor and approaches to the target drone to receive the beacon signal. If the relay drone receives the beacon signal in a beacon range of the target drone, the relay drone checks the beacon information and its flight data and transmits it to the control center. To enhance the precision of the algorithm, the relay drone checks more than two different check positions at the critical distance from the inflight target drone. The drone IFF and tracking algorithm can calculate the current position and flight route of the target drone through the two or more GPS data and flight data at the check positions from the relay drone. Since the relay drone flies heading to the inflight target drone, the precision of the drone IFF and tracking algorithm could be fluctuated according to the critical distance and the number of check positions. The experimental results with the DJI Phantom 4 Pro showed the precision of the algorithm is proportional to the product of the critical distance and flight speed and has over 92% with two check positions.

Keywords: Relay drone, IFF, Beacon, Flight tracking algorithm

Introduction

Anyone wants to fly a drone in the sky without any control or regulation by law. But the drone is a kind of flight object that can harm someone by a fault or other unpredictable situation that should be carefully controlled in the air. Many states and regional governments have a sort of drone authorization rule and operate the surveillance systems to detect unauthorized aircraft. Many of these surveillance systems have an aircraft detection system that can distinguish our force from the enemy as known as IFF (Identification Friend or Foe) system. If there is some kind of IFF among the aircraft, air traffic control can become easy to identify the aircraft and order to move or fly somewhere under the schedule. In today's airports and military areas, the IFF system is the most essential and usual system that can enhance the air traffic surveillance system.

In the drone area, the beacon-based drone surveillance system also widely used as like on airports or air force bases. But the existing drone surveillance system has short-range compare to the commercial radar system target to the aircraft and limited to the narrow area control at all. A drone has a limited power source compares to an aircraft, it cannot carry a long-range beacon to reach to the control center from the air in a wide area. Since the control center can only cover the commercial low-power beacon range less than 150m, the drone surveillance system could not become an effective control system without a high-expensive radar system. If there is a kind of bridge or repeater between the control center and target drone, the drone surveillance range can be expanded. Like the target drone, we can use a commercial drone as a relay drone that can easily make a sort of bridge between the target drone and the control center. If we use a very long-range communication system between the relay drone and control center, we just approach the relay drone near the target drone to get the beacon information as like the IFF system.

IFF Method for inflight drone

Basic Concept

The key idea of the drone IFF is a very simple method to identify the friend and foe by using a scout drone called "Relay drone" flies from the ground control center to the UAV or target drone. To identify an inflight target drone as a friend, the target drone has to carry a kind of beacon authorized by the control center. If there is an unidentified inflight drone, the control center sends a relay drone approach to the target drone. If the target drone has an authorized beacon, the relay drone can recognize it as a friend in the beacon active range. Otherwise, the target drone is recognized as a foe and handled by law or any other regulation. By using the relay drone, the control center can identify the flight authority of the target drone from the out of the beacon range, and even can track the inflight target drone by flight tracking algorithm.

Flight Tracking Algorithm

The flight-tracking algorithm also has a very simple method as known as triangulation. Fig. 1 shows a simple situation of the relay drone approached near the inflight drone. If the relay drone flight around the target inflight drone, it can check its aerial position and the azimuth to the target at two or more positions with different angles. From the aerial position data and angles, we can easily calculate the distance between the relay drone and the target drone that can identify the aerial position of the target drone.
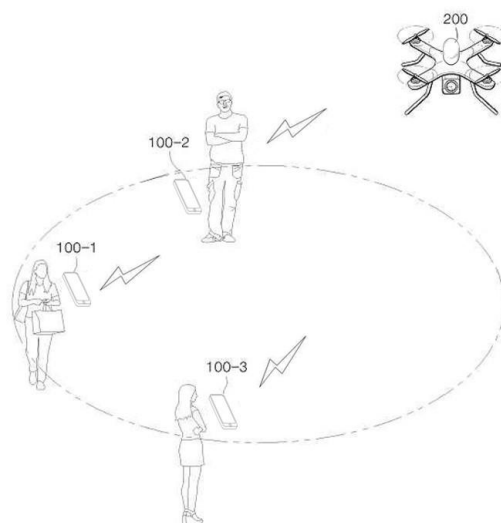
Figure 1 Basic concept of the IFF with beacon

In this work, we use the GPS data from the built-in GPS module of the relay drone as the aerial position data for triangulation. Since most of the drone system program libraries provide the GPS API and triangulation method in their development kit, we can easily estimate the distance from the relay drone on the specific position, and identify the aerial position of the target drone without any software modification of the target drone.

IFF and Tracking System Design

To identify the target drone, we attached a sort of long-range beacon module on the target drone and implemented the tracking app as shown in Fig. 2. Any of the commercial drones have no beacon module, the IFF beacon itself shows the target drone is an authorized drone for a specific control center. The tracking app can connect to the relay drone, and shows the recognized drones and its aerial position on the map. The relay drone searches the beacon signal that sends the beacon information of the target drone and its GPS data when identifies the authorized beacon signal from the target drone.

Figure 2 Beacon system design on the Phantom 4 Pro

Experimental Environments

Table 1. System environments

Environment	Item(s)	Specifications
Target Drone	Product	DJI Phantom 4 Pro
	Flight speed	P-mode:50km/s
	Weight	1,392 g
Smart device	Product	Samsung Galaxy Note 4
	OS version	Android Lollypop
Beacon	Product	BeaFon BLE C1
	Range(Max)	150 m
Total trials	Per checkpoints	8

To make sure of the proposed drone IFF and tracking algorithm, we made a series of experiments and check two major experimental results, *Critical Distance* and *Tracking Precision*. Although the drone tracking algorithm proposed in this work has a very simple method, its usability and efficiency have to by experiments under the inflight environment. Therefore, we tried 8 experiments with one relay drone and a target drone that has a beacon attached to the top of the drone. Table 1 shows all system environments in the experiments performed at the Hangang Drone Park in Seoul, Korea.

Critical Distance

The critical distance can be defined as an average distance from the relay drone to the recognized inflight target drone. If a relay drone approaches to a specific target drone that has a beacon, the relay drone can recognize the beacon signal. Since the relay drone always flies to the target drone straight, when the relay drone checks its GPS position at two or more check positions with different angle, we can estimate the distance to the target drone from the GPS data, flight angle and speed of the relay drone by the triangulation directly.

Tracking Precision

The tracking precision can be defined as a match percentile between the real aerial position and the estimated aerial position calculated by GPS data and direction of the relay drone when recognizing the target drone. The estimated aerial position of the target drone is calculated at the ground control center, not at the relay drone since the system program of the commercial drone is hardly modified by the user. If the estimated aerial position is closer to the real aerial position of the target drone, the tracking algorithm has high precision and reliability.

Experimental Results

In this work, one of the key results is the relation between the critical distance and the number of check positions for a specific target drone. To make the experiment clear, we tried multiple flights to get the critical distance from the relay drone to the target drone at constant flight speed. Table 2 shows the critical distances at

P-Mode flight speed (about 50km/sec) for a target drone with 2 check positions and 3 check positions. Although we had tried to maintain the other experimental condition despite the wind speed and temperature variation, the critical distance has a little deviation for every trial. The experimental results show that the relay drone can recognize the target drone's beacon signal almost at the same distance independent of the number of the check positions.

Table 2. Average critical distances at P-mode flight speed

Trials	*Ave.critical distance with 2 check positions*	*Ave. critical distance with 3 check positions*
1	126	123
2	105	111
3	97	101
4	111	106
5	121	112
6	108	103
7	101	102
8	107	108

Next, we check the tracking precision for a target drone at P-mode flight speed with 2 and 3 check positions. Fig. 3 shows that the tracking case with 3 check positions has higher precision than the case with 2 check positions. At the P-Mode flight speed, the tracking algorithm shows over 95% tracking precision for the target drone with 3 check positions. Even in the case of 2 check positions, the tracking algorithm has more than 92% of precision at the P-Mode flight speed. If the relay drone cannot recognize any authorized beacon signal from a UAV in the critical distance of a specific relay drone, the UAV could be recognized a sort of enemy's drone at the control center and the tracking algorithm can be worked as an effective IFF system without any expensive airplane or radar system within the drones flight range.
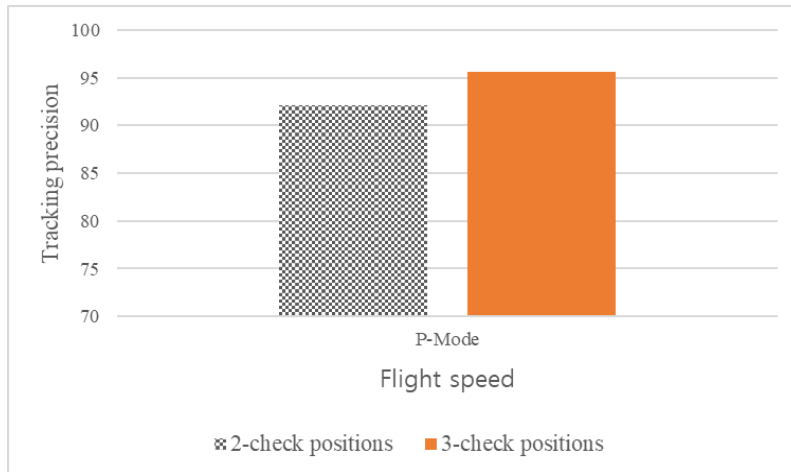
Figure 3 Tracking precision vs check positions

Conclusion

In this work, we designed and implemented an effective drone IFF and tracking algorithm with the relay drone and the beacon system. In this system, we use a relay drone to check a specific target drone is a friend or foe by using the beacon signal from the target drone. If there is a beacon signal from the target drone within the critical distance of the relay drone, we can recognize the fact that the target drone is a friend and vice versa. The critical distance can be worked as a kind of action range as like an IFF of the aircraft traffic control system. Since the critical distance could be varied according to the drone flight speed and various flight environment, we can select the appropriate method to authorized/unauthorized drone handling depends on the cost and environment. The experimental results show that the proposed drone IFF and tracking algorithm has over 92% and 95% of tracking precision at the P-Mode flight speed of the DJI Phantom 4 Pro with two and three check positions. These results enable the proposed algorithm to stretch to the commercial market or military area.

The proposed drone IFF and tracking algorithm can not only check the IFF but also check the aerial position by using the two or more GPS data of the relay drone with different target angles. Therefore, the tracking algorithm can be widely applied in the drone world, for example, regional drone traffic control, drone hunting or jamming to an illegal inflight drone, and so on. We are going to enhance the tracking algorithm works faster and simpler, and at further work, we aim to integrate the tracking algorithm into the dedicated relay drone system software along with the beacon system.

Acknowledgment

References

Dijkshoom N (2012). Simultaneous localization and mapping with the AR drone. *Master's Thesis*, University of Amsterdam

Kendoul F (2012). Survey of advanced in guidance, navigation, and control of unmanned rotorcraft systems. *Journal of the Field Robotics*, 29, 315-378.

Kim B, Jung M, Chang Y (2018). Inflight Drone Re-routing Method with Google Map on Smart Pad. Proceedings from ESCS'18. 37-40.

Mac T, Copot C, De Keyser R, Ionescu C (2018). The Development of an autonomous navigation system with optimal control of a UAV in a partly indoor environment. *Mechatronics*, 49, 187-196.

Neemat S, Inggs M (2012). Design and Implementation of a Digital Real-time Target Emulator for Secondary Surveillance radar / Identification Friend or Foe. *IEEE Aerospace and Electronics Magazine*, 27(6), 17-24.

Author Information

Yunseok Chang
Daejin University
1007 Hoikook St. Pocheon, Rep. of Korea
Contact E-mail: cosmos@*daejin.ac.kr*

IConTES 2019: International Conference on Technology, Engineering and Science

Electrochemical Study of Theophylline-Creatinine Interaction Using Square Wave Voltammetry

Asmaa M. AL-HASANY
University of Mosul

Amer Th. AL-TAEE
University of Mosul

Haitham A. AL-WAHB
University of Mosul

Abstract: In this work, the interaction between theophylline (TP) and creatinine was studied. A three electrode detection system was used, 2mm diameter glassy carbon electrode as working electrode, 1mm diameter platinum wire as auxillary electrode and Ag/AgCl. saturated KCl as reference electrode. Square wave voltammetric technique (SWV) also used, the voltammogram of theophylline shows a stable well - defined reduction peak at (1.07) V versus Ag/ AgCl Sat. KCl/ in phosphate buffer solution (pH=7) using glassy carbon electrode. The voltammograms were recorded for theophyline with serious addition of creatinine, interaction of theophyline with the sequence addition of creatinine were examined at different temperatures (288, 293, 298, 298, 303, 308 and 310) ºK and the thermodynamics parameters were calculated. The binding constant (K) between theophylene and creatinine was also measured. The results showed that the binding constant (K) decreased with increasing temperature, this is as a result of the negative value of enthalpy change (-46.6) KJ. mol-1 (exothermic binding). Negative value of Gibbs energy (-275.338 x 102 _ -36384.961 x102) KJ. mol-1 indicates that the interaction is spontaneous and could be due to van der waals forces or hydrogen bonds effect i. e the low value of Gibbs energy indicates weak interaction between the studied compounds.

Keywords: Theophylline, Cratinine, Interaction, Modified electrode

Introduction

Theophylline (1,3-dimethylxanthine) as a xanthine derivative has been commonly used as an additional treatment drug in the asthmatic acute phase in children and bronchospasm in adults (Kawai and Kato, 2000; Kanehara et al., 2008; Igarashi and Iwakawa, 2009; Fuyong Jiao et al., 2018). It is also used clinically as diuretic, cardiac stimulant and smooth muscle relaxant (Shruti et al., 2019). Thus, more and more scientists have paid increasing attention to the techniques for the quantitative determination of theophylline. The chemical structure of theophylline is shown in Fig. (1).
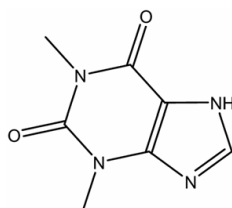
Fig. 1. The chemical structure of theophylline

At present, many methods have been employed for measuring theophylline quantitatively, such as liquid chromatography (Kalyani and Chava, 2017; Srdjenovic et al., 2008; Huang and Xu, 2005), UV spectrometry

(Sujana, 2016; Culzoni, 2005), chemiluminescent immunoassay (Zhou et al., 2005), gas chromatographymass spectrometry (GC–MS)and gas chromatography–isotope dilution mass spectrometry (GC– IDMS) (Kress et al., 2002; Arinobu et al., 2009). Nevertheless, some of these methods, such as chromatography and mass spectrometry, are time-consuming, expensive and need complicated preconcentration or multisolvent extraction as well as trained technicians. Instead, electrochemical methods are characterized by simplicity, high sensitivity, good stability, low-cost instrumentation on-site monitoring (Sadik et al., 2003). Thus, they are exploited for the determination of theophylline.

Creatinine is a metabolic waste product of the breakdown of muscle creatine. The creatinine levels in the blood serum indicate an equilibrium between production and excretion by the kidney and is an indicator of kidney function (Horne and Swearingen, 1993) . Normal concentrations of creatinine in the blood serum for adult males is 0.62 to 1.10 mg/dL and 0.45 to 0.75 mg/dL for adult women(Skurup et al., 2008). Increased serum creatinine levels, comparable to the decline in the quality of the kidneys, so that the analysis of creatinine levels in the blood is very important to know the kidneys quality work.

Creatinine analysis methods that are generally used in the medical field is the Jaffe method. Analysis of creatinine using the Jaffe method has a principle, namely by forming a colored complex solution which can be analyzed by UV-Vis spectrophotometer. The advantages of this method as an analytical process is easy and simple, while the drawback is the low selectivity. Other common methods used for the analysis of creatinine is the enzymatic method. Analysis of creatinine with this method is hardly bothered by another matrix, but it takes a long time for the analysis and the cost is quite expensive (Guo and Guo; 2005).

Another method that has been used for the analysis of creatinine is potentiometric method. In the potentiometric method used two electrodes, the working electrode and reference electrode(Darmokoesoemo, et al.; 2017). The function of the working electrode is sensoring the analyte in the solution being analyzed, so that the working electrode must be selective and sensitive to analyte. Electrodes used for potentiometric analysis can be modified with the aim to increase the selectivity and sensitivity to analyte.

In this work the determination of creatinine through its interaction with theophylline was carried out using square wave voltammetry technique (SWV).

Experiment

Apparatus

All the electrochemical experiments were performed using a797VA computrace instrument (Metrohm, Switzerland). The reference electrode was an Ag/AgCl with saturated KCl, 1.0 mm a platinum wire was used as the auxiliary electrode and 2.0 mm a glassy carbon electrode GC used as the working electrode. pH measurements were performed by using a digital pH meter (HANNA, Italy, calibrated with standard buffers.The Haake Heated Water Bath Circulator is Model G, USA.

Chemicals and Reagents

All chemicals used in this work (creatinine, theophylline, dipotassium hydrogen phosphate K2HPO4, and potassumdihydrogen phosphate KH2PO4) were of analytical grade and used without further purification, and were purchased from Fluka, and BDH.

Preparation of the Theophylline Electrode

Electropolymerisation of Theophylline at the surface of bare glassy carbon electrode GC was carried out by using cyclic voltammetric method in aqueous solution containing (1.960 x 10-4)M TP in 0.2 M PBS of pH 7.0. The TP molecules are reduced and rapidly combine with the GC surface. A uniform film is produced on GC surface, which indicates that the TP has been deposited on the GC surface by electropolymeriztion method.

Results and Discussion

Electrochemical Behaviour of Theophylline

The square wave voltammogram was recorded using (9.090 x10-5) M theophylline (TP) in phosphate buffer solution under the default instrument. After that the optimum conditions of TP has been studied, and the voltammograms of (9.090 x 10-5) M of TP Fig. (2) were recorded under each effective parameter and the results obtained are summarized in (Table 1).

Table 1. Default and the optimum conditions of TP

Condition	Defaultconditions	Optimum conditions of TP
Start Potential (V)	0.4	0.4
End Potential (V)	1.4	1.4
Deposition potential (V)	-0.9	-1.5
Deposition time (s)	60	50
Equilibration time (s)	5	5
Voltage step (V)	0.006	0.002
Amplitude (V)	0.02	0.03
Frequency (Hz)	50	100
Sweep rate (V/s)	0.3	0.1984
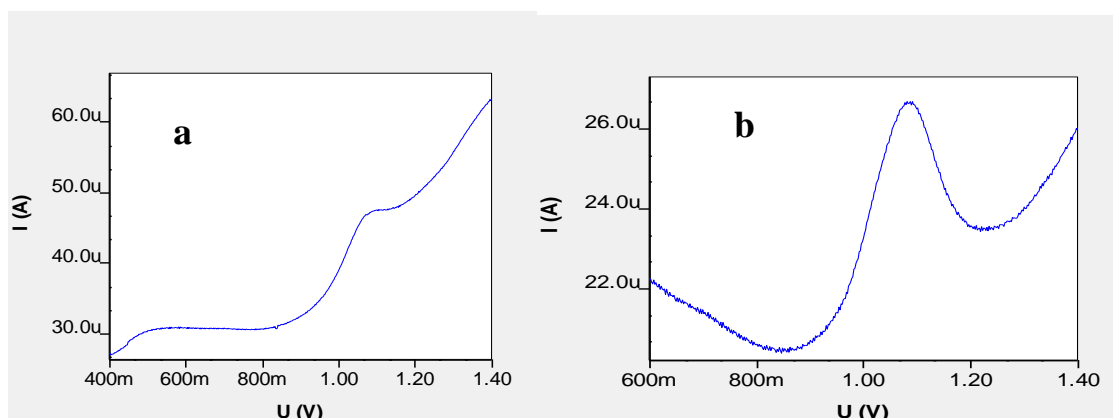
Fig. 2. The voltammogram of TP (9.090 x 10^{-5}) M (a)under the default conditions,
(b) under the studied optimum conditions

Effect of pH on the TP reduction peak

The Effect of pH on the reduction potential and diffusion current of TP reduction peak in the 0.2 M phosphate buffer (pH 4.0-9.0) was studied by square-wave voltammetry. A significant decrease of the peak current is observed at pH 4.0 to 9.0. The obtained peak shifts to the less positive potentials with the increase in the pH, and the plot of Ep versus pH is linear as shown in Fig. (3) with correlation coefficient value(R^2= 0.9172), and solpe value(0.0312 V.pH-1) which is near of the theoretical value calculated by Hillson,. this is indicate a complex electrode process in which electron exchange is significantly influenced by protons.
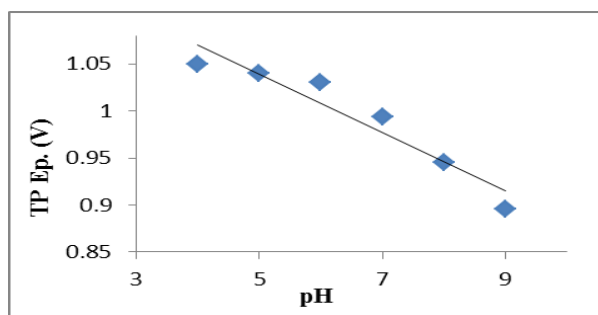
Fig. 3. The relation between the reduction potential of (1.960 x 10^{-4}) M of TP and the pH

Electropolymeriztion of TP onto glassy carbon electrode

Electropolymeriztion is a facile and efficient approach to immobilize a film onto solid state electrode surface because film properties, such as thickness, permeation and charge transportation, can be adjusted by controlling electrochemical parameters. Fig. (4) shows the successive cyclic voltammetric CV curves during the electropoly- meriztion of TP from a phosphate buffer solution (pH 7.0) containing (1.960 x 10-4)M TP. A uniform film is produced on GE surface, which indicates that the TP has been deposited on the glassy carbon electrode GC surface by electropolymeriztion method.
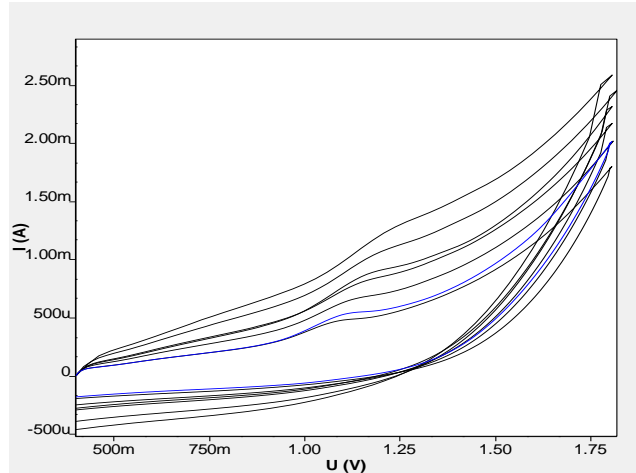
Fig. 4. Electropolymerization curve of (1.960×10^{-4}) M TPat GC

Electrochemical Behaviour of creatinine

The square wave voltammogram was recorded using (17.333 x10-5) M creatinine in phosphate buffer solution, the creatinine shows a reduction peak at (0.109) V Fig. (5).
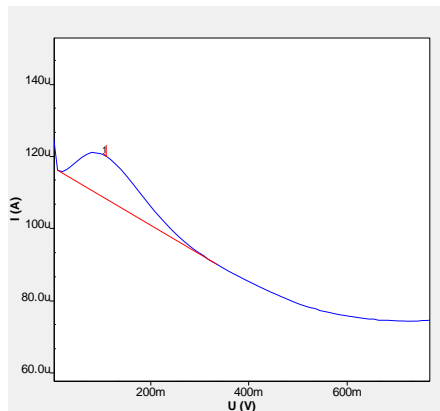
Fig. 5. Shows the creatinine reduction peak at (0.109) V.

Effect of creatinine on Theophylline Reduction Peak

The effect of creatinine on TP peak was studied by adding sequence additions of creatinine $(1.470 \times 10^{-5}$ - 38.066×10^{-5}) M to a voltammetric cell containing (1.666×10^{-3}) M of TP; a decrease in the TP current peek value was observed with the sequence additions of creatinine Fig. (6).
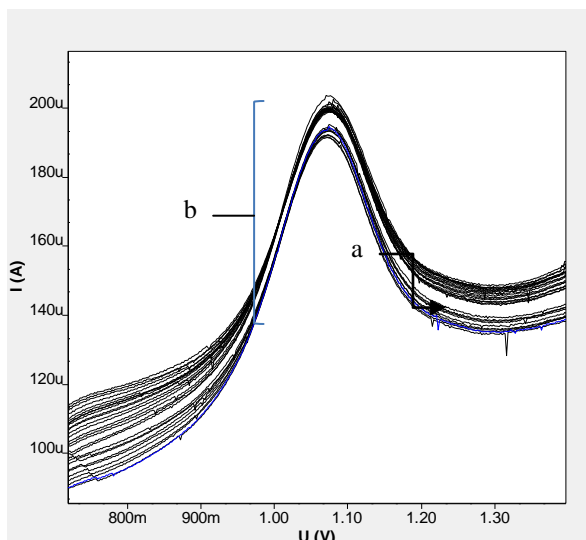
Fig. 6. The voltammograms of TP (1.666×10^{-3}) M (a) in the absence of creatinine
(b) in the presence of creatinine (1.470×10^{-5} - 38.066×10^{-5}) M

Stability of Theophylline Reduction Peak in the Presence of Creatinine

The stability of TP voltammogram (3.849×10^{-4}) M in the presence of creatinine(9.305×10^{-4}) M was measured at different times, using phosphate buffer solution (pH=7) under the previous optimum conditions of TP and the results are shown in (Table 2). The results indicate that the interaction peak was stable within the studied time (110) min.

Table 2. Stability of theophylline reduction peak in the presence of creatinine

Time (min)	Ep.(V)	Ip. (nA)
0	1.05	27200
10	1.05	26000
20	1.05	26800
30	1.05	26800
40	1.05	26400
50	1.05	26700
60	1.05	26800
70	1.05	27500
80	1.05	26600
90	1.05	27700
110	1.05	27600

Thermodynamic Calculations

The binding constant of theophylline- creatinine was calculated according to the equation (1).

$$\ln (Ip/(Ip^o -Ip)) = \ln (1/[Conc.(M)]) - \ln (K) \quad \ldots\ldots\ldots.. \quad (1)$$

Where Ip^o is the reduction current of TP alone, Ip is the reduction current of TP- creatinine complex, Conc. is the molar concentration of TP, and (K) is the binding constant of TP- creatinine complex.

The binding constant was calculated at different temperatures (288, 293, 298, 303, 308, 310) K^o, and the results are shown in Fig. (7).
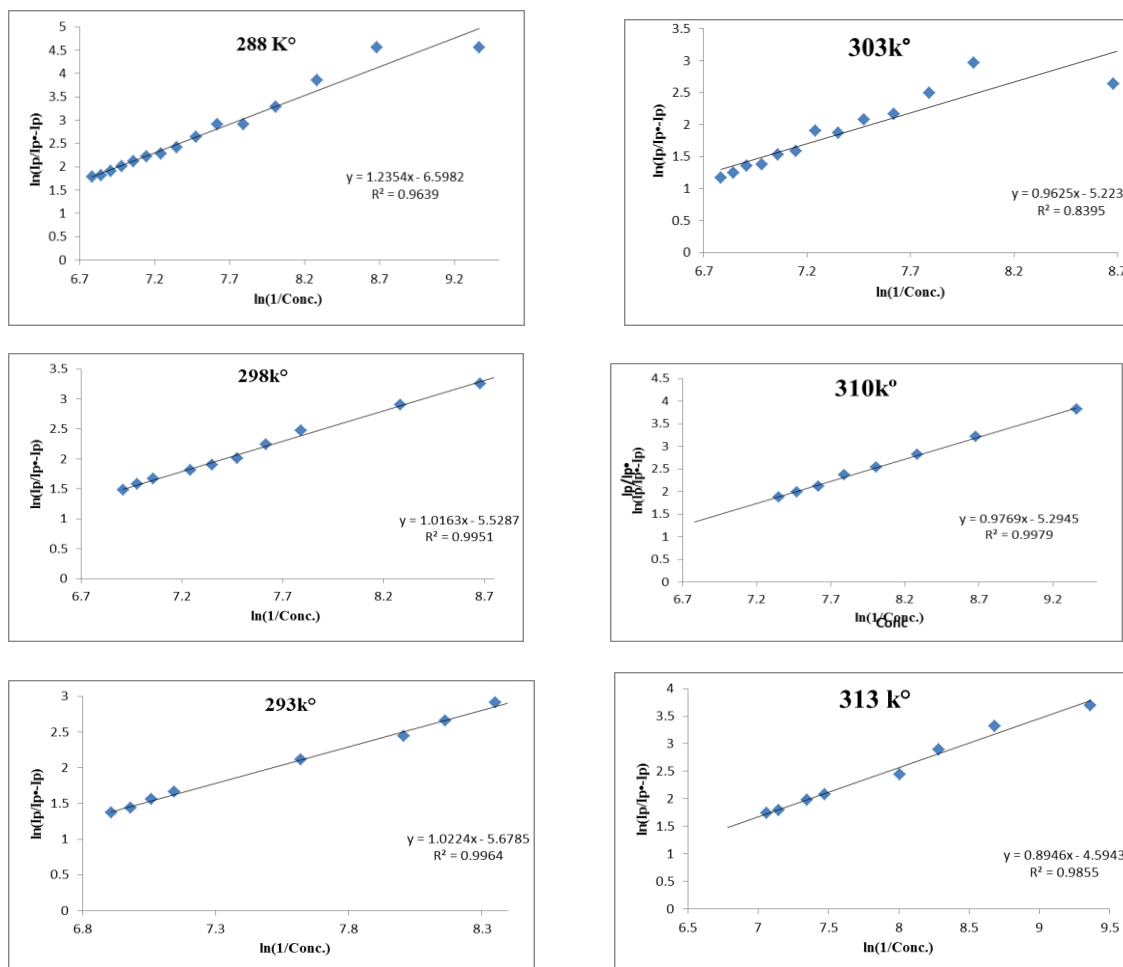
Fig. 7. Plot of ln (Ip/(Ipº –Ip)) vsln (1/[Conc.(M)]) at (288, 293, 298, 298, 303, 308, 310)ºK

Thermodynamic parameters were calculated Fig. (8) according to the equations (2) for Van't Hoff eq. and (3), the binding constant at different temperatures are shown in (Table 3).

$$\ln K = \frac{\Delta H}{RT} + \frac{\Delta S}{R} \quad \ldots\ldots\ldots\ldots \quad (2)$$

$$\Delta G = - R\,T\,\ln K \quad \ldots\ldots\ldots\ldots \quad (3)$$
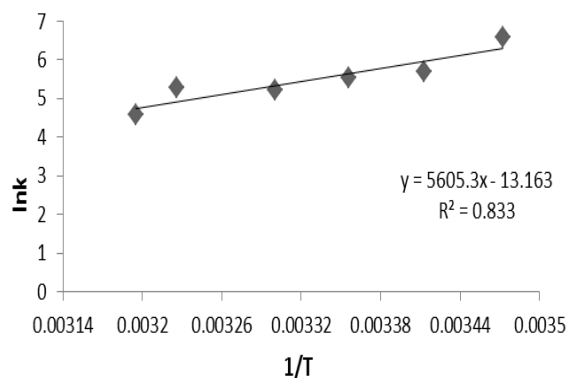
Fig. 8: Plot of ln K vs 1/T

Table 3. The relation between binding constant and temperature

T (C°)	T(K°)	Ln K_b	The binding constant $K_b (10^2)$ M	ΔH (KJ.mol^{-1})	ΔG (KJ.mol^{-1})	ΔS (J.mol^{-1}.K^{-1})
15	288	6.598	733.773		-36384.961	
20	293	5.678	292.510		-31857.024	
25	298	5.528	251.816	-46.6	-31545.923	-0.109
30	303	5.223	185.545		-30303.413	
37	310	5.294	199.237		-31426.108	
40	313	4.594	98.9188		-27533.894	

The negative value of ΔS indicates that the interaction is ordered. The negative value of ΔH means that the interaction is exothermic. From the values of ΔG, the spontaneity of interaction is decreased with increasing temperature. This agrees with the negative value of ΔH showing that the type of interaction is hydrogen bonding or vander Waals forces. From the binding constant and thermodynamic results, we find that the interaction between TP and creatinine is week, exothermic, spontaneous and stable (Ross and Subramanian, 1981).

Conclusion

Square wave voltammetry technique is a good technique to study the interaction between TP and creatinine. Thermodynamics parameters give an idea about interaction type, negative value of enthalpy change means that the interaction was exothermic, negative value of entropy change indicates that the interaction became more ordered and the shifting of Gibss free energy value to more positive caused the spontaneouity decrease. From the thermodynamics parameters we can conclude that the interaction between TP and creatinine may be due to hydrogen bonding or vander Waals forces.

References

Arinobu, T.; Hattori, H.; Kumazawa, T.; Lee, X.P.; Mizutani, Y.; Katase, T.; Kojima, S.; Omori, T.;
Kaneko, R.; Ishii, A.; Seno, H. (2009). High-throughput determination of theophylline and caffeine in human serum by conventional liquid chromatography-mass spectrometry. Forensic. Toxicol.; 27(1), 1-6.

Blake, K.; Kamada, A.K. (1996). "Textbook of Therapeutics: Drug and Disease Management".

Williams and Wilkins: Baltimore; 6, 651 p.

Culzoni, M.J.; De Zan, M.A.; Robles, J.C.; Mantovani, V.E.; Goicoechea, H.C. (2005). Chemometries-assisted uv-spectroscopic strategies for the determination of theophylline insyrups. J. Pharmaceut. Biomed., 39(5),1068-1074.

Darmokoesoemo, H.; Khasanah, M.; Sari, N.M.; Kusuma, H.S.; (2017). Analysis of creatinine by potentiometric using electrode carbon paste modified by molecularly imprinted polymer as sensor. Rasayan Journal of Chemistry • 10(2), 450 – 453.

Fuyong, J.; Nan, G.; Sheng, Z.; Yuhua, Y. (2018). A Clinical Analysis and Study of 110 Pediatric Cases with Aminophylline Poisoning. Pharmacol. and Clin. Research, 5, 2473-5574.

Guo, M.D.; Guo, H.X., Journal of Electroanalytical Chemistry, 585, 28 (2005).

Haruta, Y.; Hattori, N.; Kohno, N. (2008). Anti-inflammatory effects and clinical efficacy of theophylline and tulobuterol in mild-to-moderate chronic obstructive pulmonary disease Pulm. Pharmacol. Ther.; 21, 874.

Hillson P.J.; and P.P. Birndaun, (1950), Trans. Faraday Soc., 48, 478.

Horne, M.M.; Swearingen, P.L.; Fluids, Electrolytes and Acid-Base Balance, 2nd ed., Mosby, St Louis (1993).

Igarashi, T.; Iwakawa, S. (2009). Effect of gender on theophylline clearance in japanese pediatric patients. Biol. Pharm. Bull., 32(2), 304-307.

Kalyani, L.; Chava, V.; Rao, N. (2017). Development and validation of stability-indicating RP-HPLC method for the simultaneous analysis of Salbutamol, Theophylline and Ambroxol. Saudi J. Med. and Pharm. Sci., 2413-4929.

Kanehara, M.; Yokoyama, A.; Tomoda, Y.; Shiota, N.; Iwamoto, H.; Ishikawa, N.; Taooka, Y.; Kawai, M.; Kato, M. (2000). Theophylline for the treatment of bronchial asthma: present status Find. Exp. Clin. Pharmacol., 22(5), 309-320.

Kress, M.; Meissner, D.; Kaiser, P.; Hanke, R.; Wood, W.G. (2002). Determination of theophylline by HPLC and GC-IDMS, the effect of chemically similar xanthine derivatives on the specificity of the method and the possibility of paracetamol as interfering substance. Clin. Lab., 48(9-10), 541-551.

Minton, N.A.; Henry, J.A. (1996). Acute and chronic human toxicity of theophylline. Human Exp. Toxicol., 15(6), 471-481.

Ross, D.P.; Subramanian, S. (1981). Thermodynamics of protein association reactions: forces contributing to stability. Biochemistry, 20, 3096-3102.

Sadik, O. A.; Land, W. H.; Wang, J. (2003). Targeting chemical and biological warfare agents at the molecular level. Electroanalysis., 15(14),1149-1159.

Skurup, A.; Kristensen, T.; Wennecke G., Clinical Chemistry and Laboratory Medicine, 46(1), 3(2008).

Shruti Mouryaa; Ramesh Bodlab; Ravikant Taureanb; Akanksha Sharmab; Simultaneous estimation of xanthine alkaloids (Theophylline, Theobromine and Caffeine): High-Performance Liquid Chromatography International Journal of Drug Regulatory Affairs. 2019; 7(2),35-41.

Srdjenovic, B.; Djordjevic-Milic, V.; Grujic, N.; Injac, R.; Lepojevic, C. (2008). Simultaneous HPLC determination of caffeine, theophylline in food, drinks, and herbal products. J. Chromatographic. Sci., 46(2), 144-149.

Sujana, K.; Venu, S.; Sravani, K.; Iswarya, P. (2016). simultaneous estimation of salbutamol and theophylline in bulk drugs and marketed formulation using simultaneous equation method. International J. Pharm. Tech. Research CODEN (USA)N; 9, 274-282.

Weinberger, M.; Hendeles, L. (1996). Theophylline in asthma. N. Engl, J. Med., 334(21), 1380-1388.

Zhou, M.X.; Guan, C.Y.; Chen, G.; Xie, X.Y.; Wu, S.H. (2005). Determination of theophylline concentration in serum by chemiluminescent immunoassay. J. Zhejiang. Univ. Sci. B., 6(12), 1148-1152.

Author Information

Asmaa M. Al-Hasany
Department of Oil and Refining Engineering/ College of Petroleum and Mining Engineering/
University of Mosul, Iraq
Contact E-mail: rosefirst78@yahoo.com

Amer Th. Al-Taee
Department of Chemistry/ College of Science
University of Mosul, Iraq

Haitham A. Al-Wahb
Department of Chemistry/ College of Science
University of Mosul, Iraq

The Effect of Cataphoresis Coating on Fatigue Behaviour of Control Arms under Corrosion Environment

Cem UCAN
Teknorot Steering&Suspension Parts

Mustafa Ozgur BORA
Kocaeli University

Onur COBAN
Kocaeli University

Abstract: In this paper, the effect of the cataphoresis coating on fatigue life of control arms was evaluated under corrosion environment. The used sheet metals were manufactured by Erdemir as a technical code of S355MC grade steel according to EN 10149-2:2013 quality standard. The sheet metals were shaped at the Teknorot Automotive manufacturing processes. The shaped metals were coated with cataphoresis at the Teknorot Automotive coating facility. In order to determine the corrosion environment of the parts salt spray test was performed according to TS EN ISO 9227:2012 quality standard. Salt spray test was implemented to both cataphoresis coated and uncoated control arm bodies during 30 days. Ascott S450s brand salt spray corrosion test chamber was used for the salt spray test. After the corrosion applications, fatigue life tests were applied to the both control arm bodies, which were cataphoresis coated and uncoated, by fatigue life test machine produced by CAE Solutions for Teknorot Automotive. From test results, it was determined that cataphoresis coating was necessary for a better fatigue life performance on automobile control arms. Damage analysis was also applied to determine the damages which were occured in the coated and uncoated parts.

Keywords: Fatigue, Cataphoresis coating, Corrosion, Control arms

Introduction

The system that reduces road loads, road vibrations and ensures the connection of the wheels to the chassis is called suspension system [1,2]. Suspension systems provide more comfortable journey for passengers in the vehicles. Most of the suspension components are safety part for safe driving. The most important component is the control arms that directly connects the wheel and the chassis. In the automotive manufacturing industry, all the suspension system components are designed for infinite life and must not be damaged during the service conditions. Control arms are usually tested for fatigue life before the final assembly of the vehicle, to ensure the technical specifications of the customers and to avoid unexpected failure and accidents with vehicles [3]. The stress results of working load on the control arms should be less than the related material's endurance limit. The component would be expected to withstand these stress levels without failure during fatigue life tests and then real performance.

Material fatigue is a natural event where the structures fail when subjected to a cyclic load. Fatigue failure is one of most common source behind issues of mechanical structures. The most important parameter for the fatigue failure is the stress amplitude [4]. The fatigue failure is the greatest danger on suspension control arms during service life of a vehicle. The engineers who work at the automotive industry design the components for infinite life by reason of the fact that suspension components are under dynamic loads which cause the fatigue failure [5]. However, various parameters affect the fatigue life of the suspension control arms such as material grade, component shape, material properties and corrosion. Corrosion is one of the most dangerous issue for the component working life. Although there are different alternatives, high strength low alloy (HSLA) steels are

commonly used for control arms and as known that these type of steels have good corrosion behaviour. Corrosion fatigue is a form of material failure caused by crack growth under cyclic loading in a corrosive environment and generally corrosion has an accelerating effect on fatigue failure, and crack growth rates are substantially higher under corrosion fatigue [6]. Fisher et al. [7] claimed that the fatigue life of the steel components affected by corrosion by reason of the fact that corrosion supports the crack growth and propagation. Kim and Kim [8] investigated that corrosion evidences were intensively observed on crack initiation region, indicating that crack initiation and propagation affected by corrosion and also the result indicated that the corrosion could be an important factor of the fatigue life of suspension control arms in automotive industry.

Coating processes are an important solution against corrosion. Coating applications provide some advantages such as superior control of application conditions to ensure superior performance, corrosion prevention, ease of damage repair, as well as superior waste and pollution control. Price and Figueira [9] claimed that organic based coating systems or metallic coatings such as electroplating, diffusion, hot-dipping and thermal spraying commonly could be used to avoid the corrosion. In the automotive industry, cataphoresis coating is commonly preferred since 1970's to avoid the corrosion on the suspension components [10]. The cataphoresis coating provides the same corrosion resistance on the inner and outer surfaces independent from the component geometry [11]. The cataphoresis coating extends the life of the component and ensures its quality against corrosion. However, corrosion can be occurred on the components by reason of the fact that some problems such as coating process problems, surface damage after production, service conditions. The components under corrosion risk although coating application. For this reason, it is necessary to investigate the fatigue behaviour of the coated samples and corroded samples.

In this study, the effect of the cataphoresis coating on the fatigue life of S355MC grade steel control arms was evaluated under corrosion environment. The control arms were coated with cataphoresis technique. In order to determine the corrosion environment of the parts, salt spray test was performed according to TS EN ISO 9227:2012. After the corrosion applications, fatigue life tests were applied to the both control arm bodies which were cataphoresis coated and uncoated by fatigue life test machine. In addition, damage analysis was also applied to determine the damages which were occurred in the coated and uncoated parts.

Materials and Method

Material

The control arm bodies were produced from S355MC grade steel sheet metals which were manufactured by Erdemir according to EN 10149-2:2013 quality standard. The steel metal thickness is 4 mm. The chemical composition and the mechanical properties of the used sheet metal are shown in Table 1 and Table 2.

Table 1. The chemical composition of S355MC grade steel

Standard	Quality	%C max.	%Mn max.	%P max.	%S max.	%Si max.	%Al max.	%Nb max.	%Ti max.	%V max.
EN 10149-2	S355MC	0,12	1,40	0,025	0,020	0,50	0,02	0,09	0,15	0,20

Table 2. The mechanical properties of S355MC grade steel

Standard	Quality	R_e N/mm^2 min.	R_m N/mm^2 min.	%A		Impact KV_c (Longitudinally, d>6) Temparature: -20 °C min.	Bend (Transverse, 180°) mdb d: thickness
				d<3 A_{80} min.	d ≥3 A_5 min.		
EN 10149-2	S355MC	355	430-550	19	23	40 J	0,5 d

Where Re refers to yield strength, Rm refers to tensile strength, A refers to elongation, A5 refers to elongation (L0 = 5.65x√S0), A80 refers to elongation (L0 = 80 mm), S0 refers to cross-sectional area of the specimen

(mm²), L0 refers to original gauge length of the specimen , d refers to nominal thickness (mm), mdb refers to mandrel diameter for bending, KVc refers to impact energy (J).

Method

Production

The control arm bodies were produced by applying template cutting sheet forming operations on hydraulic presses to the steel at Teknorot Co. The used hydraulic presses are shown in Fig. 1.

Figure 1. a) Template cutting press, b) Sheet forming press

Coating

The cataphoresis coating of control arm bodies was applied to the formed bodies at Teknorot Co. after sheet forming operations. The cataphoresis coating process has four steps respectively; (a) surface cleaning, (b) surface preparation, (c) coating and (d) flash-off and oven as shown in Fig. 2. Application thickness of the cataphoresis coating was approximately 20μm.

Figure 2. a) Surface cleaning, b) Surface preparation, c) Coating, d) Flash-off and oven

In order to bond the coating with product, surface cleaning must be done perfectly. Surface cleaning process (Fig.2-a) consisted of oil-removal and rinse tanks where negative structures such as oil film, welding powders, dust on the piece were removed. Process time of surface cleaning was approximately 15 minutes. Surface preparation process (Fig.2-b) existed in cataphoresis coating by the reason of fact that held on to $ZnPO4$ crystals to metal surface and to provide bonding of coating and product. Activation tanks were consisted of $ZnPO4$ tanks and water rinse tanks on surface preparation process. Process time was approximately 5 minutes. Coating step (Fig.2-c) was applied to metal surfaces after surface preparation step. This step had application of water-based coating structure. It consisted of painting tanks and UF tanks. Process time was approximately 5 minutes. The liquid build-up in the coating was made possible by the removal of the coating from the coating as a gas and the solidification of the paint after curing was provided by this group (Fig.4-d). Process time was approximately one hour.

Salt Spray Test

The corrosion resistance of both cataphoresis coated and uncoated control arm bodies were determined by using salt spray test according to TS EN ISO 9227 quality standard. The neutral salt spray test was applied at 5 wt.% sodium chloride solution in the pH range from 6,5 to 7,2 at 25°C ± 2°C. In the saturation tower of the testing machine, the water temperature was 45°C and the pressure value was 70 kPa. The temperature of the testing machine was 35°C. The coating specification of Teknorot Co. describes the test time as minimum 720 hours for cataphoresis coating. In this study, salt spray test applied to both cataphoresis coated and uncoated control arm bodies during 720 hours (30 days). Testing machine is also shown in Fig. 3.

Figure 3.Ascott S450s brand salt spray corrosion test chamber

Weight lose that occurs due to corrosion phenomenon was checked after salt spray tests. Table 3 shows the weight lose differences between coated and uncoated control arms. Control arms are shown in Fig. 4. after salt spray test.

Table 3. Weight lose difference after 720 hours corrosion test

	After Production (gram)	After Coating (gram)	After Salt Spray Test (gram)
Coated Sample	2400	2450	2442
Uncoated Sample	2400	-	2298

Figure 4. a,b) Cataphoresis coated control arm after 720 hours salt spray test, c,d) Uncoated control arm after 720 hours salt spray test

Fatigue Test & Damage Evaluation

Fatigue tests were applied to both control arms which coated and uncoated according to related technical specification of Teknorot Co. Test parameters are 4 Hz frequency and 45° angle. The cycle load was calculated by the technical specification of Teknorot Co. as ±560 kgf. The fatigue tests carried out on 3 replications for each coated and uncoated control arm groups. Tests were finished when crack formation is detected. Damage and fracture surfaces of control arms were evaluated by visual inspection. Test apparatus was shown in Fig.5.
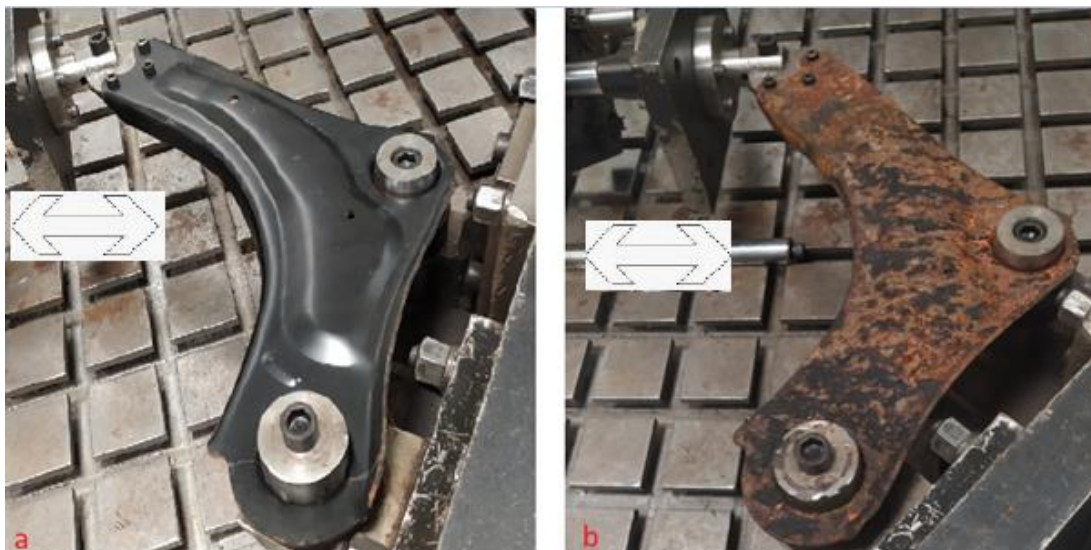
Figure 5. a) Cataphoresis coated part during fatigue test, b) Uncoated part during fatigue test

Results and Discussion

The results which were obtained from fatigue life tests were shown in Table 4.

Table 4. Fatigue life test results for coated and uncoated control arms

	Sample-1	Sample-2	Sample-3	Average	Standard Deviation (±)
Coated Control Arms	1.375.635	1.482.697	1.302.364	1.386.899	90.693
Uncoated Control Arms	681.236	653.687	709.873	681.599	28.095

Fatigue Cycles
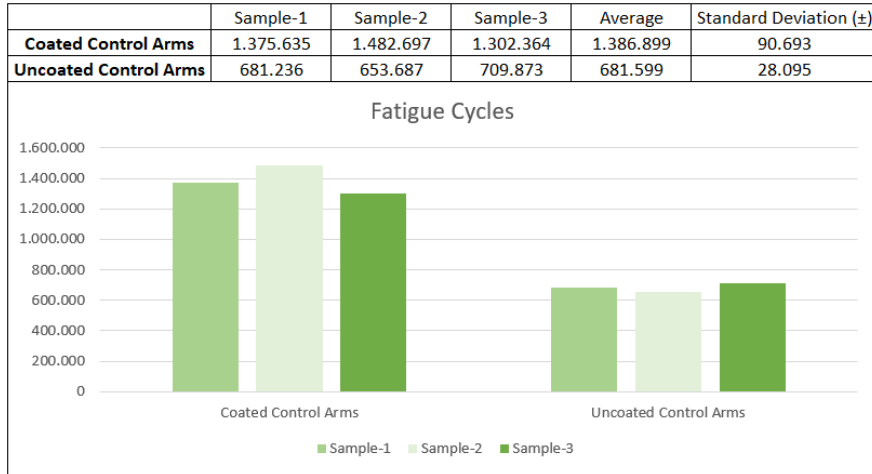
The performed control arm samples were successfully completed the fatigue tests for infinite life according to Teknorot's technical specification. However there was a significant difference between cataphoresis coated and uncoated control arms. Although all the control arms were successfully completed the fatigue tests, uncoated control arms were close to the lower limit which was described as 500.000 cycle. It was clearly shown that corrosion decreased the fatigue life of the control arms significantly. According to Table 4, the fatigue life of uncoated control arms were approximately 50% less than the fatigue life of the cataphoresis coated control arms. The reason for this was predicted that the microcracks grew earlier than they should be due to corrosion. It evaluated that the coating application provided the corrosion resistance and improved fatigue life of the control arms. As stated in ref [7,8], corrosion supported the crack growth and it affected the fatigue life of the steel components. The result indicated that the corrosion could be an important factor of the fatigue life of lower arm in automotive.

During the fatigue tests, crack formation was observed on the samples. Crack initiation regions were detected on the big bushing assembly hole for all the samples. But uncoated control arms were also damaged on different regions by the effect of the corrosion. Crack regions of coated and uncoated control arms were shown on Fig.6 and Fig.7, respectively.

Figure 6. Crack regions on the cataphoresis coated parts after fatigue test

Figure 7. Crack regions on the uncoated parts after fatigue test

Conclusion

In this study, the effect of the cataphoresis coating on the fatigue life of control arms was evaluated under corrosion environment. The obtained results are given below.

- Fatigue life was found 1,3 million cycle at cataphoresis coated control arms. However this value was fallen to 50% for the uncoated control arms compared to the fatigue life of cataphoresis coated control arms.
- The crack initiation was observed on the bushing assembly hole for cataphoresis coated control arms. However it was changeable for uncoated control arms and crack initiation was observed on anywhere according to corrosion damage.
- Cataphoresis coating application provided corrosion resistance perfectly and increased the fatigue life of the control arms that made from steel.

References

https://www.carbibles.com/guide-to-car-suspension/

https://www.thefreedictionary.com/suspension+system

L.B. Godefroid, G.L. Faria, L.C. Cândido and S.C. Araujo, "Fatigue Failure of a Welded Automotive Component", 20th European Conference on Fracture (ECF20), Procedia Materials Science 3 (2014) 1902-1907

https://www.comsol.com/multiphysics/material-fatigue

J.Marzbanrad and A. Hoseinpour, "Structural Optimization of Macpherson Control Arm Under Fatigue Loading", ISSN 1330-3651 (Print), ISSN 1848-6339 (Online)

R.W.Purvis, "An Experimental Investigation of Corrosion Fatigue Life viaThermographic Method", Louisiana State University and Agricultural and Mechanical Collage, LSU Mater'sTheses, Louisiana, 2014

J.W. Fisher, E.J. Kaufmann and A.W. Pense, "Effect of Corrosion on Crack Development and Fatigue Life", Transportation Research Record 1624

Y.S Kim and J.G Kim, "Evaluation of Corrosion Fatigue and Life Prediction of Lower Arm forAutomotive Suspension Component", Met.Mater.Int.Vol.23,No.1 (2017), Suwon, Republic of Korea

S.J. Price and R.B. Figueira, "Corrosion Protection Systems and Fatigue Corrosion in OffshoreWind Structures: CurrentStatus and FuturePerspectives", p.24-25, MDPI, 2017

http://www.boytes.com/kataforez-boya-sistemi/

https://www.teknorot.com/en/cataphoresis/

Author Information

Cem Ucan
Teknorot Steering & Suspension Parts, R&D Center
Düzce, Turkey
Address: 1. Organize Sanayi Bölgesi 1. Cadde No:5,
Beyköy/Düzce, Turkey
Contact E-mail: cem.ucan@teknorot.com

Mustafa Ozgur BORA
Kocaeli University, Faculty of Aeronautics and
Astronautics, 41285, Kocaeli, Turkey
Address: Kocaeli University, Arslanbey Campus, Faculty of
Aeronautics and Astronautics, 41285, Kartepe/Kocaeli,
Turkey

Onur Coban
Kocaeli University, Faculty of Aeronautics and
Astronautics, 41285, Kocaeli, Turkey
Address: Kocaeli University, Arslanbey Campus, Faculty of
Aeronautics and Astronautics, 41285, Kartepe/Kocaeli,
Turkey

Characterization and Comparison of the Reaction Product of (Pd, Pt, Ag and Au) in Different Solvent with Diaminothiuramdisulfide

Afyaa M.YOUNUS
University of Mosul

Ihsan A. MUSTAFA
University of Mosul

Abstract: The work presented in research describes the preparation and characterization of new complexes resulted from the reaction of diaminothiuramdisulfide(tds)with metals (or metals chlorides)of group(VIII)[Na2pdcl4,Pt(0) and K2ptcl4]in addition to group(IB)metals[Ag(0) ,AgCl and Au(o)]. The thiuramdisulfide compound (tds) reduced to the corresponding aminodithiocarbamate anion (H2NNHCS2)-in some complexes(Oxidative addition reaction) However, in the remaining complexes the (tds)were simply added to the metal chloride (addition reaction) without cleavage of the –S-S-bond.the resulting complexes can be classified as follows.

 I-The oxidative addition reactions offered complexes of the type:
1-[M(L)2]((Where L=H2NNHCS2-(aminodithiocarbamate anion) and M=Pd(II),Pt(II) , Ag(II))and [Ag2(L)4NiCl2].
2-[M(L)3][M=Au(III)]in addition to the complexes
[Au(L)3(1,10 –Phen)] .
II-The addition reactions resulted in the formation of the complexes [M(tds)Cl2] whene Pt(II).The prepared complexes were characterized using molar conductivity, UV-Vis and IR spectra in addition to magnetic measurements and metal analysis by atomic absorption .The results suggest a tetra-or hexa-coordinated complexes and also displayed the importance of using different solvents upon the type of reaction and prodect.

Keywords: Diaminothiuramdisulfide, Metals, Coordinated complexes

Introduction

Thiuramdisulfide compounds are one of the most important disulfide compounds known to have the formula [RR-NC(S)S]2 As R=R- alkyl or aryl is called tetra- alkyl or aryl thiuramdisulfide R4tds, which is derived from thiuramsulfide, known as BiS (N,N-dialkyl Thiucarbamol sulfide is the ester thiucarbamoyl for thiucarbamic acids These compounds are bio-effective(1) and when it is n=2) it is known as the (R4tds) and are antifungals that affect plants In past centuries, heterogeneous ring compounds have gained special attention in medical chemistry because they have antibacterial(2) and fungal properties, particularly potatoes and tomatoes(3,4), and in the process of accelerating the rubber accent(5,6), oxidative resistance, oxidization resistance and preventing the removal of the color from the rubber(7). In medicine, thiuram complexes use disulfide in the treatment of alcoholics(8) and have been found to be anti-virus-leading to HIV,such as AIDS(9). Thiuram disulfide ligands are the only one within thiolito ligands capable of forming the thiocarbamate ligands by breaking the sphincter (SS) in the reduction process. Thiocarbamate has the ability to spread the positive charge of the metal to the outer surface of each complex(10,11). In terms of consistency, these ligands are characterized by their compatibility with a number of transition metals, such as chelated bidentate sulfides through the two sulfur atoms.

$$R_2N\overset{+}{=}C-S-S-C\overset{+}{=}NR_2$$

(Ia

$$R_2N\overset{+}{=}C-S-S-C-NR_2$$

(Ib

$$R_2N-C-S-S-C\overset{+}{=}NR_2$$

(Ic

$$R_2N-C-S-S-C-NR_2$$

(Id
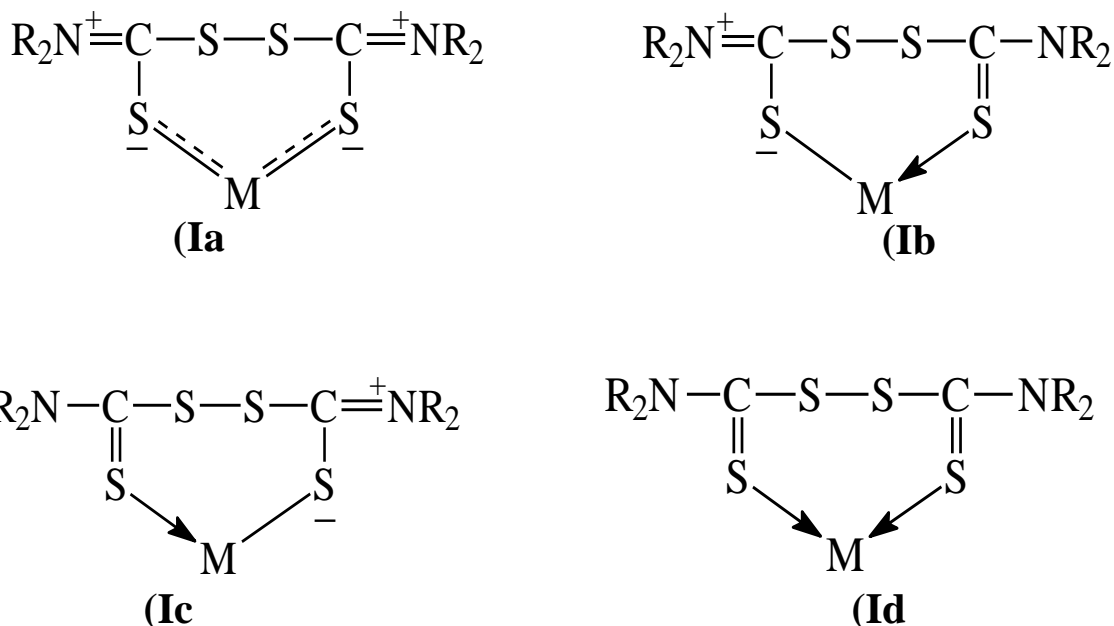
Some methods of preparation for thiuramdisulfide ligand and their complexes, Because these ligands are important, we know the methods of their preparation:

1) Indirect oxidation method:

Thiuramdisulfide compounds are prepared by oxidizing the thiocarbamate compounds using an oxidizing agent such as potassium ferrocyanide [K_3 [Fe (CN) $_6$]) [10,12] according to the following formula

$$2\ RNHCS_2Na\ +\ 2\ K_3[Fe(CN)_6]\ \longrightarrow\ RNH-\overset{S}{\overset{\|}{C}}-S-S-\overset{S}{\overset{\|}{C}}-NHR\ +\ 2\ NaK_3[Fe(CN)_6]$$

Hydrogen peroxide (H_2O_2) , sodium tetrachloride [$Na_2S_4O_6$] or bromine cyanide (BrCN) in ethanol or iodine (I_2) as in the equation:

$$2\ R_2NCS_2Na\ +\ I_2\ \longrightarrow\ R_2N-\overset{S}{\overset{\|}{C}}-S-S-\overset{S}{\overset{\|}{C}}-NR_2\ +\ 2\ NaI$$

2) Direct Oxidation method:

Thiuramdisulfide compounds are prepared directly from the reaction of the secondary amine R_2NH with carbon dioxide CS_2 in the presence of I_2 and one of the amino bases such as pyridine, or triethylamine, as in the following equation:
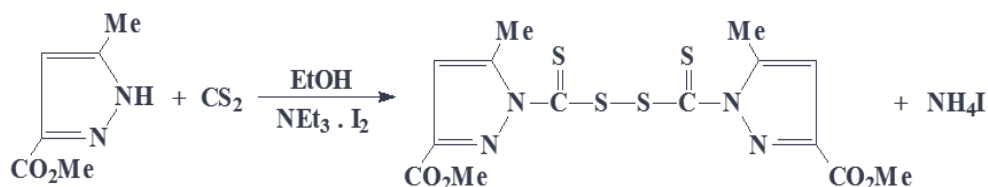
3)The thiocarbamate complexes are oxidized using one of the halogens (X_2).

In 2004(13) , heterogeneous quad-core complexes for tin metal (IV) formula [Sn (L) 3I (PPh3) 2 (M`Cl2) 3] were prepared as M` = Cu (II) and Co (II). Ni (II), L = H2NNHCS2 and PPh3 = triphenylphosphine, as shown in Figure .
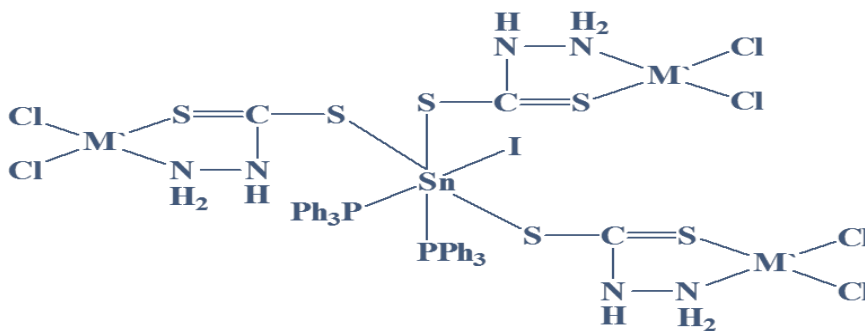
Figure of Complex [Sn(L)$_3$I(PPh$_3$)$_2$(M`Cl$_2$)$_3$]

The purpose of the research

The research aims to compare the number of (free) metals transition to the elements of the (VIII) group as well as the elements (IB) with the chlorides of these elements its ability to degrade one of the compounds (diaminothiuramdisulfide) to the dithiocarbamate ion to form complexes of the transition metals used in addition to a simple study of the effect of the solvent factor on the process of interaction and outputs of reactions.

Method

Preparation of ligand aminodithiocarbamate ammonium (NH$_4$L)

Added (6.04 ml,0.1 mol) of carbon disulfide(CS$_2$) gradually with cooling and constant stirring to (5 ml,0.1 mol) of hydroxyin water(NH$_2$NH$_2$.H$_2$O). It turns into a white dough slanted to yellow and then filters, washed and re-crystallized**.**

Preparation of ligand aminothiuramdisulfide(tds)

Add (3.95 g,0.012mol) of potassium ferrocyanide K$_3$[Fe(CN)$_6$] dissolved in (15 ml) of water to (1.25 g,0.01mol) of amino dithiocarbamate ammonium above and dissolved in an equal amount of water and ethanol and the addition is gradually done in an ice bath where yellow deposits are formed. Green and has been able to obtain a dithiuramdisulfide compound (tds) using I$_2$ dissolved in ethanol.

Preparation of Na$_2$PdCl$_4$ palladium salt solution[14].

The heating of equal amounts of palladium chloride salt (PdCl$_2$) and NaCl is brought in by a mollet ratio (2:1 in 5 ml of distilled water until palladium chloride dissolves and a red-brown solution is formed.

Preparing K$_2$PtCl$_4$ Platinum salt[15]

Melts 15 g of platin metal in 320 ml of royal water, climbs the mixture for at least(14 hours) to obtain H$_2$PtCl$_6$ acid, dissolves the resulting acid in 200ml of distilled water and is added a solution prepared from dissolved (6.4g) of potassium chloride in (60ml) of distilled water to deposit the complex (K$_2$PtCl$_6$) yellow color, filtered and washed with cold water and dried.3g dissolved from hydrochloride hydrazine (N$_2$H$_4$.HCl) prepared from the addition of concentrated hydrochloride acid to hydrochloride (N$_2$H$_4$). H$_2$O) drop-drop to be completed white deposit formation in 70 ml of distilled water and added to (20.5g) of complex K$_2$PtCl$_6$ heats the mixture to boil for half an hour to get a solution of a dark red color. For the fractional platinum, the solution cools down in the form of wild red crystals by 75%. (K$_2$PtCl$_4$)

Preparation of complexes with formulas [M (L)$_2$](M= Ag,Pd,Pt)

Add the ligand solution of tds (1.07gm,0.005mol) dissolved in 30 ml of dry toluene and climbs the mixture with constant stirring using a magnetic motor in a 14-hour glass ring with 0.539 g of silver metal or 0.717gm of AgCl and 0.975 g of platinum metal and the complex palladium was obtained using 1.472 of Na$_2$PdCl$_4$ paladium salt.

Preparation of [Au (L)₃]

Add(0.985gm) of gold metal is added with(1.605 g,0.0075 mol) from the diaminoThiuramdisulfied with 30 ml of dry toluene and using a thermal escalation and thus the complex composition.

Preparation of [Pt (tds)Cl₂]complex

Add(1.07gm,0.005mol) of tds and 20 ml dissolved compound are added in(THF) with 2.076 g of K₂PtCl₄ salt that climbs the reaction mix with continuous stirring for 2 hours until complex formation.

Preparation of [Au (L)₃ (1,10Phen)] complex

Add (1.969 g,0.01mol) of gold metal in pieces (3.210 g,0.015 mol) of diaminothiuramdisulfide and dissolved in (20ml) of dry toluene, the mixture climbs with constant stirring for 15 hours as it forms a dark green deposit and dries. Melt (5.179 g,0.01mol) from the complex prepared in 20 ml of chloroform and then added to (1.802 g,0.01 mol) of(1,10 phen) dissolved in 10 ml of methanol climbs the mixture as it filters a greenish blue deposit and dries.

Preperation of [Ag₂(L)₄NiCl₂]

Add (0.717 g, 0.005 mol) anhydrous silver (I) chloride (AgCl) is added to (1.070 g, 0.005 mol) of the diaminothiuramdisulfide compound dissolved in (20 ml) of tetrahydrofuran (THF). The mixture is stirred with constant stirring using a magnetic motor in a 50 mL glass flask for 2 hours, the precipitate is filtered and dried. Dissolve (1.609 g, 0.005 mol) of the above prepared complex in (20 ml) chloroform and add (0.324 g, 0.0025 mol) of nickel anhydrous (II) chloride (NiCl₂) dissolved in (20 ml) of dimethyl sulfoxide (DMSO). The mixture ascends with constant stirring, forming a shiny dark blue precipitate, filtered and dried.

Results and Discussion

Table 1.Analytical data and Physical Properities of ligand and their

No	Compounds	Color	M.P(ºC)	Yeild%	M%	$\Lambda m(ohm^{-1} mol^{-1} cm^2)$	μ eff. (B.M)
L1	$NH_4L(H_2NNHCS_2NH_4)$	Whitish yellow	125	70			
L2	$H_2NNHC(S)SSC(S)NHNH_2$ (tds)	Yellowish green	155	78			
1	$[Pd(L)_2]$	Green	198	58	-	3	Dia
2	$[Ag(L)_2]$	Yellow pall	161	68	33.51 33.48	4	1.72
3	$[Pt(L)_2]$	Greenish yellow	159	62	47.68 47.60	10	Dia
4	$[Au(L)_3]$	Dark green	186	75	38.02 37.22	18	Dia
5	$[Pt(tds)Cl_2]$	Brownish yellow	190	67	40.63 40.71	7	Dia
6	$[Ag_2(L)_4NiCl_2]$	Dark blue	182	67	27.89 27.99	6	2.05
7	$[Au(L)_3(Phen)]$	Bluish green	173	71	28.21 28.14	17	Dia

Λm= Molar Conductivity , μ eff= effective magnetic moment , M.P= melting point

The magnatic moment data of these Complexes Calculated from the corrected magnatic susceptibilities determined at 25 ºC are given in (Table-1). It was found that the complexes of palladium and platinum(1,3,5), which have tetra coordination arrangement with low-consistency, have magnetic moment (Dia) qualities[16]. Magnetic measurements of gold complexes (III) recorded (4 and 7) for the complex >have shown (Dia) properties that are similar to platinum (II) and are consistent with the magnetic moments found in literature[17]. Magnetic measurements of the silver complexes (II) (2 and 6) above showed magnetic moment (1.72 and 2.05) respectively and these values are consistent with the magnetic moment of torque values of a single electron perpenduation.

The palladium (II) and platinum(II) complexes with the shape of the square planner have three electronic transitions allowed[16],The electronic spectrum shows strong bands at($15000-23000 cm^{-1}$)when they return to the transition($^1A_1g \longrightarrow {}^1A_2g$) ,($24000-29000 cm^{-1}$) Attributable to the transition($^1A_1g \longrightarrow {}^1B_1g$) and appear some complexes third band ($^1A_1g \longrightarrow {}^1B_2g$) at different high ranges. The electronic spectrum showed of Pd(II) and Pt(II) complexes(1,3,5) absorption bands in range($16806-22831 cm^{-1}$)when their return to the transition ($^1A_1g \longrightarrow {}^1A_2g$) And there were other packages in the range($24900-24449 cm^{-1}$) that are back on the transition ($^1A_1g \longrightarrow {}^1B_1g$) And the appearance of strong absorptions at the range($33112-38910 cm^{-1}$) may represent the third transition ($^1A_1g \longrightarrow {}^1Eg$) Mixed with charge transition(C.T)[18] in a few cases, it's due to ligand bands. Ligand transition may be displaced to the lengths of the wave length low or higher than the complexes, indicating the composition of the complexes. Through the electronic spectrum, these values are consistent with the firm values of the order of the square planner around the metal atom.

Give the electronic spectrum of the gold complex (III) recorded above absorption packages at range($15220-20576 cm^{-1}$) and attributable to the transition($^1A_1g \longrightarrow {}^1A_2g$) and another package at($32894 cm^{-1}$)when returning to the transition($^1A_1g \longrightarrow {}^1Eg$) While no was observed The second package, which represents the transition($^1A_1g \longrightarrow {}^1B_1g$) is observed and the similarity is observed in the packet locations with platinum(II) complexes (above).

The electronic spectrum of silver complexes (II) similar to the copper(II)like electronic tetra coordination(square planner arrangement) shows two types of electronic transitions: ($^2B_1g \longrightarrow {}^2A_1g$), ($^2B_1g \longrightarrow {}^2Eg$). These transitions are shown in the area specified between($14000-18000 cm^{-1}$) and attributable to the two electronic transfers above in the form of a single package to approximate their position[19] The electronic spectrum of the prepared silver(II) complexes showed the presence of absorption packs in the range($14220-16863 cm^{-1}$) these values are consistent with the values of the electronic spectrum of silver complexes(II) the tetra coordination (square planner)[20,21,] which are often deformed towards tetra hedral.

Table 2.IR spectra of complexes

No	υ(C-S)	υ(C=S)	υ(C-N)	υ(NH$_2$)	υ(M-S)	υ(M-N)	υ(M'-N)	υ(M-N phen)	υ(S-S)
L1	1010	-	1475	3454	-	-	-	-	-
L2	980	1047	1472	3451	-	-	-	--	438
1	972	1030	1477	3336	420	510	-	-	-
2	1009	-	1481	3445/3380	422	524	-	-	-
3	1001	-	1486	3415	419	-	-	-	-
4	979/998	1022	1484	3369/3440	415	523	-	-	-
5	-	996	1485	3409	409	-	-	-	437
6	982	-	1486	3360/3429	417	530	451	-	-
7	992	1028	1487	3421	419	-	-	452	-

A technique(IR) was used to study ligands and their complex prepared within the range (400-4000cm-1) as they create new coordination bands between the ligand and the atoms of the metal lead to Electronic structure

and Energy level &Symmetry in ligands. in These changes affect the seismic frequencies of the ligand and therefore the seismic spectromeons(22).

Show the spectrum(IR) of the Diaminothiuramdisulfied two absorption packs at(1047cm-1)and(980cm-1) when they return to the two groups υ(C=S)and υ(C-S) Respectively(Table-2) These beams are displaced towards the frequencies when the ligand is connected to the metal's ion By measuring the complexes(Tabel-2), A spectrum of amino dithiocarbamate ammonium was shown an absorption pack at(1010cm-1) returning to υ(C-S) . When measuring the complex(1), two absorption packs appeared at(1030,972cm-1) its packs of the two groups υ(C=S)and υ(C-S) Respectively in a sign that these complexes are linked to amono dentate by negative sulfur ion, as research published in the field has indicated (22,23,24).

The complexes(2,3,6) showed asingle band υ(C-S)in range(982-1009cm-1) A sign of the bidentate association of the thiocarbamate ligand.while gold complex(4) is appeared three bands which are two bands υ(C-S) indicative of the presence of tri-sulfur with two metal atoms in the bi molecule and one band of υ(C=S). In IR Spectra (tds) gave a weak package in(438cm-1) that belonged to the group. υ(S-S).(25) Through a(IR) measurement of the prepared complexes it was observed that a package in the complex (17) appeared in(437cm-1) this location is near to its location in the spectrum of the ligand Which indicates that as far as it is(S-S) without breaking the ligand and the link of the ligand with metal atom through group(C=S).

Both Ligands in the (IR) spectrum gave an absorption package at (1475,1472cm-1) respectively and these bands returen to the molecular double bonds.(26,27)(C N) This value lies between the frequency of the single and the double bonds. When complexes are formed, frequency values are displaced to high frequencies in the range(1477-1487cm-1).

Vibrations υ(M-N) appeared in the complexes(1,2,4,6)at range(510-530cm-1), indicating that metal atoms were associated with the nitrogen atom in group(NH2)(Table2)While The Complex(6)is appeared band υ(M'_N)at(451cm-1) This is consistent with what he said(Nakamoto)(28), and in this area, the nickel metal has been confirmed in contact with the ligand nitrogen(29).

The complex (7) gave a pack of absorption to the insistent(M-N-phen)at(452cm-1) The firmness packets generally appear at the range (360-500cm-1)(28).

[M(L)₂] (M=Pd, Pt, Ag)

[Au(L)3(1,10-Phen)]

$$H_2N-NH$$

$$[Pt(tds)Cl_2]$$

$$[Au(L)_3]$$
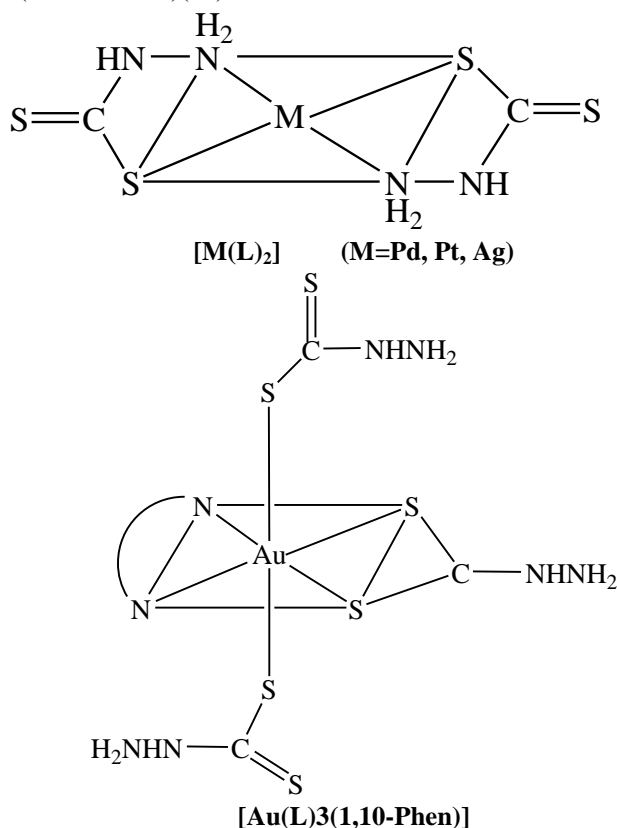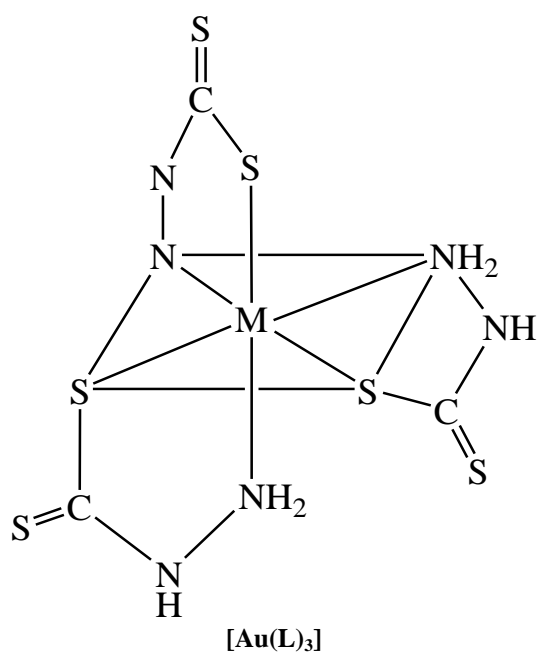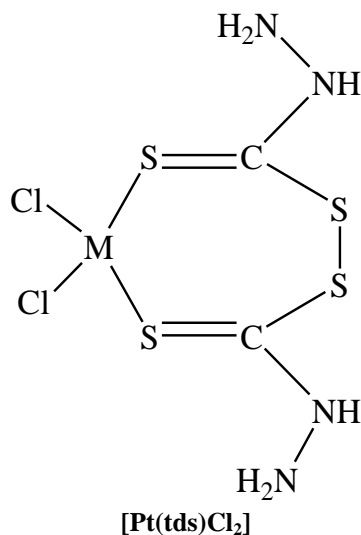
References

Angeli, E., Wagner, J., Lawrick, E., Moore, K., Anderson, M., Soderland, L., & Brizee, A. (2010, May 5). General format. Retrieved from http://owl.english.purdue.edu/owl/resource/560/01/

Calfee, R. C., & Valencia, R. R. (1991). APA guide to preparing manuscripts for journal publication. Washington, DC: American Psychological Association.

Duncan, G. J., & Brooks-Gunn, J. (Eds.). (1997). Consequences of growing up poor. New York, NY: Russell Sage Foundation.

Harlow, H. F. (1983). Fundamentals for preparing psychology journal articles. Journal of Comparative and Physiological Psychology, 55, 893-896.

Helfer, M. E., Kempe, R. S., & Krugman, R. D. (1997). The battered child (5th ed.). Chicago, IL: University of Chicago Press.

Henry, W. A., III. (1990, April 9). Making the grade in today's schools. Time, 135, 28-31.

Lastname, F. N. (Year). Title of dissertation. (Doctoral dissertation). Retrieved from Name of database. (Accession or Order Number)

Lastname, F. N. (Year). Title of dissertation. (Unpublished doctoral dissertation). Name of Institution, Location.

O'Neil, J. M., & Egan, J. (1992). Men's and women's gender role journeys: A metaphor for healing, transition, and transformation. In B. R. Wainrib (Ed.), Gender issues across the life cycle (pp. 107-123). New York, NY: Springer.

Plath, S. (2000). The unabridged journals. K. V. Kukil (Ed.). New York, NY: Anchor.

Schnase, J. L., & Cunnius, E. L. (Eds.). (1995). Proceedings from CSCL '95: The First International Conference on Computer Support for Collaborative Learning. Mahwah, NJ: Erlbaum.

Schultz, S. (2005, December 28). Calls made to strengthen state energy policies. The Country Today, pp. 1A, 2A.

Scruton, R. (1996). The eclipse of listening. The New Criterion, 15(30), 5-13.

Author Information

Afyaa M. Younus	**Ihsan A. Mustafa**
University of Mosul	University of Mosul
Mosul, Iraq	Mosul, Iraq
Contact E-mail: younis1986mmyy@yahoo.com	

A Novel Test Procedure to Determine the Behaviour of A Center Bearing of A Multi-Piece Driveshaft under Real Road Load Conditions

Efe ISIK
Tirsan Kardan A.Ş

Muzaffer KASABA
Tirsan Kardan A.Ş

Ercan GUNERI
Tirsan Kardan A.Ş

Abstract: Driveshafts are one of the most important members of the drivetrain that transmits the power and rotational movement from the engine to the rear axles. In light duty commercial vehicles, the multi- piece driveshafts have elastomeric parts called center bearing. The driveshaft center bearing usually consist of a rolling element bearing isolated in rubber and with a bracket configuration for attaching it to the vehicle chassis structure. The duty of the center bearing of the multi-piece driveshafts on the vehicle is the vibration damping function thanks to the elastomeric structure. Center bearing is an important sub-component of the multi-piece driveshaft which determines frequency response characteristic of driveshaft. The manner in which it is attached to the vehicle, whether directly to the under body or to the chassis frame, it can have a considerable effect on the center bearing's capability of providing optimum isolation and reducing the transmission of disturbances to an acceptable level in a given application. Due to both real road conditions and operation time, the elastomeric structure and the rolling ball bearings are damaged in time and the level of vibration and noise can cause disturbance on the vehicle. In this study, a test systematic has been developed to determine the change in noise characteristics of center bearing sub-assembly during the real time operation of the driveshaft. The noise characteristics of center bearing sub-assembly before and after the tests were compared and investigated.

Keywords: Driveshaft, Novel test, Drivetrain

Introduction

Vibration and noise, or NVH is the sound and vibration characteristics of ground vehicles. Sound and vibration can be measured, but noise can only be evaluated subjectively. All machines with moving parts produce dynamic forces under normal operating conditions. The mechanical behavior of the machine may change due to wear, changes in operating conditions and load changes. Understanding the dynamics of the machine and how the forces create vibration is the most important key to understand the sources of vibration.

The NVH of driveshaft is a type of NVH that causes the transmission of sound and vibration from the drivetrain system to the customer in a wide range of conditions. An error that may occur during the detection of the formation of the driveshaft NVH can create customer dissatisfaction and can lead to costly downtime and can cause fatal failures. Vibration in the automotive sector is undesirable. Because vibration means wasting energy and unwanted noise. For example, the vibration movement of the motor, vibration in electric motors or vibrations that occur in a mechanical device fall into the unwanted vibration group. Such vibrations may be caused by unbalanced rotating objects, irregular friction, collision of corresponding gears in the gearbox and other reasons. Sound and vibration are very close concepts. Sound, pressure waves are composed of vibrating structures, pressure waves are the vibration of structures. Therefore, we try to reduce the vibration level while simultaneously reducing the noise level.

When the rotational speed of the driveshaft is gradually increased, bending occurs in the center of the driveshaft tube and can gradually increase in deflection and reach an amplitude that causes the shaft to break at the critical speed of driveshaft. In order not to reach the critical speed limit during real time operation, driveshafts are designed as multi-pieces (Figure 1).

Figure 1. Multi-Piece driveshaft

In its simplest form which is depicted in Figure 2, center bearing sub-assembly consists of a rolling ball bearing in the center, a damping elastomer element around the roller ball bearing outer ring and the bracket which is attached to the chassis frame. The center bearing of driveshaft is designed to absorb vibration and noise generated by the driveshaft.
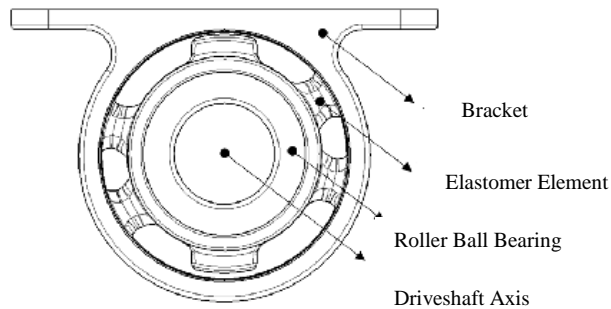
Figure 2. Driveshaft center bearing

In the book "Universal joint and driveshaft design manual "[1], noise and vibration from the propeller shaft are examined and general recommendations are given for driveshaft suspension characteristics. In the publication "NVH phenomena in light truck drivelines" [2], the causes and effects of cardan shaft noise and vibration known for the drivetrain of 4x4 vehicles are examined. In the publication "Aspects of Driveline Integration for Optimized Vehicle NVH" [3], the issues that cause noise and vibration in the drivetrain are combined with case studies and analyzes and the integration of the systems is examined. In the publication "Design and Analysis of Composite Drive Shaft" [5], the authors conducted bending mode analyzes for the propeller shaft with composite material using the finite element method. In the publication "Evaluation Method for Vibratory Forces Caused by Propeller Shaft," [8], the vibration forces that cause noise from the propeller shaft are examined. In multi flexible multibody simulation of automotive systems with non-modal model reduction techniques"[9], vehicle body simulation was performed and the effect of rigidity on vibration was investigated. In this study, a test systematic has been developed to determine the change in noise characteristics of center bearing sub-assembly during the real time operation of the driveshaft. The noise characteristics of center bearing sub-assembly before and after the tests were compared and investigated.

Theory

Sound generation or transmission in vehicles are produced in two ways, which are the result of sound waves propagating through the air (airborne sound) and generated as a result of progressive waves within the structure. The main purpose of the NVH tests on vehicles is to detect these sounds and bring them to optimal levels in terms of driver comfort. The sound pressure level is an expression of the measured sound pressure in dB, expressed in equation (1). The reference sound pressure in the equation is,

$$SPL = L_p = 10\log\left(\frac{p}{p_{ref}}\right)^2 = 20\log\left(\frac{p}{p_{ref}}\right) \ (dB)$$

Octave-Band Frequency Analysis

In order to gain an idea of the frequency distribution of the noise, the frequency scale is subdivided and the sound power per frequency range of each share is analyzed. Each portion of the frequency scale is called a band. For filtering covering the entire frequency spectrum, frequency ranges called octave bands are used. In an

octave band, the upper value of the band is twice the lower value, and the upper value of each band is the lower value of the next band. The central frequency of each band is the geometric mean of the upper and lower boundaries. The band used for detailed frequency analysis is 1/3 octave band. The ratio between the maximum and minimum values of the 1/3 octave band = 1.26. The 1/3 octave band widths are obtained by dividing the 1/1 octave band widths into three. Mathematically, 1 (one) octave band is expressed by equation (2).

$$f_2 = 2f_1$$
$$f_0 = \sqrt{2}f_1 = f_2/\sqrt{2} \tag{2}$$

In this study, for vibro-acoustic analysis, 1/1 or 1/3 octave bands are used. The center frequencies of the 1/1 and 1/3 octave bands are given in Table 1 [11].

Table 1. Octave band scale

Lower Band Limit (Hz) (Hz)	1/3 Ocave Band Center Frequency (Hz) (Hz)	Upper Band Limit (Hz) (Hz)
14,1	16	17,8
17,8	20	22,4
22,4	25	28,2
28,2	31,5	35,5
35,5	40	44,7
44,7	50	56,2
56,2	63	70,8
70,8	80	89,1
89,1	100	112
112	125	141
141	160	178
178	200	224
224	250	282
282	315	355
355	400	447
447	500	562
562	630	708
708	800	891
891	1000	1122
1122	1250	1413
1413	1600	1778
1778	2000	2239
2239	2500	2818
2818	3150	3548
3548	4000	4467
4467	5000	5623
5623	6300	7079
7079	8000	8913
8913	10000	11220
11220	12500	14130
14130	16000	17780
17780	20000	22390

Structure Borne Noise

It occurs when mechanical vibration energy is generated by a product and circulates through the structure of the product and the materials it comes into contact with. One solution to reduce structure borne noise is to prevent vibration from friction. This can be done by placing a low friction surface between mutually moving parts of a product. Another solution is to change the vibration mode of the structure by using damping material to ensure that the vibration is distributed. In this case, the structure will not vibrate as easily as before, and the vibration energy from the structure will be limited and converted into heat energy. A third solution is to isolate the vibration to prevent it from moving from one part of the product to another or to adjacent structures. Structure-borne noise is transmitted through solid structures such as steel, wood, concrete, stone.

Airborne Noise

Airborne noise arises from the interaction of a vibrating surface with the surrounding air. To reduce airborne noise; absorbers, barriers or foam can be used. Airborne sound absorbers are typically foam or fiber materials that absorb and convert sound energy into heat energy. Sound waves expand outward from the source and propagate in all directions. The difference between the structure and the noise in the air lies in the transmission medium. The sound coming from the air occurs in the progressive motion (vibrations) of the mass particles and the speed of sound is transmitted in the form of sound waves.

Test Method

Test bench at Figure 3 can excite the center bearing assembly in radial and axial directions and it can also rotate the rolling ball bearing at the same time. The interior walls of the test bench chamber are acoustically conditioned. The tests were carried out at two different temperature values. For each temperature, at the same axial and radial excitation, noise levels of the center bearing for three different speed levels were calculated. First, the ambient was cooled down to 20° C, afterwards the noise level of the center bearing assembly was calculated at 5 mm axial and radial excitation and the noise level was calculated. Then, the noise level was calculated at the same axial and radial excitation at 20° C chamber temperature and 3.000 rpm rotational speed. The same process was repeated under the same conditions but at 6500 rpm rotational speed.

The medium was allowed to warm up to 80 degrees and the operations performed at 20 ºC were repeated and the first block was completed. The block cycle was continued until the center bearing elastomer failed. As a result, the noise data calculated in the first block and the noise data calculated in the block where the failure was detected were compared.

Figure 3. Test Bench

Results and Discussion

Noise data were obtained as a result of the above described test sequences. The octave band averages of the obtained results were taken. The noise levels in the first block and the block in which the failure (last block) was observed were compared under the specified test conditions. In Figure 4, the noise levels were given when the center bearing elastomer was axially and radially moved at 20° C. In Figure 5 the center bearing elastomer was

axially and radially moved at 20° C and roller bearing was rotated at 3.000 rpm. In Figure 6, the center bearing elastomer was axially and radially moved at 20° C and roller bearing was rotated at 6.500 rpm. In Figure 7, the noise levels were given when the center bearing elastomer was axially and radially moved at 80° C. In Figure 8, the center bearing elastomer was axially and radially moved at 80° C and roller bearing was rotated at 3.000 rpm. In Figure 9, the center bearing elastomer was axially and radially moved at 80° C and roller bearing was rotated at 6.500 rpm.
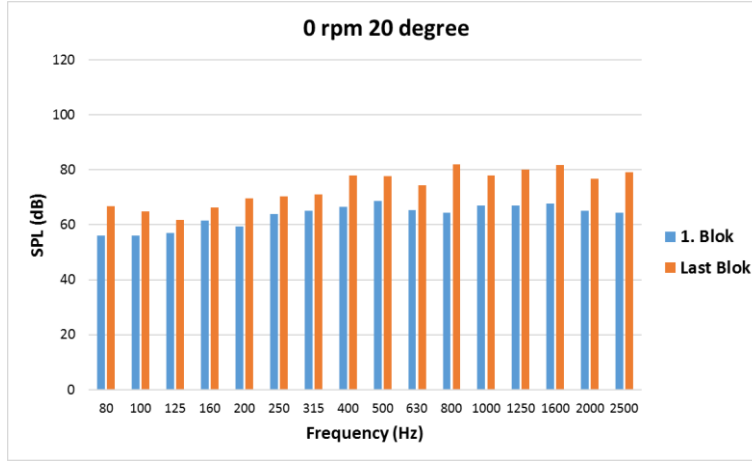
Figure 4. Sound Pressure Levels at 20ºC and 0 rpm
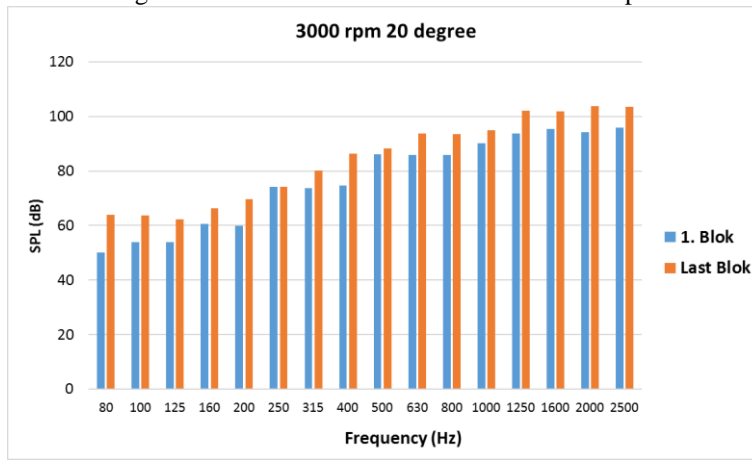
Figure 5. Sound Pressure Levels at 20ºC and 3.000 rpm

.
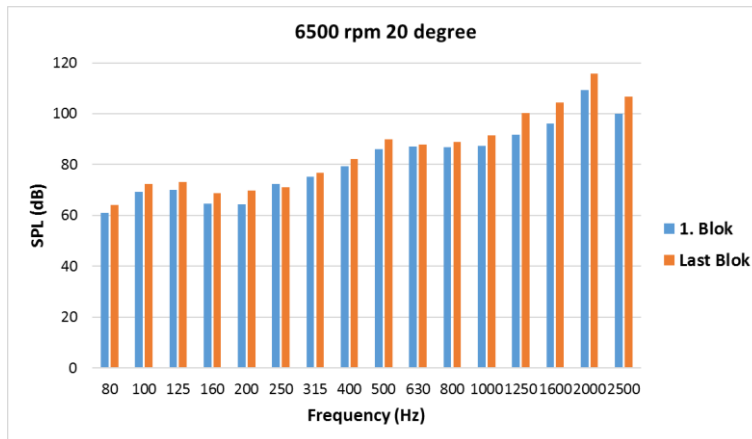
Figure 6. Sound Pressure Levels at 20ºC and 6.500 rpm
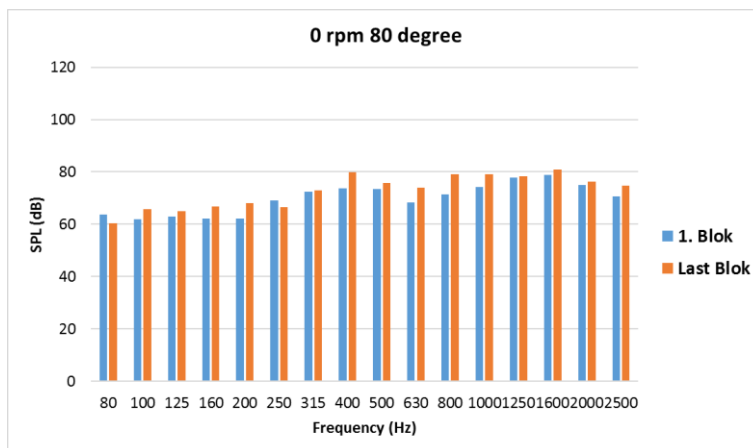
Figure 7. Sound Pressure Levels at 80 ºC and 0 rpm

.
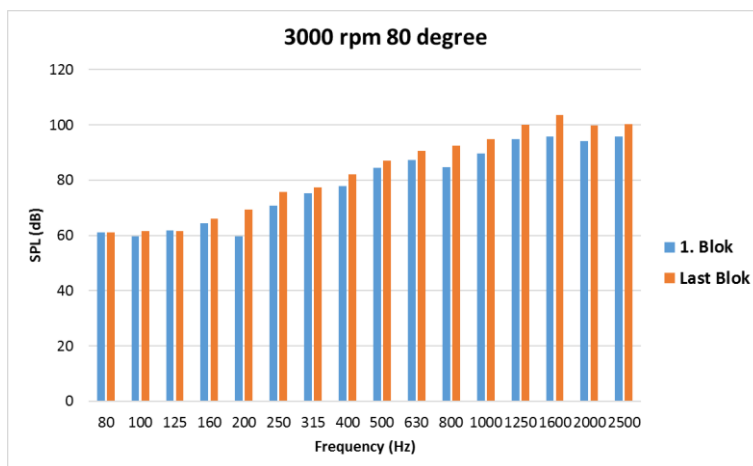
Figure 8. Sound Pressure Levels at 80ºC and 3.000 rpm
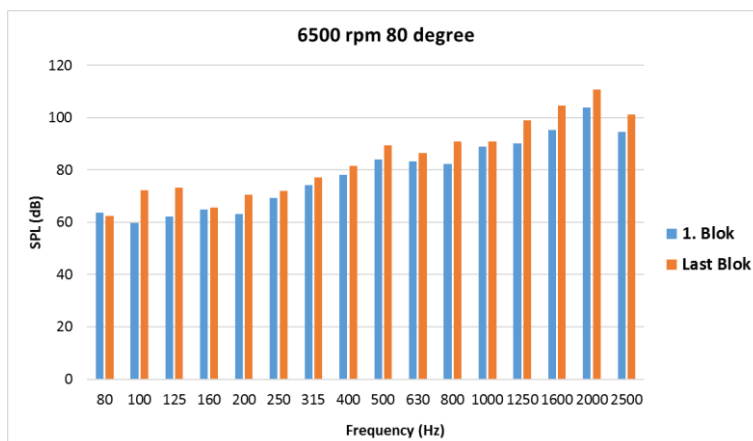
Figure 9. Sound Pressure Levels at 80ºC and 6.500 rpm

Conclusion

Table 2 shows that the equivalent noise levels for all test conditions. Results are as follows:

1. For both temperature levels, the noise level increases as the rotational speed of the roller bearings increase.
2. The comparison of noise levels in the 1st block and last block of the test at the stationary position of the roller bearing, shows that sound pressure level increases with cycles.
3. The noise level in the first block at 3000 rpm 80 degrees Celsius is 4 % lower than the noise level in the last block.

4. The noise level in the first block at 6500 rpm 80 degrees Celsius is 5 % lower than the noise level in the last block.

Table 2. Sound Pressure Levels in Test Conditions

Temp (C)	Velocity (rpm)	1. Blok SPL (dB)	Last Blok SPL (dB)
	0	85	88
20	3000	100	104
	6500	103	106
	0	87	89
80	3000	101	106
	6500	102	111

Recommendations

This study is for light duty driveshafts only, the work can be extended to all driveshaft product families in future work. In addition destructive inspection of roller bearings will be carried out to identify the root cause of the noise level increase.

Acknowledgements or Notes

References

N.N, Universal joint and driveshaft design manual, SAE, Advances in Engineering series (AE) No. 7, Second

Exner, W., "NVH Phenomena in Light Truck Drivelines," SAE Technical Paper 952641, 1995

Wellmann, T., Govindswamy, K., Braun, E., and Wolff, K., "Aspects of Driveline Integration for Optimized Vehicle NVH Characteristics," SAE Technical Paper 2007-01-2246, 2007

Xia, Y., Pang, J., Zhou, C., Li, H. et al., "Study on the Bending Vibration of a Two-Piece Propeller Shaft for 4WD Driveline," SAE Technical Paper 2015-01-2174, 2015

A.Sridhar, Dr. R. Mohan, R.Vinoth Kumar, "Design and Analysis of Composite Drive Shaft", International Journal of Scientific & Engineering Research, Volume 7, Issue 5, May-2016

P. Jayanaidu, M. Hibbatullah, Prof. P. Baskar, "Analysis of a Drive Shaft for Automobile Applications", IOSR Journal of Mechanical and Civil Engineering (IOSR-JMCE) Volume 10, Issue 2 (Nov. - Dec. 2013)

Ashwani Kumar, Rajat Jain, Pravin P. Patil, "Dynamic Analysis of Heavy Vehicle Medium Duty Drive Shaft Using Conventional and Composite Material", 2016 IOP Conf. Ser.: Mater. Sci. Eng. 149 012156

Ono, K., "Evaluation Method for Vibratory Forces Caused by Propeller Shaft," SAE Technical Paper 1999-01-1763, 1999

Taichi Shiiba , Jörg Fehr & Peter Eberhard (2012) "Flexible multibody simulation of automotive systems with non-modal model reduction techniques", Vehicle System Dynamics, 50:12, 1905-192

He, J., Fu, ZF. (2001), Modal Analysis, Butterworth Heinemann, Oxford, 304 pages

Secgin, A., Ertunç, S., Öztürk, B., Yıldırım, K., Sarıgül, S. (2009) "Bir Buzdolabı Kompresörünün Deneysel Modal Analizi, 14. Ulusal Makina Teorisi Sempozyumu, 2-4 Temmuz 2009, Kuzey Kıbrıs

Author Information

Efe Isik
Tirsan Kardan A.Ş
Organize Sanayi Bölgesi 3. Kısım M.Kemal Bulvarı No:15
Manisa, 45030 Türkiye
Contact E-mail: *e.isik@tirsankardan.com.tr*

Muzaffer Kasaba
Tirsan Kardan A.Ş
Organize Sanayi Bölgesi 3. Kısım M.Kemal Bulvarı No:15
Manisa, 45030 Türkiye

Ercan Guneri
Tirsan Kardan A.Ş
Organize Sanayi Bölgesi 3. Kısım M.Kemal Bulvarı No:15
Manisa, 45030 Türkiye

IConTES 2019: International Conference on Technology, Engineering and Science

Electrochemical Behavior of Valsartan, Glimepiride and Their Interaction with Each Other Using Square Wave Voltammetry

Amer Th. AL-TAEE
Mosul University

Aws Z. AL-HAFIDH
Mosul University

Abstract: In this work an electrochemical quantification and interaction of valsartan and glimepiride were studied on hanging mercury drop electrode (HMDE) using square wave voltammetric (SWV) technique. The effect of temperature on the interaction was investigated in eight degrees of heat and the thermodynamics parameters (enthalpy, entropy & free gibbs energy) were calculated for the interaction using Van't Hoff equation and binding constant (K) also obtained from interaction equation. From the values of the calculated thermodynamic parameters it found that the main bonding forces that predominated over the interaction were Vander Waals and Hydrogen bonding. The calibration curves of each drug was liner with R^2 value equal to 0.9819, 0.997 and the limit of detection was found to be 4.99 x 10^{-7}, 3.48 x 10^{-8} for valsartan and glimepiride respectively. Through the limit of detection, this method can be used as a standard method in estimating the pharmacists in pharmaceutics and verifying the credibility of the manufacturers of the two drugs.

Keywords: Square wave voltammetry (SWV), Valsartan, Glimepiride, Drug interaction

Introduction

Valsartan (VAL) (S)-3-methyl-2-(N-{[2'-(2H -1 ,2 ,3 ,4-tetrazol-5-yl) biphenyl -4-yl] methyl} pentanamido) butanoic acid (Fig. 1), is orally active of antihypertensive drug widely used in the treatment of hypertension (Iriarte *et al.*, 2007), belonging to the family of angiotensin II receptor antagonists acting at the ATI receptor, which mediates all known effects of angiotensin II on the cardiovascular system (Nie *et al.*, 2005).
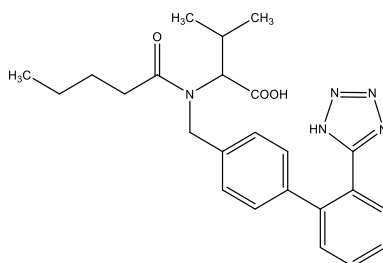
Fig. 1 Valsartan

The methods for the determination of valsartan have been reported in literature including liquid chromatography–tandem mass spectrometry (Koseki *et al.*, 2007), high performance liquid chromatography (HPLC) with a fluorescence detector (FP) (Iriarte *et al.*, 2007 ; Macek *et al.*, 2006), spectrophotometry (Tatar and Saglik, 2002), and there are electrochemical methods (Yan *et al.*, 2008 ; Ramadan *et al.*, 2012 ; Habib *et al.*, 2007).

Glimepiride, 1-[[p-[2-(3-ethyl-4-methyl-2-oxo-3-pyrroline-1-carboximido)ethyl] phenyl] sulfonyl]-3-(trans-4-methylcyclohexyl)urea, (Fig. 2), is the oral anti diabetic and second –generation sulphonylurea agent. It is

widely used in the treatment of non-insulin dependent Type II diabetes mellitus (NIDDM) in order to achieve appropriate control of blood glucose level (Davis, 2004 ; Massimo, 2002 ; Campbell, 1998 ; Draeger, 1995 ; Langtry and Balfour, 1998 ; Becic *et al.,* 2003).
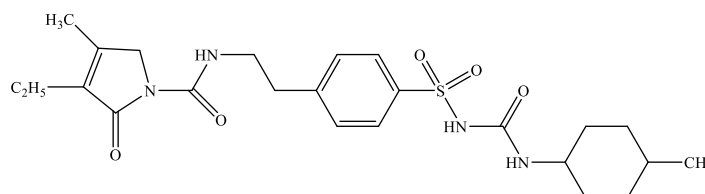
Fig. 2 Glimepiride

Glimepiride have been determination either alone or in combination with various drugs in its pharmaceutical formulations by several methods including high - performance liquid chromatography (HPLC) (Khan *et al.,* 2009), HPLC - tandem mass spectrometry (Wang *et al.,* 2009), high - performance thin layer chromatography (Patel *et al.,* 2006), UV and derivate spectrophotometry (Patel *et al.,* 2006 ; Ravindra and Singhvi, 2008), most of them needs sample preparation or high cost instrumentation.

A drug interaction is a situation in certain medicines can interact pharmacologically and affect the activity of other medicines. This action can be synergistic (when the drug's effect is increased) or antagonistic (when the drug's effect is decreased). These interactions may occur out of accidental misuse or due to lack of knowledge about the active ingredients involved in the relevant substances (Mohapatra *et al.,* 2018). It is therefore easy to see the importance of these pharmacological interactions in the practice of medicine, if a patient is taking two drugs and one of them increases the effect of the other it is possible that an overdose may occur. The interaction of the two drugs may also increase the risk that side effects will occur. On the other hand, if the action of a drug is reduced it may cease to have any therapeutic use because of under dosage (Alfonso and Gayo, 2005).

an electrochemical behaviour of valsartan and glimepiride were investigated In this work also their interaction with each other was examined for this purpose a simple, sensitive and rapid square-wave voltammetric (SWV) technique was developed. The developed method was applied to determine the valsartan and glimepiride in pharmaceutical formulations. The results obtained were compared with UV- spectrophotometric method given in the literature (Altinoz and Tekeli, 2001).

Experimental

Apparatus

SWV measurements were performed using a 797 VA Computrace connected to a computer unit supplied by Metrohm, Switzerland, coupled with a three-electrodes detection system consists of hanging mercury drop electrode (HMDE) as working electrode, an Ag/AgCl/sat. KCl as reference electrode and 1mm platinum wire was used as an auxiliary electrode.

pH measurements for prepare phosphate buffer solutions were performed using a digital pH meter supplied by HANNA company, Portugal, model pH211, microprocessor pH meter with accurate to ±0.05.
HAAKE G supplied by HAAKE company, Germany, water bath was used for controlling temperature during the measurements.

Reagents and procedure

All chemicals used were analytical grade (BDH , Fluka). The pure valsartan & glimepiride were kindly supplied by Sammira drugs industry in Iraq. Stock solution of each drugs were prepared by using an appropriate amount of valsartan and glimepiride and dissolving it in ethanol absolute and dimethyl formamide (DMF) respectively. The phosphate buffer (K_2HPO_4 & KH_2PO_4) used as supporting electrolyte.

The buffer solution was placed in polarographic cell and deoxygenated via purging with N2 gas for 5min prior the measurements, after recording the buffer voltammogram, the test solution added to the polarographic cell

and the square wave voltammograms were recorded under the optimum conditions for a sequence additions of standard stock solutions of each drugs, then the calibration curves were constructed for each drugs.

Results and Discussion

Electrochemical behavior of valsartan

Square wave voltammograms of valsartan shows a well-defined reduction peak at (-1.07)V on HMDE versus Ag/AgCl/sat.KCl under the default conditions of instrument in phosphate buffer solution (pH=7).

Optimum condition for valsartan

The square wave voltammograms were recorded for 4.97×10^{-5}M valsartan in phosphate buffer at different pHs, of phosphate buffer solution. It can be seen from figure 3, the reduction peak current, peak shape and peak potential depended strongly on pH. The optimum pH was found to be pH=6, which is used for determination, where as pH=7 (human blood pH) was used for interaction studies.
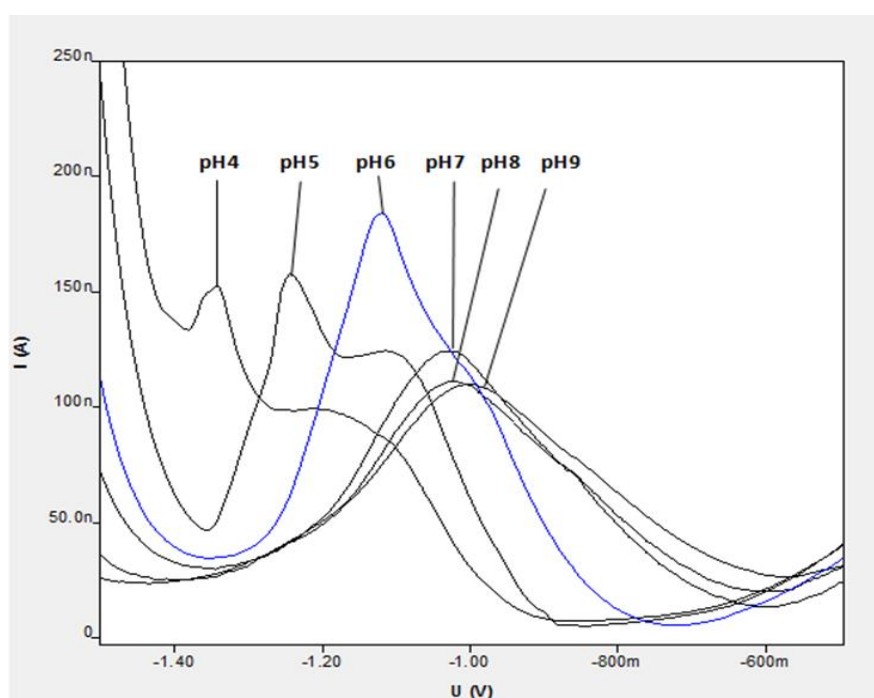
Fig. 3 Effect of pH on the reduction peak current of valsartan

In order to optimize the conditions for measurements, various instrumental and experimental variables such as frequency, scan increment, pulse amplitude, supporting electrolyte and pH were examined and optimized, using 4.97×10^{-5}M valsartan in phosphate buffer as supporting electrolyte, the results obtained are shown in table 1.

Table 1 The optimum condition for valsartan in phosphate buffer solution (pH=6)

Start Potential	-1.5 (V)
End Potential	-0.7 (V)
Deposition potential	-0.6 (V)
Deposition time	30 (s)
Equilibration time	1 (s)
Voltage step	0.006 (V)
Amplitude	0.06 (V)
Frequency	50 (Hz)
Drop size	4
Sweep rate	0.3

Stability of reduction peak

To study the stability of reduction peak of valsartan a voltammogram of 9×10^{-5}M valsartan was recorded under the mentioned optimum conditions (Table 1) versus time, the results obtained are shown in table 2, it is clear that the reduction peak current is stable within the time studied.

Table 2 Stability of reduction peak current ofvalsartan

Time (min)	Ip of VAL (nA)	Ep of VAL (V)
0	284	-1.08
5	287	-1.08
10	278	-1.08
15	278	-1.08
20	291	-1.08
25	291	-1.08
30	296	-1.08
35	276	-1.08
40	275	-1.08
45	278	-1.08
50	277	-1.08
55	279	-1.08
60	280	-1.08

Calibration curve of valsartan

The calibration curve was constructed by adding a sequence addition of standard valsartan solution (10^{-3}M) and the voltammogram was recorded for each addition (Fig. 4) under the previous optimum conditions (Table 1), the plot of peak current versus concentration (Fig. 5) gives a straight line with $R^2 = 0.9819$ concentration range $[(4.99 \times 10^{-7}$M$) - (6.95 \times 10^{-6}$M$)]$.
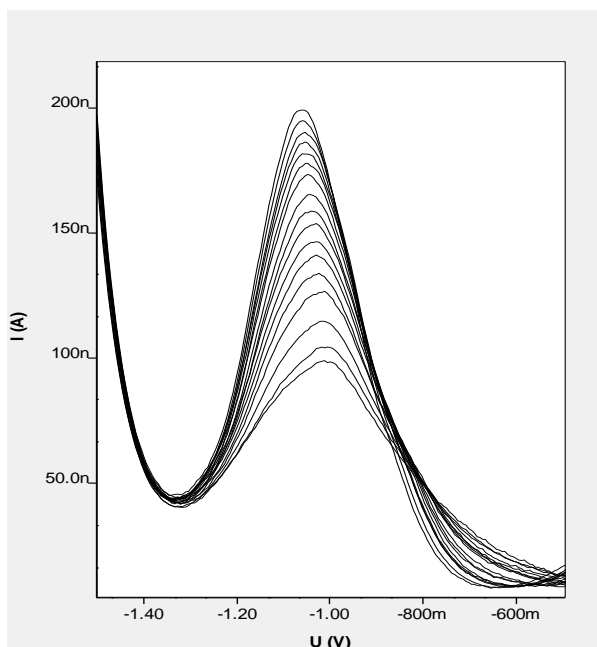
Fig. 4 Voltammograms of sequence addition of standard valsartan solution (10^{-3}M) in phosphate buffer (pH=6)
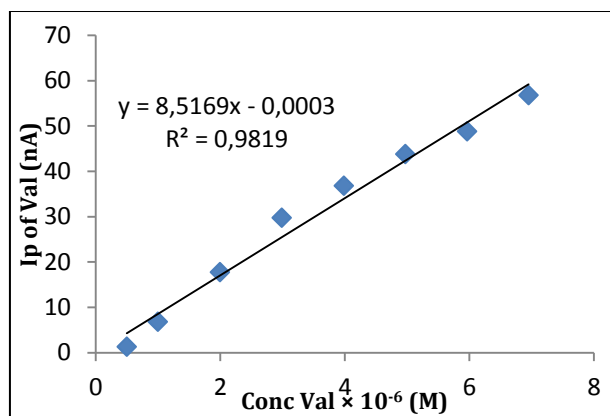
Fig. 5 The calibration curve of valsartan using phosphate buffer (pH=6)

Electrochemical behavior of glimepiride

SWV of glimepiride show a well-defined reduction peak at (-1.3)V versus Ag/Agcl/sat.KCl under the default conditions of instrument in phosphate buffer (pH=7).

Optimum condition for glimepiride

The square wave voltammograms were recorded for 4.97×10^{-5}M glimepiride in phosphate buffer solution at different pHs, It can be seen from figure 6, the reduction peak current, peak shape and peak potential depend strongly on pH. the optimum pH was found to be pH=7.
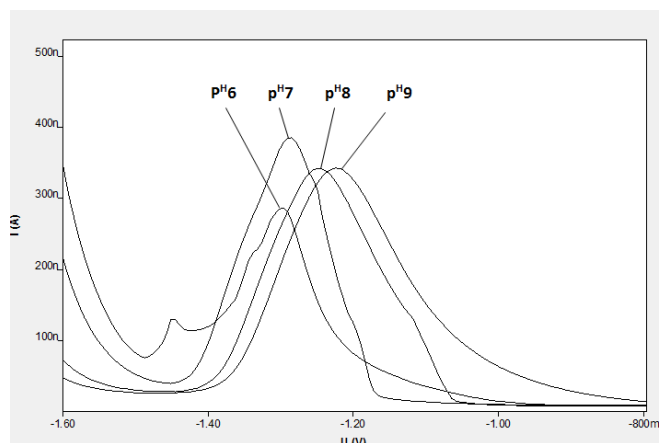
Fig. 6 Effect of pH on the reduction peak current of glimepiride

In order to optimize the conditions for measurements, various instrumental and experimental variables such as frequency, scan increment, pulse amplitude, supporting electrolyte and pH were examined and optimized, using 9.9×10^{-5}M glimepiride in phosphate buffer solution as supporting electrolyte, the results obtained are shown in table 3.

Table 3 The optimum condition for glimepiride in phosphate buffer (pH=7)

Start Potential	-1.6 (V)
End Potential	-0.8 (V)
Deposition potential	-0.8 (V)
Deposition time	70 (s)
Equilibration time	5 (s)
Voltage step	0.006 (V)
Amplitude	0.06 (V)
Frequency	50 (Hz)
Drop size	4
Sweep rate	0.3

Stability of reduction peak

To study the stability of reduction peak of glimepiride a voltammogram of 1.4×10^{-5}M glimepiride was recorded under the mentioned optimum conditions (Table 3) versus time, the results obtained are shown in table 4, it is clear that the reduction peak current is stable within the time studied.

Table 4 Stability of reduction peak of glimepiride

Time (min)	Current (nA)
0	155
5	154
10	155
15	155
20	155
25	154
30	153
35	152
40	152
45	151
50	151

The calibration curve of glimepiride

The calibration curve was constructed by adding a sequence addition of standard glimepiride solution (10^{-5}M) and the voltammogram was recorded for each addition (Fig. 7) under the previous optimum conditions (Table 3), the plot of peak current versus concentration (Fig. 8) gives a straight line with $R^2 = 0.997$ and detection limit equal to 3.48×10^{-8}M.
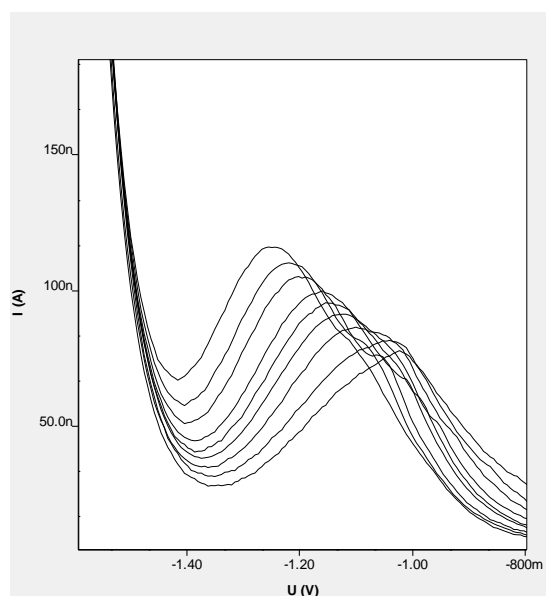
Fig. 7 Voltammograms of sequence addition of standard glimepiride solution (10^{-5}M) in phosphate buffer (pH=7)
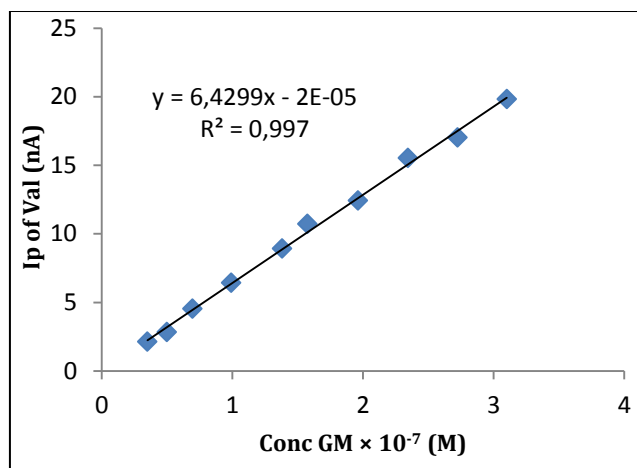
Fig. 8 The calibration curve of glimepiride using phosphate buffer (pH=7)

Interactions of valsartan with glimepiride

Square wave voltammograms of 1.4×10^{-5}M valsartan were recorded under the optimum conditions (Table 1) for a sequence additions of glimepiride solution at different temperatures using phosphate buffer pH=7 (human blood pH).

Stability of interaction

To study the stability of interaction peak a voltammogram of 1.9×10^{-4}M valsartan with 4.9×10^{-7}M glimepiride was recorded under the mentioned optimum conditions of valsartan (Table 1) in phosphate buffer pH=7 versus time, the results obtained are shown in table 5, it is clear that the interaction reduction peak current is stable within the time studied.

Table 5 Stability of interaction reduction peak current using phosphate buffer pH=7

Time (min)	Ip of Interaction (nA)
0	219
5	215
10	220
20	223
30	224
40	218
50	224

Binding constant

The decrease in peak current of valsartan with a sequence additions of glimepiride (Fig. 9) at all studied temperatures were noticed. The relations between reduction peak current and glimepiride concentrations added were linear at all studied temperatures with R^2 equal to 0.9943, 0.9964, 0.998, 0.9901, 0.991, 0.9903, 0.9412 and 0.9766 for 283^0, 289.5^0, 293^0, 298^0, 303^0, 308^0, 310^0 and 318^0K respectively. Thermodynamics parameters and binding constants were calculated (Table 6) according to equation (1) (Jalali and Dorraji, 2012) as shown in Figures 10-17.

$$ln\left(\frac{Ip}{Ip° - Ip}\right) = ln\left(\frac{1}{[GM]}\right) - lnK \dots (1)$$

where K is the binding constant, Ip° and Ip are the reduction peak currents of the free valsartan and VAL-Glimepiride complex, respectively. The plot of ln(Ip/(Ip°-Ip)) versus ln(1/[GM]) is linear and the binding constant was obtained from its intercept.
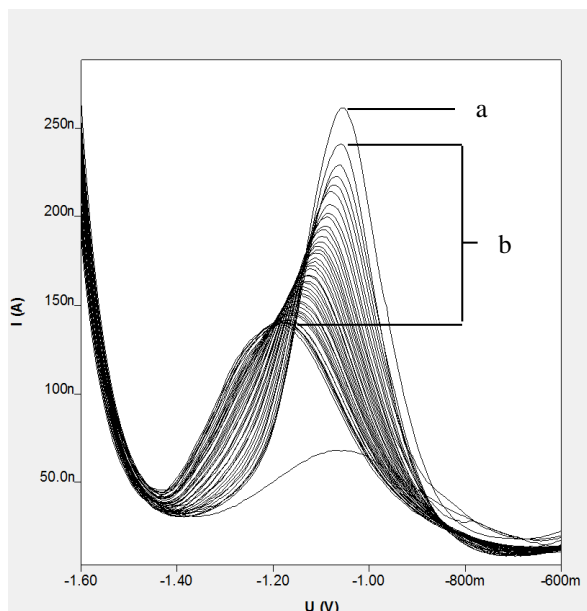
Fig. 9 The reduction peak of valsartan (a) with the sequence additions of glimepiride (b) at $(293^0 K)$
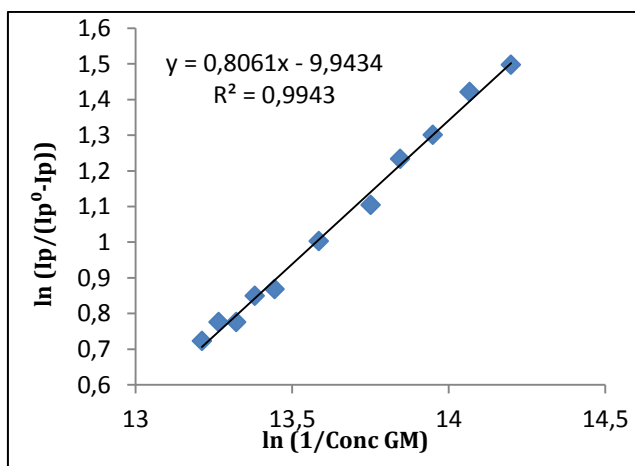
Fig. 10 ln (I p/(Ipº –Ip)) vs ln (1/[Conc(M)]) at $283^0 K$
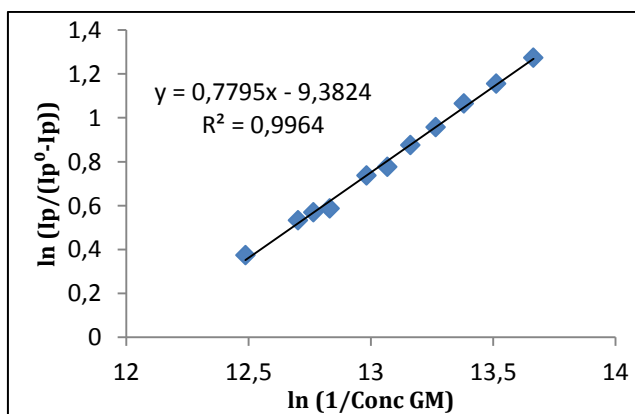
Fig. 11 ln (I p/(Ipº –Ip)) vs ln (1/[Conc(M)]) at $289.5^0 K$
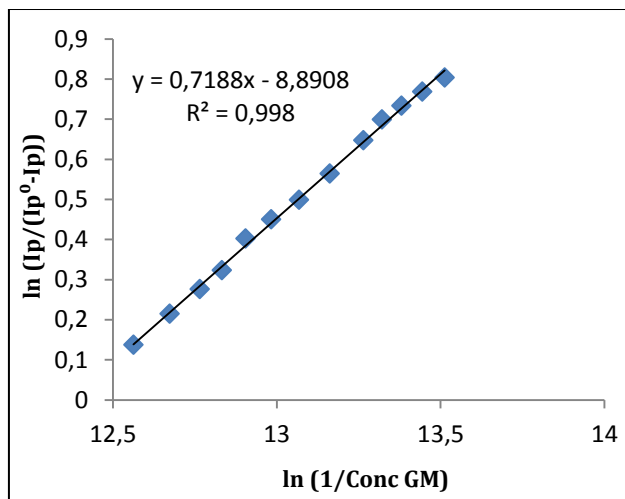
Fig. 12 ln (I p/(Ip° –Ip)) vs ln (1/[Conc(M)]) at 293^0K
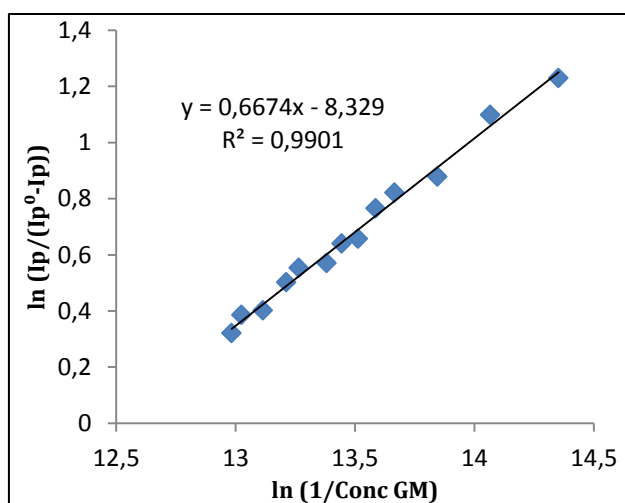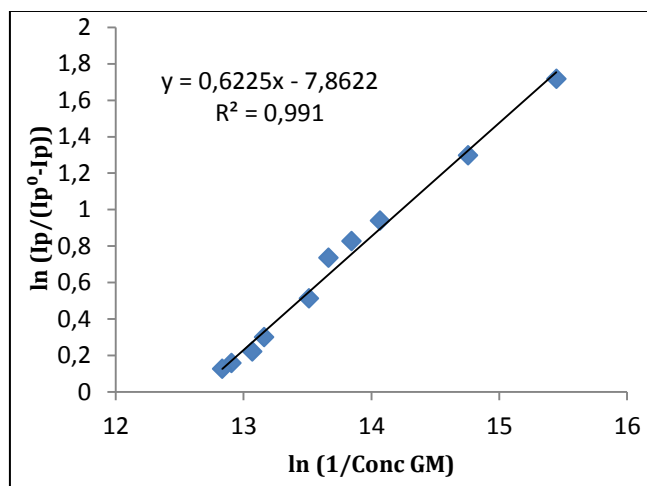
Fig. 13 ln (I p/(Ip° –Ip)) vs ln (1/[Conc(M)]) at 298^0K

Fig. 14 ln (I p/(Ip° –Ip)) vs ln (1/[Conc(M)]) at 303^0K

Fig. 15 ln (I p/(Ip° –Ip)) vs ln (1/[Conc(M)]) at $308\,^0$K

Fig. 16 ln (I p/(Ip° –Ip)) vs ln (1/[Conc(M)]) at $310\,^0$K
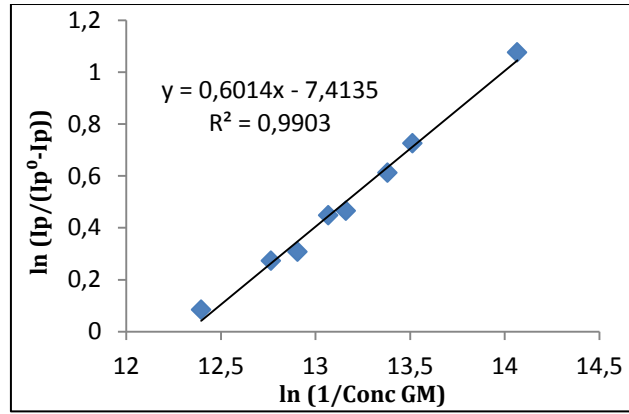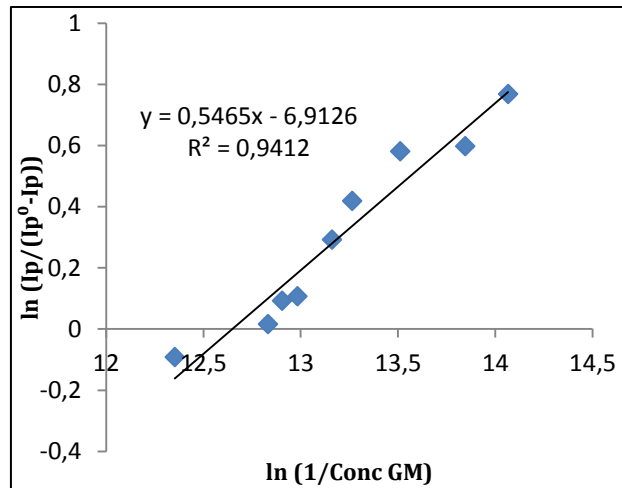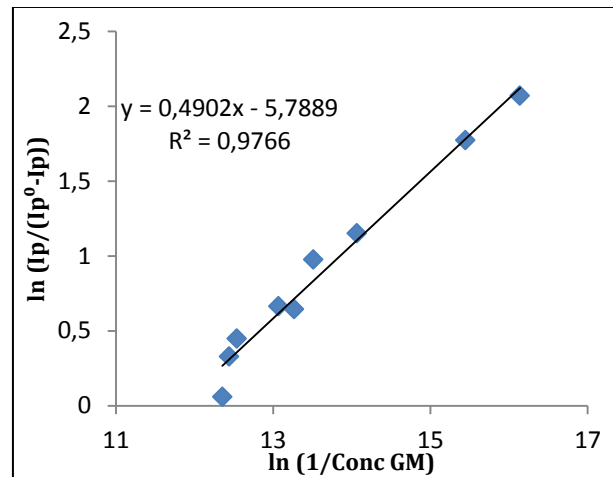
Fig. 17 ln (I p/(Ip^0 –Ip)) vs ln (1/[Conc(M)]) at $318\,^0$K

Thermodynamics parameters

The plotting of ln K against 1/T using Van't Hoff equation (2), gives linear relationship (Fig. 18). The change enthalpy (ΔH) was obtained from the slope and other thermodynamics parameters (ΔG and ΔS) were calculated as follow:-

ln K = $-\Delta H/RT + \Delta S/R$ …..(2)

Enthalpy (ΔH):-Based on the formula of Van't Hoff (3)

ΔH = - Slope $\times$ R …..(3)   (R= 8.314 J. mole^{-1}. K^{-1})

The Free energy (ΔG) was calculated from the equation (4) of Van't Hoff described below:

$\Delta G = -R \times T \times \ln K$ …..(4)

Entropy ΔS was calculated from the intercept (5)

$\Delta S = \text{Intercept} \times R$ …..(5)

The plot of ln K versus 1/T gives straight line with R^2 equal to 0.9825 (Fig. 18).
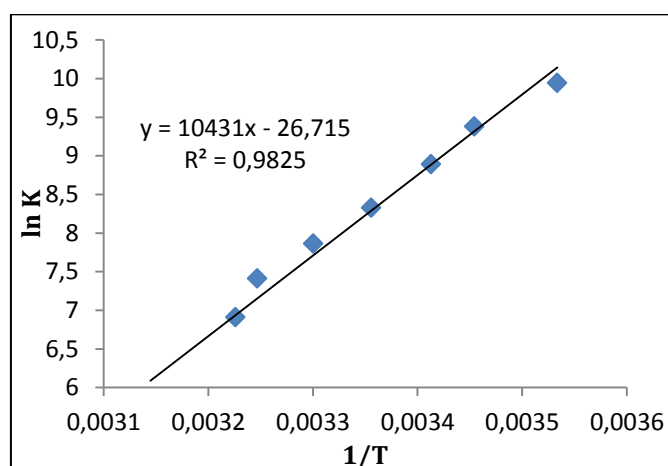
Fig. 18 Plot of ln K versus 1/T of interaction between valsartan and glimepiride

Table 6 Thermodynamics parameters and binding constants for valsartan and glimepiride interaction

Temp (K)	Binding constant $(K_b) \times 10^{-3}$ M^{-1}	ΔH (KJ.mol^{-1})	ΔG (KJ.mol^{-1})	ΔS (J.mol^{-1}.K^{-1})
283	20.8		-23.3954	
289.5	11.8		-22.5825	
293	7.26		-21.6580	
298	4.14	-86.7233	-20.6356	-222.1085
303	2.59		-19.8059	
308	1.65		-18.9838	
310	1.00		-17.8161	
318	0.326		-15.3049	

The negative charge of ΔH indicates that the binding interaction is exothermic and binding constant decrease with increasing temperature, also ΔG become more positive with increasing temperature means the spontaneously of binding decreased, where as the negative value of ΔS indicate that the system became more ordered. The negative ΔH and ΔS values for the interaction of valsartan and glimepiride indicate that the binding is mainly enthalpy and entropy driven, and the interaction may involve hydrogen bonding and van der Waals forces played major role in the interaction (Ross and Subramanian, 1981).

Conclusion

Both valsartan and glimepiride gave a well-defined reduction peak at (-1.07)V, (-1.3)V respectivily on HMDE versus Ag/AgCl/sat.KCl in phosphate buffer solution using square wave voltammetry (SWV) technique. From studying the interaction of valsartan with glimepiride and calculate thermodynamics parameters, it was concluded that the interaction is exothermic and the system became more ordered due to the hydrogen bonding and van der Waals forces between the two drugs, and the interaction becomes non-spontinous with increasing temperature and the binding constant (K_b) decreases with increasing temperature too, this is consistent with the negative value of enthalpy.

Recommendations

Apply this study as standard method on pharmaceutical drugs and calculate the percentage of active substance in them.

Acknowledgements or Notes

Acknowledgements o my supervisor Asst. Prof. Dr. Amer Th. Al-Taee.

References

Alfonso, M.S.F., Gayo, M.R. (2005). Fundamentos de Farmacología Básica y Clínica . Published by Steve Bob Billy Joe. Spain. page 232.

Altinoz, S., Tekeli, D. (2001 Jan). Analysis of glimepiride by using derivative UV spectrophotometric method. *J. Pharm. Biomed. Anal., 24(3),* 507-515.

Becic, F., Kapic, E., Becic, E. (2003). Glimepiride - an oral antidiabetic agent. *Med. Arh., 57(2),* 125-127.

Campbell, R.K. (1998 Oct). Glimepiride: role of a new sulfonylurea in the treatment type 2 diabetes mellitus. *Ann. Pharmacother., 32(10),* 1044-1052.

Davis, S.N. (2004 July). The role of glimepiride in the effective management of type 2 diabetes. *J. Diabetes Complications., 18,* 367-376.

Draeger, E. (1995 Aug). Clinical profile of glimepiride. *Diabetes Res. Clin. Pract., 28,* S139-146.

Habib, I.H.I., Weshahy, S.A., Toubar, S.S., El-Alamin, M.M.A. (2007 Dec). Stripping voltammetric determination of valsartan in bulk and pharmaceutical products, *Pharmazie., 63,* 337–341.

Iriarte, G., Ferreiros, N., Ibarrondo, I., Alonso, R.M., Maguregui, M.I., Jimenez, R.M. (2007 June). Biovalidation of an SPE-HPLC-UV-fluorescence method for the determination of valsartan and its metabolite valeryl-4-hydroxy-valsartan in human plasma. *J. Sep. Sci., 30,* 2231.

Jalali, F., Dorraji, P.S. (2012). Electrochemical and spectroscopic studies of the interaction between the neuroleptic drug, gabapentin, and DNA. *J. Pharm. and Biomed. Anal., 70,* 598– 601.

Khan, I.U., Aslam, F., Ashfaq, M., Asghar, M.N. (2009 Feb). Determination of glimepiride in pharmaceutical formulations using HPLC and firstderivative spectrophotometric methods. *J. Anal. Chem., 64(2),* 171-175.

Koseki, N., Kawashita, H., Hara, H., Niina, M., Tanaka, M., Kawai, R., Nagae, Y., Masuda, N. (2007 Jan). Development and validation of a method for quantitative determination of valsartan in human plasma by liquid chromatography-tandem mass spectrometry. *J. Pharm. Biomed. Anal., 43,* 1769.

Langtry, H.D., Balfour, J.A. (1998 Apr). Glimepiride: a review of its use in the management of type 2 diabetes mellitus. *Drugs., 55(4),* 563-584.

Macek, J., Klima, J., Ptacek, P. (2006 Jan). Rapid determination of valsartan in human plasma by protein precipitation and high-performance liquid chromatography. *J. Chromatogr. B., 832,* 169.

Massimo, M. (2002 Dec). Glimepiride in type 2 diabetes mellitus: a review of the worldwide therapeutic experience. *Clin. Ther., 25(3),* 799-816.

Mohapatra, S.S., Kafle, A., Reddy, I., Sarma, J. (2018). Drug interactions with antibiotics. *International J. Chem. Studies, 6(2),* 2120-2122

Nie, J., Zhang, M., Fan, Y., Wen, Y., Xiang, B., Feng, Y.Q. (2005, Oct). Biocompatible in-tube solid-phase microextraction coupled to HPLC for the determination of angiotensin II receptor antagonists in human plasma and urine. *J. Chromatogr. B., 828,* 62.

Patel, J.R., Suhagia, B.N., Patel, M.M. (2006). Simultaneous determination of glimepiride and pioglitazone in bulk and in pharmaceutical formulations by HPTLC method. *Asian J. Chem., 18(4),* 2873-2878.

Ramadan, N.K., Mohamed, H.M., Mostafa, A.A. (2012 Feb). Potentiometric determination of amlodipine besilate and valsartan using microsized and polymeric matrix membrane sensors. *Portugaliae Electrochimica Acta., 30(1),* 15-29.

Ravindra, N., Singhvi, I. (2008 July). Spectrophotometric estimation of glimepiride from pharmaceutical dosage forms. *Asian J. Chem., 20(6),* 4379-4382.

Ross, D. P., Subramanian, S. (1981). Thermodynamics of protein association reactions: forces contributing to stability. *Biochemistry, 20,* 3096-3102.

Tatar, S., Saglik, S. (2002 May). Comparison of UV- and second derivative-spectrophotometric and LC methods for the determination of valsartan in pharmaceutical formulation. *J. Pharm. Biomed. Anal., 30,* 371.

Wang, J., Yang, D.J., Wang, Z.T., Chen, B., Yao, S.Z. (2009 Mar). Simultaneous of illegal additives in dietary supplements and traditional medicines by high performance liquid chromatography-electrospray ionization mass spectrometry. *Food Chem., 113(1),* 227-232.

Yan, J., Wang, W., Chen, L., Chen, S. (2008 Aug). Electrochemical behavior of valsartan and its determination in capsules. *Colloids and Surfaces B., 67,* 205–209.

Author Information

Amer Th. Al-Taee
Mosul University
Mosul, Iraq
Contact E-mail: *amerthanon@yahoo.com*

Aws Z. Al-Hafidh
Mosul University
Mosul, Iraq

Cyber Security for Smart Cities

Murat DENER
Gazi University

Abstract: When the systems in smart cities are classified, there are generally eight categories. These are Smart Transportation, Smart Governance, Smart Economy, Smart Environment, Smart Health, Smart Industry, Smart Security, and Smart Life. There are dozens of intelligent systems in each category. The correct operation of these systems is as important as their security. For example, if any infiltration or intrusion into an intelligent system such as smart intersections, smart roads, crowd management, city noise mapping, smart energy, natural gas and water supply systems, early warning systems, the city may be in great danger. Natural disasters can be experienced as well as fatal consequences that affect human life. Therefore, the rulers of the smart city should always be on the alert and ensure the cyber security of the smart city. Cyber refers to electronic environments such as computer, server, device, hardware, software, protocol, algorithm, process, policy, process, laboratory, system. Cyber security is a set of methods, policies, concepts, and guidelines, risk management approaches, activities, trainings, best practice experiences and technologies used to protect the information assets of institutions, organizations and users. Intelligent strategies against cyber-attacks should be developed as the city environment created by smart systems has become very attractive for data thieves. Otherwise, a smart city can bring people closer to bad situations rather than bring people closer to technology. In this study, Cyber Security in Smart cities will be explained. The current literature review will reveal the latest trends in these two areas. The study is considered to be beneficial for smart cities technology developers.

Keywords: Smart city, Cyber security, Attack, Living, Technology

Introduction

A smart city infrastructure has many information systems such as fiber optic channels and wireless networks. Outer layers can be connected to the devices contained therein. Technologically, while these operations are performed, there is also a safety risk. In the city, there can be a power failure, water pollution, traffic incidents, material loss, loss of information, or even life-threatening.

Smart systems in smart cities have many parameters. These parameters can be either hardware or software. As examples, intelligent system forming sensor nodes, routers, gate nodes, embedded software, server required to send data detected by the gate node, database, cloud etc are given. Ensuring the high degree of security of these parameters is crucial for the safety of the smart city.

In this study, the current studies on cyber security in smart cities are shared with the elements of smart city.

Smart City

Smart city is the city where the technological opportunities for sustainable living and urbanization are implemented in the city and consequently economic, social and administrative benefits are provided. Some of the systems found in smart cities, as shown in Figure 1, are as follows.

Waste management, Electromagnetic Emissions, Smart Health, Education, Internet of Things, Smart Street Lights, Electric Vehicle Charging, Air Pollution, Smart Home, Smart Parking, Open Data, Public Safety, Smart

Environment, Smart Buildings, Traffic Management, Gas & Water Leak Detection, Intelligent Shopping, Smart Energy, Water Quality.
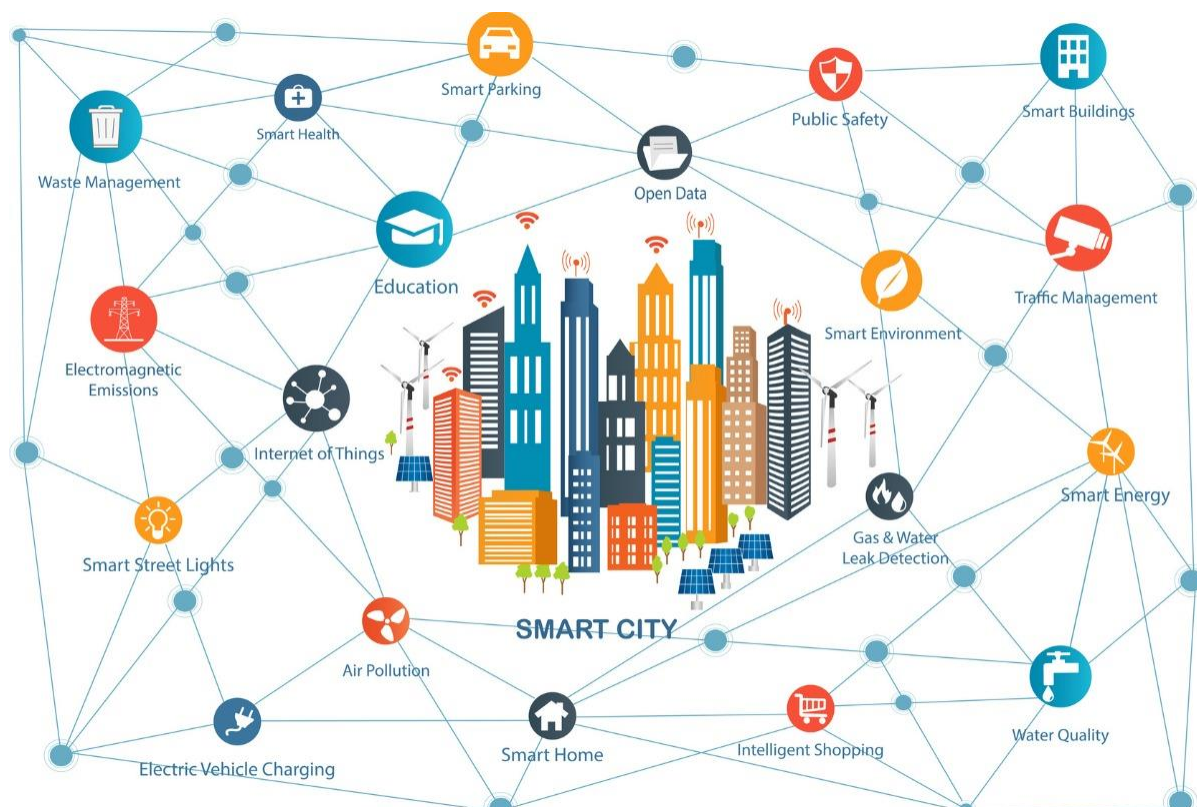
Figure 1. Smart City [SmartCitiesWorld news team, 2017]

Due to the increasing population density, cities may face many problems such as decrease in resources, pollution, increasing energy need and increasing communication need. The solution of these problems and the reduction of their effects is to make the city smart.

Cyber Security

Cyber refers to electronic environments such as computer, server, device, hardware, software, protocol, algorithm, process, policy, process, laboratory, system. Cyber security is a set of methods, policies, concepts, and guidelines, risk management approaches, activities, trainings, best practice experiences and technologies used to protect the information assets of institutions, organizations and users.

A smart city should have end-to-end protection to ensure cyber security. An attacker could infiltrate an existing vulnerability anywhere in the system and seize management.

All assets such as computers, smart devices, sensors, routers, network devices used in smart cities need to be protected. These protections must be both physical and software. Common technologies used to protect these assets include next-generation firewalls, DNS filtering, malware protection, antivirus software, and email security solutions.

Studies on cyber security in smart cities

When the literature is examined, it is seen that there are limited studies on cyber security in smart cities. These studies are described below.

In the study [Vitunskaite et al., 2019], 93 existing security standards related to smart cities were examined. Of the 93 security standards reviewed, 13 are related to cyber security. The security standards and security

measures of the smart cities of Barcelona, Singapore and London were analyzed. In addition, a new smart city security framework has been proposed.

As a threat in smart cities, a grouping is made as follows.

Threats from Intentional Attacks
Eavesdropping/wiretapping
Unauthorised use/access
Tampering/alteration
Theft
Malware/Virus
DDoS
Loss of Reputation

Threats from Accidents
Hardware failure/malfunctioning
Software error
Operator/User error
Electrical and frequency disturbance/interference
End of support
Acts of nature
Environmental incidents

The study [Parasol, 2018] reported that the Chinese government issued a law on the use of technology in the country. Due to the strict attitude of the published law, technology companies have become uneasy. There are also concerns that this law, which is prepared to protect China, will slow down China's technology. In this article, it is explained why China needs cyber security regime and the security law published by China is examined.

According to statistics from the Chinese state, the country has 731 million Internet users. Moreover, 695 million of them use the internet via their smart phones. According to the authors, this is one of the main reasons why China needs a security law.

The study [Baig et al., 2017] provides an in-depth insight into smart city security threats and digital investigation. In this study, four categories were identified as Smart Grids, Building Automation Systems, Unmanned Aerial Vehicles and Smart Vehicles and the technologies-platforms of these categories were shared. The security threats in these categories are given.

In the study [AlDairi and Tawalbeh, 2017], major security problems in smart cities and their valid solutions are given. In addition, it has been presented in many factors that affect data and information security in smart cities.

In the study [Elsaeidy et al., 2017], a new architecture has been developed for cyber attackers that affect the security of smart cities. In the architecture developed by using deep learning techniques, the behaviors of the users are taken into consideration.

The study [Wibowo, 2018] states that many smart cities in Indonesia have a web-based public services application. In order to test these services, a new method is proposed to measure the security level using the https evaluation method.

The study [Goel, 2015] examines the relationship between privacy and security and provides standards and guidelines for smart networks in smart cities.

In this study [Efthymiopoulos, 2016], smart city studies in Dubai have been given and together with these studies, necessary cyber security needs have been presented.

Conclusion

Ministry of Environment and Urbanization, Smart City concept within the scope of National Smart Cities Strategy and Action Plan 2019-2022; It is defined as a more livable and sustainable city, which is implemented

through inter-stakeholder cooperation, uses new technologies and innovative approaches, is justified on the basis of data and expertise and produces solutions that add value to life by anticipating future problems and needs.

Because smart cities are fully integrated with technology, cyber attackers can cause material, economic and even fatal losses from time to time. In order to prevent these losses, it is necessary to ensure end-to-end security of the city.

In order to ensure that the whole system is secure and not to leave any vulnerabilities at the security point, smart city security standards should be issued taking into account the standards developed by the public in the world (IEEE, ISO etc.).

Thus, each system installed in the city should be expected to meet these standards. Otherwise, a system that advances the city technologically can jeopardize the management and operation of the city due to the security gaps it contains.

References

AlDairi, A., Tawalbeh, L. (2017). Cyber Security Attacks on Smart Cities and Associated Mobile Technologies. *8th International Conference on Ambient Systems, Networks and Technologies (ANT-2017) and the 7th International Conference on Sustainable Energy Information Technology (SEIT 2017)*, 109, 1086-1091.

Baig, Z.A., Szewczyk, P., Valli, C., Rabadia, P., Hannay, P., Chernyshev, M., Johnstone, M., Kerai, P., Ibrahim, A., Sansurooah, K. (2017). Future challenges for smart cities: Cyber-security and digital forensics. *Digital Investigation*, 22, 3-13.

Efthymiopoulos, M.P. (2016). Cyber Security in Smart City of Dubai. *Proceedings of the 11th International Conference on Cyber Warfare and Security (ICCWS 2016)*, 107-118.

Elsaeidy, A., Elgendi, I., Munasinghe, K.S., Sharma, D., Jamalipour, A. (2017). A Smart City Cyber Security Platform for Narrowband Networks. *2017 27th International Telecommunication Networks and Applications Conference (ITNAC)*, 390-395.

Goel, S. (2015). Anonymity vs. Security: The Right Balance for the Smart Grid. *Communications of the Association for Information Systems*, 36, 23-32.

Parasol, M. (2018). The impact of China's 2016 Cyber Security Law on foreign technology firms, and on China's big data and Smart City dreams. *Computer Law & Security Review*, 34, 67-98.

SmartCitiesWorld news team. (2017). Smart cities services worth $225bn by 2026. Retrieved from https://www.smartcitiesworld.net/news/news/smart-cities-services-worth-225bn-by-2026-1618.

Vitunskaite, M., He, Y., Brandstetter, T., Janicke, H. (2019). Smart cities and cyber security: Are we there yet?A comparative study on the role of standards, third party risk management and security ownership. *Computers & Security*, 83, 313-331.

Wibowo, S. (2018). Enriching Digital Government Readiness Indicators of RKCI Assessment with Advance Https Assessment Method to Promote Cyber Security Awareness Among Smart Cities in Indonesia. *2018 International Conference on ICT for Smart Society (ICISS)*, 103-106.

Author Information

Murat Dener
Gazi University
Emniyet Mahallesi Abant-1 Caddesi No:10/2E Kat:8
06500 Yenimahalle / Ankara/Türkiye
Contact E-mail: *muratdener@gazi.edu.tr*

Production and Evaluation of Ethylic Biodiesel from Mixed Non-Edible Castor and Bitter Almond Oils

E. T.B. Al-TIKRITY
Tikrit University

A.B. FADHIL
University of Mosul

K. K. IBRAHEEM
Tikrit University

Abstract: Selection of low price and non-edible feedstocks for biodiesel production is a considerable target to diminish the production cost of biodiesel. Accordingly, the current work is to inspect the production of fatty acid ethyl esters (ethylic biodiesel) from mixed non-edible oils particularly; castor oil seeds (CSO) and bitter almond oil (BAO). Various blends of the CSO: BAO (10:90 -50:50 % w/w) were prepared and evaluated in order to choose the optimal blend whose properties similar to those reported for conventional raw oils. The results indicate that the equivalent blend (50:50 % w/w) possess the optimal properties. Therefore, it was chosen as a raw feedstock for producing ethylic biodiesel through the standard base-catalyzed transesterification process by using KOH as a catalyst with ethanol. Experimental parameters affecting transesterification process, such as the type and the concentration of the alkali catalyst, ethanol to mixed oils molar ratio, the reaction temperature, and the reaction time were optimized. Biodiesel with maximum yield (98.88 wt. % with purity of 97.66 % w/w) was obtained by implementing 0.50 % KOH w/w of oil, 5:1 ethanol to oil molar ratio, 35 °C reaction temperature and 30 minutes time. The 1HNMR spectroscopy affirmed the transformation of the oils blend to ethylic biodiesel. The obtained ethylic biodiesel had density and kinematic viscosity values much lower than those of ethylic biodiesel produced from CSO individually. Furthermore, the properties of the resulting biodiesel were within the acceptable limits prescribed by ASTM D 6751. It was concluded that using such blend oils could be an easy approach to improve the properties of produced biodiesel from castor oil, and to reduce production cost.

Keywords: Mixed non-edible oils, Ethylic biodiesel, Transesterification, Fuel properties evaluation, Analysis of biodiesel

Introduction

Biodiesel (BD) is manufactured on industrial scale through alcoholysis reaction of various edible oils with methanol in the presence of alkaline catalyst [1]. One of the significant key in such production process is the type and the cost of the oil feedstock. In fact, 95% of commercial BD is currently produced from edible oils, which is reported to be 70-80% of the total manufacturing cost [2, 3]. European and United States of America are producing BD from rapeseed, soybean and sunflower oils feedstock, while coconut and palm tree oils are predominantly used in Asia [4].

Regardless of that, employing edible oils in making BD has been of major awareness due to the food versus fuel dispute [5, 6]

Utilization of non-edible oils, when compared with edible oils, has received high attention in developing countries because the indigence for edible oils as food, and they are far too expensive to be utilized as fuel [5].

Consequently, exploring new innovations toward renewable and cheaper raw materials to produced low cost BD has become a new strategy for BD production feasibility.

Many inexpensive non-edible oils sources like Jatropha curcas [7,26], waste animal fats, waste cooking oil [8], and waste fish oil [9], castor oil [10], and oil from rubber seeds [11] are preferentially utilized for that purpose. This implementation arises from the reality that many of such oils are not suitable for human consumption, and could be used as successful alternative feedstock for production process.

However, castor trees (Ricinuscommunis), among many non-edible oil producer plant, are an important industrial non-food crop, it can be cultivated in wild land without special care, and can tolerate sever climate conditions [9, 10,12,13],. Its productivity for non-edible oil from their seeds (the castor seed oil, CSO) is cheap and high, as much as 51.0%. It was reported that the global production of CSO reached around 1.8 million tons per year, and that India, China and Brazil are the leading production countries [12, 13].

Unfortunately, the CSO consists of about 87 - 95% of Ricinoleic acid. This acid percent impress undesired properties, as far as BD production is concerned, like high polarity, high viscosity, and high density. It was mentioned that the kinematic viscosity of CSO amounts of 226 mm2/s at 40°C, while those of most vegetable oils are in the range 27–54 mm2/s at the same temperature. Therefore, BD derived from CSO has much higher viscosity than those of conventional biodiesels. Accordingly, many researchers suggest mixing of BD obtained from CSO with lower viscosities diesel (biodiesels or petro diesel fuel) to be within the acceptable fuel engine properties. Whereas, the other proposed mixing of CSO with another oils or animal fats, in order to select the optimum oils blend that satisfy the suitable specifications to produce BD [14-17].

On the same concept, Bitter Almond seeds, which obtained from almond tree (Prunusdulcis var. amara), gives high percent of non-edible oil about 42% and has been applied to produce BD [18-20]. Nevertheless, little literature published about synthesis of BD from bitter almond oil (BAO) via base-catalyzed transesterification, but no works were reported for production of BD from mixing of BAO with other non-edible oils [18-20].

The present research work suggests production of ethylic BD from a mixture of CSO and BAO, through optimized ethanolysis transesterification reaction. Different blends of CSO and BAO were prepared and evaluated to select the optimal blend properties. The quality of the produce BD was analyzed by FTIR, and 1H NMR spectroscopy, and the fuel properties of the obtained ethylic BD were determined following the ASTM standards.

Experimental

Materials and Reagents

Castor seeds and bitter almond seeds were collected from Nineveh and Dohuk Governorates (north of Iraq), respectively. All chemicals were of analytical reagent grade, and used as received without any further purification. Absolute ethanol (99.9 %), methanol, potassium and sodium hydroxides (KOH, NaOH, and pellets), sodium methoxide (CH3ONa), sodium ethoxide (CH3CH2ONa), iodine, acetone, sodium sulphate (Na2SO4), and diethyl ether were purchased from BDH (UK). Chloroform, n-hexane, hydrochloric acid, and cyclohexane were purchased from Fluka (Germany).

Seed Preparation and Oil Extraction

Seeds of castor and bitter almond were cleaned and oven-dried at 50°C for 24h. After grinding of the dried seeds using an electrical grinder, the oil was extracted by n-hexane in a Soxhlet extractor for 10h. The extracted oils were separated from the solvent by distillation using a rotary evaporator. The obtained oils was dried over anhydrous sodium sulfate to eliminate the residual moisture, filtered and kept in a sealed container at 5°C for further assessment and use. The yield of the oil was calculated for each type seeds, on dry bases [22].

Analysis and Characterization of the Extracted Oils

The Fatty acids composition of both CSO and BAO were determined using gas chromatography (GC, Perkin Elmer, Auto system GLX, Shelton, U.S.A.) equipped with a Supelco SP™-2380 (30 m x 0.25 mm i.d., 0.25 μm

film thickness) column equipped with flame ionization detector (FID)[22]. The average molecular weight (g/mol) of the oils was determined by a weighted average method utilizing the fatty acid profile. The iodine value of CSO and BAO was determined based on Hanus method. Properties of CSO and BAO were determined following ASTM standard methods.

Preparation of the Blended Oils

Different weight percent blends of CSO and BAO were prepared through mixing of CSO with (10, 20, 30, 40 and 50 % w/w of BAO). The prepared blends were thoroughly mixed by mechanical stirrer for 30 minutes to obtain homogeneous mixture. The physical and chemical properties of the blends oils were examined in order to select the acquired blend.

Transesterification of the Mixed CSO and BAO with Ethanol

The blend oils (100g) was placed in a three neck round-bottomed flask (500 mL), fitted with mechanical stirrer, condenser, thermostat, and sampling outlet, followed by addition(separately) a known amount of freshly prepared ethylic solutions of the catalyst salts, (NaOH, KOH, CH3ONa, and CH3CH2ONa). The mixture was, then, refluxed with stirring at 700 rpm for a specific reaction time. The reaction products were transferred into a separating funnel and left overnight to obtain two distinct phases. The lower layer (glycerin) was separated and discarded, while the upper layer (ethyl esters) was distilled under vacuum using a rotary evaporator to recover the excess alcohol, followed by washing with distilled water to remove the other impurities. Finally, the ethyl esters were dried over anhydrous sodium sulfate to dispose of any traces of leftover water. The ethyl esters yield was calculated as follow [11, 23]

$$\text{Biodiesel Yield (\% w/w)} = \frac{\text{Total weight of the purified ethyl ester X Ester content (\%)}}{\text{Total weight of the used blend oils}} \times 100$$

Analysis and Properties Evaluation of the Biodiesel

The 1HNMR spectra were used for analysis of the produced ethyl esters by using a Varian (Palo Alto, CA, USA) VNMR spectrometer operating at 300 MHz. Samples were diluted in 500 µL of deuterated chloroform (CDCl3). Properties of the produced ethyl ester were evaluated as per the ASTM standard procedures. The properties included density (ASTM D 5002), kinematic viscosity (ASTM D 445), flash point (D93), saponification value (ASTM D5555-95), the refractive index (D1747 – 09), the acid value (ASTM D664), the cloud, and pour points (ASTM D 2500). The Iodine value was measured according to Hanus method. The soap content was determined in accordance with AOCS Cc 17-95. The method proposed by Pisarello et al. [24] was used for determination of the total glycerin in the produced ethyl esters. Each property was measured in triplicate and the results were presented as the mean ± standard deviation (SD).

Results and Discussion

Properties and Analysis of the Oils

Solvent extraction of oils from castor and bitter almond seeds has given, on dry bases, 51.0 and 42.0%w/w, respectively, which are relatively high comparing to other non-edible vegetable seeds. Therefore, CSO or BAO can be exploited as potential feedstock for BD production. As mentioned earlier, the high viscosity and density of CSO may disclose unsuitable BD for engine fuel. On that subject, different blends of CSO and BAO (10/90 - 50/50 % w/w BAO/CSO) were prepared and evaluated so as to select the optimal blend properties which correspond to BD production. The results, in Table1, indicate that the density, viscosity, refractive index, and flash point of the CSO have markedly been reduced with increasing BAO content in the blends. This improvement in oil properties arise from the merits of BAO comparing to that of CSO.

Table1. Properties of CSO, BAO and their blends

Property	*CSO*	*BAO*	*Blend 90+10*	*Blend 80+20*	*Blend 70+30*	*Blend 60+40*	*Blend 50+50*
Density @ 15.6 g/mL	0.9658	0.9100	0.9397	0.9364	0.9275	0.9211	0.9193
Kinematic Viscosity@ 40°Cmm^2/s	197.43	24.12	131.42	101.21	86.66	75.33	54.77
Flash Point °C	185	180	175	170	165	145	130
Acid Value mg KOH / g oil	0.10	0.46	2.61	2.21	1.85	1.66	1.47
Refractive index@20°C	1.4780	1.4674	1.4711	1.4688	1.4665	1.4651	1.4643
Pour Point °C	-<15	-7	-15.0	-14.0	-11.0	-11.0	-10.0
Sapon. Value mg KOH / g oil	188.47	175.23	170.20	174.80	180.06	217.21	219.80

Properties of the blend in comparison to other non-edible oils			
Property	CSO+BAO (50/50%)	CJCO [a]	SMSO [b]
Density @ 15.6 g/mL	0.9193	0.9180	0.9141
Kinematic Viscosity@ 20°Cmm^2/s	54.77	35.40	42
Flash Point °C	130	186.0	230
Acid Value mg KOH / g oil	1.47	11.0	13.6
Refractive index @ 20°C	1.4643	-	1.4700
Pour Point °C	-10.0	-	-8
Sapon. Value mg KOH / g oil	219.80	-	195.0
[a] Ref.[26]; [b] Ref.[24]			

The reduction in the features of CSO, after blending with BAO, may attributed to a possible interaction between hydroxyl groups of the ricinloeic acid and the free fatty acids of BAO, or to the dilution effect. This was assured through the 1H NMR spectrum of the CSO and the blend which is depicted in Fig.1a and Fig.1b, respectively. The signals at (4.13 and 4.30 ppm) which are related to glyceride protons were separated in the CSO [25]. After blending with BAO, the signals have coalesced and become multiple as well as their integration increases. The signal at (2.32 ppm) which belongs to CH2-COO was found in the CSO and disappeared after

blending with BAO [25]. The integration of the signal at (3.4 ppm) which correspond to the proton of the hydroxyl group of the ricinoliec acid was reduced from 0.58 to 0.34 ppm after blending of CSO with BAO [25]. Hence, the equivalent blend (50/50 %) was chosen for production of BD via base-catalyzed transesterification with ethanol.
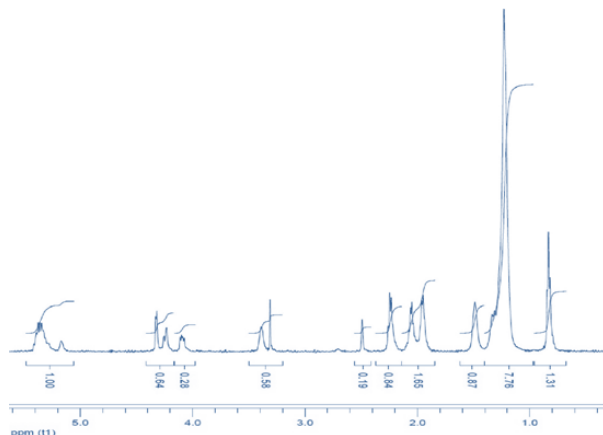
Fig.(1a). ^{1}HNMR of castor seed oil
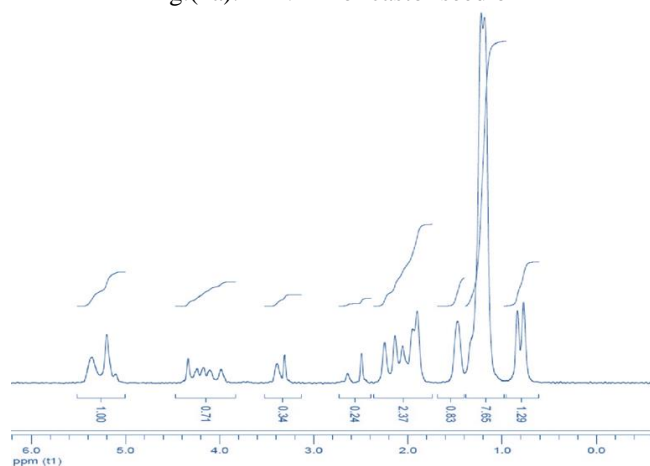
Fig.(1b). ^{1}HNMR of mixed castor oil and bitter almond oil

Biodiesel Production from the Blend of CSO and BAO

The properties of the 50:50 equivalent blends of CSO and BAO were found to be close to the feature of those conventional oils, Table 1; so, it was selected for BD synthesis. The lower acid value of the blend (0.03 mg KOH/g), in contrast to the other non-edible oils [20, 26, 27], makes it suitable feedstock for production of BD via direct optimized protocol base- catalyzed reaction. Therefore, parameters affecting the transesterification process, such as the catalyst type and concentration, ethanol to oil molar ratio, reaction temperature, reaction time, and rate of stirring were thoroughly investigated.

Influence of Catalyst type and Concentration

Effect of concentrations and catalyst type on transesterification reaction of the blend was investigated by trying various alkali catalysts (KOH, NaOH, CH3ONa and CH3CH2ONa) at different concentrations (0.25-1.50 % w/w of oil) as depicted in Fig.2. The other parameters were kept constant at 6:1ethanol: oil molar ratio, 70°C reaction temperature, 700 rpm agitation rate, and 60 minutes reaction time. It was noticed that the lower concentrations of the alkali catalysts (0.25 wt.%) led to an incomplete reaction and resulted in a low yield of BD. The yield increased and amount to maximum at 0.50 wt.% using any of the tested catalysts. Fig.2 also, exhibit that among the tested catalysts, KOH has given the highest yield of BD (92.12 wt.%) which was in accordance with many literatures published elsewhere [20-22, 28,29].
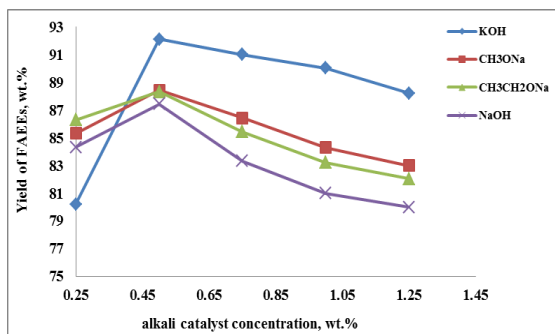
Figure 2. Effect of catalyst type and concentration on ethyl esters yield

The variation in the yield, among different alkali catalysts, could be attributed to their variation in the strength of alkalinity. Nevertheless, increasing the catalysts concentrations more than 0.50 wt.% decreased the ethyl ester yield due to the saponification reaction [28,29]. Therefore, KOH at a concentration of 0.50% w/w of oil was chosen as a type of catalyst and the optimal concentration, respectively.

Influence of Ethanol to Oils Blend Molar Ratio

Transesterification reaction is greatly influenced by alcohol to oil molar ratio. On this account, number of experiments were carried out using different ethanol to oil blends molar ratio in the range of 4:1–10:1, Fig.3, keeping the other factors fixed at 0.50 wt.% KOH, 70°C, 60 minutes, and 700 rpm. The results indicated that the maximum yield of ethyl ester (94.44 wt.%) was obtained at 5:1 ethanol to blend oil molar ratio. This finding was very low relative to other reported studies of ethanolysis of some non-edible oils. [22, 27, 30-35].
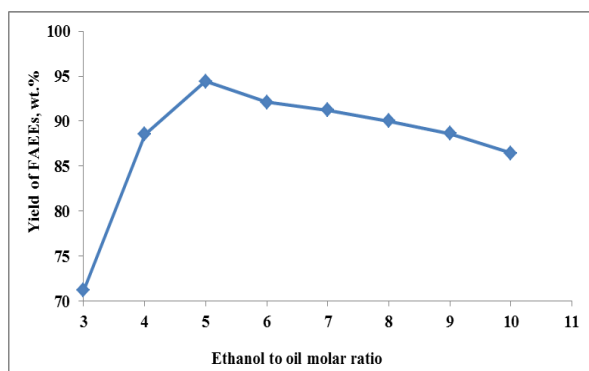
Figure 3. Effect of ethanol to oil molar ratio on ethyl esters yield

It can, also, behold that any further increase in alcohol to oil molar ratio reduced the yield of the ethyl esters due to the solubility of glycerin in the alcohol, pushes the equilibrium reaction to proceed backward to form mono-glycerides [33, 27]. Therefore, 5:1 was established as the optimal mixed alcohols to oil molar ratio.

Influence of Reaction Temperature

The reaction temperature plays a vital role on the transesterification reaction rate, yield conversion and eventually to the BD production cost. It is necessary to optimize the reaction temperature to obtain maximum yield with less energy consumption. It was reported that selecting the optimal reaction temperature for transesterification depends on the chemical composition of the raw oil feedstock, and the type of utilized alcohol [36]. Hence, different experiments were accomplished applying reaction temperature in the range of 25-75°C,whilst the other variables were fixed at 0.50% KOH w/w of oil, 5:1 ethyl alcohol to oils blend molar ratio,60 minutes reaction time and 700 rpm rate of stirring. Fig.4, display the transesterification of the oil mixture with ethanol at 25°C (room temperature) resulted in good yield of ethyl esters (90.02 wt.%), but further increase in the reaction temperature increased the ethyl ester yield. It fact, 35°C was the optimal reaction temperature because it gave highest yield of ethyl ester (96.55 wt. %). This finding is much less value than BD production from the other mixed non-edible oils and very important, as far as the cost of the production is concerned. [22, 31-33, 37, 38].
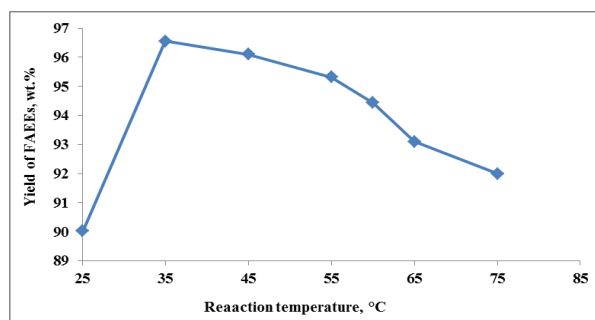
Figure 4. Effect of reaction temperature on ethyl esters yield

It was also noticed that heating more than 35°C favor the side reaction, i.e part of the esters may turned into soap (saponification reaction) leading to decreases the BD yield [35,36]. Hence, 35°C was chosen as an optimal reaction temperature.

Influence of Reaction Time

The influence of reaction duration on the ethyl ester yield was investigated by conducting the transesterification reaction at various durations (15, 30, 45, 60, 75 and 90 minutes), keeping the other parameters, for each experiment, at their optimal values Fig.5. The results exhibit that the highest ethyl ester yield (98.88 wt.%) was obtained at a time of 30 minutes which is much lower than those reported for the production of ethyl ester from various oil feedstocks in literature. [22, 31, 32, 35, 37, 39].
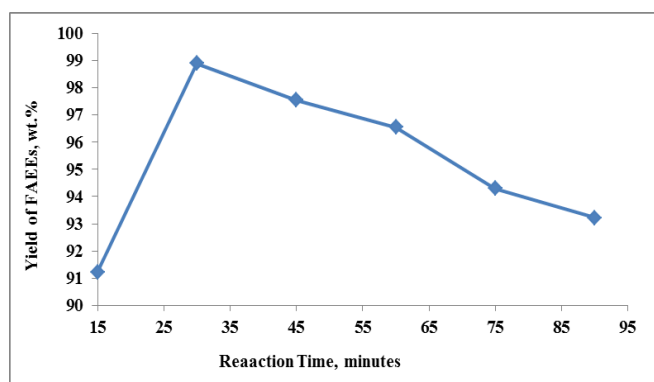
Figure 5. Effect of reaction time on ethyl esters yield

However, durations higher than 30 minutes resulted in lower ethyl ester yield due to the hydrolysis of some of the formed ethyl esters [31]. As a result, the optimal reaction duration was set as 30 minutes.

Effect of Stirring Rate

Transesterification process is induced by the stirring rate due to the mass transfer between the oil and the catalyst solution, and the reaction rate become faster as the mixing increases [27, 37]. Therefore, stirring speed was varied from 300 rpm to 900 rpm at intervals of 100 rpm, while the other parameters were kept at their optimal values. It was observed that phase change had occurred at different rate of stirring. At lower rate of stirring (300 rpm) a little phase changes formation was observed and the yield of the ethyl esters was at lowest level (88.56 % w/w) Fig.6. Whereas, the increase in the rate of stirring the phase change formation was quite clear and the BD yield increased to the maximum (98.88 %) at stirring rate of 700 rpm.
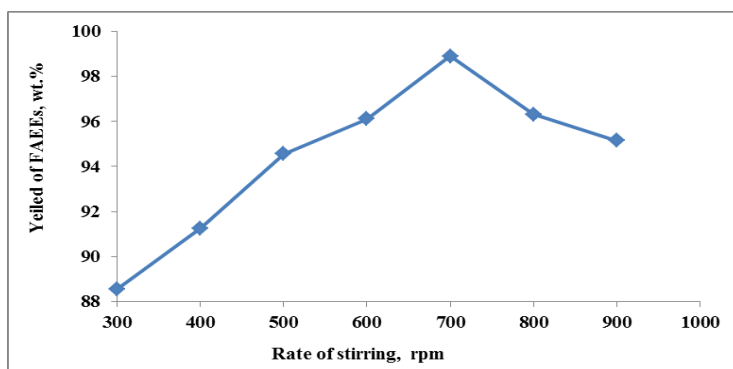
Figure 6. Effect of rate of stirring on ethyl esters yield

These results were attributed to the facts that increases the rate of stirring promotes homogeneity of the reactants, thence, raises the contact between the two immiscible phases (the blend oils and catalyst) to produce higher BD. Nevertheless, at high rate of stirring more than 700 rpm the yield was decreased because of the hydrolysis of some BD causing soap formation. These findings were in good agreement with other authors [32, 40].

Fuel Properties Evaluation

The properties of the ethylic BD obtained from the said blend are summarized in Table 2 together with the standards specified in the ASTM D 6751 and the published values of several biodiesels in literature. For comparison, ethyl esters from CSO and BAO were prepared, separately, by applying the optimal conditions as recorded previously. Following the ASTM D 6751 standards, the obtained BD has a fatty acid ethyl esters content of (97.66±1. % w/w) which was equivalent to the limit specified in that standards (96.50 % w/w). It can be seen from Table 2 that the density and viscosity of the CSO ethyl ester were much higher than those documented for other ethylic biodiesels in literature [33, 38]. Accordingly, BD from the CSO is not suitable as a successful alternative to petro diesel unless these characteristics values are reduced to the acceptable limits. Blending of the CSO and BAO impose an ethylic BD with density and viscosity values much lower than those of the ethylic BD from CSO only, and close to those published for other ethylic biodiesels in literature [32,35]. This improvement in the produced BD is related to the effect of BAO increment which its ethylic BD has much lower density and viscosity than that obtained from CSO. The cloud and pour points of the ethyl ester produced from the mixture are suitable to be used in the cold weather conditions. Moreover, other merits like flash point, refractive index, the acid value, the total content of free glycerin and soaps in the obtained ethylic BD were much lower than those established in the literature [32, 35] and the standard of the ASTM D6751 Table 2. However, the variation in properties values of the produced ethyl ester in comparison to other non-edible oils could be attributed to many factors such as; different chemical composition of the oil feedstock, the applied conditions for the transesterification and the ester content in the biodiesels. The aforementioned achievements, in general, were persuadable feedback for completion of the ethanolysis of the blend. Thus, it may recommend that blending of CSO with BAO is a manner to reduce CSO properties to become highly suitable feedstock raw materials for BD production.

Table 2. Properties of ethylic biodiesel from mixed CSO and BAO in comparison to other ethylic esters

Property	Ethylic BD from CSO	Ethylic BD from BAO	Ethylic BD from the oils blend	Ethylic BD from Used frying oil [c]	Ethylic BD from Sunflower oil [d]	ASTM D 6751
Yield (wt.%)	94.55	86.55	98.88±1.50	-	-	-
Ester content (w/w %)	92.32	81.51	97.66±1. 0	93.20	98.90	96.50
Density @15.6 °C g/mL	0.9202	0.8677	0.8702± 0.0012	0.8883	0.8810	0.9000
Kinematic viscosity @ 40 °C mm^2/s	11.22	4.07	5.18± 0.11	5.81	4.71	3.0 – 6.0
Flash point °C	145	125	±1.0130	188	163	130.0
Acid value mg KOH/g	0.08	0.11	0.03± 0.01	0.46	0.24	0.50
Refractive index @ 20°C	1.4622	1.4531	1.4511± 0.0001	-	-	-
Cloud point °C	-3.0	5.0	-1± 0.50	9.0	-2.0	-
Pour point °C	<-15	-9.0	< -10	-1.0	-10.0	-
Total glycerin content (wt.%)	0.08	0.10	0.04± 0.01	0.25	0.15	0.24
Free glycerin content (wt. %)	0.0039	0.0031	0.0033± 0.001	0.14	0.0	0.02
Soaps (ppm)	0.62	0.62	0.34± 0.02	-	-	5.0

[c] Ref.[35]; [d] Ref.[37]

Analysis of the Mixed Castor and Bitter Almond Ethyl Esters

1H NMR spectroscopy was utilized by many researchers for monitoring transesterification reaction as well as to determine the conversion of oils to their fatty acid alkyl esters [23, 38]. Hence, the obtained ethyl ester was analyzed using this technique to assure the conversion of the mixed CSO and BAO into ethylic BD. The spectrum in Fig.7 shows the disappearance of the characteristic peaks of mono-, di- and triacylglycerol hydrogens at 4.25 ppm, and the appearance of another characteristic peak at 4.11 ppm, belongs to the ethyl group of the corresponding produced ester.
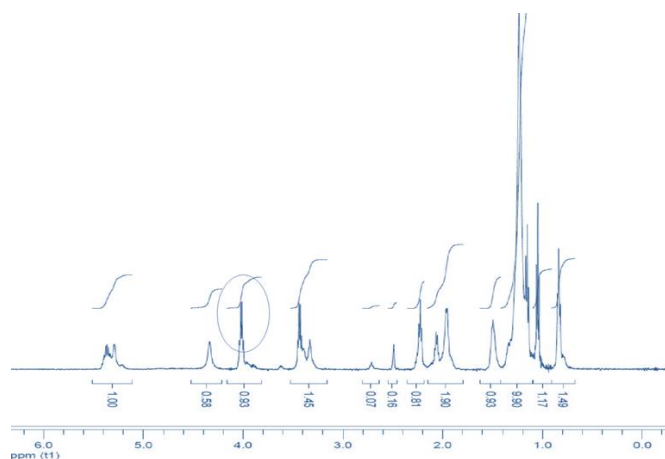
Figure 7. The ^{1}H NMR spectra of biodiesel obtained from mixed castor oil and bitter almond oil

The triplet peak at 2.26 ppm in the spectrum was attributed to α-CH2 protons, whereas the observed peak at 0.85 ppm refers to the terminal methyl protons. The strong signal at 1.26 ppm in the spectrum belongs to the methylene protons of carbon chain, while that observed at 1.58 ppm attributes to the β-carbonyl methylene protons. Finally, peak related to oliffinic hydrogen was appeared at 5.3 ppm [23, 37, 38]. This finding demonstrate the merits of transesterification process to convert low cost non-edible oils mixture into ethyl ester BD, and may considered a successful manner to alter the fuel properties of the parent feedstock into a more valuable fuel.

Conclusion

Fatty acid ethyl ester (ethylic biodiesel) was successfully prepared from mixed non-edible oils, CSO and BAO, with ethanol in the presence of an alkali catalyst. The results revealed that 50/50 v/v CSO: BAO was the acquired mixture for the preparation. Base-catalyzed transesterification of the mixture with ethanol was optimized, and the highest yield (98.88 wt.% and a purity of 97.66 % w/w) by implement 0.60 % KOH w/w, 5:1 ethanol to oils blend molar ratio, 35 °C reaction temperature, 30 minutes of reaction, and 700 rpm rate of stirring. The 1H NMR spectroscopy confirmed the conversion of the blend to their fatty acid ethyl esters. The measured properties of the biodiesel were in accordance to ASTM D 6751 standards indicating suitability of the obtained fuel for diesel engines. It was concluded that exploited the mixed oils system can reduces the required reaction temperature to give maximum conversion, which in turns reduces the cost of the biodiesel production.

Acknowledgment

References

Emaad T. Al-Tikrity, Transesterification; The Operation Role For Biodiesel Production, in : Anita Becker (Eds.) Transesterification Process, Mechanisms and Applications, Nova Science Publishers, New York, pp. 1-45 (2019) .

Knothe, G., Razon, L. F. Biodiesel fuels. Progress in Energy and Combustion Science, 58: 36 (2017) 59 DOI: 10.1016/j. pecs. 2016.08.001.

Knothe, G., Gerpen, J.V., Krahl, J., Ramos, L. P. Manual do Biodiesel. 1st edn. Edgard Blu: São Baülo, SP; pp. 1-352 (2006).

Ramachandran, K., Suganya,T., Nagendra G. N., and Renganathan, S. Recent developments for biodiesel production by ultrasonic assist transesterification using different heterogeneous catalyst. Renewable and Sustainable Energy Reviews 22 410–418 (2013).

Mustafa B. Potential alternatives to edible oils for biodiesel production – a review of current work. Energy Convers Manage; 52: 1479–92 (2011).

Ahmad AL, Yasin NHM, Derek CJC, Lim JK, Microalgae as a sustainable energy source for
Biodiesel production: a review. Renew Sust. Energy Rev; 15(1): 584-93 (2011).

Kumar, D., Kumar, G. and Poonam, S. C. P. Ultrasonic-assisted transesterification of Jatropha curcus oil using solid catalyst, Na/SiO2. Ultrasonics Sonochemistry; 17: 839–44 (2010).

Lam, M.K., Lee, K.T. Mixed methanol–ethanol technology to produce greener biodiesel from waste cooking oil: a breakthrough for SO42−/SnO2–SiO2 catalyst. Fuel Process. Technol.; 92: 1639–1645 (2011).

Fadhil,AB., Al-Tikrity, ET., Albadree, MA.. Transesterification of a novel feedstock, Cyprinuscarpio fish oil: Influence of co-solvent and characterization of biodiesel. Fuel; 162: 215–223 (2015)

Ragul Karthick Elango. Kiruthika Sathiasivan. Chandrasekaran Muthukumaran. et.al Transesterification of castor oil for biodiesel production: Process optimization and characterization Microchemical Journal 2018;145 DOI: 10.1016/j.microc.2018.12.039

Morshed, M., Ferdous, K., Khan, M.R., Mazumder, M.S.I., Islam, M.A., Uddin, Md.T. Rubber seed oil as a potential source for biodiesel production in Bangladesh. Fuel; 90: 2981–2986 (2011).

Bateni, H., Karimi, K. Biodiesel production from castor plant integrating ethanol production via a biorefinery

Tsoutsos, T., Chatzakis, M., Sarantopoulos, I., Nikologiannis, A.,Pasadakis, N., Effect of waste water irrigation on biodiesel quality and productivity from castor and sun flower oil seeds. Renew. Energy 57, 211–215 (2013).

Dantas MB, Albuquerque AR, Soledade LEB, Queiroz N. , Maia AS., Santos I MG, Souza AL, Cavalcanti EHS. Barro A K, Souza AG. Biodiesel from soybean oil, castor oil and their blends, J Therm Anal Calorim; 106: 607–611(2011).

Farias RMC, Conceicao MM, Candeia RA, Silva MCD, Valter J, Fernandes JR. Souza AG. Evaluation of the thermal stability of biodiesel blends of castor oil and passion fruit. J Therm Anal Calorim; 106:651–655 (2011).

Simoni M. Plentz Meneghetti, Mario R. Meneghetti, Tatiana M. Serra,Daniela C. Barbosa, and Carlos R. Wolf, Biodiesel Production from Vegetable Oil Mixtures: Cotton seed, Soybean, and Castor Oils. Energy & Fuels, 21, 3746–3747 (2007).

Barbosa, D C., Serra, TM., Plentz Meneghetti, SM., Meneghetti, MR. Biodiesel production by ethanolysis of mixed castor and soybean oils. Fuel; 89: 3791–3794 (2010).

Fadhil, A.B., Aziz, A.M., Altamer, M.H. Potassium acetate supported on activated carbon for transesterification of new non-edible oil, bitter almond oil. Fuel.170:130–140 (2016).

Atapour M, Kariminia HR. Characterization and transesterification of Iranian bitter almond oil for biodiesel production. Appl Energy; 88: 2377–81(2011).

Emaad T. B. Al-Tikrity, Abdelrahman . Fadhilb, and Khalid K. Ibraheem. Biodiesel production from bitter almond oil as new non-edible oil Feedstock. Energy Sources, Part A: Recovery, Utilization, and Environmental Effects; 39(7):649-656 (2017).

Al-dobouni IA, Fadhil AB, Saeed IK. Optimized alkali-catalyzed transesterification of wild mustard (Brassica juncea L.) seed oil. Energy Sources, Part A; 38(15):2319–25 (2016).

Fadhil, AB. , Abdulahad,WS.. Transesterification of mustard (Brassica nigra) seed oil with ethanol: Purification of the crude ethyl ester with activated carbon produced from de-oiled cake. Energy Conversion and Management: 77, 495-503 (2014).

Conceiço MM, Candeia RA, Dantas HJ, Soledade LEB, Fernandes Jr VJ, Souza AG. Rheological behavior of castor oil biodiesel. Energy Fuels; 19: 2185–8 (2005).

Pisarello, ML., Dall-Csta, BO.,Veizaaga ,NS.; Querini , CA. Volumetric method for free and total glycerin determination in biodiesel. Ind. Eng. Chem.Res; 49: 8935-8941 (2010).

Manuel Sanchez-Cantu, Lydia M. Pérez-Diaz a, Israel Pala-Rosas a, Eloina Cadena-Torres a,Lucia Juarez-Amador a, Efrain Rubio-Rosas a, Maricela Rodriguez-Acosta b, Jaime S. Valente. Hydrated lime as an effective heterogeneous catalyst for the transesterification of castor oil and methanol. Fuel; 110: 54–62 ((2013).

Ong, HC. , Silitonga, AS. , Masjuki, H.H., Mahlia, TMI. , Chong, WT.; Boosroh, M.H. Production and comparative fuel properties of biodiesel from non-edibleoils: Jatropha curcas, Sterculia foetida and Ceiba pentandra. Energy Conversion and Management 73, 245–255 (2013).

Suppalakpanya,K., Ratanawilai,S.B., Tongurai,C.. Production of ethyl ester from crude palm oil by two-step reaction with a microwave system. Fuel; 89: 2140–2144 (2010).

Fadhil AB, Ahmed KM, Dheyab MM. Silybum marianum L. seed oil a novel feedstock for biodiesel production.2012. Arabian J Chem; 10: S683-S690 (2017).

Alhassan, Y., Kumar, N., Bugaje, IM., Pali, H.S., Kathkar, P. Co-solvents transesterification of cotton seed oil into biodiesel: Effects of reaction conditions on quality of fatty acids methyl esters. Energy Conversion and Management; 84 : 640–648 (2014).

Sangaletti-Gerhard, N., Vieira, T.M.F., Groppo, S.S., Rodrigues, J.R., Regitanod'Arce, M.A.B. Alkaline catalyzed ethanolysis of soybean oil ethanolic miscella. Fuel; 116: 415–420 (2014).

Fadhil, AB., Ahmed, AI. Ethanolysis of fish oil via optimized protocol and purification by dry washing of crude ethyl esters. Journal of the Taiwan Institute of Chemical Engineers, 58: 71–83 (2106).

Anastopoulos, G., Zannikou, Y., Stournas, S., Kalligeros, S. Transesterification of Vegetable Oils with Ethanol and Characterization of the Key Fuel Properties of ethyl Esters. Energies; 2: 362-376 (2009).

Kumar, D., Kumar, G., Singh, P.C.P. Fast, easy ethanolysis of coconut oil for biodiesel production assisted by ultrasonication. Ultrasonics Sonochemistry; 17: 555–559 (2010).

Kurunczi, D.A., Saad, E.mir B., Wilhelm, H.M., Ramos, L.P. Optimization of the ethanolysis of Raphanus sativus (L. Var.) crude-oil applying the response surface methodology. Bioresource Technology; 99:1837–1845 (2008).

J.M. Encinar, J.F. González, A. Rodríguez-Reinares.. Ethanolysis of used frying oil. Biodiesel preparation and characterization. Fuel Processing Technology; 88:513–522 (2007).

Fadhil,AB., Al-Tikrity, ET., Albadree, MA.. Transesterification of a novel feedstock, Cyprinuscarpio fish oil: Influence of co-solvent and characterization of biodiesel. Fuel;162: 215–223 (2015).

Sánchez, B.S., Benitez, B., Querini, C.A., Mendow, G.. Transesterification of sunflower oil with ethanol using sodium ethoxide as catalyst. Effect of the reaction conditions. Fuel Processing Technology; 131: 29–35 (2015).

Filho, J.C. G., Peiter, A.S., Pimentel, W.R.O., Solett,i J.I., Carvalho, S.H.V., Meili, L. Biodiesel production from Sterculia striata oil by ethyl transesterification method. Industrial Crops and Products; 74: 767–772 (2015).

Ginting, M. S.A., Azizan, M. T., Yusup, S. Alkaline in situ ethanolysis of Jatropha curcas. Fuel; 93: 82–85 (2012).

Suppalakpanya, K., Ratanawilai, S.B., Tongurai, C.Production of ethyl ester from esterified crude palm oil by microwave with dry washing by bleaching earth. Applied Energy; 87: 2356–2359 (2010).

Ullah, K., Ahmad, M., Sofia, Qureshi, F.A., Qamar, R., Sharma, V.K., Sultana, S., Zafar. M. Synthesis and characterization of biodiesel from Aamla oil: A promoting non-edible oil source for bioenergy industry. Fuel Processing Technology; 133:173–182 (2015).

Author Information

E. T.B. Al-Tikrity
Department of chemistry, College of Science, Tikrit University, Salahaldeen, Iraq
Contact E-mail: emaad_bakir@yahoo.com

A.B. Fadhil
Chemistry Researches Laboratory, Department of Chemistry, College of Science, University of Mosul, Mosul, Iraq

K. K. Ibraheem
Department of chemistry, College of Science,
Tikrit University, Salahaldeen, Iraq

Biochemical Study of Dipeptidyl Peptidase-4 in Autistic's Patients

Safaa A. AL-AMEEN
University of Mosul

Fadwa Kh.TAWFEEQ
University of Mosul

Tareq Y. AHMAD
University of Mosul

Abstract: The research includes estimation of autistics' serum dipeptidyl peptidase-4 (DPP-4) activity. The results indicated a significant (p≤0.05) decrease in (DPP-4) activity of autism spectrum disorder groups, 57.85, 42.86, 36.47 µmol/L respectively compared to control group. By statistical analysis, the study revealed a significant (p≤0.05) relationship between DPP-4 activity with gastrointestinal disorder on one hand and with various inflammation incidence on the other hand. Partial purification of DPP-4 from serum of normal person age 14 years in Mosul city was done. Gel filtration of dialysate precipitate produced by 50% ammonium sulphate saturation has given two major proteinous components. One of them (peak A) possesses a high DPP-4 activity using sephedex G-100. The apparent molecular weight of the isolated DPP-4 was 176.6 KD. Then SDS-PAGE was performed. HPLC revealed a single peak A' at retention time 5.829 min by application the top of peak A which was isolated from gel filtration. Maximum activity of DPP-4 was obtained using 0.1 M Tris-HCl buffer at pH 8, 40°C, 4 mM of gly-pro-p-nitroanilide hydrochloride as a substrate. Maximum velocity (Vmax) was 50 µM according to Line Weaver-Burk plot while Michaelis–Menten constant (Km) was 0.5 mM. Mercuric chloride and strontium chloride hexahydrate at 5 mM revealed maximum inhibitory effect of DPP4 activity by 30.2% and 42.9% respectively.

Keywords: Dipeptidyl peptidase 4, Autism spectrum disorder, Gel filtration, Electrophoresis, High performance liquid chromatography

Introduction

Autism spectrum disorder (ASD) can be classified into five types of neuro developmental disorders which have the same main symptoms and different severity. Autism spectrum disorder (ASD) was first described in (1943) by Leo Kanner (Evans et al., 2008) and officially recognized in (1980) (Volkmar and Pauls, 2003).

ASD is beginning before the age of three years. It is classified as pervasive disorders of childhood, characterized by behavioral abnormalities in social interactions, communication and restricted repetitive and stereotyped patterns of behaviors, interest and activities which are thought to be due to abnormal brain function or structure and are also thought to have genetic bases (Rose et al., 2012). Children with ASD often present an abnormal immune and digestive system such as inflammation of the bowel, changes in digestive enzymes and suffer from bowel problems such as constipation. The cause of these changes is not entirely known (Randolph-Gips and Srinivasan, 2012).

Under conditions of high levels of oxidative stress, opioids from casein and gluten may bind too tightly to receptors in the brain. In few words, the opioid-excess theory suggests that excessive levels of incompletely metabolized peptides from foods that contain proteins, gluten and casein, pass through the intestinal and blood brain barrier (BBB) into the brain (Shattock and Whitely, 2002).

Dipeptidylpeptidase-IV (DPP-4) is the only known enzyme to break down small protein fractions from foods called peptides. The inability to break down certain peptides from gluten and casein leads to elevation of certain potentially neurotoxic peptides that formed in the gut like casomorphin, gliadorphin, dermorphin, deltorphin. These in turn are absorbed and may adversely affect neurological and immune functions. The enzyme (DPP-4), which is CD26 on T-lymphocytes, also appears on the surface of certain immune cells and serves to signal the cell into activity. When this enzyme is dysfunctional, the immune system is compromised (Shaw, 2008).

Dipeptidylpeptidase-IV (DPP-4) EC 3.4.14.5 is a protein that has a multiple functions in the body. It is known under different names depending on its location in the body. When DPP-4 is on the surface of the T- cell (lymphocyte), it is called CD26, which travels in the circulation and helps support immune functions (Lad, 2007). While when this enzyme is found on the mucosal membrane lining the intestinal tract, it is known as (DPP-4). This protein is also located on the surface tissues of the pancreatic duct, bile duct, colon, and kidney (Panchapakesan et al., 2013). Adenosine deaminase binding protein another name for DPP-4 or adenosine deaminase complexing protein-2 (Prabavathy et al., 2011).

In human, DPP-4 is encoded by the DPP-4 gene and that gene is associated with immune regulation, signal transduction and apoptosis. DPP-4 gene is located on chromosome 2q23 and spanning 70 kb. It is composed of 26 exon that encode a protein of 766 amino acids (King 2012). It is intrinsic membrane glycoprotein which possesses a unique enzymatic activity that can cleave N-terminal dipeptides from many biologically active peptides, cytokines and chemokine (Detel et al., 2012).

The enzyme DPP-4 is a member of the large family of proteases (peptidases)(Edosada et al., 2006). It is presented in a soluble form which circulates in body fluids of living organisms with a specific peptidase function (Panchapakesan et al., 2013). It cleaves dipeptides from the N-terminus of polypeptides having proline or alanine at the penultimate position (Vanderheyden et al., 2009).

Methods

This study included (67) subjects (controls and autism spectrum disorder patient. patients group included (37) cases of both sexes (6 females, 31 males) aging 2-12 years with autism spectrum disorder recruited from psychiatric research unit in Medicine College - Mosul University from January to April 2012. While control group included (30) healthy subjects of both sexes (10 females, 20 males) with the same age of patients.To estimate dipeptidyl peptidase-4, fasting blood samples were collected at (8:00-8:30 am) from the same previous groups (patients & control) from September 2012 to January 2013.

The diagnosis of autism spectrum disorder was applied by specialist psychiatric doctors, and the criteria of ASD are defined in the Diagnostic and Statistical Manuals of Mental Disorder, Fourth Edition (DSM-IV, 1994).
The patients group is divided into three subgroups: mild, moderate and severe according to symptoms severity grade and PDD scale. If the scores > 50 it is considered normal, between 50-100 it mild, between 100-150 it moderate and < 150 is considered as severe ASD (AL-Hayaly, 2010).

Venous blood samples (3-5 mL) were collected from (control and ASD) groups in clean dry plain tubes without anticoagulant and incubated in water bath at 37∘C for 10 minutes to allow the blood to clot. Centrifugation was then done at (3000 rpm) for (15 mins). Serum samples were transferred immediately by micropipette and stored at -20∘C to be analyzed later.

Also, serum sample (40 mL) was obtained from fasting normal human volunteer aging 14 years for dipeptidyl peptidase-4 activity study. The study included separation, partial purification and optimum conditions.

Assay of serum DPP-4 activity

Serum DPP-4 activity was estimated by measuring the release of light yellow product of   4-nitro aniline from an assay mixture (Kreisel *et al.*, 1982). Glycine-proline-p-nitroanilide hydrochloride was used as a substrate *in vitro*.

Protein estimation

Protein concentration was estimated by the method of modified Lowry (Schacterle and Pollack, 1973) where bovine serum albumin was used as a standard protein.

Enzyme Purification

Dipeptidylpeptidase-4 was partially purified from a serum of fasting normal human by the following steps:-

Precipitation

The protein from 40 mL serum was precipitated using 50% ammonium sulphate (Robyt and White, 1987). The mixture was left over night at 4 ºC. The proteinous precipitate was isolated using cooling centrifuge for 45min at 10000 rpm.

Dialysis

The precipitate was dialyzed against 0.1M ammonium bicarbonate. The solution was stirred slowly with a magnetic stirrer over night at 4 ºC. The buffer was changed three times during dialysis (Robyt and White, 1987). The protein concentration and enzymatic activity were performed.

Gel filtration chromatography

The dialysate 2 mL was applied to gel filtration column (2.2 x 100 cm) which contained sephadex G-100 to a height (90 cm). Elution was carried out using phosphate buffer 0.1 M, pH 7.4 and the fractions were collected at a flow rate (38.4 mL/hr) with a definite time 5 min by automatic fraction collector L C100, Haake Buchler Instruments, USA. The proteinous compounds were detected by following their absorbance at 280nm using UV/Visible spectrophotometer PD-303UV. The DPP-4 activity was estimated in each fraction.

Molecular weight determination

Sephadex G-100was used to determine the approximate molecular weight of DPP-4 using the following proteins as standard materials: phosphatase (140000 Da), hexokinase (100000 Da), bovine serum albumin (67000 Da), egg albumin (45000 Da), papain (23000 Da).

Sodium Dodecyl Sulphate Gel Electrophoresis

Protein sample, Top peak A, which was separated by gel filtration technique of normal human serum and prepared previousely, applied on SDS-Electrophoresis.

High Performance Liquid Chromatography

The top fraction of peak A which was separated by gel filtration injected into C18, 4.6X250 mm, stainless steel column. The analysis was performed using Shimadzu corporation DGU-20A5, prominenceLC 20AD LiquidChromatography in AL-Kindy State Company/Chemical Analysis Lab in Mosul city.

The optimal conditions of partial purified DPP-4

Dipeptidylpeptidase-4 was characterized with respect to its optimum temperature, buffer concentration, pH of Tris HCl buffer, substrate concentration, effect of different concentrations of some DPP-4 inhibitors.

Results and Discussion

Figure 1. demonstrated the reduction percentage of enzymatic activity of DPP-4 in mild, moderate and severe autism spectrum disorder (57.85 ± 2.35, 42.86 ± 0.7, 35.47 ± 0.94) μmol/L compared to control group (68.23 ± 3.6) μmol/L. The percentage of serum DPP-4 reduction was (48%) in severe ASD group compared to controls.
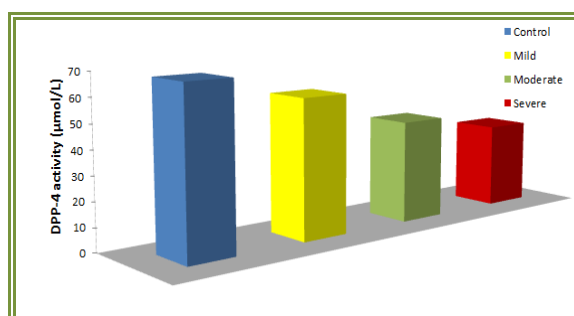
Figure 1. Serum dipeptidyl peptidase-4 activity in mild, moderate and severe ASD patients groups compared to control group.

The present study revealed a significant ($p<0.05$) relationship between DPP-4 activity and gastrointestinal disorders which occurred in ASD patients. Data revealed that the GI disorders incidence among ASD patients was (69.7%) as indicated in Table (1). Also, the results showed the percentage of various inflammations (87.9 %) occurred in ASD patients compared to controls.

Table 1:- Relationship between DPP-4 activity and some pathological disorders which occurred in ASD patients and % of disorder incidence.

Relationship between DPP-4 and pathological disorders	P value	% incidence
DPP-4 & inflammation	0.0001*	87.9
DPP-4 & gastrointestindisorders	0.035*	69.7

As mentioned in experimental part, many techniques were used to purify normal human serum DPP-4. Gel filtration chromatography was used to isolate and to find the molecular weight of normal human serum DPP-4. The results showed that there were two proteinous peaks detected at 280 nm. The dipeptidyl peptidase-4 activity was found in the first peak A as the major peak at elution volume 95.8 mL as indicated in Figure 2.
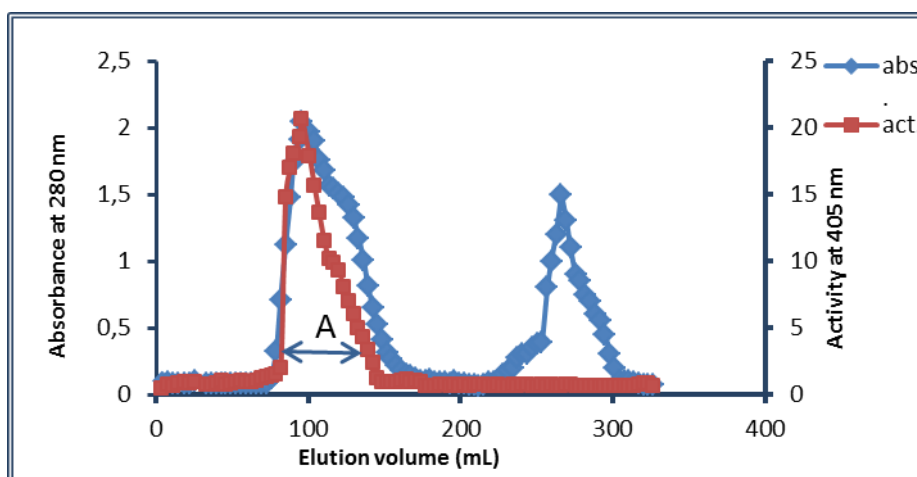
Figure 2. Elution profile of DPP-4 purified by ammonium sulphate precipitation (50%) on gel filtration column (2.2×90 cm). A represents the enzyme source collections

While Table 2 indicates the purification steps of dipeptidyl peptidase-4. The results show that the specific activity of normal human serum DPP-4 and the increment was about four folds. These results were in agreement with previous studies (Duke-Cohan *et al*., 2001) which showed a significant increase of DPP-4 activity.

Table 2. Purification steps of DPP-4 from human serum

Purification steps	Volume (mL)	Total protein (mg)	Total activity (µmol/L)	Specific activity	Fold of purification	% Recovery
Serum	40	3920	4466	1.14	1	100
Precipitate (50%) amm. sulphate	12	948	2256	2.38	2.1	50.5
Gel filtration peak A	26	351	1745	5.0	4.38	39.1

The apparent molecular weight of DPP-4 (peak **A**) which was separated by gel filtration was determined from the calibration curve (Fig. 2). It has been found that the apparent molecular weight of DPP-4 was 176.6 KD. This result is in agreement with other reported studies (Iwaki-Egawa *et al*., 1998; Duke-Cohan *et al*., 2001) where they found that molecular weight of normal human serum DPP-4 was 175 KD.

The top of peak **A** was applied to HPLC technique, a single peak (**Ã**) which appeared at retention time of (5.829 min) was obtained with flow rate 0.7mL/min. The minor peak (a) represents the elution of the solvent triflouroacetic acid as indicated in Figure 3.
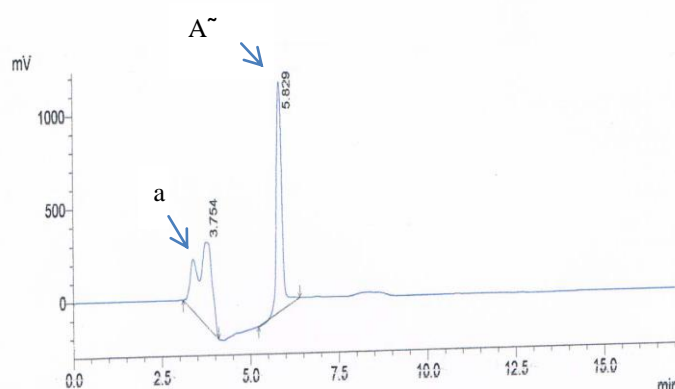
Figure 3. Chromatogram of top of the peak which was isolated from gel filtration, peak a represents the solvent triflouroacetic acid while peak Ã represents DPP-4

In this study, the top of peak A from sephadex G-100 gel filtration chromatography of normal human serum dipeptidyl peptidase-4 as indicated in Figure 2 was used in SDS-PAGE. Two bands were detected after staining and destaining with coomassie blue as shown in Figure 4 This result might indicate that DPP-4 has two

subunits. Similar results were published in the literature where DPP-4 has two subunits in SDS-PAGE (Shibuya-Saruta et al., 1996 ; Davy et al., 2000 ; Sanz and Toldra, 2001).
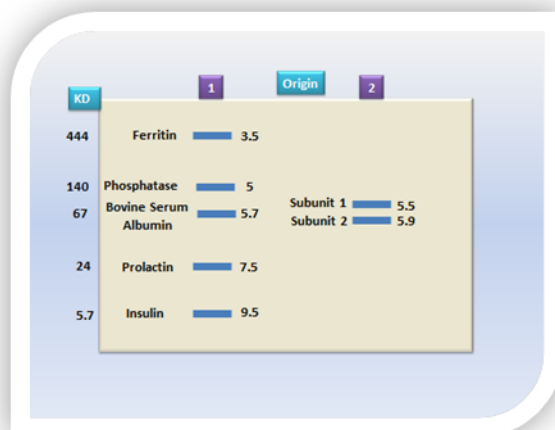
Figure 4: Representative profile of SDS-PAGE of the top peak A from sephadex G-100 of normal human serum (lane 2) compared to known materials (Lane 1). The numbers on the right hand represented relative mobility in(cm) of each material from the origin.

Kinetic Study

Effect of enzyme concentration on DPP-4 activity

The activity of enzyme was measured in the presence of different concentrations of partially purified enzyme peak A, ranged 0.1-1.2 mg/mL as shown in Fig. 5 and the concentration 0.35 mg/mL of enzyme was used for next experiments (Medium range value).
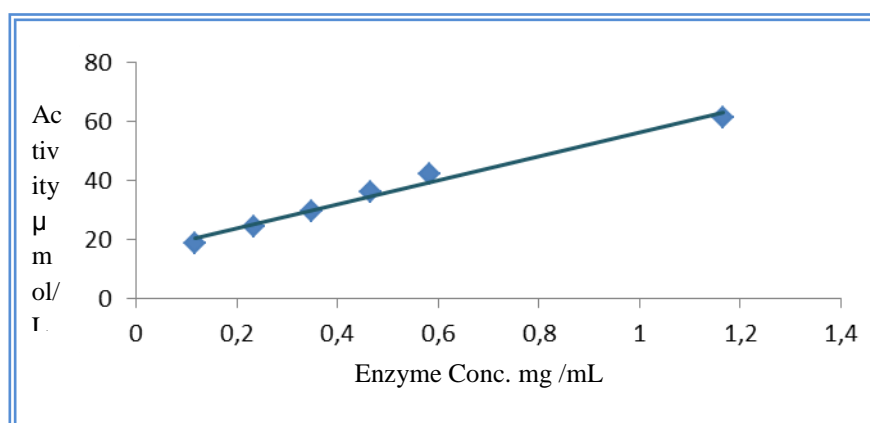
Figure 5. Effect of different concentrations of enzyme on DPP-4 activity

Effect of pH and conc. of buffer solution on DPP-4 activity

The effect of pH upon DPP-4 activity was investigated using different pH of Tris-HCl buffer between 7.2-8.8. Maximum activity was obtained at pH 8.0 which is used for the following experiments. The different concentrations 0.05-0.2M of Tris-HCl pH 8 were examined. Maximum activity was detected at concentration 0.1M of Tris-HCl pH 8 as illustrated in Fig. (6) and (Table 3). The current results are in agreement with others (Durinx et al., 2000; Davy et al., 2000). However, other investigators found that DPP-4 exhibited its highest activity over the pH range 6.7-8.9 (Scharpe et al., 1998) and it had no activity below pH 5 (Durinx et al., 2000).
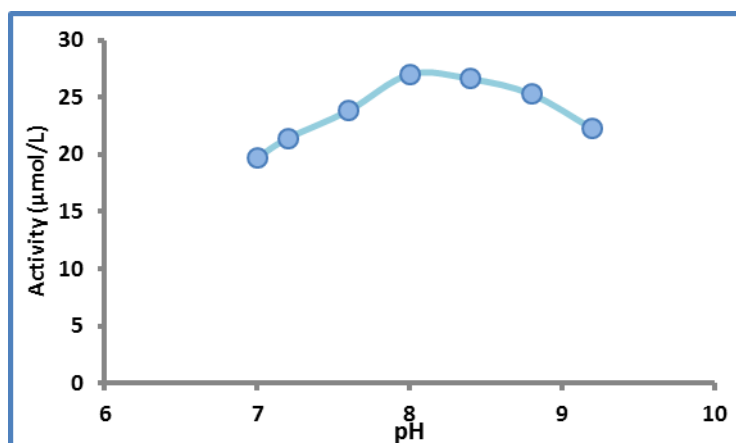
Figure 6. Effect of different pH on DPP-4 activity

Table 3: DPP-4 activity at different concentrations of Tris HCl at pH 8

Concentration of Tris HCl (M), pH 8	DPP-4 activity (μM)
0.05	22.9
0.1	28.3
0.2	27.7

Effect of temperature on DPP-4 activity

The effect of temperature on DPP-4 activity was assayed at a temp. ranging between 25-60 °C. The results showed a maximum activity of enzyme at 40 °C then dropped gradually until most of it was lost as indicated in the Fig. (7). The current results was similar to what was obtained by other investigators (Durinx et al., 2000) where they found that optimum temperature for DPP-4 activity from normal human serum is 40 °C.
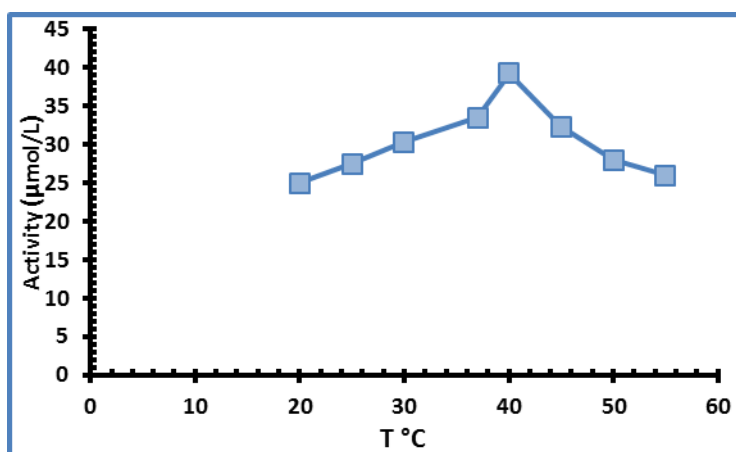
Figure7. Effect of different temp. on DPP-4 activity

Effect of substrate concentration

Different concentrations of gly-pro-p-nitroanilide as a substrate for DPP-4 were used ranging between (0-5 mM) and 4 mM gave a maximum activity of DPP-4 as indicated in Figure 8.
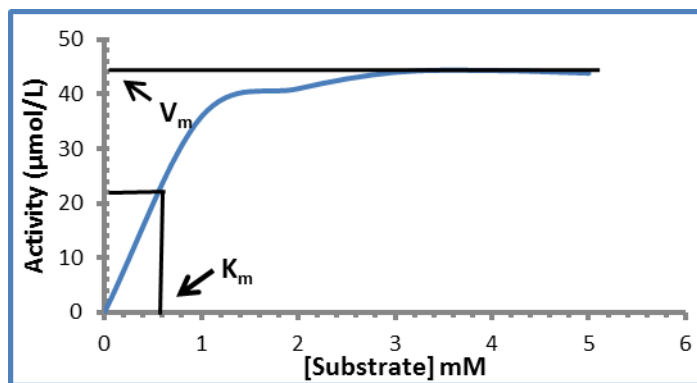
Figure 8. Effect of different concentrations of substrate on DPP-4 activity

A limiting value of substrate concentration of 0.5 mmol/L as shown in Figure 8 as Km value. Line Waver-Burk plot (Fig. 9) revealed that the values of Km and Vmax were 0.5 mM and 50 U/Lrespectively. The current results are in agreement with reported studies (Pereira et al., 2003) where they indicated that the values of Km of DPP-4 are ranging between 0.43-0.98 mM in human connective tissues and with (Davy et al., 2000) who revealed that the Km value of barley DPP-4 was 0.59 mM.
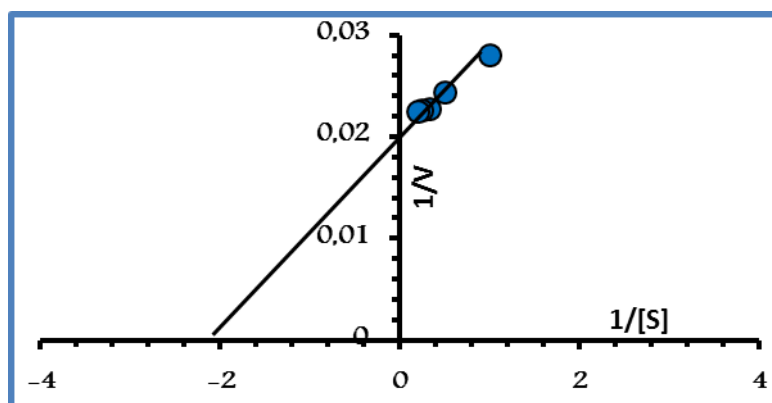
Figure 9. Lineweaver-Burk plot for DPP-4 activity

Table 4. The optimum conditions of DPP-4 activity

M DPP-4	enzyme conc. (mg/mL)	Tris HCl buffer conc. (M)	pH of Tris HCl buffer	Temp. (ºC)	Km (mM)	Vmax (µM)
Peak A	0.35	0.1	8	40	0.5	50

Effect of certain compounds on DPP-4 activity

Different conc. of mercuric chloride and strontium chloride hexahydrate on DPP-4 activity have been studied. The results in Table 5 and 6 showed that the activity was decreased with increasing their concentrations. The current results are in accord with others (Gomez et al., 2013) who they studied the effect of divalent ions on DPP-4 of rat kidney and found that Zn^{+2} and Ca^{+2} inhibited the enzyme. While (Shibuya-Saruta et al., 1996) explained activity inhibition of normal human serum DPP-4 by Ba^{+2}, Mn^{+2}, Cd^{+2}, Hg^{+2}, Co^{+2} and Sr^{+2}. So, environmental toxicants such as mercury and strontium have been found to strongly inhibit the activity of dipeptidyl peptidase (DPP-4) which are required in the digestion of the milk protein (casein) or wheat protein (gluten). The dipeptidyl peptidase-4 and cluster differentiation antigen 26 (CD26) are the same. It helps in T

lymphocyte - activation. CD26 or DPP-4 is a cell surface glycoprotein that is very susceptible to inactivation by mercury binding to its cysteinyl domain(Shibuya-Saruta et al., 1996).

Table 5. Effect of mercuric chloride on DPP-4 activity

Concentration mM	Activity µmol/L	%Inhibition
0	42.5	---
1	36.66	13.7
2	35.50	16.47
3	32	24.7
4	31.5	25.9
5	29.66	30.2

Table 6. Effect of strontium chloride hexahydrate on DPP-4 activity

Concentration mM	Activity µmol/L	%Inhibition
0	42.5	---
1	37.16	11.5
2	31.66	24.5
3	31.33	25.4
4	29.5	29.8
5	24	42.9

Conclusion

Dipeptidyl peptidase4 activity decreases in autistics' patients. Also, DPP-4 has a significant relationship with gastrointestinal disorders and different inflammations. Maximum activity of DPP-4 was obtained using 0.1 M Tris-HCl buffer at pH 8, 40°C, 4 mM of gly-pro-p-nitroanilide hydrochloride as a substrate.

Recommendations

Genetic mutations of *DPP-4,* in autistic children must be studied since mutation in this enzymes might be involved in ASD.

References

Al-Hayaly, M. Z. (2010). Estimation of lead level among children with pervasive developmental disorders. M.Sc. Thesis. College of Nursing. University of Mosul.

Davy, A.; Thomsen, K.K.; Juliano, M.A.; Alves, L.C.; Svendsen, I.; Simpson, D.J. (2000). Purification and characterization of barley dipeptidyl peptidase IV. Plant Physiology, 122, 425-431.

Detel, D.; Pugel, E.; Baticic, L.; Budjevic, P.S.; Varljen J. (2012). Development and resolution of colitis in mice with target deletion of dipeptidylpeptidase IV. Experimental physiology DOI:10.1113/expphysiol 2011.061143, 1-11.

dipeptide substrate specificity. The Journal of Biological Chemistry. 281, 7437-7444.

Duke-Cohan, J.; Moriamoto, C.; Schlossman, S.F. (2001). Form of dipeptidylpeptidase IV (CD26) found in human serum. United State Patents, 6, 325-989BI.

Durinx, C.; Lambeir, A.; Bosmans, E.; Falmagne, J.; Berghmans, R.; Heamers, A.; Schorp, S.; Meester, I.D. (2000). Characterization of dipeptidylpeptidase activity in serum soluble CD26/ dipeptidylpeptidase IV is responsible for the release of X-Pro dipeptides. Eur. J. Biochem., 267: 5608-5613

Edosada, C.Y.; Quan, C.; Weismann, C.; Tran, T.; Sutherlin, D.; Reynolds, M.; Elliott, J.M.; Raab, H.; Fairbrother, W.; Beni, B.(2006). Enzyme catalysis and regulation: Selective inhibition of fibroblast activation protein protease based on dipeptide substrate specificity. The J. Bio. Chem., 281, 7437-7444.

Evans, T. A.; Siedlak, S. L.; Lu, L.; Fu, X.; Wang, Z.; McGnnis, W. R.; Fakhoury, E.; Castellani, R. J.; Hazen, S. L.;Walsh, W. J.; Lewis, A. T.; Salomon, R. G.; Smith, M. A.; Perry, G.; Zhu, X. (2008). The autistic phenotype exhibits a remarkably localized modification of brain protein by products of free radical-induced lipid oxidation. American Journal of Biotechnology and Biochemistry, 4(2): 61-72.

Gomez, H.; Chappe, M.; Valiente, P.A.; Pons, T.; Chavez, M.A.; Charli, J.L., Pascual, I. (2013). Effect of zinc and calcium ions on the rat kidney membrane – bound form of dipeptidyl peptidase IV. J. Biosci, 38(3), 1-9.

Iwaki-Egawa, S.; Watanabe, Y.; Kikuya, Y.; Fujimoto, Y. (1998). Dipeptidylpeptidase IV from human serum : purification, characterization and N-terminal amino acid sequence. J. Biochem. 124, 428-433.

King, M.W.(2012). MedicalBiochemistryPage. /themedicalbiochemistrypage.org/

Kreisel, W.; Heussner, R.; Volk, B.; Buchsel, R.; Reutter, W.; Gerok, W. (1982). Identification of the 110000 molecular weightglycoprotein isolated from rat liver plasma membrane as dipeptidyl amino peptidase IV. FEBS Lett., 147, 85-88.

Lad, M. M. (2007). Biomedical approach for autism (Basics). Defeat Autism Now(DAN) model.

Panchapakesan, U.; Gross,S.; Komala, M. G.; Pegg, K.; Pollak, C. A. (2013). DPP-4 Inhibition in human kidney proximal tubular cells-Reno protection in diabetic nephropathy?. Journal of Diabetes & Metabolism. S9.

Pereira, D.A.; Gomez, L.; El-Cheikh, M.C.; Borojevic, R. (2003). Dipeptidyl peptidase IV(CD26) activity in the hematopoietic system: differences between the membrane-anchored and the released enzyme activity. Brazilian J. Medical and Bio. Research, 36, 567-578.

Prabavathy, N.; Vijayakumari, M.; Minil, M.; Sathiyaraj, U.; Kavimani, S. (2011). Lingaleptin–A novel DPP-4 inhibitor. International Journal of Pharma & Bio Sciences, 2(1), 438-442.

Randolph-Gips, M. M. and Srinivasan, P. (2012). Modeling autism: A systematic biology approach. Journal of clinical Bioinformatics, 2(17):1-32.

Robyt, F.J.; White, J.B. (1987). Biochemical. Theory and Practice Booke .California, U.S.A. p. 33.

Rose, S.; Melnky, R.; Trusy, T. A.; Pavliv, O.; Serdel, L.; Li, J., Todd, N.; James, S. J. (2012). Intracellular and extracellular redox status and free radicals generation in primary immune cells from children with autism. Autism research and treatment.1-10.

Schacterle, G.R.; Pollack. (1973). A simplified method for the quantitative assay of small amount of protein in biological materials. Anal. Biochem., 51, 654-655.

Sanz, Y. and Toldra, F. (2001). Purification and characterization of an X-prolyl- dipeptidyl peptidase from Lactobacillus sakei. Applied and environmental microbiology, 67(4):1815-1820.

Shattock, P. and Whitely, P. (2002). Biochemical aspects in autism spectrum disorders:Updating the opioid-excess theory and presenting new opportunities for biomedical intervention. Expert Opinion. Ther. Targets, 6(2):175-183.

Shaw, W. (2008). Biological Treatment For Autism and PDD – causes and biomedical therapies for autism and PDD-Abnormalities of the digestive system. 3rd ed.USA.pp 77-78.

Shibuya-Saruta, H.; Kasahara, Y.; Hashimoto, Y. (1996). Human serum dipeptidylpeptidase IV(DPPIV) and its unique properties. J. Clin. Lab. Anal, 10(6), 435-40.

Vanderheyden, M.; Batunek, J.; Coethals, M.; Verstraken, S.; Lambeir, A.M.; De Meester, I., Scharpe, S. (2009). Dipeptidylpeptidase IV and B type nutriuretic peptide. Clin. Chem. Lab. Med., 47(3), 248-252.

Volkmar, F. R. and Pauls, D. (2003). Autism. The Lancet, 362(9390):1133-1141.

Author Information

Safaa A. Al-Ameen
University of Mosul/Science College
Iraq- Mosul
Contact E-mail: sf_taha200@yahoo.com

Fadwa K. Tawfeeq
University of Mosul/Veterinary College
Iraq- Mosul

Tareq Y. Ahmad
University of Mosul/Science College
Iraq- Mosul

Advanced Product Quality Planning for Performance Evaluation of New Product Implementation Process: Application in a Factory

Ayse Emel UNAL
Dokuz Eylül University

Burcu FELEKOGLU
Dokuz Eylül University

Abstract: The variety of products in companies with order-based production system is high but the amount of production of each product variety is low. Therefore, each product is considered as a new product (NP) and challenges of not only producing NPs but also changing market and competitive conditions are faced. In order to overcome these difficulties and sustain the market share, it is necessary to produce high quality products at one time with minimum cost in all stages from the receipt of the order to the after-sales services in the production of NPs. In an attempt to solve this critical problem, our study focuses on the application of advanced product quality planning (APQP) technique, which is one of the most effective methods used in new product development (NPD) process control to ensure survival and continuous improvement of company and reduce the cost, time, labor and customer losses in the process of new product development. In this study, first, the NPD process and the use of APQP in NPD were explained and then an example of APQP application in a factory producing heat exchangers with order-based production system was given. APQP has been completed in three sections; process design and development, product and process validation, feedback and corrective actions. Process management and control activities and tools such as establishment of team, selection of NP, feasibility studies, determination of workflow, reduction of risks, determination of process capability and measurement systems analysis, creation of control plan, production, dimensional and performance tests were performed. As a result of this study, it has been proved that NPs produced by following an NPD process that is continuously evaluated with APQP method, fully meet both customer and company requirements. By using APQP method in NPD, process is controlled and scrap rates, costs and customer complaints are reduced.

Keywords: New product development, Advanced product quality planning, Order-based production system

Introduction

The order-based production system is a production model used to create a new service or product. It is a production system covering a small quantity but high level of product range. In addition to the similarity of the products to be produced at some points, a special effort is required in order to achieve innovation in the order-based production system. It is a production model that is mostly privatized according to customer and has the least standards. Nowadays, with the changing market and competition conditions, the companies realize customer specific production in order not to fall behind the market and not to decrease their market share.

In the order-based production systems, to put business rules and to measure and control the processes by making them a certain standard is difficult. Product variety and low production quantity reduce the repetition in processes to a minimum. Therefore, right production in one time is an extremely important criterion.

During the product development process that begins with the receipt of the order until the customer's use of the product, pre-determination of the failures and risks that may occur, taking the necessary measures, reducing of scraps, re-processing time, time and cost losses, customer losses and quality losses, offering the products to the market quickly are important requirements for companies to be ahead of their competitors. In line with these reasons, in today's conditions, application of the quality management by the companies which has this type

production system provides excellent advantages to them. Quality management is defined as a fullest extent of planned and systematic activities applied to ensure sufficient confidence in the fulfillment of the requirements of a new product or service.

When the studies in the literature are examined, application of Advanced Product Quality Planning (APQP) technique in new product development (NPD) process in mass production system has generally been seen. In our country, enterprises that have project-based production system in global competition takes an important place. However, there are not sufficient studies in implementing APQP in NPD which minimizes the risk rates in this production system where the risk ratio, costs, customer satisfaction, quality, and product offer more rapid conditions. This study was inspired by the lack of appropriate solutions in the NPD process in companies that have a project-based production system. For companies that have such production systems, APQP technique, which is an effective method for NPD process management, has been proposed. APQP technique is thought to provide significant benefits for both literature and enterprises.

New Product Development

NPD means the research and development efforts that are revealed by the firms to develop original products, product changes or new brands that are required by the customer (Armstrong, Kotler, Saunders, & Wong, 2005). The new product may be something that has never been produced or changes in the existing product such as style, color, performance variations, dimensional differences etc. (Onal, 2009). NPD process includes strategic formulation, distribution, resource allocation and coordinated cooperation between people from different professions and nations, and many issues and challenges in a company such as systematic planning, monitoring and control. Therefore, the NPD activity is essentially a selection, transformation and coordination work (Loch & Kavadias, 2008). NPD process consists of three stages. These include; Pre-development activities, development phase activities, decision to production and market entry.

Performance Criteria in NPD Process

There are many factors to achieve success in developing a new product to a new market or to the existing market. Cooper (2000) collected the performance criteria in the NPD process in 10 different categories. These factors include; differentiated and superior products, preliminary studies - homework, listening to the customer's voice, clear, stable and early product definition, market research, go / kill decision points for the project, cross-functional project teams, determination of strong points and using them is the creation of a market and the support of top management (Cooper, 2000). Ernst (2002) based on the literature studies on NPD, divided critical success factors into 5 categories, namely, NPD process, organizational structure, firm culture, senior management role and commitment and strategy. Desai, Mital, and Subramanian (2008), based on Cooper and Montoya-Weiss and Calantone studies, identified NPD performance criteria under the headings of uniqueness, customer orientation and adaptation to the market, preliminary studies, clear and early product promotion, the execution of activities, organizational structure, project selection decisions, marketing, the role of senior management, speed without compromising on quality, systematic finding of new product process, market attractiveness, experience and foundation competences.

Advanced Product Quality Planning (APQP) in NPD

APQP defines the activities that determine customer needs and develops products and processes to meet these needs. In short, product quality planning is a structured method for identifying and realizing the steps in all processes such as production and marketing, where a new product idea is designed, researched, and designed to ensure customer satisfaction (Sanongpong, 2009). In APQP, directing resources to appropriate activities, determining the changes in advance, avoiding late changes, providing a quality product on time and at low cost are the biggest benefits (Khanna, 2005). APQP is used in new product manufacturing process and product or process change.

APQP Process

The success of a project depends on meeting customer needs and expectations on time. Product Quality Planning provides failure prevention works with time diagram. If the problem solving methodology is not

sufficiently comprehensive, the solution will not be correct and the problem will reappear sooner or later. As shown in Figure 1, problems with an activity schedule will be prevented from occurring with Concurrent Engineering studies. The Product Quality Planning Team is responsible for ensuring that the timings are appropriate or earlier than the customer schedule (Kaushik, Khanduja, & Mittal, 2012; Book, Fick, Hopkins, Minkler, & Williams, 2008).
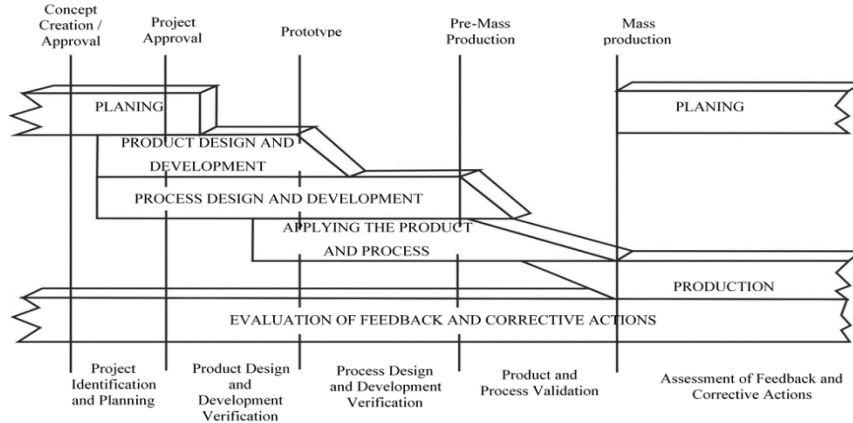
Figure 1 Advanced product quality planning time diagram (Book et al., 2008, s.5)

As shown in Figure 1, the APQP process consists of a total of five main stages. These stages are; project identification and planning, product design and development, process design and development, product and process validation, evaluation of feedback and corrective actions.

While suppliers with design responsibility have to implement all processes, suppliers with production responsibility are only required to apply process design and development, product and process validation, evaluation of feedback and corrective actions.

Problem Definition and Methodology

In this study, the name of the application company is kept anonymous for privacy purposes and is referred to as the ABC company. ABC Company has order-based production system where each order is in the scope of the new product. Approximately 15% of the production amount is reproduction in terms of product types produced on annual basis. The remaining 85% production is evaluated within the scope of new product. Many factors, such as product type, dimensional characteristics of the product, material type, product circuit, direction and notation are differentiated the order. For this reason, material properties and production methods are varied for each product which is differentiating. There are exponentially increasing risks in the process of delivering the product on time, in quality and in desired quantity to the customer due to changing conditions. Such risks lead to increased scrap rates, time and cost losses and, most importantly, prestige and consequently customer losses. Along with to order a different product is very difficult and also the number of products ordered is very low. For this reason, making accurate production is required at one time. Under all these circumstances, new product manufacturing and process management at ABC are considerably complex and difficult. Along with the challenges of having an order-based production system, in order to survive in a competitive environment, the company must offer products to the market quickly, in addition to products that fulfill customer requests and does not compromise on quality. Since the deadline of raw material is 6 weeks but deadline of product is 2 weeks, NPD process was more difficult. By managing all these challenges in the NPD systematically, producing on the right amount and on correct quality products at the first time is an important constraint for the company. The works to be done for it will put the company ahead of its competitors and increase its profit margin.

In this study, considering the difficulties in ABC Company has to deal with, a systematic process and product management approach based on key performance indicators will be developed for more effective and quality management of the NPD process. Within the scope of the research, APQP process will be applied for quality planning to avoid potential failures which might occur, which is aimed at continuous improvement and meeting specific customer requests in the production of new type heat exchanger. With efficient using of APQP in NPD process, will increase the success rate of the company and enable to meet the demands and expectations of the customers, increase the speed to market according to the competitors and achieve a competitive advantage.

Application

APQP methodology will be applied for NPD process in ABC company.

Section 1 and 2: Project Identification and Planning and Product Design and Development: Since the product design belongs to the customer, all necessary information has been provided by the customer.

Introduction of the Product that is Subject to Study: The product was an evaporator which is the main component of the vehicle air conditioner system that will minimize the heat transfer of the part allocated to carry the perishable product. The frame sheet, pipes, honeycombs and auxiliary parts of the product were designed as aluminum.

Feasibility Studies: The feasibility studies and whether the product can be made without order approval were evaluated by all relevant departments in terms of time, money, raw material and labor. The product can be made under the conditions of ABC company and the packaging conditions were in the standards that ABC can provide. Product raw materials were evaluated and stock controls were provided. Some changes have been requested on the customer's technical drawing in order to use the product effectively and to avoid nonconformities. It was communicated to the customer by the sales and marketing department and customer approval was obtained. According to the meeting resolution, Sales and Marketing Manager was selected as the leader for this project.

Section 3: Process Design and Development: In this section, production workflow, product material list, process failure mode effects analysis (PFMEA), measurement statistical analysis (MSA), Statistical Process Control (SPC), Control Plan and Packaging standards studies were performed.

New Product Production Flow Diagram: New product production flow diagram was same as standard production line

Material List for New Product: According to the product drawing, the materials to be used to produce the product, raw material list, usage amounts were determined on the basis of quantity and kg.

Process failure mode effects analysis (PFMEA): In order to determine risks in advance and to take precautions, the following PFMEA application steps were performed: Determination of Scope, Formation of the Team, Examination of the Process, Determining Possible Failure Types, Determining Possible Causes of Failure, Determination of Possible Failure Effects, Identification of Existing Controls, Determination of Severity, Occurrence, Detection Values, Calculation of R.P.N Value according to Equation 1, Evaluation of R.P.N. value according to Table 1, Determination and Implementation of Measures to be Taken, Calculation of the new R.P.N. value.

$$RPN = \text{Precaution (P) x Frequency of occurrence (F) x Determination (D)} \qquad \text{Eq (1)}$$

Tablo 1 R.P.N. Evaluation (Duru, Koç, & Taş, 2011, p.62)

R.P.N Points	Activities
R.P.N <= 40	There is no need to take precautions.
40 < R.P.N <= 100	It is useful to take precautions.
R.P.N > 100	Precautions must be taken.

According to PFMEA analysis, the R.P.N value of the four failure modes were greater than 100 and measures have been taken for these failure modes. The first of these four critical failure modes were the failure of the collector axis measurement and the second of them was failure of the distributor axis measurement. For these failure modes; special fixing fixture was made to prevent dimensional failure for fixing during brazing process. In addition, part support sheet was made to prevent dimensional deformation that may occur due to transport for the purpose of fix the collector and distributor to the mirror sheet. The third failure mode was improper brazing operation. To prevent this failure from occurring; brazing operator was trained and brazing wire with borax was introduced. The fourth failure mode detected was deformation of the mirror sheets due to brazing heat. To prevent this failure from occurring; a cooling pool was developed in order to made of the brazing process by cooling. As a result of the improvements, the new R.P.N values of all failure modes have been reduced to below 100.

Measurement statistical analysis (MSA): Method of measurement analysis was used to determine the adequacy of measurement systems. MSA Steps involved; determining the critical part and critical characteristics, to make the necessary settings to the instrument, selection of parts, numbering of parts, selection of operators, informing operators about measurement, 3 repetition of measurements, calculation of ranges, range average, UCLR value, the average of the operators and part, difference between the largest and smallest average, Repeatability - equipment variance (EV), The reproducibility - Appraiser variance (AV) value, Repeatability and reproducibility (GRR) value, The part variance (PV) value, the total variance (TV) value, The percentages of EV, AV, PV, and GRR in the TV, % GRR Evaluation, calculation and evaluation of number of distinct categories (ndc) value.

According to MSA, the GRR value was calculated as 12.88%. The value was acceptable because it was between 10% and 30%. The APQP team decided not to make improvements based on the accuracy of the part. The ndc value was calculated to be 10.888 as a result of the analysis. Since the value was over 5, the part category value was acceptable.

Statistical process control (SPC): This method was used to determine process variation after measurement variation was determined by MSA. SPC is a method used to monitor the process for detecting abnormal behavior in a process that is caused by specific reasons that are unnatural, unpredictable, and unregulated for the process, consisting of an uncertain source. (Baldan et al., 2018). Steps to apply SPC involved; determination of part and part number, the feature to be checked, the upper tolerance limits (UTL) and lower tolerance limits (LTL) of the feature to be checked, control frequency and sample size, measuring tool, machine, the date, shift, day and time of the measurement, making measurements, calculation of mean and range values, Calculation of Upper Control Limit (UCLX), Lower Control Limit (LCLX) for average and Upper Control Limit (UCLr), Lower Control Limit (LCLr) for ragne, drawing and evaluating graphs, calculation of standard deviation, calculation of process capability values (cp,cpk).

According to all basic control situations; measurements were within the control limits. The number of measurements between the centerline and UTL and the number of measurements between the centerline and ATL were similar. All measurement results were distributed randomly within the control limits. According to the calculated Cp = 1.96532317 and Cpk = 1.949601, the process capability was appropriate. Although the process meets the desired conditions, there would be unsuitable parts in the process outputs. However, the probability of detection was quite high.

Control Plan: The control plan includes all the controls planned to be carried out in accordance with the production workflow, customer, manufacturer, legal conditions and regulations. Steps to creating control plan involved; determination of scope, setting the team, examination of process will be applied, preparation of control plan. In accordance with the prototype production, all processes with their numbers, process characteristics in accordance with the product drawing, products subject to the process, all control methods, measurement method, frequency, sample size, registration forms and actions to be taken in case of inappropriate product were specified in the control plan. The approved control plan was informed in detail to the relevant process owners and production and quality control personnel. If necessary, instructions regarding the controls were prepared and trainings were given.

Packaging Standards: Product packaging standards were realized in accordance with customer packaging conditions, ABC company packaging conditions and legal regulations. Packaging standards were prepared as instructed and forwarded to the packaging and final quality control department.

At the end of each study, all data, documents, analyzes, findings and preventive studies were presented to the APQP team by the study leaders. As a result of the studies, all risks that may cause loss of time, money and firm prestige in product production were eliminated.

Section 4: Product and Process Validation: At this stage, production was carried out in accordance with the product technical drawing and control plan, bubble test was performed in the pool under 35 bar pressure with dry air for 2.5 minutes and dimensional measurements were performed for performance test. The product was packaged according to the specified packaging standards. All stages of pre-shipment packaging were photographed for customer approval. A Part Submission Warrant form was prepared for customer approval and sent to the customer with all documents.

Section 5: Feedback and Corrective Actions: The product has been checked by the customer and the product has received customer approval. No corrective action was requested for the product. On the customer side, the product was included in the approved product list in the approved supplier category.

Application Evaluation and Results

In the ABC company, which has an order-based production system, APQP technique was applied for evaluating the performance of the new aluminum evaporator product impentation process, all stages were carried out effectively and the results were analyzed. APQP team applied PFMEA as the first analysis after determining the feasibility, production flow diagram and material list. As a result of the analysis, 72 potential failure modes were determined. R.P.N. value of 17 potential failures were below 40, the R.P.N. value of 51 of them were between 40 to 100, The R.P.N. value of four of them was found to be over 100. Failure modes with a value of R.P.N. over 100 were focused on and preventive actions were initiated. With preventive actions, the R.P.N value of four critical failure modes was reduced to less than 100. As a second analysis, MSA was applied. Flare Sleeve semi-finished products to be used in new aluminum evaporator product have been selected for MSA. 10 samples taken from the production were randomly measured by three different quality personnel with three replications. According to the MSA, the GRR value was found to be 12.88%. Since the measurement system was between 10% and 30%, it is determined that the measurement systems are acceptable. In addition, the ndc value was found to be 10.858. Since the ndc value is greater than 5, it has been found that the measuring equipment has sufficient distinguishing feature. As the third analysis, SPC was applied to determine process adequacy levels. For SPC, flare aluminum union semi-finished products to be used new aluminum evaporator product were selected. Five semi-finished products were selected. Five sets were taken at different times provided that there were Five samples in each set. As a result of SPC application on a total of 25 samples, all measurement results were in the range of part tolerance. For the measurement range, UCLr was calculated as 0.50 and LCLr was calculated as 0. The calculated range values for all sets remained within the limits range and Cp and Cpk values were calculated to measure process capability. Cp value was calculated as 1.96 cpk values was calculated as 1.94. According to the common conditions of the customer and ABC company, Cpk value was required to be above 1.67 to indicate that the process was carried out under sufficient conditions. After eliminating the risks for the production of new products and determining that the measurement systems and processes were sufficient, a control plan was prepared in which all the processes that would enable the possible failures to be minimized were included. Information training was organized for all departments related to the control plan and necessary documentation was provided. Dimensional measurement and leakage test was performed on the product which was produced according to the determined work flow and provided accuracy according to the control plan. Dimensional measurements were within tolerances. According to the leakage test, it was confirmed that there was no brazing leakage on the new product. All these analyzes, dimensional measurements and performance tests were documented and presented to the customer with the product. The product has been approved based on the customer's documentation review and product controls.

Discussion and Conclusions

The APQP technique in NPD provides benefits such as ensuring product quality in new product production, reduction in delivery speed, customer satisfaction, lowering costs, and controlling processes. This technique ensures the systematic management of the processes by sustaining the participation of all employees with the continuous improvement of all activities in this technical organization. The APQP technique, which ensures that product realization activities are carried out under controlled conditions, was proposed and applied in ABC company which has an order-based production system where 85% of the product variety is evaluated as a new product and where the competitive conditions are the most difficult, and has a costly product and production line such as a heat exchanger. All activities to implement the APQP model in the production of new products in the company where the research is conducted were planned. APQP team was determined and new product to be applied was selected among the demands from the customer. The application was completed in five main sections. The first two parts of APQP are related with product design. Since the company has not design responsibility and it belongs to the manufacturer, the documents of the first two sections have been provided by the customer. Three main sections of the other APQP application were realized in the company. These sections are Process Design and Development, Product and process validation, Feedback and corrective actions. Inter-departmental critical meetings were held with the APQP team. Evaluations were made about the studies and the progress of the process. First, feasibility studies were conducted and the feasibility of the company was investigated. Product workflow was determined. The sections were completed according to the determined product flow. Some statistical techniques were used in practice. These are PFMEA, SPC, Process capability

analysis, MSA. Using these statistical techniques, TV was measured, capabiilities were evaluated and risks were reduced. Then, production was made according to work flow. The whole process was controlled according to the determined control plan. Dimensional measurements control and performance tests have been performed on the completed product and it has been proved that it meets customer requirements and company requirements. The product, which has been approved, has been sent to the customer with all documents in accordance with the packaging and transportation conditions determined by the joint decision of the company and the customer. Thanks to the communication established between the customer and the company in the whole process from the order to the delivery of the product to the customer, many studies became easy to understand and unnecessary time losses were prevented. The customer has reviewed and approved the new product and documents. The APQP model was approved as an evaluation model for new product performance by the top management due to the advantages of APQP technique such as ensuring the right production of the product at one time and thus reducing the labor, time, cost and scrap rates, detecting and eliminating the failures at the source before supplying them to the customer, ensuring customer satisfaction, preparing the control plan for the product. Since 85% of the production is a new product, APQP technique has been used in the production of all products. In this way, the company has achieved a significant advantage over its competitors in terms of both price and quick return to the customer. As a result, it is aimed to increase the current market rate of the enterprise and to enter new markets.

In the production of new products, the APQP model is frequently used by companies in the automotive and aerospace sectors, which have a mass production system. Unlike these sectors and production systems, our work was carried out in the air conditioning and refrigeration sector and a company that has an order-based production system. The results of our study show that, the companies applying the APQP model in the NPD process, which have an order-based production system and which have high product and production costs, will have gains such as reduced product cycle times, increased productivity, reduced costs, increased customer satisfaction. In addition, increasing the quality of the final product, providing competitive advantage, increasing the existing market share, increasing the opportunities to enter new markets are among the other advantages. As a result, companies that follow a systematic approach such as APQP to evaluate and control their new product implementation process can ensure continuous improvement of company and reduce the cost, time, labor and customer losses in the process and hence increase their profitability rates.

As a result of this study, the APQP model, which is thought to be beneficial for the new product implementation processes in the automotive and aerospace sectors with only mass production systems, has been proven to be beneficial for the air-conditioning and cooling sector with order-based production systems. In future studies, APQP model can be developed for enterprises with production systems other than mass production and order-based production systems. Academic studies can be conducted on generic APQP models for enterprises with order-based production systems. Similar studies can be conducted in sectors other than air conditioning and refrigeration, automotive, automotive sub-industry.

References

Armstrong, G., Kotler, P., Saunders, J., & Wong, V. (2005). New-product development and product life-cycle strategies. In *Principles of marketing* (4th ed.) (pp. 579-619). UK: Prentice Hall Financial Times Press.

Baldan, F. J., Benítez, J. M., Fuente, M. J., Sainz-Palmero, G. I., & Sanchez-Fernandez, A. (2018). Fault detection based on time series modeling and multivariate statistical process control. Chemometrics and Intelligent Laboratory Systems, 182(2018), 57-69.

Book, B., Fick, W., Hopkins, R., Minkler, R., & Williams, C. (2008). Plan and define program. In *Advanced product quality planning and control plan* (2nd ed.) (pp. 7-14). USA: Chrysler LLC, & Ford and General Motors Press.

Cooper, R. G. (2000, July/August). Doing it right: Winning with new products. Retrieved from www.stage-gate.com.

Desai, A., Mital A., & Subramanian, A. (2008). Developing successful products. In *Product development* (pp. 17-36). UK: Butterworth Heinemann Press.

Duru, N., Koç, K. H, & Taş, Y. (2011). İşletmelerde hatasızlığa yönelim, altı sigma ve hata türü etkileri analizi. *Ormancılık Dergisi, 7*(1), 56-57.

Ernst, H. (2002). Success factors of new product development: A review of the empirical literature. *International Journal of Management Reviews, 4*(1), 1–40.

Kaushik, P., Khanduja, D., & Mittal, K. (2012). Evidence of APQP in quality improvement: An SME case study. *International Journal of Management Science and Engineering Management, 7*(1), 20-27

Khanna, V. K. (2005). Role of APQP and PPAP in supply chain management. *Paradigm, 9*(2), 86-95.

Loch, C. H., & Kavadias, S. (2008). Managing new product development: an evolutionary framework. In *Handbook of new product development management* (pp. 1-26). UK: Butterworth Heinemann Press.

Onal, Ş. (2009). *The effect of corporate culture and new product development process on new product development success and an application in Turkey*. (MSc dissertation), Retrieved from Council of Higher Education Thesis Center. (240631)

Sanongpong, K. (2009). Automotive product realization; A process-based management. *Proceedings of the International MultiConference of Engineers and Computer Scientists 2009, 2,* 1915-1921. http://www.iaeng.org/publication/IMECS2009/

Author Information

Ayse Emel Unal
The Graduate School of Natural and Applied Sciences, Dokuz Eylül University
Izmir, 35390, Turkey
Contact E-mail: *emel_biricik@hotmail.com*

Burcu Felekoglu
Dept. of Industrial Engineering, Dokuz Eylül University
Izmir, 35390, Turkey

Determination of Uric Acid by Voltammetric Method (DPASV) Comparing with Spectrophotometric Methods

Eman A.M. ALJAWADI
Mosul University

Haitham A.A. AL-WAHAB
Mosul University

Abstract: The study includes determination of uric acid in urine by DPASV technique and comparing the results with those obtained by the routine spectrophotometric technique, the estimation of the products from using direct method to detect uric acid in patients with renal, renal failure comparing with normal these disease cause obvious decrease in uric acid concentration in patients urine.Determination of uric acid by chemical method using voltammetric technique (DPASV), it showed an obvious reduction current peak at potential (-0.592V)vs Ag/AgCl(3M KCl) as reference electrode .DPASV technique gave better result comparing with spectrophotometric method in Economy ,Accuracy ,Effort, time and the speed.

Keywords: Uric acid, DPASV, Voltammetric

Introduction

Uric acid is a chemical produced when our body breaks down foods that contain organic compounds called purines. Most uric acid is dissolved in the blood, filtered through the kidneys, and expelled in the urine. Sometimes the body produces too much uric acid or doesn't filter out enough of it. Hyperuricemia is the name of the disorder that occurs when you have too much uric acid in your body.

Uric acid is the final product of the metabolism of purines in the human body (End product of purines metabolism) where he poses with diuresis. Figure 1 shows the structural formula of uric acid.
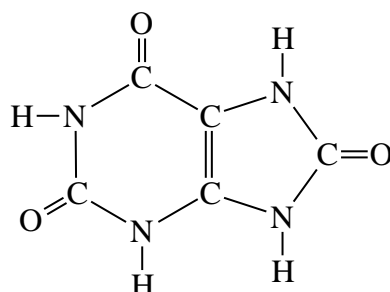
Figure 1.Structural formula of uric acid

The Voltammetric properties of uric acid were studied by DPASV after the initial and final fixation and optimum conditions were determined for the compound. Uric acid is a compound that can be analyzed using the voltometric techniques. It contains an electroactive functional group that gives a clear reduction wave by DPASV (as figure 2).
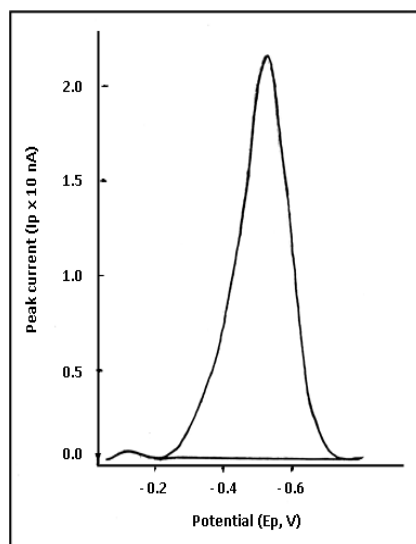
Figure 2. DPASV of uric acid

Method

Method of measurement using DPASV technique with sample:
1. 5 ml of pH solution (pH = 7.0) was taken in the measuring cell (clean and dry).
2. Transfer the nitrogen gas for 10 minutes after which the measurement is done for the reference (Blank).
3. Add 0.02 mL of the sample , nitrogen gas (5) minutes and then measure.

Results and Discussion

Optimization of the conditions

The optimum conditions for the study of DPASV The optimum conditions were determined for the study of uric acid voltammogram which gave the highest value of the propagation current (Ip) and the best form of the Uric acid reduction wave, by adding 5 milliliters of phosphate buffer with pH 7.0 by adding 0.1) Of the uric acid and then the nitrogen gas emitters. The output current (Ip) is then read at a voltage of -0.592 volts against the reference electrode (Ag / AgCl) with a concentration of (3M) KCl. Figure (3-14) shows the reduction wave of uric acid. The optimal conditions were determined under the following factors:

Effect of Deposition Time

Voltamogram was measured with different pulse deposition rates of the uric acid at varying levels of precipitation on the surface of the HMDE. The table (1) shows the values of the propagation current (Ip) obtained by changing Sedimentation time.

Table 1. The effect of Deposition time on Voltamogram shows the differential pulse anodic pulse of uric acid

Deposition time (sec.)	0	5	10	15	20	25
Ip (nA)	9.340	11.66	9.970	9.370	8.430	7.920

It is noticed from Table (1) that, following the results obtained, the sedimentation time (5) seconds gave the best and highest value of the propagation current. Therefore, this value was selected and adopted in subsequent measurements.

Effect of Conditioning Time

A study was conducted on the effect of the time of conditioning conditions after the deposition time was fixed at (5) seconds, as shown in Table (2), which shows the measurement time and different times between 0-20 seconds.

Table 2.The effect of Conditioning Time on voltammogram illustrates the DPASV of uric acid

Conditioning time (sec.)	0	5	10	15	20
Ip (nA)	8.750	9.070	9.340	8.420	7.610

The results obtained in Table 2 indicate that the Conditioning Time is 10 seconds

Effect of Equilibration Time

A study was conducted on the effect of equilibrium time, as shown in Table 3

Table 3. The equilibrium time on voltammogram shows the DPASV of the uric acid

Equilibration time (sec.)	0	5	10	15	20	25
Ip (nA)	7.710	7.860	7.920	8.140	8.780	7.800

It is noted from Table (3) that the values of the propagation current (Ip) increase to 20 seconds and then begin to decrease with the increase of the equilibrium time. Therefore, the b equilibrium time (20) was chosen because it gave the highest value of the propagation current (Ip).

Effect of Scan Rate

voltammogram uric acid was recorded after the previous conditions were established. A study was conducted on the effect of the Scan Rate, as shown in Table (4).

Table 4. The effect of the Scan Rate on voltammogram illustrates the DPASV of uric acid

Scan rate (mV/sec.)	1	2	3	4	5	6
Ip (nA)	12.840	13.370	17.150	17.230	17.650	15.450

Effect of Conditioning Potential

After stabilizing the previous influencing factors, the diffusion current (Ip) was measured by changing the Conditioning Potential as shown in Table (5).

Table (5): The effect of Conditioning Potential on voltammogram illustrates the DPASV of uric acid

Effect of Pulse Height

voltammogram was recorded in uric acid after the optimal conditions for the influencing factors were determined to determine the effect of pulse height in the propagation current (Ip). Table (6) shows the obtained results.

Table 6. The effect of Pulse Height on voltammogram illustrates the DPASV of uric acid

Pulse height(Mv)	0.020	0.022	0.024	0.026	0.028	0.030	0.032	0.034	0.036	0.038	0.040
Ip (nA)	7.980	8.640	9.210	9.710	9.800	11.440	11.460	12.520	12.820	14.570	13.300

Effect of Height of Uric Acid without Addition of Urine

The effect of increasing the concentration of uric acid was studied after the optimal conditions were achieved by taking (5) milliliters of the pH solution (pH 7.0) and the measurements by adding successive quantities of solution (10-3) molar uric acid and concentrations ranging from (29,126* 10-6 - 1.990*10-6) molar as shown in figure (3).The correlation coefficient value (R) is 0.99512. These results indicate that the reduction process was regular and the figure.2 show this
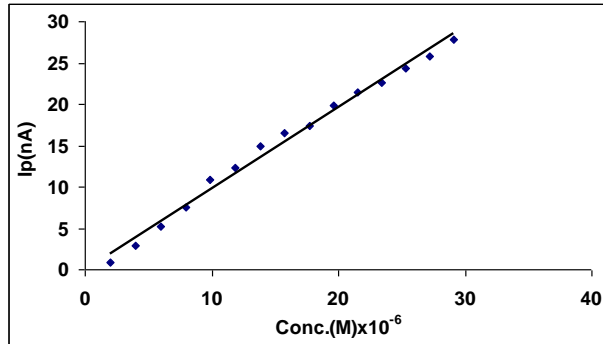
Fig.3. The relationship between the concentration of uric acid and the current values of the addition

Effect of increased uric acid in the presence of urine

voltammogram was measured with the DPASV excretion of uric acid with concentrations ranging from (13.67188*10-6 - 1.976285*10-6) molar, and measurements were made at optimal conditions previously determined for measurement.I n the relationship between the concentration and the current values of the addition, a straight line of 338636.8 was obtained and the correlation coefficient (R) was 0.997. This indicates that the reduction process was regular. Figure (4)show the relationship between the concentration of uric acid and the current values of the addition.
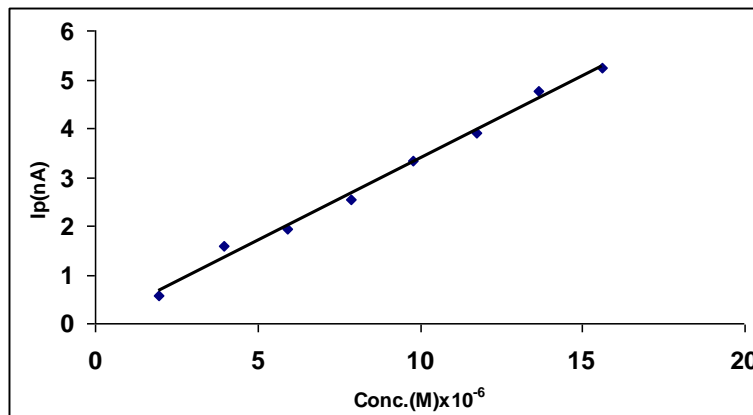
Figure 4 . the relationship between the concentration of uric acid and the current values of the addition Results and Discussion

Clinical Application of Uric Acid by DPASV

The amount of uric acid (mg / 24hr) was estimated in the administration of healthy and sick people using the (DPASV)¸ to measure uric acid in urine samples A reduction of uric acid was observed in the urine sample as shown in (Fig. 5)
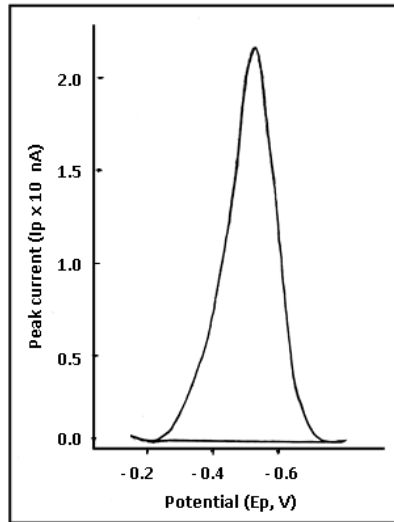
Fig .5. DPASV voltammogram of Uric acid in urine sample

Relationship between DPASV Method and Spectrophotometric Method

(DPASV) and the colorimetric method used to measure uric acid (mg / 24hr) in generation. A total of 24 samples were obtained from 8 samples of healthy individuals and 16 patients with renal diseases and renal failure and hypertension.

The uric acid was measured according to the color method, which is one of the methods routinely used in the pathological analyzes to estimate uric acid, which is based on an enzymatic reaction that produces a light pink color in the natural state and a deeper pink color in the cases of the disease. 510) nanometer.

Figure (6) shows the comparison between the proposed method of spectrometry (DPASV) and the color method of measuring the concentration of uric acid in the administration of people with kidney disease, kidney failure, hypertension and healthy people.
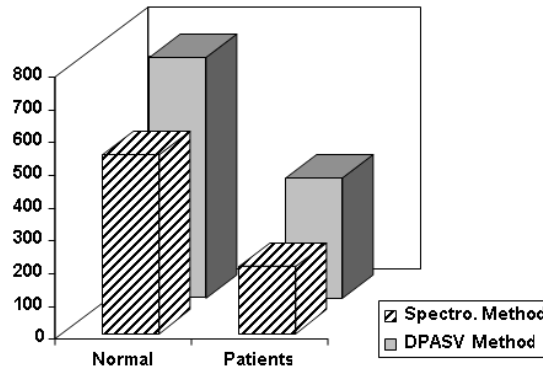
Figure 6. Shows the comparison between the suggested method of voltmeter (DPASV) and the color method for the concentration of uric acid in both natural and pathological condition

In order to prove the accuracy of the comparison between the suggested method and the color method to estimate the concentration of uric acid, the following correction equation is used:

DPASV method = [(202.0606) + (0.982511× colorimetric method)]

Conclusion

The use of DPASV is one of the most recently proposed methods for estimating uric acid in mg / 24hr in healthy individuals with renal disease and renal failure and hypertension. Comparison of the results obtained from this

method with the chromatic method routinely used in pathological analyzes. It was found through the results obtained between the two methods that the proposed polarographic method gave results consistent with the results obtained in the color method with the distinction of the first method of the following: Economic ,Characteristics of solutions ,Interferences, and Sensitive

References

S.P.Kounaves, Voltammetric techniques, (Ch. 37), (2001), from: http://www. Yahoo.com/science,chemistry,electrochemistry, ch.37. htm. p. 709-725, yahoo.inc., Accessed: Sept., 15, 2003.

D.S. Hier, J. Butler and R. Lewis, "Hole's Human Anatomy and Physiology". 9th ed., McGraw-Hill, New York, (2002), pp. 824, 842-843.

Eman A.M. A L Jawadi et al., The Eurasia Proceedings of Science, Technology, Engineering & Mathematics (EPSTEM), 2018,Volume 4, Pages 156-161 . ISSN: 2602-3199

J. Guo, M. Chen, H. Fa, X. Luo and Y. Ma, Sens. Actuators B 238 (2017) 1316.

H.W. Yu, J.H. Jiang, Z. Zhang, G.C. Wan, Z.Y. Liu, D. Chang and H.Z. Pan, Anal. Biochem. 519 (2017) 92.

P. Zuman, In "Polarography of biomolecules. Experimentals Methods in Biophysical Chemistry". (C. Nicotan, Ed.), Wiley, New York, (1973), pp. 393-414.

Y. Wang, Y. Huang, B. Wang, T. Fang, J. Chen and C. Liang, J. Electroanal. Chem. 782 (2016) 76.

C.A. Burtis and E.R. Ashwood, "Titz Textbook of Clinical Chemistry". 3rd ed., W.B. Saunders Company, Philadelphia, (1999), pp. 1241-1242, 1245-1249.

Z. Bai, C. Zhou, H. Xu, G. Wang, H. Pang and H. Ma, Sens. Actuators B 243 (2017) 361.

Author Information

Eman A.M. Aljawadi	**Haitham A.A. Al-Wahab**
Mosul University/College of science / Biophysics Dept., Iraq	Mosul University/College of science / Chemistry Dept., Iraq
Contact E-mail : e_abd2012@yahoo.com	

IConTES 2019: International Conference on Technology, Engineering and Science

Isolation and Studying the Effect of Protein Fractions of Red chili pepper (Capsicum annuum L.) on Some Biochemical Parameters in Experimental Diabetic Rats

Zena A.M. ALJAWADI
Mosul University

Abstract: The research was an attempt to Isolate and study the active protein compounds from the aqueous extract of red chili pepper (Capsicum annuum L.), using different biochemical techniques. Two compounds (A and B) were isolated using gel filtration chromatography for the precipitate produced by ammonium sulphate precipitation. The results predicted that, glucose level was lowered by intraperitoneally administration of the concentrated aqueous extract and the protein compound (B) compared with oral administration. The comparative molecular weight of the isolated protein active compound (peak B), was found to be 24000 Dalton, also it included the effect of the aqueous extract and the protein compound (B) in four doses (50, 75, 100 and 125 mg/kg body weight) on certain blood constituents in normal and alloxan induced diabetic rats. In normal rats, the blood glucose level was significantly lowered by crude aqueous extract and the protein compound in a dose (75 mg/kg body weight) compared with control group. and in a same dose showed a significant decrease in serum cholesterol and total lipids level. In diabetic rats, the protein compound in a dose of (75mg/kg body weight) showed a significant decrease in serum glucose, cholesterol and total lipids levels.

Keywords: Red chili pepper, (Capsicum annuum L.), Diabetes disease

Introduction

The red chili pepper (Capsicum annuum L.) is the fruit of plants from the genus Capsicum. Red chilies contain a substance called capsaicin, which gives peppers their characteristic pungencies, producing mild to intense spice when eaten. In addition, peppers are a good source of vitamin C and small amounts of carotene (provitamin A) and B vitamins (vitamin B6 in particular). They are very high in potassium, magnesium, and iron. Their very high vitamin C content can also substantially increase the uptake of non-heme iron from other ingredients in a meal, such as beans and grains [1,2].

Red chili peppers (Capsicum annuum L.), such as cayenne, have been shown to reduce blood cholesterol, triglyceride levels, and platelet aggregation, while increasing the body's ability to dissolve fibrin, a substance integral to the formation of blood clots. Cultures where hot pepper is used liberally have a much lower rate of heart attack, stroke and pulmonary embolism [3,4], and a very large study found some indications that humans who consume spicy foods, especially fresh chili peppers, were less likely to die of cancer or diabetes [5] Fig.(1).

Fig.1. Red chili pepper(Capsicum annuum L.)

The aim of the study is to investigate the effect of the protein compounds isolated from the aqueous extract of the red chili pepper on some biochemical parameters in experimental animals. Hopping to isolate an active compounds having insulin-like action and / or structure.

Materıals and Methods

Preparation of the Crude Aqueous Extract

Red chili pepper (Capsicum annuum L.) from local market in Iraq (0.75 kg weight) which were used in the study were cut into small pieces, mixed with cold distilled water in a ratio 1:3 w/v, and then homogenized for five minute using a blender. The crude homogenate was stirred for additional two hours in ice bath, and then allowed to stand in a refrigerator overnight. The mixture was then filtered through several layers of shahs to remove all residual materials. Finally, the filtrate or the mixture was then centrifuged at a refrigerated centrifuge for 15 minutes at 8000 xg to obtain the supernatant. The volume of the resulting supernatant was reduced to about 1/3 by lyophilization and kept for further investigation. Total protein was determined by modified Lowry method.

Precipition of the Proteins

Protein materials were separated from the cold extract using ammonium sulfate precipitation. It was added to cold crude aqueous extract in a ratio (75:100w/v) with slow stirring at 0°C. The mixture was left in a refrigerator for 24h and the precipitated protein was isolated by centrifugation for 15 minutes at 8000xg.The protein precipitate was dried by lyophilization then kept in a tight sample tube in a freezer for the next step.

Fractionation of the Protein Extract

A concentrated sample 5 ml (clear aqueous solution obtained by dissolving a sample of 150 mg in 5 ml distilled water and centrifuged) of the protein material from plant was fractionated by gel-filtration chromatography using Sephadex G-75 (2.56x87cm) column. Distilled water was used as eluent in the separation.

Intrapertioneal Injection

Group of healthy adult rats (150-170 gm weight), the rats were fasted for (16h) and divided randomly into two main groups. The first group was normal while the second group was injected intraperitoneally with the alloxan (125 mg/kg) to induce diabetic rats. Each group was then sub divided into eight group(each containing 4 rats). Group one in the sub group was kept as a control group while the remaining subgroups were injected intraperitoneally with the crude aqueous extract and the fractionated proteins (75,100mg/kg). After two hours of injection blood samples were collected for analysis by the orbital sinus puncture under ether anesthesia using non-heparinized micro-hematocrit capillary tubes.

Determination of Glucose, Cholesterol and Total Lipids

Serum blood glucose and cholesterol level was measured according to the enzymatic methods using Randox kit for glucose, U. K.[6, 7]. Serum blood total lipids level was measured by Chabral and Chardonnet method[8].

Statistical Analysis

The statistical methods used to analize the data including mean, standard deviation, minimum and maximum, while student T-test was used to compare between control and diabetic rats at $p \leq 0.05$ level[9].

Results and Discussion

Precipitation of the Protein

Precipitation of total proteins from the crude aqueous extract was accomplished by ammonium sulfate technique [10]. The protein content of the precipitate was determined and found to be 54.19% in the crude extract. The efficiency of the precipitation of the protein is 30.12%.

Fractionation of Total Protein

Fractionation of total Protein was accomplished by gel filtration chromatography using Sephadex G75 to give mainly one major peak with elution volume of 411 ml, Fig.(2).
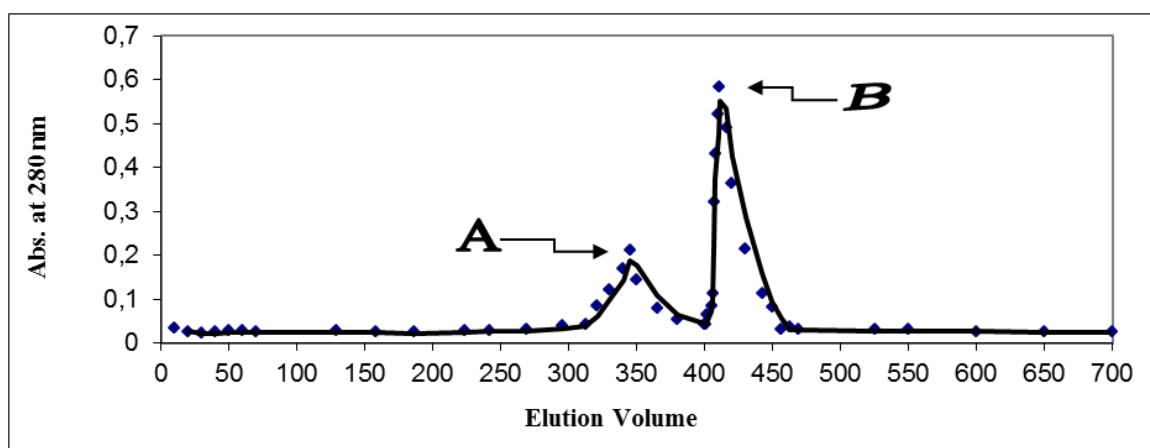
Fig.2. Elution profile of total protein precipitate from red chili pepper (Capsicum annuum L.) berry on Sephadex G75 column with a dimension (2.56x87cm). Distilled water was used as eluent, each fraction is 10 ml at flow rate 40 ml/h.

Quantitative determination of the protein in the peak after gel filtration chromatography was performed and then the percent of the component (peak A) was found to be 15.9% and (peak B) was found to be 46.1%. Comparative molecular weight of the isolated protein compound were determined by gel filtration chromatography on a pre-calibrated column using known molecular weight proteins as shown in Table(1). Peak A which approximately 42000 Dalton while the peak B approximately equal to 24000 Dalton were shown in Fig.(3).

Table 1. Molecular weights and their elution volumes of different protein compounds on Sephadex G 75

Compounds	Molecular weight (Dalton)	Elution volume (ml)
Blue dextran	2000000	121
Bovine serum albumin (BSA)	67000	246
α- amylase	58000	324
Eggs albumin	45000	345
Pepsin	36000	375
Insulin hormone	5750	418
Tryptophan	204	446
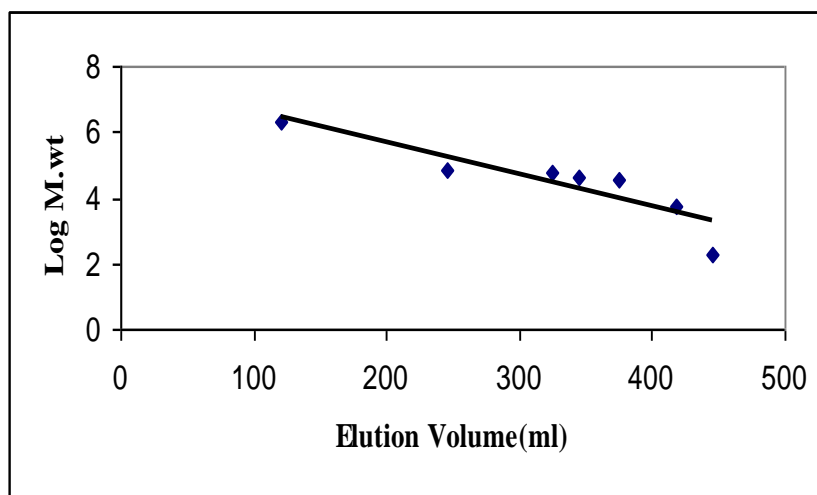
Fig.3. A plot of the logarithm molecular weights of known proteins versus elution volumes on a Sephadex G 75

Effect of crude aqueous extract and the isolated protein compound on glucose, cholesterol and total lipids in normal rats after intraperitoneally administration

The results in Table(2) showed the effect of crude aqueous extract and protein products on glucose, cholesterol and total lipids in normal rats. Results indicated not significant decrease of serum glucose in normal rates for protein fraction (Peak A).

Table 2. Effect of crude aqueous extract and isolated protein compound on serum glucose, cholesterol and total lipids in normal rats intraperitoneally administration

Groups	Glucose (mmol/l)	Cholesterol (mmol/l)	Total lipids (mg/dl)
Control	4.70±0.435	2.90±0.158	487.1±11.762
Crude aqueous extract	3.50±0.506*	2.44±0.20	403.8±99.97
Protein(peak A) at (125 mg/kg)	3.94±0.19	2.65±0.10	413.5±78.90
Protein(peak A) at (100 mg/kg)	3.90±0.25	2.50±0.13	409.5±78.78
Protein(peak A) at (75 mg/kg)	3.76±0.39	2.21±0.21	393.9±70.30
Protein(peak A) at (50 mg/kg)	3.75±0.32	2.16±0.29	383.8±73.53
Protein(peak B) at (125 mg/kg)	3.76±0.53	2.61±0.14	377.5±51.77*
Protein(peak B) at (100 mg/kg)	3.71±0.54	2.58±0.17	371.5±31.66**
Protein(peak B) at (75 mg/kg)	3.53±0.23*	1.85±0.52**	261.3±72.22**
Protein(peak B) at (50 mg/kg)	3.77±0.23	1.97±0.53	387.3±63.46*

*Significant difference at $P<0.05$
**Significant difference at $P<0.001$

The results in Table(2) showed a reduction of blood glucose to low significant level after intraperitoneal injection of the rats with crude aqueous red chili pepper(Capsicum annuum L.) extract compared with control

[10]. When chili-containing meals are a regular part of the diet, insulin requirements drop even lower. Plus, chili's beneficial effects on insulin needs get even better as body mass index (BMI, a measure of obesity) increases [4]. In overweight people, not only do chili-containing meals significantly lower the amount of insulin required to lower blood sugar levels after a meal, but chili-containing meals also result in a lower ratio of   C-peptide/ insulin, an indication that the rate at which the liver is clearing insulin has increased [11]. The amount of C-peptide in the blood pointer how much insulin is being produced by the pancreas. The pancreas produces proinsulin, which splits into insulin and C-peptide when secreted into the bloodstream. Each molecule of proinsulin breaks into one molecule of C-peptide and one molecule of insulin, so less C-peptide means less insulin has been secreted into the bloodstream. The results also showed lowering level in cholesterol and total lipids in the blood compared with control group, the lower cholesterol levels maybe by reducing accumulation of cholesterol in the body and increasing its breakdown and excretion in the feces [4, 10].

The results also showed that the protein compound (peak B) in red chili pepper(Capsicum annuum L.) at a dose of (75 mg/kg) led to maximum depression (64%) of blood glucose level compared to control group as listed in Table(2). This depression might be due to insulin like action of the protein content of red chili pepper(Capsicum annuum L.) [11], or might be due to insulin like structure of the protein product that binds with insulin receptors and lower blood glucose level. The protein compound (peak B) at a dose of (75 mg/kg) in the same table showed a significant lower level in cholesterol and total lipids. This might be due to inhibit cholesterol synthesis or increases the rate of cholesterol ejection loss from the body and insulin like action may help to lower the level of cholesterol [12].

Effect of crude aqueous extract and the isolated protein compound on glucose, cholesterol and total lipids in normal rats after orally administration

The results in Table(3) showed the effect of crude aqueous extract and protein products on glucose, cholesterol and total lipids in normal rats. Results indicated not significant decrease of serum glucose in normal rates for protein fraction (Peak A, peak B).

Table 3. Effect of crude aqueous extract and isolated protein compound on serum glucose, cholesterol and total lipids in normal rats after orally administration

Groups	Glucose (mmol/l)	Cholesterol (mmol/l)	Total lipids (mg/dl)
Control	4.70±0.435	2.90±0.158	487.1±11.76
Crude aqueous extract	4.25±0.33*	2.53±0.26	435±51.5
Protein(peak A) at (125 mg/kg)	4.76±0.07	2.84±0.16	457±63.10
Protein(peak A) at (100 mg/kg)	4.75±0.21	2.82±0.19	456±68.00
Protein(peak A) at (75 mg/kg)	4.77±0.74	2.78±0.16	435±78.12
Protein(peak A) at (50 mg/kg)	4.76±0.77	2.71±0.17	438±79.17
Protein(peak B) at (125 mg/kg)	4.76±0.90	2.71±0.13	433.4±76.10
Protein(peak B) at (100 mg/kg)	4.67±0.86	2.78±0.12	438.4±71.33
Protein(peak B) at (75 mg/kg)	4.74±0.74	2.77±0.26	391±83.11*
Protein(peak B) at (50 mg/kg)	4.73±0.86	2.73±0.16	337±75.19*

*Significant difference at $P<0.05$
**Significant difference at $P<0.001$

The results indicated that the orally administration of crude aqueous extract red chili pepper (Capsicum annuum L.) extract and protein fractions (Peak A, peak B) produced an increase of serum glucose. This might due to the crude aqueous extract which contains many materials or constituents such as polysaccharides, proteins, fats and amino acid. The metabolism of these compounds due to an increase of serum glucose, because the glycolysis, glycogenolysis, glugoneogenesis becomes active. Also, the protein fraction (Peak A, peak B) caused increase of serum glucose in orally administration, the proteins may be destroyed by the gastric juice or easily inactivated by the proteolytic enzymes. For all of these, the intraperitoneally administration of extract and protein fraction of the plant has hypoglycemic effect more than orally administration and it was a preferable route.

Effect of crude aqueous extract and the isolated protein compound on glucose, cholesterol and total lipids in diabetic rats after intraperitoneally administration

To test the effect of crude aqueous extract and the protein compound of active peak from red chili pepper(Capsicum annuum L.) on blood glucose, cholesterol and total lipids in diabetic rats, alloxan was used to induce diabetic experimental animals. Alloxan can damage the langerhans cells leading to decrease the production and secretion of insulin [4, 13, 14]. thus diabetes will occur. The results of intraperitoneal injection into diabetic rats were listed in Table(4).

Table 4. Effect of crude aqueous extract and isolated protein compound on serum glucose, cholesterol and total lipids in diabetic rats

Groups	Glucose (mmol/l)	Cholesterol (mmol/l)	Total lipids (mg/dl)
Control	29.6±1.019	3.02±0.680	657.15±29.747
Crude aqueous	20.6±3.65*	2.14±0.43	478.51±32.92*
Protein(peak B) at (125 mg/kg)	23.2±4.13	2.37±0.43	485.53±15.62*
Protein(peak B) at (100 mg/kg)	20.5±4.24	2.32±0.72	487.34±13.32*
Protein(peak B) at (75 mg/kg)	17.6±8.10*	1.71±0.37*	294.40±32.38**
Protein(peak B) at (50 mg/kg)	25.6±3.81	2.58±0.81	473.40±35.73*

*Significant difference at $P \leq 0.05$
** Significant difference at $P < 0.001$

The results in Table(4) showed that the protein compound injection caused a maximum depression of glucose, cholesterol and total lipids in diabetic rats in the same fusion as for normal rats. However, the protein product (peak B) at a dose of 75mg/kg is more effective in lowering the biochemical parameters under investigations in diabetic rats compared to normal. This lowering effect in this study could help reduce the risk of hyperinsulinemia (high blood levels of insulin) a disorder associated with type 2 diabetes[16]. because insulin was secreted after the chili rich diet and meal. This is also further evidence that the protein compound possessing insulin-like action mechanism that facilitates the entrance of glucose inside the cells and increases its metabolism[14, 15].

Conclusion

Novel of this research showed that the red chili pepper (Capsicum annuum L.) has the potential in the treatment of diabetes as it contain active protein compounds In addition, the C-peptide/insulin ratio was highest after the chili-containing meal, indicating an increase in the liver's ability to clear insulin. besides capsaicin, chilies contain antioxidants, including vitamin C and carotenoids, which might also help improve insulin regulation. that have the employability to reduce the concentration of blood sugar and lipids.

References

M. K. Hwang, A. M. Bode, S. Byun, N. R. Song, H. J. Lee, K. W. Lee and Z. Dong. Cancer Research. 70 (17): 6859–6869, 2010.

J. J. Tewksbury and G. P. Nabhan. Nature., 412 (6845): 403–404. 2001.

KD. Ahuja and MJ. Ball. Br J Nutr., 96(2): 239-242. 2006.

KD. Ahuja, IK. Robertson and DP. Geraghty. Am J Clin Nutr., 84(1): 63-69. 2006.

SK. Sharma and AS. Vij. Pharmacol Eur J., 720: 55-62, 2013.

H. Passing and W. Bablok. J. Clin. Chem. Clin. Biochem., 24: 863-869, 1983.

N.W. Tietz. Text book of clinical chemistry,3rd ed .C.A. Burtis, E.R. Ashwood, W.B. Saunders, pp.809-856,1999.

Chabral and Chardonnet , Cited by Geloson Torol, Philip G. Ackermann, Drac. Clin. Chem. Little, Brown and Company, Boston, 1975.

R.G. Steel and J.H. Torrie. Principles and Procedures of Statistics a Biometrical Approach. 2nd ed., McGraw-Hill, Inc., Singapore, 1980.

M.M. Abdel Magied, N.A. Salama and M.R. Ali. Journal of Food and Nutrition Research, 2(11): 850-856, 2014.

L. Nordquist, R. Brown, A. Fasching, P. Persson and F. Palm. Am. J. Physiol. Renal Physiol., 297(5): F1265–1272, 2009.

K. Esayas, A. Shimelis, F. Ashebir and R. Negussie. Bulletin of the Chemical Society of Ethiop, 25(3): 451-454. 2011.

Y.T. Liang, X. Tian, J.N. Chen, C. Peng, K.Y. Ma, Y. Zuo, R. Jiao, Y. Lu, Y. Huang and Z. Chen. European Journal of Nutrition., 52(1): 379-388, 2013.

M. Ozgur1, T. Ozcan, A. Akpinar-Bayizit and L. Yilmaz-Ersan. African Journal of Agricultural Research., 6 (25): 5638-5644, 2011.

R. Chandini, V. Udayabhaskaran, J.P. Binoy and K.P. Ramamoorthy. International Journal of Diabetes in Developing Countries, 33(2): 83–85, 2013.

Author Information

Zena A.M. Aljawadi
Chemistry Department, Science College,
Mosul University, Mosul, Iraq
Contact E-mail zena_aljawadi@yahoo.com

Study the Effect of Isolated Osteocalcin from Human and Rats on Lipids Profile in Normal and Alloxan-Induced Diabetic Male Rats

Thikra AL- ALLWSH
University of Mosul

Liqa'a ABDULLA
University of Mosul

Abstract: This study concerned with an attempts to isolate and purify osteocalcin from healthy human blood plasma and healthy rats serum using different biochemical techniques. This included precipitation by cold acetone and gel filtration chromatography. It was found that only the second peak (peak B) from human and rats had concentration of osteocalcin, and showed that fold of purification of isolated osteocalcin 57 and 43 for human and rats respectively. The research also included study the effect of isolated osteocalcin from human plasma and rats serum on lipids profile in normal and alloxan induced diabetic males rats. The results showed after one week of treatment by the isolated osteocalcin from human plasma and rats serum at the dose (1ng/Kg of body weight/d) caused a significant decrease in the concentration of all from total lipids, total cholesterol, triglycerides, VLDL-C, LDL-C, atherogenic index, and a significant increase in the concentration of HDL-C, and antiatherogenic index in normal and alloxan induced diabetic rats.

Keywords: Osteocalcin, Isolation, Lipids profile, Diabetes, Rats

Introduction

Osteocalcin is a bone matrix protein, Osteocalcin, also called bone Gla-protein or the vitamin k-dependent protein of bone and synthesized predominantly by osteoblasts and in lower way by odontoblasts, is incorporated into the extracellular matrix of bone (Rehder et al., 2015). In particular, osteocalcin or is a small abundant non-collagenous calcium binding protein, indigenous to the organic matrix of bone dentin and possibly other mineralized tissue, which circulates in the blood It is accepted as a marker of osteoblast activity(Shao et al., 2015 ; Zoch et al., 2016). In 2007 research from Columbia University Medical Center demonstrates that bone cells release a hormone called osteocalcin, which controls the regulation of blood sugar (glucose) and fat deposition through synergistic mechanisms, so osteocalcin directs the pancreas' beta cells, which produce the body's supply of insulin, to produce more insulin, at the same time, osteocalcin directs fat cells to release a hormone called adiponectin, which improves insulin sensitivity, this discovery showed for the first time that one hormone has a synergistic function in regulating insulin secretion and insulin sensitivity, and that this coordinating signal comes from the skeleton, additionally, osteocalcin enhances the production of insulin-producing beta cells, which is considered one of the best, to treat diabetes(Zoch et al., 2016; http://www.columbia.edu/cu. (2007)). The scientists reported that osteocalcin-deficient mice were glucose intolerant, insulin resistant, obesity prone, and characterized by decreased secretion of insulin and adiponectin (Lee et al., 2007).

Aim of the Research

Because there is few previous studies in Iraq about effect of osteocalcin on normal and diabetes experimental animals. So, there was suggestion to study the effect of isolated osteocalcin from human plasma and rats serum on the concentration of lipids in normal and diabetes experimental animals.

Method

Samples

A human fresh plasma (45 mL) was obtained from one healthy male person age (35 years), with assistance of Blood Bank in Mosul city, and male albino rats serum (25 mL) was separated by centrifugation from blood of male albino rats (13±1 week old) from animal house, college of veterinary medicine, university of Mosul.

The methods used to purification of osteocalcin

Organic solvent precipitation

Proteinous materials were precipitated by using acetone (Robyt and White 1987). Gradual addition (60:40 v/v) cold acetone to plasma with slow stirring at 4°C for 60 min. The mixture was left in a refrigerator for 24 h and the precipitated protein was isolated by centrifugation for 30 minutes (12000 g) at a refrigerated centrifuge. Protein and osteocalcin concentration were estimated after dissolving the precipitate in a lowest volume of distilled water. Then the solution of proteinous precipitate was kept in a tight sample tube for further step.

Gel Filtration Chromatography

Packing of the column: It has a dimension of (2 × 100 cm) which contained a gel sephadex G-50. Proteinous precipitates solutions which were prepared in section (1) were applied to this column.

Lyophilization Technique

Peaks B (from the column) were dried by freeze drying, this technique was performed in the department of chemistry, college of science, university of Mosul.

Osteocalcin Assay

Osteocalcin concentration was determined by enzyme linked immunosorbent assay (ELISA) technique (Nagasue et al., 2003) using Epitope Diagnostics, Inc kit (USA). This analysis was performed in the immunity laboratory in Al-Salam hospital in Mosul city by using (BIO-TEK INSTRUMENTS, INC), USA.

Determination of Protein Concentration

Protein was determined by the method of modified lowry (Schacterle and Pollack 1973). Bovine serum albumin was used as a standard protein.

Effect of isolated osteocalcin from human plasma and rats serum in normal and alloxan–induced diabetic rats

Animals used

Forty six healthy male albino rats with age (13±1 week old), and weight (300±35g) obtained from animal house, college of veterinary medicine, university of Mosul were used in the experiments. They were housed under standard environmental conditions, pelleted food and water were available ad Libitum.

Induction of diabetes

The animals were fasted for (24 h) and made diabetes by injecting with alloxan tetrahydrate (180 mg/ Kg of body weight, i.p) dissolved in sterile normal saline (Miura et al., 1995). The diabetic state was monitored by

hyperglycemia (Colorimetric assay kit, Randox, United Kindom) along the next ten days. Rats with blood glucose concentration more than (250 mg/dL) were considered diabetic and used for study.

Experimental Design

The dose of isolated osteocalcin was (1ng/kg of body weight) (Dou *et al*., 2014; Sabek *et al*., 2015).
The male rats were divided into six group and all groups were injected for one week as shown   below:
1. The first group: non fasted control male rats group was injected intraperitoneally with physiological saline solution.
2. The second group: non fasted male rats group before and after induced them diabtes by injecting with alloxan tetrahydrate (180 mg/ Kg of body weight, i.p).
3. The third group: non fasted healthy male rats group was injected intraperitoneally with (1 ng/kg of body weight) isolated osteocalcin from human plasma.
4. The fourth group: non fasted healthy male rats group was injected intraperitoneally with (1 ng/kg of body weight) isolated osteocalcin from rats serum.
5. The fifth group: non fasted and alloxan induced diabetic male rats group was injected intraperitoneally with (1 ng/kg of body weight) isolated osteocalcin from human plasma.
6. The sixth group: non fasted and alloxan induced diabetic male rats group was injected intraperitoneally with (1 ng/kg of body weight) isolated osteocalcin from rats serum.

Collection of blood

Fasting (16 h) blood samples were collected from six groups by orbital sinus puncture technique, using capillary tube without anticoagulant (Tomoda et al., 1990). Serum was separated and used to estimate the following clinical parameters:

Total lipids: was found by colorimetric method manually (Chabrol and Chardonnet 1937).
-Total cholesterol: was determined by enzymatic colorimetric method (Allain *et al*., 1974), using BIOLABO kit (France).
-Triglycerides: was determined by enzymatic colorimetric method (Fossati and Principle 1982), using BIOLABO kit (France).
-Very low density lipoprotein-cholesterol (VLDL-C): was calculated by using the following equation: VLDL Conc. (mmol/L) = TG Conc./2.2 (Yeboah *et al*., 2017).
-Low density lipoprotein-cholesterol (LDL-C): was calculated by using the following equation:
LDL Conc. (mmol/L) = Total cholestrol Conc.-HDL Conc.-(TGconc./2.2) (Burtis and Ashwood 1982).
-High density lipoprotein-cholesterol (HDL-C): was determined by precipitation method (Burtis and Ashwood 1982), using BIOLABO kit (France).
-Atherogenic Index(AI): was calculated by using the following equation:
Atherogenic Index (AI) = Log(TG/HDL-C) (Nagasue *et al*., 2003).
   -Antitherogenic Index(AAI): was calculated by using the following equation:
100 / (TC -HDL-C) (Saravanan et al., 2011).× Antiatherogenic index (AAI) = HDL–C

Data Analysis

The data obtained in the current study was analyzed using statistical package for social science (SPSS).
1. Standard statistical method used to determined the mean and standard error.
2. Indepent – sample T-test to compare between two parameters.
3. One way anova (Duncan-test) is used to compare between more than two parameters.
4. P-value ≤ 0.05 was considered to be statistically significant (Kirkwood, 1988).

Results and Discussion

Purification of osteocalcin from human plasma and rats serum

Organic solvent precipitation

The precipitate solution which obtained by cold acetone from plasma human was with high concentration of osteocalcin (23.77 ng/mL) compared with plasma (16.55 ng/mL), while the filtrate was not obtained any concentration of osteocalcin hormone. So, the filtrate was neglected. The precipitate solution which obtained by cold acetone from rats serum was with high concentration of osteocalcin (2.1 ng/mL) compared with plasma (1.33 ng/mL), while the filtrate was not obtained any concentration of osteocalcin hormone. So, the filtrate was neglected.

Gel filtration chromatography

This technique was applied to separate the proteinous materials, which were obtained by acetone precipitation method from human plasma and rats serum. The results of elution of isolated osteocalcin from human and rats shown in figure (1) and (2) respectively and indicated that there were two peaks (A & B). The elution volume of peak A & B were (89.47 mL) , (223 mL) respectively for isolated osteocalcin from human, and elution volume of peak A & B were (93.0 mL) , (230 mL) respectively for isolated osteocalcin from rats. Only peak (B) from human plasma and rats serum was obtained with high concentration of osteocalcin.
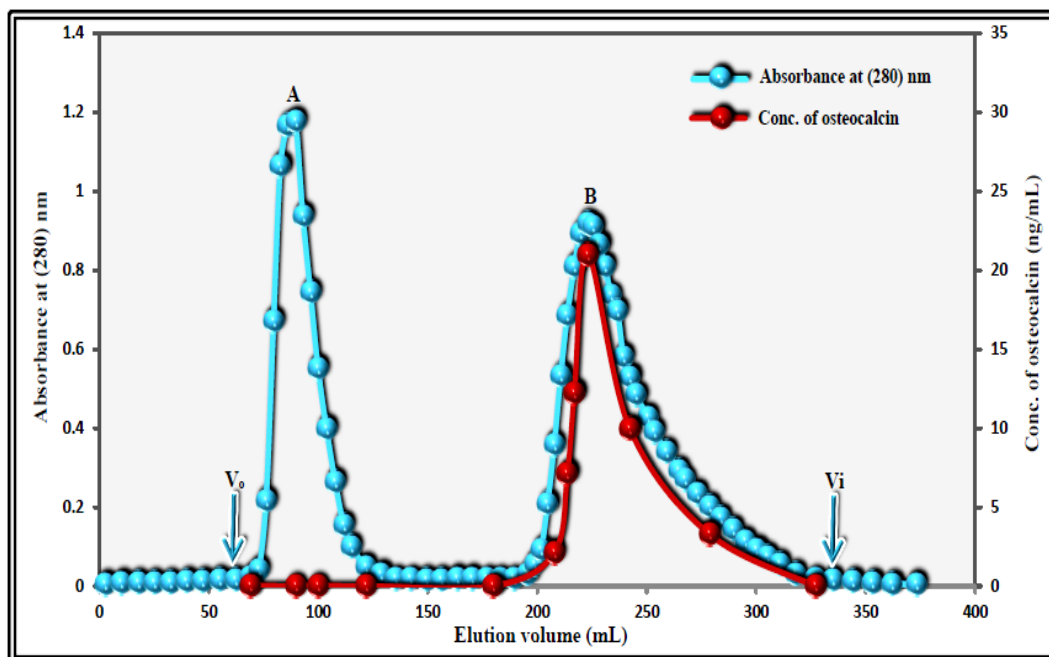
Figure 1.Elution profile of proteinous precipitate solution obtained from acetone precipitation of human plasma on Sephadex G-50.The dimensions of the column are (2×100 cm).
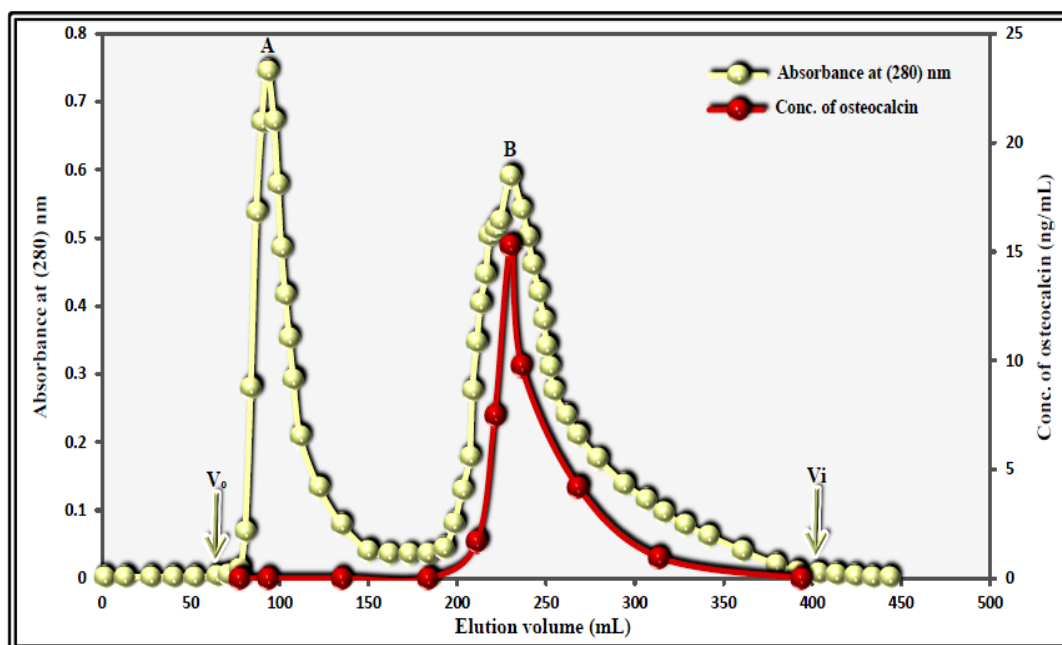
Figure 2.Elution profile of proteinous precipitate solution obtained from acetone precipitation of rats serum on Sephadex G-50.The dimensions of the column are (2×100 cm)

The results of all purification steps for osteocalcin from human plasma and rats serum were listed in table (1) and table (2) respectively:

Table 1.Partial purification of osteocalcin from human plasma

Purification steps	Volume (mL)	Total protein (mg)	Total conc. Of osteocalcin (ng)	Total specific conc. Of osteocalcin (ng/mg)	Recovery %	Fold of purification
Plasma	45	319.5	744.75	2.33	100	1
Proteinous precipitate solution by cold acetone	30	143.4	713.1	4.97	95.75	2
Gel filtration/Sephadex G-50 (peak B)	10	4.7	620	131.91	83.24	57

The results in Table (1) showed that the concentration of osteocalcin was increased from (16.55 ng/mL) in plasma to (23.77 ng/mL) for proteinous precipitate solution concentration of osteocalcin and to (62 ng/mL) for peak B concentration of osteocalcin used in gel filtration by using (Sephadex G-50).While the concentration of protein was decreased.

Table 2.Partial purification of osteocalcin from rats serum

Purification steps	Volume (mL)	Total protein (mg)	Total conc. Of osteocalcin (ng)	Total specific conc. Of osteocalcin (ng/mg)	Recovery %	Fold of purification
Serum	25	158.5	33.25	0.21	100	1
Proteinous precipitate solution by cold acetone	14	60.34	29.4	0.49	88.42	2
Gel filtration/Sephadex G-50 (peak B)	5	2.65	23.85	9	71.73	43

The results in Table (2) showed that the concentration of osteocalcin was increased from (1.33 ng/mL) in serum to (2.1 ng/mL) for proteinous precipitate solution concentration of serum rats and to (4.77 ng/mL) for peak B concentration of osteocalcin used in gel filtration by using (Sephadex G-50).While the concentration of protein was decreased.

Effect of isolated osteocalcin on some clinical parameters in serum of normal and alloxan-induced diabetic rats:

When injected intraperitoneally the isolated osteocalcin from human plasma and rats serum at the dose (1ng/Kg of body weight/d) in healthy and alloxan induced diabetic male rats for one week, the results show effect of osteocalcin on lipids profile as shown bellow:

1. Total lipids, Total cholesterol, Triglycerides, Very low density lipoprotein cholesterol, Low density lipoprotein cholesterol & High density lipoprotein cholesterol

The results revealed that the percentage of reduction in the third group and the fourth group in the concentration of all from total lipids were (-13.62%) and (-7.99%) respectively, total cholesterol were (-40.89%) and (-31.06%) respectively, triglycerides were (-19.88%) and (-11.37%) respectively, very low density lipoprotein cholesterol were (-19.51%) and (-10.66%) respectively, low density lipoprotein cholesterol were (-75.16%) and (-56.50%) respectively, while the percentage of reduction in the fifth group and the sixth group in the concentration of all from total lipids were (-34.13%) and (-27.24%) respectively, total cholesterol were (-44.62%) and (-38.39%) respectively, triglycerides were (-45.51%) and (-38.76%) respectively, very low density lipoprotein cholesterol were (-45.20%) and (-38.77%) respectively, low density lipoprotein cholesterol were (-59.01%) and (-49.90%) respectively after one week of treatment with osteocalcin as shown in the tables (3), (4), (5), (6), and (7).

Table 3. Effect of intraperitoneally administration of isolated osteocalcin for one week on total lipids concentration in normal and alloxane-induced diabetic male rats

Group No.	Treatment	TL conc. (mg/dL) Mean ± S.E		Change %
		Pre-treatment (Zero time)	Post-treatment (After one week)	
1	Control group+ 0.9%NaCl	572.84 ± 5.18A	b,c,d,e 586.33 ± 8.85A	2.35
2	Diabetic rats+0.9%NaCl	577.01 ± 1.71A	a,c,d,e,f 798.54 ± 8.81B	38.39
3	Normal rats + (1ng/Kg/d) of isolated human osteocalcin	590.82 ± 7.84A	a,b,d,f 510.33 ± 1.33B	-13.62
4	Normal rats + (1ng/Kg/ d) of isolated rats osteocalcin	587.16 ± 6.09A	a,b,c,e,f 540.24 ± 3.03A	-7.99
5	Diabetic rats + (1ng/Kg/d) of human osteocalcin	790.57 ± 8.12A	a,b,d,f 520.73 ± 1.20B	-34.13
6	Diabetic rats + (1ng/Kg/d) of rats osteocalcin	797.32 ± 5.98A	b,c,d,e 580.11 ± 1.14B	-27.24

Different letters horizontally A,B indicate different significant at (P≤0.05) in the lipid parameter concentration between pre-treatment and post-treatment, while differents letters vertically (a), (b), (c), (d), (e) and (f) indicate that the mean is different significantly at (P≤0.05) in the lipid parameter concentration between each group after one weak (post-treatment).

$$Change\% = \frac{Post\text{-}treatment\ Conc. - Pre\text{-}treatment\ Conc.}{Pre\text{-}treatment\ Conc.} \times 100$$

The cause may be due to that osteocalcin increases energy consumption in muscles and adipose tissues (Lacombe et al., 2013), also (Pi and Quarles 2012) showed when injected osteocalcin, it enhace insulin sensitivity via its direct effect on its GPRC6A receptor activating on skeletal muscles, liver, and adipose cells, and through its role in enhance adiponectin secretion from adipose cells, so adiponectin regulates energy metabolism through increases fatty acid oxidation in liver and skeletal muscle, inhibits gluconeogenesis in liver, and enhances glucose uptake in skeletal muscles, as well as osteocalcin decreases leptin concentration when leptin rises at fat mass increasing (Grau et al., 2010).

Whereas the results showed that the percentage of elevation of HDL-C concentration in the third group and the fourth group were (17.33%) and (11.76%) respectively, while the percentage of elevation in the fifth group and the sixth group were (63.76%) and (56.45%) respectively after one week of treatment with osteocalcin as shown in the table (8), these elevation could be attributed to that osteocalcin stimulates insulin secretion, so the activity of lipoprotein lipase will increase and lead to increase HDL-C, or the cause may be due to that osteocalcin promotes adiponectin secretion, so osteocalcin correlated positively with HDL-C (Zoch et al., 2016, Albadah et al., 2015).

Table 4. Effect of intraperitoneally administration of isolated osteocalcin for one week on total cholesterol concentration in normal and alloxane-induced diabetic male rats

Group No.	Treatment	TC conc. (mmol/L) Mean ± S.E		Change%
		Pre-treatment (Zero time)	Post-treatment (After one week)	
1	Control group+ 0.9%NaCl	4.94 ± 0.10A	b,c 5.17 ± 0.12A	4.65
2	Diabetic rats+0.9%NaCl	5.52 ± 0.14A	a,c,d,e,f 7.01 ± 1.06B	26.99
3	Normal rats + (1ng/Kg/d) of isolated human osteocalcin	5.38 ± 0.07A	a,b 3.18 ± 0.30B	-40.89
4	Normal rats + (1ng/Kg/ d) of isolated rats osteocalcin	5.44 ± 0.05A	b 3.75 ± 0.21A	-31.06
5	Diabetic rats + (1ng/Kg/d) of human osteocalcin	7.26 ± 0.73A	b 4.02 ± 0.13B	-44.62
6	Diabetic rats + (1ng/Kg/d) of rats osteocalcin	7.11 ± 0.52A	b 4.38 ± 0.10B	-38.39

Table 5. Effect of intraperitoneally administration of isolated osteocalcin for one week on triglycerides concentration in normal and alloxane-induced diabetic male rats

	Treatment	TG conc. (mmol/L) Mean ± S.E		Change%
		Pretreatment (Zero time)	Post-treatment (After one week)	
1	Control group+ 0.9%NaCl	1.73 ± 0.07A	b 1.66 ± 0.06A	-4.04
2	Diabetic rats+0.9%NaCl	1.96 ± 0.03A	a,c,d,e,f 3.27 ± 0.23B	66.83
3	Normal rats + (1ng/Kg/d) of isolated human osteocalcin	1.81 ± 0.01A	b,f 1.45 ± 0.14B	-19.88
4	Normal rats + (1ng/Kg/ d) of isolated rats osteocalcin	1.67 ± 0.05A	b,f 1.48 ± 0.23B	-11.37
5	Diabetic rats + (1ng/Kg/d) of human osteocalcin	3.23 ± 0.41A	b 1.76 ± 0.07B	-45.51
6	Diabetic rats + (1ng/Kg/d) of rats osteocalcin	3.25 ± 0.48A	b,c,d 1.99 ± 0.10B	-38.76

Table 6. Effect of intraperitoneally administration of isolated osteocalcin for one week on VLDL-C concentration in normal and alloxane-induced diabetic male rats

Group No.	Treatment	VLDL-C conc. (mmol/L) Mean ± S.E		Change %
		Pretreatment (Zero time)	Post-treatment (After one week)	
1	Control group+ 0.9%NaCl	0.78 ± 0.03A	b 0.75 ± 0.02A	-3.84
2	Diabetic rats+0.9%NaCl	0.89 ± 0.01A	a,c,d,e,f 1.48 ± 0.10B	66.29
3	Normal rats + (1ng/Kg/d) of isolated human osteocalcin	0.82 ± 0.005A	b,f 0.66 ± 0.06B	-19.51
4	Normal rats + (1ng/Kg/ d) of isolated rats osteocalcin	0.75 ± 0.02A	b,f 0.67 ± 0.11B	-10.66
5	Diabetic rats + (1ng/Kg/d) of human osteocalcin	1.46 ± 0.18A	b 0.80 ± 0.03B	-45.20
6	Diabetic rats + (1ng/Kg/d) of rats osteocalcin	1.47 ± 0.21A	b,c,d 0.90 ± 0.04B	-38.77

Table 7. Effect of intraperitoneally administration of isolated osteocalcin for one week on LDL-C concentration in normal and alloxane-induced diabetic male rats

Group No.	Treatment	LDL-C conc. (mmol/L) Mean ± S.E		Change%
		Pretreatment (Zero time)	Post-treatment (After one week)	
1	Control group+ 0.9%NaCl	2.62 ± 0.06A	b,c,d 2.92 ± 0.03A	11.45
2	Diabetic rats+0.9%NaCl	3.11 ± 0.05A	a,c,d,e,f 4.89 ± 1.03B	57.23
3	Normal rats + (1ng/Kg/d) of isolated human osteocalcin	3.06 ± 0.15A	a,b,f 0.76 ± 0.23A	-75.16
4	Normal rats + (1ng/Kg/ d) of isolated rats osteocalcin	3.15 ± 0.17A	a,b 1.37 ± 0.17A	-56.50
5	Diabetic rats + (1ng/Kg/d) of human osteocalcin	5.10 ± 0.53A	b 2.09 ± 0.12B	-59.01
6	Diabetic rats + (1ng/Kg/d) of rats osteocalcin	5.01 ± 0.63A	b,c 2.51 ± 0.08B	-49.90

Table 8. Effect of intraperitoneally administration of isolated osteocalcin for one week on HDL-C concentration in normal and alloxane-induced diabetic male rats

Group No.	Treatment	HDL-C conc. (mmol/L) Mean ± S.E		Change %
		Pretreatment (Zero time)	Post-treatment (After one week)	
1	Control group+ 0.9%NaCl	1.54 ± 0.13A	b,f 1.50 ± 0.19A	-2.59
2	Diabetic rats+0.9%NaCl	1.52 ± 0.10A	a,c,d,e 0.63 ± 0.01B	-58.55
3	Normal rats + (1ng/Kg/d) of isolated human osteocalcin	1.50 ± 0.21A	b,e,f 1.76 ± 0.02B	17.33
4	Normal rats + (1ng/Kg/ d) of isolated rats osteocalcin	1.53 ± 0.23A	b,e,f 1.71 ± 0.04B	11.76
5	Diabetic rats + (1ng/Kg/d) of human osteocalcin	0.69 ± 0.01A	b,c,d 1.13 ± 0.17B	63.76
6	Diabetic rats + (1ng/Kg/d) of rats osteocalcin	0.62 ± 0.02A	a,c,d 0.97 ± 0.14B	56.45

Atherogenic index

The results demonstrated that the percentage of reduction of atherogenic index (AI) in the third group and the fourth group were (-214.28%) and (-200%) respectively, while the percentage of reduction in the fifth group and the sixth group were (-69.69%) and (-54.92%) respectively after one week of treatment with osteocalcin as shown in the table (9).The cause may be due to that osteocalcin correlates by negative correlation with triglycerides and by positive correlation with HDL-C (Kang, 2016), therefore osteocalcin may be a marker for assessing the risk of atherosclerosis and cardiovascular in type II diabetes (Alfadda *et al*., 2013), and these results were in agreement with those obtained by other investigators (Dou *et al*., 2014) who demonstrated that osteocalcin had protective effect from atherosclerosis and cardiovascular.

Table 9. Effect of intraperitoneally administration of isolated osteocalcin for one week on atherogenic index (AI) in normal and alloxane-induced diabetic male rats

Group No.	Treatment	Atherogenic index (AI) Mean ± S.E		Change %
		Pretreatment (Zero time)	Post-treatment (After one week)	
1	Control group+ 0.9%NaCl	0.05 ± 0.05A	b,f 0.06 ± 0.19A	20
2	Diabetic rats+0.9%NaCl	0.11 ± 0.06A	a,c,d,e,f 0.71 ± 0.43B	545.45
3	Normal rats + (1ng/Kg/d) of isolated human osteocalcin	0.07 ± 0.21A	b,e,f -0.08± 0.07A	-214.28
4	Normal rats + (1ng/Kg/ d) of isolated rats osteocalcin	0.06 ± 0.21A	b,e,f -0.06 ± 0.14A	-200
5	Diabetic rats + (1ng/Kg/d) of human osteocalcin	0.66 ± 0.58A	b,c,d 0.20 ± 0.07B	-69.69
6	Diabetic rats + (1ng/Kg/d) of rats osteocalcin	0.71 ± 0.69A	a,b,c,d 0.32 ± 0.08B	-54.92

Antitherogenic index

The results showed that the percentage of elevation of antitherogenic index (AAI) in the third group and the fourth group were (241.09%) and (112.87%) respectively, while the percentage of elevation in the fifth group and the sixth group were (277.80%) and (192.11%) respectively after one week of treatment with osteocalcin as shown in the table (10). These elevation could be attributed to that osteocalcin correlates by positive correlation with HDL-C and by negative correlation with total cholesterol (Kang, 2016), and these results were in agreement with those obtained by other investigators (O'Connorand Durack 2017) who demonstrated the correlation of osteocalcin concentration with clinical parameters concentration of atherosclerosis in type II diabetes.

Table 10. Effect of intraperitoneally administration of isolated osteocalcin for one week on antitherogenic index in normal and alloxane-induced diabetic male rats

Group No.	Treatment	Antitherogenic index (AAI) Mean ± S.E		Change%
		Pretreatment (Zero time)	Post-treatment (After one week)	
1	Control group+ 0.9%NaCl	45.41 ± 4.26A	c,d 40.99 ± 5.90A	-9.73
2	Diabetic rats+0.9%NaCl	38.14 ± 1.22A	c,d 10.74 ± 4.62B	-71.84
3	Normal rats + (1ng/Kg/d) of isolated human osteocalcin	39.15 ± 6.89A	a,b,d,e,f 133.54 ± 22.66A	241.09
4	Normal rats + (1ng/Kg/ d) of isolated rats osteocalcin	39.85 ± 7.42A	a,b,c,e,f 84.83 ± 5.04A	112.87
5	Diabetic rats + (1ng/Kg/d) of human osteocalcin	10.77 ± 1.27A	c,d 40.69 ± 9.66B	277.80
6	Diabetic rats + (1ng/Kg/d) of rats osteocalcin	9.76 ± 0.72A	c,d 28.51 ± 4.45B	192.11

Conclusion

From this research we concluded that the isolated osteocalcin from human plasma and rats serum had a major role in the metabolism of glucose and lipids profile in normal and alloxan induced diabetic rats, also it was concluded that isolated osteocalcin from human plasma was more effect than isolated osteocalcin from rats

serum on the concentration of lipids in normal and alloxan induced diabetic males rats, especially the effect of isolated osteocalcin from human plasma was higher than isolated osteocalcin from rats serum on the concentration of lipids in alloxan induced diabetic males rats compared with normal male rats.

References

Albadah, M.S.; Dekhil, H.; Shaik, S.A.; Alsaif, M.A ; Shogair, M; Nawaz, S. and Alfadda, A.A. (2015). " Effect of weight loss on serum osteocalcin and its association with serum adipokines". Internat. J. Endocrinol. 10: 1-10.

Alfadda, A.A.; Masood, A.; Shaik, S.A.; Dekhil, H. and Goran, M. (2013). "Association between osteocalcin, metabolic syndrome, and cardiovascular risk factors: Role of total and undercarboxylated osteocalcin in patients with type 2 diabetes". Internat. J. Endocrinol. 10: 1-6.

Allain, C.C.; Poon, L.S.; Chan, C.S.; Richmond, W. and Fu, P.C. (1974). "Determination of serum total cholesterol by enzymatic colorimetric method". J. Clin. Chem. 20(4): 470-475.

Burtis, C. A. and Ashwood, E.R. (1982). " Teits Fundamental of Clinical Chemistry". 2nd ed., W.B. Saunders Company, U.S.A. Philadelphia. :302, 337, 539, 901.

Chabrol and Chardonnet. (1937). Cited by AL-Mollah, L. A. M. (1990). "Studies of some metabolic effects of noradrendine insulin inpresence of Ca++. M.Sc. Thesis, University of Mosul.

Dou, J.; Li, H.; Ma, X.; Zhang, M.; Fang, Q.; Nie, M.; Bao, Y. and Jia, W. (2014). "Osteocalcin attenuates high fat diet-induced impairment of endothelium-dependent relaxation through Akt/eNOS-dependent pathway". J. Cardiovascular Diabetol. 13(74): 1-12.

Fossati, P. and Principle, L. (1982). "Serum triglycerides determined colorimetrically with an enzyme that produces hydrogen peroxide". J. Clin. Chem. 28(10): 2077-2080.

Grau, G.A.; Ara, I., Dorado, C.; Rodriguez, V.G.; Gomez, P.J.; Cabrero, J.C.; Sanchez, S.J.A.; Santana, A. and Calbet, J.A. (2010). "Osteocalcin as a negative regulator of serum leptin concentration in humans: insight from triathlon competitions". Eur. J. Appl. Physiol. 110(3): 635-643.

Kang, J.H. (2016). " Association of Serum Osteocalcin with Insulin Resistance and Coronary Atherosclerosis". J. Bone Metab. 23: 183-190.

Kirkwood, B. R. (1988). Essentials of Medical Statistics. 1st edn., Black well Scientific Publication, Oxford; 43-56.

Lacombe, J.; Karsenty, G. and Ferron, M. (2013). "In vivo analysis of the contribution of bone resorption to the control of glucose metabolism in mice". J. Molecular. Metab. 8: 1-7.

Lee, N.K.; Sowa, H.; Hinoi, e.; Ferron, M.; Ahn, J.D.; Confavreux, C.; Dacquin, R.; Mee, P.J.; Mckee, M.D.; Jung, D.Y.; Zhang, Z.; Kim, J.K.; Mauvais,J. F; Ducy, P. and Karsenty, G. (2007). "Endocrine regulation of energy metabolism by the skeleton". J. Cell. 130: 456-469.

Miura, T.; Usami, M.; Tsuura, Y.; Ishida, H. and Seino, Y. (1995). "Hypoglycemic and hyolipidemic effect of chitosan in normal and neonantal streptotocin induced diabetic mice". J. Biol. Pharm. Bull. 18(1): 1623-1625.

Nagasue, K.; Inaba, M.; Okuno, S.; Kitatani, K.; Imanishi, Y.; Ishimura, E.; Miki, T., Kim, M. and Nishizawa, Y. (2003). "Serum N-terminal midfragment vs. intact osteocalcin immunoradiometric assay as markers for bone turnover and bone loss in hemodialysis patients". J. Biomed. Pharmacother. 57(2):98-104.

Nansseu, J.R.N.; Moor, V.J.A.; Nouaga, M.E.D.; Awona, B.Z.; Tchanana, G. and Ketcha, A. (2016). " Atherogenic index of plasma and risk of cardiovascular disease among Cameroonian postmenopausal women". J. Lipids in Health and Disease. 15:49: 1-5.

O'Connor, E.M. and Durack, E. (2017). " Osteocalcin: The extra-skeletal role of a vitamin K-dependent protein in glucose metabolism". J. Nutr. & Intermed. Metab. 7: 8-13.

Pi, M. and Quarles, L.D. (2012). "Multiligand specificity and wide tissue expression of GPRC6A reveals new endocrine networks". J. Endocrinol. 153(5): 2062-2069.

Rehder, D.S.; Gundberg, C.M.; Booth, S.L. and Borges, C.R. (2015). " Gamma-carboxylation and fragmentation of osteocalcin in human serum defined by mass spectrometry". J. Mol. & Cell. Proteomics. 14(6): 1546-1555.

Research shows skeleton to be endocrine organ. http://www.columbia.edu/cu. (2007).

Robyt, F.J. and White, J. B. (1987). "Biochemical Techniques Theory and Practice". Books Cole Publishing Co., U.S.A., 141, 235-236, 246, 263, 269

Sabek, O.M.; Nishimoto, S.K.; Fraga, D.; Tejpal, N.; Ricordi, C. and Gaber, A.O. (2015). "Osteocalcin effect on human β-cells mass and function". J. Endocrinol. 156(9): 3137-3146.

Saravanan, G; Kalaiselvi, .B. and Reddy, G.P.(2011). "Hypolipidemic effect of zignidd (polyherbal formulation) in streptozotocin-induced diabetic rats". INT. J. Drug Formulation and Research. 2(6): 151-160.20.

Schacterle, G.R. and Pollack , R. L. (1973). "A simplified method for the quantitatiue assay of small amounts of protein biological material". J. Anal. Biochem. 51: 654-655.

Shao, J.; Wang, Z.; Yang, T.; Ying, H.; Zhang, Y. and Liu, S. " (2015). "Bone regulates glucose metabolism as an endocrine organ through osteocalcin". Internat. J. Endocrinol. 10: 1-9.

Tomoda, M.; Shimizu, N.; Gonda, R.; Kanari, M.; Yamada, H. and Hikino, H. (1990). "Anti-Complementary and hypoglycemic activities of the glycans from the seeds of malva verticillata". J. Planta. Med. 56:168-170.

Yeboah, J.O.; Owiredu, W.K.B.A.; Norgbe, G.K.; Lokpo, S.Y.; Gyamfi,J.; Allotey, E.A.; Aduko, R.A.; Noagbe, M. and Attah, F.A. (2017). " The Prevalence of metabolic syndrome and its components among people with type 2 diabetes in the Ho Municipality, Ghana: A cross-sectional study". Internat. J. Chronic Dis. 10: 1-8.

Zoch, M.L.; Clemens, T.L. and Riddle, R.C. (2016). " New insights into the biology of osteocalcin". J. Bone and diabetes. 82: 42–49.

Author Information

Thikra A. Al-Allwsh	**Liqa'a S. Abdulla**
Mosul University	Mosul University
Department of chemistry, College of science,	Department of chemistry, College of science,
Mosul university, Iraq	Mosul university, Iraq
Contact E-mail:Allwsh2007@yahoo.com	

Effect of Some Biochemical Parameters on the Level of Enzymes in the Serum and Placenta of the Infected Pregnant Woman with Toxoplasmosis

Layla A. MUSTAFA
University of Mosul

Muna I. IBRAHEEM
University of Mosul

Abstract: The present study was conducted aiming at investigating the medical, biological and biochemical importance of toxoplasmosis and the effect of the causative agent, *Toxoplasma gondii* ,on the level of the enzymes in the serum and placentae of infected pregnant women compared to non- pregnant, non- infected women (control group) he study included 450 specimens of women , 225 out of them were non- infected and 225 were infected with toxoplasmosis.A significant increase (p≤0.01) in activity of Px, GST ,LDH and AchE whereas non-significant decrease in activity of SOD and AE was noticed, compared to control group.Interference between infection and different pregnancy periods showed a significant increase (p≤0.01) in activity of SOD, Px, LDH and AE in serum of pregnant, infected women during 1-3 months pregnancy period , whereas GST increased significantly (p≤0.01) in activity during 3-6 months pregnancy period and AchE during 6-9 months pregnancy period.The result related to the placentae of the pregnancy women who are infected with Toxoplasmosis showed a non-significant increasing in activity of: SOD, GST, LDH, and AchE through period of pregnancy ranged (6-9) months. Also; efficiency of AE increased through period of pregnancy ranged (1-3) months; but activity of Px through period of pregnancy in placentae of the pregnant infected women decreased.

Keywords: Toxoplasmosis, Arylesterase, Acetylcholineesterase, Peroxidase

Introduction

Toxoplasmosis is a disease caused by a kind of the parasitic prophylaxis called Toxoplasma gondii parasite, which considered one of the intracellular parasites, that can cause many kinds of the intermediate hosts like: the rodents, birds, wild animals and the human beings. (Remington *et. al.,* 2000).

Cats and the other kinds related to the family felidae are considered specialist final enforcing and intermediate hosts in the life cycle of the parasite. (Dubey, 2003). The name of Toxoplasma was derived from its Crescent Shape; whereas toxin means an arch and plasma means a form. (Buxton; 1983).

The patients are classified into two groups according to the way of causing with the disease: the first one represents the placenta Toxoplasmosis which occurs as a result of transpoting the parasite from the mother to the embryo across the placenta; and the second kinds is produced by many ways including the mouth through taking some materials like: water, fruits and vegetables polluted in Sporulated Oocytes; dealing with polluted soil with the excrement of the caused cats; or taking the tissue hosts existing in the raw or uncooked well intermediate tissues, less common ways like through the nose by inhaling. (Prescott and *et. al.,* 2002). Besides; through blood transfusion whereas the parasite can stay in the blood stored in 4_oC for more than 50 days, or by members transplantation. (Al-Nuaimy, 2010). Also; pregnancy is considered a kind of the oxidative stress: that causes to increase oxidation levels and decrease anti-oxidation because the oxidative stress represents the unbalance state among oxidants (free radicals and their products resulting from the metabolic processes) and anti-oxidants, more than anti-oxidants causing to destroy the biochemical particles in the body like: proteins, fats, and nucleic acids. (Robinson and *et. al.,* 2008).

Then, it is necessary to point out that the free *radicals*s are chemical compounds consist of one electron or more undoubled in the cell; whereas; they are severe in the interaction process; that the particle tries to reach at state of stability as quick as possible then attacks the neighboring particles and obtains the electron required from the stable particle. (Gleeson and *et. al.,* 2006).

Free radicals play an important role in many diseases that cause the human being. (Liu; 2003). So; the reactive oxygen species (ROS) generated inside the body attack the cells and destroy their components of protein, fats, and nucleic acids like: Ribonucleic acid RNA and Deoxy Ribonucleic acid DNA, carbohydrate and other components in the cell then cause to damage the cellular wall. (Stahl & Sies; 1997, Bartosikova *et. al.,* 2003). Also; reactive oxygen species affect on the proteins through their effect on the double bond and its oxidation, besides; oxidation of SH group that causes to change in composition of the proteins with modifications on them that affect on their work and inhabit enzymes activities (Tritto & Ambrosio; 1999, Michael, 2001).

Therefore; the study is an attempt to limit the change that can be taken place in efficiency of the enzymes like: Superoxide Dismutase (SOD), Peroxidase, Glutathione- S- transferase, Lactet dehydrogenase LDH, Arylesterase, and Acetyl Choline esterase as anti-oxidants in serum of the women caused with the disease whether the aborted or non-aborted ones.

Method

Collection of Placenta Specimens

Placenta specimens were collected from aborted and non-aborted women. Then, 24 specimens were collected from Al-Khansa' Gynecology and Obstetrics Hospital. Hence, 18 placentae specimens were collected from women suffered from repeated abortion cases through various pregnancy periods as shown (1-3), (3-6) and (6-9) months. Thereafter it became certain to be caused with Toxoplasmosis by using the direct microscopic examination of the placenta extract and isolation the parasite in its pure form from the infected placentae. (Sharma & Dubey; 1981, Dubey & Livington, 1986; Al-Khaffaf ; 2001).

Collection of Blood Specimens

Blood specimens were taken from various groups of the pregnant women aiming at estimation of some enzymes as following: healthy pregnant and infected women with Toxoplasmosis for each period of pregnancy through (1-3), (3-6) and (6-9) months.

Group of infected women and non-infected with *Toxoplasma Condii*

Scientifically speaking, 450 blood specimens were collected from pregnant women who were non-infected and infected with Toxoplasma Condii whose cases were diagnosed by female diagnosticians Obstetrics Hospital / Consultative Section; whose ages ranged (20-45) years; whereas 10 milliliters of the venious blood were taken and put in a plain tubes then left for clotting for 10 minutes in a water bath at $37 \circ C$; thereafter a centrifugal was made at speed 5000 rpm to get the blood serum to be maintained at $-20 \circ C$ for estimation the biochemical variables. (Tietz; 1999).

Estimation of SuperOxide Dismutase (SOD)

SuperOxid Dismutase (SOD) was estimated by using the modification method; Tetrazolum Blue Nitro/Riboflavin Modified. (Beyer *et. al.,* 1991).

Estimation of Peroxidase

A colouring method was used for estimation the total Peroxidase efficiency by using the material called amino antipyrine-4 which interacts with hydrogen peroxide with existence of peroxidase enzymes to give pink complex; whereas the absorbance of which was estimated at 510 nm resulting from decomposition of hydrogen peroxide (Tinder; 1996).

Estimation of Glutathione-S-Transferase

The enzyme was estimated according to the method used by the researchers (Habig *et. al.,* 1974).

Estimation of Lactate Dehydrogenase and Arylesterase

Lactate Dehydrogenase was estimated by using ready equipment from SRYBio company; and an Aryle estrase according to the method of (Thomas *et. al.,* 2000).

Estimation of Acetyl Choline Esterase

Electrometric Techniques was used to estimate Acetyl Choline Esterase. (Mohammed & Omar, 1982).

Results and Discussion

The results showed on table (5) highly significant effect for each of: Peroxidase, Glutathione-S-Transferase, Lactet Dehydrogenase LDH, and Acetyl Choline Esterase in the serum of the pregnant women who are infected and non-infected through the periods of pregnancy; besides the interaction among the cases and periods of pregnancy at the probability level estimated $P \geq 0.01$. But; Superoxid Dismutase (SOD) and Arylesterase did not show a significant effect in the serum of the pregnant women. According to the results appeared; it was noted a significant increasing in each of Peroxidase and Glutathione-S-Transferase. Lactate Dehydrogenase LDH, and Acetyl choline Esterase in the serum of the pregnant women who are infected with *Toxoplasmosis* reaching 22.55 ± 16.66, 24.35 ± 13.42, 279.87 ± 129.38, IU/L, 0.69 ± 0.20 μmol/L in comparison with their counterparts the pregnants who are non-infected; whereas Superoxide Dismutase and Arylesterase decreased ; that the values did not reach at the statistical significant.

Therefore; results of the study conducted on the interaction among the cases and periods of pregnancy showed an significant increasing in: Superoxide dismutase, Peroxidase, Lactate dehydrogenase LDH, and Arylesterase reaching $0.09 \pm 0.001 \pm 0.09$ μmol/L, 33.75 ± 19.71, 339.06 ± 15.09 , 158.001 ± 12 IU/L in the serum of the pregnant women caused in the period of pregnancy (1-3) months; then the activity of Glutathione-S-transferase through period of pregnancy increased (3-6) months reaching 26.21 ± 13.2 IU/L. but; activity Acetyl choline esterase decreased in the serum of the pregnant women infected with disease in the period of pregnancy (6-9) months in comparison of their non-infected counterparts reaching 0.772 ± 0.17 μmol/L.

Thus, activity increasing of some enzymes may belong to increasing of the free radicals production as a result of the case that to loss of balance state among levels of anti-oxidations and the reactive oxygen species; that generated a state of oxidative stress; then emphasized the necessity of giving anti-oxidation like the vitamins such as C and E (Vasdev *et. al.,* 2006), (Senti *et. al.,* 2003), and (Mullah Alo, 2011).

Whereas reason for decreasing in other enzymes activity belongs to effect of oxidative stress especially through the advanced stages of the pregnancy on the enzymatic anti-oxidant and changing of these enzymes like Glutathione peroxidase GPX and Glutathione reductase GR; accordingly this go with previous study results conducted on the blood- pressure patients; whereas a decreasing activity of some enzymes was noted in comparison with the control group. (Rodrigo *et. al.,* 2007, Al Sabawi,2009)

Table1.Show the average and standard deviation for enzymes in serum of infected and non infected women

Parameters	Mean ±SD µmol/L	Mean ±SD U/L				Mean ±SD µmol/L	
	Acetyl choline esterase	Arylester ase	Lactet dehydroge nase	Glutathion e-S-Transfera se	Peroxida se	Superoxide Dismutase	NO
non-infected pregnant women	0.67±0.13 B	147.91±11.14 A	109.03±6.22B	13.97±7.31 B	7.84±3.43B	0.06±0.03A	225
infected pregnant women	0.69±0.20 A	147.22±22.10 A	279.87±129.38A	24.35±13.47A	22.55±16.66 A	0.05±0.8A	225
	Interference between infection and different pregnancy periods						
non-infected(1-3)months	0.68±0.05 B	151.81±17.37B C	107.71±4.35C	7.11±2.77 D	7.58±3.07D	0.005±0.001 C	75
non-infected(3-6)months	0.54±0.12 D	142.62±4.52D	109.12±7.14C	19.88±6.01 B	6.86±4.10D	0.006±0.001 BC	75
non-infected(6-9)months	0.77±0.09 A	149.30±2.77C	110.25±6.61C	14.92±5.84 C	9.07±2.59D	0.007±0.001 B	75
infected(1-3)months	0.61±0.18 C	158.01±12.46 A	339.06±15.09 A	22.78±13.08 AB	33.75±19.71 A	0.09±0.001 A	75
infected(3-6)months	0.70±0.21 B	127.44±18.70E	258.28±12.48 B	26.21±13.02 A	19.99±14.17 B	0.003±0.001 D	75
infected(6-9)months	0.77±0.17 A	156.36±19.28 AB	243.06±83.82 B	24.04±14.24A	14.07±6.90 C	0.003±0.001 D	75

Within columns, means having the same letters don't differ significantly at p≤ 0.05 probability level

Activity of Enzymes in the Placentae of Infected and Non-Infected Pregnant Women

Clarifying results showed on table (2) indicate to existence of high significant effect in activity of Glutathione - S- transferase and Arylesterase in the placentae of the pregnant infected and non-infected women at the $P<0.01$. Also; according to what the clarified studies showed on table (2); it was noted that there was a significant increasing in activity of: Superoxide dismutase, Glutathione-S-transferase, Lactate dehydrogenase, and Acetyl choline esterase in placentae of the pregnant infected and non-infected women through period of pregnancy (6-9) months. Also; it was noted that each of Lactate dehydrogenase, Acyte choline esterase did not reach at that statistical significant; whereas the values estimated $0.010 ± 0.001$ µmol/L, $10.13 ± 3.90$, $88.37 ± 6.13$ IUL $0.140± 0.05$ µmol/L respectively.

Whereas Peroxidase decreased in the placenta of the pregnant infected and non-infected women through period of pregnancy (6-9) months that reached $1.85 ± 0.28$ IUL ; but Arylesterase in placentae of the pregnant infected and non-infected women through period of pregnancy (1-3) months; whereas reached $91.62 ± 0.01$ IUL. Perhaps the reason for that is attributed to anti-toxoplasmosis drugs taken by the pregnant infected women through period of pregnancy that may play a role in increasing the activity of anti-oxidant; whereas sparamycin, one of the drug used in treatment of toxoplasmosis, its concentration in the placenta ranged (3-5) times higher than its concentration in the other tissues (Stray), 1999), (Mulla Allo, 2011), or increasing the oxidation in large quantities inside the body of the pregnant infected women causing certain increasing in production the harmful compounds resulting from oxidation the fats or proteins; then increasing in activity of enzyme in taking off the

poisonous compounds inside the body by way of Glutathione-S-transferase which is called also Detoxification Enzyme.

Besides; results of this study went with the results offered by many researchers like: (Al-Gubori *et. al.*, 2004; Kaynar *et. al.*, 2005, and Mullah Allo, 2011).

Also; we note existence of non-significant decreasing in activity of Lactate dehydrogenase in placentae of the infected women through various stages of pregnancy in comparison with the non-infected placentae; whereas the results of these studies agree with the study of (Dawood, 2007); also with results of many researchers like: (Al-Gubori *et. al.,*., 2004; Kaynar *et. al.,*., 2005; and Mullah Alo, 2011).

Thus, the results of this study agree with results of previous of other diseases; whereas it was noted an important increasing as to efficiency of other enzymes came synchronous with other diseases such as cancerous tumours. (Al-Abachi, 2006).

Thereafter, enzymes in the serum of healthy non-infected with any disease individuals were estimated; and it was noted also that some of them are affected came and decreased with old-aged according to sex, variety of ecological factors, difference in nutrition, pattern of life, in addition to genetic factors and mutations which affect on the azo enzymes. (Nevin *et. al.,* 1996). Also; that was happened with those patients caused with certain diseases like: arteriosclerosis, blood- pressure, and diabetes that caused decreasing in activity of oxidative stress processes with the patients (Al-Rubaiae, 2006). Also; they agree with results of previous studies conducted on those patients who are caused with blood pressure; whereas it was noted decreasing in activity of enzymes in comparison with the control group. (Rodrigo *et. al.,* 2007; Al-Sabawi; 2009). Besides; they agree with results of studies related to other diseases like those patients who are caused with Rheumatoid arthritis drugs; whereas the activity of enzyme decreased after treatment using one medicine with those who were treated using common medicine in comparison with those who were infected but not treated. (Al-Jammas, 2006), with patients caused with amnesia who were treated with Vitamin E which increases composition of nervous carrier in nervous clashes places like Acetyl choline through staying of nerves in the brain area (Morris; 2002).

Table 2. Show the average and standard deviation for enzymes in placentae of infected and non-infected women

Placentea in pregnancy periods	Mean ± SDµmol/L	Mean ± SDU/L				Mean ± SDµmol/L	
	Acetyl choline esterase	Arylesterase	Lactet dehydrogenase	Glutathione-S-Transferase	Peroxidase	Superoxide Dismutase	N0.
non-infected placentae	0.10±0.05A	74.62±9.64B	80.14±20.11A	5.11±1.80B	18.63±1.99A	0.008±0.001A	6
infected(1-3)months	0.14±0.01A	91.62±0.01A	76.90±0.01A	7.18±0.01B	5.80±0.01AB	0.004±0.001B	6
Infected3-6)months	0.10±0.01A	69.78±0.01B	70.42±2.21A	4.12±2.22B	3.08±0.69B	0.005±0.001B	6
Infected(6-9)months	0.14±0.05A	73.12±2.49B	88.37±6.13A	10.13±3.90A	1.85±0.28B	0.01±0.001A	6

Within columns, means having the same letters don't differ significantly at p≤ 0.05 probability level

References

Al-Abachi S ZM (2006) Enzymatic and other biochemical changes in blood serum and tissues of benign and malignant brian cancer. Ph.D. Thesis,College of Science. Mosul University.

AL-Gammas ,M.H.A.(2006) Study of physiological and biochemical variables of blood and articular fluid for some patients with pulmonary arthritis. . M.Sc. Thesis .College of Sciences, University of Mosul. Iraq.

Al Gubory KH; Bolifraud P; Cermain GN; Cole A; Ceballos Bico TI (2004) Antoxidant enzymatic defence systems in sheep Corpus luteum throughout pregnancy. Soci. Repr.Fert.,128:767-774.

AL- Nuaimy .Y.S.A.(2010) Comparison of latex and polymerase sequencing methods in the diagnosis of *Toxoplasma gondii* in Nineveh province. M.Sc. Thesis .College of education, University of Mosul. Iraq.

AL-Robaiey ,.R . F.G.M. (2006) Isolation and Studing Arylesterase in Blood Serum and Its Relation with Atherosclerosis in Mosul. M .Sc. Thesis in chemistry. College of Sciences, University of Mosul.

AL-Sabaawy , OM . (2009) Measurement of lipid peroxidation irdices and some antioxidations in both blood and sweat fluid of hypertensive patients. M.Sc. Thesis in Biochemistry ,College of Sciences, University of Mosul.

AL Khaffaf, F.H.O.(2001) Isolation and study of epidemiological seroprevalence of toxoplasmosis age in Nineveh province . M.Sc. Thesis .College of Sciences, University of Mosul. Iraq.

Ambrosio G and Tritto I (1999) Reperfusion injury experimental evidence and clinical implications. Am.Heart.138:569-575.

Beyer W;Mlay J and Fridovich I (1991) Superoxide dismutase. Prog nuclic acid Res.Mol.Biol.,40:221-253.

Bartosikova L; Necas J; Suchy V; Kubinova D; Vesela L and Benes L (2003) Effect of morine in alloxan-induced diabetes mellitus in the laboratory rat. Acta Vet.,72:191-200.

Buxton D (1983) Toxoplasmosis. In martin WB (ed.) Diseases of sheep. Black well scientific Publication, Oxford.

Dawood M N (2007) Study of liver function tests in non pregnant women with toxoplasmosis. M.Sc. Thesis ,College of Medicine University of Mosul.

Dubey JP and Livington JR (1986) *Sarrcocystis capracanis* and *Toxoplasma gondii* infection in range goat from Texas. Am. J.Vet.,47(3):523-524.

Dubey JP (2003) *Toxoplasma gondii*. Vet. Parasitol., 86:235-248.

Gleeson M; Bishop NC; Blannin AK;Burns VE;Lancaster GI; Robson –Ansley P;Walsh NP and Whitham M(2006) Immune function in sport and exercise. Elsevier Churcill Livingston. China., 22,296.

Habig W H;Pabst MJ and Jakoby W B (1974) Glutathione S- transferase. the frist enzymatic step in merca pturic acid formation. J. Biochem., 249(22):7130-7139.

Kabaroglu C; Mutaf I; Boydak B; Ozmen D; Habif S; Erdener D; Polritader Z and Bayindir O (2004) Associatation between serum paraoxonase activity and oxidation stress in acute coronary syndromes . Acta Cordiol.,59(6):606-611.

Kaynar H; Meral H; Turhan H; Keles M; Celik G and Acay F (2005) Glutathione peroxidase, glutathione-S-Tansferase, catalase, xanthine oxidase Cu- Zn superoxide , dismutase activities, total glutathione, nitric oxide, and malondialdehyde levels in erythrocytes of patients with small cell and non cancer.

Liu   J (2003) Classic Glutathione Peroxidase. Free Radical and Radiation Biology Program. The University of Iowa City, IA.52224-228.

Michael L (2001) The Peroxy Radical. Department of Chemistry, University of Iowa, Iiwa City, IA.52242.

Mohammad   FK and Omer St.V.E.V (1982) Modifications of michel's electrometric method for rapid measurement of blood cholinesterase activity in animals:a minireview. Vel.Hum. Toxicol.,24:119-121.

Morris   MC ;Evans DA; Bienuas JL;Tangney CC and Wilson RS (2002) Vitamin E and congnitive decline in older persons. J. Arch. Neural.,59:1125-1132.

Mla-ALw .F. Y.H (2011) Oxidative stress for pregnancy in the Ninawa governorate. M .Sc. Thesis in Biochemistry. College of Sciences, University of Mosul.

Nevin D; Zambon A; Furlong CE; Richter R J; Humbert R; Hokonson JE and Brunzell JD (1996) Paraoxonase genotyper, lipoprotein lipase activity and HDL. Arteriosclar. Thromb. Vasc.Biol.,16:1243-1249.

Prescott LM; Harley JP; Klein DA (2002) Microbiology (5th ed.). McGraw Hill. New York.

Remington JS; McLeod R; Thulliez P; Desmants G (2000) Toxoplasmosis: In   Remington JS; Klein JO Infectius diseases of the fetus and new born infants". (5th ed.) .WB Saunders Rodrigo R; Prat H and Passalacqua W (2007) Relationship between oxidative stress and essential hypertension .J.Cardiovasc Pharmacol.,46:1159-1167.

Robinson IP; Yamka RM and Friesen K G (2008) Food with lipoic acid and elevated levels of vitamin E and vitamin C correlate with whole blood antioxidant concentrations and may protect geriatric dogs form oxidative stress. Int. J. Appl. Res. Vet. Med., 6(2):93-100.

Rodrigo R; Prat H and Passalacqua W (2007) Relationship between oxidative stress and essential hypertension .J.Cardiovasc Pharmacol.,46:1159-1167.

Senti   M; Tomas M; Fito M; Weinbernner T; Covas M; Sala J; Masia R and Marrugat J (2003) Antioxidant paraoxonase 1 activity in the metabolic syndrome J. Clin. Endocrinol.Metab.,88(11):5422-5426.

Sharma   SP and Dubey JP (1981) Quantitative survival *Toxoplasma gondii* tachyzoites and bradyzoites in pepsin and trypsin solution. Ann. J. Vet. Res., 42:128-130.

Stahl   W and Seis H (1997) Antioxidant defense vitamin E and C and carotonoids. Diabetes,46:14-18.

Stary   PB (1999) Treatment of toxoplasmosis in pregnant mother and new born . Child. Scand. J. Infect. Dis.,84:23-31.

Tietz NW (1999) Textbook of Clinical Chemistry. (3rd edn.) W.B.Saunders Company, Philadephia,1239-1250.

Tomas M; Senti M; Gareia- Faria F; Vila J; Torrents A;Govas A and Marrugat J (2000) Effect of simvastatin therapy on paraoxonase activity and related lipoprotein in familial hypercholestrolemic patients. Arteriosclar. Thromb. Vasc.Biol.,20:2113.

Trinder P (1966) Determination of glucose in blood using glucose oxidase with an alternative oxygen accepted. Am. Clin. Biochem.,6:24.

Vasdev   S; Gill VD and Singal PK (2006) Madulation of oxidative stress- induced hypertension and atherosclerosis. Exp. Clin.Cardiol.,11(3):206-216.

Author Information

Layla A. Mustafa
University of Mosul
Mosul, Iraq
Contact E-mail: anmar1930@yahoo.com

Muna .I.Ibraheem
University of Mosul
Mosul, Iraq

A Correlation Study of an FEA Method Developed for Heavy Duty Driveshaft Applications

Muzaffer KASABA
Tirsan Kardan A.Ş

Sedat TARAKCI
Tirsan Kardan A.Ş

Efe ISIK
Tirsan Kardan A.Ş

Onur AKKAS
Tirsan Kardan A.Ş

Abstract: The driveshafts are responsible for transmitting power and rotational movement from the engine to the rear axles. In order to fulfill high torque transmission requirements, driveshaft components are generally produced from steel by hot forging process. For steel components, reduction of the weight is limited by geometrical alterations due to boundary conditions, functionality requirements etc. For this reason, verification method of design iterations must be conducted accurately. Although verification on physical component is much reliable, regarding high material, die, tooling and machining costs an alternative verification method is needed. Generally finite element analysis (FEA) is preferred as design verification method. The major phenomenon is to build the simulation as similar as possible with real conditions in order to have accurate results. In this study, an FEA method was developed for design verification of heavy duty driveshafts. The results from FEA analysis of heavy duty driveshaft were compared with the results from the bench tests and a correlation study was conducted to reveal the consistency of developed FEA method.

Keywords: Finite element method, Data acquisition, Stress, Strain

Introduction

Today, the expectations in the automotive industry are increasing day by day. Accordingly, the lightweight driveshaft design and implementation in drivetrain systems is one of the biggest expectations. Increasing ecological concerns have led automobile manufacturers around the world to seek new solutions. Developing lightweight but high-strength components for ground vehicles that will led to less fuel consumption without compromising safety and comfort is one of the major goals of automobile manufacturers.

For steel components, reduction of the weight is limited by geometrical alterations due to boundary conditions. Therefore, reduction of the weight should be carried out very carefully. Verification of the developed lightweight designs is the most important step of the studies. Although design verification by experimental methods is the best solution for validating the design, it has some disadvantages like test costs, long testing durations and labor expenses. For these reasons, there is a need to create a finite element model which can be used in place of the experimental method and simulate the actual state of the driveshaft in the most appropriate way.

Within the scope of the study, the main technical characteristics of the relevant cardan shafts (yield point, ultimate torsional strength, torsional stiffness value) were determined. Then, finite element models were established, and non-linear static analyzes were performed according to the determined mechanical properties.

After the non-linear FE analysis, stress distributions on the heavy duty driveshaft were revealed. In parallel, data acquisition studies were conducted. By performing static torsion test, the strain data from the each sub-components of the heavy duty driveshafts were collected and the regions where the stress lines and points were concentrated revealed. Finally, finite element analyzes results and the test results were compared and the results were presented with percentage deviations.

Finite Element Method

The finite element method (FEM), or finite element analysis (FEA), is a computational technique used to obtain approximate solutions of boundary value problems in engineering. Boundary value problems are also called field problems. The field is the domain of interest and most often represents a physical structure. (Kasaba, 2017)

The field variables are the dependent variables of interest governed by the differential equation. The boundary conditions are the specified values of the field variables (or related variables such as derivatives) on the boundaries of the field. For simplicity, at this point, we assume a two-dimensional case with a single field variable $\varphi(x, y)$ to be determined at every point $P(x, y)$ such that a known governing equation (or equations) is satisfied exactly at every such point. (Kasaba, 2017)

A General procedure of finite element analysis is as follows:

Preprocessing

        Define the geometric domain of the problem.

        Define the element type(s) to be used.

        Define the material properties of the elements.

        Define the geometric properties of the elements (length, area, and the etc.)

        Define the element connectivities (mesh the model).

        Define the physical constraints (boundary conditions). Define the loadings.

Solution

        Computes the unknown values of the primary field variable(s)

        Computed values are then used by back substitution to compute additional, derived variables, such as reaction forces, element stresses, and heat flow.

Post processing

        Postprocessor software contains sophisticated routines used for sorting, printing, and plotting selected results from a finite element solution.
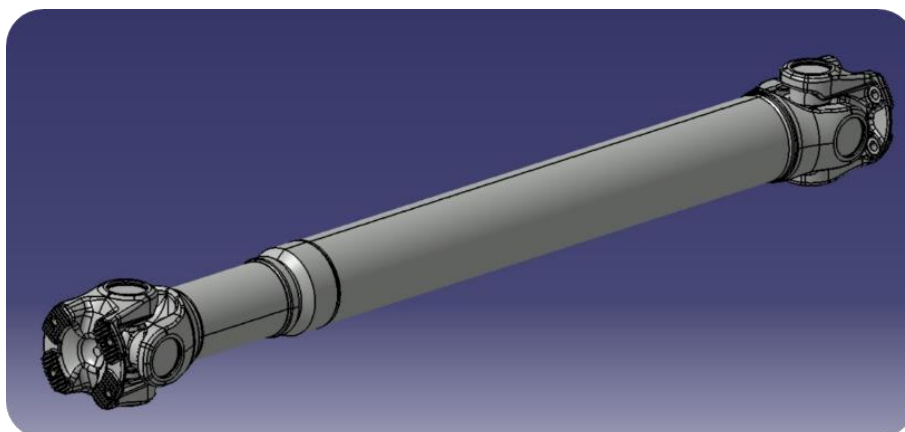
Figure 1. CAD Model of the Driveshaft

The driveshaft was modeled by using Catia V5 2014 software as shown in Figure 1. After the solid model was obtained, a finite element model was generated by using pre-processing steps as shown in Figure 2, and a non-linear finite element analysis was performed by considering the vehicle interface restrictions and contact definitions. The boundary conditions are given in Table 1.

However, in the design stage, the additional costs such as equipment, prototype and personnel required for the implementation of the experimental method, as well as time loss occur. For these reasons, there is a need to create a finite element model which can be used in place of the experimental method and simulate the actual state of the driveshaft in the most appropriate way. In this study, a finite element analysis method has been developed to meet these expectations.
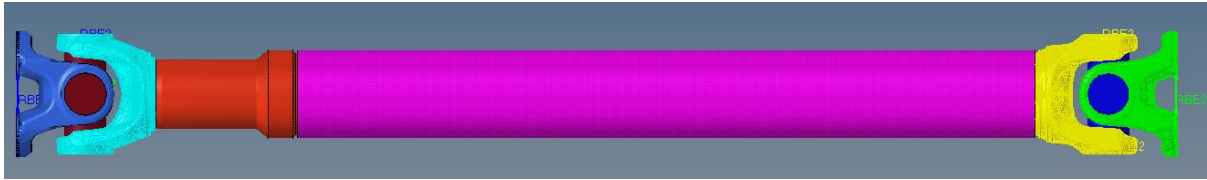
Figure 2. Finite Element Model

Table 1. Boundary conditions

Fixed B.C	Moment
B.C 1,2,3,4,5,6 (fixed) RBE2s are bounded to master node	B.C 2,3,5,6 (fixed) RBE2s are bounded to master node
	Moment is bounded to master node (RBE2)

Data Acquisition Study

In order to specify the strain levels on specific areas of driveshaft sub-components at different levels of torsional loads, the driveshaft test sample was installed on a static torsion test bench which is depicted in Figure 3. Before the installation of the test sample onto the test bench, the test sample was instrumented by following steps:

1. Data collection regions were determined.
2. Surface was prepared with handle sandpaper.
3. Adhesive was applied to the surface which was cleaned with alcohol and degreaser and rosette type strain-gauge was bonded.
4. Terminals were placed on the paper tapes.
6. The quarter bridge connection was generated by soldering the strain gauges wires onto the terminals.
7. Connections checked with ohmmeter (120 Ω).
8. Strain-gauge was covered with liquid silicon for protection.

Static torsion test was conducted at different levels of torque loads and at each torque load strain data of specific areas on driveshaft were recorded for stress calculations.
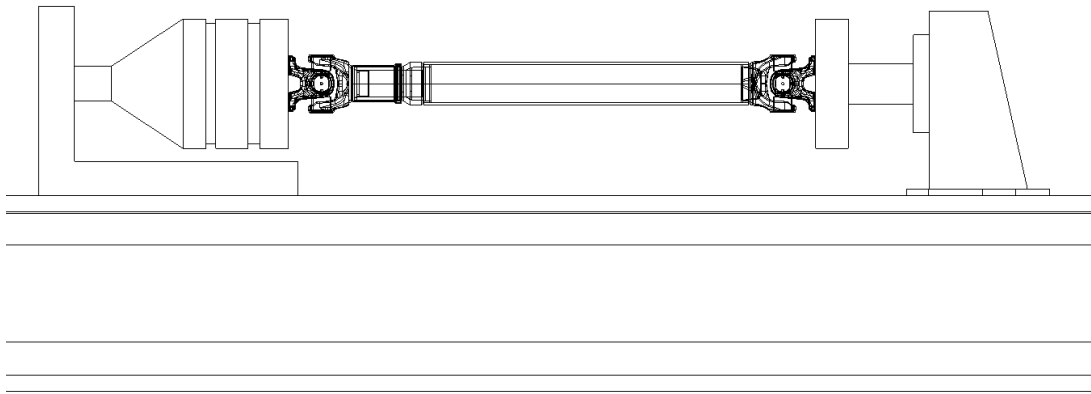
Figure 3. Static torsion test system

Results

Within the scope of this study, it was aimed to generate stress map of heavy-duty driveshaft by measuring strain at specific points / areas (Figure 4) and compare the results with the stress values obtained from finite element analyzes. After installation of test sample onto the test bench, LMS Bridge calibration was done and then static torsion test were performed in clock-wise and counter clock-wise directions with 500 Nm load steps up to 20 kNm torsional load. During static torsion test, strain data was collected using 21 different channels at the specified torque levels from the driveshaft sub-components. By using strain data, equivalent stress (Von Mises) was calculated. The strain values obtained from the driveshaft sub-components are presented in Figure 5.
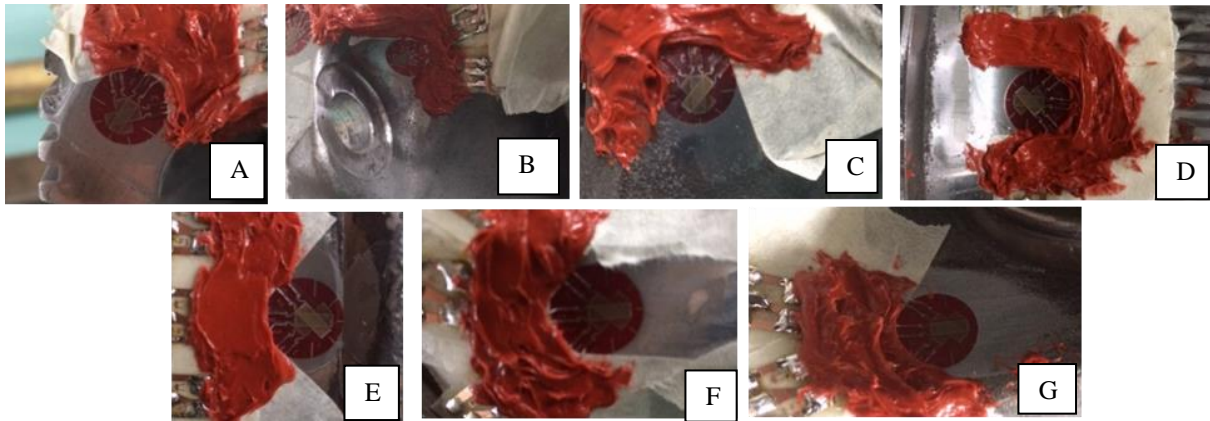
Figure 4. Strain gauge points on instrumented driveshaft test sample
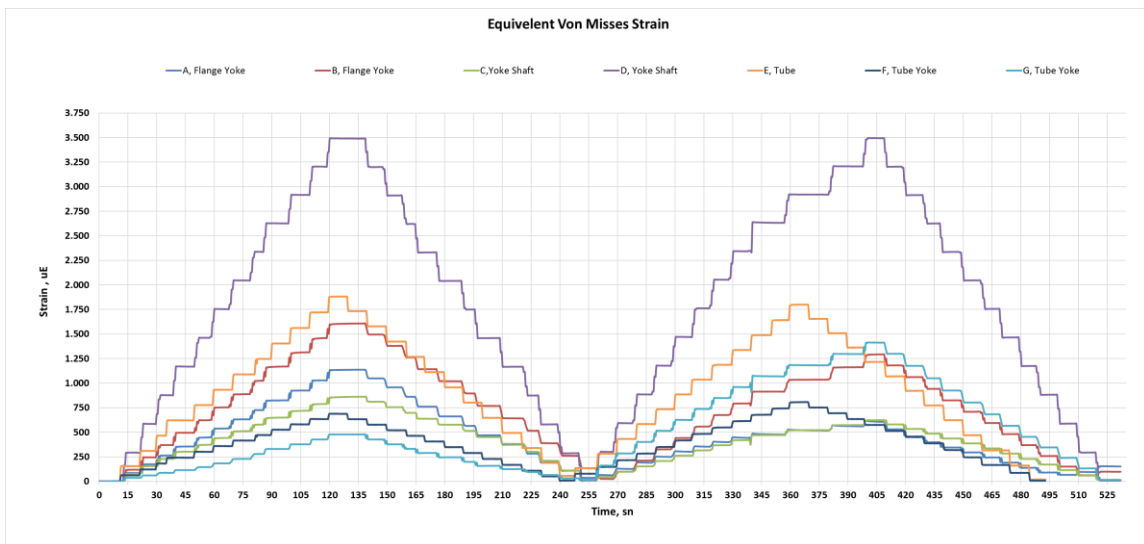
Figure 5. Data acquisition strain results

Finite element models are constructed in accordance with the testing conditions. All driveshafts were analyzed under 20 kNm torque load. The FEA results (Figure 6) are compared with data acquisition results and the comparison is given in Table 3.

When the percentage deviation values were examined in Table 3, it was determined that the difference between the test results and the finite element analysis results did not exceed 10%.
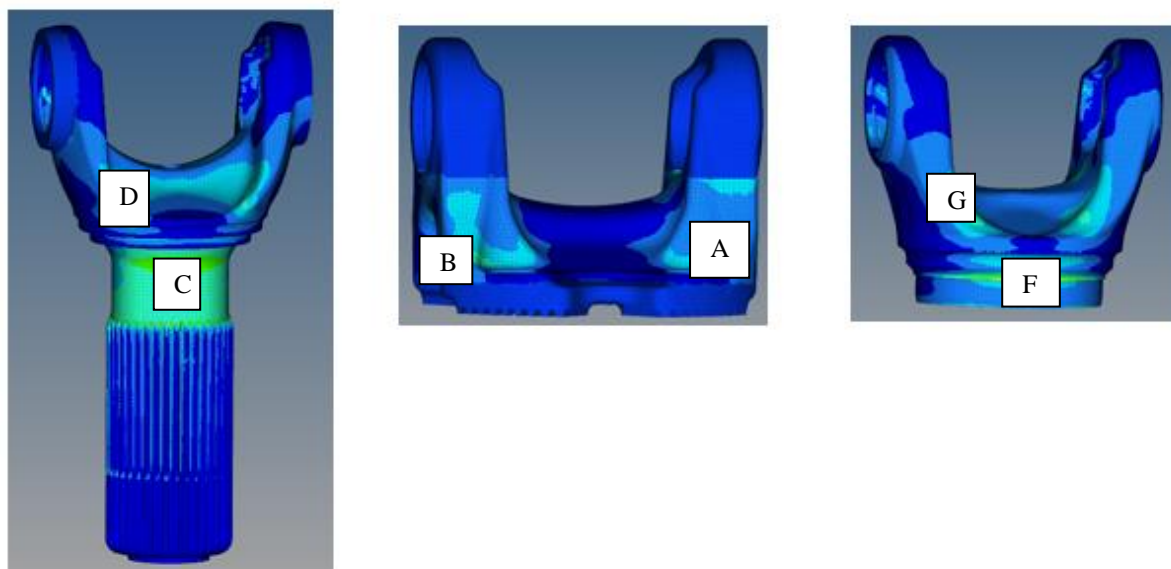
Figure 6. Finite element analysis results

Table 3. Static torsion test & fea results comparison table

	A	B	C	D	E	F	G
% Deviation	9,78	6,29	10,32	3,74	7,67	8,16	9,15

Conclusion

As a result, it has been shown that proposed non-linear finite element model can be used safely without the need for a driveshaft test sample in the design stages with a maximum allowable deviation of 10 %. In this way, production and test costs will be reduced which will create a competitive advantage within the market.

Recommendations

This study is conducted for heavy duty driveshafts only, therefore our study can be extended to all driveshaft product families in the future work.

Acknowledgements or Notes

We would like to thank Tirsan Kardan R & D Center and Test Center for their support in the studies.

References

Kit, H., Khaj, M., & Mykhaskiv, V. (1996). Analysis of dynamic stress concentration in an infinite body with parallel penny-shaped cracks by BIEM. Engineering Fracture Mechanics, 55(2), 191–207.

Noda, N. (1995). Stress concentration factors for round and flat test specimens with notches. International Journal of Fatigue, 17(3), 163–178.

Bhattacharya, S., & Kumar, A. (1995). Modelling of rotational factor in notched bend specimen under general and local yield situation. Theoretical and Applied Fracture Mechanics, 24(1), 33–46.

Davies, D., & Jenkins, S. (2012). Influence of stress and environment on the fatigue strength and failure characteristics of case carburised low alloy steels for aerospace applications. International Journal of Fatigue, 44, 234–244.

Shen, W., & Choo, Y. S. (2012). Stress intensity factor for a tubular T-joint with grouted chord. Engineering Structures, 35, 37–47.

Cheng, B., Qian, Q., & Zhao, X.-L. (2015). Stress concentration factors and fatigue behavior of square bird-beak SHS T-joints under out-of-plane bending. Engineering Structures, 99, 677–684

She, C., & Guo, W. (2007). Three-dimensional stress concentrations at elliptic holes in elastic isotropic plates subjected to tensile stress. International Journal of Fatigue, 29(2), 330–335.

Ndiaye, A., Hariri, S., Pluvinage, G., & Azari, Z. (2007). Stress concentration factor analysis for notched welded tubular T-joints. International Journal of Fatigue, 29(8), 1554–1570.

Yu, P., Guo, W., She, C., & Zhao, J. (2008). The influence of Poisson's ratio on thickness-dependent stress concentration at elliptic holes in elastic plates. International Journal of Fatigue, 30(1), 165–171.

Zheng, M. (1997). Analysis of the stress concentration factor for a shallow notch by the slip-line field method. International Journal of Fatigue, 19(3), 191–194.

Fielder, R., Millwater, H., Montoya, A., & Golden, P. (2019). Efficient estimate of residual stress variance using complex variable finite element methods. International Journal of Pressure Vessels and Piping, 173, 101–113.

Paroissien, E., Lachaud, F., Silva, L. F. D., & Seddiki, S. (2019). A comparison between macro-element and finite element solutions for the stress analysis of functionally graded single-lap joints. Composite Structures, 215, 331–350.

Hu, H., Zou, Z., Jiang, Y., Wang, X., & Yi, K. (2019). Finite element simulation and experimental study of residual stress testing using nnlinear ultrasonic surface wave technique. Applied Acoustics, 154, 11–17.

Kasaba, M. (2017). Numerical Analyses Of Structural Acoustic Systems Based On Monte Carlo Simulations And Modal Impedances. Graduate School of Natural and Applied Sciences of Dokuz Eylül University

Author Information

Muzaffer Kasaba
Tirsan Kardan A.Ş
Organize Sanayi Bölgesi 3. Kısım M.Kemal Bulvarı No:15
Manisa, 45030 Türkiye
Contact E-mail: *m.kasaba@tirsankardan.com.tr*

Sedat Tarakci
Tirsan Kardan A.Ş
Organize Sanayi Bölgesi 3. Kısım M.Kemal Bulvarı No:15
Manisa, 45030 Türkiye

Efe Isik
Tirsan Kardan A.Ş
Organize Sanayi Bölgesi 3. Kısım M.Kemal Bulvarı No:15
Manisa, 45030 Türkiye

Onur Akkas
Tirsan Kardan A.Ş
Organize Sanayi Bölgesi 3. Kısım M.Kemal Bulvarı No:15
Manisa, 45030 Türkiye

Effects of Crude Aqueous Extract of the Palmito on some Biochemical Parameters in Serum of Healthy Rats

Saba Z. AL-ABACHI
University of Mosul

Sameer M. AL-GORANY
Middle Technical University

Abstract: This study was designed to evalute the protective effects of the cold crude aqueous extract of palmito and in different doses (100, 250, 500 mg / kg BW) on some biochemical parameters, including: hepatic enzymes, (alkaline phosphatase ALP, alanine aminotransferase ALT and aspartate aminotransferase AST), total protein, albumin, globulin, bilirubin (total, direct and indirect) and total lipid in the blood serum of healthy adult rats and compared with control group treated with distilled water orally, daily for two weeks. A (24) white adult male rats were used aging between (12-14 weeks) and weighting (215.3 ± 9.7 gm). They were divided randomly, each of which contain (6) animals. The results showed that the palmito aqueous extract led to the high significant of the liver enzymes activity, and in the concentration of total protein, albumin, globulin and in the concentration of total lipid, while led to a reducing in the concentration of total, direct and indirect bilirubin in the blood serum of healthy adult rats when compared with control group.

Keywords: Bilirubin, Hepatic enzyme, Liver, Palmito, Total protein

Introduction

Medicinal plants, also called medicinal herbs, are plants or parts of a plant, have been discovered and used in traditional medicine practices since prehistoric times. Plants synthesis hundreds of chemical compounds for functions including defense against insects, fungi, diseases, and herbivorous mammals. Numerous phytochemicals with potential or established biological activity have been identified. However, since a single plant contains widely diverse phytochemicals, the effects of using a whole plant as medicine are uncertain. Herbal medicine products are dietary supplements that people take to improve their health, but some of these products can cause health problems, while others do not have any effectiveness. And has taken a great place, especially in recent years, because people believe that herbal medicines have no side effects, as well as being cheap and available locally (Belay, et al., 2016 ; Thiyagarajan and Venkatachalam, 2012).

Palmito: heart of palm is a vegetable harvested from the inner core and growing bud of certain palm trees . Harvesting of many uncultivated or wild single-stemmed palms results in palm tree death. When harvesting the cultivated young palm, the tree is cut down and the bark is removed, leaving layers of white fibers around the center core. During processing, the fibers are removed, leaving the center core or heart of palm (Masoomeh et al., 2013).

The palmito are commonly medical used in supplements to improve prostate health, anti-cancer, balance hormone levels, and prevent hair loss in men (Masoomeh et al., 2013). It's also associated with other benefits, including decreased inflammation and improved urinary function. Also, it is protect the stomach, kidney and liver (Baliga et al., 2011).

The aim of this research is to study the effect of the cold crude aqueous extract of palmito in different doses on some biochemical parameters, as (ALP, ALT and AST), total protein, albumin, globulin, bilirubin (total, direct and indirect) and total lipid in the blood serum of healthy adult rats.

Materials and Methods

Preparation of cold crud aqueous palmito extract

The fresh date palm (type Al-Kastawi) was cut off which were collected from Baaquba city/ Dyala/ Iraq. The plant was positively identified by Biologist literature in Biological department /College of Science /University of Mosul / Iraq. the leaves and fibers were peeled from the base of the seed. After the cleaning and washing with tap water, the plant was cut into small parts. About (300 g) of the palmito was crush and mix with cold distilled water (1/3 w/v) with continuous stirring for one hour (Robyt and White, 1987). Then the mixture was subjected to the ultrasonic device and filtrated through glass woods, and separate the extract with a cooled centrifuge for 20 minutes at a speed of 33520 xg to obtain a clear extract, the volume of filtrate was measured, and then estimated the amount of protein by modified Lawry (Schacterle and Pollack, 1973). The volume of crude extract were concentrated by the lypholyzer device.

Experimental animals

In the study, (24) healthy male adult albino rats ageing between (12 and 14 weeks) and the main of weighting between (215.3 ± 7.9 g) were obtained from the animal house in the medicine faculty / Mosul University / Iraq. Animals were randomly distributed and placed in special plastic cages (10 x 20 x 40 cm) covered with stainless steel wire, (6) animals were placed in each cage. Rats were housed under standard laboratory condition, light and dark cycles of 12h, in a polypropylene cages and allowed free access to feed and tap water under strictly controlled pathogen free conditions with room temperature (25±2ºC), humidity (50±5%).

Experimental design

The experiment showed the effect of different concentrations of the crude aqueous extract of the plant on some of the biochemical variables in the healthy adult rats. In this experiment, 24 samples were distributed into four groups and in equal numbers, as follows:

Group I: Received (0.5ml/kg) body weight of distilled water orally for 2 weeks and used as the normal control. The animals in all groups were killed by anesthetic ether on the day 15.

Group II: Received (0.5 ml/kg) body weight of cold crude aqueous extract of the palmito plant with a concentration of (100 mg / kg) orally by gavages tube daily for two weeks.

Group III: Received (0.5 ml/kg) body weight of cold crude aqueous extract of the palmito plant with a concentration of (250 mg / kg) orally by gavages tube daily for two weeks.

Group IIII: Received (0.5 ml/kg) body weight of cold crude aqueous extract of the palmito plant with a concentration of (500 mg / kg) orally by gavages tube daily for two weeks.

Blood collection

At the end of the experiment, anesthetize the animals for a few seconds and then draw the blood from all groups weekly from the Orbital sinus puncture using special capillary tubes, left stand in serum tubes for (30 minutes) to be coagulated. Serum samples were collected by centrifugation at (3000 rpm) for (20 minutes) at room temperature. The clear, non-haemolysed sera was separated and stored at (- 20 C°) for measurements of biochemical analyses of liver functions (Atta et al., 1983).

Estimation of serum biochemical parameters

-The ALT and AST activities were measured spectrophotometrically by using the method of Reitman and Frankle (Anderson and Cockayne, 1993).
-ALP was measured by the method devised by Bowers and McComb, which allows calculation of ALP activity basing on the molar absorptive of P-nitrophenol (Tietz, 1999).

-Total serum protein was measured by Biuret method using kit from BIOLABO (Bishop et al., 2005) and serum albumin was determined quantitively by colorimetric method used bromocresol green (Doumas et al., 1971).
-The total proteins minus the albumin gives the globulin.
-The total and direct bilirubin concentrations were calculated by the colorimetric method used sulfanilic acid method (Walters and Gerarde,1970).
-The indirect bilirubin concentrations was estimated by the equation:

$$\text{Bilirubin indirect Conc.} \atop \mu\text{mol/L} = \text{Total bilirubin Conc.} \atop \mu\text{mol/L} - \text{Bilirubin direct Conc.} \atop \mu\text{mol/L}$$

-The total lipid determined by heated the serum with concentrated sulphuric acid, then react the mixture with phosphovaniline reagent (Toro and Ackermann, 1975).

Statistical Analysis

The data presented in this investigation were expressed as the mean ± Standard Diviation (mean ± SD) of the mean. The significant difference among the means has been statistically analyzed by one-way analysis of variance Duncan, ($p < 0.05$) was considered as statistical significance using SPSS 19 Software (Snedecor and Cochran, 1986).

Results and Discussion

Amount of total protein and percentage in cold crud aqueous palmito extract

The amount of total protein in cold crud aqueous palmito extract was found and it was equal (8433.75 mg), then we found the percentage of the plant which estimate (2.318%), as shown in table (1).

Table 1. Amount of total protein and percentage in cold crud aqueous palmito extract

Extract	Protein concentration (mg/cm^3)	Total volume of extract (cm^3)	Total protein in extract (mg)	Protein percentage in plant (%)	Plant weigh (gm)	Practical weight of protein (mg)
Cold crud aqueous palmito extract	8.65	975	8433.75	2.318	300	6955

Effect of different doses (100, 250, 500 mg / kg) of crude aqueous extract of the palmito on some biochemical parameters in serum of healthy adult male rats:

Enzymes activity (ALP, ALT, AST):

The activity of alkaline phosphatase was evaluated in serum of healthy adult male rats and treated with cold crude aqueous extract of the plant. The treatment of (500 mg / kg) in the first week showed a significant increase ($p \leq 0.05$) compared with control group, while the two doses (100, 250 mg / kg) did not show significant differences when compared with the control group. When compared between the doses in the first week, the dose (250 mg / kg) was significantly reduced when compared to the two doses (100, 500 mg / kg) as shown in table (2). In the second week of the treatment, there were no significant differences in the treatment group with the cold crude aqueous extract of the palmito plant in the two doses (100, 250 mg / kg) compared with the control group. While the dose (500 mg / kg) showed a significant increase when compared with the control group. Statistical analysis showed that the two doses (100, 250 mg / kg) showed no significant differences between them, while the two groups showed a significant decrease in the activity of ALP enzyme when compared with the aqueous extract group of (500 mg / kg).

The dose (500 mg / kg) of the cold crude aqueous extract of the palmito plant by oral resulted in a significant increase of the activity of ALP in the serum of adult male rats compared with control group during the first and two weeks as shown in table(2). The reason for the high activity of ALP enzyme is due to the presence of the

enzyme in the liver cells and when affected these cells by the overdose of the extract will lead to the collapse of some of these cells and then released the enzyme into the serum causing increased of the activity of this enzyme (Uskokovic et al., 2007).

The treatment with the cold crude aqueous extract of the palmito plant in doses (100, 250, 500 mg / kg) showed no significant differences when compared with control group at the first week, also when comparison of each group with the other in the activity of ALT in the serum of healthy adult male rats as shown in table (2).

In the second week, the treatment with the cold crude aqueous extract of the palmito plant showed an effect on serum ALT activity. Statistical analysis showed that the dose (250 mg / kg) showed a significant decrease when compared with control group, while the groups which are treated at doses (100, 500 mg / kg) showed no significant differences compared with control group. When comparing the three experimental groups, there were no significant differences between them as shown in table (2).

The treatment of the cold crude aqueous extract of the palmito plant at doses (100, 500 mg / kg) for male rats by oral did not show significant differences in ALT activity when compared with control group in the first and second weeks. This indicates that the activity of enzyme was not affected by these doses of extract. For the group of (250 mg / kg) dose, it was significantly decreased and improved well when compared with control group for both weeks.

Statistical analysis in the first week of treatment showed that the three trial groups (100, 250, 500 mg / kg) showed no significant differences compared to control group, when measuring the activity of the AST in the serum of healthy adult rats. When comparing groups between them, there was no significant difference between the two groups (100, 250 mg / kg) and between the two groups (250, 500 mg /kg) while the dose (500 mg / kg) showed a significant increase when compared with the dose (100 mg / kg).

In the second week, two doses of treatment (100, 250 mg / kg) showed a significant decrease when compared with control group, while dose group (500 mg / kg) has no significant differences when compared with control group. In addition, the two groups of doses (100, 250 mg / kg) showed no significant differences between them in the activity of serum AST, while the dose group (500 mg / kg) gave a significant increase compared to the previous two doses as shown in table (2).

The treatment with the cold crude aqueous extract of the three-dose of palmito plant showed no significant differences in AST activity during the first week when compared with control group, while in the second week of the treatment, the two groups of doses (100, 250 mg / kg) were significantly lower than the control group.

These results are identical to those found by (Abuelgassim, 2010), noting that the concentration of some biochemical measured (glucose) in serum of healthy rats after two and four weeks of treatment with date palm leaf extract did not give any significant changes compared with the non-treated control group. The date palm leaf extract was found to reduce the concentration of cholesterol significantly in the serum of healthy rats four weeks after the extract was given, while no significant difference was observed in the concentration of triglyceride at the same time in serum of healthy rats. Researchers have shown that the palm extract contains effective compounds that act as scavenger free radicals. And that the moral effect found after the four weeks indicates that the plant extract contains effective antioxidants that reduce oxidative stress (Saafi et al., 2010).

The cold crude aqueous extract of the palmito plant causes a significant decrease in the activities of AST and ALT. These decrement due to the antioxidant contained in the plant extract (Chaira et al., 2007). Or may be due to the presence of multiple phenolic compounds that play an important role in the synthesis of proteins and improve liver function, or may be due to the fact that the extract may have systematic effects of mitochondrial and cellular membrane permeability, resulting in increased membrane stability (Masoomeh et al. , 2013).

Table 2. Effect of cold crude aqueous extract of the palmito plant at doses (100, 250, 500 mg / kg) on the biochemical variables (ALP, ALT, AST) in serum of healthy male adult rats

Groups	ALP U/L		ALT U/L		AST U/L	
	1st week	2nd week	1st week	2nd week	1st week	2nd week
Control	275.60±11.31 ab	287.67±9.01 a	67.17±9.39 a	66.90±4.58 b	232.80±10.82 ab	254.05±15.05 b
100 mg/kg	304.72±13.15 b	287.50±16.55 a	63.90±9.46 a	49.17±6.68 ab	191.67±12.66 a	203.82±8.14 a
250 mg/kg	267.45±10.05 a	318.73±9.48 a	45.57±2.76 a	39.43±3.22 a	228.57±8.07 ab	172.17±6.77 a
500 mg/kg	340.46±12.08 c	358.60±1.94 b	54.43±11.86 a	51.67±2.65 ab	246.07±27.29 b	246.56±11.80 b

Different letters vertically mean a significant at ($p \leq 0.05$).
The values above refer to the mean ± standard deviation.

Total protein, albumin and globulin concentrations

The analysis showed that the group of dose (500 mg / kg) has a significant increase when compared with control group in the first week, while the two dose groups (100, 250 mg / kg) showed no significant difference. In the second week, shows that the two groups (250, 500 mg / kg) showed a significant increase compared to the control group, while the dose group (100 mg / kg) showed a non -significant difference compared to the control group as shown in table (3). When comparing the groups, the treatment group (100 mg / kg) showed a significant decrease when compared with the two groups of doses (250, 500 mg / kg) and the latter two groups showed no significant differences between them in the total protein concentration in healthy adult male rats.

Table 3. Effect of cold crude aqueous extract of the palmito plant at doses (100, 250, 500 mg / kg) on the biochemical variables (total protein, albumin, globulin) in serum of healthy male adult rats

Groups	Total protein gm/dl		Albumin gm/dl		Globulin gm/dl	
	1st week	2nd week	1st week	2nd week	1st week	2nd week
Control	5.26±0.32 a	5.76±0.09 a	2.84±0.26 a	3.31±0.03 a	2.42±0.12 a	2.45±0.24 a
100 mg/kg	6.03±0.29 ab	6.14±0.19 a	3.43±0.02 b	3.42±0.04 a	2.60±0.31 a	2.72±0.34 a
250 mg/kg	5.57±0.05 ab	6.90±0.26 b	3.52±0.19 b	3.79±0.05 b	2.05±0.33 a	2.11±0.18 a
500 mg/kg	7.01±0.34 b	7.05±0.69 b	3.40±0.04 b	4.13±0.19 c	3.61±0.06 b	3.92±0.38 b

Different letters vertically mean a significant at ($p \leq 0.05$).
The values above refer to the mean ± standard deviation.

The albumin concentration in the first week for all doses showed significantly increased when compared with control group, while there are no significant differences compared between them. In the second week, the two groups (250, 500 mg / kg) showed a significant increase when compared with control group, while the dose (100

mg / kg) did not appear any significant changes when compared with the control group. When comparing the three dose groups among them, a dose of (500 mg / kg) was found to be significantly higher when compared with the dose (250 mg / kg) and the latter has significantly increased compare with the dose (100 mg / kg) in the concentration of serum albumin.

From table (3) and from the two weeks of the treatment with the cold crude aqueous extract of the palmito plant at dose (500 mg / kg) showed a significant increase when compared with control group in the concentration of globulin. The two dose groups (100, 250 mg / kg) did not show a significant difference when compared with the control group. In addition, the three dose groups did not show significant differences when compared among them at two weeks in the concentration of serum globulin of healthy adult male rats.

The increase in the cold crude aqueous extract of the palmito plant in total protein, albumin and globulin concentrations was due to the susceptibility of the extract to the stimulation the hepatic tissues, which led to increased protein synthesis in the liver and improved functional status of hepatic cells (Hussein et al., 2007).

Total bilirubin, direct, indirect and total lipid concentrations

From table (4) and from the first week in the measurement of total bilirubin concentration in serum adult rats, the dose group (500 mg / kg) showed a significant decrease when compared with control group, while the two doses (100, 250 mg / kg) did not show significant differences compared to the control group, and we note from the same table that the groups of three doses did not show significant differences when comparing among them during the first week of the treatment. In the second week, the treatment with the three-doses with aqueous extract showed better improvement than in the previous first week, with the statistical analysis that the three doses of the extract showed a significant decrease when compared with the control group. When compared with the doses, the dose group (100 mg / kg) showed a significant increase when compared with the two groups of doses (250, 500 mg / kg), while note the results showed that the last two doses did not show any significant differences between them in the total bilirubin concentration. These results were identical to those found by the researcher (Al-Azzawi, 2015) that the extract is the regeneration and repair of liver cells, which leads to the expansion and opening of bile ducts within the liver and the lack of flow of bilirubin into the blood.

The results of the direct bilirubin concentration in serum adult male rats showed that there was a similarity in the results of the statistical analysis between the first and second weeks of this characteristic. Table (4) shows that each dose of the three group doses showed a significant decrease when compared with the control group during the first and second weeks of treatment. When comparing between the three doses, the dose group (500 mg / kg) showed a significant decrease when compared with both doses (100 , 250 mg / kg) for both the first and second weeks of treatment, but there are no significant differences between the two doses in the above when

In table (4) and in the first week of treatment with the cold crude aqueous extract of the palmito plant, it was found that the three dose groups showed a significant decrease in indirect bilirubin concentration when compared with the control group. When comparing dose groups among them we showed that the dose (500 mg / kg) did not show a significant difference when compared with the two doses (100, 250 mg / kg), while the dose group (250 mg / kg) was significantly lower when compared with the dose group (100 mg / kg). In the second week, we note from table (4) that the three dose groups showed a significant decrease when compared with the control group, especially the dose group (500 mg / kg). Compares among the doses, the dose group (500 mg / kg) decreased significantly with the dose group (250 mg / kg) and the latter decreased significantly compared to the dose group (100 mg / kg) in indirect bilirubin concentration in the serum. . The reason for the low concentration of direct bilirubin in both weeks is to increase the effectiveness of the hepatic enzyme glucuronyl transferase, which converts the direct bilirubin into indirect bilirubin. As a result of the increased the activity of this enzyme the reduced of the direct concentration of bilirubin in the serum (Travis and Anupam, 2014).

In the first week of treatment, we observed in table (4) that the two doses (100, 250 mg / kg) showed a significant decrease in total lipid concentration in compares with control group, while the dose (500 mg / kg) did not show a significant difference. The latter dose showed a significant increase when compared with the two groups of doses (100, 250 mg / kg), while the two doses did not show significant differences when comparing them.

In the second week of treatment, we note from the same table that the two dose groups (250, 500 mg / kg) showed a significant decrease when compared with the control group, while the dose group (100 mg / kg) was no significant when compared with the control group. When comparing the three doses, the dose group (500 mg

/ kg) was significantly lower than the dose group (250 mg / kg) and the latter also decreased from the dose group (100 mg / kg) in the total lipid concentration in adult male rats treated with cold crude aqueous extract of the palmito plant. This indicates that increasing the dose of cold crude aqueous extracts of palmito lead to a decline in total lipid decomposition process. These results are consistent with what he found (Abuelgassim, 2010). This reduction was due to the presence of compounds acting as antioxidants in date palm leaf extracts that reduce oxidative stress. The decrease may be explained by the fact that these antibodies are associated with bile acids, which inhibit the hydroxymethyl glutaryl coenzyme A enzyme, which reduces the level of cholesterol (Saafi et al. , 2010).

Table 4. Effect of cold crude aqueous extract of the palmito plant at doses (100, 250, 500 mg / kg) on the biochemical variables (total, direct, indirect bilirubin and total lipid) in serum of healthy male adult rats

Groups	Total bilirubin µmol/L		Direct bilirubin µmol/L		Indirect bilirubin µmol/L		Total lipid mg/dl	
	1st week	2nd week	1st week	2nd week	1st week	2nd week	1st week	2nd week
Control	5.19±0.51 b	7.39±0.43 c	2.03±0.36 c	4.38±0.29 c	3.16±0.38 c	4.01±0.47 c	398.5±16.03 b	568.83±35.79 c
100 mg/kg	4.18±0.38 ab	5.34±0.52 b	1.77±0.16 b	2.71±0.21 b	2.41±0.19 b	2.63±0.33 b	264.5±32.08 a	568.80±18.77 c
250 mg/kg	3.17±0.33 ab	4.73±0.27 a	1.67±0.22 b	2.85±0.18 b	1.50±0.27 a	1.88±0.11 ab	308±10.42 a	474.63±8.26 b
500 mg/kg	2.91±0.34 a	2.96±0.36 a	1.20±0.19 a	1.30±0.16 a	1.71±0.39 ab	1.66±0.14 a	418.4±12.15 b	385.85±20.38 a

Different letters vertically mean a significant at ($p \leq 0.05$).
The values above refer to the mean ± standard deviation.

Conclusions

The treatment of adult male rats with the cold crude aqueous extract of the palmito plant in different doses (100, 250, 500 mg / kg) of body weight showed significant increases in the activities of hepatic enzymes, especially in the second week of the treatment from the concentration of total protein, albumin and globulin and to a significant decrease in total, direct and indirect bilirubin concentrations and in total lipid.

References

Abuelgassim, O. Abuelgassim, (2010). Effect of flax seeds and date palm leaves extracts on serum concentrations of glucose and lipids in alloxan diabetic rats. Pakistan Journal of Biological Sciences 13(23): 1141-1145.

Al-Azzawi, H. H., (2015). Effect of smoking cigarettes on the activity of enzymes AST, ALT, ALP and the levels of electrolytes in the plasma of smokers. Master Thesis, College of Education for Pure Sciences, Diyala University,Iraq.

Anderson, S., Cockayne, S., (1993). Clinical chemistry: Concepts and Aplications. Philadelphia; W.B. Saunders Company. pp.248-264.

Atta, A.H.; Shalaby, M.A.; Shokry, I.M. and Ahmed, A.A., (1983). Interaction between oral hypoglycemic and antibiotics on blood glucose level of normal fasted and alloxan-diabetic rats. Vet. Med. J., 31(1): 11-18.

Baliga, M.S.; Baliga, B.R.; Kandathil, S.M.; Bhat, H.P. and Vayalil, P.K., (2011). A review of the chemistry and pharmacology of the date fruits (Phonix dactylifera L.) J. food Res Int; 44: 1812-1822.

Belay, B.; Belachew, B.; and Habitamu, D., (2016). Review on Application and Management of Medicinal Plants for the Livelihood of the Local Community. Journal of Resources Development and Management. Vol.22, pp.33-39.

Bishop, M., Fody, E., Schoeff, L., (2005). Clinical chemistry: Principle, Procedures, Correlations. 5th ed., Baltimore: Lippincott Williams. Pp: 250-253. 476-486.

Chaira, N.A.; Ferchichi, A. M. and Sghairoun, M., (2007).Chemical composition of the flesh and the pit of date palm fruit and radical scavenging activity of their extracts. Pak. J. Biol. Sci., 10: 2202-2207.

Doumas, B.T. ; Watson, W.A. And Biggs, H.G., (1971). Albumin standards and the measurement of serum albumin with bromocresol green. Clinica Chimica Acta. pp: 392-402.

Hussein, J. S.; Oraby, F. S. and El-Shafey, N., (2007). Antihepatotoxic effect of garlic and onion oils on ethanol-induced liver injury in rats. J. Applied Sciences Research, 3 (11): 1527-1533.

Masoomeh, D.; Hojatallah, K.J.; Nader, T. and Negar, A., (2013). Effects of heart of palm (palmito) extract on reproductive system of adult male rats. Asian pacific J. of Reproduction 2(4): 272-276.

Robyt, F.J. and White, J.B., (1987). Biochemical Techniques. Theory and Practice. Brookes/Cloe Publishing Company, Monterey, California, pp. 115-118.

Saafi, E.B.; Louedi, M.; Elfeki, A.; Zakhama, M.F.; Najjar, M. H. and Achour L., (2010). Protective effect of date palm fruit extract (Phoenix dactylifera L.) on dimethoate induced-oxidative stress in rat liver. Exp. Toxicol pathol. 14:15-22.

Schacterle, G.R. and Pollack J.K., (1973). A simplified method for the quantitative assay of small amount of protein in biological materials. Anal. Biochem., 51: 654-655.

Snedecor G., Cochran, G., (1986). Statistical Methods. 4th Edn. Iowa State University Press, Ames, Iowa, USA.

Thiyagarajan, M., and Venkatachalam, P.,) 2012). Large-scale in vitro propagation of Stevia rebaudiana (Bert) for commercial application: Pharmaceutically important and antidiabetic medicinal herb. Industrial Crops Products, 37(1): 111-117.

Tietz, N.W., (1999). Text book of clinical chemistry, 3rd Ed. Burtis C.A., Ashwoodm E.R. , Saunders W.B.; pp.819-861.

Toro, G. and Ackermann, P.G., (1975). Practical Clinical Chemistry. Little Brown, Boston, U.S.A., p: 354.

Travis D. Hull and Anupam Agarwal, (2014). Bilirubin: A Potential Biomarker and Therapeutic Target for Diabetic Nephropathy, Diabetes Volume 63: 2613–2616.

Uskokovic-Markovic, S. , Milenkovic, M. , Topic, A. , Kotur-Stevuljevic , J. , Stefanovic, A. , Antic-Stankovic, J., (2007). Protective effectives of tungstophoric acid and sodium tungstate on chemically inducedliver necrosis in wistar rats. J Pharm Pharmaceut Sci, 10 (3): 340-349.

Walters, M. and Gerarde, H., (1970). An ultramicromethod for the determination of conjugated and total bilirubin in serum or plasma. Micro chem. J. 15(2):231-243.

Author Information

Saba Z. Al-Abachi	Sameer M. Al-Gorany
Mosul University, Iraq	Middle Technical University
Contact E-mail: Saba_alabachi@yahoo.com	Iraq

IConTES 2019: International Conference on Technology, Engineering and Science

Synthesis and Electrochemical Performance of the $(Mg_{0.2}Co_{0.2}Ni_{0.2}Zn_{0.2}Li_{0.2})$ O High Entropy Oxide as Anode Material for Li-ion Batteries

Mustafa ANIK
Osmangazi University

Ersu LOKCU
Osmangazi University

Abstract: Presently intercalation type graphite anode electrodes were being used mainly in the commercial Li-ion batteries. Graphite electrodes, however, have reached their theoretical capacity values ($\approx$ 372 mAhg^{-1}). Therefore large amount of studies on the synthesis of the novel electrode types were conducted all over the world. One of the novel electrode groups is conversion type electrode. The high entropy design approach is especially utilized in this multi-component oxide electrode synthesis. In this study a new high entropy oxide $(Mg_{0.2}Co_{0.2}Ni_{0.2}Zn_{0.2}Li_{0.2})$O was synthesized for the first time in the literature by mixing and grinding of the oxide powders, followed by solid-state reaction at 1000 ºC. The microstructure of the material was characterized using XRD and FESEM-EDX methods, showing single-phase rocksalt structure. The electrochemical performances of the synthesized $(Mg_{0.2}Co_{0.2}Ni_{0.2}Zn_{0.2}Li_{0.2})$O as anode material for Li-ion batteries was determined using LIR2016 coin cell. The results showed that $(Mg_{0.2}Co_{0.2}Ni_{0.2}Zn_{0.2}Li_{0.2})$O, which has good potential to be used as anode in lithium-ion batteries, had the highest capacity value in 1.0 M LiTFSI-DME electrolyte (1725 mAhg^{-1}).

Keywords: High entropy oxide, Li-ion battery, Conversion type anode

Introduction

Recently, lithium-ion batteries have been regarded as the main technology for powering portable devices and consumer electronics. Commercial lithium-ion batteries, based on intercalation type electrodes, are generally stable, but they have low specific energy (Puthusseri et al., 2018). Therefore, is very important and necessary to develop new type anode materials with high specific energy. Metal oxides are alternative electrodes for lithium-ion batteries that working through conversion reactions. These reactions are associated with much higher energy densities than intercalation reactions. Simply, the concept of a conversion reaction can be expressed as:

$$M_xO_y + 2yLi^+ + 2ye^- = xM + yLi_2O$$
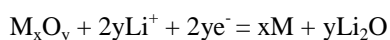
where, M generally denotes a transition metal. Transition metal oxides can undergo this reaction, yielding high theoretical capacity from 500 to 2000 mAhg^{-1} (Puthusseri et al., 2018; Meister et al., 2016).

Since the day it was discovered, the concept of high entropy alloy (HEA) has led to the emergence of many new materials under the name of high entropy materials (HEMs) such as high entropy carbides, nitrides, borides, sulfides, oxides etc. The key concept of HEMs is to use multiple components (usually five or more in equiatomic amount), in order to maximize the configurational entropy to achieve a single phase, simple solid solution structures. Inspired by this phenomenon, Rost et al. reported the first high entropy oxide (HEO) or entropy stabilized oxide (ESO), which has rocksalt type crystal structure, single-phase solid solution (Mg,Co,Ni,Cu,Zn)O system. Further, many functional and structural properties have been reported for (Mg,Co,Ni,Cu,Zn)O. Berardan et al. reported that (Mg,Co,Ni,Cu,Zn)O possesses promising electrical

properties. Li-substituted (Mg,Co,Ni,Cu,Zn)O showing larger ionic conductivity because of oxygen vacancies formed due to substitution of a nonisovalent element into the structure. The reaction sequence and mechanical properties of (Mg,Co,Ni,Cu,Zn)O were studied by Hong et al.

Very recently, Sarkar et al. was explored the lithium storage properties of (Mg,Co,Ni,Cu,Zn)O as conversion type anode material for lithium-ion batteries. (Mg,Co,Ni,Cu,Zn)O exhibit reversible lithium storage properties, and it was demonstrated that the improvements in cycling stability are related with entropy stabilization. In another study in which the performance of (Mg,Co,Ni,Cu,Zn)O nanoparticles as an anode material for lithium-ion batteries, which was examined, the electrode with a first discharge capacity of 1585 mAhg^{-1} reached a reversible capacity of 920 mAhg^{-1} after 200 cycles (Chen et al.,2018).

In this work, synthesis and characterization of a new high entropy oxide $(Mg_{0.2}Co_{0.2}Ni_{0.2}Zn_{0.2}Li_{0.2})O$ was carried out. Furthermore, we studied the anode performance and cycling behavior of synthesized $(Mg_{0.2}Co_{0.2}Ni_{0.2}Zn_{0.2}Li_{0.2})O$ for lithium-ion batteries in LIR2016 coin cell.

Method

MgO, CoO, NiO, ZnO and Li_2O oxides were mixed with a ball milling (Fritsch Pulverisette 7 Premium Line) for 2 hours at 300 rpm and then uniaxially pressed into pellet under a pressure of 300 MPa. Subsequently, the samples which were heat treated at 1000 °C for 12 hours before air quenching. X-ray Diffraction (XRD) and scanning electron microscopy (SEM) techniques were performed to characterize the synthesized $(Mg_{0.2}Co_{0.2}Ni_{0.2}Zn_{0.2}Li_{0.2})O$.

For the preparation of electrode, electrode slurry were made by mixing with a ball milling of $(Mg_{0.2}Co_{0.2}Ni_{0.2}Zn_{0.2}Li_{0.2})O$ powders (70 wt%), Super P acetylene black (20 wt%) and PVDF (10 wt%) in NMP for 3 h at a speed of 300 rpm. The resulting slurries were coated on a Cu foil by brushing and then dried in a vacuum atmosphere at 80 °C for 12 h. LIR2016 coin type cells with a Li metal foil as counter electrode and glass microfiber soaked in 1M LiTFSI:DME as a electrolyte were assembled inside an argon filled glovebox. Discharge/charge tests were performed galvanostatically at 100 mAg^{-1} between the potential range of 0.05-3.00 V (vs. Li^{+}/Li) by using Gamry Reference 3000 Potentiostat/Galvanostat/ZRA.

Results and Discussion

Fig. 1 shows the (XRD) pattern of a synthesized $(Mg_{0.2}Co_{0.2}Ni_{0.2}Zn_{0.2}Li_{0.2})O$. The pattern shows that the sample is crystalline and in a form of single phase rocksalt crystal structure. The diffraction peaks at 2θ values 36.8˚, 42.8˚, 62.0˚, 74.5˚ and 78.4˚, are corresponded to the (111), (200), (220), (311) and (222), planes of the rocksalt crystal structure, respectively. A heat treatment temperature of 1000 °C seems to be sufficient for the synthesis of $(Mg_{0.2}Co_{0.2}Ni_{0.2}Zn_{0.2}Li_{0.2})O$ and additional peaks corresponding to secondary phases is not observed.
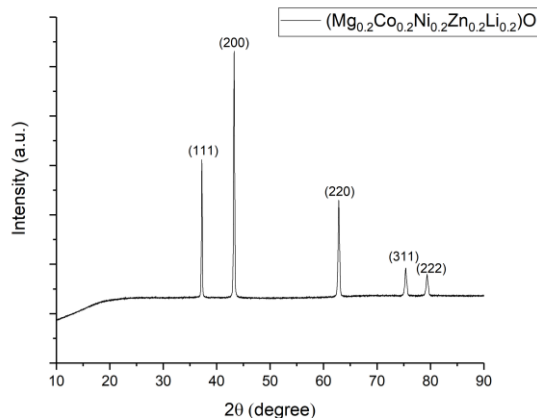
Figure 1. XRD patterns of the $(Mg_{0.2}Co_{0.2}Ni_{0.2}Zn_{0.2}Li_{0.2})$ O sample

The SEM image in Fig. 2 reveals a very dense microstructure for $(Mg_{0.2}Co_{0.2}Ni_{0.2}Zn_{0.2}Li_{0.2})$ O. The sample was successfully sintered at 1000 °C and any pore and secondary phases were not observed in the microstructure. The average grain size of the sample was determined about 1 μm from the SEM observation.
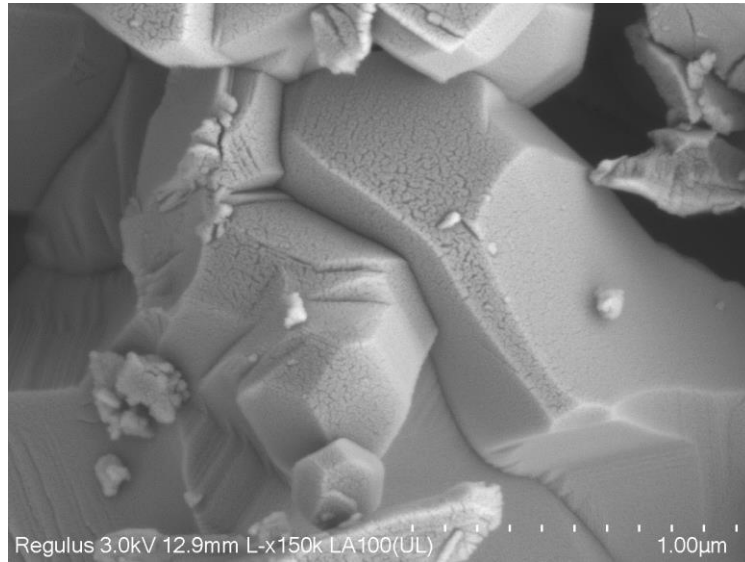
Figure 2. SEM image of the $(Mg_{0.2}Co_{0.2}Ni_{0.2}Zn_{0.2}Li_{0.2})$ O sample

Fig. 3 shows the discharge/charge curves of the $(Mg_{0.2}Co_{0.2}Ni_{0.2}Zn_{0.2}Li_{0.2})O$ anode at a current density of 100 mAg^{-1}. Charging and discharging corresponds to lithiation and delithiation of the $(Mg_{0.2}Co_{0.2}Ni_{0.2}Zn_{0.2}Li_{0.2})O$ anode, respectively. As can be seen from Fig. 3, a specific capacity of about 1725 mAhg^{-1} was achieved in the first discharge with a discharge voltage of ~0.65 V. According to the literature, the $(Mg_{0.2}Co_{0.2}Ni_{0.2}Zn_{0.2}Li_{0.2})O$ anode show a typical voltage profile of metal oxide (Co_3O_4, ZnO, NiO etc.) anode in lithium ion battery for the first discharge process (Lu et al., 2018). It is attributed to the reduction of HEO to Co, Ni, and Zn. After the first cycle, the irreversible capacity loss is observed due to formation of solid electrolyte interphase at the interface of the electrode surface and the electrolyte and initial lithium loss, mainly due to anode conversion (Lu et al., 2018; Chen et al.,2018). On the other hand, after the first cycle, the discharge plateau of the $(Mg_{0.2}Co_{0.2}Ni_{0.2}Zn_{0.2}Li_{0.2})O$ anode were changed at higher potentials and into one slope during the reduction process. A reversible capacity of$(Mg_{0.2}Co_{0.2}Ni_{0.2}Zn_{0.2}Li_{0.2})O$ anode is 720 mAhg^{-1} after 10 cycles.
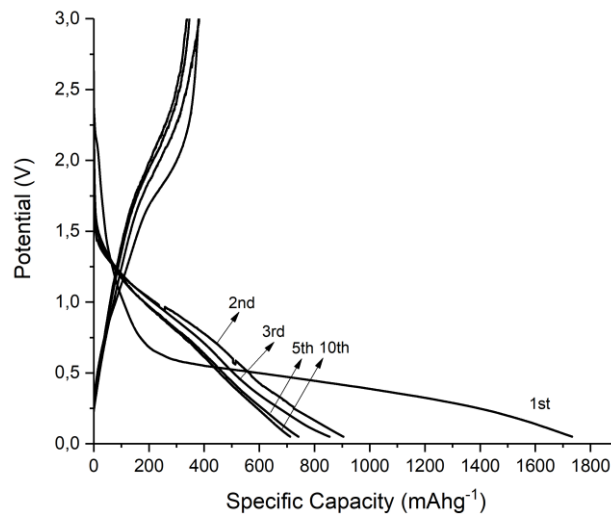
Figure 3. Discharge-charge voltage profiles of $(Mg_{0.2}Co_{0.2}Ni_{0.2}Zn_{0.2}Li_{0.2})$ O for the 1st, 2nd, 3rd, 5th, and 10th cycles in the voltage range of 0.05-3.00 V

Conclusion

In summary, $(Mg_{0.2}Co_{0.2}Ni_{0.2}Zn_{0.2}Li_{0.2})O$ high entropy oxide was synthesized and characterized successfully and was applied as a negative electrode material for lithium-ion batteries. A specific discharge capacity of 1725 $mAhg^{-1}$ was observed in the first cycle and maintained at 720 $mAhg^{-1}$ after 10 cycles in LIR2016 coin cell. To determine possible combinations of new HEO based anode materials by revealing the effects of different oxides (cations) on battery performance is highly promising for the future studies.

References

D. Bérardan, S. Franger, A.K. Meena, N. Dragoe, (2016). "Room temperature lithium superionic conductivity in high entropy oxides", J. Mater. Chem. A. 4, 9536–9541.

Chen, H., Qiu, N., Sun, S., Wang, Y., Cui, Y., Yang, Z., (2018). "A high entropy oxide (Mg0.2Co0.2Ni0.2Cu0.2Zn0.2O) with superior lithium storage performance", J. Alloys Compd., 777, 767-774.

W. Hong, F. Chen, Q. Shen, Y.H. Han, W.G. Fahrenholtz, L. Zhang, (2019). "Microstructural evolution and mechanical properties of (Mg,Co,Ni,Cu,Zn)O high-entropy ceramics", J. Am. Ceram. Soc. 102,2228–2237.

Lu, Y., Yu, Li., Lou, X.W. (2018). "Nanostructured Conversion-type Anode Materials for Advanced Lithium-Ion Batteries", Chem., 4, 972-996.

Meister, P., Jia, H., Li, J., Kloepsch, R., Winter, M., Placke, T. (2016). "Best Practice: Performance and Cost Evaluation of Lithium Ion Battery Active Materials with Special Emphasis on Energy Efficiency", Chem. Mater., 28, 7203-7217.

Puthusseri, D., Wahid, M., Ogale, S. (2018). "Conversion-type Anode Materials for Alkali-Ion Batteries: State of the Art and Possible Research Directions", ACS Omega, 3, 4591-4601.

Rost, C.M., Sachet, E.,. Borman, T., Moballegh, A., Dickey, E.C., Hou, D., Jones, J.L., Curtarolo, S.,Maria, J.P. (2015). "Entropy-stabilized oxides", Nat. Commun. 6, 1-8.

Sarkar, A., Wang, Q., Kübel, C., Wang, D., Talasila, G., Brezesinski, T., Hahn, H., de Biasi, L., Velasco, L., Bhattacharya, S.S., Breitung, B. (2018). "High entropy oxides for reversible energy storage", Nat. Commun. 9, 1-9.

Author Information

Mustafa Anik
Department of Metallurgical and Materials Engineering,
Eskisehir Osmangazi University, 26480, Eskisehir, Turkey
Contact E-mail: manik@ogu.edu.tr

Ersu Lokcu
Department of Metallurgical and Materials Engineering,
Eskisehir Osmangazi University, 26480, Eskisehir, Turkey

IConTES 2019: International Conference on Technology, Engineering and Science

Comparison of TEC Prediction Methods in Low Latitudes with GIM Maps

Galina GLEBOVA
Southern Federal University

Olga MALTSEVA
Southern Federal University

Abstract: For the high-latitude part of the low-latitude region, the errors in determining the TEC from the data of Rostov and Ankara stations in 2015 were estimated. The estimates obtained for the IRI-Plas model turned out to be better than for the NeQuick model, with an average absolute error in the range of 3-3.6 TECU, a relative RMS error in the range of 21-27% which is acceptable for use in positioning systems. For a short-term forecast, the best results were obtained by the Standard Persistence Model with an average absolute error in the range of 1.95-2.5 TECU, a relative RMS error in the range of 17-21%. For the proposed method, these estimates were 2.04–2.5 TECU and 12–14%.

Keywords: Ionosphere, Total electron content, Models, Prediction, Disturbance

Introduction

Low latitudes are one of the areas where there are few ionosondes that provide information on the state of the ionosphere necessary for the operation of various communication systems using a critical frequency. With the advent of GPS, GLONASS navigation satellites, on the one hand, it became possible to study the behavior of the total electron content TEC of the ionosphere, providing even more complete information, on the other hand, there is a need for modeling and prediction of TEC. There are a number of global models of ionospheric parameters, such as the International Reference Ionosphere IRI, IRI-Plas, NeQuick, and others that could be used in areas where there are no ionosondes and GPS receivers. But these models must be tested in each such local area. In this work, testing is carried out according to the data of Rostov and Ankara stations, which can be attributed to the high-latitude part of the low-latitude zone. This region needs testing, which is confirmed by a number of papers (e.g., Arikan et al., 2007). For testing, GIM maps are used (Hernandez et al., 2009), which are the most comprehensive database. A comparison is made for the IRI-Plas and NeQuick models. Despite the fact that the IRI model is the most used, no comparison is made for it. Firstly, there are a lot of papers on such a comparison, and secondly, such a comparison is not entirely correct due to the difference in the upper boundary of the TEC definition: for the IRI model, it is 2,000 km, for GPS satellites, 20,200 km. IRI-Plas and NeQuick models provide a long-term forecast. No less important role is played by short-term forecasting methods. For a short-term forecast, are compared the Standard Persistence Model (SPM), a 27 day median model, considered in (Badeke et al., 2018), and the proposed method for 1 day in advance, using data from 2015.

Experimental Data and Models

As experimental data the values of global maps JPL GIM-TEC calculated from IONEX files from steps of 2 hours (ftp://cddis.gsfc.nasa.gov/pub/gps/products/ionex/), for 2015 for stations Juliusruh (54.6 °N, 13.4 °E), Rostov (47.2 °N, 39.7 °E) and Ankara (39.89 °N, 32.76 °E) were used. Calculations of TEC with use of models IRI-Plas and NeQuick were carried out in online on websites: http://www.ionolab.org/index.php?language=en and https://t-ict4d.ictp.it/nequick2/nequick-2-web-model.

Comparison of Long-Term TEC Results for 2015

Figure 1 compares IRI-Plas and NeQuick for three stations and 2015 with global JPL maps for medians and deviations from them.
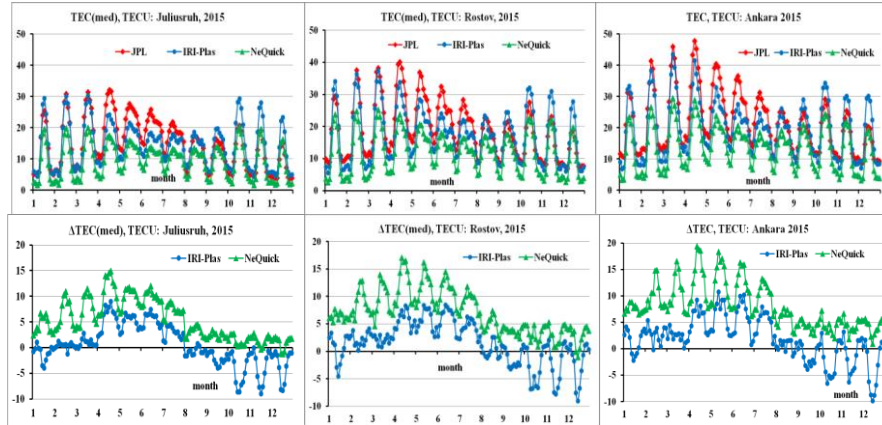
Figure 1. Comparison of TEC values calculated by different methods (upper part) and their deviations from observational medians (lower part) for three stations in 2015

One can see that values of TEC increase with decreasing latitude, however the seasonal variation of values is similar: maximum in March-May, minimum in August-September. The NeQuick model always underestimates values ($\Delta TEC > 0$). The IRI-Plas model underestimates values in the first eight months, then starts to overestimate. Quantitative estimations are given in Table 1 for absolute and relative deviations.

Table 1. Model accuracy comparison in 2015 for JPL map

	$|\Delta TEC|$, TECU		σ, TECU		σ, %	
	IRI-Plas	NeQuick	IRI-Plas	NeQuick	IRI-Plas	NeQuick
Juliusruh	3.04	5.49	3.96	6.7	26.79	45.30
Rostov	3.39	7.14	4.16	8.15	22.02	43.17
Ankara	3.59	8.15	4.48	9.15	20.77	42.39

It can be seen that the deviations increase with decreasing latitude, although the relative deviations decrease with decreasing latitude due to large values. The results for the NeQuick model are almost 2 times worse than for the IRI-Plas model. This does not correspond to the global results of the work (Okoh et al., 2018), in which at low latitudes the best results were obtained for the NeQuick model.

Comparison of short-term TEC results for 2015

This section compares the results of methods such as SPM, Med, presented in (Badeke et al., 2018), with the results of the proposed method according to TEC for three stations in 2015. A brief description of the proposed method is as follows. The annual sequence of TEC contains values for every 2 hours (in accordance with the availability of experimental data) of each day for all months. This sequence is approximated on each 27-day interval by samples representing the decomposition for each day in accordance with the formula $y_{ij} = A_j * \sin(\omega_{i-1}\Delta t * (i-1)) + B_j$, where A_j is the harmonic amplitude and B_j is the constant component for every day. ω is selected based on the spectrum of the 27-day observation. The coefficients A_j and B_j are found by the least squares method. The first stage of the method work, the approximation of the TEC sequence, is illustrated by y_{ji} samples in Figure 2. The horizontal axis represents the day of the 27-day period. The blue rhombuses show the observational values, the red circles concern the approximation results.

The approximation accuracy depending on the period ranged from 0.5 TECU to 3.5 TECU with a relative RSME of 4 to 20%. The average annual accuracy was 1.49 TECU for Juliusruh station, 1.63 TECU for Rostov station, 1.63 TECU for Ankara station. The corresponding average RSMEs are 11.04, 9.66 and 8.36%.

Then, for each period, the decomposition spectra for each day are found, examples of which for the 10th 27-day period for three stations are shown in Figure 3.
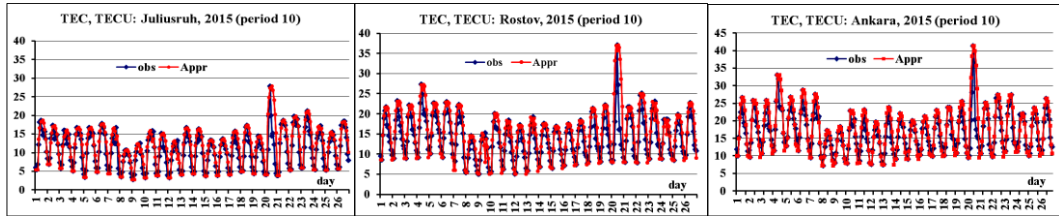
Figure 2. The results of the approximation of the TEC sequence for the 10th period
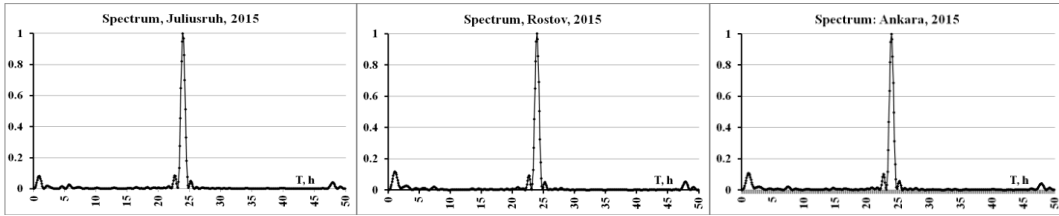
Figure 3. The decomposition spectra of the TEC sequence for the 10th 27-day period

The spectrum for Ankara is similar to two another. An example of a forecast is given in Figure 4. Observational TEC values (obs icon), 27-day medians (med icon), predicted values (pred icon), and forecast errors (Err) are presented.
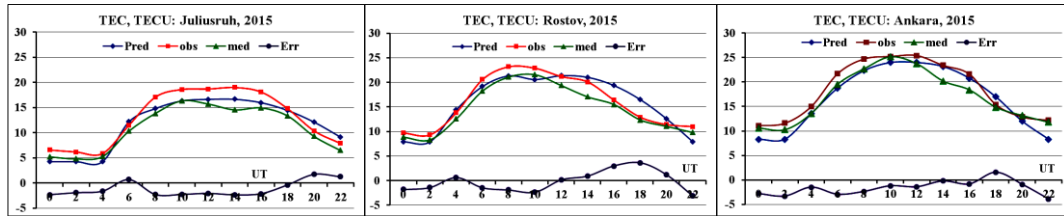
Figure 4. Example of forecast for the day following the 10th 27-day period

A comparison of the forecast accuracy for the three stations is given in Table 2 for the SPM method, for using the median (Med), and for the proposed method (Pred).

Table 2. Annual accuracy statistics of various forecast methods in 2015

2015	|ΔTEC|,TECU			σ, %		
	Pred	SPM	Med	Pred	SPM	Med
Julius	2.04	1.95	3.10	14.07	21.03	20.87
Rostov	2.19	2.14	3.38	12.01	17.80	17.54
Ankara	2.48	2.48	3.72	11.58	17.56	16.73

These results should be compared with data of (Badeke et al., 2018), which can be presented as Table 3.

Table 3. Statistical results of comparing short-term forecast methods

database	SPM	MediMod	Fourier	NTCM-GL
SWACI	2.75	2.86	2.81	4.0
UPC	2.66	3.15	3.28	4.73

It can be seen that in both tables the SPM model gives the best result, while the climatological model gives the worst result. This even coincides with the results of the paper (Lean, 2019), in which a statistical model for forecasting TEC at time scales Δt exceeding 1 day was developed. In (Lean, 2019), is shown that the SPM model gives better results than the new and climatological models, with Δt = 1. The average absolute error varies from 2.5 to 3.2 TECU with a relative RMSE error of 16 to 20%. In our case, the absolute and relative errors are less. Moreover, these deviations are smaller than those provided by the IRI-Plas and NeQuick models, shown in the Table 1. It should be noted that in contrast to (Badeke et al., 2018), quiet days were not selected. This allows us to reveal the dependence of the predicted values on the index Dst, which is chosen to characterize

the disturbed conditions. Figure 5 shows the predicted values for Ankara station along with the Dst index, reduced by 10 times. Correlation coefficients for each period are also given.
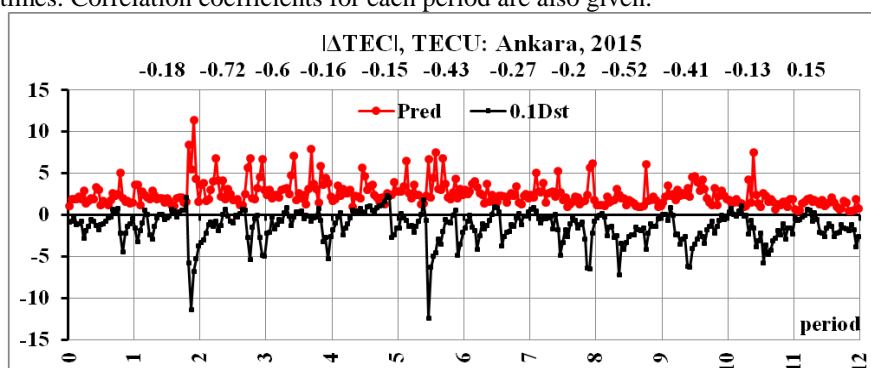
Figure. 5. The behavior of the predicted values of |ΔTEC| for all periods under consideration

For the Juliusruh station, the correlation coefficients for the periods were -0.13, -0.77, -0.47, -0.15, 0.14, -0.39, -0.1, -0.34, -0.1, -0.25, 0.02, 0.37, for Rostov -0.26, -0.8, - 0.47, -0.08, -0.02, -0.44, -0.38, -0.27, -0.57, -0.32, -0.09, 0.27. The values for Rostov and Ankara are close, also the graphs are similar. The average annual values of the correlation coefficients were -0.25, -0.36 and -0.34 for the stations Juliusruh, Rostov and Ankara, respectively. It can be seen that there are practically no quiet periods and the correlation is negative. The forecast for disturbed days is much worse than on quiet days. Apparently, in the future it will be necessary to switch to the forecasting scheme for the Dst index and, accordingly, adjusting the TEC values.

Conclusion

For the high-latitude part of the low-latitude region, the errors in determining the TEC from the data of Rostov and Ankara stations in 2015 were estimated. It is shown, that results of global model can differ from results in local area. The estimates obtained for the IRI-Plas model turned out to be better than for the NeQuick model, and are acceptable for use in positioning systems. TEC database for a specific receiver allows using the Standard Persistence Model as a short-term forecasting method. The proposed method provides the results no worse, while the relative errors are significantly reduced. It is important to notice, that accuracy of the forecast for this zone is close to results for the middle-latitude zone which are the etalon.

Acknowledgments

References

Arikan, F., Arikan, O. & Erol, C. B. (2007). Regularized estimation of TEC from GPS data for certain midlatitude stations and comparison with the IRI model. *Advances in Space Research, 39, 867–874.*

Badeke, R., Borries, C., Hoque, M. M. & Minkwitz D. (2018). Empirical forecast of quiet time ionospheric Total Electron Content maps over Europe. *Advances in Space Research, 61, 2881-2890.*

Hernandez-Pajares, M., Juan, J. M., Sanz, J., Orus, R., Garcia-Rigo, A., Feltens, J., Komjathy, A., Schaer, S. C. & Krankowski, A. 2009. The IGS VTEC maps: a reliable source of ionospheric information since 1998. *Journal of Geodesy, 83, (3–4), 263–275*.

Lean, J. L. (2019). One-to 10-day forecasts of total electron content using a statistical model. *Space Weather*, *17, 2, 313-338.*

Okoh, D., Onwuneme, S., Seemala, G., Shuanggen, J., Rabiu, B. Nava, B. & Uwamahoro J. (2018). Assessment of the NeQuick-2 and IRI-Plas 2017 models using global and long-term GNSS measurements. *Journal of Atmospheric and Solar-Terrestrial Physics, 170, 1–10.*

Author Information

Galina Glebova
Institute for Physics, Southern Federal University
344090, Stachky 194, Rostov-on-Don, Russia

Olga Maltseva
Institute for Physics, Southern Federal University
344090, Stachky 194, Rostov-on-Don, Russia
Contact E-mail: *mal@ip.rsu.ru*

Investigation of the Dynamic Systems' Phase Portraits

Irina ANDREEVA
Peter the Great St. Petersburg Polytechnic University

Tatiana EFIMOVA
Peter the Great St. Petersburg Polytechnic University

Abstract: Dynamic systems in a broad sense may be considered as mathematical models of processes and phenomena, where any statistical events we may disregard. The dynamic systems theory investigates curves, defined by differential equations. The same time the laws of Nature are written using the language of differential equations, as the great French mathematician and encyclopedist of the nineteenth and twentieth centuries J.H. Poincare has taught. Thus, these laws are written using dynamic systems. A study of a given family of dynamic systems depending on several parameters means splitting of a phase space belonging to the dynamic system under consideration into trajectories and investigation of the limit behavior of them with the aim to reveal and describe their positions of equilibrium, and to find the so-called sinks and sources. Also, very important are the question of the stability of equilibrium states and their types, as well as the question of a roughness of a system. Rough dynamic systems can preserve their qualitative character of motion under some considerably small changes in parameters of the system. The paper is devoted to the original investigation of a broad family of polynomial dynamic systems, depending on multiple parameters.

Keywords: Dynamic systems, Trajectories, Phase portraits, Equilibrium states, Differential equations, Poincare sphere, Poincare disk, Singular points, Separatrices, Limit cycles

Introduction

The unique "scientific position" of a dynamic system is to serve as a mathematical model of some process, where any statistical events (fluctuations, for example) could be omitted and put out of investigator's consideration. Any dynamic system has the two main features, the two main characteristics of it. Namely those characteristics are: 1) the initial state of a dynamic system, and 2) a law of this system's transformation into some different state. A totality including all admissible states of a given dynamic system is called a *phase space* of it. There can be separated the two main categories of dynamic systems: one of them includes all dynamic systems with the discrete time (the so-called *cascades*), while the other category includes dynamic systems with the continuous time (the *flows*). For cascades their behavior is described with a sequence of different states. For flows their state is defined on an imaginary or on a real axis per each time moment. Flows and cascades represent the key fields of investigations in such branches of science as the topological dynamics and the symbolic dynamics.

But the same time the both abovementioned principally different types of dynamic systems usually can be described using a certain autonomous system of differential equations, which is defined in some domain and satisfies in this domain the conditions of the Cauchy theorem. The Cauchy theorem of existence and uniqueness of solutions of differential equations is the one of main theorems in the theory of differential equations. Under such an approach the singular points of differential equations will be matched to dynamic systems' equilibrium positions, while periodical solutions of differential equations will match to dynamic systems' closed phase curves.

The actual key problem of the dynamic systems' theory is an investigation of curves, which are defined with differential equations.

A process of such a study involves the following several stages:
1) we need to split a phase space of a taken dynamic system into trajectories and then
2) investigate their limit behavior.
That means:
2.1) find out and identify classification types of equilibrium positions,
2.2) reveal and investigate possible attracting and repulsive manifolds of a dynamic system under consideration.

The additional key (greatly important) notions introduced in the dynamic systems theory are the following notions:
1) a notion of a stability of equilibrium states of the system. Here we mean the following property of the dynamic system: its ability to remain near some equilibrium state - or on an indicated manifold - for a voluntary prolonged time period provided that small enough changes of initial data take place, as well as
2) a notion of a dynamic system's roughness (this property means an ability of saving of its characteristics in the face of small changing of the whole model itself). A rough dynamic system shows such a type of its behavior, that it preserves the (qualitative) character of motion in the face of a (satisfactory) small changes in the very system's parameters.

Modern specialists in the field of the theory of dynamic systems honor Jules Henri Poincare, the great French mathematician and encyclopedist (1854 – 1912), as the founder of the qualitative theory of differential equations. J. H. Poincare was one of the last encyclopedists – being able to keep in his mind almost all contemporary to him branches - not only of the pure mathematics, but also of physics, celestial mechanics, astronomy etc. For example, J.H. Poincare has laid the very foundation of the relativity theory.

J.H. Poincare has revealed, that each normal second-order autonomous differential system having polynomials in its right parts principally allows the total exhaustive qualitative investigation of it on an (extended) real plane $\bar{R}^2_{x,y}$ [1].

Several special different types of such polynomial dynamic systems were satisfactory studied since the J.H. Poincare times. Modern mathematicians have exhaustively investigated some categories of such systems, i.e. the quadratic polynomial dynamic systems [2], dynamic systems involving nonzero linear terms in their right parts, cubic homogeneous polynomial systems, and also polynomial dynamic systems including nonlinear homogeneous terms of some odd degrees (such as 3, 5, 7) [3], dynamic systems, which have a center or a focus in a singular point O (0,0) [4], and several additional different system's types.

In the present paper let us discuss some special broad family of dynamic systems on an arithmetical (real) plane of their phase variables *x, y*

$$\frac{dx}{dt} = X(x, y), \qquad \frac{dy}{dt} = Y(x, y), \qquad (1)$$

where *X (x, y), Y (x, y)* be the reciprocal polynomial forms of *x* and *y, X* be a cubic, while *Y* be a square polynomial form, *X (0,1) > 0, Y (0, 1) > 0*.

The first of our established goals is to reveal and construct in a Poincare disk all possible types of phase portraits, which are appear to be admissible for the Eq. (1) – dynamic systems.

The second of our established goals is to determine and describe the (close to the coefficient ones) criteria of every such a phase portrait existence. The J.H. Poincare's sequential mapping method helps us to achieve our goal on this way: at first it is necessary to proceed the central mapping of an augmented with a line at infinity phase real plane $\bar{R}^2_{x,y}$ (from the center (0, 0, 1) of the Poincare sphere $\sum$) onto the sphere $\sum : X^2 + Y^2 + Z^2 = 1$ where the diametrically opposite points are considered to be identified, and after this step, at the second, we proceed the orthogonal mapping of the enclosed lower semi sphere of a Poincare sphere $\sum$ to the Poincare disk $\bar{\Omega}: x^2 + y^2 \leq 1$, where we consider to be identified the points of its boundary Γ which are diametrically opposite one to another.

As it was already mentioned above in the context, the disk $\bar{\Omega}$ and the sphere $\sum$ are further called correspondingly the Poincare disk and the Poincare sphere [1].

Some Important Notations and Definitions

$\varphi(t, p)$, $p = (x, y)$ —a fixed point := a motion (a solution) of
an Eq.(1) – system with initial data $(0, p)$.

$L_p : \varphi = \varphi(t, p), t \in I_{max}$. a trajectory of a motion $\varphi(t, p)$.

$L_p^{+(-)} := +(-)$- a semi trajectory of a trajectory L_p.

O-curve of a system := the system's semi trajectory L_p^s ($p \neq O$, $s \in \{+, -\}$), which is adjoining to a point O with the condition $st \to +\infty$.

$O^{+(-)}$- curve of a system := this system's O-curve $L_p^{+(-)}$.

$O_{+(-)}$-curve of a system := this system's O-curve, which is adjoining to a point O from a domain $x > 0$ ($x < 0$).

TO-curve of a system := this system's O-curve, which, being supplemented by a point O, touches some ray in the point O.

A nodal bundle of NO-curves of a system := an open continuous family of this system's TO-curves L_p^s, where $s \in \{+, -\}$ is a fixed index, $p \in \Lambda$, Λ - is a simple open arc, $L_p^s \cap \Lambda = \{p\}$.

A saddle bundle of SO-curves of a system, a separatrix of the point O:= is a fixed TO -curve, which is not included into any bundle of NO-curves of a system.

E, H, P : an elliptical, a hyperbolic, a parabolic O-sectors of a system.

A topological type (T-type) of a finite singular point O of a system := a word A_O including letters *N, S* (a word B_O including letters *E, H, P*), which is used to describe a circular order of nodal and saddle bundles *N, S* of this system's O-curves (of this system's elliptical, hyperbolic, parabolic O-sectors *E, H, P*) while traversing the finite singular point O counterclockwise = in the «+»-direction, starting from some of them.

$$P(u) := X(1, u) \equiv p_0 + p_1 u + p_2 u^2 + p_3 u^3,$$
$$Q(u) := Y(1, u) \equiv a + bu + cu^2.$$

Note A. For each Eq.(1) - system:

1) The T-type of a finite singular point O in its form B_O is easy to construct using the T-type of this singular point in the form A_O , and backwords (we ought to know the both forms, see the Corollary 1 below);

2) the real roots of a polynomial $P(u)$ (polynomial $Q(u)$) appear to be in fact the angular coefficients of the isoclines of infinity (the isoclines of a zero);

3) writing out the real roots of the system's special polynomials $P(u)$, $Q(u)$, separately or all together, we agree always to number the roots of each one of those polynomials in an ascending order.

A Singular Point O (0, 0) and Its Topological Type

Now we need to:
1) reveal and enlist all the existing for these dynamic systems of Eq. (1) O-curves, and
2) to split the whole their totality into the nodal and saddle bundles *N, S*.

The method of exceptional directions of a dynamic system in the finite singular point O will be used in order to achieve this established goal [1]. The exceptional directions' equation for the point O of the Eq.(1) – dynamic systems family will be written in the form

$$xY(x, y) \equiv x(ax^2 + bxy + cy^2) = 0.$$

So the several different cases which are listed below may be realized for this equation:

1) $d \equiv b^2 - 4ac > 0$ - in this case the exceptional directions' equation defines the simle straight lines described with the equations $x = 0$ and $y = q_i x$, $i = 1, 2$, $q_1 < q_2$,

2) $d = 0$ - in this case the exceptional directions' equation defines a straight line described by the equation $x = 0$ as well as a double straight line described with equations $y = qx, q = -\frac{b}{2c}$,

3) $d < 0$ − under this condition the exceptional directions' equation defines only one straight line $x = 0$.

Theorem A. A topological type of a finite singular point O (0, 0) of a family of dynamic systems corresponding to the equations (1) is described with the so-called words A_O and B_O

These words can obtain the following structures:

1) if $d > 0$ - depending on signs of values $P(q_i), i = 1,2$, have forms, indicated in a Table 1,

2) if $d = 0$ - depending on signs of values q and $P(q)$ - have forms, indicated in a Table 2,

3) if $d < 0$ a form: $A_O = S_0 S^0$, $B_O = HH$: [5].

Table 1. Topological type of a finite singular point $O(0, 0)$ in the case when $d > 0$

r	$P(q_1)$	$P(q_2)$	A_O	B_O
1, 4	+	+	$S_0 S_+^1 N_+^2 S^0 N_-^1 S_-^2 = S_0 S_+^1 N S_-^2$	PH^2
2	−	−	$S_0 N_+^1 S_+^2 S^0 S_-^1 N_-^2 = N S_+^2 S^0 S_+^1$	PH^2
3, 6	−	+	$S_0 N_+^1 N_+^2 S^0 S_-^1 S_-^2$	$PEPH^3$
5	+	−	$S_0 S_+^1 S_+^2 S^0 N_-^1 N_-^2$	$H^3 PEP$

Table 2. Topological type of a finite singular point $O(0, 0)$ in the case when $d = 0$

q	$P(q)$	A_O	B_O
+	+	$S_0 S_+ N_+ S^0$	$H^2 P$
−	−	$S_0 N_+ S_+ S^0$	PH^2
+	−	$S_0 S^0 S_- N_-$	$H^2 P$
−	+	$S_0 S^0 N_- S_-$	PH^2
0	+	$S_0 S_+ N S_-$	$H^2 P$
0	−	$N S_+ S^0 S_-$	PH^2

Note B. Explanations and meanings of the new symbols, introduced in the Theorem A.

The symbol S_0 is used to indicate a saddle bundle S, which is adjoining to the finite singular point $O(0, 0)$ from the domain $x > 0$ along the semi axis $x = 0, y < 0$, with the condition that $t \to +\infty$.

Similarly, the symbol S^0 is used to indicate a saddle bundle S, which is adjoining to the finite singular point $O(0, 0)$ from the domain $x > 0$ along the semi axis $x = 0, y > 0$, with the condition that $t \to -\infty$.

A lower sign index «+» or «-» of each nodal or saddle bundle N or S, different from S_0 or S^0, is used to indicate will the bundle under consideration consist of O_+-curves or of O_--curves. An upper index 1 or 2 of each bundle means: will the O-curves of this bundle be adjoining to the finite singular point O along a straight line defined with the equation $y = q_1 x$ or, oppositely, along a straight line defined by the equation $y = q_2 x$.

In the Table 2 above, see lines with the numbers 5 and 6, the node bundle N has not any lower sign index, since it contains both O_+ -curves and O_- -curves together.

Corollary A. As we can conclude from the Theorem A above, all the dynamic systems belonging to the broad family described with the Equations (1) have no limit cycles on the arithmetical plane of their phase variables $R^2_{x;y}$.

Really, such an important feature of the dynamic system as the limit cycle principally could exist and surround a finite singular point O (0,0) of the Eq.(1) - system, and in this situation the Poincare index of that singular point will necessarily be equal to 1 [1]. But let us take into consideration the very important formula for calculation of the index of an isolated singular point of a smooth dynamic system, the formula of Bendixon, which looks like the follows:

$$I(O) = 1 + \frac{e-h}{2},$$

where *e* is a number of elliptical *O*-sectors of the dynamic system, and *h* is a number of its hyperbolic *O*-sectors. The Bendixon's formula together with the formulated above Theorem A mean, that for the finite isolated singular point *O (0, 0)* of any smooth dynamic system described with the Equations (1) the Poincare index *I(O)* = 0. So there are no limit cycles among the trajectories of these systems.

Corollary B. There exist 11 (eleven) different topological types for the isolated finite singular point *O (0, 0)* of the Eq.(1) – systems family. After the detailed thorough analysis of these eleven topological types we can conclude, that for each Eq. (1) – dynamic system there may exist no more than 4 (four) separatrices of the isolated finite singular point *O (0, 0)*. The actual amount of such separatrices may vary from 2 to 4 ones.

Investigation of the İnfinitely Remote Singular Points

Obviously a question of a great interest is the investigation of a behavior of trajectories of the dynamic systems under consideration in the neighborhood of infinity. Such a field of studies demands using of the sequential mappings method. The sequential mappings method is a powerful instrument in the qualitative theory of differential equations and dynamic systems. It was invented by Jules Henri Poincare and provides for the sequential implementation of the two Poincare transformations (famous enough among the researches in this field) [1].

   The first Poincare transformation

$$x = \frac{1}{z}, \quad y = \frac{u}{z} \quad (u = \frac{y}{x}, \quad z = \frac{1}{x})$$

maps a phase arithmetical plane $R^2_{x,y}$ of the dynamic systems described by the equations (1) anambiguosly onto the so-called Poincare sphere $\sum$: $x^2 + y^2 + z^2 = 1$ (where $z = -Z$ [1]).The diametrically opposite points on the Poincare sphere $\sum$ we consider to be identified. Firstly we consider the Poincare sphere $\sum$ without it`s equator *E*. But also the first Poincare transformation maps the infinitely remote straight line of a plane $\overline{R^2_{x,y}}$ onto the equator *E* of the Poincare sphere $\sum$. The diametrically opposite points on the equator *E* of the Poincare sphere $\sum$ we considered to be identified similarly.

The described above first Poincare transformation (and mapping) translates the dynamic system described by the equations (1) into the system, which in the new coordinates of the first Poincare transformation u, z (and after a time change) has the form

$$\frac{du}{d\tau} = P(u)u - Q(u)z, \quad \frac{dz}{d\tau} = P(u)z,$$

where $P(u) :\equiv X(1, u)$ and $Q(u) :\equiv Y(1, u)$ are reciprocal polynomials (this special term means that they would not have common roots and, consequently, would not have common multipliers in their decompositions into the forms of lower degrees).

The obtained new dynamic system will be considered and determined on the whole Poincare sphere $\sum$, including the equator *E* of it. Also this new system will be determined on the whole $(u, z) -$ plane α^*, which is tangent to a sphere $\sum$ at a point $C = (1, 0, 0)$. We need to investigate the new system on the plane $\overline{R^2_{u,z}}$, and it will be necessary to project the results received in this study onto a closed Poincare disk (or a Poincare circle in the other varient of this term) $\overline{\Omega}$, mapping firstly a plane $R^2_{u,z}$ onto the Poincare sphere $\sum$ from the center of the sphere $\sum$, and secondly the lower semi sphere $\overline{H}$ of the Poincare sphere $\sum$ onto the Poincare disk $\overline{\Omega}$, that means – (via the orthogonal mapping) onto a closed unit disk of a plane $R^2_{x,y}$.

For the appeared as a result of the described above first Poincare mapping new dynamic system the axis $z = 0$ will be the invariant axis (that mean it will consist of trajectories of this system). On this axis now will lie the singular points $O_i (u_i, 0), i = \overline{0, m}$, where $u_i, i = \overline{1, m}$ are all existing real roots of the polynomial $P(u)$, and $u_0 = 0$; the same time may exist $i_0 \in \{1, ..., m\}$: $u_{i_0} = 0$. Further we are going to name such singular points the infinitely remote (IR) points of the 1st kind for the dynamic systems described by the equations (1).

   The second Poincare transformation

$$x = \frac{v}{z}, \quad y = \frac{1}{z} \quad \left(v = \frac{x}{y}, \quad z = \frac{1}{y}\right)$$

somehow similarly maps a phase real plane $R^2_{x,y}$ anambiguosly onto a sphere $\sum$, where the diametrically opposite points are also considered to be identified. At first we again consider the Poincare sphere $\sum$ without it`s equator. The second Poincare transformation translates each Eq.(1) - system into a new dynamic system. This newly obtained dynamic system in the new coordinates of the second Poincare mapping τ, v, z looks like:

$$\frac{dv}{d\tau} = -X(v,1) + Y(v,1)vz, \quad \frac{dz}{d\tau} = Y(v,1)z^2.$$

It is considered and determined on the whole Poincare sphere $\sum$, as well as on the whole (v,z) – plane $\hat{a}$, which is tangent to a sphere $\sum$ at a point $D = (0,1,0)$ [1].

A set described with the equation $z = 0$ is the invariant set for the new dynamic system. On this set will lie the singular points $(v_0, 0)$, where v_0 is any real root of the polynomial $X(v,1) \equiv p_3 + p_2 v + p_1 v^2 + p_0 v^3$. We could name those singular points the infinitely remote points (IR-points) of the 2nd kind for the dynamic systems described by the equations (1), but every singular point of the 2nd kind, for which $v_0 \neq 0$, naturally coincide to someone among the IR-points of the 1st kind, and precisely to the point $\left(\frac{1}{v_0}, 0\right)$,

while $v_0 = 0$ won't be a root for the polynomial $X(x, 1)$, since $X(0, 1) = p_3 \neq 0$ for the dynamic system described by the equations (1). As a result, we can formulate the

Corollary C. Any dynamic system belonging to the broad family described by the equations (1) has infinitely remote singular points only of the 1st kind.

Using the orthogonal projection, further we proceed a mapping of a closed lower semi sphere $\bar{H}$ of a Poincare sphere $\sum$ onto a real plane x, y. As a result of this mapping the open part H of a lower semi sphere of a Poincare sphere $\sum$ maps one-to-one onto the open Poincare disk Ω, and an equator of the Poincare sphere $\sum$ (its boundary) E maps onto a very circle, a bondary of the Poincare disk, $\Gamma = \partial\Omega$. =>

1) All the own trajectories of any dynamic system described by the equations (1), including the isolated finite singular point $O (0, 0)$, now displayed into the disk Ω, and they are filling the Poincare disk. They are called trajectories of the system under consideration (the Eq.(1) – system) in the Poincare disk Ω.

2) The infinitely remote trajectories, including the infinitely remote singular points, are displayed now on a boundary Γ of a Poincare disk Ω, and they are filling this boundary. They are called trajectories of the system under consideration (the Eq.(1) – system) on the Poincare disk's boundary – the circle Γ.

Each infinitely remote singular point O_i $(u_i, 0)$ of the Eq.(1) – system, $i \in \{1, ..., m\}$, now corresponds to the two diametrically opposite points situated on the Poincare disk's boundary – the circle Γ .

$O_i^{\pm}(u_i, 0)$: O_i^+ $(O_i^-) \in \Gamma^{+(-)} := \Gamma|_{x>0\,(x<0)}$.

$\forall\, i \in \{1, ..., m\}$ for the point O_i^+ (O_i^-) we now need to introduce the necessary and important notations.

1) O_i^+ (O_i^-)—curve be a semi trajectory of the Eq.(1) – system in the Poincare disk Ω, which is adjacent to a singular point $O_i^{+(-)}$. It starts in the some ordinary point $p \in \Omega$.

2) Notations of nodal and saddle bandles N, S, which are adjacent to the singular point O_i^+ (O_i^-) from the Poincare disk Ω, will correspond to the notations introduced for the isolated singular point $O (0, 0)$.

3) We introduce the notations of the words A_i^+ (A_i^-) containing letters $N, S,$ which are fixing the order of bandles of O_i^+ (O_i^-)-curves at a semi circumvention of the point O_i^+ (O_i^-) in the Poincare disk Ω. This semi circumvention is proceeded in the direction of increasing of u.

We are going to describe the topological type of the singular point O_i^+ (O_i^-) with a word A_i^+ (A_i^-), while we describe the topological type of a singular point O_i with words $A_i^{\pm}$.

For the topological types of the infinitely remote singular points $O_0^{\pm}$ $(0,0)$ of the family of dynamic systems described by the equations (1) the following theorem is formulated and proved.

Theorem B. If we consider a number $u = 0$ as the root of a polynomial $P(u)$ of the Eq.(1) – system, having the multiplicity $k \in \{0, ..., 3\}$, then the words $A_0^{\pm}$, used to describe the topologycal types of the infinitely remote singular points $O_0^{\pm}$ $(0,0)$ of the system, may only have the forms, written in the Table 3 below. The precise form will depend on the sign of a number ap_k and the value of k (here a and p_k are the coefficients of the system) [5].

Table 3. Topologycal types of infinitely remote singular points $O_0^{\pm}$ $(0,0)$.

k	ap_k	A_0^+	A_0^-
0	0	N	N
0, 2	+ (-)	$N_+(N_-)$	$N_-(N_+)$
1, 3	+ (-)	$N_-N_+(\emptyset)$	$\emptyset(N_-N_+)$

Corollary D. Infinitely remote singular points $O_0^{\pm}$ of any dynamic system described by the equations (1) has no separatrices.

Theorem C. If we consider a real number u_i $(\neq 0)$ as the root of a polynomial $P(u)$ of the Eq.(1) – system, having the multiplicity $k_i \in \{1,2,3\}$, then the words $A_i^{\pm}$, as well as the value $g_i = P^{(ki)}(u_i)Q(u_i) \neq 0$, which describe and determine the topologycal types of the infinitely remote singular points $O_i^{\pm}$ $(u_i,0)$ of the system under consideration, may have only forms written in the Table 4 below. The precise form will depend on the value of k_i and signs of numbers u_i and g_i, [5].

Table 4. Topological types of the infinitely remote points $O_i^{\pm}$ $(u_i,0)$, $i \in \{1, ..., m\}$.

u_i	k_i	g_i	A_i^+	A_i^-
+(-)	1, 3	+	$N_+(N_-)$	$S_-(S_+)$
+(-)	1, 3	–	$S_-(S_+)$	$N_+(N_-)$
+(-)	2	+	$S_-N_+(\emptyset)$	$\emptyset(N_-S_+)$
+(-)	2	–	$\emptyset(N_-S_+)$	$S_-N_+(\emptyset)$

Corollary E. We can conclude using the Theorems B and C, that for the infinitely remote singular points of the family of dynamic systems described by the equations (1), only the finite number, and namely 13 (thirteen) separate topological types are existing. The thorough detailed study of those 13 topological types makes clear, that the infinitely remote singular points of every Eq.(1) - system may have only *m* separatrices: one separatrice for every singular point O_i $(u_i, 0), i = 1, m$.

Note C. In the Tables 3, 4 the lower sign index «+» or «-» of every nodal or saddle bundle *N* or *S*, shows will the given bundle adjust to the singular point O_i^+ (or to the point O_i^-) from the side where $u > u_i$ or from the side where $u < u_i$ of the isocline described with the equation $u = u_i$.

In the Table 3, see line 1, a nodal bundle *N* has no lower sign index at all, that means that it contains O_i^+-curves (O_i^--curves) in each domain where $|u| > 0$ [5-9]].

Conclusions

The present paper is written as a result of the original study in the field of the qualitative theory of differential equations and dynamic systems.

The main aim of the study is to investigate and construct all different in the topological and topo-dynamical sense phase portraits of a broad family of dynamic systems. The systems belonging to this family are clearly characterized with their reciprocal polynomial right parts. A total broad family has numerical subfamilies, interesting in the different applications.

The whole family of dynamic systems under consideration was studied using the first and the second Poincare mappings on the Poincare sphere, in the Poincare disk and on its boundary - the Poincare circle. We have constructed all topologically different phase portraits which are possible for the systems of this family, about 250 types of phase portraits. All those types were constructed basing on the theoretical precise proofs. [6, 7].

For this aim it was necessary to investigate all finite and infinitely remote singular points of systems under consideration. Purposes of such an investigation demanded developing of new powerful special and totally new research methods. [8-10].

Recommendations

Despite of the theoretical nature of the present investigation, due to obtained pioneer results and developed in this study new research methods [11-15], authors consider the work to be useful for different applied studies of dynamic systems having polynomial right parts [16, 17].. The paper will be interesting and addressed to students, postgraduates and scientific researchers.

References

Andronov, A.A., Leontovich, E.A., Gordon, I.I., & Maier, A.G. (1973). *Qualitative theory of second-order dynamic systems*. New York, NY: Wiley.

Andreev, A.F., & Andreeva, I.A. (1997). On limit and separatrix cycles of a certain quasi quadratic system. *Differential Equations, 33 (5),* 702 – 703.

Andreev, A.F., & Andreeva, I.A. (2007). Local study of a family of planar cubic systems. *Vestnik St. Petersburg University: Ser.1. Mathematics, Mechanics, Astronomy, 2*, 11- 16. DOI: 10.3103/S1063454107020021, EID: 2-s2.0-84859730890.

Andreev, A.F., Andreeva, I.A., Detchenya, L.V., Makovetskaya, T.V., & Sadovskii, A.P. (2017). Nilpotent Centers of Cubic Systems. *Differential Equations*, *53*(8), 1003 - 1008. DOI: 10.1134/S0012266117080018, EID: 2-s2.0-85029534241.

Andreev, A.F., & Andreeva, I.A. (2007). Phase flows of one family of cubic systems in a Poincare circle. I. *Differential Equations and Control, 4*, 17-26.

Andreev, A.F., & Andreeva, I.A. (2008). Phase flows of one family of cubic systems in a Poincare circle. II. *Differential Equations and Control, 1,* 1 - 13.

Andreev, A.F., & Andreeva, I.A. (2008). Phase flows of one family of cubic systems in a Poincare circle. III. *Differential Equations and Control/, 3*, 39 - 54.

Andreev, A.F., & Andreeva, I.A. (2009). Phase flows of one family of cubic systems in a Poincare circle. IV_1, *Differential Equations and Control, 4*, 181 - 213.

Andreev, A.F., &Andreeva, I.A. (2010). Phase flows of one family of cubic systems in a Poincare circle. IV_2, *Differential Equations and Control, 4*, 6- 17.

Andreev, A.F., & Andreeva, I.A. (2017). Investigation of a Family of Cubic Dynamic Systems. *Vibroengineering Procedia, 15,* 88 – 93. DOI: 10.21595/vp.2017.19389.

Andreev, A.F., & Andreeva, I.A. (2017). Phase Portraits of One Family of Cubic Systems in a Poincare Circle.I. *Vestnik RAEN,* 17, 4, 8 – 18. ISSN 1682-1696.

Andreev, A.F., &Andreeva, I.A. (2018) On a Behavior of Trajectories of a Certain Family of Cubic Dynamic Systems in a Poincare Circle, *IOP Journal of Physics, Conference Series,* 1141.

Andreeva, I.A. (2018) Phase Portraits of Cubic Dynamic Systems in a Poincare Circle. *(A Chapter in the Monograph "Differential Equations- Theory and Current Research". IntechOpen, UK,* ISBN 978-953-51-6120-2.

Andreev, A.F., & Andreeva, I.A. (2018). Phase Portraits of a Family of Cubic Dynamic Systems in a Poincare Circle.II. *Vestnik RAEN,* 18, 4, 11 – 15. ISSN 1682-1696.

Andreeva, I.A., &Efimova, T.O. (2019) Phase Portraits of a Special Class of Dynamic Systems in a Poincare Circle, *IOP Journal of Physics, Conference Series,* 1236.

Aksenova, O.A., & Khalidov, I.A. (2016). Analytic Model of the Effect of Poly-Gaussian Roughness on Rarefied Gas Flow near the Surface, *Rarefied Gas Dynamics*, *AIP Conference Proceedings, 1786, American Institute of Physics, Melville, NY*, 1000071 - 1000078.

Aksenova, O.A., & Khalidov, I.A. (2016). Unstable Rarefied Gas Flow Conditions in a Channel, *Rarefied Gas Dynamics, AIP Conference Proceedings 1786, American Institute of Physics, Melville, NY*, 1000091-1000097.

Authors Information

Irina Andreeva	**Tatiana Efimova**
Peter the Great St. Petersburg Polytechnic University	Peter the Great St. Petersburg Polytechnic University
195251 St. Petersburg, Polytechnicheskaya, 29.	195251 St. Petersburg, Polytechnicheskaya, 29.
Russian Federation	Russian Federation
Contact E-mail: *irandr2@gmail.com*	

IConTES 2019: International Conference on Technology, Engineering and Science

Experimental Spray Investigation of Biodiesel Fuels Derived from Corn Oil and Canola Oil

Anılcan ULU
Izmir Institute of Technology

Seven Burcin CELLEK
Izmir Institute of Technology

Alvaro Diez RODRIGUEZ
Izmir Institute of Technology

Unver OZKOL
Izmir Institute of Technology

Abstract: Spray characteristics of fuels are one of the most important factors for engine research owing to their relationship between performance output and emission level. The aim of this study was to investigate the spray behavior of biodiesel fuels derived from corn oil and canola oil, utilizing a piezo injector. Effects of ambient pressure and injection pressure on spray characteristics like spray penetration length and spray cone angle were investigated in a constant volume combustion chamber. Ambient and injection pressures were in range of 0-15 bar and 600-1000 bar, respectively. As a result of this study, sampled biodiesel fuels have longer penetration and smaller spray angles. This can be explained by having higher viscosities resulting in slower evaporation and atomization.

Keywords: Biodiesel, Constant volume combustion chamber, Spray investigation

Introduction

Diesel engines have been very important devices for power generation so far owing to their higher torque capability and energy density than their gasoline counterparts. Although their widespread usage, they are focus of criticism due to their pollutant emission levels and utilization of nonrenewable fossil fuels. Important organizations like European Union (EU) and Environmental Protection Agency (EPA) of United States of America brought strict regulations to pollutant levels from automobiles. These regulations have been obligating researchers to find ways of decreasing emissions since 1990s (Rodriguez, 2009). Therefore, investigation of pollutant emissions in every aspect has had an important place in engine research up to now.

One of the promising ways to overcome the problems of diesel engines is to develop renewable fuels from vegetable oils or animal fats, which are called as biodiesel fuels. Many studies have been performed to obtain a biodiesel from a source, such as pyrolysis, transesterification, gasification followed by Fischer-Tropsch synthesis (Oumer, Hasan, Baheta, Mamat, & Abdullah, 2018). Among these techniques, transesterification is the most common method owing to its simplicity and efficiency. Plenty of raw materials have been employed for biodiesel production, such as palm oil, jatropha, soybean oil, coconut oil, rapeseed, canola, sunflower, corn, and olive oils (Mirhashemi & Sadrnia, 2019). In Turkey, sunflower, olive, canola, and corn oils are the most widespread oils for biodiesel generation.

Biodiesel fuels have several advantages which are subject of current research in this field. Firstly, it is mechanically advantageous to use biodiesel fuels instead of diesel fuels in diesel engines (Mirhashemi & Sadrnia, 2019) because lubrication properties of biodiesel fuels are better than those of mineral diesel fuels and

biodiesels have higher flash points. Furthermore, some biodiesels have higher cetane numbers than those of diesel fuels while some of them possess lower cetane numbers (How, Masjuki, Kalam, & Teoh, 2018). Biodiesels having higher cetane number can be comparable with conventional diesel fuels in terms of ignition properties. Hence, these advantages may lead to a replacement of diesel fuel with biodiesel fuel.

On the other hand, biodiesels own some disadvantages over mineral diesels. Firstly, biodiesel fuels possess higher viscosities than conventional diesels (Deng, Li, Hu, Wu, & Li, 2010). Thence, biodiesels perform slower atomizations which cause slower break-up. Secondly, biodiesels have higher densities which affect the spray pattern (Gupta & Agarwal, 2016). Thirdly, calorific values of biodiesels are lower than those of mineral diesels (Gharehghani, Mirsalim, & Hosseini, 2017). Besides, biodiesels are more expensive and less available than conventional diesel fuels. According to drawbacks of biodiesel fuels, it is undesirable to use pure biodiesel in compression ignition engines. Instead, the use of diesel-biodiesel blends is desirable to achieve good physicochemical properties. By this way, a fuel which can utilize both advantages of diesel and biodiesel may be presented.

Numerous studies are available in the literature about performance of diesel-biodiesel blends. An et al. (2012) researched the pure biodiesel performance in a diesel engine. They found that the power reduced on average by 12.2% from 1600 rpm to 3600 rpm. Moreover, Özkan et al. (2005) observed greater reductions in power for diesel-biodiesel blends. On the contrary, Al-Widyan et al. (2002) reported that diesel-biodiesel blends performed higher power output than conventional diesel fuel. Forson et al. (2004) also found greater power output and higher brake thermal efficiency for diesel-biodiesel blends.

Emissions from a diesel engine consists primarily of nitric oxides (NO_x), carbon monoxide (CO), hydrocarbons (HCs). Although emissions vary from engine to engine depending on the operating conditions, fuel properties and engine design, a general inference can be made (Oumer et al., 2018). HC and CO emission levels decrease with the use of diesel-biodiesel blends. However, significant decrease in NO_x level can not be observed. In many times, NO_x increases with the utilization of biodiesel in mineral diesel fuel.

Moreover, spray investigation is crucial for diesel engine research. Because, it directly affects the combustion behaviour thus the performance and emission levels. Hence, spray behaviour of biodiesel fuels has to be researched in order to understand the development pattern and to develop an idea on the combustion properties of fuels (Baumgarten, 2006). Some of the key parameters of interest are spray break-up length, spray penetration length, and spray cone angle for a spray analysis. These parameters can help researchers predict how fuel mixes with surrounding air. Moreover, a constant volume combustion chamber (CVCC) which is covered with transparent windows can be used to perform the spray tests where transparent windows allow the light to pass the chamber for spray visualization.

In literature, several studies can be found for spray investigation of biodiesel fuels. For example, Deng et al. (2010) observed that spray penetration lengths of biodiesel fuels are longer than conventional diesel fuel due to higher density and viscosity. They also reported that spray penetration length and spray cone angle get larger as the injection pressure increases for both diesel and biodiesel fuels. Also, Desantes et al. (2009) concluded that biodiesel shows longer spray penetration and smaller cone angle compared to conventional diesel due to the higher density and surface tension. On the other hand, Gupta et al. (2016) found that biodiesel spray pattern is not significantly different from the conventional diesel. They concluded that biodiesel and diesel fuels are comparable in terms of spray tip penetration and spray cone angle.

The aim of this study was to investigate the spray characteristics of biodiesel fuels in terms of spray penetration length and spray cone angle for biodiesel fuels derived from corn oil and canola oil. Biodiesels were selected due to their abundance in Turkey. Tests were performed in a constant volume combustion chamber with a common rail system. Then, desired spray parameters of biodiesel fuels are obtained and compared with those of diesel fuels.

Experimental System

Experimental Setup

A schematic sketch of the spray test rig which consists of three subsystems is shown in Figure 1. These three subsystems are gas filling system, fuel injection system and constant volume combustion chamber. A high-speed camera is utilized to record an injection event at 20,000 fps, shutter speed of 1/62,000 with a resolution of

512x512 pixels during the experiments. After the experiments, spray characteristics can be obtained from the videos which are recorded by the camera. These videos are then post processed to acquire the required parameters.
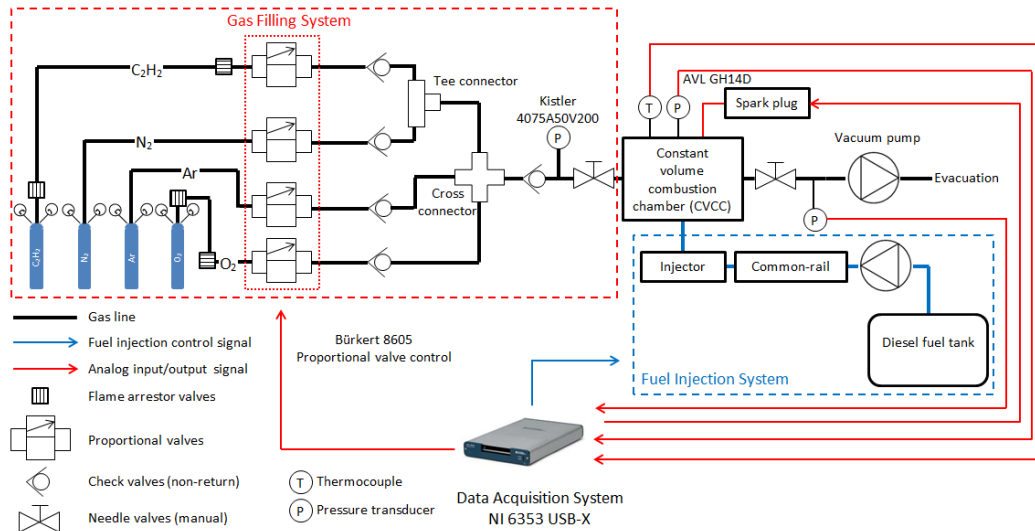
Figure 1. Schematic of experimental setup

Constant Volume Combustion Chamber (CVCC)

CVCC is a useful chamber to simulate an engine-like environment in order to obtain the spray characteristics of any fuel with any injector. Chamber is filled with nitrogen gas to control the ambient pressure which can be measured via data acquisition system with pressure sensors. Besides, CVCC has an optical window allowing the spray visualization via various optical techniques.

Gas Filling System

Gas filling system consists of 4 different gases which are nitrogen, oxygen, argon, and acetylene to simulate air and flammable gases. However, only nitrogen is used for spray investigation to prevent burning any portion of the fuel. Furthermore, proportional valves are used to fill the chamber from the gas tubes. PID control is available for more accurate filling.

Fuel Injection System

Fuel tank, fuel filter, high pressure pump, common rail, fuel lines, and the injector are the components of the fuel injection system. Injector is a piezo type injector.

Fuel Properties and Test Conditions

Three samples are prepared from corn oil, canola oil, and diesel fuel. Canola oil and corn oil are named as CAB100 and COB100, respectively. Table 1 shows the viscosity and density values of the tested fuels. Diesel fuel has the lowest viscosity and density values. Although both biodiesel fuels have similar density and viscosity values, biodiesel derived from corn oil has higher density and viscosity than the biodiesel derived from canola oil.

Table 1. Properties of tested fuels

Test Fuel	Viscosity @ 40°C (mPa.s)	Density @ 25°C (kg/m^3)
Diesel	3.071	829.546
CAB100	5.149	869.915
COB100	5.868	877.069

During the experiments, three different injection pressures were utilized, which are 600, 800, and 1000 bars. Ambient pressure was adjusted from 0 bar to 15 bar by increasing the pressure 5 bars. Operating conditions are presented in Table 2.

Table 2. Test conditions

Injector type	Piezo CRDI injector
Number of the nozzle holes	1
Injection angle	145°
Injection duration (ms)	1
Injection pressure (bar)	600, 800, 1000
Ambient pressure (bar)	0, 5, 10, 15

Image Processing Algorithm

An example for an original and its post processed images is shown in Table 3. Then, spray penetration length and spray cone angle are obtained by a MATLAB based in house code and ImageJ. The logic behind the algorithm is that a threshold pixel intensity search given at the below charts, Figure 2 and Figure 3.

Spray penetration measurement from the video is obtained by taking four images of the respective sequence before fuel injection. These images are used for correction of the raw images taken from each complete injection. Background subtraction is applied. After that, a threshold value is calculated, and the last pixel of each image is defined, and spray penetration is calculated by using the formula for finding the distance between two points.

Spray angle measurement is obtained by an angle measurement tool created in house code. This tool creates 2 vectors according to the position of the injector tip as shown in Figure 3. After obtaining these vectors, end points of the vectors can be moved towards the desired point manually while keeping the vectors tangentially to the spray outline.
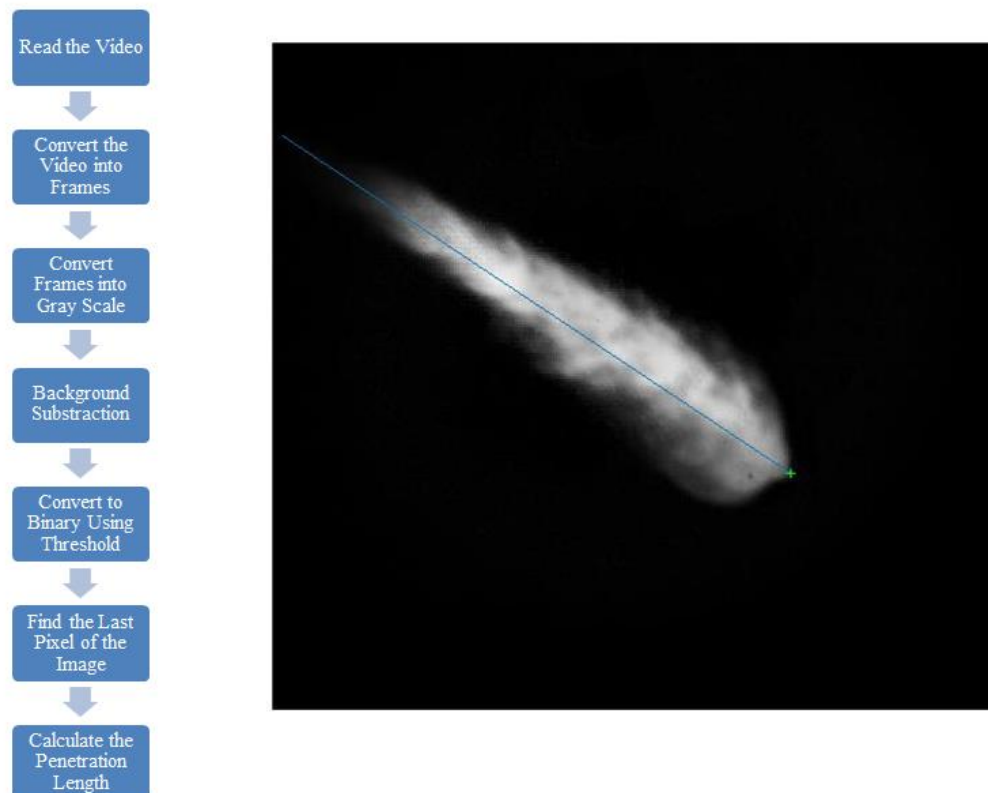
Figure 2. Schematic of spray penetration algorithm
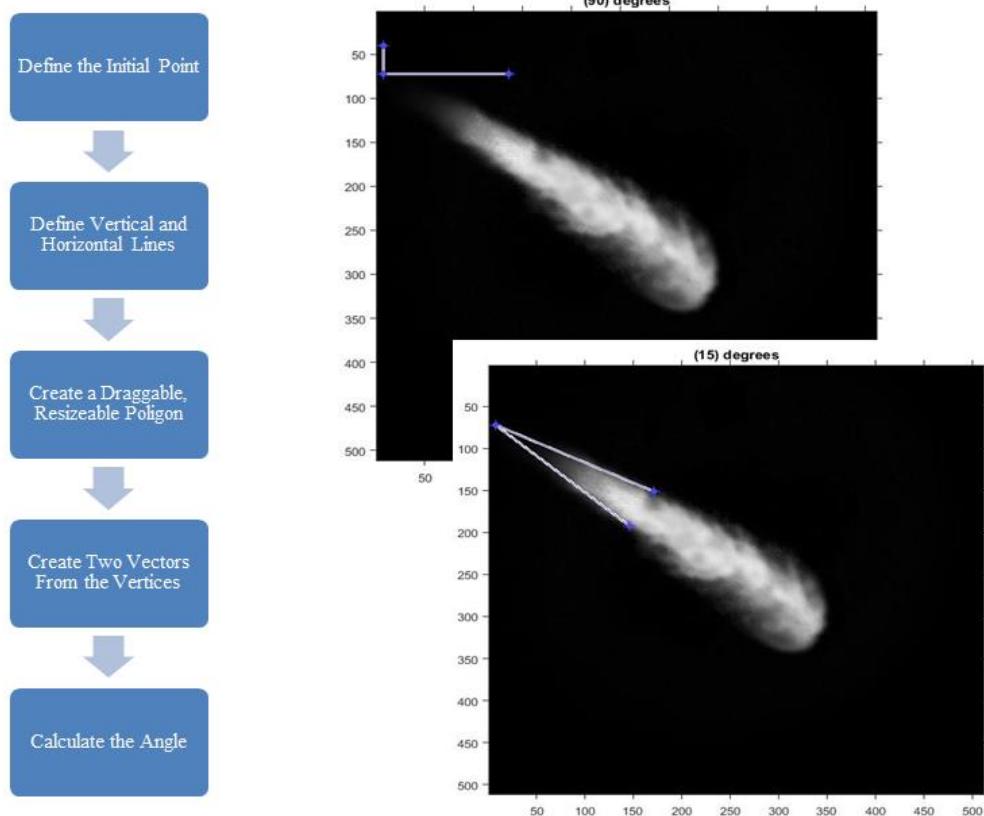
Figure 3. Schematic of spray angle algorithm.

Table 3. Comparison of original image and processed image

Conditions	Original Image	Processed Image
Injection pressure: 800 bar Ambient pressure: 1 bar Time after start of injection: 0.7 ms Frames per second: 20,000 Fuel: Mineral diesel		

Results and Discussion

The definition of spray penetration is the maximum distance measured from the injector tip to the spray tip. The definition of spray angle is the angle between two lines being tangent to the spray outline. Both parameters are affected by injection pressure and ambient pressure. Figure 4 and Figure 5 represent the comparision of spray penetration under different conditions.

Figure 4a to 4d shows how spray penetration length develops in time at three different injection pressures (600, 800 and 1000 bars) and four ambient pressures (0, 5, 10 and 15 bars). These graphs show that the spray penetrates longer when COB100 is used as fuel. CAB100 fuel spray penetration length follows it and, the diesel's spray penetration length is the least. Biodiesel fuels evaporates slower than diesel fuel due to their higher density and viscosity. Biodiesel fuels penetrate longer when compared to neat diesel fuel spray for all ambient pressures. As the injection pressure increases, spray penetration length increases for all fuel types (Figure 5). As expected, spray penetration length decreases as the ambient pressure increases due to higher drag forces.

(a)　　　　　　　　　　　　　　　　(b)

(c)　　　　　　　　　　　　　　　　(d)
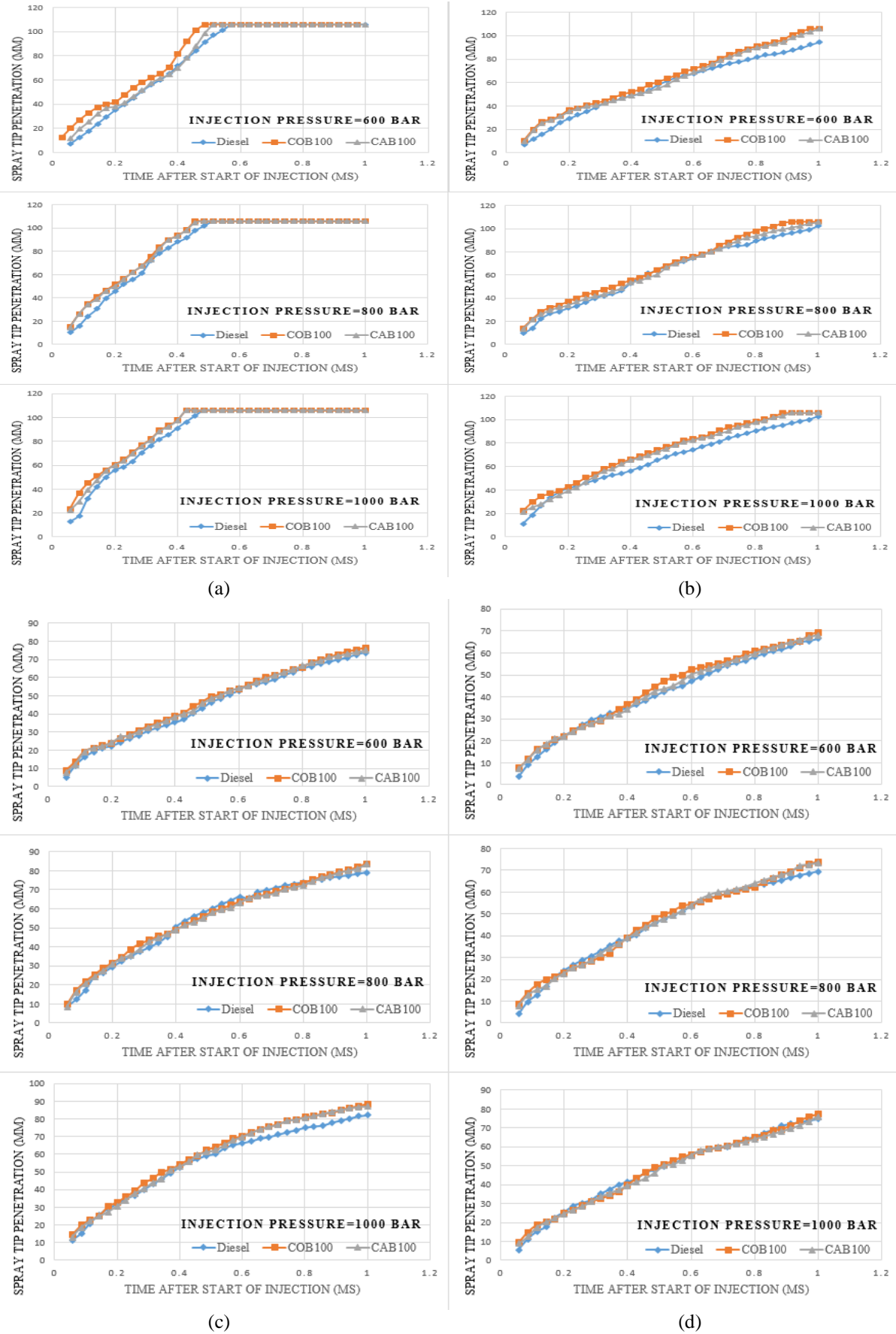
Figure 4: Comparison of spray tip penetration for diesel, COB100 and CAB100 at (a) 0 bar, (b) 5 bar, (c) 10 bar and (d) 15 bar ambient pressure of spray chamber

(a)

(b)

(c)

(d)
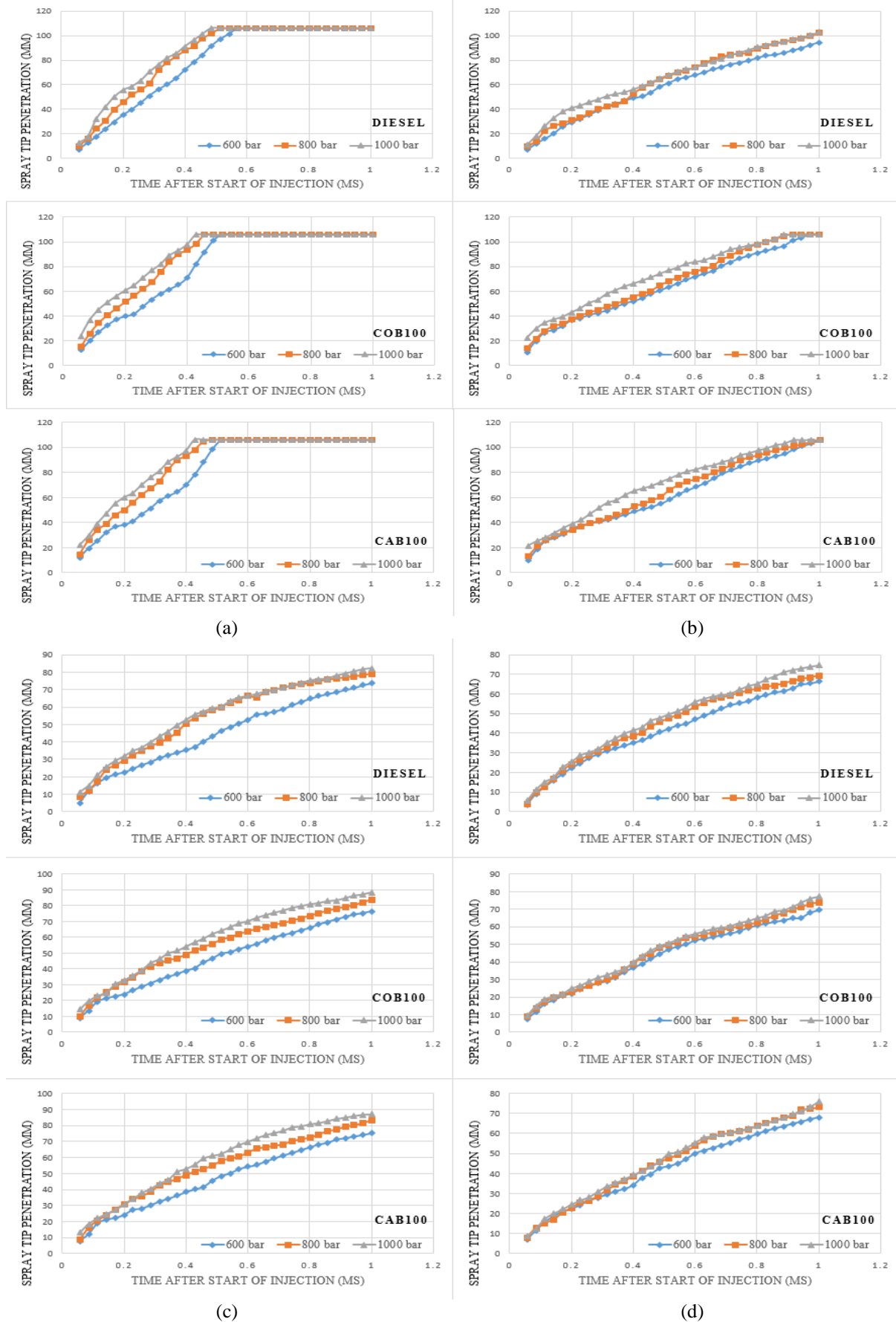
Figure 5. Effect of injection pressure on spray tip penetration for diesel, COB100 and CAB100 at (a) 0 bar, (b) 5 bar, (c) 10 bar and (d) 15 bar ambient pressure of spray chamber

(a)   (b)

(c)   (d)
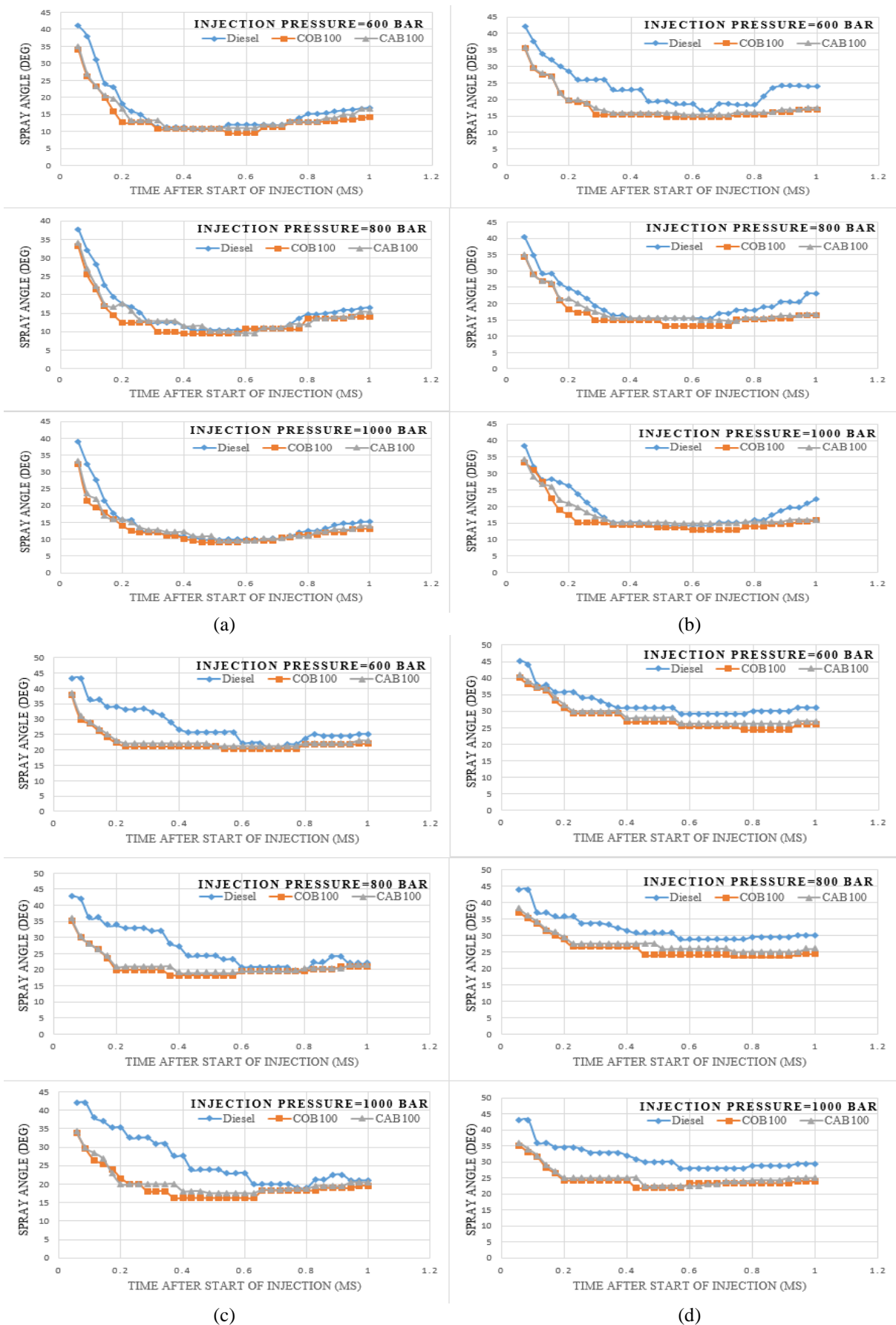
Figure 6. Comparison of spray cone angle for diesel, COB100 and CAB100 at (a) 0 bar, (b) 5 bar, (c) 10 bar and (d) 15 bar ambient pressure of spray chamber.

(a)

(b)

(c)

(d)
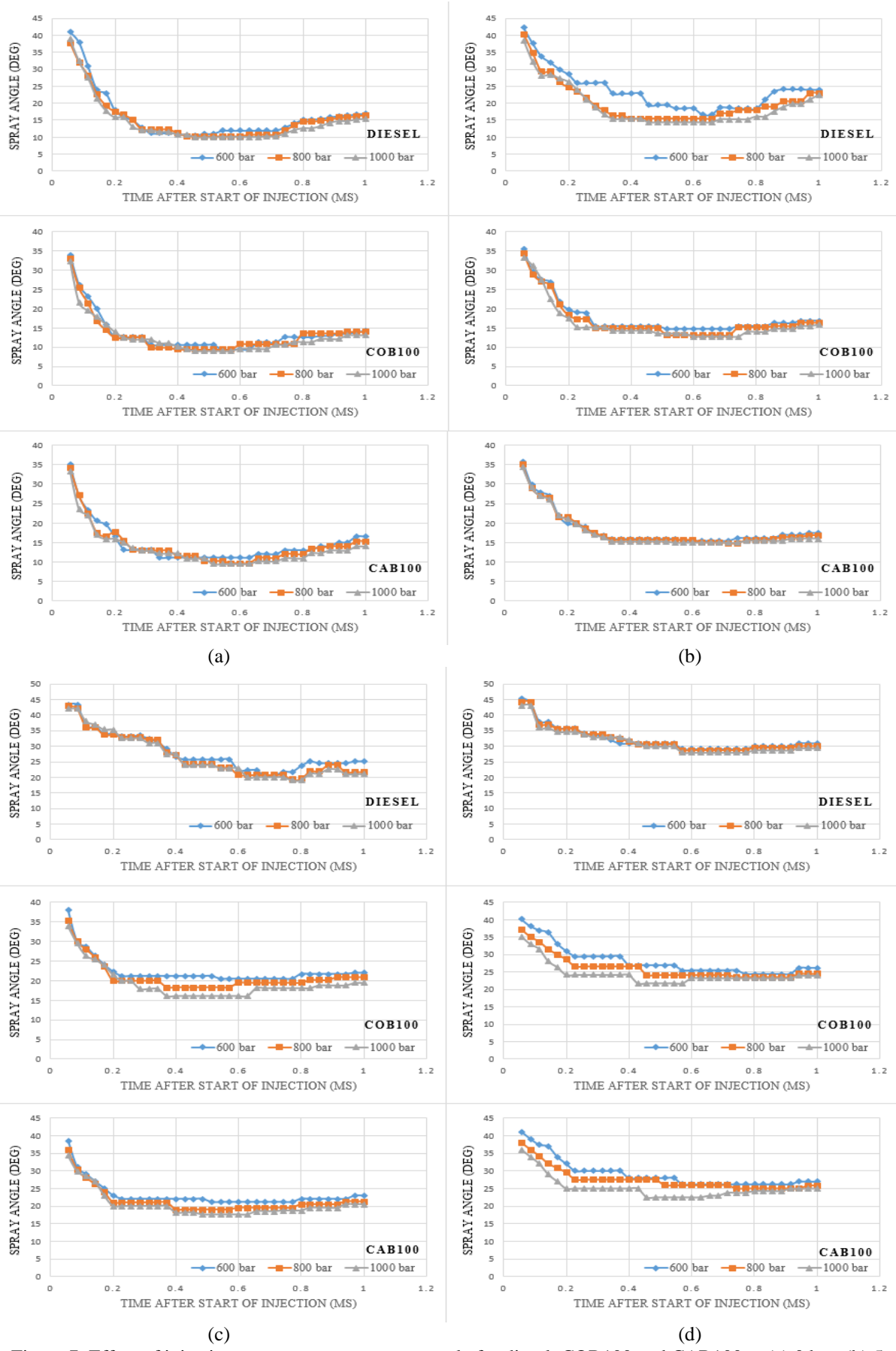
Figure 7. Effect of injection pressure on spray cone angle for diesel, COB100 and CAB100 at (a) 0 bar, (b) 5 bar, (c) 10 bar and (d) 15 bar ambient pressure of spray chamber.

Figure 6 and Figure 7 represent the comparison of spray angle under conditions similar to Figure 4 and 5. Spray angle gets narrower when using biodiesels as fuel. It is because of the slowness of evaporation speed as a consequence of higher density and surface tension of biodiesel fuels. Furthermore, spray angle decreases as the injection pressure increases (Figure 7) due to its higher momentum.

Conclusion

The purpose of the study was investigation of spray characteristics – spray penetration and spray angle – of biodiesel fuels derived from canola oil and corn oil. In the direction of this purpose, a CVCC and high-speed optical system was utilized. The experiments were performed under different ambient and injection pressures. Ambient pressure varied from 0 bar to 15 bar with increment of 5 bar. Injection pressure varied from 60 Mpa to 100 Mpa with increment of 20 Mpa. The experiments were recorded by a high-speed camera and investigated by using a Spray Angle and Spray Penetration Calculation algorithm.

According to the results, biodiesel fuel had longer spray than diesel spray. Due to higher viscosity and density of biodiesel, spray was longer. The longest spray is obtained under 0 bar ambient pressure for biodiesel derived from corn oil. The penetration length decreased as the ambient pressure increased. It is caused by higher drag forces due to higher ambient pressures. Spray angle was narrower for biodiesel fuels due to viscosity and density difference between diesel and biodiesel.

Recommendations

Although spray penetration length and spray cone angle are important parameters, they are insufficient to explain how biodiesel fuels affect the engine performance and emission levels. Also, atomization behaviors of biodiesels are needed to be researched in order to better understand the effects of viscosity and density. Furthermore, combustion properties like flame lift-off length and flame angle should be analyzed to better explain the combustion behavior of biodiesel fuels.

Acknowledgements

References

Al-Widyan, M. I., Tashtoush, G., & Abu-Qudais, M. (2002). Utilization of ethyl ester of waste vegetable oils as fuel in diesel engines. *Fuel Process Technol*, 91-103.

An, H., Yang, W., Chou, S., & Chua, K. (2012). Combustion and emissions characteristics of diesel engine fueled by biodiesel at partial load conditions. *Applied Energy*, 363-71.

Baumgarten, C. (2006). *Mixture formation in internal combustion engines.* New York: Springer.

Deng, J., Li, C., Hu, Z., Wu, Z., & Li, L. (2010). Spray characteristics of biodiesel and diesel fuels under high injection pressure with a common rail system. *SAE International 2010-01-2268*.

Desantes, J. M., Payri, R., Salvador, F. J., & Manin, J. (2009). Influence on diesel injection characteristics and behavior using biodiesel fuels. *SAE Technical Paper Series 2009-01-0851*.

Forson, F., Oduro, E., & Hammond-Donkoh, E. (2004). Performance of jatropha oil blends in a diesel engine. *Renewable Energy*, 1135-1145.

Gharehghani, A., Mirsalim, M., & Hosseini, R. (2017). Effects of waste fish oil biodiesel on diesel engine combustion characteristics and emission. *Renewable Energy*, 930-936.

Gupta, J. G., & Agarwal, A. K. (2016). Macroscopic and microscopic spray characteristics of diesel and karanja biodiesel blends. *SAE International 2016-01-0869*.

How, H., Masjuki, H., Kalam, M., & Teoh, Y. (2018). Influence of injection timing and split injection strategies on performance, emissions, and combustion characteristics of diesel engine fueled with biodiesel blended fuels. *Fuel 213*, 106-114.

Mirhashemi, F. S., & Sadrnia, H. (2019). NOx emissions of compression ignition engines fueled with various biodiesel blends: A review. *Journal of the Energy Institute*.

Oumer, A. N., Hasan, M. M., Baheta, A. T., Mamat, R., & Abdullah, A. A. (2018). Bio-based liquid fuels as a source of renewable energy: A review. *Renewable and Sustainable Energy Reviews*, 82-98.

Özkan, M., Ergenç, A. T., & Deniz, O. (2005). Experimental performance analysis of biodiesel , traditional diesel and biodiesel with glycerine. *Turk J Eng Environ Sci*.

Rodriguez, A. D., & Zhao, H. (2010). Investigation of split injection in a single cylinder optical diesel engine. *SAE Technical Paper 2010-01-0605*. doi:https://doi.org/10.4271/2010-01-0605

Szybist, J. P., & Boehman, A. L. (2003). Behavior of a Diesel Injection System with Biodiesel Fuel. *SAE Technical Paper Series 2003-01-1039*.

Author Information

Anılcan Ulu
Izmir Institute of Technology
Gulbahce Campus 35430 Urla, Izmir, Turkey
Phone: +902327506743
Fax: +902327506701
Contact E-mail: *anilcanulu@iyte.edu.tr*

Seven Burçin Çellek
Izmir Institute of Technology
Gulbahce Campus 35430 Urla, Izmir, Turkey
Phone: +902327506743
Fax: +902327506701

Alvaro Diez Rodriguez
Izmir Institute of Technology
Gulbahce Campus 35430 Urla, Izmir, Turkey
Phone: +902327506743
Fax: +902327506701

Ünver Özkol
Izmir Institute of Technology
Gulbahce Campus 35430 Urla, Izmir, Turkey
Phone: +902327506770
Fax: +902327506701

Evaluation and Correlation of Friction Head Losses in Smooth and Rough Pipes

Abdelkrim HADDAD
Université 8 Mai 1945

Abstract: In order to transport a fluid, the energy losses mainly due to friction have to be overcome. Expressed in fluid height and referred to as head reduction, they are essentially dependent on pipe roughness and fluid low regime, and constitute the basis for the computation of fluid transportation and distribution networks design and analysis. The present paper reviews the diverse relationships that lead to the computation of friction head losses, and compare the results obtained to those of the experimentations carried out on pipes of diverse roughness and fluid flow regimes. The Hazen-Williams and Strickler relationships have been found to be the most appropriate to predicting the friction head losses in smooth and rough pipes respectively. Second-order polynomial correlations of the experimental results are developed for the cases investigated.

Keywords: Head loss, Friction, Fluid flow transportation, Distribution networks

Introduction

Due to internal friction and turbulence, the energy of a flowing fluid is spent through maintaining its movement. It is present throughout the length of the pipes and expressed in terms of height or head loss. Appurtenances and accessories present in a pipe network and usually termed ad minor losses contribute to this loss of energy. However in petroleum and water distribution systems that are constituted of pipelines of considerable length, minor losses are usually found to be insignificant compared to their major counterparts, and may thus be neglected. (Weisbach, 1845) came out with the first relationship that expresses the head loss. (Darcy, 1857) contributed to the application of the derived relationship that has been since known as the Darcy-Weisbach formula. It essentially depends on the relative roughness and the friction coefficient, this latter being a function of the flow regime characterized by the Reynolds number. Several explicit and implicit relationships were since proposed for the friction coefficient. (Moody, 1944) produced the universally known diagram called after him. It allows the determination of the friction coefficient as a function of the Reynolds number and the relative roughness coefficient.

Several other investigators such as (Blasius, 1913), (Colebrook, 1939) and (Ger and Holly, 1976) provided the literature with diverse equations that are of implicit type, thus requiring a try-and-error procedure in order to achieve a solution leading to a value of the friction coefficient. Explicit relationships expressing the friction coefficient for all regimes are available. An interesting review of the diverse formulas is presented by (Lahiouel and Haddad, 2002). As reported by (Powell, 1968) and (Williams, 1970) and as early as 1891, (Manning, 1891) derived such a formula. (Strickler, 1923) suggested a simpler relationship based on a fixed coefficient. (Williams and Hazen, 1933) expressed the head loss as a function of the pipe diameter and length, and the flow rate. They used an empirical coefficient that essentially depends on the pipe material, as described later by (Lamont, 1969). Similar to that of (Williams and Hazen, 1933), (Scobey, 1966) derived a relationship that uses a fixed coefficient. In 1965, Calmon and Lechapt (CEMAGREF, 1983) used three coefficients instead and suggested a relationship that varies with the pipe roughness.

Experimentations were carried out by the author using pipes of various roughness and diameters inside which water was made to flow at different regimes. The linear head losses were measured, and the results obtained were subsequently compared to those achieved by the computations using the six most common pipe flow formula presented.

Theoretical Approach

The main advantage of determining the frictional head losses in pipes lies in finding out the optimal solution that enables their reduction leading to saving energy. Frictional losses are mainly generated by fluid viscosity and flow regime, and may be presented throughout the length of the pipe.

Table 1. Friction head loss relationships

Name	Relationship	Constants
Darcy-Weisbach	$j = \dfrac{f}{12.1\,D^5}Q^2$	$\dfrac{1}{\sqrt{f}} = -2\log\left\{\dfrac{\varepsilon}{3.7D} - \dfrac{5.02}{R_e}\log\left[\dfrac{\varepsilon}{3.7D} - \dfrac{5.02}{R_e}\log\left(\dfrac{\varepsilon}{3.7D} + \dfrac{13}{R_e}\right)\right]\right\}$
Manning	$j = \dfrac{h_f}{L} = \dfrac{10.29\,N^2}{D^{\frac{16}{3}}}Q^2$	For PVC: $N=0.0095$
Hazen & Williams	$j = \dfrac{h_f}{L} = \dfrac{10.68}{C_{HW}^{1.852}\,D^{4.87}}Q^{1.852}$	For PVC: $D=14$mm ; $C_{HW}=145$ - $D=25$mm ; $C_{HW}=146$ $D=13.3$mm ; $C_{HW}=148$ - $D=23.5$mm ; $C_{HW}=150$
Strickler	$j = \dfrac{10.29}{K^2\,D^{16/3}}Q^2$	$K=0.95$ (PVC)
Scobey	$j = \dfrac{h_f}{L} = \dfrac{1.58}{C_S^{1.886}\,D^{4.87}}Q^{1.887}$	$C_S = 37$ (PVC pipes)
Calmon-Lechapt	$j = \dfrac{h_f}{L} = a\dfrac{Q^n}{D^m}$	Smooth pipes: $a=0.916.10^{-3}$, $n=1.78$, $m=4.78$ Rough pipes: $a=1.01.10^{-3}$, $n=1.84$, $m=4.88$

Numerous relationships approaching the solution have been developed, and can be integrated into computer software. The most common is known as the Darcy-Weisbach equation (Weisbach, 1845 and Darcy, 1857). It expresses the head loss in terms of the friction coefficient, the flow velocity and the pipe length and diameter. All the other empirical relationships proposed have the merit of expressing the head loss without the complexity introduced by the friction coefficient. They are resumed in Table 1.

A dimensional analysis of the Darcy-Weisbach equation shows that the Darcy friction coefficient (f) is a function of both the relative roughness coefficient (ε/D) and the Reynolds number (Re). Numerous relationships have been derived for the computation of the Darcy friction coefficient, some of them being of implicit type hence requiring a recursive solution. In 1982, a complex relationship expressing the friction coefficient that possesses the advantage of being explicit and highly accurate was derived by (Zigrang and Sylvester, 1982). All the other empirical relationships proposed have the merit of expressing the head loss without the complexity introduced by the friction coefficient.

The pipe roughness coefficients are provided by the manufacturer, and the computation procedure starts by expressing the Reynolds number in terms of the volume flow rate and the pipe dimensions. The Reynolds number is one of the key parameters in the computation of the pressure losses. It allows the determination of the flow regime considered and along with the relative pipe roughness coefficient (ε/D), will influence the approach to determining the coefficient of friction.

Experimental Approach

A hydraulic system apparatus (Boudebza and Bouachari, 1999) essentially constituted of the hydraulic bench illustrated in Figure 1 was used to carrying out the experimentations. It uses diverse pumps and measuring devices. The characteristics of the pipes are represented in Table 1

Table 2. Characteristics of the pipes [14]

Pipe number	Diameter D_i (mm)	Roughness ε (mm)
1	8.5	8.5×10^{-6}
2	13.3	15.0×10^{-5}
3	23.5	23.5×10^{-6}
4	14.0	2.0×10^{-2}
5	25.0	$15.0.10^{-4}$

The hydraulic bench is of volumetric type. It provides a continuous and valve-controlled amount of water supplied through two centrifugal pumps. The pressure loss is determined in terms of head difference using water and mercury manometers, and the volume flow rate is measured by a direct rotameter. The network comprises PVC pipes with different diameters and roughness.
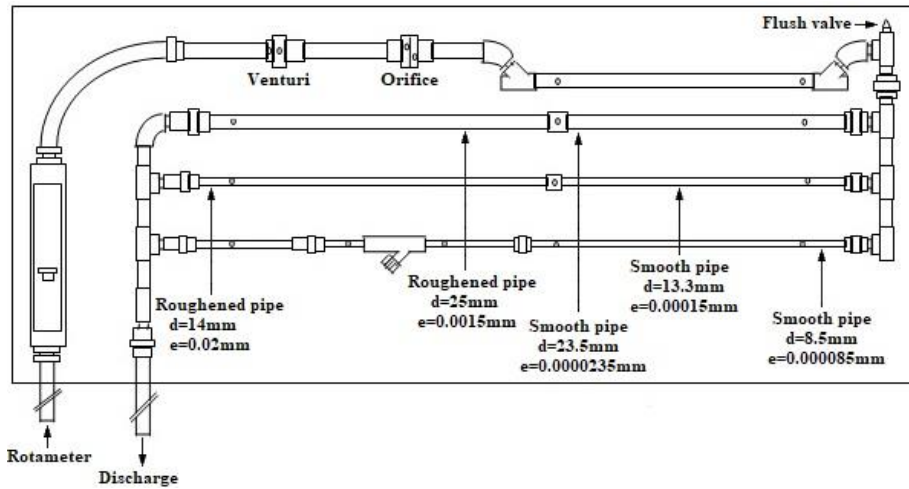
Figure 1. PVC variable diameters and roughness pipes network

Results and Discussion

The friction pressure losses are computed using the six relationships presented in Table 1, and the experimental results are derived from the measurements carried out on the pipe network and hydraulic bench represented in Table 2 and Figure 1.

Figures 2, 3 and 4 present the friction head losses obtained for the three 'smooth' pipes while Figures 5 and 6 show those of the two remaining rough pipes. All the results are expressed in terms of the dimensionless pressure loss (j) versus the Reynolds number (Re), and all the flow regimes have been found to be turbulent.
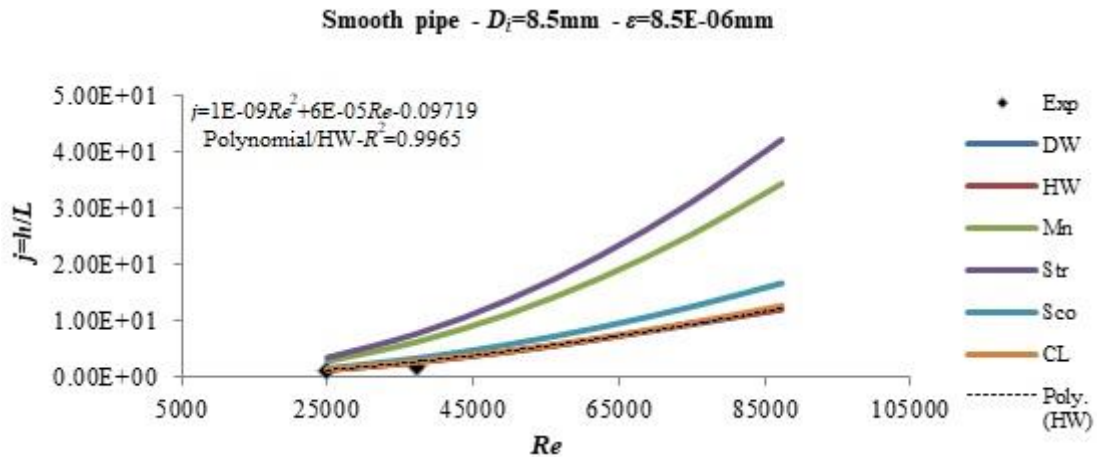
Figure 2. Head loss for a smooth pipe (D_i=8.5mm ; ε=8.5.10^{-6}mm)

The Hazen-Williams approach is found to be the most likely to predicting the head loss for the smooth pipes whose results are presented in Figures 2, 3 and 4. This relationship is essentially based on a complex large-spectrum expression for the friction coefficient that leads to satisfactory results. It is widely used in the United States of America since its derivation in 1933.

The increase in the Reynolds number leading to higher errors is noteworthy. This seems to be generated by the displacement of the flow regime from laminar-transitional to turbulent. This difference can be decreased through integrating more relevant coefficients that will take into account the development of the flow regime. It shows the complexity of the problem particularly when faced with distribution networks incorporating numerous pipes of different diameters and roughness.
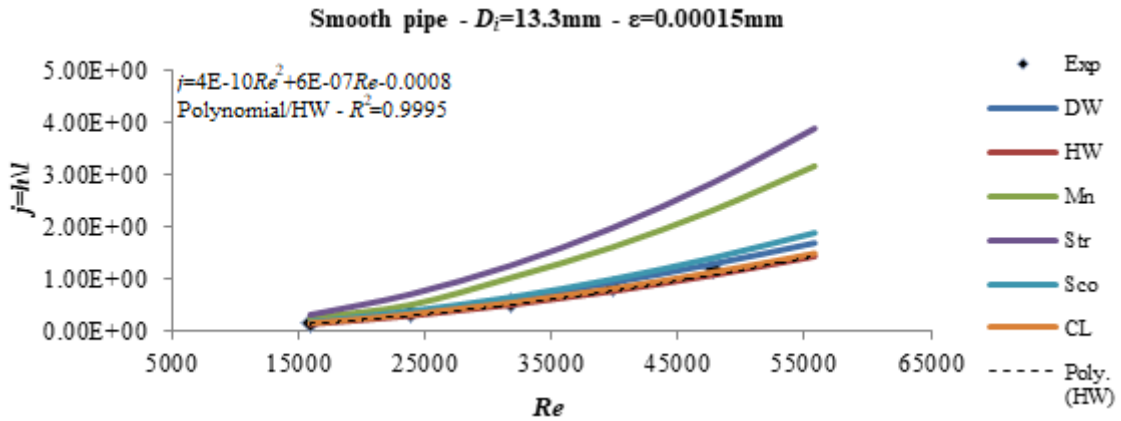
Figure 3. Head loss for a smooth pipe (D_i=13.3mm ; ε=15.0.10^{-5}mm)

An approach consisting of simulating the experimental results by second-order polynomials produced nearly-similar equations that resulted in a residue approaching 0.98 (Maoui, 2016). However, this cannot be ascertained, the approach needing more profound examination.
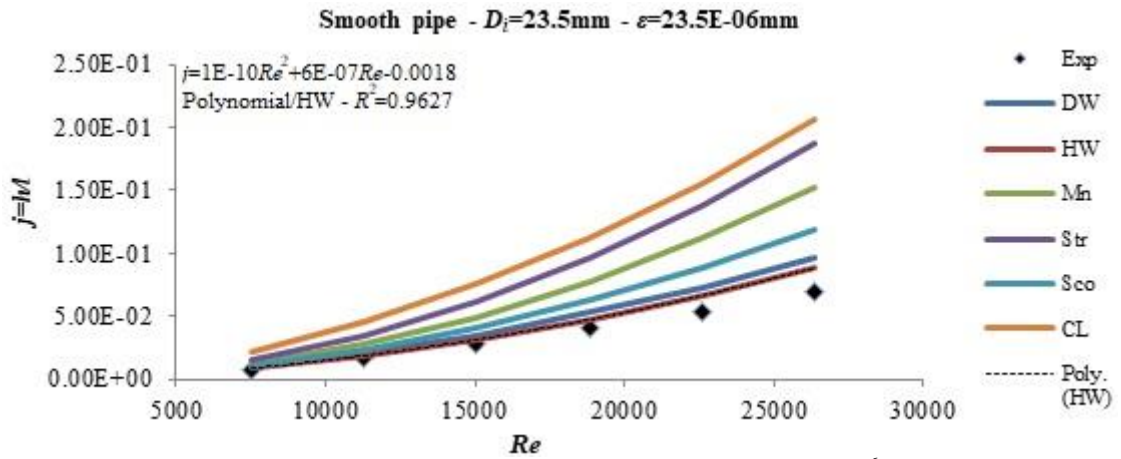
Figure 4. Head loss for a smooth pipe (D_i=23.5mm ; ε=23.5.10^{-6}mm)

The same observations can be made for the case of the two rough pipes whose results are illustrated in Figures 4 and 5. The experimental results show greater head losses than those computed by the different empirical relationships. This difference seems to be essentially generated by the difficulty of correctly predicting the pipe roughness. It is the most important parameter and its value was that proposed by the manufacturer for a new pipe thus omitting the fact that with time, deposits have been accumulating leading to the decrease of the pipe diameter along with the increase of its roughness and consequently boosting the head loss along the pipe.
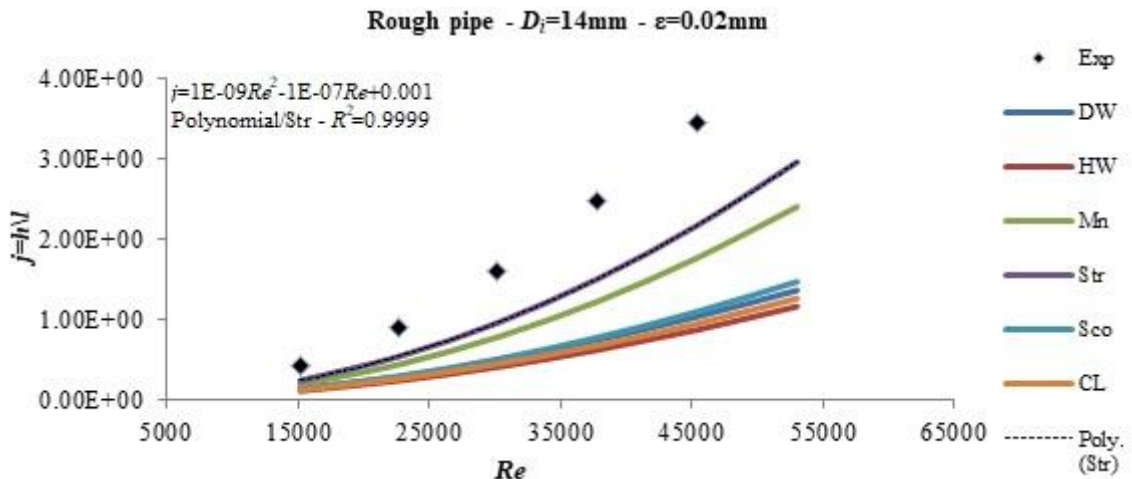
Figure 5. Head loss for a rough pipe (Di=14.0mm ; ε=0.02mm)
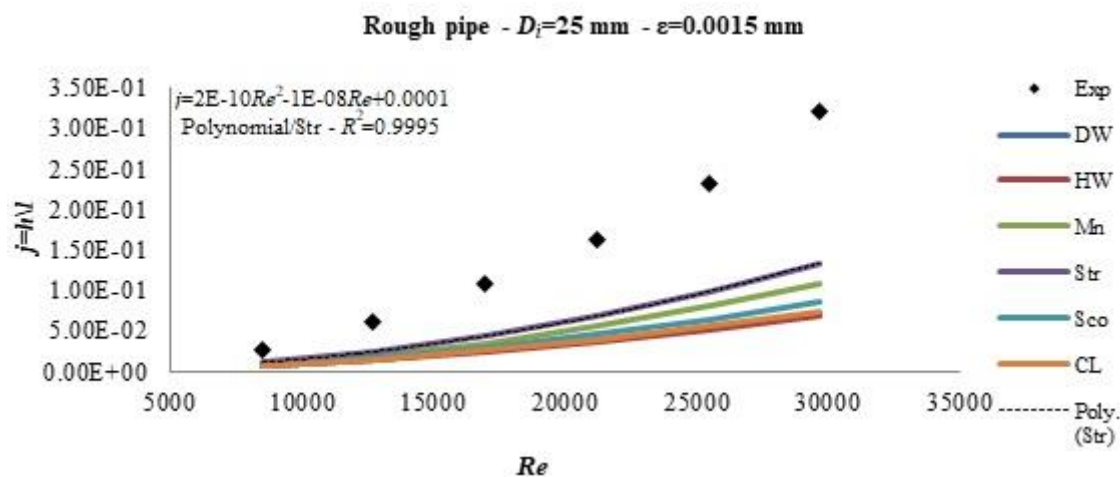
Figure 6. Head loss for a rough pipe (Di=25mm ; ε=0.0015mm)

From what preceded, one can conclude that the transport capacity of the pipes decreases with time (i.e. aging). This reduction is essentially generated either by a decrease in the cross-section due to an accumulation of deposits and an increase in the roughness, or both. The obstruction and the encrustation are the most common forms of such deposits which can vary from 1mm to 10mm in thickness. For the Hazen-Williams formula, the value of 140 is the most commonly used for the coefficient (C_{HW}). It is however understood that for an old pipe in good condition, a value comprised in the interval 100-120 should be acceptable, while for a used pipe 40 to 80 is mostly used. This situation shows the great difficulty faced by the authors in achieving an 'acceptable' value for the coefficients (C_{HW} as well as f and N) used in the developed relationships, and this seem to be the main reason for the relative disparity of the results obtained.

Conclusions

The present study reviewed and applied the different approaches developed over the last decades for the determination of head losses in pipes. These losses are mainly due to friction. The experimental results obtained and their comparison to those computed through applying these relationships show:
1. a preponderance of the Hazen-Williams approach in the case of smooth pipes (i.e. of limited roughness),
2. a better approach by the Strickler relationship in the case of highly rough pipes,
3. the difficulty in determining the friction coefficient particularly when the flows are turbulent,
4. the complexity of evaluation of the roughness coefficient, the value of which is solely provided by the manufacturer in the case of new pipes. Due to erosion and depositing caused by aging, the used pipes are not provided with corresponding roughness coefficients.

An adjustment of the results obtained was attempted through a polynomial approach. This procedure can be interesting and should be further investigated. The present results do however constitute a set of reference data that may be of profit to those interested in the transportation of incompressible fluids inside pipes.

Recommendations

The results and conclusions presented may be subjected to improvements when: (1) considering the determination of the roughness coefficient of aging pipes resulting mainly from erosion-corrosion and deposits etc., (2) determining the pressure losses due to singularities. Indeed, the intermediate region downstream of any accessory is a mixture of both friction and turbulence phenomena, and (3) attempting an adjustment through a polynomial or another function approach.

References

Blasius, H. (1913). Das ahnlichkeitsgesetz in flussigkeiten, Verein Deutscher Ingenieure, Forschungsheft, 131.

Boudebza, C. & Bouachari, A. (1999). Etude des approches de calcul des pertes de charge par frottement et singulières et comparaison avec l'expérimentation, Dipl. Ing., Institut de Génie Mécanique, université 8 Mai 1945, Guelma, Algeria.

CEMAGREF (1983), Calcul des réseaux ramifiés sous pression, 506, Antony, France.

Colebrook, C. F. (1939). Turbulent flow in pipes with articular reference to the transition region between the smooth and rough pipe laws, J. Inst. of Civil Engrs., I1, 133-156.

Darcy H. (1857). Recherches expérimentales relatives au mouvement de l'eau dans les tuyaux, Mallet-Bachelier, atlas, Paris, France.

Ger, A.M. & Holly, E.R. (1976). Comparison of single point injections in Pipe Flow, J. Hydraul. Div., Am. Soc. of Civil Engrs., 102(HY6), 731-746.

Lahiouel, Y. & Haddad, A. (2002). Evaluation of energy losses in pipes, 6th Saudi Engineering Conference, KFUPM, Dhahran, Saudi Arabia, 5, 577-589.

Lamont, P. (1969). The choice of the pipe flow laws for practical use, Water and Water Engineering, 55-63.

Manning R., (1891). On the flow of water in open channels and pipes, Transactions of the Institution of Civil engineers of Ireland.

Maoui, K. (2016). Approche, application et comparaison des pertes de charge dans les conduites de systèmes de distribution d'eau, Master2, Département de Génie Mécanique, Faculté des Sciences et de la Technologie, université 8 Mai 1945, Guelma, Algeria.

Moody, L.F. (1944). Friction factors for pipe flow, Trans. ASME, 66, 671-684.

Powell, R.W. (1968). The origin of Manning formula, J. Hydraul. Div., American Society of Civil Engrs., 1179-1181.

Scobey, F.C. (1966). The flow of water in commercially smooth pipes, Water Resources Center Archives, Series report 17, Univ. of California, Berkeley, USA.

Strickler A., (1923). Beiträge zur Frage der Geschwindigkeitsformel und der Rauhigkeitszahlen fur Ströme, Kanäle und Geschlossene Leitungen, Berna.

Weisbach J. (1845). Lehrbuch der Ingenieur - und Maschinen-Mechanik, vol. 1. Theoretische Mechanik, Vieweg und Sohn, Braunschweig, Germany.

Williams, G.P. (1970). Manning Formula-A Misnomer?, J. Hydraul. Div., American Society of Civil Engrs., 193-200.

Williams, G.S. & Hazen, A. (1933). Hydraulic tables, 3rd Edition, John Wiley & sons inc., USA.

Zigrang, D.J.& Sylvester, N.D. (1982). Explicit Approximations to the Solution of Colebrook's Friction Factor Equation, J. Am. Inst. of Chemical Engrs, 514-515.

Author Information

Abdelkrim Haddad
Laboratoire de Mécanique Appliquée des Nouveaux Matériaux (LMANM),
Université 8 Mai 1945.
PO Box 401, Guelma, Algeria.
Contact E-mail:haddad.abdelkrim@univ-guelma.dz

IConTES 2019: International Conference on Technology, Engineering and Science

Evaluation of Theoretical and Experimental Spectroscopic Properties of 3-Methyl-4-[4-methoxy-3-(*p*-toluenesulfonyloxy)-benzylidenamino]-4,5-dihydro-1*H*-1,2,4-triazol-5-one

Murat BEYTUR
Kafkas University

Haydar YUKSEK
Kafkas University

Abstract: In this study, 3-methyl-4-[4-methoxy-3-(p-toluenesulfonyloxy)-benzylidenamino]-4,5-dihydro-1H-1,2,4-triazol-5-one was synthesized according to literature. Experimental data were obtained from the literature. The synthesized title compound was optimized by using B3LYP/6-311G(d,p) basis set. ^{1}H-NMR and ^{13}C-NMR spectral data values were calculated according to the method of gauge including atomic orbital (GIAO) and continuous set of gauge transformations (CSGT) methods using the program package Gaussian G09W Software. Experimental and theoretical values were inserted into the graphic according to equitation of δexp=a+b. δ calc. The standard error values were found via SigmaPlot program with regression coefficient of a and b constants. Also, the calculated IR data of compound were calculated in gas phase by using of 6-311G(d,p) basis set of B3LYP method and are multiplied with appropriate adjustment factors. Theoretical infrared spectrums are formed from the data obtained according to B3LYP method. In the identification of calculated IR data was used the veda4f program. The calculated and experimental results were exhibited a very good agreement.

Keywords: 1,2,4-Triazol-5-one, GIAO, CSGT, B3LYP, Experimental, Theoretical

Introduction

Heterocyclic compounds that possess 1,2,4-triazole ring have relevance to the pharmacological properties. These properties are fungicidal, antioxidant, antimicrobial, anticancer and antiviral activities (Li et al., 2004; Kritsanida et al., 2002; Holla et al., 2002; Gürsoy Kol and Yüksek, 2010; Sancak et al., 2010; Çiftçi et al., 2018). In addition to this kind of relevance, it was reported that Schiff bases that were originated from triazole compounds possessed some biological activities (Çiftçi et al., 2018). Triazole derivatives have been widely used as antifungal agents, especially, many known triazole agents presently play a leading role in the treatment of agricultural fungal infections, including epoxiconazole, tebuconazole and triadimefon, et al. What's more, triazole agents have a big market share in the field of pesticide because of strong systematic and unique mechanism property.

Density functional theory calculations (DFT) are reported to showed excellent vibrational frequencies of organic compounds if the calculated frequencies are scaled to compensate for the approximate treatment of electron correlation, for basis set deficiencies and for the anharmonicity (Abramov et al., 1999; Handy et al., 1992). A number of papers have recently appeared in the literature concerning the calculation of Nuclear Magnetic Rezonans chemical shift by quantum-chemistry methods (Forsyth and Sebag, 1997; Sebag et al., 2001; Turhan Irak and Gümüş, 2017; Beytur et al., 2019; Turhan Irak and Beytur, 2019). These papers indicate that geometry optimization is a crucial factor in an accurate determination of computed NMR chemical shift. Moreover, it is known that the DFT (B3LYP) method adequately takes into account electron correlation contributions, which are especially important in systems containing extensive electron conjugation and/or electron lone pairs (Forsyth and Sebag, 1997). However, considering that as molecular size increases, computing-time limitations are introduced for obtaining optimized geometries at the DFT level, it was proposed that the single-point calculation

of magnetic shielding by DFT methods was combined with a fast and reliable geometry-optimization procedure at the molecular mechanics level (Forsyth and Sebag, 1997).

The gauge-including atomic orbital (GIAO) (Ditchfield, 1972, Wolinski et al., 1990) method is one of the most common approaches for calculating nuclear magnetic shielding tensors. It has been shown that the results obtained by GIAO method are often more accurate than those calculated with other approaches, at the same basis set size (Cheeseman et al., 1996). DFT methods have been preferred in the study of large organic molecules (Friesner et al., 1999) and for GIAO ^{13}C calculations (Cheeseman et al., 1996) in all those cases in which the electron correlation contributions were not negligible.

Density Functional Theory (B3LYP) methods are used for the determination of the structure of molecules and the investigated of spectroscopic properties. Firstly, 3-methyl-4-[4-methoxy-3-(p-toluenesulfonyloxy)-benzylidenamino]-4,5-dihydro-1H-1,2,4-triazol-5-one compound was obtained according to the literature (Aktaş Yokuş, 2012). The compound was analyzed with IR, ^{1}H-NMR and ^{13}C-NMR and experimental spectrums were drawn. The titled compound has been optimized using B3LYP/6311G(d) basis set (Frisch et al., 2009; Wolinski et al., 1990). ^{1}H-NMR and ^{13}C-NMR isotropic shift values were calculated by the methods of GIAO and CSGT using the program package Gaussian G09W (Frisch et al., 2009). Experimental (Aktaş Yokuş, 2012) and theoretical values were inserted into the graphic according to equitation of δ exp_a+b. δ calc. The standard error values were found via SigmaPlot program with regression coefficient of a and b constants. IR absorption frequencies of analyzed molecule were calculated by two methods. The veda4f program was used in defining IR data, which were calculated theoretically (Jamróz, 2004).

Computational Details

The title compound was optimized based on the 3-methyl-4-[4-methoxy-3-(p-toluenesulfonyloxy)-benzylidenamino]-4,5-dihydro-1H-1,2,4-triazol-5-one. The optimized molecular structures of the title compound in the ground state (in vacuo) were computed by performing DFT by a hydrid functional B3LYP functional (Becke's three parameter hybrid functional using the LYP correlation functional) methods (Becke, 1993; Lee, 1998) at 6-311G(d,p) level. The gauge-including atomic orbital (GIAO) (Ditchfield, 1974; Rohling et al., 1984; Wolinski et al., 1990) and continuous set of gauge transformations (CSGTs) (Keith and Bader, 1992) methods are three of the most common approaches for calculating nuclear magnetic shielding tensors (Pir et al., 2013, Rani et al., 2010; Turhan Irak and Beytur, 2019; Beytur et al., 2019). In the present study, ^{1}H and ^{13}C NMR chemical shifts were calculated within GIAO and CSGT approach applying B3LYP method with 6-311G(d,p) basis set.
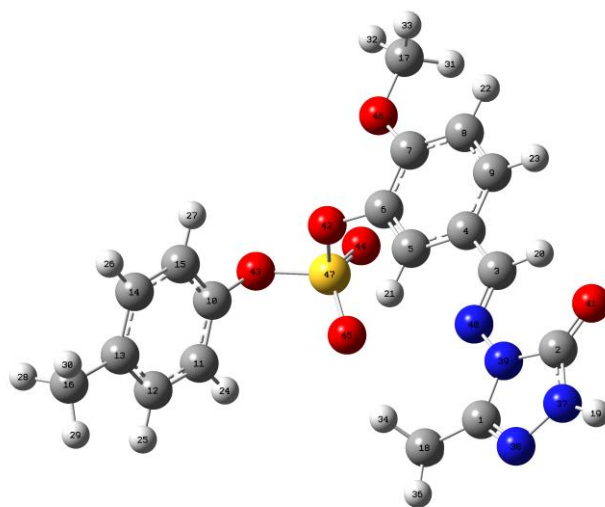
Figure 1. The optimized molecular structure of 3-methyl-4-[4-methoxy-3-(p-toluenesulfonyloxy)-benzylidenamino]-4,5-dihydro-1H-1,2,4-triazol-5-one with DFT 6-311G(d,p) level.

Results and Discussion

NMR spectra of 3-methyl-4-[4-methoxy-3-(p-toluenesulfonyloxy)-benzylidenamino]-4,5-dihydro-1H-1,2,4-triazol-5-one

In nuclear magnetic resonance (NMR) spectroscopy, the isotropic chemical shift analysis allows us to identify relative ionic species and to calculate reliable magnetic properties which provide the accurate predictions of molecular geometries (Rani et al., 2010; Subramanian, Sundaraganesan, & Jayabharathi, 2010; Wade, 2006). Initially, molecular structure of 3-methyl-4-[4-methoxy-3-(p-toluenesulfonyloxy)-benzylidenamino]-4,5-dihydro-1H-1,2,4-triazol-5-one is optimized by using B3LYP method with 6-311G(d,p). Then, both GIAO and CSGT ^{13}C and ^{1}H calculations of the title compound have been made by using B3LYP method with 6-311G(d,p) basis set. The GIAO and CSGT methods according to ^{1}H and ^{13}C chemical shift values (with respect to TMS) have been calculated for the optimized structures of the title compound and compared to the experimental 1H chemical shift values (Aktaş Yokuş, 2012) (Table 1). In the present paper, ^{1}H-NMR and ^{13}C-NMR spectral data values were calculated according to the method of gauge including atomic orbital (GIAO) and continuous set of gauge transformations (CSGT) methods using the program package Gaussian G09W Software. Theoretical and experimental (Aktaş Yokuş, 2012) values were plotted according to δ exp=a. δ calc.+ b, Eq. a and b constants regression coefficients with a standard error values were found using the SigmaPlot program.

Table 1. Data calculated ^{13}C and ^{1}H-NMR DMSO(B3LYP/6311G(d,p) isotropic chemical shifts of the molecule according to GIAO and CSGT Methods (δ/ppm)

No	Experim.	DFT/6311(d,p) DMSO GIAO	Diff./DMSO	DFT/6311(d,p) DMSO CSGT	Diff/DMSO
1C	146,18	150,35	-4,17	147,56	-1,38
2C	152,63	153,59	-0,96	147,95	4,68
3C	151,65	152,10	-0,45	151,68	-0,03
4C	126,73	131,02	-4,29	130,17	-3,44
5C	121,35	123,63	-2,28	121,22	0,13
6C	132,51	144,02	-11,51	141,74	-9,23
7C	154,33	161,77	-7,44	158,88	-4,55
8C	114,02	114,59	-0,57	114,11	-0,09
9C	129,87	137,93	-8,06	137,62	-7,75
10C	144,59	154,11	-9,52	152,29	-7,70
11C	128,75	127,87	0,88	126,05	2,70
12C	130,38	134,14	-3,76	133,24	-2,86
13C	138,50	146,39	-7,89	145,72	-7,22
14C	130,38	134,26	-3,88	133,48	-3,10
15C	128,75	127,17	1,58	125,57	3,18
16C	21,61	21,31	0,30	23,40	-1,79
17C	56,45	55,76	0,69	46,43	10,02
18C	11,44	12,43	-0,99	13,51	-2,07
19H	11,80	7,25	4,55	7,20	4,60
20H	9,86	10,01	-0,15	9,12	0,74
21H	7,89	7,93	-0,04	7,65	0,24
22H	7,28	7,00	0,28	7,15	0,13
23H	7,62	7,52	0,10	7,41	0,21
24H	7,72	7,38	0,34	7,38	0,34
25H	7,47	7,50	-0,03	7,66	-0,19
26H	7,47	7,51	-0,04	7,68	-0,21
27H	7,72	7,56	0,16	7,55	0,17
28H	2,43	2,57	-0,14	3,11	-0,68
29H	2,43	2,23	0,20	2,71	-0,28
30H	2,43	2,35	0,08	2,84	-0,41
31H	3,62	3,76	-0,14	4,24	-0,62
32H	3,62	4,3	-0,68	4,82	-1,20
33H	3,62	3,88	-0,26	4,32	-0,70
34H	2,09	2,17	-0,08	2,56	-0,47
35H	2,09	2,22	-0,13	2,6	-0,51
36H	2,09	1,93	0,16	2,29	-0,20
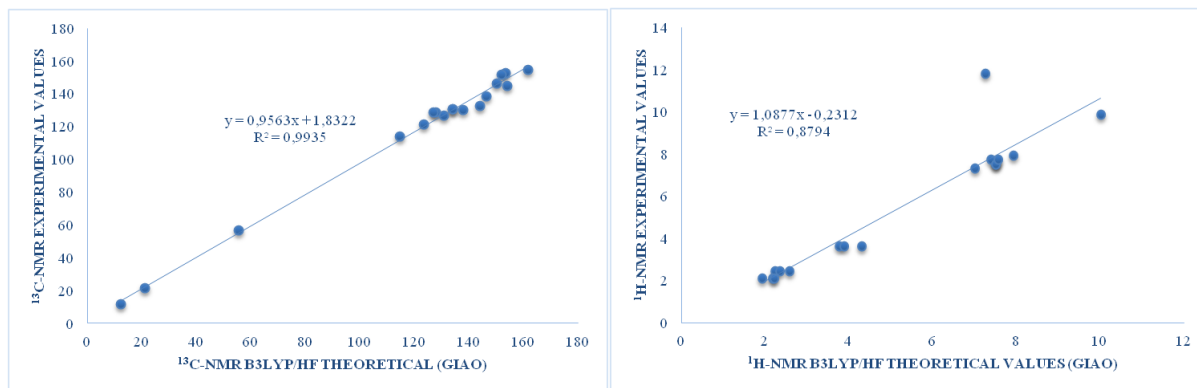
Figure 2. The correlation graphics for ^{13}C-NMR (DMSO) and ^{1}H-NMR (DMSO) chemical shifts of the molecule according to GIAO
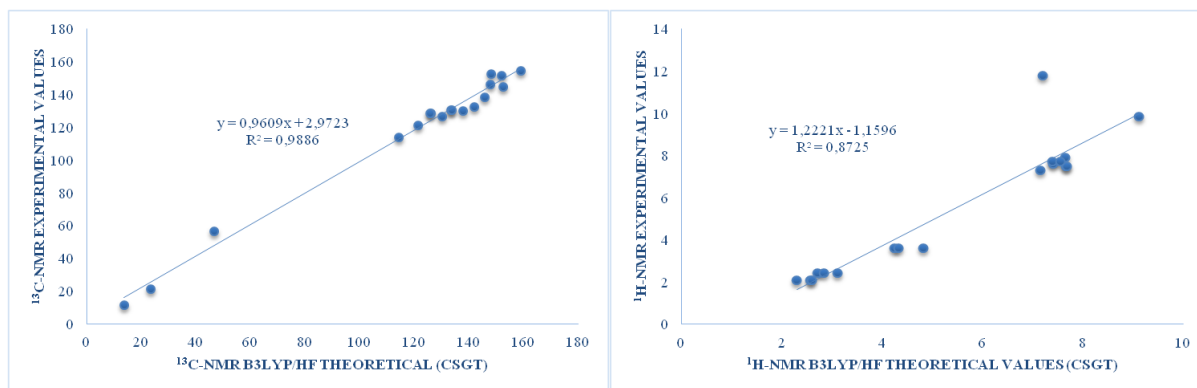
Figure 3. The correlation graphics for ^{13}C-NMR (DMSO) and ^{1}H-NMR (DMSO) chemical shifts of the molecule according to CSGT

The relation between R^2 values of the compound

B3LYP/6311G(d,p) (GIAO): ^{13}C: 0.9935, ^{1}H: 0.8794 and B3LYP/6311G(d,p) (GIAO): ^{13}C: 0.9886, ^{1}H: 0.8725. There is such a relationship between R^2 values of the 3-methyl-4-[4-methoxy-3-(p-toluenesulfonyloxy)-benzylidenamino]-4,5-dihydro-1H-1,2,4-triazol-5-one. Found standard error rate and a, b constants regression values were calculated according to formula exp $=a +b.\delta$ calc Eq.

Assignments of the vibrational modes of the compound

Experimental vibrational data of the title compound has been taken by from (Aktaş Yokuş, 2012). We have calculated the theoretical vibrational spectra of the title compound using B3LYP method with 6-311G(d,p) basis set. We have compared our calculations of the title compound with the experimental results and the comparison is shown in Table 2. The vibrational bands assignments have been made by using Gauss-View Molecular Visualisation Program (Frisch et al., 2003). To make comparison with experiment, we present correlation graphic in Figure 3 based on the calculations. As we can see from the graph in Figure 3 experimental data are in better agreement with the scaled data and are found to have a good correlation for B3LYP. Theoretically IR values were calculated with the veda4f program and scalar values were obtained. The negative frequency in the data was not found. This result shows that the structure of compound was shown to be stable. IR spectrums were drawn with obtained values according to DFT method. Theoretical IR values were compared with experimental IR counterparts. The result of this compare were found corresponding with each other of values (Aktaş Yokuş, 2012).

As can be seen from Table 2, the N-H vibrations of the title compounds have been calculated by using B3LYP method with 6-311G(d,p) basis set observed at 3148 cm^{-1} (Aktaş Yokuş, 2012). This vibration band was calculated at 3647 cm^{-1} (for B3LYP). The C=O experimental vibrations band of title compound were observed

at 1689 cm^{-1}, that have been calculated with B3LYP at 1787 cm^{-1} (see Table 2). As can be seen from Table 2, there is good agreement beetween experimental and theoretical vibration data for the C–H asymmetric and symmetric stretch and the others.

Table 2. The calculated frequencies values of the molecule.

Vibration Types	Experimen.	B3LYP
COSO (83)		5
CCOS (19), OSOC (49)		14
OSOC (23), NCCC (28), CNNC (15)		19
OSOC (24), HCCC (43)		27
HCCC (10), CCOS (31), OSOC (18)		29
OSOC (38), HCCC (22)		32
CCCC (14), NCNN (14), NNCN (11), COCC (11)		44
NCC (24), CCC (20), CCOS (13)		61
COS (25), CCCO (13), OSOC (11)		80
NCNN (13), CNNC (21), COCC (17)		91
CNNC (30)		157
NCCC (24), CNNC (20)		189
OSO (24), CCCO (10)		223
CNNC (47), HNNC (19)		295
CCO (12), CCN (12), COC (10), OOOS (15)		308
CCCO (45), CCCC (10), NNCN (10), NCNN (16)		317
CNN (18), OCN (15), NNC (10), CCN (14)		359
OCCC (16), CCCC (11)	406	416
OCC (20), OSO (18)		434
HNNC (51), ONNC (11)		457
OSO (31)		481
OSO (12), CCCO (10), CCCC (14), OCCC (13)	479	498
OOOS (44)		525
CCO (18)	542	556
OOOS (10)	581	579
CC (11), OCN (12), CNN (12)		604
CC (18)	626	629
CCCC (10)		638
CCC (46), OCC (10)	665	648
ONNC (76)	721	738
CC (15), CCC (24)	761	782
CC (14), SO (15), CCC (11)		794
NC (20), CNN (36)		800
HCCC (72), OCCC (11)	813	819
HCCC (59), CCCC (10)		859
CCCC (10), HCCC (59)	900	909
HCCC (81)	951	966
HCH (12), NNC (10), HCCN (33)		987
HCH (18), HCCC (54)		999
CCC (66)		1026
CCC (11), OC (67)	1014	1043
HCH (19), HCCC (54)		1053
HCH (21), HCCN (69)		1058
NN (38), HNN (10), HCCN (17)	1087	1093
CC (22), HCC (39)		1120
OC (13), SO (46)		1143
HCH (13), HCOC (65)		1160
HCOC (38)	1179	1197
NC (12), HCOC (129)		1202
CC (54)		1219
CC (14), HCC (23)		1231
HCC (29)		1266
NCN (12)	1277	1292
NN (13), NCN (129)		1296

|		
NC (24), HCN (26), HCH (18)	1309	**1314**
NC (24), HCN (26), HCH (10)	1361	**1368**
HCH (16), HNN (58)		**1383**
NC (10), HCN (16), HCH (14)		**1440**
CC (41), HCC (13)	1429	**1443**
HCH (76), HCCN (22)		**1458**
HCH (77)		**1465**
HCH (75), HCCC (16)	1457	**1477**
HCOC (23), HCH (75)		**1481**
HCH (67), HCCC (14)		**1483**
OC (14), CCC (14), HCC (25)	1510	**1531**
CC (51), CCC (10)		**1586**
CC (21), NC (20)		**1628**
NC (60)	1599	**1650**
NC (13), OC (73)	1689	**1787**
CH (99)	2643	**2984**
CH (91)		**3017**
CH (98)	3049	**3071**
CH (91)		**3113**
CH (98)		**3117**
CH (98)		**3122**
CH (100)		**3137**
CH (97)		**3140**
CH (98)		**3143**
CH (94)		**3177**
CH (93)		**3178**
CH (99)		**3182**
CH (98)	3148	**3189**
NH (100)	3252	**3647**
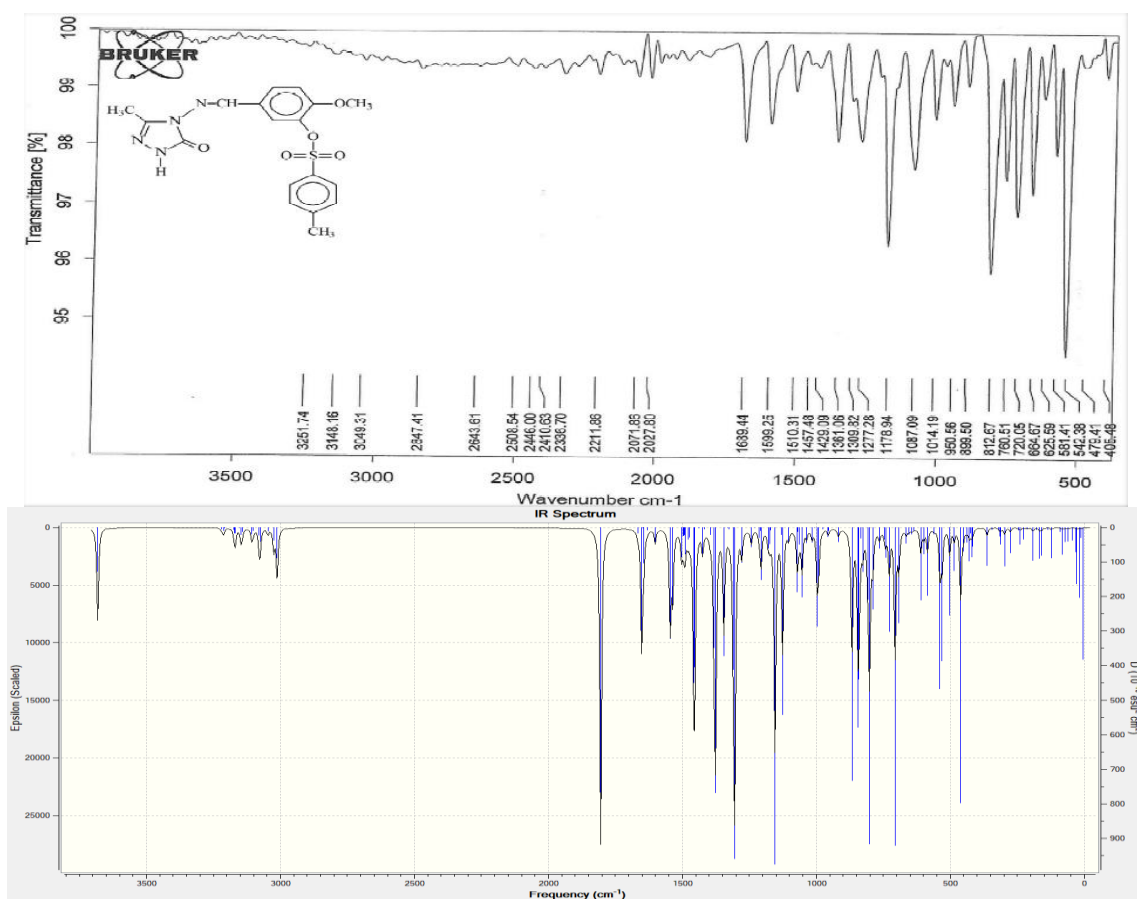
Figure 3. IR spectra experimental and simulated with DFT/B3LYP/6311G(d,p) levels of the molecule

Conclusion

In this work we have calculated the vibrational frequencies and ^{13}C NMR and ^{1}H NMR chemical shift values of the title compound (3-methyl-4-[4-methoxy-3-(p-toluenesulfonyloxy)-benzylidenamino]-4,5-dihydro-1H-1,2,4-triazol-5-one) by using B3LYP method with 6-311G(d,p) basis set. To fit the theoretical vibrational frequency results with experimental ones for B3LYP we have multiplied the data by 0.9905. Multiplication factors results gained seemed to be in a good agreement with experimental data. In particular, the results of B3LYP method has shown better fit to experimental data in evaluating vibrational frequencies. Likewise, B3LYP method seems to be appropriate for the calculation of geometrical parameters of molecules.

To test the different theoretical approaches (DFT/B3LYP) reported here, computed and vibrational frequencies and ^{1}H NMR and ^{13}C NMR chemical shift values according to GIAO and CSGT methods of the 3-methyl-4-[4-methoxy-3-(p-toluenesulfonyloxy)-benzylidenamino]-4,5-dihydro-1*H*-1,2,4-triazol-5-one were compared. More commonly, however, the IR and NMR spectra are used in conjunction with other forms of spectroscopy and chemical analysis to determinate the structures of complicated organic molecules.

References

Abramov, Yu. A., Volkov, A. V. & Coppens, P. (1999). On the evaluation of molecular dipole moments from multipole refinement of X-ray diffraction data. *Chemical Physics Letters, 311 (1-2)*, 81-86.

Aktaş Yokuş, A. (2012). Bazı Yeni 1,2,4-Triazol Türevlerinin Sentezi ve Biyolojik Aktivitelerinin İncelenmesi. *Doktora Tezi, Kafkas Üniversitesi Fen Bilimleri Enstitüsü,* Kars.

Becke A. D. (1993). Density functional thermochemistry. III. The role of exact Exchange, The Journal of Chemical Physics, 98, 5648-5652.

Beytur, M., Turhan Irak, Z., Manap, S., and Yüksek, H. (2019). Synthesis, Characterization and Theoretical Determination of Corrosion Inhibitor Activities of Some New 4,5-Dihydro-1H-1,2,4-Triazol-5-one Derivatives, *Heliyon*, 5 (6), e01809, 1-8.

Cheeseman, J. R., Trucks, G. W., Keith, T. A. & Frisch. M. J. (1996). A comparison of models for calculating nuclear magnetic resonance shielding tensors. *The Journal of Chemical Physics, 104 (14)*, 5497.

Çiftçi, E., Beytur, M., Calapoğlu, M., Gürsoy Kol, Ö., Alkan, M., Toğay, V. A., Manap, S., & Yüksek, H. (2018). Synthesis, Characterization, Antioxidant and Antimicrobial Activities and DNA Damage of Some Novel 2-[3-alkyl (aryl)-4,5-dihydro-1H-1,2,4-triazol-5-one-4-yl]-phenoxyacetic acids in Human Lymphocytes, *Research Journal of Pharmaceutical, Biological and Chemical Sciences*, 9 (5), 1760-1771.

Ditchfield, R. (1974). Self-consistent perturbation theory of diamagnetism. *Molecular Physics, 27 (4)*, 789-807.

Frisch, M. J., Trucks, G., Schlegel, H. B., Scuseria, G. E., Robb, M. A., Cheeseman, J. R., Scalmani, G., Barone, V., Mennucci, B., Petersson, G. A., Nakatsuji, H., Caricato, M., Li, X., Hratchian, H. P., Izmaylov, A. F., Bloino, J., Zheng, G., Sonnenberg, J. L., Hada, M., Ehara, M., Toyota, K., Fukuda, R., Hasegawa, J., Ishida, M., Nakajima, T., Honda, Y., Kitao, O., Nakai, H., Vreven, T., Montgomery, J. A., Jr. Vreven, T., Peralta, J. E., Ogliaro, F., Bearpark, M., Heyd, J. J., Brothers, E., Kudin, N., Staroverov, V. N., Kobayashi, R., Normand, J., Raghavachari, K., Rendell, A., Burant, J. C., Iyengar, S. S., Tomasi, J., Cossi, M., Rega, N., Millam, J. M., Klene, M., Knox, J. E., Cross, J. B., Bakken, V., Adamo, C., Jaramillo, J., Gomperts, R., Stratmann, R. E., Yazyev, O., Austin, A. J., Cammi, R., Pomelli, C., Ochterski, J. W., Martin, L. R., Morokuma, K., Zakrzewski, V. G., Voth, G. A., Salvador, P., Dannenberg, J. J., Dapprich, S., Daniels, A. D., Farkas, O., Foresman, J. B., Ortiz, J. V., Cioslowski, J. & Fox, D. J. (2009). Gaussian Inc., Wallingford, CT.

Friesner, R. A., Murphy, R. B., Beachy, M. D., Ringnalda, M. N., Pollard, W. T., Dunietz, B.D. & Cao, Y. (1999). Correlated ab Initio Electronic Structure Calculations for Large Molecules, *The Journal of Physical Chemistry A*, 103 (13), 1913-1928.

Forsyth, D. A. & Sebag. A. B. (1997). Computed ^{13}C NMR Chemical Shifts via Empirically Scaled GIAO Shieldings and Molecular Mechanics Geometries. Conformation and Configuration from [13]C Shifts, *Journal of the American Chemical Society*, 119 (40), 9483-9494.

Gürsoy Kol, Ö., and Yüksek, H. (2010). Synthesis and invitro antioxidant evaluation of some novel 4,5-dihydro-1H-1,2,4-triazol-5-one derivatives, *E-Journal of Chemistry*, 7 (1), 123-136.

Handy, N. C., Maslen, P. E., Amons, R. D., Audrows, J. S., Murroy, C. W. & Lawing, G. (1992). The harmonic frequencies of benzene. *Chemical Physics Letters, 197 (4-5)*, 506-515.

Holla, B.S., Poojary, K.N., Rao, B.S. & Shivananda, M. K.. (2002). New bis-aminomercaptotriazoles and bis-triazolothiadiazoles as possible anticancer agents. *European Journal of Medicinal Chemistry, 37 (6)*, 511-517.

Jamróz, M. H. (2004). Vibrational Energy Distribution Analysis: VEDA 4 program, Warsaw.

Lee, S. Y. (1998). Molecular Structure and Vibrational Spectra of Biphenyl in the Ground and the lowest Triplet States. Density Functional Theory Study, Bulletin of the Korean Chemical Society, 19 (1), 93-98.

Li, W., Wu, Q., Ye, Y., Luo, M., Hu, L., Gu, Y. & Niu. F. (2004). Density functional theory and ab initio studies of geometry, electronicstructure and vibrational spectra of novel benzothiazoleand benzotriazole herbicides. *Spectrochimica Acta Part A, 60*, 2343-2353.

Keith, T. A., Bader, R. F. W., (2002). Calculation of magnetic response properties using a continuous set of gauge transformations. *Chemical Physics Letters, 210 (1-3)*, 223-231.

Kritsanida, M., Mouroutsou, A., Marakos, P., Pouli, N. & Papakonstantinou-Garoufalias. C. (2002). Synthesis and antiviral activity evaluation of some new 6-substituted-3-(1-adamantyl)-1,2,4-triazolo[3,4-b][1,3,4]thiadiazoles. *Farmaco, 57*, 253-257.

Pir, H., Günay, N., Tamer, Ö., Avcı, D. & Atalay, Y. (2013). Theoretical investigation of 5-(2-Acetoxyethyl)-6-methylpyrimidin-2, 4-dione: Conformational study, NBO and NLO analysis, molecular structure and NMR spectra, Spectrochimica Acta Part A: Molecular and Biomolecular Spectroscopy, 112, 331-342.

Rani, A. U., Sundaraganesan, N., Kurt, M., Çınar, M., & Karabacak, M. (2010). FT-IR, FT-Raman, NMR spectra and DFT calculations on 4-chloro-N-methylaniline, *Spectrochimica Acta Part A: Molecular and Biomolecular Spectroscopy*, 75, 1523-1529.

Rohling, C. M., Allen, L. C., & Ditchfield, R. (1984). Proton and C-13 chemical-shifts-comparison between theory and experiment. *Chemical Physics, 87*, 9-15.

Sancak, K., Unver, Y., Kazak, C., Dugdu, E., and Arslan, B. (2010). Synthesis and characterizations of some new 2,4-dihydro-[1,2,4]-triazol-3-one derivatives and X-ray crystal structures of 4-(3-phenylallylideneamino)-5-thiophen-2-yl-methyl-2,4-dihydro-[1,2,4]triazol-3-one, *Turkish Journal of Chemistry*, 34 (5), 771-780.

Sebag, A. B., Forsyth, D.A. & Plante, M. A. (2001). Conformation and configuration of tertiary amines via GIAO-derived (13)C NMR chemical shifts and a multiple independent variable regression analysis. *The Journal of Organic Chemistry, 66 (24)*, 7967-7973.

Wolinski, K., Hinton, J. F. & Pulay, P. (1990). Efficient implementation of the gauge-independent atomic orbital method for NMR chemical shift calculations. Journal of the American Chemical Society, 112, 8251-8260.

Turhan Irak, Z. & Gümüş, S. (2017). Heterotricyclic compounds via click reaction: A computational study. *Noble International Journal of Scientific Research*, 1(7), 80-89.

Turhan Irak, Z. & Beytur, M. (2019). 4-Benzilidenamino-4,5-dihidro-1H-1,2,4-triazol-5-on Türevlerinin Antioksidan Aktivitelerinin Teorik Olarak İncelenmesi, *Iğdır University Journal of the Institute of Science and Technology*, 9 (1), 512-521.

Wolinski, K., Hinton, J. F. & Pulay, P. (1990). Efficient implementation of the gauge-independent atomic orbital method for NMR chemical shift calculations. *Journal of the American Chemical Society*, 112, 8251-8260.

Author Information

Murat Beytur	**Haydar Yuksek**
Kafkas University	Kafkas University
Faculty of Science and Letters, Department of Chemistry, Kars, Turkey	Faculty of Science and Letters, Department of Chemistry, Kars, Turkey
Contact E-mail: *muratbeytur83@gmail.com*	

Spectroscopic and Nonlinear Optical Properties of Biologically Active 3-(2/3/4-Pyridyl)-4-amino-1,2,4-triazole-5-thiones by Density Functional Theory Method

Zeynep Turhan IRAK
Igdir University

Murat BEYTUR
Kafkas University

Abstract: In the present study, vibrational frequencies and gauge including atomic orbital (GIAO) 13C-NMR and 1H-NMR chemical shift values of 3-(2/3/4-pyridyl)-4-amino-1,2,4-triazole-5-thiones in the ground state have been calculated by using the density functional method (B3LYP) with 6-311G(d,p) basis set. The vibrational spectra of the title compounds which is calculated by DFT methods, reproduces vibrational wave numbers and intensities with an accuracy which allows reliable vibrational assignments. The title compounds have been studied theoretically in the 4000–400 cm^{-1} region and the assignment of all the observed bands were made. In the identification of calculated IR data was used the veda4f program. Theoretical infrared spectrums are formed from the data obtained according to B3LYP method. The calculated IR data of title compounds were calculated in gas phase by using of 6-311G(d,p) basis sets of B3LYP method and are multiplied with appropriate adjustment factors. Also, The ^{1}H- and ^{13}C- nuclear magnetic resonance chemical shifts values of 3-(2/3/4-pyridyl)-4-amino-1,2,4-triazole-5-thione molecules have been calculated by the gage including atomic orbital (GIAO) method. The calculated ^{13}C-NMR and ^{1}H-NMR chemical shift values compared with the experimental values. Experimental data were obtained from the literature. Furthermore, total static dipol moment (μ), the mean polarizability ($<\alpha>$), the anisotropy of the polarizability ($\Delta\alpha$), the mean first-order hyperpolarizability ($<\beta>$), of title compounds have been investigated by using B3LYP levels with the 6-311G(d,p) basis set.

Keywords: 1 2 4-Triazole-5-thione, GIAO, B3LYP, Polarizability, Hyperpolarizability

Introduction

The 1,2,4-Triazole compounds has showed widespread attention due to their different biological activities (Çiftçi et al., 2018), and the 1,2,4-Triazole containing amino group is also important for obtaining various Schiff bases with well-established antimicrobial properties as well. 1,2,4-Triazole skeleton are indeed known as important polar pharmacophore, both as a donor to hydrogen bond and as a acceptor, and thus readily to interact with a variety of partners in biological systems (Zhane et al.,2016). Several well- known pesticides containing 1,2,4-Triazole are Triadimefon (Crofton, 1996), Itraconazole, Voriconazole, Fluconazole, Diniconazole and Tebu- conazol (Küçükgüzel et al., 2015). 1,2,4-Triazole has an ambident nucleophilic centers and is a good starting material for the synthesis of several interesting N and S-bridged heterocycles (Aggarwal et al., 2011). Therefore, 1,2,4- Triazole is of significance for the design of new molecular entities with unique structural features. 1,2,4-Triazole and its derivatives are reported to possess a broad spectrum of biological activities such as antimicrobial, antifungal, antitumor, anti-HIV, antiviral, anticancer, anti-inflammatory, analgesic and antioxidant properties (Bayrak et al., 2010; Gürsoy Kol and Yüksek, 2010; Sancak et al., 2010; Çiftçi et al., 2018; Beytur et al., 2019; Turhan Irak and Beytur, 2019). Also, several articles reporting the synthesis of some 1,2,4-triazol derivatives have been published (İkizler and Yüksek, 1994; Yüksek et al., 2005; Yüksek et al., 2006; Turhan Irak and Gümüş, 2017; Beytur et al., 2019).

In the present study, the optimized molecular structure, vibrational frequencies, spectroscopic parameters of the 3-(2/3/4-pyridyl)-4-amino-1,2,4-triazole-5-thiones have been calculated by using DFT/B3LYP method with 6-311G(d,p) basis set. All quantum chemical calculations were carried out by using Gaussian 09W (Frisch et al., 2009; Wolinski, Hilton & Pulay, 1990) program package and the GaussView molecular visualization program (Frisch, Nielson & Holder, 2003). The molecular structure and vibrational calculations of the molecule were computed by using Becke-3-Lee Yang Parr (B3LYP) (Becke, 1993; Lee et al.,1998) density functional method with 6-311G(d,p) basis set in ground state. IR absorption frequencies of analyzed molecule were calculated by density functional method. Then, they were compared with experimental data (Nadeem and Ashraf, 2012), which are shown to be accurate. The assignments of fundamental vibrational modes of the title molecule were performed on the basis of total energy distribution (TED) analysis by using VEDA 4f program (Jamroz, 2004). Furthermore, the mean polarizability ($<\alpha>$), the anisotropy of the polarizability ($\Delta\alpha$), the mean first-order hyperpolarizability ($<\beta>$) of titled compound have been investigated by using B3LYP and HF levels with the 6-311G(d,p) basis set.
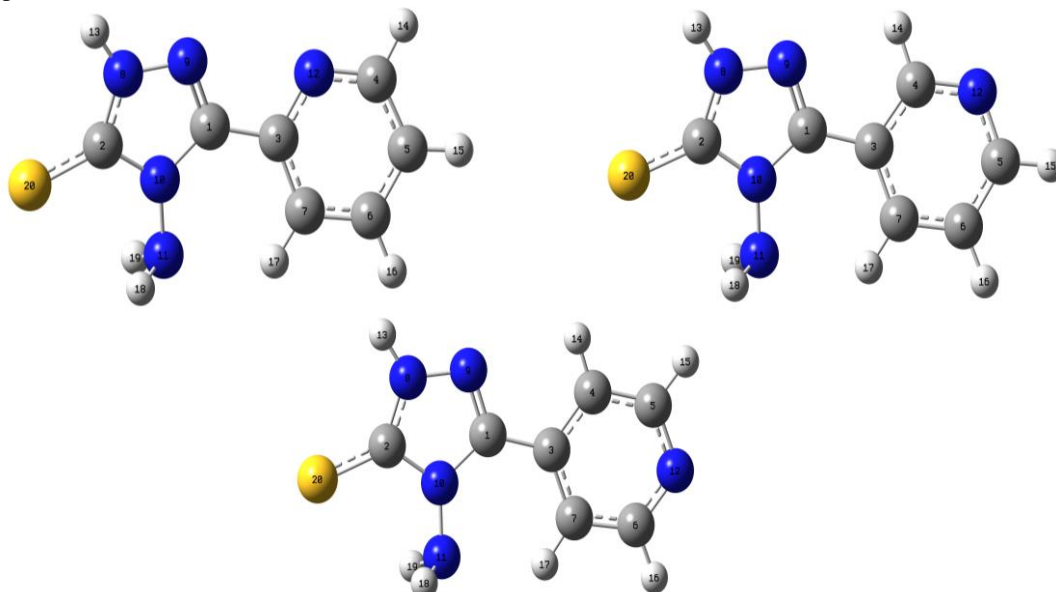
Figure 1. The optimized molecular structure (Gaussview Appearance) of compounds 1-3 with DFT/B3LYP 6-311G(d,p) level.

Method

The molecular structure of the title compound in the ground state is computed by performing both the density functional theory (DFT) and Hartree-Fock (HF) (Becke, 1993; Lee, 1998) at 6-311G+(d,p) level. Density functionals for all studies reported in this paper have been in the following form

$$E_{XC} = (1-a_0)E_X^{LSDA} + a_0 E_X^{HF} + a_X \Delta E_X^{B88} + a_C E_C^{LYP} + (1-a_C)E_C^{VWN}$$

where the energy terms are the Slater exchange, the Hartree-Fock exchange, Becke's exchange functional correction, the gradient corrected correlation functional of Lee, Yang and Parr, and the local correlation functional of Vosko, Wilk and Nusair (Vosko et al., 1980). The theoretical geometric structure of the title compound is given in Figure 1. Molecular geometry is restricted and the optimized geometrical parameters of the title compound in this study are carried out by using Gaussian 09W program package (Frisch et al., 2009) and the visualization parts were done with GaussView program (Dennington et al., 2009) on personal computer employing 6-311G+(d,p) basis set. Additionally, harmonic vibrational frequencies for the title compound are calculated with these selected methods and then scaled by 0.9516 and 0.9905, respectively (Avcı and Atalay, 2008) and these results were compared with the experimental data (Nadeem and Ashraf, 2012).

Experimantal Data

3-(2-Pyridyl)-4-amino-1,2,4-triazole-5-thione (1): IR (KBr, ν, cm^{-1}): 3430-3330 (NH$_2$), 1630 (Ar C=C), 1567 (C=N), 1238 (C=S). ^{1}H NMR (300 MHz, DMSO-d$_6$, δ, ppm): 13.8 (s, 1H, NH/SH), 8.60 (d, 1H, J=5.0 Hz, H-6),

8.03 (d, 1H, J=7.9 Hz, H-3), 7.81 (t, 1H, J=6.7 Hz, H-4), 7.37 (t, 1H, J=5.3 Hz, H-5), 5.54 (s, 2H, NH$_2$), (Nadeem and Ashraf, 2012).

3-(3-Pyridyl)-4-amino-1,2,4-triazole-3-thione (2): IR (KBr, ν, cm^{-1}): 3436-3334 (NH$_2$), 1627 (Ar C=C), 1570 (C=N), 1247(C=S). ^{1}H NMR (300 MHz, DMSO-d$_6$, δ, ppm): 12.6 (s, 1H, NH/SH), 9.13 (d, 1H, J=1.5 Hz, H-2), 8.68 (d, 1H, J=3.5 Hz, H-6), 8.36 (d, 1H, J=7.9 Hz, H-4), 7.56 (dd, 1H, J=7.9 Hz, J=4.9 Hz, H-5), 5.79 (s, 2H, NH2), (Nadeem and Ashraf, 2012).

3-(2-Pyridyl)-4-amino-1,2,4-triazole-5-thione (3): IR (KBr, ν, cm^{-1}): 3272 (NH$_2$), 1629 (Ar C=C), 1566 (C=N), 1218 (C=S). ^{1}H NMR (300 MHz, DMSO-d$_6$, δ, ppm): 13.7 (s, 1H, NH/SH), 8.82 (d, 2H, J=5.9 Hz, H-3, H-5), 7.83 (d, 2H, J=6.0 Hz, H-2, H-6), 5.53 (s, 2H, NH2), (Nadeem and Ashraf, 2012).

Results and Discussion

Analysis of vibrational modes

In spectroscopic field, the vibrational spectra of substituted benzene derivatives have been greatly investigated by various spectroscopic, since the single substitution can have a tendency to put greater changes in vibrational wavenumbers of benzene (Pir et al., 2013). In other words, molecular system of benzene is greatly affected by the nature of substituents. The number of potentially active fundamentals of non-linear molecule which have N atoms is equal to (3N-6) apart from three translational and three rotational degrees of freedom. The 3-(2/3/4-pyridyl)-4-amino-1,2,4-triazole-5-thiones contains 20 atoms and 54 normal vibration modes have C1 symmetry (Table 1). Experimentally (Nadeem and Ashraf, 2012), the investigated titled compound, as expected the IR spectra data, the NH$_2$ stretching vibration at the range of 3430-3330 cm^{-1} for compound 1, the range of 3436-3334 cm^{-1} for compound 2 and 3272 cm^{-1} for compound 3 respectively. The C=S peak at 1238, 1247 and 1218 cm^{-1} range was observed respectively. Theoretically and experimentally (Nadeem and Ashraf, 2012), the calculated vibrational frequencies for the 3-(2/3/4-pyridyl)-4-amino-1,2,4-triazole-5-thiones are summarized in Table 1. Finally, the experimental IR (Nadeem and Ashraf, 2012) and simulated spectra by using B3LYP/6-311G+(d,p) level of the titled compounds under investigation are given in Figure 2.

Table 1. The calculated scaled frequencies values of the titled compounds (1-3)

Vibration Types	Compound 1		Compound 2		Compound 3	
	Experim.	skalalı DFT	Experim.	skalalı DFT	Experim.	skalalı DFT
1		**17**		24		14
2		**67**		68		66
3		**130**		128		134
4		**163**		170		163
5		**183**		201		202
6		**227**		230		230
7		**265**		260		264
8		**302**		292		298
9		**319**		313		322
10		**341**		344		336
11		**409**		405		383
12		**494**		485		512
13		**513**		516		512
14		**549**		549		555
15		**616**		603		603
16		**626**		637		671
17		**671**		670		677
18		**701**		714		708
19		**717**		717		711
20		**742**		721		729
21		**754**		741		756
22		**802**		827		850
23		**921**		946		900

|							
24			**957**		956		947
25			**975**		985		994
26			**1000**		1010		1002
27			**1008**		1019		1007
28			**1058**		1033		1029
29			**1075**		1057		1086
30			**1104**		1096		1096
31			**1112**		1116		1102
32			**1146**		1143		1129
33			**1179**		1214		1221
34	C=S	1238	**1236**	1247	1222	1218	1235
35			**1280**		1265		1259
36			**1304**		1274		1268
37			**1322**		1330		1332
38			**1347**		1352		1343
39			**1377**		1358		1356
40			**1446**		1414		1420
41			**1458**		1463		1446
42			**1490**		1478		1478
43			**1508**		1494		1511
44	C=N	1567	**1567**	1570	1560	1566	1548
45	Ar-C=C	1630	**1623**	1627	1602	1629	1594
46	Ar-C=C	1630	**1627**	1627	1617	1629	1621
47			**1720**		1694		1693
48			**3144**		3124		3121
49			**3168**		3149		3126
50			**3187**		3158		3181
51	NH_2	3330	**3225**		3198	3272	3204
52	NH_2	3330	**3390**	3334	3413	3272	3415
53	NH_2	3430	**3460**	3436	3474	3272	3477
54	NH_2	3430	**3632**	3436	3631	3272	3629
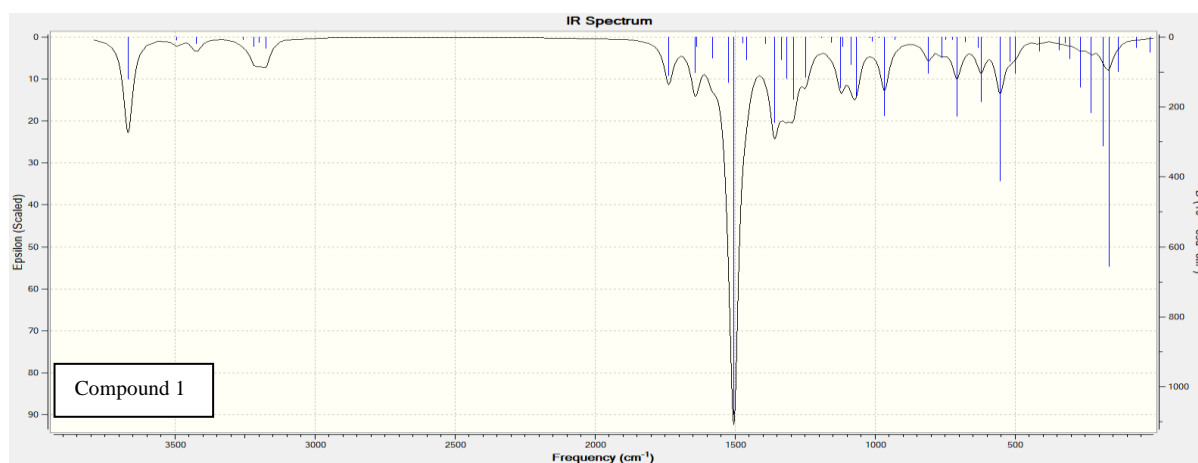
Figure 2. IR spectra simulated with DFT/B3LYP/6-311G+(d,p) level of the titled compounds (1-3)

NMR Spectral Analysis

The chemical shift analysis allows us to identify relative ionic species and to calculate reliable magnetic properties in nuclear magnetic resonance spectroscopy which provide the accurate predictions of molecular geometries, (Wade, 2006; Rani, et al., 2010; Subramanian et al., 2010). The optimized molecular geometry of the 3-(2/3/4-pyridyl)-4-amino-1,2,4-triazole-5-thiones were obtained by using B3LYP method with 6-311G+(d,p) basis level in DMSO solvent. The ^{1}H and ^{13}C NMR chemical shift values were calculated at the same level by using Gauge-Independent Atomic Orbital method (Table 2-4). Theoretically and experimentally values (Nadeem and Ashraf, 2012) were plotted according to δ exp=a. δ calc.+ b, Eq. a and b constants regression coefficients with a standard error values were found using the SigmaPlot program. The correlation graphics are given Figure 3. The (R^2) values (DFT) for ^{1}H NMR (DMSO) chemical shifts in different solvents have been found as 0.489, 0.585 and 0.448 for the 3-(2/3/4-pyridyl)-4-amino-1,2,4-triazole-5-thiones (1-3)respectively(Figure 3). In our study, the ^{1}H-NMR spectrum of the titled compounds were observed belong to H13 proton peak at 13.80, 12.60 and ppm, respectively because acidic show feature(Yüksek et al., 2005; Yüksek et al., 2006, Çiftçi et al., 2018).

Table 2. The calculated and experimental ^{1}H and ^{13}C NMR isotropic chemical shifts of the compound 1.

No	Experim.	DFT/6311+(d,p) DMSO	Diff./DMSO
1C		136,00	-136,00
2C		158,95	-158,95
3C		131,69	-131,69
4C		136,24	-136,24
5C		112,41	-112,41
6C		123,45	-123,45
7C		112,43	-112,43
13H	13,80	8,49	5,31
14H	8,03	8,46	-0,43
15H	7,37	7,08	0,29
16H	7,81	7,57	0,24
17H	8,60	8,87	-0,27
18H	5,54	3,72	1,82
19H	5,54	3,48	2,06

Table 3. The calculated and experimental ^{1}H and ^{13}C NMR isotropic chemical shifts of the compound 2

No	Experim.	DFT/6311+(d,p) DMSO	Diff./DMSO
1C		152,52	-152,52
2C		177,54	-177,54
3C		126,52	-126,52
4C		152,80	-152,80
5C		155,86	-155,86
6C		127,04	-127,04
7C		138,10	-138,10
13H	12,60	9,00	3,60
14H	8,68	9,50	-0,82
15H	8,36	8,85	-0,49
16H	7,56	7,54	0,02
17H	9,13	9,70	-0,57
18H	5,79	4,11	1,68
19H	5,79	3,84	1,95

Table 4. The calculated and experimental ^{1}H and ^{13}C NMR isotropic chemical shifts of the compound 3

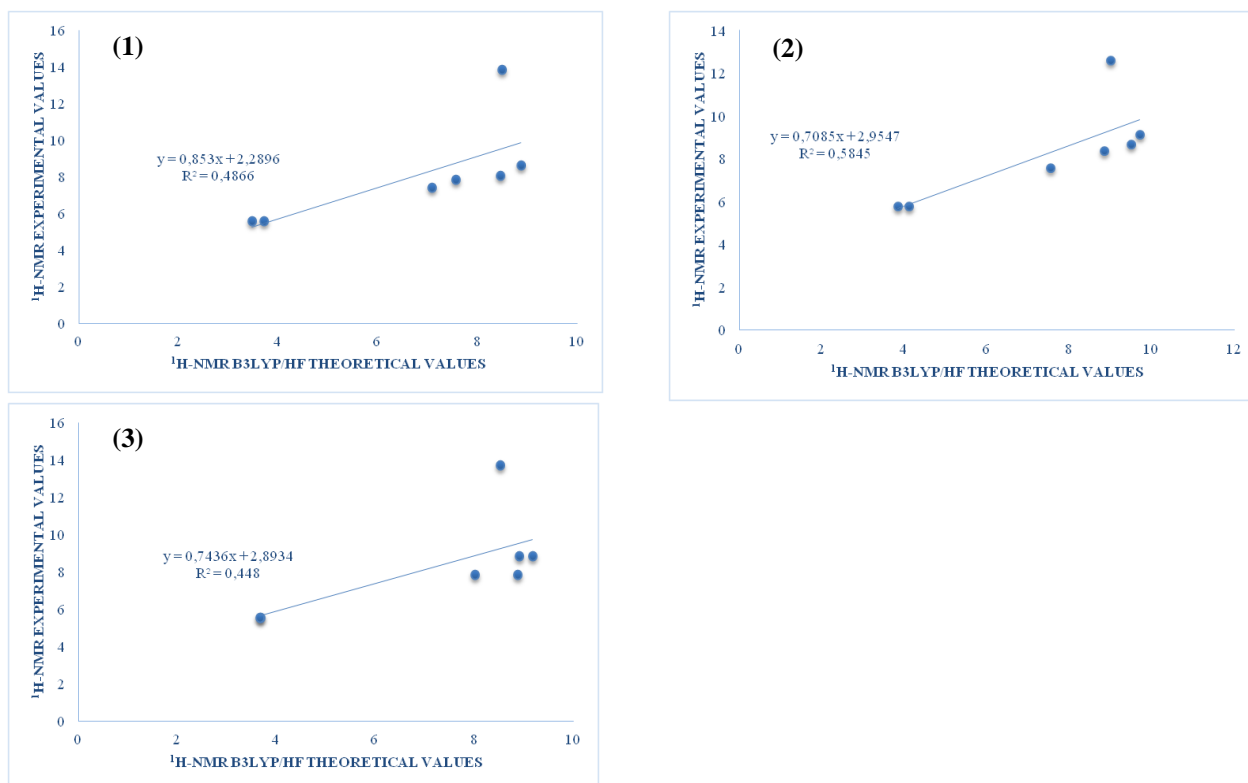| No	Experim.	DFT/6311+(d,p) DMSO	Diff./DMSO
1C		151,53	-151,53
2C		178,56	-178,56
3C		136,29	-136,29
4C		122,73	-122,73
5C		154,73	-154,73
6C		155,23	-155,23
7C		121,79	-121,79
13H	13,70	8,52	5,18
14H	7,83	8,01	-0,18
15H	7,83	8,88	-1,05
16H	8,82	8,91	-0,09
17H	8,82	9,17	-0,35
18H	5,53	3,68	1,85
19H	5,53	3,67	1,86

Figure 3. The correlation graphics for ^{1}H-NMR (DMSO) chemical shifts of the titled compounds (1-3)

Nonlinear Optic Properties

The materials having nonlinear activity possess a nonlinear response to the electric fields associated with the light of a laser beam. It is well known that the higher values of dipole moment, polarizability, and hyperpolarizability are important for more active NLO properties. In this study dipole moment, polarizability and first hyperpolarizability of the titled molecule were investigated by using B3LYP method at 6-311G+(d,p) basis set. The following formulas are used for calculating the magnitude of total static dipole moment (μ), polarizability (α) and first hyperpolarizability (β):

$$\mu = \left(\mu_x^2 + \mu_y^2 + \mu_z^2 \right)^{\frac{1}{2}}$$

$$\alpha = \frac{1}{3}\left(\alpha_{xx} + \alpha_{yy} + \alpha_{zz} \right)$$

$$\beta = \sqrt{\left(\beta_{xxx} + \beta_{yyy} + \beta_{zzz} \right)^2 + \left(\beta_{yyy} + \beta_{xxy} + \beta_{yzz} \right)^2 + \left(\beta_{zzz} + \beta_{xxz} + \beta_{yyz} \right)^2}$$

Where, the total static dipole moment (μ), linear polarizability (α) and the first hyperpolarizability (β) using the *x*, y, z components are defined as (Abraham et al., 2008; Karamanis et al., 2008). The linear polarizability (α) and the first hyperpolarizability (β) values of conformer ct of the titled molecules (1-3) are investigated as a function of the two torsional angle using B3LYP/6-311G+(d,p) level of theory (Govindarajan et al., 2012) (Table 5).

Tablo 5. Calculated polarization and hyperpolarizability values of the molecules 1-3 (B3LYP/6-311G+(d,p))

B3LYP	1	2	3
α_{xx}	31,446 a.u.	32.472 a.u.	31.776 a.u.
α_{yy}	17.426 a.u.	18.157 a.u.	18.802 a.u.
α_{zz}	7.419 a.u.	8.484 a.u.	8.340 a.u.
A	18.76×10^{-24} esu	19.71×10^{-24} esu	19.64×10^{-24} esu
$\Delta\alpha$	20.90×10^{-24} esu	20.90×10^{-24} esu	20.34×10^{-24} esu
β_x	9352.32 a.u.	-7046.56 a.u.	-8440.32 a.u.
β_y	2191.08 a.u.	-3524.06 a.u.	-2571.32 a.u.
β_z	113.45 a.u.	59.77 a.u.	-0.81 a.u.
β_{xxx}	8936.28 a.u.	-6049.28 a.u.	-7886.06 a.u.
β_{xxy}	1732.66 a.u.	-2301.53 a.u.	1949.72 a.u.
β_{xyy}	480.00 a.u.	-768.52 a.u.	-384.46 a.u.
β_{yyy}	183.67 a.u.	-745.51 a.u.	-172.86 a.u.
β_{xxz}	85.44 a.u.	46.20 a.u.	-0.80 a.u.
β_{xyz}	-44.36 a.u.	-64.36 a.u.	0.27 a.u.
β_{yyz}	-80.13 a.u.	-120.10 a.u.	0.50 a.u.
β_{xzz}	-63.96 a.u.	-228.76 a.u.	-169.80 a.u.
β_{yzz}	274.76 a.u.	-477.03 a.u.	-448.75 a.u.
β_{zzz}	108.14 a.u.	133.68 a.u.	-0.51 a.u.
B	9.61×10^{-30} esu	7.88×10^{-30} esu	8.82×10^{-30} esu

Conclusion

In this study, The vibrational frequencies, ^{1}H and ^{13}C NMR chemicals shifts of 3-(2/3/4-pyridyl)-4-amino-1,2,4-triazole-5-thiones obtained have been calculated by using DFT/B3LYP methods. By considering the results of experimental works it can be easily stated that the ^{1}H chemical shifts, and vibrational frequencies spectroscopic parameters obtained theoretically are in a very good agreement with the experimental data. Finally, The nonlinear optical properties of the investigated compounds were calculated theoretically. It was found that the molecule concerned had a higher hyperpolarizability value than urine (0.77×10^{-30} esu) (Zyss, 1994). It was found that molecules whose structures were examined theoretically had higher hyperpolarizability values than urea. The sequence is 1> 3> 2> urea.

References

Abraham, J. P., Sajan, D., Hubert, Joe I. H., & Jayakumar, V. S. (2008). Molecular structure, spectroscopic studies and first-order molecular hyperpolarizabilities of p-amino acetanilide, *Spectrochimica Acta Part A: Molecular and Biomolecular Spectroscopy*, 71 (2), 355-367.

Aggarwal, N., Kumar, R., Dureja, P. & Khurana, J. M. (2011). Synthesis, antimicrobial evaluation and QSAR analysis of novel nalidixic acid based 1,2,4-triazole derivatives, *European Journal of Medicinal Chemistry*, 46 (9), 4089-4099.

Avcı, D. & Atalay, Y. (2008). Theoretical analysis of vibrational spectra and scaling-factor of 2-aryl-1,3,4-oxadiazole derivatives, *International Journal of Quantum Chemistry*, 109, 328-341.

Bayrak, H., Demirbas, A., Demirbas, N., & Karaoglu, S. A. (2010). Cyclization of some carbothioamide derivatives containing antipyrine and triazole moietieses and investigation of their antimicrobial activities, *European Journal of Medicinal Chemistry*, 45 (11), 4726-4732.

Becke A. D. (1993). Density functional thermochemistry. III. The role of exact Exchange, *The Journal of Chemical Physics*, 98, 5648-5652.

Beytur, M., Turhan Irak, Z., Manap, S., and Yüksek, H. (2019). Synthesis, Characterization and Theoretical Determination of Corrosion Inhibitor Activities of Some New 4,5-Dihydro-1H-1,2,4-Triazol-5-one Derivatives, *Heliyon*, 5 (6), e01809, 1-8.

Çiftçi, E., Beytur, M., Calapoğlu, M., Gürsoy Kol, Ö., Alkan, M., Toğay, V. A., Manap, S., & Yüksek, H. (2018). Synthesis, Characterization, Antioxidant and Antimicrobial Activities and DNA Damage of Some Novel 2-[3-alkyl (aryl)-4,5-dihydro-1H-1,2,4-triazol-5-one-4-yl]-phenoxyacetic acids in Human Lymphocytes, *Research Journal of Pharmaceutical, Biological and Chemical Sciences*, 9 (5), 1760-1771.

Crofton KM. 1996. A Structure-Activity Relationship for the Neurotoxicity of Triazole Fungicides. Toxicology Letters (Shannon). 84 (3), 155-159.

Dennington, R., Keith, T., & Millam, J. (2009). GaussView, Version 5, Semichem Inc., Shawnee Mission KS.

Frisch, A., Nielson, A.B., & Holder, A.J. (2003).Gaussvıew User Manual, Gaussian, Inc., Wallingford, CT,

Frisch, M. J., Trucks, G., Schlegel, H. B., Scuseria, G. E., Robb, M. A., Cheeseman, J. R., Scalmani, G., Barone, V., Mennucci, B., Petersson, G. A., Nakatsuji, H., Caricato, M., Li, X., Hratchian, H. P., Izmaylov, A. F., Bloino, J., Zheng, G., Sonnenberg, J. L., Hada, M., Ehara, M., Toyota, K., Fukuda, R., Hasegawa, J., Ishida, M., Nakajima, T., Honda, Y., Kitao, O., Nakai, H., Vreven, T., Montgomery, J. A., Jr. Vreven, T., Peralta, J. E., Ogliaro, F., Bearpark, M., Heyd, J. J., Brothers, E., Kudin, N., Staroverov, V. N., Kobayashi, R., Normand, J., Raghavachari, K., Rendell, A., Burant, J. C., Iyengar, S. S., Tomasi, J., Cossi, M., Rega, N., Millam, J. M., Klene, M., Knox, J. E., Cross, J. B., Bakken, V., Adamo, C., Jaramillo, J., Gomperts, R., Stratmann, R. E., Yazyev, O., Austin, A. J., Cammi, R., Pomelli, C., Ochterski, J. W., Martin, L. R., Morokuma, K., Zakrzewski, V. G., Voth, G. A., Salvador, P., Dannenberg, J. J., Dapprich, S., Daniels, A. D., Farkas, O., Foresman, J. B., Ortiz, J. V., Cioslowski, J. & Fox, D. J. (2009). Gaussian Inc., Wallingford, CT.

Govindarajan, M., Periandy, S., & Carthigayen, K. (2012). FT-IR and FT-Raman spectra, thermo dynamical behavior, HOMO and LUMO, UV, NLO properties, computed frequency estimation analysis and electronic structure calculations on α-bromotoluene. *Spectrochimica Acta Part A: Molecular and Biomolecular Spectroscopy*, 97, 411-422.

Gürsoy Kol, Ö., and Yüksek, H. (2010). Synthesis and invitro antioxidant evaluation of some novel 4,5-dihydro-1H-1,2,4-triazol-5-one derivatives, *E-Journal of Chemistry*, 7 (1), 123-136.

İkizler, A. A. & Yüksek, H. (1994). Reaction of 4-amino-4,5-dihydro-1H-1,2,4-triazol-5-ones with 2,5-dimetoxytetrahydrofuran, *Collection of Czechoslovak Chemical Communications*, 59 (3), 731-735.

Jamróz, M. H. (2004). Vibrational Energy Distribution Analysis: VEDA 4 program, Warsaw.

Karamanis, P, Pouchan, C., & Maroulis, G., (2008). Structure, stability, dipole polarizability and differential polarizability in small gallium arsenide clusters from all-electron ab initio and density-functional-theory calculations, *Physical Review A*, 77, 013201-013208.

Küçükgüzel, Ş. G., & Çıkla Süzgün P. (2015). Recent advances bioactive 1,2,4-triazole-3-thiones, *European Journal of Medicinal Chemistry*, 97, 830-870.

Lee, S. Y. (1998). Molecular Structure and Vibrational Spectra of Biphenyl in the Ground and the lowest Triplet States. Density Functional Theory Study, *Bulletin of the Korean Chemical Society*, 19 (1), 93-98.

Nadeem, H. & Ashraf, Z. (2012). Regiospecific synthesis of some novel N-nucleosides of 4-amino-5-substituted-1,2,4-triazole-3-thiones and their in-vitro antimicrobial activity, *European Journal of Chemistry*, 3 (4), 485-492.

Pir, H., Günay, N., Tamer, Ö., Avcı, D. & Atalay, Y. (2013). Theoretical investigation of 5-(2-Acetoxyethyl)-6-methylpyrimidin-2, 4-dione: Conformational study, NBO and NLO analysis, molecular structure and NMR spectra, *Spectrochimica Acta Part A: Molecular and Biomolecular Spectroscopy*, 112, 331-342.

Rani, A. U., Sundaraganesan, N., Kurt, M., Çınar, M., & Karabacak, M. (2010). FT-IR, FT-Raman, NMR spectra and DFT calculations on 4-chloro-N-methylaniline, *Spectrochimica Acta Part A: Molecular and Biomolecular Spectroscopy*, 75, 1523-1529.

Sancak, K., Unver, Y., Kazak, C., Dugdu, E., and Arslan, B. (2010). Synthesis and characterizations of some new 2,4-dihydro-[1,2,4]-triazol-3-one derivatives and X-ray crystal structures of 4-(3-phenylallylideneamino)-5-thiophen-2-yl-methyl-2,4-dihydro-[1,2,4]triazol-3-one, *Turkish Journal of Chemistry*, 34 (5), 771-780.

Subramanian, N., Sundaraganesan, N., & Jayabharathi, J. (2010). Molecular structure, spectroscopic (FT-IR, FT-Raman, NMR, UV) studies and first-order molecular hyperpolarizabilities of 1,2-bis(3-methoxy-4-hydroxybenzylidene)hydrazine by density functional method, *Spectrochimica Acta Part A: Molecular and Biomolecular Spectroscopy*, 76, 259-269.

Turhan Irak, Z., & Beytur, M. (2019). 4-Benzilidenamino-4,5-dihidro-1H-1,2,4-triazol-5-on Türevlerinin Antioksidan Aktivitelerinin Teorik Olarak İncelenmesi, *Iğdır University Journal of the Institute of Science and Technology*, 9 (1), 512-521.

Yüksek, H., Üçüncü, O., Alkan, M., Ocak, Z., Bahçeci, Ş., & Özdemir, M. (2005). Synthesis and Determination of pKa Values of Some New 3,4-Disubstituted-4,5-Dihydro-1H-1,2,4-triazol-5-one Derivatives in Non-aqueous Solvents, *Molecules* 10, 961-970.

Yüksek, H., Küçük, M., Alkan, M., Bahçeci, S., Kolaylı, S., Ocak, Z., Ocak, U., Şahinbas, E., & Ocak, M. (2006). Synthesis and antioxidant activities of some new 4-(4-hydroxybenzylidenamino)-4,5-dihydro-1H-1,2,4-triazol-5-one derivatives with their acidic properties, *Asian Journal of Chemistry*, 18 (1), 539-550.

Tereci, H., Askeroğlu, İ., Akdemir, N., Uçar, İ., & Büyükgüngör, O. (2012). Combined experimental and theoretical approaches to the molecular structure of 4-(1-formylnaphthalen-2-yloxy)phthalonitrile, *Spectrochimica Acta Part A: Molecular and Biomolecular Spectroscopy*, 96, 569-577.

Turhan Irak, Z. & Gümüş, S. (2017). Heterotricyclic compounds via click reaction: A computational study. *Noble International Journal of Scientific Research*, 1(7), 80-89.

Turhan Irak, Z. & Beytur, M. (2019). 4-Benzilidenamino-4,5-dihidro-1H-1,2,4-triazol-5-on Türevlerinin Antioksidan Aktivitelerinin Teorik Olarak İncelenmesi, *Iğdır University Journal of the Institute of Science and Technology*, 9 (1), 512-521.

Vosko, S. H., Wilk, L. & Nusair, M. (1980). Accurate spin-dependent electron liquid correlation energies for local spin density calculations: a critical analysis, *Canadian Journal of Physics*. 58, 1200.

Wade, Jr. L.G. (2006). Organic Chemistry, 6nd ed.; Pearson Prentice Hall: New Jersey.

Wolinski, K., Hinton, J. F. & Pulay, P. (1990). Efficient implementation of the gauge-independent atomic orbital method for NMR chemical shift calculations. *Journal of the American Chemical Society*, 112, 8251-8260.

Zhang, L.Y., Wang, B.L., Zhan, Y.Z., Zhang, Y., Zhang, X. & Li, Z. M. (2016). Synthesis and biological activities of some fluorine- and piperazine-containing 1,2,4-triazole thione derivatives. *Chinese Chemical Letters*, 27, 163-167.

Author Information

Zeynep Turhan Irak
Igdir University
Department of Environmental Engineering, Igdir, Turkey
Contact E-mail: *zeynepsilanturhan@hotmail.com*

Murat Beytur
Kafkas University
Faculty of Science and Letters, Department of Chemistry, Kars, Turkey

Computational Studies on Quinoline Based Metal Chemosensors

Selcuk GUMUS
Van Yuzuncu Yil University

Aysegul GUMUS
Van Yuzuncu Yil University

Abstract: The design and synthesis of sensors that selectively sense metal ions have a very important place in biological and environmental processes. Fluorescence sensor is one of the most important chemical sensors and is a powerful tool for imaging target molecules and ions in living organisms. Because it has high sensitivity and simultaneous imaging. Although there are many metal sensors available commercially, chemists are still designing sensors that are simpler, easier to synthesize, higher in sensitivity, selectivity and reliability to meet their needs. Hydroxy quinolines are used as fluorophore in metal chemosensors. 8-Hydroxyquinoline (8-HQ), an important fluorophore, exhibits poor fluorescence due to intramolecular proton transfer from oxygen to nitrogen (ESIPT-excited state intramolecular proton transfer). But they show bright fluorescence and photostability after they are attached to metal ions. Thus, the 8-HQ framework is commonly used to construct fluorescence sensors for many important metal ions. However, since the 8-HQ molecule has poor binding selectivity to many metal ions, chemosensors are designed by combining the appropriate binding units (ionophores). Computational calculations of the designed chemosensors have beenperfomed to determine the 3D geometries of the structures, to calculate the spectroscopic properties and to elucidate the mechanism of metal bonding. Calculations will be performed using the Density Functional Theory, the B3LYP hybrid function and the basic set of 6-311++(d,p).

Keywords: Chemosensors, Quinoline, Computational calculations, Metal chemosensors

Introduction

Detecting cations is of great interest to many scientists, including chemists, biologists, clinical biochemists and environmentalists. Sodium, potassium, magnesium, calcium are involved in *biological processes* such as transmission of nerve impulses, muscle contraction, regulation of cell activity, etc. Moreover, various metal ions belong to metalloenzymes. In *medicine*, it is important to control the serum levels of lithium in patients under treatment for manic depression, and potassium in the case of high blood pressure. Regarding aluminium, its toxicity has long been recognized and there is a controversy about its possible implication in Alzheimer's disease. In *chemical oceanography*, it has been demonstrated that some nutrients required for the survival of microorganisms in sea water contain zinc, iron, manganese as enzyme cofactors. Finally, it is well known that mercury, lead and cadmium are toxic for organisms, and early detection in the environment is desirable.

Among the numerous analytical methods that are available for the detection of cations, flame photometry, atomic absorption spectrometry, ion sensitive electrodes, electron microprobe analysis, neutron activation analysis, etc., are expensive, often require samples of large size and do not allow continuous monitoring. In contrast, the methods based on fluorescent sensors [1–6] offer distinct advantages in terms of sensitivity, selectivity, response time, local observation (e.g. by fluorescence imaging spectroscopy). Moreover, remote sensing is possible by using optical fibres with a molecular sensor immobilized at the tip [7]. Therefore, considerable efforts are being made to develop selective fluorescent sensors for cation detection.

Such fluorescent sensors consists of a fluorophore linked to an ionophore and is thus called a fluoroionophore (Fig. 1). In the design of such sensors [8], attention should be paid to both recognition and signaling moieties. The *signaling moiety* acts as a signal transducer, i.e. it converts the information (recognition event) into an

optical signal expressed as the changes in the photophysical characteristics of the fluorophore. These changes are due to the perturbation (by the bound cation) of photoinduced processes such as electron transfer, charge transfer, energy transfer, excimer or exciplex formation or disappearance, etc. These aspects are relevant to the field of *photophysics*.

As regards the *recognition moiety*, it is responsible for selectivity and efficiency of binding which depend on the ligand topology, on the characteristics of the cation (ionic radius, charge, coordination number, hardness, etc.), and on the nature on the solvent (and pH, ionic strength in the case of aqueous solutions). These aspects are relevant to the field of *supramolecular chemistry*. It should be noted that the signaling moiety can be linked to the ionophore moiety via a spacer or not. Even in the latter case, some atoms of the fluorophore may participate in the complexation. Therefore, the selectivity of binding often results from the whole structure involving both signaling and recognition moieties.

It should be emphasized that, under the conditions of detection, the dissociation constant of the complex should match the expected range of cation concentration which is very different according to the field. For instance, the concentration of calcium ion inside a living cell is in the micromolar range, whereas in blood plasma and urine it is in the millimolar range. Therefore, the well-known calcium sensors designed by Tsien (Indo-1, Fura-2, etc.) [9] are suitable for cellular biology but not for clinical diagnosis.

Method

The three-dimensional ground state (S_0) geometry of the compound was geometry optimized using Density Functional Theory (DFT) [10] by using the Gaussian 09W [11] package program and the hybrid functional B3LYP. The B3LYP is composed of Becke's three parameter exchange functional (B3) [12] and the nonlocal correlation functional by Lee, Yang, and Parr (LYP) [13]. The basis set used for all atoms was 6-31++G(d,p) in both DFT and time-dependent density functional theory (TD-DFT) method. We have applied default G09 grid for computations.

For the nonel compound, vibrational analyses were carried out using the same basis set employed in the corresponding geometry optimizations. The frequency analysis of none of the compounds yielded any imaginary frequencies, indicating that the structure of each molecule corresponds to at least a local minimum on the potential energy surface. The normal mode analysis was performed for 3N-6 vibrational degrees of freedom, N being the number of atoms in the molecule.

The low-lying triplet (T) and singlet excited states (S) of the compounds were relaxed to obtain their minimum energy geometries using the TD-DFT as implemented in G09 package program [14]. The vertical excitation energies and oscillator strengths were obtained for the lowest triplet and singlet transitions at the optimized ground state equilibrium geometries by using TD-DFT at the same hybrid functional and basis set [14]. Optimized ground state structures were utilized to obtain the electronic absorption spectra, including maximum absorption wavelengths, oscillator strengths, and main configuration assignment by using TD-DFT.

Results and Discussion

In the present study a quinoline based metal chemosensor has been considered for its spectroscopic properties at B3LYP/6-31++G(d,p) level of theory.

First of all, geometry optimization of the quinoline based antracene derivative has been performed to obtain the ground state structure. Front and side view of the structure after geometry optimization can be seen in Figure 1. As can be observed the triazole moiety is directed out of the coordination center which was unfortunate for us since the triazole nitrogen units had been thought to be a very well coordination part of this potential chemosensor. Although the geometry optimized structure has been obtained out of what we were expecting, the coordination computatons for metal till went on because there are more complexation sites (quinoline nitrogen and connecting oxygen) in the structure.
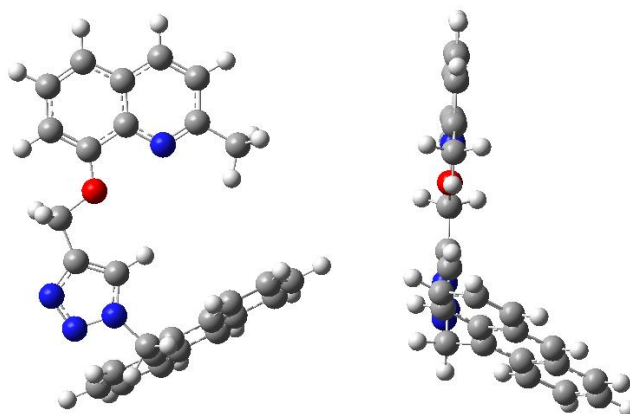
Figure 1. Chemical structure of triazophenone

Geometry optimized structures of the Zn^{2+} and Hg^{2+} coordinated structures are shown in Figure 2. As we performed the ground state search the triazole moiety rotated towards the coordination center which is more obvious in Hg coordination. Moreover anthracene unit came closer to the metal to make a π-π-stacking interaction.
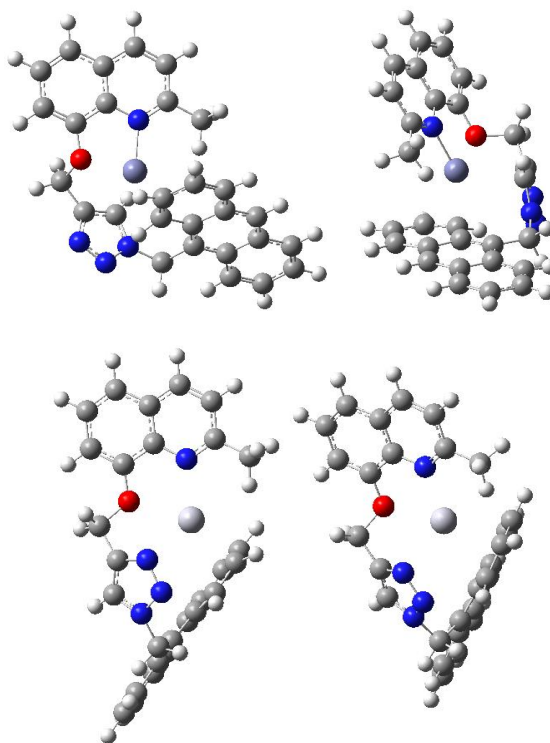

Figure 2. Geometry optimized structure of Zn and Hg complexes

The UV-VIS spectra of the compounds have been obtained by the same method of computation. The non-metal quinoline compound has got two major peaks at around 200-300 nm and a non-intense peak at 390 nm. Zn and Hg complexes possess a new band at around 350 nm and 400 nm, respectively. Moreover the non-intense band of the parent compound shifted to blue in both cases.
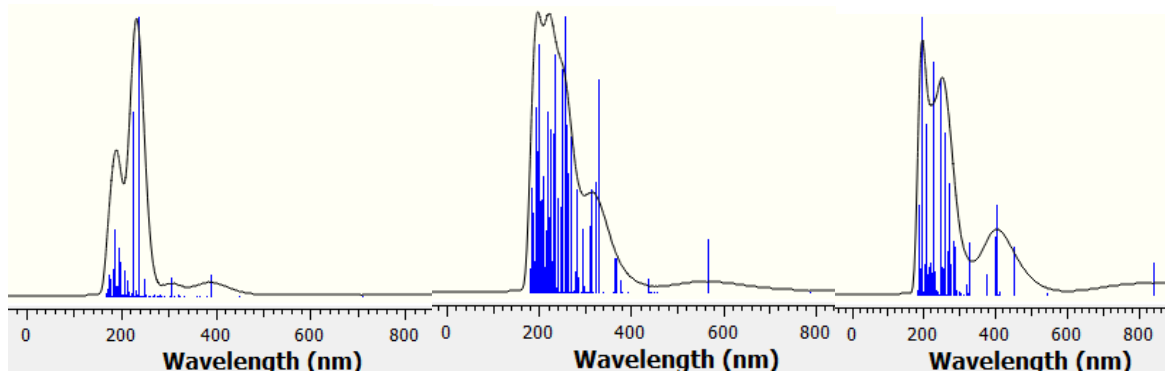
Figure 3. UV-VIS spectra of the present compounds

Conclusion

In the present study, we performed a computational study by the application of Density Functional Theory at B3LYP/6-31++G(d,p) level on a quinoline based anthracene derivative.

The triazole in the parent structure changed conformation towards coordination in the metal complex. The charge on the metal cation decreased from +2 to 0.845 and 0.873 on Zn and Hg, respectively, which proves the coordination.

Moreover, the changes in the UV-VIS spectra clearly indicated the coordination and complex formation.

Acknowledgements or Notes

References

Krämer, R. (1998). Fluorescent Chemosensors for Cu^{2+} Ions: Fast, Selective, and Highly Sensitive. *Angew. Chem. Int. Ed*. 37, 772–773.

Uauy, R., Olivares, M., Gonzalez, M. (1998). Essentiality of copper in humans. *Am. J. Clin. Nutr.* 67, 952–959.

de Silva, A. P., Gunaratne, H. Q. N., Gunnlaugsson, T., Huxley, A. J. M., McCoy, C. P., Rademacher, J. T., Rice, T. E.(1997). Signaling Recognition Events with Fluorescent Sensors and Switches. *Chem. Rev*. 97, 1515–1566.

Czarnik, A.W. (1992). *Fluorescent Chemosensors for Ion and Molecule Recognition*, first ed., A.C.S, Washington.

Chen, Y., Wan, L., Yu, X., Li, W., Bian, Y. and Jiang, J. (2011). Rational Design and Synthesis for Versatile FRET Ratiometric Sensor for Hg^{2+} and Fe^{2+}: A Flexible 8-hydroxyquinoline Benzoate Linked Bodipy-Porphyrin Dyad. *Org. Lett.*, 13, 5774-5777.

Jotterand, N., Pearce, D. A. and Imperiali, B. (2001). Asymmetric Synthesis of a New 8-Hydroxyquinoline-Derived α-Amino Acid and Its Incorporation in a Peptidylsensor for Divalent Zinc. *J. Org. Chem*., 66, 3224-3228.

Zhao, Y., Lin, Z., Liao, H., Duan, C. and Meng, Q. (2006). A highly selective fluorescent chemosensor for Al3+ derivated from 8-hydroxyquinoline. *Inorg. Chem. Commun.,* 9, 966-968.

Li, Z., Xi, P., Huang, L., Xie, G., Shi, Y., Liu, H., Xu, M., Chen, F. and Zeng, Z. (2011). A highly selective fluorescent chemosensor for Cd(II) based on 8-hydroxyquinoline platform. *Inorg. Chem. Commun.,* 2011, 14, 1241-1244.

Tian, H., Li, B., Wang, H., Li, Y., Wang, J., Zhao, S., Zhu, J., Wang, Q., Liu, W., Yaoa, X. and Tang, Y. (2011). A nanocontainer that releases a fluorescence sensor for cadmium ions in water and its biological applications. *J. Mater. Chem*., 21, 10298-10304.

W. Kohn, L.J. Sham, Self-consistent equations including exchange and correlation effects. *Phys. Rev.* 140, 1133-1138 (1965).

M. J. Frisch, G. W. Trucks, H. B. Schlegel, G. E. Scuseria, M. A. Robb, J. R. Cheeseman, G. Scalmani, V. Barone, B. Mennucci, G. A. Petersson, H. Nakatsuji, M. Caricato, X. Li, H. P. Hratchian, A. F. Izmaylov, J. Bloino, G. Zheng, J. L. Sonnenberg, M. Hada, M. Ehara, K. Toyota, R. Fukuda, J. Hasegawa, M. Ishida, T. Nakajima, Y. Honda, O. Kitao, H. Nakai, T. Vreven, J. A. Montgomery, Jr., J. E. Peralta, F. Ogliaro, M. Bearpark, J. J. Heyd, E. Brothers, K. N. Kudin, V. N. Staroverov, T. Keith, R. Kobayashi, J. Normand, K. Raghavachari, A. Rendell, J. C. Burant, S. S. Iyengar, J. Tomasi, M. Cossi, N. Rega, J. M. Millam, M. Klene, J. E. Knox, J. B. Cross, V. Bakken, C. Adamo, J. Jaramillo, R. Gomperts, R. E. Stratmann, O. Yazyev, A. J. Austin, R. Cammi, C. Pomelli, J. W. Ochterski, R. L. Martin, K. Morokuma, V. G. Zakrzewski, G. A. Voth, P. Salvador, J. J. Dannenberg, S. Dapprich, A. D. Daniels, O. Farkas, J. B. Foresman, J. V. Ortiz, J. Cioslowski, and D. J. Fox, *Gaussian 09, Revision D.01*, Gaussian, Inc., Wallingford CT, 2013.

A.D. Becke, Density-functional exchange-energy approximationwith correct asymptotic behavior. *Phys. Rev. A* 38, 3098–3100 (1988).

C. Lee, W. Yang, R.G. Parr, Development of the Colle–Salvetti correlation energy formula into a functional of the electron density. *Phys. Rev. B* 37, 785–789 (1988).

M.E. Casida, C. Jamorski, K.C. Casida, D.R. Salahub, Molecular excitation energies to high-lying bound states from timedependent density-functional response theory: characterization and correction of the time-dependent local density approximation ionization threshold. *J. Chem. Phys.* 108, 4439–4449 (1998).

Author Information

Selcuk Gumus
Van Yuzuncu Yil University
Department of Chemistry
Contact E-mail: *gumuss@gmail.com*

Aysegul Gumus
Van Yuzuncu Yil University
Department of Chemistry

IConTES 2019: International Conference on Technology, Engineering and Science

Spectrophotometric Determination of Sulfacetamide

Zena TALAL
Mosul University

Wadala A. BASHIR
Mosul University

Abstract: Sulfacetamide is a sulfonamide antibiotic that is used as a cream to treat skin infections and as eye drops infections. On the skin it is used to treat acne and seborrheic dermatitis. In Sulfacetamide Sodium is the sodium salt of sulfacetamide, a synthetic sulfanyl acetamide derivative with bacteriostatic activity. Sulfacetamide [N (4 – aminophenyl) sulphonyl] acetamide is a N – subistituted derivatives of sulfanilamide which is widely used in the treatment of urinary tract infection and burn therapy. A spectrophotometric method for the determination of trace amounts of sulfacetamide, based on coupling of diazotized sulfacetamide with m-aminophenol to form an intense orange coloured, water soluble monoazo dye which exhibits maximum absorption at 436 nm. Adherence to Beer`s law is observed over the concentration range (0.4 – 8) ppm with a molar absorptivity of (1.68×10^4) mol^{-1}. Cm^{-1}, Sandell sensitivity index of (1.4×10^4) mg.cm^{-2}, precision of (+. 0.28 - +. 0.8) and accuracy of (0 – 0.3) indicating that the method is accurate and precise. the proposed method has been successfully applied to the assay of sulfacetamide eye drops.

Keywords: Sulfacetamide, N (4 – aminophenyl) sulphonyl] acetamide, Diazotized, Eye drops

Introduction

Sulfacetamide [1] is a white crystalline powder that dissolves in water and alcohol and its water solution is evenly acidic. Sulfacetamide has a half age in plasma of about 7 hours [2]. Sulfacetamide is an early discovered sulfa drug [3], but at present, sulfacetamide is an important bacterial antibiotic used in ophthalmic solutions and ophthalmic. Sulfacetamide is a well_water soluble sulfonamide and has several scientific names, including : N_sulfanilyl acetamide or N_acetyl sulfanilamide or N-[(4- aminophenyl) sulfonyl] _acetamide] [2]. Including the following composition [4].

Metholodgy

Apparatus

Spectral and absorbance measurements are carried out using Shimadzu UV-160 UVVisible computerized double-beam spectrophotometer. In all measurements, 1-cm matched cells are used. The pH measurements are carried out using HANA pH meter.

Chemicals

All chemicals used are of analytical reagent grade

Sulfacetamide sodium solution (100 ppm): 0. 011 g of Sulfacetamide was dissolved in distilled water then the volume was completed to 100 ml with distilled water in a dry and clean volumetric flask. Then, the solution was transferred to a dark bottle to be stable for at least 10 days.

Sulphuric acid 1N: 98% concentration sulphuric acid solution has been used for preparing 1N of sulphuric acid solution in 100 ml volumetric flask.

Sodium nitrite solution (1%): Prepare this solution by dissolving (1) g of sodium nitrite and complete the volume to (100) in a volumetric bottle with distilled water.

Sulfamic acid solution (3%): Prepare this solution by dissolving (3) g of sulfamic acid with distilled water and complete the volume to (100) ml in a volumetric bottle with distilled water. This solution is stored in a dark volume volumetric vial and is stable for at least 20 days.

Meta-amin-phenol solution (0.5%): Prepare this solution by dissolving (0.5) grams of meta-amino-phenol in distilled water and complete the volume to (100) ml in a volumetric bottle with distilled water. This solution is stored in a dark volume volumetric vial and is stable for 10 days after which the solution becomes yellowish brown.

Sodium acetate solution (1N): Prepare a sodium acetate solution at a concentration of (1N) by dissolving (8.2) grams of the substance with distilled water and complete the volume to (100) ml in a volumetric bottle with distilled water. This solution is stored in a dark plastic bottle

Drug solutions:
First: Samacetamide Drops (SDI): The solution is prepared by taking (0.1) ml of the drop after shaking and diluted to (100) ml using distilled water.
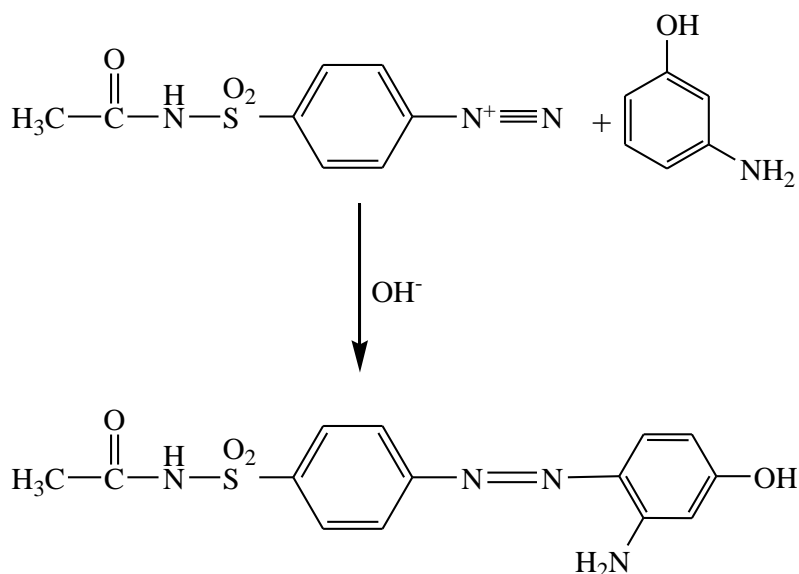 Second: Samacetamide Drops (Shifa Drug Factory - Iraq): The solution is prepared by taking (0.1) ml of the drop after shaking and diluted to (100) ml using distilled water.

Results and Discussion

(30) μg of sulfamethoxazole in a final volume (25) ml was used for subsequent experiments at wavelength (436) nm.

Principle of the Suggested Method

$$HNO_2 + H_2N\text{-}SO_3H \longrightarrow N_2 + H_2O + H_2SO_4$$
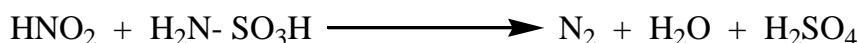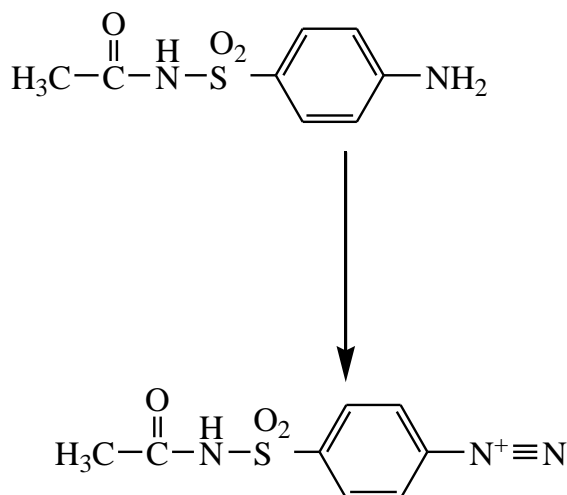
Study the optimal conditions for the reaction

The effect of different conditions on the optical properties of the dye produced by the reaction of sulfacetamide with an increase of nitrite in acidic medium was studied to be diazonium salt.

Effect of acid amount

The effect of different acids on the dye absorption intensity was studied (HCl, H_3PO_4, HCOOH, CH_3COOH, HNO_3, H_2SO_4). The results showed that the use of 3.5 ml of a solution of sulfuric acid at a concentration of 1 Ml gave the best results and was adopted in subsequent experiments.

Effect of nitrite quantity and time

The use of 0.7 ml of sodium nitrite solution at a concentration of 1% and the reaction time of 3 minutes gave the best results and was adopted in subsequent experiments. (Table 1).

Table 1. Effect of nitrite quantity and time

ml of NaNO$_2$ solution	Absorbance / min. standing time							
	0	**1**	**2**	**3**	**5**	**10**	**15**	**20**
0.1	0.092	0.113	0.086	0.113	0.098	0.102	0.113	0.062
0.3	0.097	0.108	0.109	0.096	0.070	0.076	0.074	0.074
0.5	0.098	0.105	0.105	0.113	0.096	0.104	0.110	0.100
0.7	0.267	0.239	0.211	0.211	0.203	0.201	0.200	0.212
1.0	0.164	0.140	0.128	0.118	0.120	0.122	0.124	0.122
1.5	0.145	0.134	0.177	0.186	0.203	0.190	0.218	0.270
2.0	0.190	0.075	0.263	0.297	0.113	0.221	0.175	0.252

Effect of meta-amino phenol intake

The results showed that using different volumes of the meta-amino-phenol reagent solution, 1.5 ml of the reagent at 0.5% concentration gave the highest value of r at 0.999041 and was therefore used in subsequent experiments.

Base effect

By studying several types of weak and strong bases such as (KOH, NaOH, NH4OH, Na_2CO_3, $NaHCO_3$, CH_3COONa, HCOONa) and at a concentration of 1 molar it was found that the use of a solution of 7 ml CH_3COONa gives the best results for this use in subsequent experiments.

Effect of surfactants

The purpose of adding surface tensile agents is to increase the sensitivity of the method and increase the speed [5]. In addition, colloidal systems are stable and non-toxic. (SDS), Cetyl pyridinium chloride (CPC) and Alkyl phenol ethoxylate (Triton X-100) and practical results showed that the addition of surface tensile agents does not improve the properties of the resulting dye.

Final absorption spectrum

When the meta-amino-phenol reagent is added to the solution containing sulfacetamide, which is obtained under experimentally optimal conditions, an orange colored pigment is formed and gives the highest absorption at the wavelength of 436 nm compared to the image solution, which gives weak absorption at the same wavelength. Figure 1 shows the absorption spectrum. The resulting dye vs. solution solution and the absorption spectrum of the solution solution versus distilled water and the wavelength of the highest absorption of 436 nm were used for subsequent experiments.
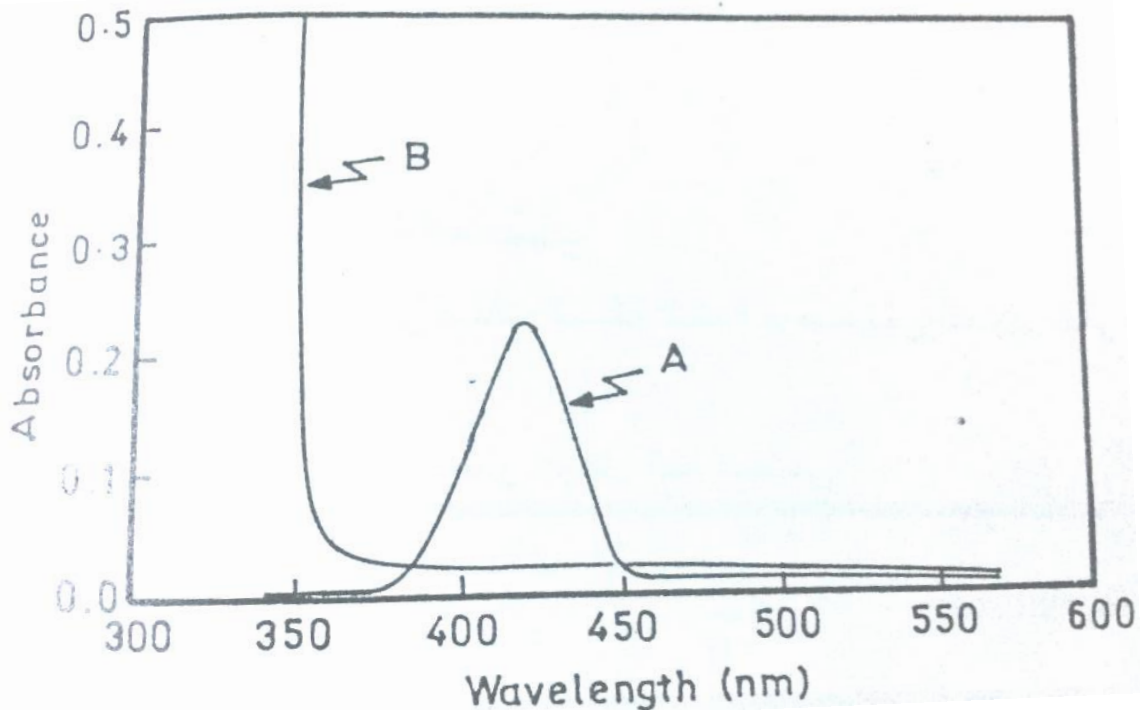

Fig.1: Final absorption spectrum of 30 µg /25 ml of sulfacetamide measured against (A): reagent blank, (B): reagent blank against distilled water

Standard working method and standard curve

To a series of volumetric bottles (25) ml add (5) ml distilled water to (0.1, 0.3, 0.5, 0.7, 1.0, 1.5, 2.0) ml solution (100) ppm sulfacetamide and then add (4) ml of sulphuric acid (1N)) And (0.7) ml solution (1%) sodium nitrite and leave the solution for (3) minutes to complete the reaction and then add (1.5) ml solution (3%) sulfamic acid and leave the solution for (2) minutes to complete the destruction of the increase Nitrite was then added (1.5) ml of the reagent solution (0.5%) m-aminopheol and then added (7) ml of the solution (1M) sodium acetate then the volume was completed to the extent of the mark with distilled water and then measured absorption immediately

after dilution at the wavelength (436) nm . Figure (2) represents the standard curve, which is in accordance with Bear's law, in the range of concentrations (10-200 µg / 25 ml). the value of molar absorptivity and sandell sensitivity are $1.68 \times 10^4 \ 1.mol^{-1}.cm^{-1}$, $1.4 \times 10^{-4} \ µg / cm^{-2}$.
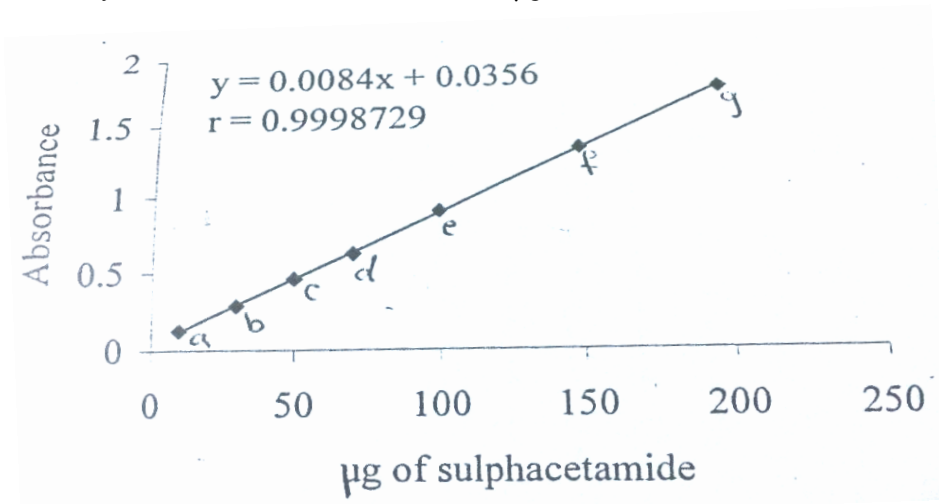

Fig.2. Standard curve for sulfacetamide assay

Accuracy Method

The accuracy of the method of estimating sulfacetamide has been determined by applying the method of work used to find the standard curve for three different concentrations (10, 30, 50, 100) micrograms of sulfacetamide (each of 5 readings) as shown in the following table:

Table 2. Compatibility and accuracy of the proposed method

µg of sulphacetamide	Er, %	R.S.D%
10	0	± 0.8
30	0.3	± 0.39
50	0.040	± 0.43
100	0.070	± 0.28

Nature of dye formed

The continuous change method (Job's method) was used to determine the reaction rate of sulfacetamide with the reagent. It was noted that the coupling ratio between sulfacetamide and meta-aminophenol reagent is 1: 1. Accordingly, the proposed wording would be as follows:
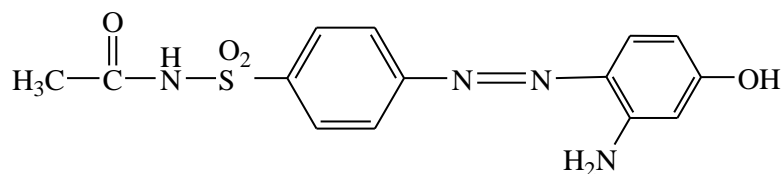
Application Method

For the purpose of checking the validity of the method was applied to different samples , the recovery of Samacetamide Drops (SDI) was (93%), while the recovery of Samacetamide Drops (Shifa Drug Factory - Iraq) was 97.

Comparison of method

Table 4 shows the comparison between the analytical variables of the present method with those of other method for sulfacetamide determination

Table 7. Comparison of method

Analytical parameters	Present method	Literature method[6]
Reagent	m-aminophenol	chromotropic acid
Medium	Basic	Basic
λ_{max} (nm)	436	511.5
Beer's law range ($\mu g \cdot ml^{-1}$)	10-200	0.5-20.0
Molar absorptivity ($l.mol^{-1}.cm^{-1}$)	1.68×10^4	3.2186×104
Color of the product	orange	orange
Application of the method	Pharmaceutical preparations	Pharmaceutical preparations

Conclusions

The method is based on the coupling of sulfacetamide with the meta-aminophenol reagent and the formation of a water-soluble colored dye. The proposed method does not require temperature control, use of organic solvents or solvent extraction and has been successfully applied in the determination of sulfacetamide in pharmaceutical preparations.

References

British Pharmacopeia on CD-Rom ;(2013), 7th Edn., System Simulation Ltd. The stationary office, London.

Wilson and Gisvold"text book of organic medicinal and pharmaceutical chemistry", 8th edn., J.B.Liippincott company, New York, (1982), 629-630.

Kucers A and Mck bennett N., "the use of antibiotics", 3rd edn. , Lowe and Brydone.(printers) ltd., london, (1979), 657-659.

Budavari S., O'Neil,J.M., and Smith A, "the merck index", 11th edn., Merk and co. İnc., New York, 1989, 669-670.

Zaki M.T., and El-Didamony A.M., Analyst, (1988), 113, 1277-1281.

Darweesh S. A. , Al-Haidari I. A. , Mohammed A.K. , Dikran S. B. , Spectrophotometric Determinations of Sulfacetamide Following Simple Diazotization and Coupling with Chromotropic Acid", Ibn Al-Haitham Jour. for Pure & Appl. Sci., 26 (3) 2013.

Author Information

Zena Talal
Dep. of Chemistry, College of Science,
Mosul University, Mosul, Iraq
Contact E-mail: safazena@yahoo.com

Wadala A. Bashir
Dep. of Chemistry, College of Science,
Mosul University, Mosul, Iraq